ADVANCED JOINING PROCESSES

Welding, Plastic Deformation, and Adhesion

ELSEVIER

Edited by

Lucas da Silva, Mohamad El-Zein, and Paulo Martins

ADVANCED JOINING PROCESSES

This page intentionally left blank

ADVANCED JOINING PROCESSES

WELDING, PLASTIC DEFORMATION, AND ADHESION

Edited by

Lucas da Silva

Departamento de Engenharia Mecânica, Faculdade de Engenharia (FEUP), Universidade do Porto, Porto, Portugal

Mohamad El-Zein

John Deere Moline Technology Innovation Center, Moline, IL, United States

Paulo Martins

IDMEC, Instituto Superior Tecnico, Universidade de Lisboa, Portugal

ELSEVIER

Elsevier
Radarweg 29, PO Box 211, 1000 AE Amsterdam, Netherlands
The Boulevard, Langford Lane, Kidlington, Oxford OX5 1GB, United Kingdom
50 Hampshire Street, 5th Floor, Cambridge, MA 02139, United States

Library of Congress Cataloging-in-Publication Data
A catalog record for this book is available from the Library of Congress

British Library Cataloguing-in-Publication Data
A catalogue record for this book is available from the British Library

ISBN: 978-0-12-820787-1

For information on all Elsevier publications visit our website at
https://www.elsevier.com/books-and-journals

Publisher: Matthew Deans
Acquisitions Editor: Edward Payne
Editorial Project Manager: Mariana L. Kuhl
Production Project Manager: Sojan P. Pazhayattil
Cover Designer: Victoria Pearson

Typeset by TNQ Technologies

Contents

6. Explosive welding

A. Loureiro, G.H.S.F.L. Carvalho, I. Galvão, R.M. Leal and R. Mendes

7. Ultrasonic welding

Jean Pierre Bergmann, Tobias Köhler and Pascal Pöthig

C

Adhesive bonding

8. Manufacture and testing

Ricardo J.C. Carbas, Catarina Borges, Eduardo A.S. Marques, Alireza Akhavan-Safar and Lucas F.M. da Silva

9. Simulation

Alireza Akhavan-Safar, Eduardo A.S. Marques, Ricardo J.C. Carbas and Lucas F.M. da Silva

10. Hybrid joining techniques

H. Fricke and T. Vallée

Contributors

Alireza Akhavan-Safar Instituto de Ciência e Inovação em Engenharia Mecânica e Engenharia Industrial (INEGI), Porto, Portugal

L.M. Alves IDMEC, Instituto Superior Tecnico, Universidade de Lisboa, Lisboa, Portugal

N. Bay Department of Mechanical Engineering, Technical University of Denmark, Lyngby, Denmark

Jean Pierre Bergmann Technische Universität Ilmenau, Ilmenau, Germany

Catarina Borges Instituto de Ciência e Inovação em Engenharia Mecânica e Engenharia Industrial (INEGI), Porto, Portugal

Daniel F.O. Braga LAETA, IDMEC, Instituto Superior Técnico, Universidade de Lisboa, Av. Rovisco Pais, 1, Lisbon, Portugal

Ricardo J.C. Carbas Instituto de Ciência e Inovação em Engenharia Mecânica e Engenharia Industrial (INEGI), Porto, Portugal; Departamento de Engenharia Mecânica, Faculdade de Engenharia (FEUP), Universidade do Porto, Porto, Portugal

G.H.S.F.L. Carvalho Universidade de Coimbra, CEMMPRE, Departamento de Engenharia Mecânica, Coimbra, Portugal

Lucas F.M. da Silva Instituto de Ciência e Inovação em Engenharia Mecânica e Engenharia Industrial (INEGI), Porto, Portugal; Departamento de Engenharia Mecânica, Faculdade de Engenharia (FEUP), Universidade do Porto, Porto, Portugal

M. El-zein John Deere Moline Technology Innovation Center, Moline, IL, United States

Shayan Eslami INEGI, University of Porto, Rua Dr. Roberto Frias, 400, Porto, Portugal

H. Fricke Fraunhofer Institute for Manufacturing Technology and Advanced Materials IFAM, Bremen, Germany

Stefan Gach Welding and Joining Institute, RWTH Aachen University, Aachen, Germany

I. Galvão Universidade de Coimbra, CEMMPRE, Departamento de Engenharia Mecânica, Coimbra, Portugal; ISEL, Department of Mechanical Engineering, Polytechnic Institute of Lisbon, Lisbon, Portugal

Arnold Gillner Fraunhofer Institute for Laser Technology ILT, Aachen, Germany

G. Glinka Mechanical and Mechatronics Engineering, University of Waterloo, Waterloo, ON, Canada

R. Goyal John Deere Asia Technology Innovation Center, Pune, MH, India

Tobias Köhler Technische Universität Ilmenau, Ilmenau, Germany

R.M. Leal Universidade de Coimbra, CEMMPRE, Departamento de Engenharia Mecânica, Coimbra, Portugal; LIDA-ESAD.CR, Polytechnic Institute of Leiria, Caldas da Rainha, Portugal

A. Loureiro Universidade de Coimbra, CEMMPRE, Departamento de Engenharia Mecânica, Coimbra, Portugal

Eduardo A.S. Marques Instituto de Ciência e Inovação em Engenharia Mecânica e Engenharia Industrial (INEGI), Porto, Portugal

P.A.F. Martins IDMEC, Instituto Superior Tecnico, Universidade de Lisboa, Lisboa, Portugal

R. Mendes Universidade de Coimbra, ADAI/LEDAP, Departamento de Engenharia Mecânica, Coimbra, Portugal

P.M.G.P. Moreira INEGI, University of Porto, Rua Dr. Roberto Frias, 400, Porto, Portugal

C.V. Nielsen Department of Mechanical Engineering, Technical University of Denmark, Lyngby, Denmark

Alexander Olowinsky Fraunhofer Institute for Laser Technology ILT, Aachen, Germany

Dirk Petring Fraunhofer Institute for Laser Technology ILT, Aachen, Germany

Pascal Pöthig Technische Universität Ilmenau, Ilmenau, Germany

Uwe Reisgen Welding and Joining Institute, RWTH Aachen University, Aachen, Germany

C.M.A. Silva IDMEC, Instituto Superior Tecnico, Universidade de Lisboa, Lisboa, Portugal

T. Vallée Fraunhofer Institute for Manufacturing Technology and Advanced Materials IFAM, Bremen, Germany

Preface

This book is intended to be a reference for people needing a quick, but authoritative, description of advanced topics in the field of joining processes. It is intended for scientists and engineers of many different backgrounds who need to have an understanding of various aspects of joining technology. These will include those working in research or design, as well as others involved with production. It is expected to be a valuable resource for both undergraduate and research students.

The joining technology is in constant development. There are many books and several international journals dealing with this subject. From time to time, it is important to summarize the most important recent developments and have it available in only one book for an easy access. The originality of this book is that it includes in one volume all the methods of joining available: thermal, mechanical and chemical. In general, these subjects are treated separately but they are increasingly being used simultaneously in many structures and it is important for the designer to have all the necessary information in a single document.

The transport industry is facing very important challenges at the moment with the use of lightweight materials compatible with electrical energy, and efficient joining techniques play an important role in that process.

This book is intended to fill a gap between the necessarily simplified treatment of the student textbook and the full and thorough treatment of the research monograph and review article. The subject is treated very comprehensively and with the most up to date information so that the end-user has in a single book a proper guidance and fundamental knowledge required for many joining applications.

There are in total 10 chapters written by internationally renowned authors who are authorities in their fields.

The editors wish to thank all the authors for their participation and cooperation, which made this volume possible. They would also like to thank the team of Elsevier, especially Dr. Edward Payne, for the excellent cooperation during the preparation of this volume. Finally, Lucas da Silva and Paulo Martins would like to acknowledge the support by Fundação para a Ciência e a Tecnologia of Portugal under LAETA-UIDB/50022/2020.

Lucas F. M. da Silva
Paulo Martins
Mohamad El-Zein

This page intentionally left blank

PART A

Welding

This page intentionally left blank

CHAPTER

1

Laser joining

Arnold Gillner, Dirk Petring, Alexander Olowinsky
Fraunhofer Institute for Laser Technology ILT, Aachen, Germany

1. Introduction

Laser joining is already known as a versatile technology almost since the invention of the laser itself. Compared to other joining technologies, laser joining is characterized by

- Low overall energy and heat input
- Very local modification of the base material
- High spatial accuracy
- The ability to join different materials together
- Very high joining speeds

Therefore laser joining is used for a wide variety of applications from electronics, medical technology, automotive industry, machine building to erospace and ship building. In general laser joining is based on localized melting of both joining partners by absorption of the photon energy and mixing together the materials of the joining partners. Depending on the type of material, the absorption of the laser energy takes place at the surface of the material or within the volume, when the transmittance of material corresponding to the used laser wavelength is high. In der following figure the different laser joining methods for the different material classes are listed and typical laser powers are given (Fig. 1.1).

In the following the different laser joining technologies are described in detail.

2. Laser heat conduction welding

In laser heat conduction welding the material is heated up by surface absorption of the laser radiation well above the melting but below the evaporation temperature. The shape of the melt pool and therefore the welding depth are depending on the heat conduction of the material. Important factors, which are influencing the heat conduction are the thermophysical constants like heat conduction coefficient, specific heat and density of the material,

Advanced Joining Processes
https://doi.org/10.1016/B978-0-12-820787-1.00001-2

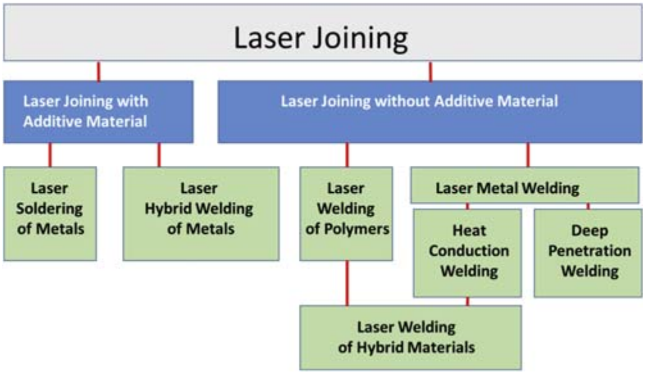

FIG. 1.1 Overview of laser joining technologies.

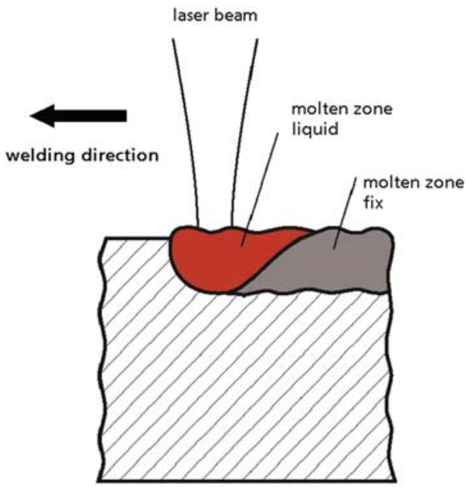

FIG. 1.2 Principle of laser heat conduction welding.

the geometry of the joint and the part and the temperature of the work piece. Fig. 1.2 shows the principle of the heat conduction welding process.

The energy transport into the depth of the material follows the heat conduction mechanism, which can be described by the 3-dimensional heat conduction equation, in which the source term is defined by the absorbed laser intensity [1]. The absorbed energy forms an isothermic field in the depth of the material. At the material specific melting temperature, a melt is formed and by temperature and surface tension driven melt flow a mixing of the molten material of two parts occur. If the melt pool is placed at the interface of two workpieces, these two parts are joined and fixed after resolidification of the melt. A typical isothermic field for heat conduction welding is shown in Fig. 1.3 as a cross section and also as a section along the welding direction. Here it can be seen, that at the welding front the distances between the isotherms are shrinking and high temperature gradients occur. At the back of the melting

FIG. 1.3 Cross section of a heat conduction weld seam.

region, the melt is still there, even the laser beam is not heating the surface of the melt. After a certain time, which is defined by the specific heat conduction conditions of material and part geometry, the melt resolidifies, forming a melting joint.

Heat conduction welding can be realized by gas laser, solid-state laser and diode laser. The intensity I of the laser radiation must be high enough to heat up the workpiece to its melting temperature but less the threshold intensity for evaporation. If the intensity exceeds this threshold intensity, the heat conduction welding process changes into the deep penetration welding process [2].

The threshold intensity for deep penetration welding depends on the heat conduction, the specific heat, the density of the material, the absorption coefficient of the material with respect of the used laser radiation as well as the evaporation temperature of the material or the oxide layer on top of the material. Especially in aluminum welding, heat conduction welding is difficult due to the very high melting temperature of the aluminum oxide layer compared to the low melding temperature of the aluminum. However in steel and even in copper heat conduction welding is a good choice, when thin materials have to be welded and a very high surface quality of the resulting weld bead is needed. In heat conduction welding the melt flow is mainly driven by marangony convection, which results from the differences in surface tension at different temperatures. The principle of marangony convection is shown in Fig. 1.4 together with the dependence of the surface tension on the temperature.

With low temperature gradients in the melt respectively in the surface of the part, a smooth surface can be achieved and very low surface roughness is the result. In contrast, at high temperature gradients or even partial evaporation of the material and resulting vapor

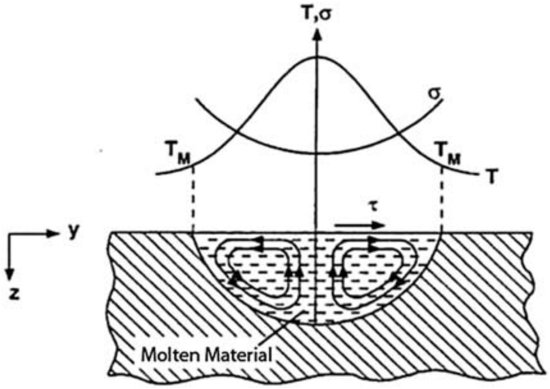

FIG. 1.4 Principle of marangony convection and responsive temperature dependent surface tension.

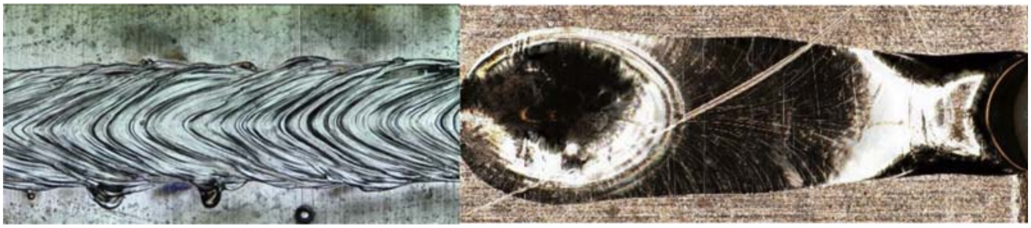

FIG. 1.5 Surface pictures of representative heat conduction welds with low temperature gradient and high temperature gradient.

FIG. 1.6 Example of heat conduction welding application in watch industry.

pressure a rough surface is the result. In Fig. 1.5 two typical surface roughness pictures with high temperature and low temperature gradients are shown.

Low temperature gradients can be achieved by large laser spot sizes, where the outer regions of the irradiation zone is heating up the material but does not reach the melting temperature. For this purpose high power diode lasers provide the best performance and high power diode lasers are used to join components from medical industry and also a large variety of stainless steel products for white goods and related products. In Fig. 1.6 an example of heat conduction welded components is shown.

3. Laser keyhole welding

In contrast to the heat conduction welding in Laser keyhole welding the material is heated up above the evaporation temperature. This causes evaporation pressure on the molten material and thus flow of molten metal, which forms a vapor channel (keyhole) into the melting pool. This effect is named deep welding effect DIN 32511 [3,4] and allows high aspect ratios (seam deep/-width approximately zR/w0) greater than 10:1. Fig. 1.7 illustrates the process schematically.

Within the welding process, the keyhole is moved along the desired welding path and the melt flows around the keyhole. In front of the vapor channel the material is completely molten. The molten material flows around the vapor channel and solidifies behind the keyhole to the weld seam. To reach the evaporation temperature a material characteristic intensity is necessary. Fig. 1.8 shows the increase of the welding depth at a characteristic laser intensity of typical $I = 10^6\ W/cm^2$. At this intensity a vapor channel is formed and the laser radiation is coupled to the channel thus increasing the overall absorption of the laser radiation by a factor of more than 5.

Above a laser intensity I, the keyhole and the vapor capillary is associated with metal vapor plasma, which is developed from the absorption of the laser irradiation and partially by ionization of the metal vapor which forms a plasma inside the keyhole. This phenomenon assists the input coupling of laser beam into the workpiece by further absorption of the laser radiation in the plasma. The energy transfer is carried out by hot gases and the plasma to the capillary wall. Furthermore the absorption of the laser irradiation in front of the vapor capillary can be described by the Fresnel formula. Because of multiple reflections and multiple absorption in the vapor capillary it is possible to a reach high absorption rates even at high reflective materials, such as copper. By suitable geometrical conditions of the vapor capillary the absorption rate increases by more than a factor of 10 [5] (Fig. 1.9).

When the laser irradiation increases, the vaporization rate increases and the metal vapor density is rising. This leads to dense plasmas, which shields the laser radiation so that the energy is absorbed in the plasma and isolates the laser beam from the working area. When the energy input is too high, the plasma removes from the workpiece and interrupts the working process.

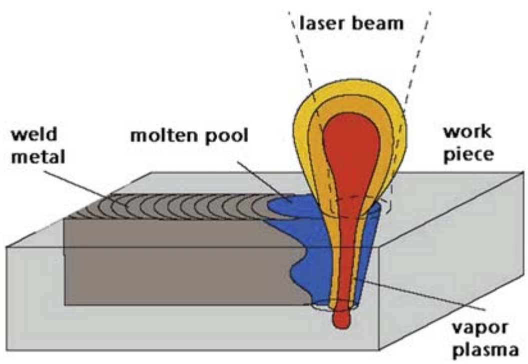

FIG. 1.7 Principle of keyhole welding.

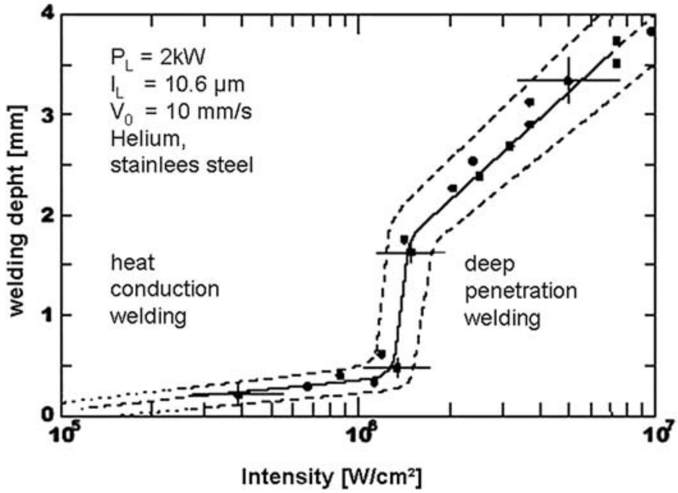

FIG. 1.8 Increase of welding depth by reaching the threshold for deep penetration welding.

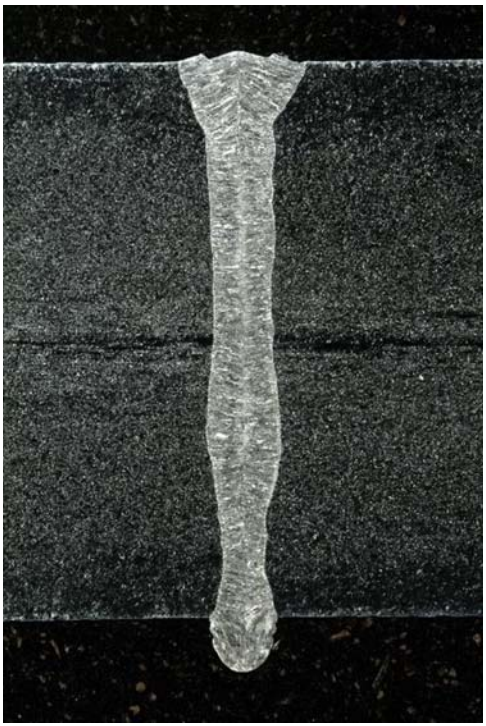

FIG. 1.9 Welding with disk laser bead on plate welding stainless steel $s = 10$ mm $P_L = 8$kw, $v_s = 3$ m/min.

The geometry of the capillary is determined first by the intensity distribution and a homogenous intensity within the keyhole and second by the vapor pressure inside the keyhole. The vaporized metal streams up in a vertical direction to the capillary wall, so that one part of the vapor condenses by hitting the back wall. At butt welds, another part of vaporized metal streams through the upper capillary aperture. On full penetration welds an additional part vapor streams through the lower aperture. The generated pressure inside the capillary is in balance with the pressure outside, so that the vapor capillary achieves:

$$p_i = p_a$$

Inside the vapor capillary the gas pressure and the ablations pressure are added. On the other hand, from the outer side, there is the inertia of the melt, the curvature pressure and the solid pressure. The pressure balance in the vapor capillary is regulated through the plasma pressure $p = pkT$ and the ablation pressure. The geometry of the vapor capillary depends on laser- and process parameters. Its size is in a range of the laser beam diameter.

The plasma plume develops, when there is sufficient metal vapor with adequate density. The required threshold intensity depends on different process parameters. Assist gases (e.g. Helium, Argon) have great influence of the vapor plume. Their size depends on the kind of gas and escape proportion [6].

The application spectrum for using this process is wide spread. This process is useful for materials like steel, aluminum, titanium and different alloys. With the application of solid-state-lasers with high beam quality and small spot sizes in the range of a few 10 μm the area of non-ferrous material for the deep penetration welding is worth mentioning. This holds especially for copper and aluminum, materials which normally show very low absorption coefficients. With deep penetration keyhole welding the restrictions of the low absorption can be overcome and copper based contacts for e-mobility and batteries can be securely welded. The material thickness which can be welded with keyhole welding is on a scale from some tenths of millimeters to 20 mm, in some cases more than 20 mm.

Deep penetration welding can be used for various joining configurations like butt-joint, t-joint, lap joint and fillet-weld, in different welding positions. The application areas extend in the micro technique, in the automotive industry, in off shore applications and in shipping- and tank constructions. Deep penetration welding is used by manufacturing shops for welding simple geometric parts as well as for 3D-machining. The comprehension of filler materials and the laser-hybrid-technology considerably extend the spectrum of laser deep penetration welding, while the small tolerance zone of laser beam welding will be major.

With regard to conventional welding techniques like MIG/MAG/TIG/UP e.g., the laser beam welding has a higher efficiency. The relatively low efficiency of the lasers applied in comparison with the conventional sources is overcompensated by the much better process efficiency. This is the reason for the high welding speed and precision by using CNC handling systems. More advantages are given in the low distortion of the welded parts, cost reduction, as well as contactless and wear less machining with the laser tool. This are characterized advantages of the deep penetration welding.

However, by using this process with all advantages, it is necessary that the constructions of welding parts are suitable for the laser technology. The accessibility for the laser beams e.g. the optical components and the material specific properties of the welding parts must be considered as well as part tolerances to avoid gaps between the components, which would lead to insufficient laser absorption.

4. Laser hybrid welding

The expression "laser hybrid welding" represents welding processes which use – beside the laser beam – a second welding source, acting in the same melt pool as the laser beam. The second source provides additional heat and – as the case may be – also filler material [7].

Beside the combination of different laser beams, the most established hybrid welding variant is the support of lasers by arc power. Laser-arc hybrid welding processes are meanwhile recognized for their robustness, efficiency and flexibility. Especially the coupling of a deep-penetrating laser beam with the heat and molten metal supplying gas metal arc (GMA) is a proven hybrid technique. It significantly expands the original welding application range of lasers.

The laser-arc hybrid process is characterized by the simultaneous application of a focused laser beam and an arc, creating and moving a common melt pool along the weld pass (see Fig. 1.10). The combination offers an increased number of parameters compared to the single processes, thus allowing flexible control of the welding process adapted to the demands of material, design and manufacturing conditions.

The main benefits of the hybrid technique compared to laser beam welding with or without filler wire are:

- Better gap bridging capability at lower laser beam power.
- Better leveling of edge offset.
- Lower demands on edge preparation and clamping.
- Improved adjustment of the thermal cycle.

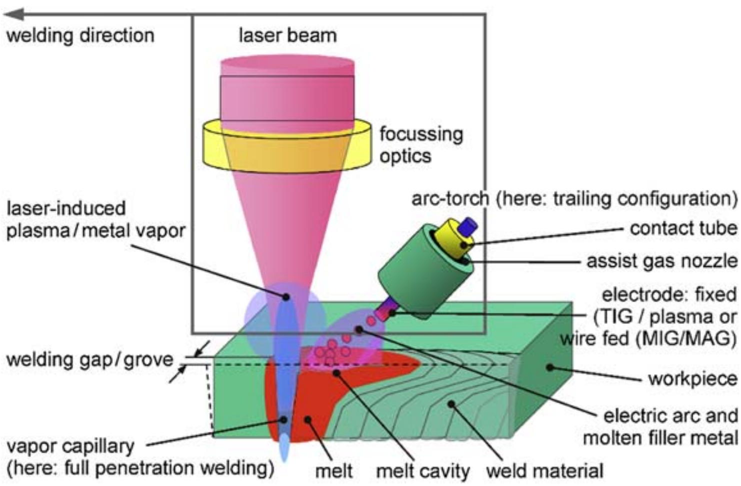

FIG. 1.10 Principle of laser-arc hybrid welding [8].

And there are also significant benefits compared to arc welding techniques:

- Higher welding speed.
- Weldability of zero-gap and I-seam at lap joint.
- Single-pass full-penetration welding even at high welding depth.
- Lower heat input.
- Lower distortion.
- At T-joints or in corners: smaller fillet, more clearance.

The result is a more flexible and robust welding process providing higher productivity and quality.

The arrangement of the arc relative to the laser beam axis (leading, trailing or co-axial type, inclination and distance between laser and arc) depends on the material to be welded and its surface properties. Also important are type of joint, edge preparation and welding position. The laser and arc power, the laser focusing parameters, and the laser wavelength, as well as the striven metal-transfer mode (MIG/MAG) and special boundary conditions, e.g. the accessibility for a seam tracking sensor, are other factors with strong influence on the design of hybrid process and equipment.

Normally, the smallest possible arc inclination is desired. Angles in the range of 15–30° relative to the laser axis work with technically acceptable effort. Nd:YAG, disk and fiber laser radiation, due to a lower interaction with the arc's plasma, allows a closer approach to the arc than CO_2 laser radiation, as long as the laser induced vapor jet is not leading to detrimental interaction effects.

The currently most preferred laser-arc hybrid welding process is using MIG/MAG. The process can be controlled in such a way that the MIG/MAG part provides the appropriate amount of molten filler material to bridge the gap or fill the groove while the laser is generating a vapor capillary within the molten pool to ensure the desired welding depth at high speed. The combination of processes increases the welding speed above the sum of the single speeds, and produces an increased regularity of the weld bead. Improvements of metallurgical properties regarding hardness and toughness as well as diminished porosity due to promoted escaping of gas out of the enlarged melt pool are noted.

The correct setting of gas parameters is an important factor in hybrid welding, where laser and arc-specific criteria have to be taken into account simultaneously. Using Nd:YAG, disk or fiber laser radiation, beam absorption within the plasma and resulting plasma shielding can be neglected due to the shorter wavelength compared to CO_2 lasers. Thus, with these lasers the selection of process gas can be determined according to the arc stability demands and bead shielding properties. In this case argon will be the dominant portion of the gas used. For MIG/MAG al-so droplet detachment and spatter-free metal-transfer have to be considered. Small addition of oxygen promotes the droplet detachment and reduces spatter. Admixtures of helium lead to higher arc voltage and the corresponding power in-crease results in wider seams, but also leads to a destabilizing of the arc. Nevertheless, using CO_2 lasers, a helium mixture is necessary to avoid plasma shielding. Fortunately, the presence of the laser beam enables acceptable arc stability even with a significant helium portion.

With the standard approach of combining a discrete arc-torch in off-axis configuration with a laser focusing head, there are certain limitations on the possible position and orientation of the arc. In order to prevent the torch nozzle from interfering with the laser beam, it has

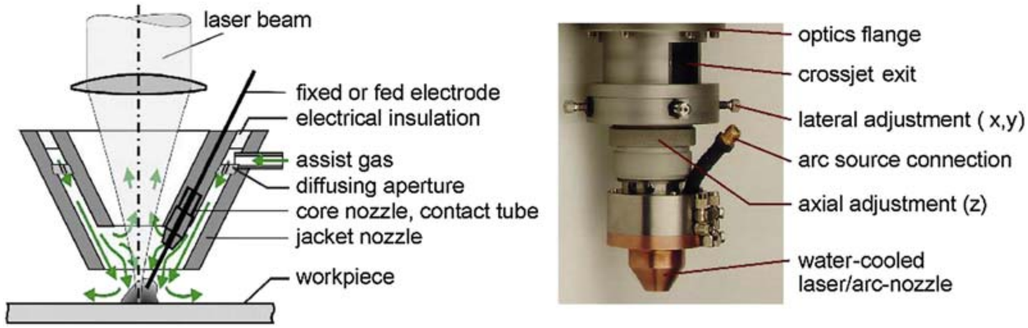

FIG. 1.11 Principle (left) and practical device (right) of the "Integrated Hybrid Welding Nozzle" [9].

to be positioned at sufficient distance and inclination. Another problem with this off-axis configuration approach is that it pro-motes entrainment of air into the weld by the Venturi effect.

To address these problems, a more sophisticated approach uses a welding head where the laser beam and arc are surrounded by a common water-cooled nozzle device with integrated contact tube for contacting and stable guiding of the wire electrode (see Fig. 1.11) [2]. This arrangement provides the closest laser and arc proximity at the steepest arc inclination. The process gas flows out of an annular channel coaxially to the laser beam. A diffusing aperture within the channel enables a homogeneously distributed stream of the assist gas onto the welding zone. Thus, a transverse suction of air by the Venturi effect is avoided and effective protection of the weld bead is ensured (Fig. 1.11). Moreover, a minimal but sufficient leak gas flow in the upward direction avoids process gas contamination by air entrainment via the laser beam entrance.

To demonstrate the general capabilities of laser-MIG/MAG hybrid welding, typical macro sections of seams in aluminum and steel are shown in Fig. 1.12. The examples provide evidence of fast speed, wide gap bridging, smooth leveling of misalignment and high quality.

Further examples shall illustrate some hybrid welding features in more detail. In Fig. 1.13 the gap variation at butt joint in 4 mm aluminum sheets could be bridged even without any backing melt support or root protection. Fillet welds at lap joint (Fig. 1.14) get an effective reinforcement by the contribution of the MIG process. Furthermore, thick section welds can be produced up to 25 mm in a single pass in structural steel plates (Fig. 1.15). The respective laser beam powers, welding speeds and gap bridging capabilities can be read from Fig. 1.16. Corresponding fatigue results are shown in Fig. 1.17.

5. Laser beam micro welding

Laser beam micro welding is a versatile and flexible manufacturing technology, which has found its way into various industrial applications. In the past electron guns for CRT displays have been produced using Nd:YAG lasers since the seventies of the last century. In watch industry gear wheels and arbors are joint together by means of laser beam welding. Today numerous applications can be found in consumer products like smart phones and also in a

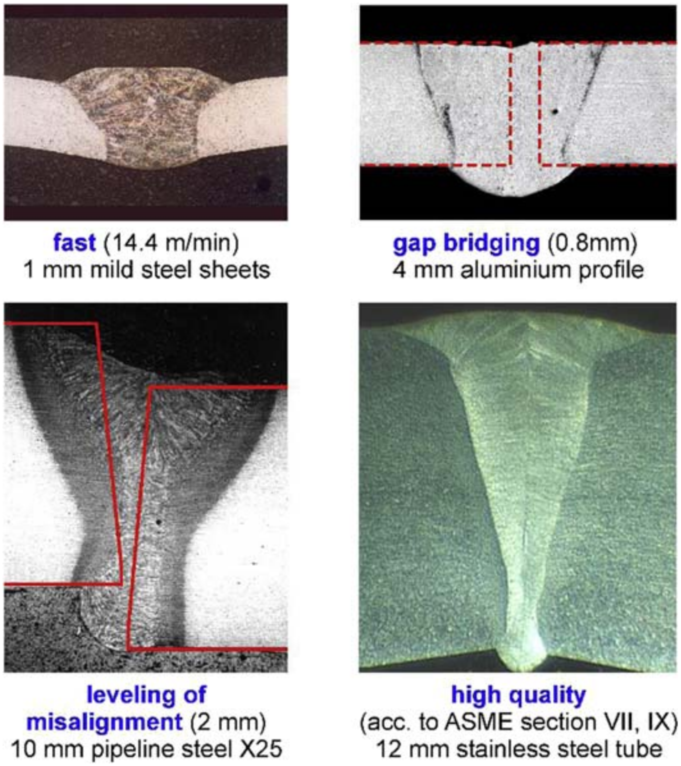

FIG. 1.12 Cross sections and related parameters showing benefits of hybrid welding [8].

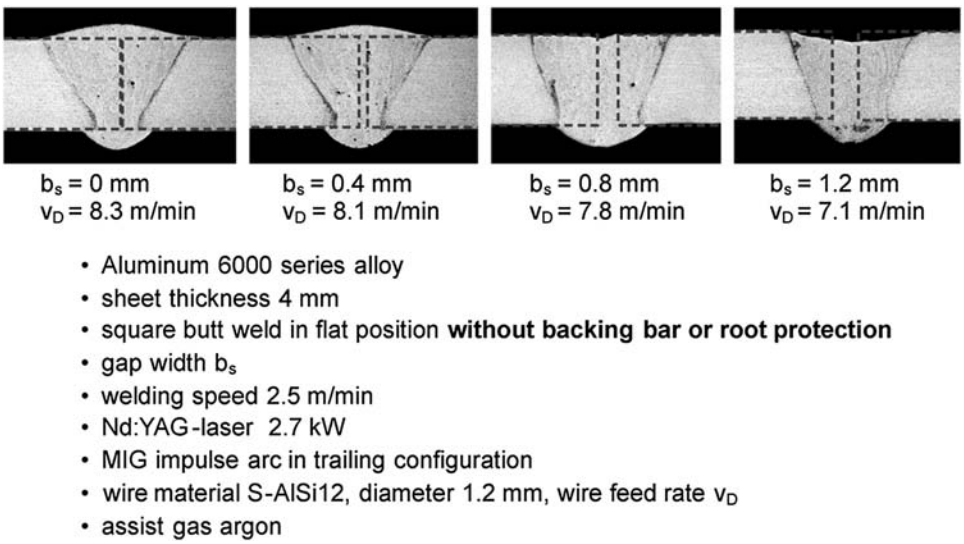

FIG. 1.13 Gap bridging capability in an aluminum alloy [8].

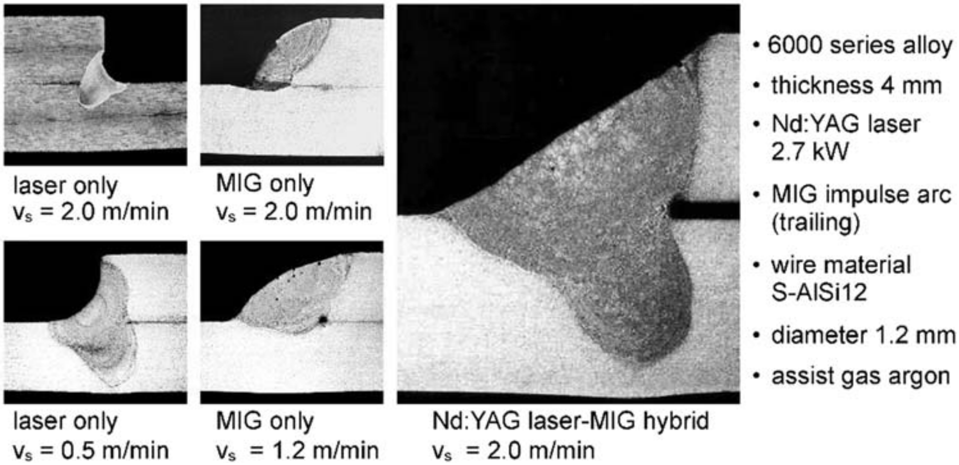

FIG. 1.14 Hybrid welding of fillet weld at lap joint and comparison with the welding result using the single processes alone [9].

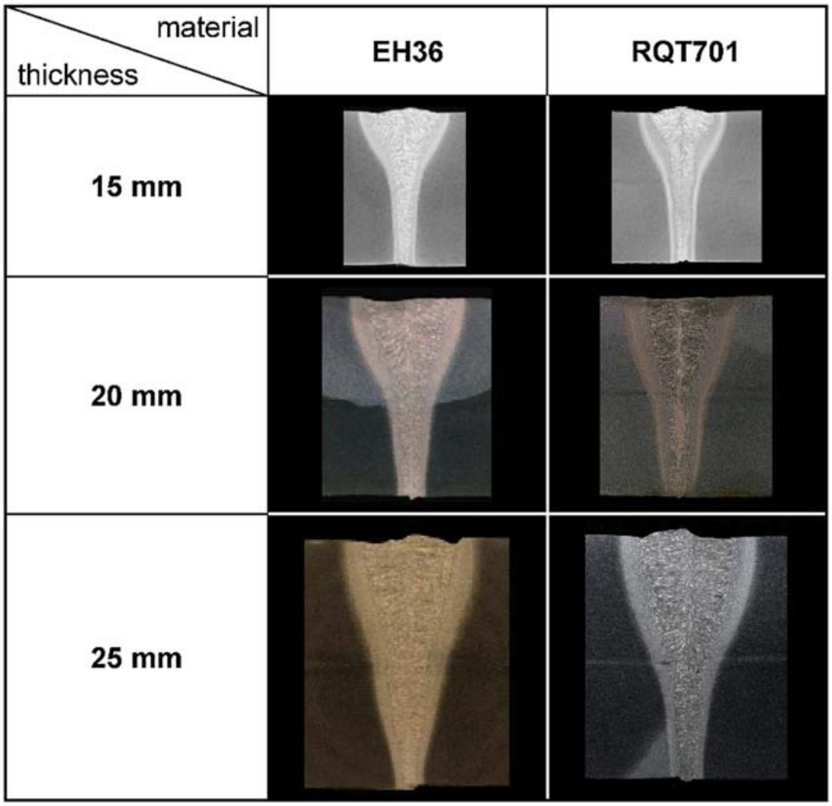

FIG. 1.15 Cross sections of hybrid welded high-strength steel plates up to 25 mm thickness using a 20 kW CO_2 laser at adapted power level [10].

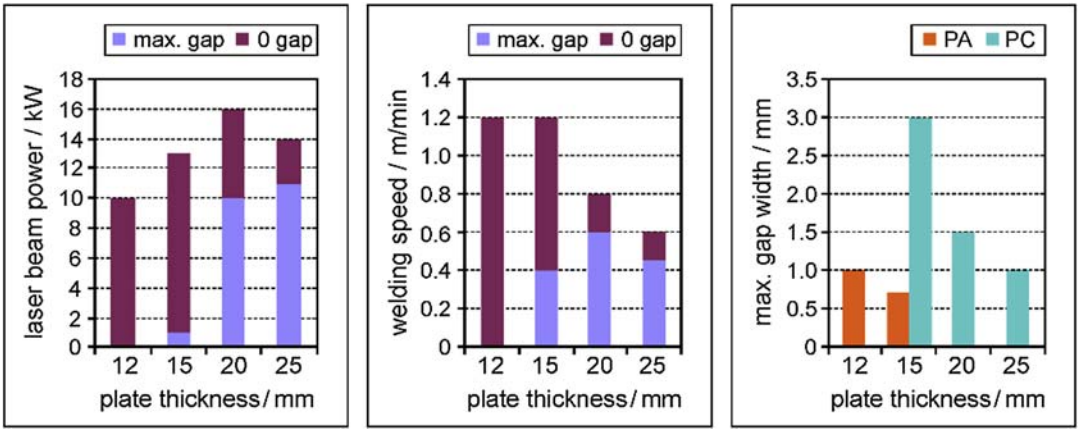

FIG. 1.16 CO_2-Laser-MAG hybrid welding parameters versus thickness, gap size and welding position for butt joints in structural steel [10].

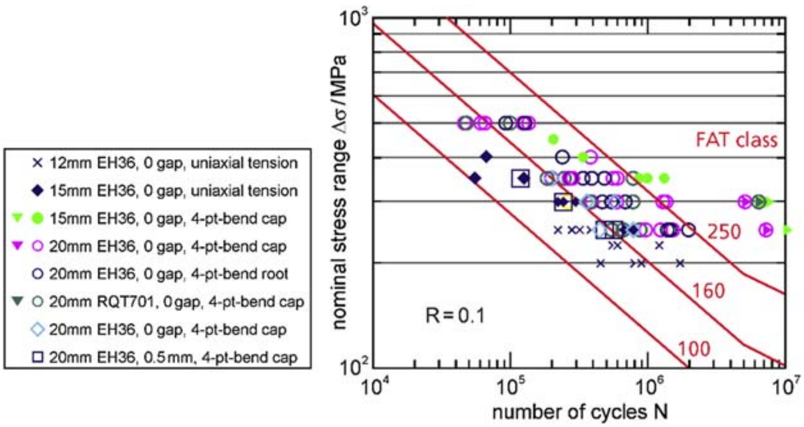

FIG. 1.17 Fatigue results of heavy section laser hybrid welds [10].

variety of electrical contacts, as it is in electrical tooth brushes and hearing aids. Especially in automotive industry more and more sensors and components such as relays and control units are mounted directly under the hood and have to undergo heavy vibrations and high temperatures. The joints in these components have to survive with long estimated lifetime and a very low failure probability these stresses, as they are part of the safety equipment. Laser beam micro welding is a versatile solution for this applications as it is a non-contact process without any tool wear-out. The process duration is shorter than comparable techniques with low restrictions from material and accessibility to the joint. The joining process may be finished within a few milliseconds whereas the whole cycle time within the production is determined by loading and unloading of the components to be joint [11].

One main advantage of laser beam welding is the flexibility: part geometry, material and materials' combination can be changed very easily because the energy input can be controlled

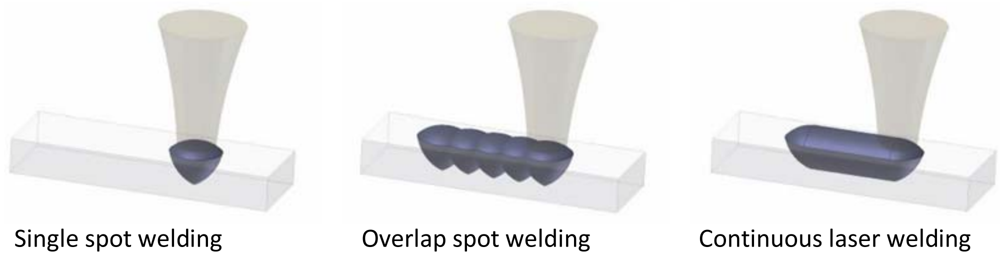

FIG. 1.18 Principles strategies of laser micro welding. (A) Single spot welding (B) Overlap spot welding (C) Continuous laser welding.

and the intensity and the power can be adapted to the task in a wide range. Spot welds as well as continuous weld seams can be applied. Process monitoring as a main requirement in industrial production lines can easily be integrated as inline weld monitor or offline inspection of the weld.

In laser micro welding of metals, in principle three different welding approaches are used:

- Laser spot welding
- Overlap laser spot welding
- Continuous laser welding

In recent years several techniques have been developed to modify the dynamics of the laser molten material and tailor the joint zone by fast laser beam oscillation or an overlay of several laser beams in the welding zone.

In Fig. 1.18 the principle basic strategies for micro laser welding are shown.

5.1 Spot welding

Spot welding will be applied if only a small connection cross sections are needed or the available space is not sufficient for elongated weld seams. The diameter ranges from 100 to 800 μm depending on the beam diameter, the material and the laser power. The spot welding process can be divided into four phases: Heating, Melting, melt flow dynamics and cooling. Depending on the intensity evaporation of material may occur.

By means of pulse forming the intensity can be adapted to the sequence of the process phases. For some materials a preheating as shown in the left picture above is favorable. Other materials such as copper alloys require high intensities at the beginning of the pulse in order to crack existing oxide layers and to assure a stable incoupling of the laser energy. A post heating with well controlled cooling conditions may reduce the risk of cracks. Typical pulse durations range from 1 to 15 ms [12].

For pure heat conduction welding the weld depth amounts to the radius of the weld spot diameter. Increasing the intensity leads to evaporation of material and to establishing a capillary. The now developing keyhole welding process creates deeper weld depths. The discrimination between pure heat conduction welding and keyhole welding cannot be given for micro parts due to the given facts of heat accumulation and dimensions of the parts.

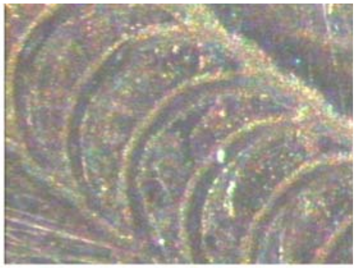

FIG. 1.19 Examples of laser overlap spot welding. (A) Top view of pacemaker casing (B) Top view of overlap spot welds.

5.2 Overlap spot welding

Overlap spot welding is realized be placing several spot welds at a certain overlap in order to achieve a seam weld. The length of the seam scalable but the heat input is very high because for each spot all process phases of spot welding have to be passed through. On the other hand, if the dimensions of the part is very small, the control of the heat input has a higher accuracy, especially when machine accelerations limits the necessary speed for continuous welding. The following Fig. 1.19 shows a cover of battery housing for a pace-maker, which is sealed by pulsed laser overlap welding.

Important process parameters beside pulse power and pulse duration are pulse repetition rate and feed rate. The latter two determine together with the spot diameter the overlap of two consecutive spots which is usually in the range of 60%.

5.3 Continuous laser micro welding

In the past continuously emitting lasers have been rarely used for applications in micro welding due to the low beam quality and thus large spot diameters. However, with the upcome of high brilliant fiber and disc lasers new cost effective and high quality process solutions are available using tightly focused laser beams and fast bema modulation.

Continuous (cw) laser welding is used firstly for longer joints and for larger parts. Using fast scanning technologies, cw-lasers are also used for micro spot welding with small circular weld joints. For continuous laser welding of metals a high average laser power, Pav >500 W, and a high processing velocity, $v > 5$ m/min are required. Due to the homogenous energy input and the continuous melt pool motion with low disturbances cw laser welding show a smooth surface and an optimized microstucture nearly without any pores. The energy per length is less for cw laser welding than for pulsed laser welding. Moreover the use of the pulse forming (temporal shape of the laser pulse) enables the joining of dissimilar materials like steel to copper.

A successful and stable joining process between the components depends on one basic criterion: The heat energy input. Especially for micro welding the overall heat input has to minimized. Due to the fact, that all metallic materials have high thermal transfer properties, thermal stress occur with high energy input. Since the alloys of the frequently used metallic

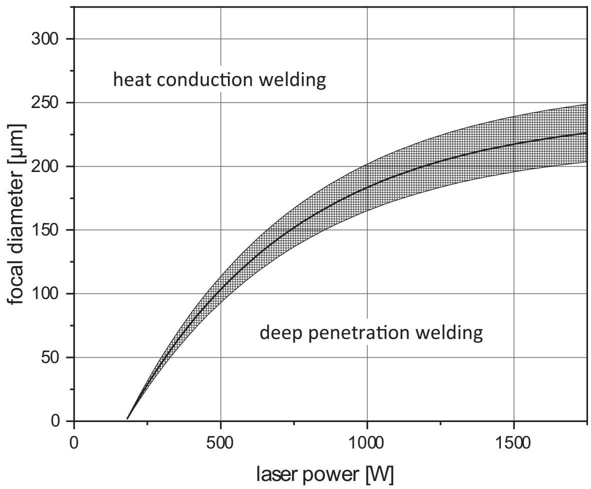

FIG. 1.20 Threshold between deep penetration and heat conduction welding of Cu-ETP by using a Gaussian intensity distribution. The measurement has been conducted using a fiber laser with a wavelength of 1070 nm.

connector materials copper and aluminum have a low absorption rate (<10 %) with simple interaction between light and material - so called heat conduction welding - when conventional laser beam sources in the wavelength range around 1 µm are used. The formation of a vapor capillary − so called deep penetration welding - leads to a sudden increase in absorption and thus in the efficiency of the joining process. To generate this vapor capillary, it is necessary to exceed the intensity threshold for deep penetration laser beam welding. Fig. 1.20 show the different regimes of heat conduction welding and deep penetration welding in dependence of the laser power and the spot diameter.

This allows the intensity to be influenced in two ways. Firstly, by increasing the laser power even with larger focus diameters (>100 µm), the intensity threshold for deep penetration welding can be exceeded. This also results in an increase in the energy input and thermal load of the batteries to be joined, which can lead to permanent damage to the cells. Due to the larger focus diameter, however, the resulting weld seam has a larger connection area. On the other hand, when using moderate laser power (<500 W), the focus diameter can be reduced (<40 µm) so that a deep penetration welding process can be realized, while keeping the energy input to a minimum level. This results in narrow and slender weld seams, which are characterized by smaller connection areas but reduced thermal load. By using a spatial power modulation − a linear feed with superposed circular motion − or increasing the number of weld seams, possibly with cooling breaks in between for a thermal stress relief, however, the joint cross-sections can be increased [13].

As already mentioned, high brightness lasers, such as fiber lasers, are increasingly being used. When workable focusing conditions are applied, it is possible to obtain focal diameters of about several tens of micrometers. Those small focal diameters result, on the one hand, in advantageous smaller thermal energy input but, on the other hand, in lesser width of the weld seam. In an overlap joint welded by a high brightness laser beam, the connection area is small, which renders it less suitable for such applications. To increase the seam width and, thus, the strength of the connection, the line energy needs to be increased, resulting in a greater energy input per unit length.

To enlarge the cross-section and to stabilize the welding process, spatial power modulation can be used. This means a linear feed with superposed circular oscillation, resulting in a stir movement. The circular oscillation is defined by an oscillation amplitude, A_s, which is equivalent to the radius of a circle, and an oscillation frequency, f_s. This technique was introduced by Martukanitz et al. [14] for laser macro welding with low feed rates, vf, $\leq$33.3 mm/s, fs $\leq$ 50 Hz and large As $\leq$ 2.00 mm. That technique already resulted in an enlarged fusion zone. The first usage of spatial power modulation with high brightness laser sources was published by Boglea et al. [15] for welding of plastic materials. The galvanometer scanners allowed for higher vf $\leq$ 200.0 mm/s, higher fs $\leq$ 1 kHz and small As $\leq$ 0.20 mm), which are common for laser micro welding. This process was adapted for laser micro welding of metals and applied for a patent as SHADOW® welding using a Nd:YAG laser source [16] and for micro welding using a fiber laser. But due to the limitations of galvanometer scanners and necessary frequencies for higher feed rates, this technique is still limited to a few hundred mm/s.

In contrast to a conventional laser welding process, spatial power modulation leads to a higher energy efficiency, which does not depend on the higher energy input, but on a better usage of the thermal energy inside the oscillation [17]. Fig. 1.21 shows the movement of the laser beam by spatial power modulation including the effects of thermal conduction.

The analysis of the welding process with spatial power modulation show three different regimes of the molten pool. These different regimes are presented in Fig. 1.22. For the

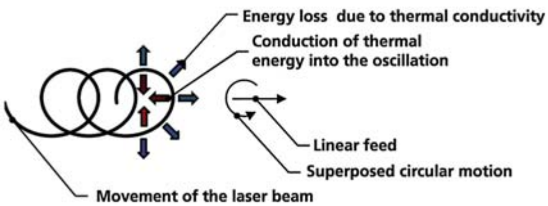

FIG. 1.21 Schematic sketch of the energy losses and conduction of thermal energy into the oscillation by spatial power modulation.

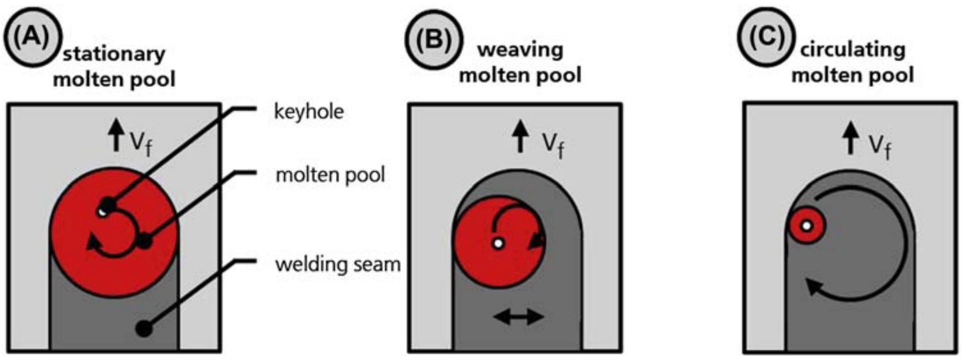

FIG. 1.22 Schematic representation of the regimes for the molten pool by laser welding of CuSn6 with spatial power modulation: (A) stationary molten pool; (B) weaving molten pool; and (C) circulating molten pool.

stationary molten pool, the molten pool only moves with the linear feed, and the keyhole circulates continuously inside the molten pool. In this case, the diameter of the molten pool is the same as the width of the weld seam on the surface. A weaving molten (see Fig. 1.22B) pool arises if the molten pool moves orthogonally to the feed movement. The diameter of the molten pool is smaller than the width of the weld seam. A circulating molten pool (see Fig. 1.22C) can be observed if the molten pool follows the keyhole along its path. Here the width of the molten pool is much smaller than the width of the weld seam. These movement types depend very much on the characteristic variables of the welding process. It can be assumed that when the thermal conductivity, oscillation amplitude or the feed movement rise, a more circulating molten pool is generated. Also it can be assumed that a more stationary molten pool is caused by higher laser power or a higher oscillation frequency. Obviously, not only is a modification of the process parameters able to change the movement types of the molten pool, but the movement types also change during the whole laser welding process. At the beginning of this process, when spatial power modulation is used, right after the formation of the keyhole, a circulating molten pool could always be observed. The characteristic variables determine if the movement types of the molten pool will be maintained or changed into other types until a constant behavior can be detected.

Fig. 1.23 shows the cross-sections of Laser welds in CuSn6 using different oscillation parameters. The weld made without using spatial power modulation is characterized by a high aspect ratio; this means the ratio of weld depth to weld width is high. To keep the degree of overlap constant, the oscillation amplitude was increased and the oscillation frequency decreased, which, in turn, lowers the aspect ratio. On the one hand, the weld depth decreased, while on the other hand, the weld width increases because of the higher oscillation

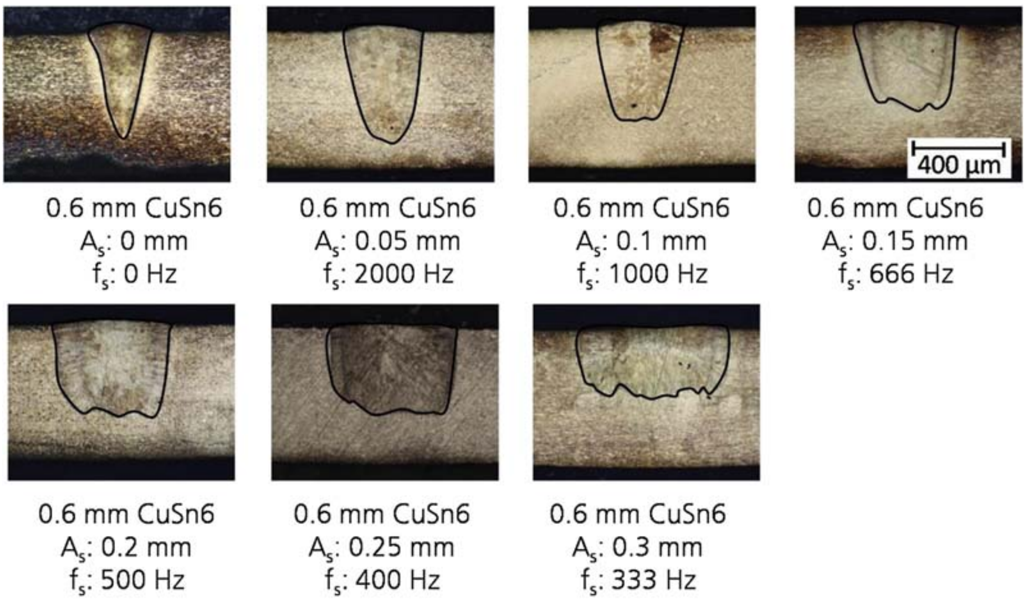

FIG. 1.23 Optical micrographs of CuSn6 cross-sections of welds by different spatial power modulation.

amplitude. The aspect ratio decreases linearly as expected with an increase of the oscillation amplitude. The weld cross-sectional area increased with a rising oscillation amplitude. At lower oscillation amplitudes (As $\leq$ 0.15 mm), a small increase in the cross-sectional area can be seen. When the oscillation amplitude is further increased, the cross-sectional area rose rapidly up to about 210,000 μm^2 at an amplitude of 0.25 mm. This maximum in the cross-sectional area indicates that the thermal energy input is used more efficiently at larger oscillation amplitudes for examined amplitudes up to 0.30 mm.

Laser micro joining is a rapidly growing application, especially in the field of high power electronics and energy storage systems, like Li-Ion-Batteries. Laser joints can withstand high forces and high temperatures and they are fast to apply and highly flexible. With the use of fiber lasers even cost effective solutions can be provided as long as some major requirements are kept in mind. In laser micro welding spatial power modulation should be used to generate larger molten pool areas with a sinusoidal shape during the individual oscillations by a degree of overlap of $\approx$ 0.5. Using this technology the efficiency during laser welding can increased by a factor of two at constant energy input per unit length [18].

5.4 Laser soldering

Laser soldering is one of the most important joining process in addition to welding and adhesive bonding. Soldering is a thermal process for substrate-to-substrate bonds and coating of materials whereas a liquid phase is formed by melting an additional solder alloy or by diffusion at the interfaces. The solidus temperature of the basic material is not being exceeded. During the soldering process a liquid phase is caused by melting of a solder alloy or by diffusion processes within the intermediate layer. In principle, the joining process is based on interaction reactions between the joining partners and the melted solder. Therefore, a direct, oxide- and contamination-free contact between the metal surfaces of the joining partners and the solder alloy is one of the most important process requirements. If the melting temperature of the additional material is below 450 °C (840 °F) the process is called soldering, while when above 450 °C the process is called brazing.

For a successful and high quality soldering process a process adapted heating cycle is necessary for the soldering process. This heating cycle, as shown in Fig. 1.24, with specific temperature values is responsible for the different process stages, like surface activation, melting of the solder alloy, wetting of the surfaces, spreading and filling of the gap between the components to be joined. Each heating cycle involves four important parameters: the heating rate and dwell time for heating, the peak soldering temperature, the dwell time above the melting point of the solder alloy and the cooling rate. In general, it is desirable to use a high heating rate for short process cycle times, but the maximum heating rate is normally constrained by the form of the energy input. By means of laser energy and its high energy density it is possible to realize a maximum heating rate. The dwell time during heating is necessary for the evaporation of vapors and constituents of the flux and for the uniform heating of the joining partners up to the wetting temperature. This temperature is below the melting temperature of the solder alloy. The soldering temperature needs to be at a value for completely melting the solder, but at the same time the solder alloy should not be overheated so that it degrades or evaporates with a loss solder alloys. The peak temperature is normally set to about 20–30 °C above the melting point. At this temperature the components

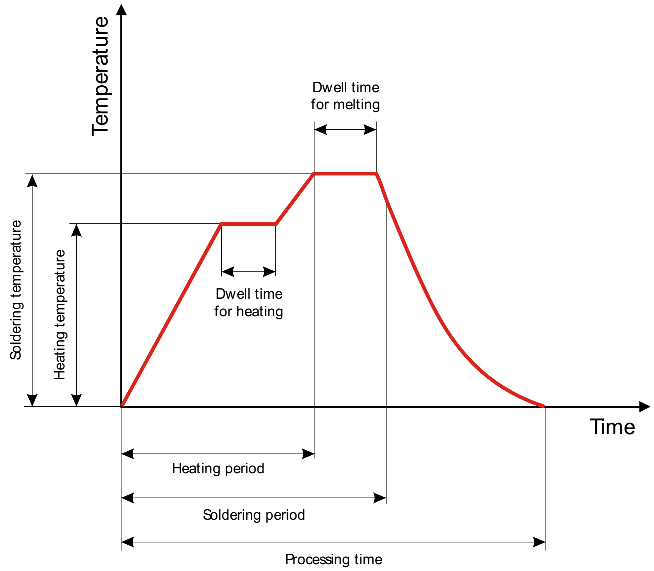

FIG. 1.24 Heating cycle for a laser soldering process.

are continuously heated to ensure overall melting of the solder and wetting of the components with the molten solder. Extended holding times will result in excessive spreading of the molten solder alloy, possible oxidation and deterioration of the properties of the components. Cooling takes place by self quenching due to heat conduction in the components. For laser processing it is very fast because of the instantaneous switch-off of the laser power, resulting in a fine-grained microstructure of the joint [19].

Laser soldering is a highly selective soldering process with very defined energy input and low overall energy deposition. Compared to other conventional selective soldering techniques laser beam soldering is contactless, temporally and spatially well controllable and allows continuous measurement of the temperature during soldering. Because of these characteristics laser beam soldering is predestined for joining tasks where miniaturization and reduced thermal and mechanical stresses are required. Special features of laser beam soldered joints are fine-grained microstructure and the low amount of intermetallic phases due to the fast heating and cooling rates of this process. In principle laser beam soldering is characterized by temporally and spatially selective energy input by surface absorption in the joining area, successive heat conduction and interface processes. The joining process is determined by characteristics of the laser beam source, chosen process parameters and thermo-physical properties of the joining partners (Table 1.1).

By using diode free beam systems or continuous Nd:YAG lasers, joining geometries $<$ 100 μm can currently be processed. Fig. 1.25 shows a fine pitch soldering on a semiconductor component, which was created by means of a diode laser. In these applications, the solder is usually applied in the form of solder paste before the soldering process. This is followed by an initial reflow of the solder in the reflow process, followed by the actual laser soldering, in which only flux has to be applied again. For a high quality soldered joint, a special

TABLE 1.1 Typical lead free solder pastes for laser soldering.

Solder	Solidus temperature	Liquidus temperature	Application
SnBi	138 °C	139 °C	Consumer
SnZn	198.5 °C		Consumer
SnAgBi	206 °C	213 °C	Military/Aerospace Consumer
SnAg	221 °C	226 °C	Automotive
SnAgCu	217 °C		Automotive Telecommunications
SnCu	227 °C		Consumer Telecommunications

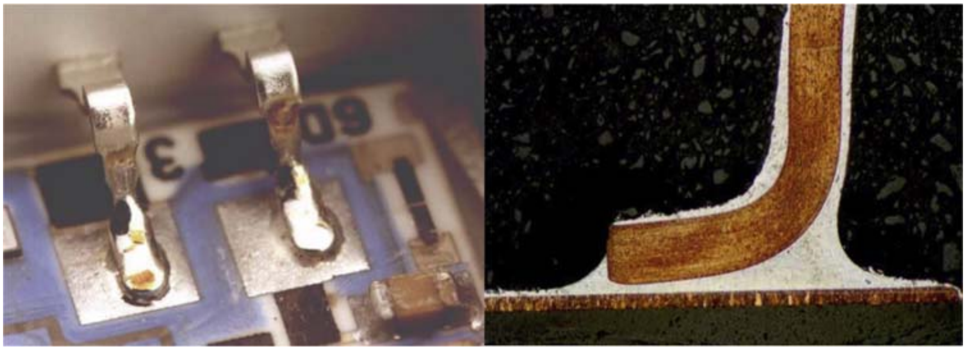

FIG. 1.25 Laser soldered contact and cross section of laser soldered contact pin.

temperature profile must be set at the soldering point, which ensures both uniform heating of the soldering point and complete wetting. The different temperature plateaus are achieved by sequential power variation during irradiation. In laser beam soldering, a pyrometric temperature measurement is usually used to control the temperatures actually reached. Ideally, this is done coaxially through the laser processing optics [20].

Soldering is divided into different subcategories. Below a liquidus temperature of 450 one speaks of soft soldering. If the liquidus temperature of the solder is higher than 450 °C, we speak of brazing.

Laser beam brazing is mainly used where, firstly, high strength and long-term stability even under the influence of large forces are required and, secondly, where high surface qualities with low roughness of the seam upper beads are required. These requirements are found above all in the automotive industry, where laser beam brazing is used to join body components and where large gaps have to be bridged [21]. Laser beam brazing is shown schematically in Fig. 1.26 using the example of a flared joint. The laser beam is projected onto the process zone. There, the base materials are heated and the brazing alloy melts away so that the materials can be wetted by the liquid brazing alloy. The solder is continuously fed in wire form through the wire conveyor and via the wire nozzle to the process zone. The laser beam and wire nozzle are guided in the feed direction over the workpieces to be soldered so

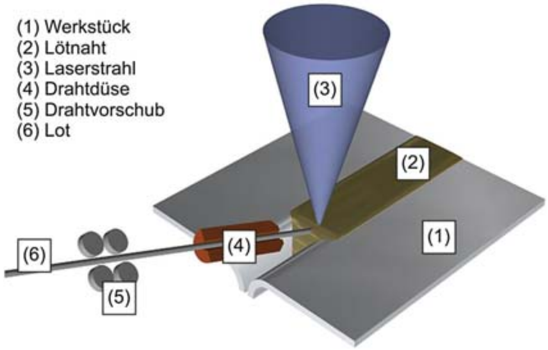

FIG. 1.26 Principle set up of laser brazing technology.

that a uniform soldered seam is produced. The solder wire is usually fed at an angle of 45° to the incident laser beam. The laser beam is guided vertically or slightly trailing to avoid direct back reflections on the component. The laser spot is formed in such a way that the base materials are brought to working temperature and the solder reaches its liquidus temperature. To ensure this, the exact positioning of the solder wire and laser spot relative to the joint is necessary.

A disadvantage of the established process principle is the fact that the wire, which is introduced into the process zone in a dragging manner, covers the joint in the lead-up to the process zone. As a result, the base materials, which must be heated in advance for good wetting, can only absorb part of the laser radiation in advance of the process zone. To counter this problem, various approaches are being pursued to channel more energy into the base materials. One variant is the use of two laser spots, which are introduced into the process zone in an elliptical shape laterally offset to the feed direction and can thus couple more energy into the base materials. A second variant guides the solder perpendicular to the joint into the process zone, so that both the upstream and downstream of the process zone are accessible to the laser radiation. Here, too, the laser radiation is distributed to two laser spots, so that one partial beam can preheat the base materials, while the second partial beam allows the brazing alloy to melt. Another variant uses an axicon optics to create an annular beam distribution and guides it coaxially to the solder wire into the process zone [22] (Fig. 1.27).

These two-beam or coaxial systems are intended to achieve improved wetting of the base materials. Some of the methods also postulate directional independence and higher feed rates. However, none of these systems has yet been able to establish itself in industrial production. Due to their usually large design, an associated increased interference contour, and high investment costs, these systems have not yet been able to establish themselves in series production.

The latest approaches from research deal with a dynamic adjustment of the intensity distribution in which the laser spot is moved across the process zone with the help of a galvo scanner. The laser spot can be deflected laterally to the feed direction and should thus ensure a better energy input into the base materials. Currently, approaches are being pursued which generate two smaller forward laser spots in addition to the main laser beam. These leading laser spots are laterally offset so that they can radiate past the incoming solder. In addition

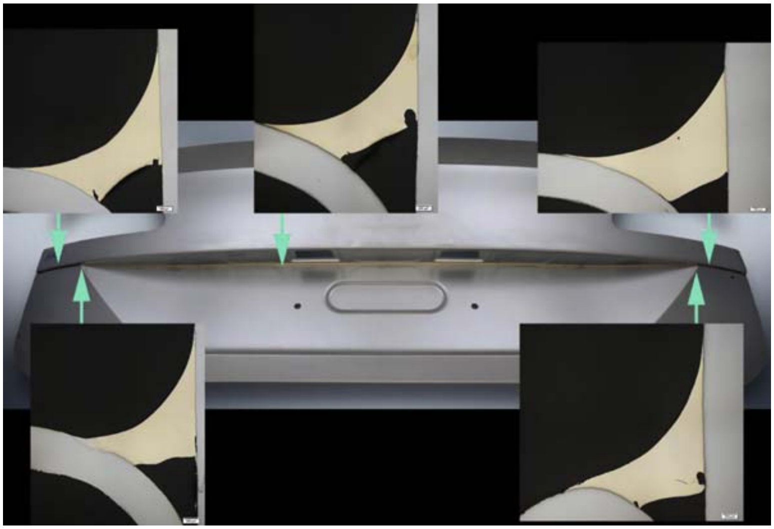

FIG. 1.27 Several cross sections of laser brazed joints at a rear car hood.

to the increased energy input into the base materials, the aim of this trifocal approach is to remove interfering zinc or oxide layers and thus achieve a higher quality soldering result. Especially for hot-dip galvanized steel sheets, this process represents a promising approach, as it can prevent undesirable spattering and irregular seam spurs. The implementation of this trifocal intensity distribution can be achieved by using a multi-core light guide cable, in which several laser beams can be guided to the processing optics at the same time. Alternatively, solutions exist in which the intensity distribution within the processing optics is adjusted. With this solution, several laser spots can also be generated. In addition, it is possible to adjust the geometric arrangement of the partial beams to each other individually to the process. In contrast to the two-beam or coax solution, these approaches offer the advantage that they can be easily and cost-effectively integrated into existing systems and thus represent an extension of the established process principle.

5.5 Laser welding of thermoplastic polymers

Thermoplastic polymer parts are generally joined by adhesive bonding, mechanical crimping, hot plate welding, vibrational welding and ultrasonic welding. Compared to this conventional technologies laser polymer welding technology offers significant advantages, such as low mechanical influence to the parts, power scalability, flexible geometry and contour shaping, joining capability without additional material, and process stability. Moreover laser joining of plastic parts offers the possibility for on-line process control, which have already established laser polymer welding as a versatile process for high quality assembly in many industrial applications [23].

Laser polymer welding allows a contactless and locally defined energy deposition without thermal damage of the joining partners and without any geometry change of the components.

The mechanical stress is also being reduced or avoided since during the joining process the components experience no relative movement to each other as it is the case in ultrasonic of vibrational welding. For optimal plastic material combination the welding strength is close to the one of the base material. Furthermore, tight, pore-less and optical high quality weld seams can be achieved through laser beam welding of plastic materials. The quality of the welding as well as the various applications that can be covered by the laser beam welding reveal its great market potential. At present the laser beam welding can be considered for approximately 20% of the plastic processing market in fields like electronics, automotive applications or packaging.

Laser beam welding of plastic material is based on the use of different transmission and absorption properties of the electro-magnetic radiation in the thermoplastic material. Beside general melting approaches known from metal welding, polymer welding is mainly used with an overlap geometry of the joint, in which one of the joining partners is transparent or translucent for the wavelength of the laser radiation and the other one is absorbing the laser light. So the laser beam can pass through the upper joining partner and is absorbed at the contact surface between the two joining partners. Here, the electro-magnetic energy is converted by the absorbing joining partner with almost no losses into thermal energy. Through heat conduction the transparent joining partner is also melted. To guarantee an efficient heat transfer a firm contact between the joining partners is required. In the case of transmission welding a thin film of molten material in the range of 30–300 μm is resulting in the welding zone [23] (Fig. 1.28).

Basic requirement for this approach is a high transparency of the upper joining partner for the wavelength of the laser light. Therefore in general high power diode lasers in the wavelength range from 800 nm to 1 μm are used. In this wavelength range all thermoplastic polymers show a high transparency of more than 85%. At some polymers a high degree of

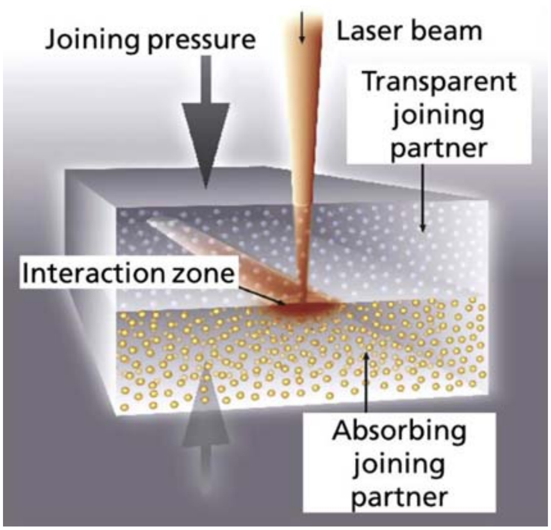

FIG. 1.28 Basic principle of laser transmission welding of thermoplastic polymer parts.

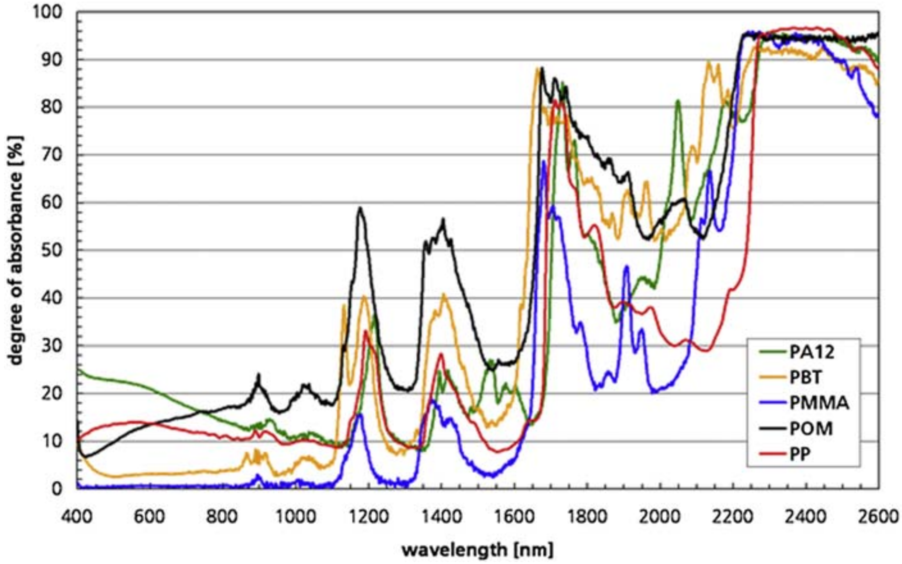

FIG. 1.29 Absorption spectra of different polymers in the infrared.

crystallization scatters the laser light, like in PBT which leads to a broadening of the laser spot. However as long as intensities of $> 10^3\,W/cm^2$ can be achieved at the interface of the partners, a sufficient weld can be performed. To achieve a high absorbance of the laser radiation in the second joining partner, this component has to be equipped with an absorber. A common and cheap absorber is black carbon with is directly mixed with the basic polymer and which is extruded in injection molding. Other absorbers can be wavelength specific pigments or other filler materials, which are normally used for strengthening the polymer. Also other wavelengths can be used to allow a direct absorption of the polymer as it can be seen from Fig. 1.29 from the absorption spectra for different polymers in the infrared wavelength region. With a matching of the laser wavelength according to the absorption peaks specific absorbers can be eliminated and even transparent polymers can be welded.

For laser polymer welding different processing approaches can be used as indicated in Fig. 1.30. For large parts and long weld seams, contour welding is used, where the laser beam is focused to about 1 mm spot size and guided along the welding contour. Here classical robots or machining systems are used for part or laser beam movement. For smaller parts quasi-simultaneous welding can be used, where the laser beam is tightly focused and scanned with a multiple path along the welding contour. Due to the low thermal conductivity of the polymer the entire weld seam contour is molten and the joint is performed. This technology can be used, when large gaps between the parts have to be bridged and the parts are moved to each other during the melting phase. Mask welding is used at very small weld seam widths for example in polymer microfluidic parts. In this approach a transmissive mask is placed on top of the component and the light shines through the mask openings and the weld here is performed. For very large parts also simultaneous welding can be used and separate diodes are placed along the welding contour [24].

In order to achieve a high quality joining results, a specific process management is an essential aspect. A detailed process shows different process regimes which are represented as a "characteristic curve" of the laser beam welding process (Fig. 1.31). On this characteristic curve the different stages or situations of a laser transmission welding process can be identified. At low line energies, the absorbing joining partner is just molten but the transparent joining partner is only heated. For this case the weld seam has a poor strength. With the increase of the energy a sufficient molten volume is produced and a strong weld seam can be achieved. The optimal process parameters for achieving the strongest weld seam are within this domain of the characteristic curve. A further increase of the energy will lead to thermal decomposition of the absorbent joining partner and the strength of the weld is decreased. However in particular cases an increase of the weld strength can be noticed but the process instability will rise, too. One of the most common consequences of such a situation is the formation of pores in the weld seam, which will eventually cause the failure of the weld seam or will compromise the leakage tightness of the assembly.

5.6 Laser joining of polymer-metal hybrid components

Lightweight components require joining technologies to combine different materials such as metals and polymers. The combination of different materials, such as plastics, especially

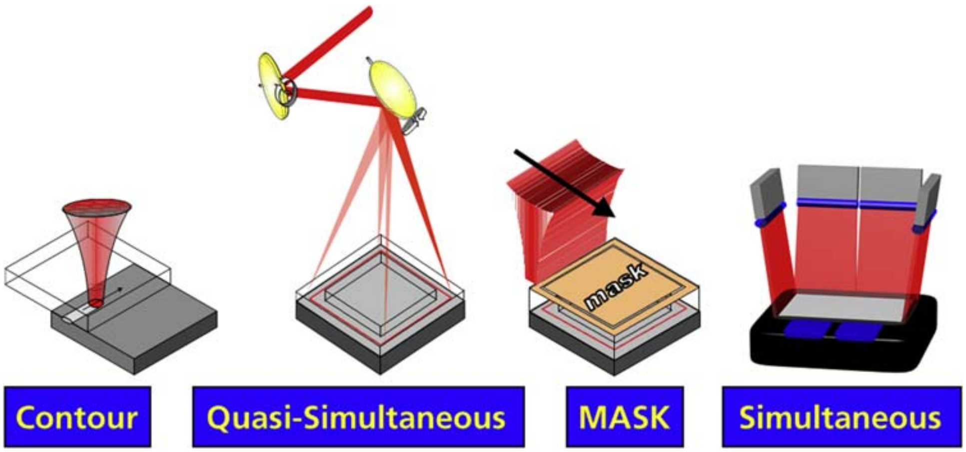

FIG. 1.30 Laser polymer welding process strategies.

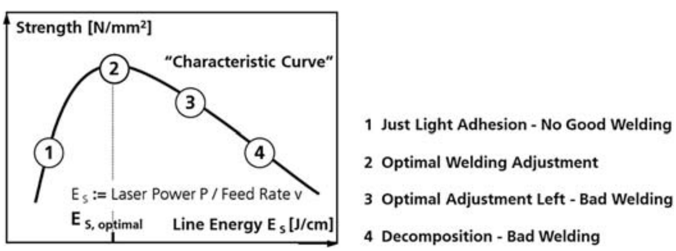

FIG. 1.31 Characteristic curve of laser transmission welding of polymers.

fiber reinforced plastics (FRP), and metals, adapted to local loads opens up new paths for weight reduction. While metals can withstand high loads due to their mechanical properties, polymers are characterized by low weight, attractive price and nearly endless shaping possibilities. Though, a direct joint between both materials, e.g. by welding, fails due to their different physical and chemical properties. Therefor until now adhesive joining is the most used technology for the combination of metals and polymers.

Thermal direct joining of plastics and metals is a novel approach to join polymers and metals. Due to low specific adhesion between polymers and metals, a surface pretreatment of the metal is essential to achieve high joint strengths. The energetic state, electrical potential, morphology, geometry and chemical structure have a decisive influence on the bond strength. Commonly used techniques are sandblasting, plasma pretreatment or etching, but these techniques rarely enable mechanical interlocking between the materials.

With laser based polymer metal joining high strengths of the joint can be achieved and a fully automated process can be realized. The process principle of the laser-based process chain is shown in Fig. 1.32. Within the first process step the metal surface is micro structured with laser radiation in order to create undercut structures for the interlocking of polymer into the metal and to enlarge the boundary surface to increase specific adhesion. In the second process step, the metal is heated up and due to thermal contact of polymer and metal the matrix of the thermoplastic composite material melts. The plasticized material flows into the cavities by applying an external joining force. After resolidification a strong and durable connection is formed, which is mostly based on mechanical interlocking [25].

For the surface structuring of the metal several strategies can be used. When using continuous wave (cw) single-mode fiber laser beam sources, the material is ablated in a linear fashion at high scanning speeds by a combination of sublimation and melt removal. With a tightly focused (30–40 μm) and fast scanned (>10 m/s) laser beam the metal is partially vaporized and the resulting sublimation pressure presses the melt from the base of the structure to the edge of the structure, where part of the melt solidifies as it is expelled. The depth of the structure can be increased by repeated passes of the laser beam and at the same time an undercut is formed by the material solidified at the neck of the structure. The cavities with a drop-shaped cross section enable a reproducible bonding of the plastic in the sub-sequent joining process. The structure sizes are typically in the range of structure depths from 100 to 150 μm and structure widths between 30 and 50 μm. Due to the combination of

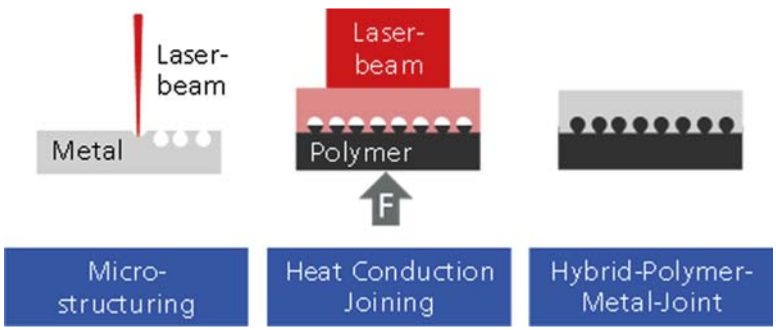

FIG. 1.32 Process principle of laser based polymer metal joining.

sublimation and melting, the process speed is much faster compared to conventional structuring processes (Fig. 1.33).

Using ultrashort pulsed lasers in the femtosecond and picosecond pulse duration range self-organizing microstructures can be generated in the metal surface. During the ablation of metals with ultrashort laser pulses the formation of numerous self-organized microstructures can be observed e.g. mounds, spikes, micro- and nanoripples or cone-like protrusions (CLP). The structure is characterized by a random orientation and an extremely enlarged surface with a high surface roughness due to nano-substructures covering the microstructures (Fig. 1.34). In contrast to the microstructuring approach with fiber lasers, the achievable joints strengths are even higher due to the higher structure density. Depending on the material combination, loads of more than 25 MPa are achievable for tensile shear load. For pure shear load joint strengths of nearly 50 MPa are possible. Due to low process speed compared to cw-structuring, the ultrashort pulsed microstructuring approach is only suitable for applications where high process speeds are not required but the priority is set to achieve extremely high joint strengths [26].

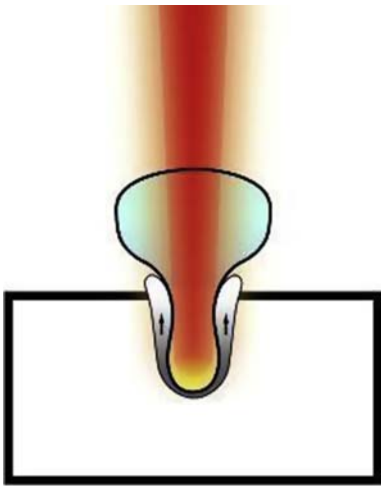

FIG. 1.33 Laser surface structuring for polymer-metal joints using cw-lasers.

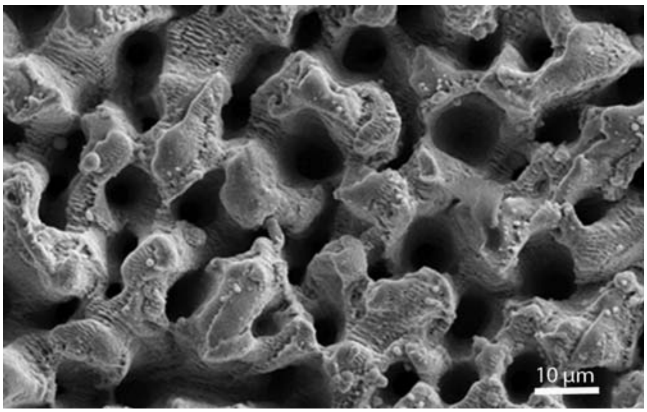

FIG. 1.34 With ultrafast lasers structured surface for polymer-metal joints.

After micro structuring of the metal surface both polymer and metal components have to be pressed together. In the thermal joining process of plastic-metal hybrids, the thermoplastic polymer is plasticized by applying heat and the metal surface and its cavities are wetted with molten plastic by applying joining pressure. When the plastic solidifies, a connection is formed which is based on a form fit or chemical and physical interaction. For this process the energy input can be applied via different methods, e.g. ultrasonic joining, induction joining, heating element joining and laser joining. When the process is optimized, the type of heating has a negligible influence on the achievable composite strengths and should be adapted to the respective application.

Using laser radiation as an energy source for joining of plastic-metal hybrids, the energy is introduced into the joining zone via laser heating. Here two different irradiation strategies can be used. For laser transmission joining, a laser-transparent plastic material faces the beam source and transmits the incoming laser radiation. The transmitted radiation is then absorbed on the metal surface. The heat output in the metallic joining partner is proportionally transferred into the plastic by heat conduction at the interface. The plastic melts, wets the metal surface and flows into any existing surface structures by the applied joining pressure. This process is only applicable for laser-transparent plastics with a transparency of at least 20% and therefore not suitable for most FRP.

Alternatively, for laser heat conduction joining, the metallic joining partner is irradiated directly and the plastic component is melted by heat conduction through the metal. Especially for carbon fiber reinforces polymers this strategy favorable, because the optical properties of the plastic have no influence on the joining process and the process is only dependent on the heat conduction properties and the material thickness of the metal. For both irradiation approaches, sufficient thermal contact between both joining partners is necessary.

Besides direct thermal joining processes, it is also to include the joining process into the forming part of the polymer component, e.g. injection molding or compression molding. Therefore micro structured metal parts can be placed into a molding tool and the joining takes place as molten plastic penetrates the structures during the forming process. In order to guarantee the filling of the micro-structures the metal parts need a certain temperature, to avoid solidification of the melt on the cold metal surface.

5.7 Laser sources for laser joining processes

According to the different process parameters, different laser beam sources are used for laser joining. Continuous beam sources are particularly suitable for laser soldering due to the long joining times. With the exception of a few special cases where cw-Nd:YAG lasers are used, only high-power diode lasers are used for this purpose today. These diode lasers consist of GaAs semiconductor components, which, as so-called semiconductor single bars, today emit powers up to several 10 W up to 100 W. The wavelength of these diode lasers can be adjusted by selecting the doping and layer sequence in the semiconductor. For material processing, diode lasers with wavelengths of $\lambda = 809$ nm, 940 nm and 980 nm are usually offered today. Due to their design, the emitted light has an elliptical beam shape and must first be converted to line or circular form with suitable optical elements before it can be used. By interconnecting several bars via polarization and wavelength coupling, outputs in the multi-kilowatt range are now achieved. Since fiber-coupled systems are generally

FIG. 1.35 Fiber guided diode laser. *Source: Laserline.*

easier to integrate into production machines for industrial use, diode lasers are increasingly being offered as well. With newer developments of diode lasers and their combination to higher powers the beam quality is rising continuously, so that fiber diameters less than 100 μm are available even at higher laser power (Fig. 1.35).

For laser beam welding of metals in the past lamp-pumped pulsed and cw Nd:YAG lasers have been used. With the upcome of diode pumped solid state lasers continuous wave Nd:YAG lasers with high beam quality are increasingly used for cw welding. In all solid-state lasers, the beam is transported to the processing location via an optical fiber. If the laser system is designed accordingly, several processing stations can be supplied by a single beam source. The switching time from one fiber to the next is only a few 10 ms. After being coupled out of the fiber, different processing heads such as simple focusing optics or complex beam scanners can be connected, depending on the application. In some cases, the laser beam can also be split into several partial beams and thus produce several welds simultaneously.

Lamp-pumped solid-state lasers have a limited beam quality due to their design, which limits the achievable focus diameter. To achieve smaller beam diameters, diode-pumped lasers must be used. In the case of continuously emitting diode-pumped solid-state lasers, two system variants have become established for this purpose, both of which deliver very high beam quality in the fundamental mode range and accordingly enable very small spot diameters in the range of 20–50 μm in the focus of the processing lens. With the resulting high laser beam intensities, new process principles can be realized and the thermal impact of the laser welding process can be further minimized.

The disk laser consists of a wafer-thin crystal disk made of Yb:YAG, which sits on a heat sink that dissipates the heat and also serves as a resonator mirror. The crystal is excited by almost coaxial irradiation with a diode laser. The beam quality is much higher than that of a rod laser and independent of power. This is due to the fact that - unlike in a rod laser - almost no thermal lens is formed in the disk to deform the laser beam. There is also a temperature difference between the top and bottom of the disk. However, this difference runs axially in the direction of the laser beam and not radially, as in the rod. Thus, the optical path is the same for all photons and the beam is not deformed.

Very high beam qualities can be achieved with fiber lasers, where the laser light is generated inside the fiber. This makes the entire resonator concept simpler and less complex than with other laser types. Fiber-coupled single emitter diodes with a very long lifetime are used as pump sources, which pump the active fiber - doped with rare earth elements such as Ytterbium (Yb), Erbium (Er) or Thulium (Tm). Due to the long resonator length and small fiber dimensions, passive cooling is sufficient for fiber lasers, which simplifies integration into production lines. By combining fiber modules, the laser can be scaled up into the high multi-kilowatt range while maintaining good beam quality.

Beside the different laser set ups and principles, recent developments on high power lasers are related to the use of new laser wavelengths. Especially for joining copper based materials green and even blue laser wavelengths lead to a significant increase in the absorption [27]. Thus blue high power diodes as well as frequency doubled solid state lasers become important candidates for high efficiency laser joining processes. Moreover diode and solid state lasers in the mid-infrared spectral range from 1.5 to 2 μm allows a low energy joining process for polymers with hidden joining zones in the middle of the part at the contact interface of the joining partners. So new wavelengths and higher laser powers will enlarge the application areas for high quality laser joining processes.

6. Summary

Highly brilliant laser beam sources such as multi-kilowatt fundamental mode fiber lasers and disk lasers as well as fiber-guided diode lasers with high beam quality and power have helped laser joining technology to become a widely established industrial technology. Due to low-cost systems and the possibility to guide the laser beam in flexible fibers, these tools can be integrated into simple handling and assembly equipment. The technology has become established in a variety of application areas, such as the automotive industry, electronics, ship and aircraft construction and medical technology. Especially in the field of energy technology, such as Li-ion batteries and fuel cells as well as the corresponding electronic components, laser joining technology is increasingly used due to the material and component friendly energy supply. With new wavelengths in the blue spectral range as well as in the mid-infrared, the areas of application are further expanded through increased process efficiency and improved reproducibility.

References

[1] A. Paul, T. Debroy, Free surface flow and heat transfer in conduction mode laser welding, Metallurgical Transactions B 19 (6) (1988) 851−858.
[2] P. Stritt, R. Weber, T. Graf, S. Müller, C. Ebert, Utilizing laser power modulation to investigate the transition from heat-conduction to deep-penetration welding, Physics Procedia 12 (Part A) (2011) 224−231.
[3] DIN 32511.
[4] C. Benter, D. Petring, Investigation of the transition from heat conduction to deep penetration welding with high power diode lasers, in: Proceedings of Lasers in Manufacturing, vol. 3, Springer, 2005, pp. 67−72.
[5] E. Beyer, Schweißen mit CO2-Hochleistungslasern. Technologie Aktuell, VDI-Verlag, 1987.
[6] R. Fabbro, Melt pool and keyhole behaviour analysis for deep penetration laser welding, Journal of Physics D: Applied Physics 43 (44) (2010).

[7] M. Eboo, W.M. Steen, J. Clark, Arc-augmented laser welding, in: Proc. 4th Int. Conf. On Advances in Welding Processes, UK, 9–11 May 1978, 1978, pp. 257–265.
[8] D. Petring, Hybrid laser welding, Industrial Laser Solutions (2001) 12–16.
[9] D. Petring, C. Fuhrmann, Hybrid laser welding: laser and arc in concert, The Industrial Laser User (33) (2003) 34–36.
[10] D. Petring, C. Fuhrmann, N. Wolf, R. Poprawe, Progress in laser-MAG hybrid welding of high strength steels up to 30 mm thickness, in: Proceedings of 26th Interna-Tional Congress on Applications of Lasers & Electro-Optics ICALEO 2007, Orlando, USA, 2007, pp. 300–307.
[11] A. Olowinsky, A. Boglea, J. Gedicke, Innovative laser welding processes, Laser Technik Journal 5 (2008) 48–51.
[12] A. Blom, P. Dunias, P. van Engen, W. Hoving, J. de Kramer, Process spread reduction of laser microspot welding of thin copper parts using real-time control, Proceedings of SPIE 4977 (2003) 493–507.
[13] S. Hollatz, P. Heinen, E. Limpert, A. Olowinsky, A. Gillner, Overlap joining of aluminium and copper using laser micro welding with spatial power modulation, Welding in the World 64 (2020) 513–522.
[14] R. Martukanitz, I. Stol, J.F. Tressler, C.J. Warren, Development of the laser stir welding process for aluminum laser beam welding, in: Proceedings of 24th International Congress on Applications of Lasers and Electro-Optics (ICALEO 2005). 31 October 31 – 3 November 2005, Miami, FL., USA, 2005, pp. 712–718.
[15] A. Boglea, L. Bosse, A. Olowinsky, S. Bou, Fiber laser pick-and-join tool for welding of thermoplastics, in: Proceedings of the 25th International Congress on Applications of Lasers and Electro-Optics (ICALEO 2006). 30 October – 2 November 2006, Scottsdale, AZ., USA, 2006, pp. 383–388.
[16] J. Gedicke, A. Olowinsky, J. Artal, A. Gillner, Influence of temporal and spatial laser power modulation on melt pool dynamics, in: Proceedings of the 26th International Congress on Applications of Lasers and Electro-Optics (ICALEO 2007). 29 October – 1 November 2007, Orlando, FL., USA, 2007, pp. 816–822.
[17] F. Schmitt, Laserstrahl-Mikroschweißen mit Strahlquellen hoher Brillanz und örtlicher Leistungsmodulation, Dissertation, RWTH Aachen, 2012 (in German).
[18] W.-S. Chung, A. Haeusler, A. Olowinsky, A. Gillner, R. Poprawe, Investigation to increase the welding joint area with modulated laser beam welding over gap, Journal of Laser Micro Nanoengineering 13 (2) (2018) 117–125.
[19] A. Gillner, J. Holtkamp, C. Hartmann, A. Olowinsky, J. Gedicke, K. Klages, L. Bosse, A. Bayer, Laser applications in microtechnology, Journal of Materials Processing Technology 167 (2-3) (2005) 494–498.
[20] L. Bosse, A. Schildecker, A. Gillner, R. Poprawe, High quality laser beam soldering, Microsystem Technologies 7 (5-6) (2002) 215–219.
[21] P. Hofmann, R. Dierken, E. Beyer, T. Morris, The story of laser brazing technology, in: SPIE LASE, SPIE Proceedings, vol. 10, SPIE, 2012, pp. 823–903.
[22] K. Loeffler, The latest laser applied technology of the auto industry in europe on the example of the body in white applications of the volkswagen golf V, Yosetsu Gakkai Shi/Journal of the Japan Welding Society 73 (8) (2004) 15–18.
[23] U.A. Russek, A. Palmen, H. Staub, J. Pöhler, C. Wenzlau, G. Otto, M. Poggel, A. Koeppe, H. Kind, Laser beam welding of thermoplastics, Proceedings of SPIE - The International Society for Optical Engineering 4977 (2003) 458–472.
[24] A. Boglea, A. Olowinsky, A. Gillner, Extending the limits of laser polymer welding using advanced irradiation strategies, Journal of Laser Micro Nanoengineering 5 (2) (2010) 138–144.
[25] K. Van Der Straeten, S. Britten, F. Schneider, S. Janssen, C. Engelmann, Laser technology for lightweight industrial applications, Kunststoffe International 106 (5) (2016) 13–17.
[26] K. van der Straeten, J. Sparla, A. Olowinsky, A. Gillner, Influence of self-organizing microstructures on the wettability of molten plastic on steel for hybrid plastic-metal joints, Welding in the World 63 (5) (2019) 1431–1441.
[27] S. Engler, R. Ramsayer, R. Poprawe, Process studies on laser welding of copper with brilliant green and infrared lasers, Physics Procedia 12 (Part B) (2011) 339–346.

CHAPTER

2

Electron beam welding

Uwe Reisgen, Stefan Gach

Welding and Joining Institute, RWTH Aachen University, Aachen, Germany

1. Introduction

Electron beam welding (order number acc. to DIN EN ISO 4063:51), also abbreviated as EBW, uses highly accelerated electrons in a vacuum as energy carrier. The energy which is released when these electrons are decelerated, is used to melt the material [1]. An electron beam welding system can be divided into three functional units, Fig. 2.1 [3]:

- Beam generation
- Beam guidance (beam focusing, deflection, guidance)
- Beam effect

The beam generation follows the principle of a cathode ray tube. A negatively charged tungsten ribbon cathode is heated via Joule resistance heating thus allowing electrons to escape from the tungsten metal lattice. The electrons are accelerated in the direction of the

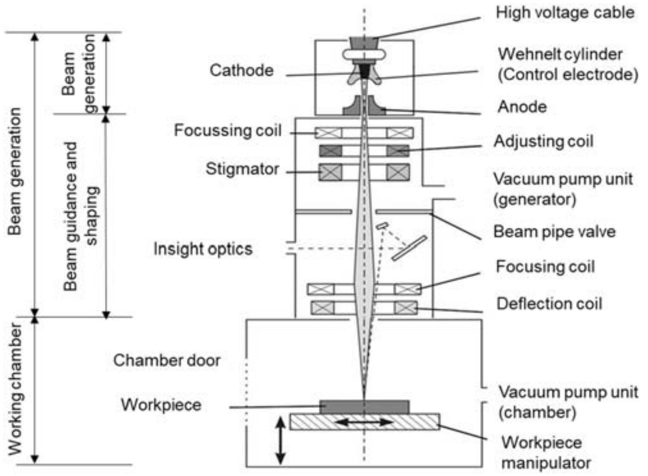

FIG. 2.1 Systematic set-up of an electron beam welding machine [2].

https://doi.org/10.1016/B978-0-12-820787-1.00002-4

anode by the electric field resulting from the potential difference between the negatively charged cathode and the anode at earth potential and reach speeds of up to 2/3 of the speed of light depending on the acceleration voltages. The intensity of the electron beam can be influenced by the voltage of the negatively charged control electrode (relative to the cathode). The arrangement of the beam generation from the three elements cathode, control electrode and anode is called triode. The electrons leave the beam generator area via the anode bore in the form of a bundled electron beam which then passes through various electro-optical systems. The function of these systems is to shape and focus the electron beam on its way to the workpiece as required for the specific application and to deflect it statically or dynamically from the beam axis if required.

Both the process of beam generation and beam guidance takes place in a vacuum, since on the one hand which is oxygen present during beam generation oxidizes and thus destroys the cathode, and on the other hand a collision of the emitted electrons with air molecules would lead to divergence of the beam. In addition, the electrons would lose their kinetic energy due to the impact reactions with the air molecules which would then no longer be available for material processing [4]. The focusing coil (or focusing lens) consists of ring shaped wire windings, surrounded on three sides by high permeability iron which coaxially encloses the beam path. When energized, the focusing coil generates a magnetic field that acts like a focusing lens. The electrons leave the focusing coil on slightly curved spiral paths without loss of speed. The electron beam resembles a cone standing on its tip [4]. The electro-optical systems use the principle of the Lorenz force which acts on electrons when they pass through an electromagnetic field. Depending on the direct current (lens current) flowing through the ring coil, the strength of the electromagnetic field is influenced which in turn affects the amount of Lorentz force acting on each electron in the electromagnetic field. Thus, by changing the lens current, the opening angle of the "beam cone" and thus the distance of the smallest diameter to the focusing coil can be controlled. Thus, focusing on varying working heights or welding in the defocused area is possible.

A deflection system is arranged in the beam path below the focusing lens. It consists of four pairs of coils, alternately connected and each wound around an iron core. The deflection system is arranged coaxially around the beam path and the coil pairs are orthogonal to each other in the main axes X and Y. When current flows, a pair of coils generates the electromagnetic field which deflects the beam out of the beam axis. By combining both pairs of coils, controlled by a function generator with amplifiers, the coils deflect the beam at any angle between the main axes at constant current flow. If dynamic alternating currents are applied to the coils, the beam can oscillate. By varying the phase and frequency, different pendulum figures are achieved [4].

The deflection coils allow the shape of the electron beam to be varied as needed. This allows a free shaping of the heat source. High-frequency beam deflection also allows the almost inertia-free electron beam to switch between several effective points. For example, several melting pools/vapor capillaries can be kept open simultaneously. A synchronization between deflection and focus coil allows a change between high and low intensities. Thermal fields can thus be applied simultaneously next to high intensity weld pools [3].

2. State of research on electron beam welding

In the time from 2013 until today, more than 100 scientific and technical publications related to electron beam technology have been published. These can be assigned mainly to the 3 main topics Materials, Simulation and Processes which have been adopted as subchapters in the following.

2.1 Publications related to materials

A more detailed review of the materials-related publications shows that the main focus is on the structural materials steel and aluminum on the one hand. On the other hand, titanium and its alloys can unite the highest number of publications and show the importance of the electron beam in the welding processing of this refractory metal. A decisive role in this respect is certainly being played by the system-immanent vacuum of the EB process, see above which favors the processing of this oxygen-affine material group. The other publications cannot be clearly assigned to one material group. Worth mentioning are the nickel materials and magnesium materials. All of these investigations use the electron beam primarily as a tool for processing the materials, or for investigating material-specific imperfections, etc. For this reason, no detailed evaluation of the contents will be made here.

3. Publications related to simulation

Simulation-based research makes it possible, based on theoretical models, to investigate the processes in the vapor capillaries which have a temperature of several thousand degree Celsius and in the surrounding melt mantle. These processes are difficult to measure. In the following, individual examples will be presented:

3.1 Transmissivity of the vapor channel

Novokreshchenov and Rodyakina [5] present a theoretical analysis of the kinetics of the interaction of particles in the vapor capillary during deep penetration welding in the PC constrained position. Their findings can be summarized as follows:

In the upper part of the capillary, at a particle density in the vapor phase between 10^{16} and 10^{17} cm^{-3}, the vapor phase is almost transparent for electrons, as a result of which the energy density of the beam remains almost constant. If the energy density in the lower part of the capillary increases significantly (between 5×10^{18} and 5×10^{19} cm^{-3}), a significant energy exchange takes place through interaction of the electrons with the vapourous material. The relevant particle density depends on the size of the molecule in the vapor: The highest energy input in the vapor phase occurs at 5×10^{18} cm^{-3} for iron and titanium, but at 5×10^{19} cm^{-3} for copper, molybdenum and aluminum.

3.2 Melt pool dynamics and kinetics of the vapor capillary

Huang et al. [6] present a mathematical model for the three-dimensional representation of the capillary and the melt pool dynamics taking into account the effects of energy and mass flow in the melt. A novel physical heat source is used which represents the self-consistent capillary and weld pool dynamics at EBW. The weld seam dimensions and the coupling dynamics between vapor capillary and weld pool during electron beam welding in a Ti6Al4V alloy could thus be successfully predicted, as shown by good agreement with experimental and literature data. The main conclusions are: The frequency of dynamic oscillation of the vapor capillary, measured at 1–2 KHz, with a characteristic period in the order of milliseconds, was unstable for the entire penetration process, except at the beginning of welding. The main forces controlling the stability of the vapor capillary are the recoil pressure, the surface tension and the impact force of the liquid flow. Increasing the welding speed or reducing the surface tension weakened the vapor capillary vibrations. The characteristic flow patterns in the weld pool were numerically determined and systematically discussed for the first time. The flow of the fluid is complex and varies considerably with the welding time; two typical vortices often occur at the back of the weld pool, and high-speed flows with a velocity of 5 m/s or even more occur at the wave fronts on the capillary interface. During the welding process, obvious lateral flows around the capillary become visible in the weld pool. The most important driving forces of the weld pool dynamics, including recoil pressure, surface tension and thermocapillary force, were determined and discussed. The recoil pressure is responsible for the penetration force which determines the penetration depth of the capillary. In addition, the recoil pressure is a main driving force of high velocity fluid flows. A decrease of the surface tension and the thermocapillary force weakened the flows in the weld pool. The transient capillary and weld pool dynamics during the EBW process were self-consistent and strongly coupled.

Luo et al. [7]. used the model of Huang et al. [6]. and derived findings on the melt pool dynamics and kinetics of the vapor capillary as a function of varying frequencies and oscillation radii of circular beam oscillations. Experimental and theoretical studies using the titanium alloy TiAl6V4 as an example are the basis. Circular beam deflection can influence the movement of high temperature areas on the capillary wall and contribute to an increased homogeneity of the weld pool dynamics behind the capillary. However, the temperature distribution in the vapor capillary remains irregular when welding with beam oscillation and the temperature profile tends to oscillate. Low-frequency oscillation can lead to an increase in welding defects such as porosity, spiking and spattering, as it increases the tendency for capillary oscillation. High frequency beam oscillation could stabilize the capillary to a certain degree and positively change the fluid flow of the weld pool by regularization. The radius of beam oscillation should be chosen neither too small nor too large, too small a radius increases the susceptibility to welding defects, too large a radius significantly reduces the penetration depth.

These findings are not new from a welding technology point of view, but the visualization of the flow effects of the melt along the wall of the vapor capillaries and the temperature distribution which substantiate the empirical values with physical effects, is interesting.

Based on the physical understanding of the electron beam welding process, a dual direction energy uniformity criterion (DDEU criterion) was developed which describes the degree of energy uniformity in the welding direction and orthogonally to it. This allows a selection of stable oscillation parameters. The essential process parameters, including beam scanning frequency and radius, can be successfully optimized with the proposed criterion.

Should this criterion prove to be robust also for other oscillation figures and materials, this would be a possibility to reduce cost-intensive experimental studies.

3.3 Equivalent heat source and residual stress simulation

The welding simulation pursues the goal of determining the geometric parameters of the molten pool, the temperature cycles in the molten pool and the heat-affected zone (HAZ) in its immediate vicinity. It can be divided into the three areas of process simulation, design simulation (or structure simulation) and material simulation.

The process simulation shows the melting zone geometry, process efficiencies and process stability, while the material simulation shows the microstructural state in the cooling melting zone and the heat affected zone, the hardness that develops and the hot and cold crack tendency. The design simulation (or structure simulation) is used to determine residual stresses and distortion and to estimate their influence on strength and stiffness. For this, information about the heat source in equivalent form and the relevant mechanical material characteristics including the transformation strain are required from the process [8].

Unwanted component distortion is a major quality issue in welding technology. Therefore, the mathematical prediction of residual stresses and distortion caused by the welding process is important. For the welding simulation of the temperature field, the residual stresses and the distortion the structure simulation is used [9].

A substitute heat source is usually used to simulate the temperature field. The temperature field simulation represents the central aspect of the welding simulation, as the subsequent mechanical behavior of the component is derived from these calculations. For the mathematical description, the equivalent heat source method is used with the aim of obtaining a representation of the heat distribution in the component as close to reality as possible.

In the electron beam welding process, a narrow conical molten pool is generated inside the component. To be able to reproduce this, the model of a conical heat source is used. A near-surface area dominated by heat conduction is modeled on the Gaussian-normally distributed double-ellipsoid volume heat source according to Goldak, Fig. 2.2.

Reisgen et al. [10]. show the thermal influence on distortion and residual stresses on the basis of EB welds in carbon manganese steels. They define the Goldak heat source as a hemispherical volume source with normal distribution of heat density in radial direction according to Ref. [8]:

$$q_G(x,y,z) = (1 - EBP) * \frac{Q * 6 * \sqrt{3}}{\pi * \sqrt{\pi} * R_G^3} * \exp\left(-3 * \left(\frac{x - x_0}{R_G}\right)^2 - 3 * \left(\frac{y}{R_G}\right)^2 - 3 * \left(\frac{z}{R_G}\right)^2 \right) \quad (2.1)$$

R_G describes the radius of the heat source. Because of the structure of the simulation it is sufficient to consider it as spherical. For this reason, the geometry is determined by the

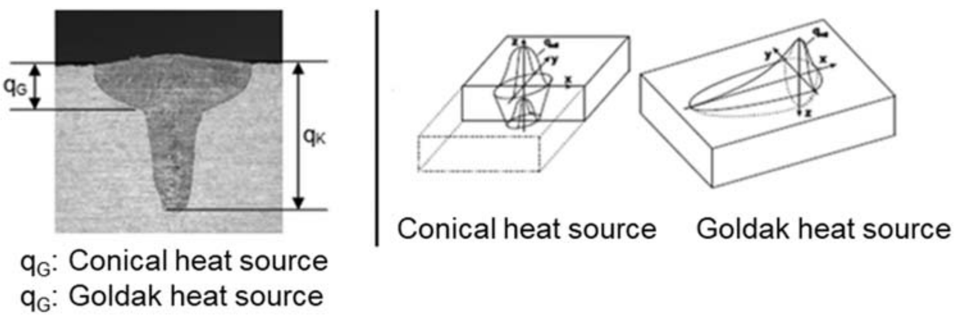

FIG. 2.2 Cross section of an electron beam weld (left); Mathematical models of heat sources in comparison (right) [9].

radius. The term *EBP* describes the percentage of the Goldak or conical heat source. The energy input is introduced via the power Q. The conical heat source is composed as follows:

$$q_k(x,y,z) = EBP * \frac{Q*3}{\pi * H * R_0^2} * \exp\left(-3 * \left(\frac{x-x_0}{R_0}\right)^2 - 3 * \left(\frac{y}{R_0}\right)^2 \right) * \left(1 + 0.5 * \frac{H-z}{H}\right) * step(H-z) \tag{2.2}$$

Apart from the coordinates x, y and z, the conical heat source is composed of geometrical factors that determine the inclination of the cone flanks. In addition, the geometric outer contour is described by the cone radius R_0 and the weld seam depth H. The step function is a measure for a simulation specification so that the heat input in direction z never exceeds the weld depth H.

The simulation of the equivalent heat source is performed using the program "Ansys CFX 17.2", a simulation software that uses the finite element method.

A.Bonakdar et al. [11] demonstrated the application of a three-dimensional finite element model, implemented in the ABAQUS software, for the analysis of residual stresses and distortion in electron beam welded gas turbines made of crack susceptible Inconel-713 The heat source consists of a superposition of a hollow sphere with linear distribution and a conical heat source with Gaussian distribution which was constructed on the basis of macrosections taken from a transverse sections. The model was validated experimentally by means of the borehole method and by comparison with the literature. It showed a sufficient average accuracy in predicting the residual stresses and distortions to be expected.

A hollow sphere instead of a spherical heat source model with Gaussian distribution, as classically described by Goldak et al. [12]. has the elegance to avoid the problem of heat accumulation which is caused by the superposition of the spherical and conical heat source. This probably allows a less fault-sensitive calculation of the temperature distribution.

Based on the previous investigations (see above [10]) Reisgen and Bleck [13] extended the residual stress simulation which previously only considered thermal stresses, by the influence of transformation stresses. The material basis of the investigations are dual-phase steels which are welded by means of the electron beam and subsequently investigated by means of the borehole method with regard to the resulting residual stresses. The calculation of the residual stresses is carried out by means of a sequentially coupled 3D finite element model. In order to accurately predict the sharp temperature gradients that occur during beam welding across the different welding zones, a movable volumetric heat source model was developed that combines a spherical and a conical thermal flow distribution. The temperature profiles calculated with this heat source model matched the measured temperatures. The simulated weld geometry was compared with the microscopic images of the weld cross-section to validate the parameters of the heat source model. The time-temperature history recorded at each node of the FE-mesh served as input for the metallurgical and mechanical analyses, in which the kinetics of the phase transformations, the volumetric dilatations and thus the residual stresses in the weld were calculated.

A metallurgical framework was established, into which the development of different phase fractions and the thermal and transformation stresses were introduced. The simulations showed that the electron beam welding process leads to a constant heat input along the weld seam which is associated with high longitudinal tensile residual stress along the welding direction. The martensite transformation which took place in the melting zone and the heat-affected zone during the rapid cooling cycle of the weld, led to massive volumetric expansion in the weld areas near the base material. As a result, high longitudinal residual stresses in the weld center and residual compressive stresses in the transverse direction were observed. The experimental and simulated results showed a similar trend in residual stresses with marginal differences due to the limitations of the quantification methods used.

The results show that the solid-state phase transition occurring during cooling in a welding process can have a great influence on the level of the resulting residual stresses and also that a prediction of the resulting residual stresses is possible by simulation, as the comparison with the experimental borehole test results shows.

4. Process-related publications

The electron beam, in industrial use for welding since the late 1950s [4] and continuously being developed further since then, has been overshadowed in public perception by the futuristic-looking laser. M. Magda poetically describes electron beam welding as "the rose that blooms in the shadows", because, on the one hand, the public is easily dazzled by the laser beam and its marketing in the form of publications and, on the other hand, the process takes place in a more or less dark vacuum chamber [14]. This rather unobjective, poetic description may be polemically exaggerated, but it nevertheless hits the core of the current state of research. Over the last 30 years, the price per kilowatt laser beam power has fallen continuously and the beam quality and efficiency of commercially available lasers has increased significantly. Consequently, lasers have dug out more and more fields of application for EB. Nevertheless, applications in which the electron beam is the undisputed technology of choice remain, such as the processing of refractory metals (titanium and niobium) by application in a vacuum, as well as copper and aluminum thick sheet metal joints which can only be processed by the laser to a limited extent due to the low energy coupling. The possibility of beam modulation allows the free design of the heat source shape as well as the high-frequency time-based splitting of the beam into several beam effect areas, such as melting baths or, depending on the intensity, pre- and post-heating fields, just to name a few potentials. Nevertheless, there are areas, especially in the field of analytics, where the laser has an advantage due to its better accessibility to the process.

5. Process diagnostic — online monitoring

Electron beam welding (EBW) is a well-established welding process that is used in the production of cost-intensive individual components and small series of thick-walled components or components made of materials that benefit from the joining process in the process-immanent vacuum. In addition, there are also a number of series and large series components that are welded using the process and which benefit from the advantages such as high seam quality, low thermal influence due to heat input with high intensity and excellent welding speeds and possibilities for beam manipulation.

In both cases, documentation and assurance of the seam quality is becoming increasingly important. In particular in the field of welding in series production, seamless monitoring and documentation of the weld seam quality at component and seam level is already being demanded and is implemented in various industrial production fields.

In arc processes, this can be done by recording and comparing the measurable process variables with empirically developed value ranges. When using laser beam welding (LBW), there are also proven systems that record direct process emissions and evaluate them in a comparable manner. In addition, further data from upstream sensors (e.g. seam tracking) and downstream sensors (e.g. filling degree determination for quality assurance and documentation) can be used. In some cases, direct control loops have already been implemented on the basis of the recorded data. In laser beam welding, for example, there are measuring devices that can record the welding depth achieved during the process and, in the event of deviations, directly adjust the beam power. By means of an envelope curve comparison with values of a number of good welds, a production-related assessment of the joining quality of the current series can be carried out and, possibly, the general inspection effort can be reduced or limited to those components which have shown irregularities in the QA data. In addition, with suitable component identification, data can also be stored subsequently down to the component and seam level, thus ensuring production documentation.

In contrast to the welding processes presented as examples above, electron beam welding has an enormous backlog demand with regard to direct process monitoring. Although most of the welding machines record machine parameters to varying degrees and with varying temporal resolution, direct welding process measurement variables such as process signals are not usually recorded. The comparison of measured process variables with envelopes of good welds for process-accompanying quality assessment and documentation does not usually happen. The recording of process emissions in the area of optical radiation in the spectrum from UV to IR which has been used in the LBW area for decades, has not been carried out in electron beam welding up to now. Methods based on triangulation and time-of-flight measurement which have recently been used for in-process capillary depth measurement at the LBW, have also not been tested yet. One of the reasons for this is that a reliable protection of the optical sensors and optics against process emissions (metal vapor) has not been realized with sufficient service life and safety. Nevertheless, the electron beam offers some secondary effects which can be used analytically for process diagnostics:

5.1 Secondary effects

At the point of impact of the electron beam on the sample surface, the accelerated electrons of the beam (primary electrons) interact with the atoms of the sample. In this interaction, the kinetic energy of the primary electrons is converted into heat of the atoms of the sample, based on several physical principles, Fig. 2.3.

- Excitation of oscillations in molecules or phonons in the solid body
- Excitation of collective oscillations (plasmons) of electrons in the valence or conduction band
- Excitation of an electron from one energy level to another, or from one shell to another
- Ionization of atoms by the interaction of primary electrons with electrons of the atomic shell.

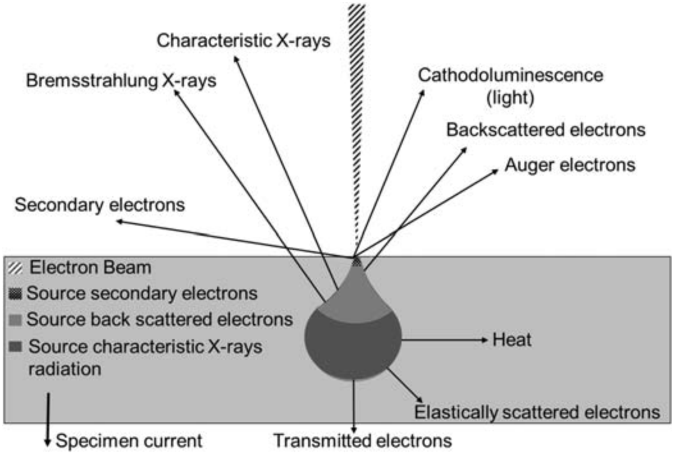

FIG. 2.3 Secondary effects at the point of impact of the electron beam [15,16].

Besides energy conversion, several other effects occur which can be measured and used for process diagnostics. For example, the primary electrons are partially deflected without energy loss by the influence of the Coulomb fields of the atomic nuclei and are sometimes scattered back from the sample (back-scattered electrons (BSE)), unless they interact again with the plasma in the vapor channel or with the melt at the capillary wall with energy loss [15].

The energy transfer can lead to an emission of electrons in the outer shells of the atoms which leave the sample as so-called secondary electrons (SE). Secondary electrons have only a lower energy (<50 eV) as backscattered electrons and can only leave the sample from a small depth [16]. The ionization of the atoms leads to the formation of Auger electrons and characteristic X-rays. The latter is element-specific and allows a quantitative analysis of the composition of the sample body when detected, e.g. by energy dispersive X-ray analysis (EDX) performed by scanning electron microscopy (SEM) [16]. In addition to element-specific X-rays, X-braking radiation is also released during the deceleration of highly accelerated electrons. Furthermore, cathodoluminescence occurs, the emission of photons whose wavelengths are sometimes in the visible spectrum.

Backscattered electrons, secondary electrons and X-rays can be measured by special detectors. The line-by-line scanning of the sample surface allows a spatially resolved assignment of the signals to the respective position of the electron beam. This information of BSE and SE can be measured by means of detectors and optically reproduced by image processing as gray scales, as is already used by commercially available systems, for example. There are many possible applications, for example for joint search and for detailed positioning of the beam. For this, the beam is guided over the seam in a grid pattern before welding, the seam is automatically detected by image processing and the deflection coils can compensate for waviness or similar. Online welding observation is also possible. For this purpose, the electron beam is scanned defocused over the joint 10% of the time, the backscattered electrons are processed for imaging and a picture of the capillary, weld pool, seam joint and weld seam is created, Fig. 2.4. An evaluation of the weld seam quality based on the cover layer can be done by subsequent scanning of the weld seam after the actual welding process [17].

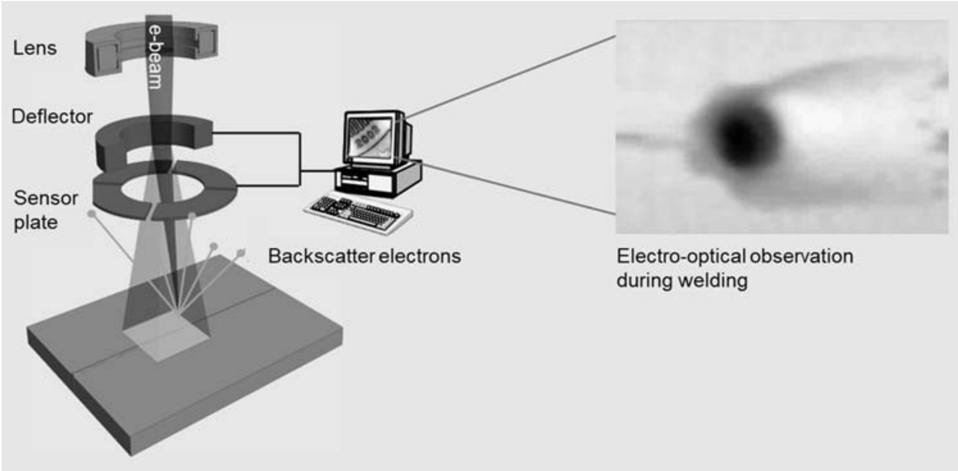

FIG. 2.4 Online-Elo Weld seam observation [17].

5.2 Backscatter electron signal

D.N. Trushnikov et al. [18,19] showed investigations of the formation of the secondary current signal in the plasma during electron beam welding with oscillation. This is composed of backscattered and secondary electrons, distinguishable by their energy level. A ring-shaped "collector" positively biased at 50V was positioned over the welding process. The secondary current signals were recorded on a computer system via a multi-channel analog-digital interface. A synchronous storage method was used, a modification of the synchronous detection method, whereby the detected signal is converted into a square wave with a low duty cycle. The reference signal is shifted by a value t less than the period T of the oscillation of the deflection coil, multiplied by the secondary electron signal data(t) and then integrated (summed or averaged) over time. The method provided information about the processes taking place in the steam channel during oscillation and could be used to analyze the synchronization of the secondary current pulses with the oscillation frequency of the beam in the deflection coils. Thus it was possible to describe the range of maximum power distribution. This area moved along the walls of the vapor capillary during the oscillation process of the electron beam. For each position of this area the cumulative value of the current collected in the plasma was displayed.

This data can help to select different oscillation parameters. Several high-frequency pulses can be identified which are related to the oscillation frequency. The signal is composed of harmonic multiples of the oscillation frequency. Simple deflection figures such as longitudinal and transverse oscillation were investigated. In the case of longitudinal oscillation along the seam, the secondary electron signal contains both the first and the second harmonic; in the case of an underfocused beam, the first harmonic is dominant, whereas in the case of an overfocused beam, the second harmonic is dominant. A possible explanation is that in the first case the beam interacts primarily with the front capillary wall, whereas in the second case the beam interacts with both the front and the rear capillary wall.

Furthermore, the author [20] presents an evaluation based on wavelet analysis of the secondary electron signals and compares this with the evaluation based on the classical Fourier transformation.

5.3 Ion current

The vapor capillary in electron beam penetration welding is filled with a metal vapor plasma which is transmissive for the electron beam depending on the particle density, see above. Since, among other things, the vapor pressure is a relevant variable in the equilibrium of forces and acts in all directions, it also spreads spherically above the capillary. This plasma cloud is enriched with positively charged ions which, similar to backscattered or secondary electrons, are information carriers from the place of their origin.

Trushnikov et al. [21] positioned a negatively polarized electrode over the weld seam and were thus able to collect ions from the plasma cloud above the vapor capillary. This electrode was shielded against the primary electron beam, so that no negative effects occur. By means of the "coherent accumulation" method, the random impulses were converted into evaluable signals. In addition, an evaluation of maxima, in absolute value and time interval, was carried out in comparison to the changes in the deflection coil, on the one hand and the size of the capillary in the molten pool on the other. This technology enables new control possibilities such as the determination of the focus during welding and the analysis of seam defects. For example, the transition from a weld-in to a through-weld can be measured in a drop of the ion current.

5.4 X-ray braking radiation

The work of Varushkin et al. [22]. was aimed at evaluating the signal of the X-ray braking radiation from the processing zone which can be measured during electron beam surfacing with solid wire. During the experiments, a scintillation detector based on monocrystalline iodine-caesium and silicon photomultiplier was used to record the X-ray signal. Circular oscillations of the electron beam produced the informative component. The synchronous storage method was used for a mathematical evaluation of the recorded signal. It was shown that the dependence of the processing result - the relative delay value $\Delta t0/T$ of the function $S(\tau)$ on the filler wire deviation ΔL - can be approximated by a linear function. The application of the braked X-ray signal in the control systems enables the positioning of the filler wire during electron beam cladding.

5.5 Magnetic field

Bagshaw et al. [23]. reports on the origins and effects of magnetic fields on the electron beam process. Magnetic fields can be caused by residual magnetism in the workpiece or by large thermoelectric currents which are generated when welding dissimilar materials in mixed joints. It is generally assumed that a magnetic flux density of 5 Gauss or less is an acceptable level of magnetism in materials for EB welding. If the magnetization is above this, a demagnetization method or active compensation should be used.

Unfortunately, the authors omit a detailed description of the compensation. Such a compensation which could be imagined via beam deflection in the coils, requires a precise knowledge of the position and magnitude of the magnetic fields in the workpiece and their effect on the electron beam. Also the authors do not provide any justification for proposed limits of the magnetic flux of 5 Gauss.

One possibility for compensation was provided in 2016 by Laptenok et al. [24]. They presented a method to avoid the influence of magnetic fields on the position of the electron beam during the welding process.

When highly accelerated electrons hit a workpiece, they convert their kinetic energy into heat. During these physical processes, the electrons are decelerated which leads to the release of X-ray braking radiation. The intensity of the X-ray braking radiation depends on the surface through which the radiation flow passes. A deflection of the beam from the optical beam axis, for example by a magnetic field, leads to a change in this radiation component. This was detected by means of an X-ray detector which was equipped with a slit diaphragm in the direction of the beam. The seam was scanned upstream and the deflection was detected by the intensity of the X-ray radiation. Using an approximation formula to calculate the angle of deflection and the misalignment of the electron beam from the optical axis, a mathematical model of the effect of the magnetic field induced by thermoelectric currents was created.

Comparable studies show [25] the relationship between changing X-rays and the position of the beam relative to the joint in the absence of melt by analyzing mathematical models. For this purpose, the authors used a scintillator based on sodium iodine as an X-ray detector which is activated by thallium and makes the signals electronically evaluable by means of a photoelectric effect. In contrast to the work of [24], the deflection of the beam was recorded online during welding. The upstream measuring beam which was temporarily pulled out of the vapor capillary to perform the measurements, led to a systematic error in determining the position of the beam relative to the joint and higher signal noise, as the research group demonstrated in an earlier publication [26]. Furthermore, this approach required additional commutated operations to ensure sufficient velocity of the beam movement which required the use of additional equipment and resulted in lower reliability. Instead, the possibility of obtaining the required information directly from the welding channel by means of self-powered X-rays was analyzed as an alternative. For this purpose, the influence of edge offset of the joining partners as well as dissimilar welded joints of copper and steel were analyzed. Edge offsets only showed an influence on the X-ray intensity up to welding depths of up to 15 mm.

5.6 Secondary signals on the underside of the weld seam

Varushkin et al. [27]. examined four secondary signals on the underside of the weld seam for welds with the capillary opened downwards with regard to their suitability for monitoring complete penetration. These were electron and ion current in the root-side plasma, the passage current and penetrating X-rays. Similar to the detection of the backscatter and ion current signals on the upper side of the workpiece, a preloaded detector was mounted below the workpiece. The passage current was detected with the same detector. This was shielded by a precharged metallic grid which in turn was covered with a metal foil. The X-ray braking radiation was detected directly at the root of the seam using a scintillator based on a single-crystal-activated cesium iodide and a photomultiplier.

The secondary electron flow showed a pulsed signal on the detector in the root-side plasma when the capillary was fully penetrated. This signal coincided with the frequency of the deflection coils, whereas it remained unchanged with only partial penetration. Ion current as well as electron current did not show any dependence on the oscillation of the deflection coil. The author suspects that the passage current is more strongly influenced by fluctuation effects of the fluid dynamics in the vapor channel and thus no statistical dependence can be detected. The X-ray retardation, on the other hand, provides a signal close to full penetration and its fluctuations reflect the penetration depth of the vapor capillary.

5.7 Goniometry

During electron beam welding, process instabilities can occur which are due to the molten pool dynamics. Due to its property as a charge carrier beam, it is possible to oscillate the beam at high frequency via electromagnetic control. It is well known that the welding process can be stabilized by beam oscillation. If the aspect ratio (depth to width of the weld seam) is greater than 2, this is generally referred to as deep penetration welding. The simplified representation of the deep penetration welding process with vapor capillary usually specifies a quasi-static process, as this is sufficient for the macroscopic specification of the processes and the development of the welding geometry. In reality, the development and maintenance of the vapor capillary is a highly dynamic, non-stationary process with a complex balance of forces that has not been fully understood so far [28]. For the extension of the process parameter for EBW, a better understanding of the fluid dynamic processes around the vapor capillary on the one hand and measuring methods for monitoring the process stability in real time on the other hand are necessary. The latter serve both basic research and quality monitoring in practical application. For this purpose, a novel polarization goniometer is used which enables the determination of the inclinations of the plane of the observed surfaces and thus, in particular, the 3D monitoring of the capillary geometry with very high temporal resolution. The associated work is presented in Ref. [29]. A correlation of the geometry with the flow measurement, as is usual with EBW, and the self-luminescence of the capillary (X-rays) should contribute to a better interpretation of the melt pool dynamics. This serves to extend the analytical process model of the melt pool dynamics and its interactions with defined beam parameters on the basis of the measurement results obtained for a temporal change of the vapor capillary geometry in three spatial dimensions.

In an electron beam welding machine an atmospheric chamber was installed which allows the use of two high speed cameras. Those cameras record the X-ray luminescence of the capillary as well as the infrared luminescence in the vacuum chamber close to the process, Fig. 2.5. A scraper mirror which is positioned in the beam path and allows a concentric observation of the capillary, provides a coaxial inside view. A beam splitter allows four beam paths with polarization directions directed at 45° against each other for two-dimensional determination of the angle of the reflected beam.

First tests on welds of steel, titanium and nickel base showed that the molten surface of the resulting capillary emitted enough light in the range of 800 nm to record videos with a frame rate of several kHz. The main part of the tests was carried out on the material 1.4301 with a thickness of 10 mm.

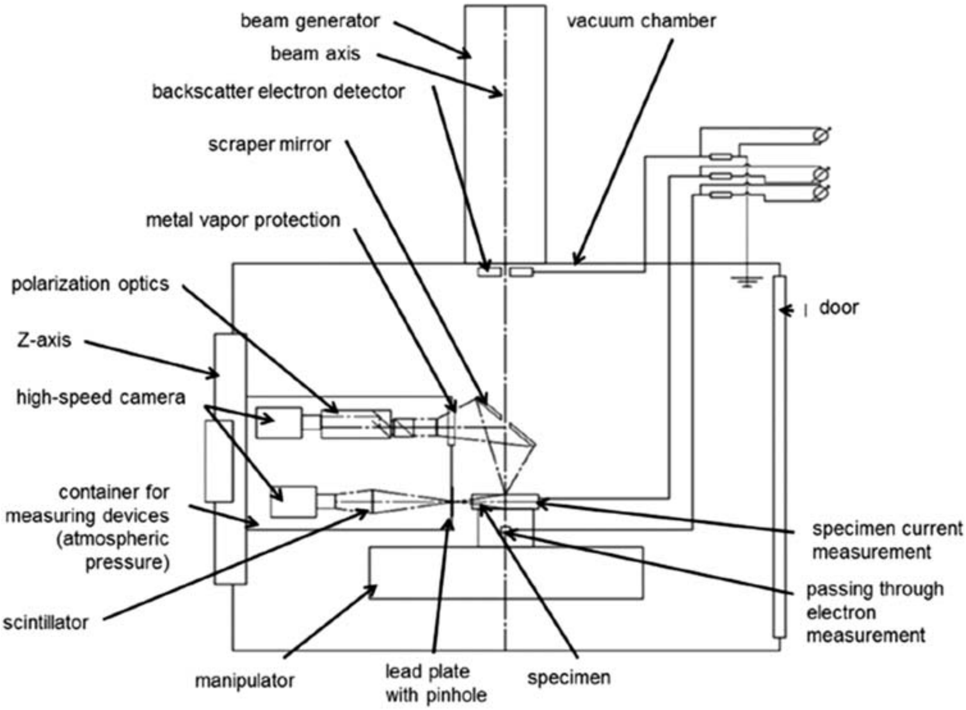

FIG. 2.5 Sketch of test stand Goniometry in [29].

5.8 Beam measurement

Electron beam welding is the preferred method for welding joints that have to meet the highest demands. Research and development and the aerospace industry place great importance on the high process reliability of the electron beam. In the automotive sector, the electron beam is convincing due to its high degree of automation in combination with its reproducible, high quality. Particularly the joining tasks in the aerospace industry require a joining tool that meets the highest requirements in terms of seam quality and reproducibility in series production. To achieve this standard, an optimally set-up beam is absolutely necessary. Deviations from the intended value, resulting from changed geometric or electrical boundary conditions, can lead to drastic joining errors. With regard to constancy and reproducibility - both in mass production and in individual production - the control of the beam parameters is of great importance. A major problem with all electron beam welding machines is the objective measurement and documentation of the quality of the electron beam. Although many modern electron beam machines have a monitoring system for the electron beam, there is no standardized procedure for manufacturer-independent measurement and analysis of the electron beam. With a powerful beam diagnostic system it is possible to guarantee the high standards of seam quality and reproducibility. Such a measuring instrument is a basic prerequisite for easy transferability of processes between different plants. A simple application is for example the determination of the real focus position at high beam power.

This information is especially necessary for thick sheet metal welding tasks. Furthermore, it is possible to determine the optimum power range and the task-related best working distance. It can be verified whether a cathode or triode change was carried out correctly. Information about the change of focus shift with increasing beam current correlates directly with the geometric conditions in the triode. An incorrect installation of the cathode, a changed distance between Wehnelt cylinder and anode and an incorrect heating current can be measured immediately.

The measurement of the beam quality can basically be performed following different principles. The simplest method is the Arata-Beam-Test, in which the penetration shape is analyzed on special test plates [30]. The measurement of the electron beam with photographic/optical methods (fluorescent screen) is only possible for very low beam powers [31]. Furthermore, it is possible to derive the beam quality from the backscattered electron image of a defined geometry while the beam oscillates on a test set-up [32]. Alternatively, it is possible to measure the power density distribution directly. In this case, the beam oscillates over a pinhole or slit-aperture sensor, whereby the power density can be discretely resolved, Fig. 2.6.

Various techniques and devices for characterizing electron beams for welding have been developed over time and are discussed in Ref. [33]. The techniques used include slot, pinhole and wire rotation techniques. In each variant, the beam must be measured and the signals

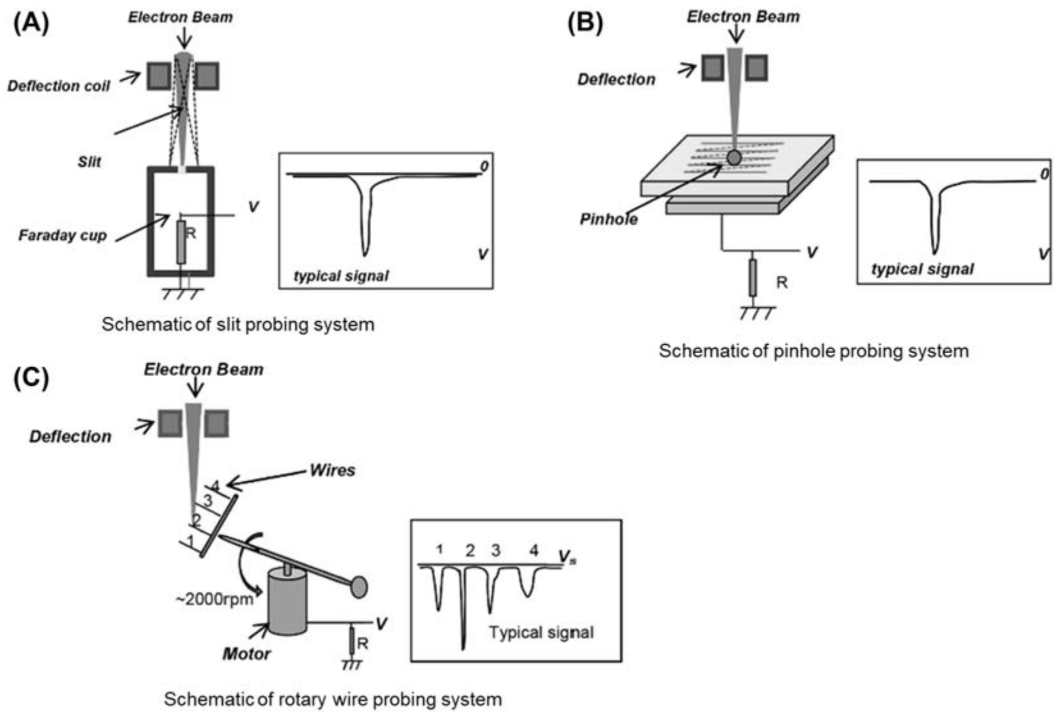

FIG. 2.6 Measuring principles of beam measurement — (A) Slit Aperture; (B) Pinhole; (C) Rotating Wire Sensor [33].

subsequently processed to obtain relevant information such as beam characteristics. The measuring systems have in common that they measure the energy distribution over the beam cross-section. For welding applications, high-energy electron beams are used which are focused on the smallest possible beam cross-section in order to achieve the high energy densities required for deep penetration welding. In order to avoid damage to the measuring equipment, the beam is scanned over the measuring device at high speed (slot and pinhole method), or a rotating wire is passed at high peripheral speed through a stationary beam (wire rotation method) [34], as used for example for measuring non-vacuum EB systems [33].

In the slot aperture method, the beam is guided across a narrow gap under which a Faraday cage with measuring resistance to earth potential is located. The advantage of the slit diaphragm is the rather simple and compact design of the measuring device, the immunity to electrical noise and signal degradation by backscattered electrons, since the sensor itself is encapsulated and shielded. The pinhole method is based on a similar principle, except that the slit is replaced by a pinhole which must be much smaller in diameter than the smallest beam diameter to be measured. The beam is guided over the pinhole in a grid pattern. Since only a small part of the beam power is detected at each pass, the voltage signal at the measuring resistor is very small and requires amplification. The pinhole method is susceptible to changes in the geometry of the pinhole, e.g. due to melting, clogging, breakout, etc. which results in a changed or reduced resolution [33].

The rotation wire method is based on a patent from 1970 by Sanderson et al. [35] and allows qualitative statements about beam shape and current distribution and quantitative measurement data regarding the beam width and is only mentioned here for completeness. Currently there are several commercial systems available on the market which have published their results in beam measurement in the last years:

5.8.1 Diabeam-system − combination of slotted ring aperture and pinhole

The beam measuring system "DiaBeam" combines two different measuring principles. With the integrated slit aperture in circular form and a centrally arranged pinhole aperture, the electron beam is analyzed within the sensor. The compact design of the sensor allows measurements, even in small electron beam chambers. In order to prevent damage or destruction of the measurement sensor due to the very high energy density of the electron beam, the electron beam is moved very shortly over the sensor. The electron beam moves at a speed between 200 and 800 m/s. Between two measurements the electron beam is directed onto a cooled copper block. The energy introduced here is dissipated by a cooling water circuit. The basic measured value obtained is the power density of the electron beam. Based on this value it is possible to calculate the beam diameter. With repeated measurements at different working distances by moving the sensor in the height axis, the beam caustics and the expansion of the beam, the so-called aperture angle, can be determined, Fig. 2.7.

By separating signal recording, transmission and amplification, measurements at high beam powers up to 30 kW are possible. A circular slit aperture in the sensor helps the system to calibrate the electron beam automatically. The online display of the electron beam diameter makes it possible to determine the deviation of the electron beam from its ideal geometry. The rotationally symmetrical Gaussian intensity distribution of an optimally aligned beam is clearly visible. Besides the intensity distribution, it is also possible to determine the maximum

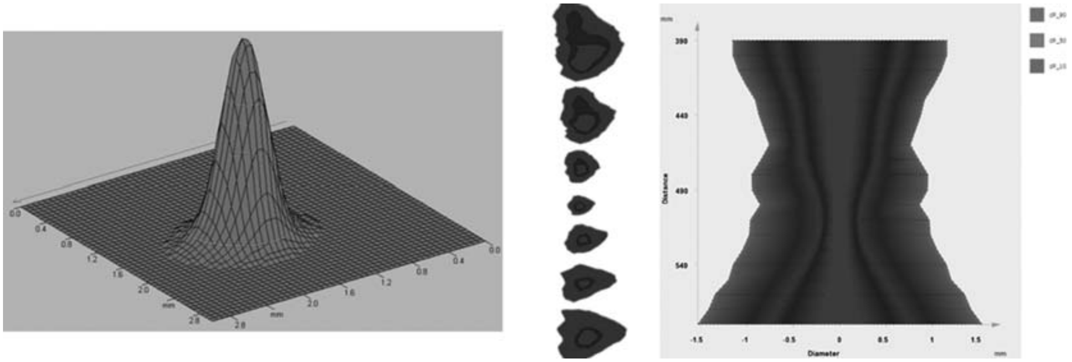

FIG. 2.7 Exemplary measurement result of the Diabeam system - power distribution (left), beam caustic (right).

intensity, the beam shape and the beam diameter. With this system, electron beam machines or different operating conditions can be compared. By shifting the height of the sensor via the integrated Z-axis, the measuring system can measure the caustics of the electron beam and, among other things, the ideal focal point can be determined [36,37].

5.8.2 Slit apertures and beam on circular path

Kaur et. Al. presented a different approach to the characterization and quality assurance of electron beams in Refs. [33]. For this purpose, they formed a correlation of beam characteristics and the resulting weld quality. Here, a slit-based measuring device records a small part of the electron beam by means of four radially arranged slit apertures which are also designed as Faraday cages. The beam is guided on a circular path over the radial slit diaphragms. Due to the radial arrangement, the energetic resolution of the beam in both main axes can be measured in only one circular overflow in the slit apertures which are offset by 90°. The acquired signals are processed to generate a series of features by means of wavelet transformations. Energy distribution between different decomposition stages was derived from wavelet coefficients. A correlation between beam characteristics and weld quality is established by radiographic testing and microsections. Using the parameter weld depth, the authors showed that wavelet transformations are suitable for the characterization of electron beams to map defined parameters of weld quality [38].

5.8.3 TechScan - rotating disk scanner

Oving [39] showed another possibility for beam measurement by means of a rotating disk scanner, called TechScan. This scanner analyses the beam in a stationary state without deflection. Up to now, the only solution for systems without active beam deflection was the rotating wire sensor or a rotating slotted disk aperture. However, these sensor designs are susceptible to high thermal stress and only provide a single angular position scan. The TechScan system is based on a rotating disk sensor with a large dissipation area that allows medium power beams to be analyzed. The instantaneous heat load on the disk at high speed (6000 rpm) is relatively low due to the power distribution of the beam and is distributed over an annular section of the disk. The rotary disk sensor can measure beams of 15 kW beam power without the need for water cooling. The turntable is equipped with a large number of pinholes and rotates directly above fixed Faraday cages. The pinholes in the disc are arranged with a radially increasing distance to the center and allow a small part of the beam current to pass under the beam. The traces of each pinhole through the beam follow an arc section. The knowledge of pinhole position and angular position allows the allocation of the measured points on an XY plane and thus a measurement of the beam with respect to its power distribution.

5.8.3.1 Optical beam measurement

Tactile beam measurement systems are all limited by the beam impact of the electron beam on an aperture with more or less low power. As an alternative concept, Goncharov et al. [40]. shows a non-contact measuring method which evaluates light emission of the beam from free space. This occurs when the beam electrons interact with the residual gases and atoms in the vacuum atmosphere. A digital camera-based method for image generation is described which allows to obtain information about the power distribution of an electron beam by means of image processing.

To get an image, a digital camera with a long focal length lens was used. The camera was placed outside the vacuum chamber. A specially designed target was used to minimize light radiation from the area of interaction between the beam and the material. The images are taken with a stationary electron beam. A steel scale with a pitch of 0.5 mm in the field of view of the camera allows a quantitative measurement. The beam images obtained are processed by means of a graphic editor, and a mathematical treatment of the original images is carried out to quantitatively determine the beam parameters.

The amount of light from each beam point detected by the sensor is proportional to the number of interaction events between an incident (primary) electron beam and residual gases and atoms; this number in turn is proportional to the beam current at a specific point in space. The latter assumption is valid if the density of the residual gas particle distribution is kept uniform over the range of beam propagation. Each beam image is subjected to a mathematical treatment by software. The idea of such a processing is based on the assumption that the pixel luminance in the image is directly proportional to the intensity of the light radiation hitting the photosensitive sensor during exposure. This assumption is valid if a characteristic curve of the sensor is straight. It should be noted that the image is actually an integral beam projection onto the detector plane. The image therefore contains information about a current density distribution over all beam cross sections parallel to the detector plane. To obtain information about the current density distribution over the entire beam j(x,y,z) or any beam cross section j(x,y) at a given distance z above the focal position, three- or two-dimensional tomographic reconstructions are necessary. To solve such a problem without an a priori assumption regarding the shape of the restored function, it is necessary to obtain at least some object projections. Nevertheless, it is possible to determine a number of quantitative beam parameters using a single beam projection.

The proposed method for determining beam parameters can be used for monitoring the plant condition, for example to determine the accuracy of the triode system setup and the cathode condition from the behavior of the power density distribution.

Although the presented work only evaluates beams of up to 6 kW, the system will certainly be able to analyze higher power beams in the future.

5.9 Beam quality

An ideal electron beam for welding applications involves a symmetrical power distribution of the beam in both spatial directions and has a high power peak in the beam center. As a result, it generates high intensities at its focal point. Real electron beams however, diverge from this ideal. This is due to various influences. On the one hand, the raw beam already varies before being projected through the lens system due to a fluctuating installation position of the filament in the filament carrier, the filament carrier in the triode system or due to manufacturing tolerances of the filament itself. This affects the position in the triode system and the virtual crossover. The varying raw beam leads to beam aberrations on its way through the electro-optical imaging system which influence the shape of the spot in the focus.

Modern electron beam systems use a triode system for beam generation and control of the beam power. Electrons are emitted from the hot cathode by the thermoelectric effect. The electrons are accelerated by the expanding electric field toward the circular anode and pass the anode in the form of a directed beam. The potential difference between anode and cathode depends on the electron gun and is typically between 60 and 175 kV. The Wehnelt cylinder serves as a control electrode: an adjustable voltage opposing the cathode (approx. max. 2000 V), generates a negative electrostatic field and influences the number of electrons passing and thus regulates the beam current.

The research group led by Reisgen and Böhm [41] is investigating the influence of the cathode on the welding result which is the central part of the beam generator and the only consumable part of a vacuum electron beam system. Thus, manufacturing tolerances, deviations from the installation position, deformations due to thermal expansion, and discontinuous wear of the cathode are analyzed. They evaluated their results with the Diabeam measuring system.

5.9.1 Influence of mounting position

Displacement of the cathode in the z-direction, e.g. due to an incorrect installation position, causes a change in the beam current which can, however, be adjusted by the programmable logic controller (PLC) by regulating the voltage at the control electrode. But as the control electrode also has a focusing function, the crossover in the beam generator also changes slightly with the potential change and thus changes the energy distribution in the focal spot. Even a deviation in the position of 0.01 mm leads to significant changes. Especially at the high acceleration voltage of 150 kV, the beam diameter can vary by up to 50%. Studies have shown that when using a precision mounting device for filaments, a deviation of ±0.01 mm in the z-direction can be expected when the same cathode is repeatedly mounted. For processes with very high beam quality requirements, it is necessary to check the mounting position, e.g. under a measuring microscope in an air-conditioned measuring room. While changing the mounting position in the z-direction primarily affects the focus diameter, the energy distribution in the spot is changed by an inclined installation. The ideal Gaussian beam current distribution is deformed linearly or triangularly. The detection of such deviations is difficult without a beam measuring device, since they do not necessarily lead to significantly different welding depths. Therefore they are small or even not detectable if only a wedge sample is used. Furthermore, fabrication characteristics of the cathode have an influence on the position of the filament in the electrostatic field of the electron gun. This includes a possible crowning of the emission surface as well as deviations from specified bending angles which cause a change in position when the filament is fixed. Due to differences in the thickness of the filament, different surface temperatures can occur in the heated state. In addition, thermal expansion and production-related residual stresses can lead to deformations that are difficult to quantify. However, the effects on the beam quality are comparable to those of faulty installation [41].

5.9.2 *Influence of cathode wear*

Damage to the cathode has a significant influence on the beam quality. The authors observed an increase of the spot diameter by 0.15 mm at an initial spot of 0.3 mm after 16h welding of steel. Several possible phenomena are suggested as the cause of this 50% increase in spot diameter: Firstly, the high operating temperatures result in a slight evapouration of the material despite the high vapor pressure of the tungsten in a vacuum. The authors estimate the decrease to be 12.7 $\mu g/(mm^2h)$ at 2652 °C operating temperature, resulting in a cathode decrease of 10^{-3} mm/h. Secondly, recrystallization processes lead to a change in the microstructure and, as a result, to a change in the surface topography. Third, ion bombardment damages the cathode at its point of impact, sometimes knocking out tungsten atoms and leaving a crater landscape. The ions come from the welding zone and are additionally accelerated toward the cathode by the acceleration field in the triode system. The higher the vapor pressure of the processed material, the higher the number of ions hitting the cathode. This also explains the shorter life cycles of a cathode when processing aluminum or even magnesium [41].

Oving [39] shows alternative measurement data for cathode wear, measured with the TechScan system after 0, 10h and 20h cathode heating. The cathode was baked out to 130 mA at 45 kV acceleration voltage. The author reports a material loss of 0.03 mm after 10 h and 0.06 mm after 20 h of cathode heating. Thus, the results are in a comparable order of magnitude to the measurement data of the research group around Reisgen and Böhm [41]. The results showed that for the same focus setting, the peak current density decreases with the life of the cathode. This is due to the change in cathode geometry, whereby cathode retraction induces a change in the geometry of the extraction field. This change in the field geometry leads to a change in beam formation and the position of the virtual radiation transition (crossover). The decrease of the peak current density is accompanied by an increase of the beam diameter. With the same focus current setting, the weld spot shows the same changes, lower peak current density and larger diameter. This development is directly related to cathode retraction.

5.10 Plasma cathode

A plasma electron source is a device used to extract electrons from the plasma environment. It thus replaces the thermally heated filaments in a thermionic system. There are different designs and excitation methods of the plasma. A plasma chamber in a vacuum, the so-called discharge chamber, is the central component and is fed with a gas, for example compressed air or argon gas, via a vacuum feedthrough. It can be designed in the form of a hollow cathode with a cylindrical anode. The supplied gas is ionized, for example by an

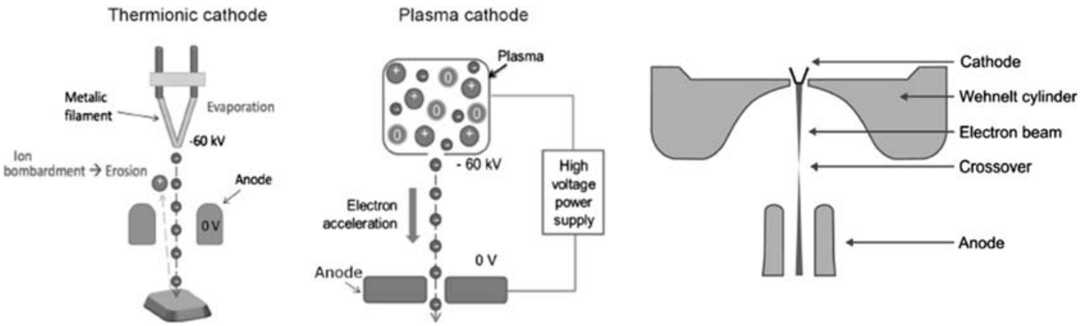

FIG. 2.8 Principle sketch thermionic cathode (left), plasma cathode (middle) as diode systems [42], Principle sketch triode system thermionic cathode (right) [41].

applied DC voltage or, in more recent designs, also by an HF signal. Excited plasma with low temperature and low pressure is created. The electrons move away from the atoms and begin to move freely together with the neutral atoms. The electron beam is extracted from the plasma chamber into the vacuum chamber. Similar to a thermionic EB gun, this is done by a potential field, for example 60 KV between the plasma cathode and an anode, often in the form of a grid anode, Fig. 2.8. Geometry and design of the plasma chamber influence the properties of the electron beam and are the object of current research. Usually, low pressures are used in the plasma chamber to minimize gas leakage through the acceleration gap into the beam generator space, as this could lead to a high voltage flashover.

Plasma cathodes have several advantages over conventional thermionic cathodes. On the one hand, their lifetime is unlimited, whereas thermionic cathodes are worn out in their lifetime due to evapouration and erosion which is accompanied by a change in beam properties as [39,41] impressively demonstrate, see above. On the other hand, conventional thermionic cathodes require a third electrode for power control, called the Wehnelt cylinder or control electrode. However, this leads to the formation of beam aberrations and makes the triode system susceptible to high-voltage flashovers. A plasma cathode, in contrast, can be designed in the form of a diode system consisting of cathode and anode. A high-frequency (HF) modulation can be used for power control which, among other things, greatly simplifies beam pulsing. In principle, thermionic cathodes may also be operated as diode systems, but these systems are sluggish in terms of power ramps, as these can only be controlled by the magnitude of the acceleration voltages, and therefore do not play a noteworthy role in welding. Current research work is primarily concerned with the layout and design of a plasma cathode.

Rempe et al. [43]. measure the electron beam of a hollow plasma cathode in terms of diameter and beam quality (brightness). Diameter and beam quality of the plasma hollow cathode are compared with measurement data of a Lab6 cathode and a tungsten filament. The measured data was collected with a slot sensor and a wire rotation sensor. The beam quality was determined between 10 and 60 mA at an acceleration voltage of 60 kV. It was found that the beam quality of the plasma cathode is comparable to thermionic cathodes based on Lab-6, while both are superior to the beam quality of tungsten filaments. The authors contrasted the measurement results with cross sections of weld samples in order to visualize the effect.

The results are promising, but the plasma emitters still have to prove themselves at higher beam currents as well as higher acceleration voltages.

Del Pozo et al. [44]. presented a novel high-frequency (HF)-excited plasma cathode-electron beam gun design operating at a frequency of 84 MHz. The electrons were extracted from the plasma chamber and accelerated by an electric field applied in a vacuum chamber at a pressure of 10^{-5} to 10^{-6} hPa, producing a collimated electron beam. Air at a pressure of about 0.5 hPa was used as ionized gas. The EB gun was operated at 60 kV accelerating voltage and generated beam powers of up to 3.2 kW. The modulation of the HF signal was used to control the beam power. The advantages of this system are the avoidance of beam aberration and the fast pulsing of the beam. The beam can be switched on in 200 ns and off within 800 ns. Due to the HF excitation, the emissivity of the plasma cathode can be changed quickly compared to the conventional control of triode guns. This leads to a faster and more precise control of the beam parameters, not only compared to DC plasma source guns but also to thermionic cathode guns. In some applications, the beam needs to be switched on and off quickly which can be done easily and cost-effectively in less than 1 μs. There is no delay for cooling-down a metal cathode as with thermionic emitters and no capacity to be discharged as with rectified plasma source guns [45]. The use of an HF signal offers additional advantages, such as controlling the beam power by amplitude modulation and controlling the average beam power by pulse width modulation. However, the minimum beam pulse duration is determined by the decay time of the plasma in the chamber after the HF excitation voltage is switched off. At atmospheric pressure this is about 20 ns, since the ions are recombined with the gas molecules of the environment. At low pressure this can take several milliseconds. The diameter of the plasma chamber has been kept small so that the ions collide against the walls and recombine faster which accelerates the plasma extinction when the excitation is stopped. The dimensions of the plasma chamber are preferably chosen to be smaller than the average path length of the ions in the plasma to ensure that the plasma decay occurs shortly after the RF excitation is stopped.

Derived from the findings, Ribton et al. [42]. present the development of a genetic optimization algorithm which forms an interface to simulation-based electron beam gun design. This provides a rapid method for the design of gun shapes and allows radical design approaches to be explored. The design process is outlined and the practical implementation is described. The influence of different design features was also investigated:

- Varying plasma pressure from $\sim 10^{-2}$ to 2×10^{-1} mbar
- Plasma excitation power from ~ 5 to 100 W
- Beam extraction aperture with a diameter of 0,7−2 mm
- Plasma chamber geometry: flat electrode and hollow electrode design

It was found that low plasma pressures produce higher beam currents, both in a flat plasma chamber and in the hollow cathode design. Low pressure was also a better option to avoid metallic deposits on the plasma chamber wall caused by the high energy electrons. The beam current also increased with the HF excitation power in all design configurations. The maximum applied power was 100 W, and the maximum current was generated at 38 mA at 60 kV from a hollow electrode design with 2 mm aperture. Hollow cathode designs generated higher beam currents than the flat electrode design. It was observed that some of the hollow cathode dimensions are critical to increasing the extracted beam current. The gap between the end of the hollow cylinder and the diaphragm electrode was varied and an optimum was found at about 7 mm. The beam current increased with the diameter of the opening in the diaphragm electrode. An aperture diameter of 0.7 mm generated about 5 mA less current than the 2 mm aperture diameter, while all other plasma parameters remained fixed. However, there is a limitation on how much the diameter of the aperture can be increased: the quantity of gas flow must be sufficient to keep the pressure in the plasma chamber constant in order to maintain a permanent discharge.

Koval and Vorobyov [46] showed a wide aperture electron source (750 × 150 mm) with a lattice plasma cathode based on a low-pressure arc discharge and a large cross-sectional beam through an outer foil window. However, this was not used for welding, but, for example, for processes such as radiation curing of natural latex without chemical additives that accelerate the vulcanization process, the formation of carbon structures in polyvinyl chloride films and electron beam disinfection of agricultural products such as barley, and is mentioned here only for the sake of completeness. The beam was brought to atmosphere through a thin film (30 μm thick) of AlMg-2 stretched over a supporting grid.

5.11 Non-vacuum electron beam welding technology (NV-EBW)

Electron beam welding in atmosphere (NV-EBW) combines the known advantages of electron beam welding in vacuum with the possibility to work under normal ambient pressure. The process has a high energy efficiency and the available beam power allows very high welding speeds. However, the beam quality and the welding result depend on many influencing variables.

The electron beam which is guided from the vacuum to atmosphere over several pressure levels and used there, is an ideal tool for welding conventionally manufactured and formed sheet metal parts. The upper bead of the weld seam is similar to that of an arc weld and thus does not have the narrow, deep geometry typical of electron beam welding in a vacuum. The use of the NV-EBW process is recommended where high welding speeds and short working times with not too great seam depths are required. Thin sheet welds up to 5 mm are the preferred application. Another application for the NV-EBW is the welding of tailored blanks which are widely used by car and plant manufacturers.

Hasselt et al. presented the various application possibilities of the NV-EB process and projected the results into a possible future process chain which serves several applications with only one plant technology. In addition to welding of thin steel and aluminum sheets, primarily in the automotive industry, the authors focused on the robustness of the NV-EB process with respect to process tolerances and the good gap bridging capability which makes this process ideal for welding thermally cut sheets in I-butt joint. With reference to an older publication of the research group [47,48], the NV-EBW technique could be used for thermal cutting with the aid of a vacuum pot which is moved along on the underside of the workpiece and sucks the melt downwards. Since the electron beam, as a particle beam, carries a pulse, but is not effective as an expelling medium due to the low electron mass, this method must be used in this case. The method is characterized by high cutting speeds with good cutting quality. In addition to welding and cutting, the authors also mention the possibilities of heat treatment and marking of components. All these operations can be carried out in successive steps without extensive retooling of the NVEB system. Welding process, heat treatment and marking differ only in the working distance and beam current parameters. An example from crane construction served as a feasibility study of a typical process chain. For this purpose, round cut-outs in 5.4 mm thick sample sheets made of S1000QL with 420 mm diameter were first produced using NVEBC at a cutting speed of 5 m/min. In the next process step, a sheet made of S960QL with 5 mm material thickness was inserted into the cut-out in the I-butt joint and welded in place using cold wire [49,50].

The research group Reisgen, Senger, Olschok [51] show investigations on aluminum die-casted alloys by electron beam welding in atmosphere. Different casted alloys, on the one hand cast under vacuum and on the other hand cast under atmosphere, based on the alloy AlSi10MnMg are considered. It is shown that welding porosities of less than 5% can be achieved. This applies both to die cast parts with low hydrogen content and even to parts cast in atmosphere. The NV-EB process is robust against pores and blowholes caused by casting technology. As with other thermal fusion welding processes, the welding porosity increases with the hydrogen content in the base material. The welding speed as the main process parameter has a high influence on the degassing of pores when welding die cast parts. Thus, higher welding speeds have a positive influence on the welding porosity of die cast components with a higher hydrogen content. With increasing hydrogen content and slow welding speeds, micropores grow into macropores and deteriorate the mechanical properties. In contrast to pores and gas inclusions, blowholes have no direct negative influence on the weldability of die castings. As a hypothesis, it is assumed that strontium as an alloying element can increase the porosity in the weld as strontium hydroxide.

A comparison with other published work shows that the NV-EBW process achieves the welding porosities of electron beam welding under vacuum and laser beam welding at comparable die casting qualities. Its advantages are a fast and cost-effective operation for high volume production and the possibility to weld a wider range of joint configurations with one system configuration.

5.12 Additive Manufacturing

Additive manufacturing (AM), formerly known as “shape welding”, is a revived manufacturing technology that enables the production of complex geometric structures that cannot be produced in conventional ways. In addition, it offers the potential for significant savings in the area of material and reduction of processing times and throughput costs, especially for components with a high chip volume. Furthermore, additive technologies allow for promising new developments in areas such as mechanical engineering and medical technology [52].

5.13 Differentiation of AM manufacturing processes

Laser and vacuum electron beam welding have so far been successfully used with this new type of production. In principle, processes can be differentiated into powder bed-based and wire-based processes with regard to their material feed. Powder bed-based processes include selective laser melting (SLM), selective laser sintering (SLS) and (selective) electron beam melting ((S)EBM). Laser-additive-manufacturing (LAM) and Electron-beam-additive-manufacturing (EBAM) use the filler material in wire form.

There is a wide range of research work in the field of powder-based processes which will not be discussed here in favor of focusing on EBAM with direct deposition which is related to electron beam welding.

Barrier to the implementation of SLM methods in manufacturing is their low efficiency. For example, powder bed based SLM systems offer buildup rates of up to 105 cm^3/h. The most efficient additive manufacturing (AM) processes use direct deposition (DD), where powder or wire is fed directly into the laser or electron beam. Sciaky Ltd. offers such systems using a vacuum electron beam with a working space of up to 5791 ч 1219 ч 1219 mm and deposition rates of up to 3—9 kg/h. The filler wire is fed directly into the electron beam. In comparison between electron beam additive manufacturing (EBAM) and conventional manufacturing, the AM process offers not only reduced material costs, but also up to 80% faster production times compared to conventional manufacturing [53].

Both, wire and powder-based EBAM processes can process a wide range of materials such as steel, Ti, Cu, Al and other alloys [54—56]. Their great advantage, the processing under exclusion of oxygen in a vacuum which predestines these systems for the processing of e.g. refractory metals, is at the same time their greatest disadvantage due to the limited space of the working chamber. These require additional pumps and limit the workpiece geometry.

An overview of the fields of application of wire-based - EBAM at the Nuclear AMRC (Advanced Manufacturing Research Center, Sheffield, UK) is given by Baufeld [57,58] highlighting the challenges and solution strategies. The author states that the motivation for using the EBAM process is the elimination of the production bottleneck for large forgings such as nuclear pressure vessels. These require features such as holding lugs or nozzles which are machined from the forging blank using state-of-the-art technology. EBAM offers the potential to add these features to a forging blank and thus reduce the size of the forged parts, Fig. 2.9 above. Steam generator support plates, on the other hand, contain complex trefoil features which are currently produced by the cost-intensive broaching technique and introduce high residual stresses into the component Fig. 2.9 below. In comparison, the author argues that with the competing direct energy deposition (DED) processes the higher purity of the products is due to the fact that the process takes place in vacuum under exclusion of oxygen, a superior fast beam control by electromagnetic beam guidance, and higher material deposition rates. The latter is due to the higher energy intensity of the EB and the effective coupling of the beam power into any electrically conductive material such as aluminum or copper. Disadvantages are the additional costs for the provision of vacuum and radiation protection as well as the evapouration of alloying elements with a low evapouration point and the reduced cooling rates in vacuum. The author mentions the sensitivity of EBW to magnetic fields, a disadvantage compared to arc or laser-based processes which is particularly relevant for rotating components and deflects the beam away from its intended effective spot in the area of the wire nozzle. The author also discusses the phenomenon of a gradual decrease in height when creating linear wall constructions in a single direction and explains this with the direction of the material flow opposite to the beam movement. The extent of the effect is possibly related to the high welding speed and the low cooling rates in vacuum. The materials steel and the titanium alloy TiAl6V4 the latter of which is relevant for the erospace and medical sector, were taken into account.

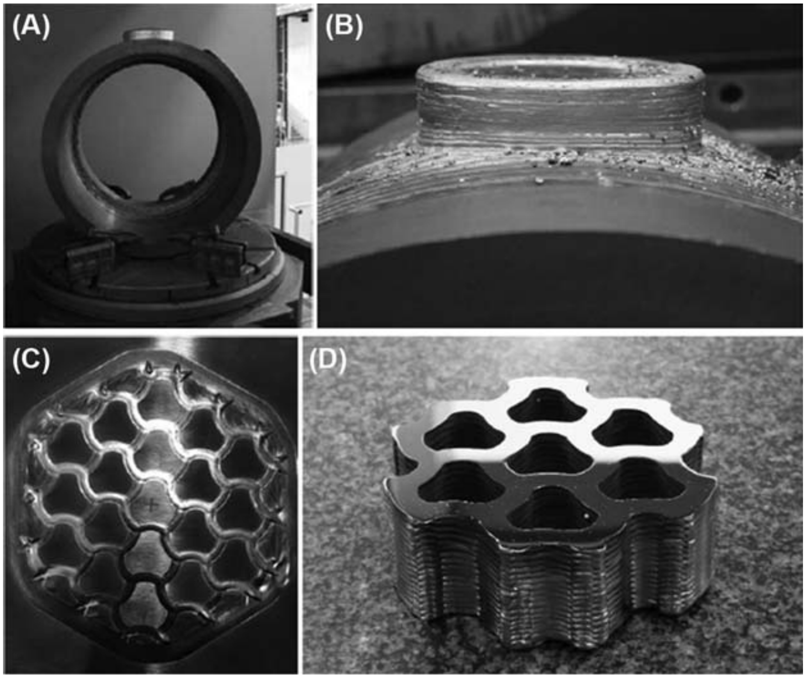

FIG. 2.9 Application examples for EBAM in the nuclear sector: Overview on a steel feature added on a cylinder (A); detailed view on the steel feature (B); Trefoil − fist two layers (C), polished cross-section (D) [59].

The application of atmospheric electron beam welding (NV-EB) for additive manufacturing is currently not yet used in industry, but there are research activities in this field, among others at the Leibnitz University of Hannover [57]. The NV-EB process with wire for direct deposition is particularly suitable for the additive fabrication of components made of copper and copper alloys which, due to the low absorption coefficient for laser radiation, can only be processed with great difficulty using the laser-based processes.

Klimov et al. [57] patented a non-vacuum electron beam welding (NVEB) approach to wire-based additive manufacturing. The NV-EBAM process is predestined for the production of components made of copper materials. The high degree of absorption of the electron beam on copper materials allows a high deposition rate and thus a high efficiency of the process. This gives the process a clear advantage over competing laser beam processes. During the experiments, a number of samples with different geometries were produced on steel substrates using CuSi3 welding wire. Tubular and conical geometries were selected which were produced by NVEB-AM using a tilting and rotating table to move the substrate. The use of the axisymmetric geometry and the tilting and rotating table allowed a simplified wire feed from only one direction. The front feed of the filler wire proved to be the most stable position during the experiments. The typical microstructure of the deposited welding samples consisted of columnar grains. The cross-section of the deposited layer showed a fine dendritic structure. Energy-dispersive X-ray analyses (Edx) show that the deposited material has a single-phase structure. The structure determination with the scanning electron microscope revealed that iron atoms diffuse in quantities from the substrate into the printed structure up to a height of about 0.88 mm.

The research group Chang, Gach, Senger [58] are showing results on 3D deposition welding of unalloyed steels on a non-vacuum electron beam system in the form of multilayer deposition welds. Linear seams consisting of up to 10 individual layers are evaluated. The tests are carried out at 150 KV acceleration voltage, a beam current of 30 mA and a welding speed of 0.4 m/min. The influences of the wire feeding speed, the height offset when building up increasing layers and the type of drop transfer of the filler wire into the melt are examined. An increasing wire feeding speed increases the material deposition and reduces the penetration in the substrate, as evaluations in the form of cross sections prove. Varying height offsets between 0.5 and 0.7 mm above the previously welded top layer do not show any noticeable effects on the outer appearance of the multilayer weld. The height of the point of wire entry into the beam path above the component determines the type of drop transition of the wire into the melt. If this is too large, a drop-shaped periodic detachment of the filler material into the melt occurs. At medium to small distance, a continuous input of the filler material into the melt is observed. If the distance becomes negative, the wire penetrates the melt and is melted by convection. A disadvantage in the latter case is that the wire is deflected by contact with the substrate plate which leads to process irregularities.

5.14 Distortion simulation EBAM

Wire-based additive manufacturing using electron beam has a relatively high deposition rate compared to other additive manufacturing processes. Similar to any other manufacturing process with heat input, repeated thermal cycles lead to plastic deformation and corresponding residual stresses in the area of heating which can lead to an unfavourable effect on component geometry. The cost of subsequent straightening is an additional factor that must be taken into account when assessing the productivity and commercial attractiveness of the process. Experiments and finite element modeling were carried out by Ref. [60] using a linear multilayer deposition on a substrate plate, creating wall like structures made of the titanium alloy TiAl6V4 to investigate the potential benefits of applying distortion control methods in the processing of W-EBAM components (wire-based electron beam welding for additive manufacturing). A number of layers were built up to understand distortion propagation. An FEA model of distortion formation in the process was developed and validated. Both the experimental results and the FEA model showed a stiffening effect with increasing structure height. The FEA model was used to investigate the results of a number of distortion reduction solutions. The most promising method was investigated experimentally. It was shown that preheating the substrate and maintaining a high substrate temperature gives the best results in terms of distortion minimization. Improvements in processing quality were also achieved by reducing processing power with increasing height to compensate for the decreasing heat sink effect of the baseplate.

6. Conclusion

Although electron beam welding is a rather old welding process, especially in direct comparison to the competing laser beam welding, there are several fields of activity in the research community. In the last 5 years, especially material-related, simulation-based or process-related publications have been published.

The electron beam is used for processing a wide variety of electrically conductive materials. Primarily these are steel and aluminum. EB-Processing plays a special role for the refractory metal titanium, which is used both in medical technology and in the erospace industry. Due to its high affinity to oxygen, the electron beam, which works in a vacuum, is predestined for its processing. The achievable high seam quality has an additional positive effect in these high-tech fields of application.

Studies based on simulation deal with different areas of electron beam welding. Some of them are dedicated to phenomena in the vapor capillaries, especially with regard to the kinetics and dynamics of capillaries and the molten pool on the one hand, or on the pressure dependency of the transmissivity of the vapor channel for electrons on the other. Studies, which focus on the generation and propagation of residual stress, neglects these highly dynamic processes above the liquidus temperature by introducing an equivalent heat source, which simulates the geometry and heat input of the vapor capillaries and the melt pool and acts as input variable for a structure simulation. The design of the equivalent heat source on the one hand and the simulation of the processes relevant for residual stress and distortion during cooling such as shrinkage and phase transformation on the other hand are fields of current research activity.

Process-related publications currently deal with different aspects such as process diagnostics, online monitoring and beam measurement. A large field of research is the evaluation of secondary parameters of the electron beam welding process for process diagnostics and online monitoring. Backscattered and secondary electrons, ions from the plasma cloud as well as the braking radiation are considered. For example, a deflection of the beam due to magnetic fields can be measured using an X-ray detector. Oscillation frequencies in the deflection coils can be measured in the backscattered electron signal. Conclusions about the behavior of the capillaries as well as melt pool dynamics can be drawn from goniometric investigations, in which a high-speed camera coaxially monitors the capillary as well by analyses of the X-ray self-luminosity.

Modern measurement technology allows to determine the beam intensity and thus to characterize the electron beam as a tool. Different beam measurement systems have been intensively investigated in recent years. They use either a slit or a pinhole aperture or a combination of both. A particular challenge is the handling of the high energy densities and beam powers that modern electron beam systems can deliver. By means of the beam measurement methods a comparison of different welding machines, the reproducibility of the beam quality after cathode change or the change of the beam quality over the lifetime of a cathode can be monitored. Different measuring systems deliver comparable results: The wear of the cathode due to ion bombardment and evaporation during high voltage flashovers leads to a reduction of the its thickness, which in turn leads to a decrease of the current density of the beam. Even a slight mispositioning of the cathode or a variation in the material thickness due to manufacturing tolerances has a great influence on the resulting beam diameter and ultimately on the welding result.

The plasma cathode promises to be an innovation in the field of electron beam welding. The electrons are provided by an excited plasma gas instead of a heated filament. The negative influences due to incorrect positioning or wear of the classical filament cathodes can thus be eliminated. The design and control of such a welding system a plasma cathode is the subject of current research efforts.

Additive manufacturing is becoming increasingly important, especially in the production of complex geometries. Basically powder bed based processes, which have their origin in prototype production, and wire based additive production are distinguished The latter has long been known in welding technology as shape welding and is experiencing a renaissance with the trend toward additive manufacturing. Although there is a lot of work on powder-based processes, the focus here is on wire-based processes, as this is related to classical electron beam welding. Possible applications of the additive processes using EB-Technology can be found wherever complexity and small quantities are required. With regard to the materials to be processed, the oxygen-affine refractory metals should be mentioned on the one hand, as well as materials which can only be processed with great difficulty with the competing laser beam processes due to their low absorption, such as copper and its alloys. The latter also speaks for the use of electron beam welding in atmosphere for additive manufacturing.

References

[1] U. Reisgen, L. Stein, Grundlagen der Fügetechnik: Schweißen, Löten und Kleben, DVS Media GmbH, Düsseldorf, 2016.
[2] U. Dilthey, Schweißtechnische Fertigungsverfahren 1: Schweiß- und Schneidtechnologien, third ed., Springer-Verlag Berlin Heidelberg, Berlin, Heidelberg, 2006.
[3] K.-J. Matthes, E. Richter (Eds.), Schweißtechnik: Schweißen von metallischen Konstruktionswerkstoffen ; mit 130 Tafeln, fourth ed., Fachbuchverl. Leipzig im Carl-Hanser-Verl., München, 2009.
[4] H. Schultz, Elektronenstrahlschweißen, in: Verl. für Schweißen und Verwandte Verfahren DVS-Verl, 2000. Düsseldorf.
[5] V.V. Novokreshchenov, R.V. Rodyakina, Kinetics of interaction of particles in the penetration channel in electron beam welding, Welding International 27 (2013) 976−979, https://doi.org/10.1080/09507116.2013.796648.
[6] B. Huang, X. Chen, S. Pang, R. Hu, A three-dimensional model of coupling dynamics of keyhole and weld pool during electron beam welding, International Journal of Heat and Mass Transfer 115 (2017) 159−173, https://doi.org/10.1016/j.ijheatmasstransfer.2017.08.010.
[7] M. Luo, R. Hu, T. Liu, B. Wu, S. Pang, Optimization possibility of beam scanning for electron beam welding: physics understanding and parameters selection criteria, International Journal of Heat and Mass Transfer 127 (2018) 1313−1326, https://doi.org/10.1016/j.ijheatmasstransfer.2018.07.014.
[8] D. Radaj, Schweißprozeßsimulation: Grundlagen und Anwendungen, Verl. für Schweißen und Verwandte Verfahren DVS-Verl, 1999. Düsseldorf.
[9] C. Schwenk, FE-Simulation des Schweißverzugs lasergestrahlter dünner Bleche: Sensitivitätsanalyse durch Variation der Werkstoffkennwerte, 2007. Dissertaionsschrift.
[10] U. Reisgen, S. Olschok, O. Mokrov, S. Gach, F. Akyel (Eds.), Simulation des thermischen Einflusses auf Verzug und Eigenspannungen in Kohlenstoff-Mangan-Stählen im Elektronenstrahlschweißprozess, 2017.
[11] A. Bonakdar, M. Molavi-Zarandi, A. Chamanfar, M. Jahazi, A. Firoozrai, E. Morin, Finite element modeling of the electron beam welding of Inconel-713LC gas turbine blades, Journal of Manufacturing Processes 26 (2017) 339−354, https://doi.org/10.1016/j.jmapro.2017.02.011.
[12] J. Goldak, A. Chakravarti, M. Bibby, A new finite element model for welding heat sources, Metallurgical Transactions B 15 (1984) 299−305, https://doi.org/10.1007/BF02667333.
[13] K. Komerla, S. Gach, F. Akyel, T. Vossel, U. Reisgen, W. Bleck, Finite element simulation of residual stress induced by high energy beam welding in dual phase steel, Lasers in Manufacturing and Materials Processing 246 (2020) 123, https://doi.org/10.1007/s40516-020-00112-4.
[14] M. Magda, Prozessbeobachtung des Elektronenstrahlschweißens in slow motion, 2018. Friedrichshafen.
[15] S. Gach, A. Schwedt, S. Olschok, U. Reisgen, J. Mayer, Confirmation of tensile residual stress reduction in electron beam welding using low transformation temperature materials (LTT) as localized metallurgical injection − Part 1: metallographic analysis, Materialprüfung 59 (2017) 148−154, https://doi.org/10.3139/120.110957.

[16] L. Reimer, Scanning Electron Microscopy: Physics of Image Formation and Microanalysis, Springer Berlin Heidelberg, Berlin, Heidelberg, s.l., 1998.
[17] C. Vogelei, Faszination Elektronenstrahl. EB-Schweißen von Großbauteilen und -strukturen, 2013 (Accessed 1 February 2020), https://www.slv-halle.de/fileadmin/user_upload/Rostock/6RST/09_Vogelei__Christian__ProBeam.pdf.
[18] D.N. Trushnikov, V.Y. Belen'kii, Investigation of the formation of the secondary current signal in plasma in electron beam welding with oscillations of the electron beam, Welding International 27 (2013) 877–880, https://doi.org/10.1080/09507116.2013.796645.
[19] D.N. Trushnikov, G.M. Mladenov, V.Y. Belenkiy, Controlling the electron beam focus regime and monitoring the keyhole in electron beam welding, Quarterly Journal of the Japan Welding Society 31 (2013) 91s–95s, https://doi.org/10.2207/qjjws.31.91s.
[20] D.N. Trushnikov, Using the wavelet analysis of secondary current signals for investigating and controlling electron beam welding, Welding International 27 (2013) 460–465, https://doi.org/10.1080/09507116.2012.715932.
[21] D.N. Trushnikov, G.M. Mladenov, V.Y. Belenkiy, E.G. Koleva, Ion current, collected from plasma above the welding zone during electron beam welding, Electrotechnica and Electronica E+E 49 (2014) 22–29.
[22] S. Varushkin, D. Trushnikov, E. Koleva, D. Shamov, Using bremsstrahlung X-Ray for positioning of the filler wire during electron beam surfacing, Journal of Physics 1089 (2018) 12009, https://doi.org/10.1088/1742-6596/1089/1/012009.
[23] Understanding the origins and effects of magnetic fields in electron beam welding, in: N. Bagshaw, C. Ribton, C. Punshon (Eds.), Proceedings of the 9th International Conference Beam Technology, TWI, Cambridge, UK, 2013.
[24] V.D. Laptenok, A.A. Druzhinina, A.V. Murygin, Y.N. Seregin, Siberian state aerospace university, Krasnoyarsk, RU, Siberian federal university, in: R.U. Krasnoyarsk (Ed.), Method to Eliminate the Impact of Magnetic Fields on the Position of the Electron Beam during EBW, 2016.
[25] V. Braverman, V. Bogdanov, Dependency of the X-ray radiation on the welding channel placement relative to the joint during electron beam welding, Journal of Physics 1089 (2018) 12006, https://doi.org/10.1088/1742-6596/1089/1/012006.
[26] V. Braverman, V. Bogdanov, V. Belozertsev, N. Uspenskiy, Tracking on the joint during the electron beam welding, IOP Conference Series: Materials Science and Engineering 155 (2016) 12023, https://doi.org/10.1088/1757-899X/155/1/012023.
[27] S. Varushkin, V. Belenkiy, D. Trushnikov, Researching signals from workpiece backside during electron beam welding in full penetration mode, KEM 743 (2017) 231–235, https://doi.org/10.4028/www.scientific.net/KEM.743.231.
[28] U. Reisgen, AIF Vorhaben 15.560N: Qualifizierung und Optimierung des Fügens mit dem Elektronenstrahl in Zwangspositionen, 2011. Abschlussbericht.
[29] U. Reisgen, S. Olschok, S. Ufer, T. Graf, P. Berger (Eds.), Observing Weld Pool Dynamics of the Vapour Capillary by Using the Real-Time Polarisation Intensity Quotient Goniometry, 2017.
[30] Y. Arata, Evaluation of Beam Characteristics by the AB Test Method, IIW-Doc. IV-340, 1983.
[31] K. Kanaya, Measure of focus properties of an electron probe by means of a shadow image, Bulletin of the Electrotechnical Laboratory (1967) 185–205.
[32] A.G. pro-beam, C. KGaA (Eds.), Elektronenstrahlschweißen: Grundlagen einer faszinierenden Technik, Eigendruck im Selbstverlag, 2011.
[33] A. Kaur, C. Ribton, W. Balachandaran, Electron beam characterisation methods and devices for welding equipment, Journal of Materials Processing Technology 221 (2015) 225–232, https://doi.org/10.1016/j.jmatprotec.2015.02.024.
[34] H. Masny, Elektronenstrahlschweißen an Atmosphäre – von der Entwicklung bis zum industriellen Einsatz, Mat.-wiss. u. Werkstofftech. 38 (2007) 528–532, https://doi.org/10.1002/mawe.200700168.
[35] A. Sanderson, J. Martin, Adams 3534387A, 1968.
[36] U. Reisgen, J.d. Vries, A. Backhaus, H.-P. Bauer, S. Ufer, B. Reichenberg, T. Schmitz-Kempen 10 2012 102 608.4 (2012).
[37] U. Reisgen, S. Olschok, S. Ufer (Eds.), Accurate Diagnostic of Electron Beam Characteristics: Electrontechnica & Electronica E+E, 49th ed., 2014.
[38] A. Kaur, C. Ribton, W. Balachandran, Development of a novel approach for characterising electron beams and quality assurance of welds, Journal of Manufacturing Processes 24 (2016) 217–224, https://doi.org/10.1016/j.jmapro.2016.09.005.

[39] P. Oving (Ed.), Development of a New Electron Beam Probing Device and Analyses Method, 2017.
[40] A.L. Goncharov, V.K. Dragunov, A.V. Shcherbakov, E.V. Terent'ev, M.A. Portnov, I.S. Chulkov, A technique to determine processing parameters of electron beams in welding electron guns, Russian Electrical Engineering 86 (2015) 594–597, https://doi.org/10.3103/S1068371215100077.
[41] S. Hellberg, S. Ufer, S. Böhm, U. Reisgen, D.E. Universität Kassel, D.E.R.W.T.H. Aachen, Influence of Fluctuating Cathode Characteristics on Beam Quality and Welding Results in Electron Beam Welding, Aachen, 2017.
[42] C.N. Ribton, S. del Pozo, D.R. Smith, W. Balachandran, Design of a Plasma Cathode Electron Gun Using Evolutionary Optimization, Aachen, 2017.
[43] N. Rempe, S. Kornilov, A. Beniyash, N. Murray, T. Hassel (Eds.), Characterisation of Electron Beams Generated by a Plasmacathode Gun: Electrontechnica & Electronica E+E, 49th ed., 2014.
[44] S.d. Pozo, C.N. Ribton, D.R. Smith, A novel RF excited plasma cathode electron beam gun design, IEEE Transactions on Electron Devices 61 (2014) 1890–1894, https://doi.org/10.1109/TED.2014.2299339.
[45] S.I. Belyuk, V.A. Gruzdev, Y.E. Krejndel, R.Y. Raznikov, Automat Weldg 47–48.
[46] N.N. Koval, M.S. Vorobyov, Possible applications of the electron source with a wide-grid plasma cathode and the output beam into the atmosphere, Journal of Physics: Conference Series 1089 (2018) 12011, https://doi.org/10.1088/1742-6596/1089/1/012011.
[47] N. Murray, A. Beniyash, R. Konya, F.-W. Bach, T. Hassel, Non-Vacuum Electron Beam Cutting, 2009. Chichago.
[48] T. Hassel, N. Murray, R. Konya, A. Beniyash, F.-W. Bach, Nonvacuum electron beam cutting and welding - two parnering processes for fast and highly efficient metal working, Welding in the World 57 (2013) 315–322.
[49] t. Hassel, N. Murray, A. Beniyash, G. Klimov, Anwendungspotentiale der atmospärischen Elektronenstrahltechnik als universelles Fertigungsverfahren für die Blechbearbeitung, 2016. Leipzig, DE.
[50] N. Murray, G. Klimov, A. Beniyash, T. Hassel, Non-vacuum Electron Beam Technology as a Universal Tool for Material Processing, Aachen, 2017.
[51] U. Reisgen, A. Senger, S. Olschok, Electron beam welding in atmosphere of aluminum die casting alloys made of different qualities, Welding in the World 62 (2018) 1207–1213, https://doi.org/10.1007/s40194-018-0640-4.
[52] B. Langefeld, Additive Manufacturing - A Game Changer for the Manufacturing Industry?, 2013. www.rolandberger.com.
[53] Sciaky Inc, Additive Manufacturing, 2020. https://www.sciaky.com/additive-manufacturing/electron-beam-additive-manufacturing-technology.
[54] P. Frigola, O.A. Harrysson, T.J. Horn, H.A. West, R.L. Aman, J.M. Rigsbee, E. Rodriguez, Fabricating Copper Components with Electron Beam Melting. http://www.radiabeam.com/upload/1423166106amp17207p20.pdf (Accessed 25 March 2020).
[55] C.A. Terrazas, S.M. Gaytan, E. Rodriguez, D. Espalin, L.E. Murr, F. Medina, R.B. Wicker, Multi-material metallic structure fabrication using electron beam melting, International Journal of Advanced Manufacturing Technology 71 (2014) 33–45, https://doi.org/10.1007/s00170-013-5449-0.
[56] W.U.H. Syed, L. Li, Effects of wire feeding direction and location in multiple layer diode laser direct metal deposition, Applied Surface Science 248 (2005) 518–524, https://doi.org/10.1016/j.apsusc.2005.03.039.
[57] G. Klimov, N. Murray, A. Beniyash, A.A. Bataev, O.G. Lenivtseva, T. Tassel (Eds.), Additive Manufacturing Using Non-vacuum Electron Beam Technology, 2017.
[58] S. Chang, S. Gach, A. Senger, H. Zhang, D. Du, A new 3D printing method based on non-vacuum electron beam technology, Journal of Physics: Conference Series 1074 (2018) 12017, https://doi.org/10.1088/1742-6596/1074/1/012017.
[59] B. Baufeld, T. Dutilleul, R. Widdison (Eds.), Wire Based Electron Beam Additive Manufacturing, 2017.
[60] N. Bagshaw, A. Buxton, T.P. Mitchel, V. Jefimovs, M.E. Nunn (Eds.), Electron Beam Wire-Fed Additive Manufacture and Distortion Control, 2017.

This page intentionally left blank

CHAPTER

3

Computational weld analysis and fatigue of welded structures

R. Goyal[a], M. El-zein[b], G. Glinka[c]

[a]John Deere Asia Technology Innovation Center, Pune, MH, India; [b]John Deere Moline Technology Innovation Center, Moline, IL, United States; [c]Mechanical and Mechatronics Engineering, University of Waterloo, Waterloo, ON, Canada

1. Introduction

Welding process has been widely accepted for joining of structural components for large range of industrial applications especially in mechanical and civil engineering domains. In general, the structural components are designed for an intended fatigue life. In case of structures involving welded joints, the most obvious location of fatigue failure is either at the toe or root of the weld. It's imperative that welded joints need to be designed to ensure those joints do not fail before their intended fatigue life. At the same time, over designed welded joints would result into bulky structures, thereby increasing cost and reducing efficiency. Hence, this is critical to accurately determine fatigue life of the welded joints during the early design process. Continuous enhanced usage of virtual design and verification methods has been well adopted strategy across the industries to reduce dependency on expensive and time-consuming physical builds in line with the "first time right" design philosophy. However virtual design and verification of welded joints poses many challenges due to several complexities associated with it.

Majority of the issues associated with virtual design and fatigue life prediction of welded joints can be broadly categorized into three categories:

(a) Geometric stress concentration factor: For structural applications, welds are mainly needed to facilitate transfer of loads from one part to another. However, this load transfer must pass through complex geometric shape of the weld. The arc welds are typically either of fillet or grove type, which can be applied to join parts for achieving five types of joints namely butt, T, lap, corner and edge resulting into complex geometric shape at a macro scale. The geometric weld shape is also influenced by the welding

https://doi.org/10.1016/B978-0-12-820787-1.00003-6

process e.g. nugget shaped weld could be produced through resistance, laser or friction welding processes. Additional complexity is introduced through geometric transition between the weld and parent material in terms of small radius and angle of transition, also known as micro geometrical features. Both macro and micro geometric features of the weld joint produce stress concentration i.e. resistance to the load transfer, eventually affecting fatigue life of the joint. While the macro level weld geometry is specified by design on the drawings and controlled through various weld quality standards e.g. AWS D14.3 or ISO 5817, there is no provision for weld micro-geometrical features. The authors strongly feel the need to incorporate these micro features into design and quality control procedures. In any case, those must be carefully accounted for during the fatigue design life assessment of welded structures.

(b) Weld and HAZ related material changes: Material properties play key role in influencing the strength and fatigue behavior of the structure. Addition of micro alloying elements for grain refinement or further material processing such as rolling, or heat treatment are quite common techniques to enhance specific physical properties, hardness, strength and fatigue properties of the engineering materials. The welding process typically involves melting of the parent material and may involve filler wire metal with certain chemistry (typically enriched with Mn and Si) resulting into different chemistry into the solidified weld as compared to the parent material. Furthermore, next to the weld zone, some portion of the parent material is affected by thermal heat (known as heat affected zone or HAZ) and typically would undergo softening or hardening behavior due to microstructural changes, influencing strength and fatigue performance of the overall weld joint.

(c) Residual stress and distortion: Welding process involves localized melting, heating and cooling of the material in a structure typically constrained using fixtures and clamps resulting into differential strains and displacements. The complex thermal cycles from welding heat input also leads to a residual stress state in and around the welded joint, which could be detrimental to fatigue life of the weld joint. Distortion from the process could produce mis-alignment in the welded assembly causing additional stresses which may not have been considered in design. On the other hand, compressive residual stress could be beneficial to enhance fatigue life of welded joints. Several of the weld fatigue life improvement techniques rely on this fundamental principal of introducing compressive residual stresses at the weld toe either by using low temperature transformation (LTT) weld wires or high frequency mechanical impact treatment (HFMI) methods.

Fatigue causes irreversible damage of a component subjected to repeated loading leading to cracks and failure. Conventionally, total fatigue life is divided mainly into two parts – fatigue cycles to crack initiation and the subsequent cycles required for propagating this initial crack up to the final fracture. This convenient but arbitrary division of total life into initiation and propagation phases deals with the dilemma of initial crack size, possible a biggest drawback of the theory due to lack of consistency. There is no universal agreed definition of initial crack size, while its well agreed that initial crack size has significant influence on the crack propagation life. Initial crack size would ideally be the size which can be measured in a consistent manner and is dependent on the resolution of NDT methods employed for this purpose. In the engineering sense though, typically initial crack is assumed to be semi-elliptical surface crack, about 0.5 mm in depth and 2 mm in length for typical industrial applications.

Fatigue damage of weldments is one of the most frequent modes of failure of engineering structures leading to fracture of essential load carrying welded joints subjected to cyclic or fluctuating loads. For fatigue phenomena to happen, there must be some plasticity introduced into the material by the applied cyclic loads. Even though global working loads applied to the welded structure may be well within elastic limit of material, local stress at the weld toe or root due to geometric stress concentration can be high enough to cause localized plasticity. This is the main reason that fatigue cracks initiate from either weld toe or root locations in welded structures. The magnitude and distribution profile of the stresses in the potential crack plane controls the relative proportions of the crack initiation and propagation.

Due to significance of the subject, fatigue phenomenon has been studied over several decades in a wide variety of industrial applications using metallic and non-metallic materials e.g. in Refs. [1–4]. Even though significant progress has been made to understand fatigue process and mechanics associated with the phenomenon, there is no generalized approach for fatigue assessment for welded joints. There is enormous amount of literature available covering theoretically as well as engineering aspects dealing with design and analysis of welded joints.

A concise yet highly informative flow chart describing the information path for stress and fatigue analysis is shown in Fig. 3.1. The essential inputs required for any fatigue life analysis

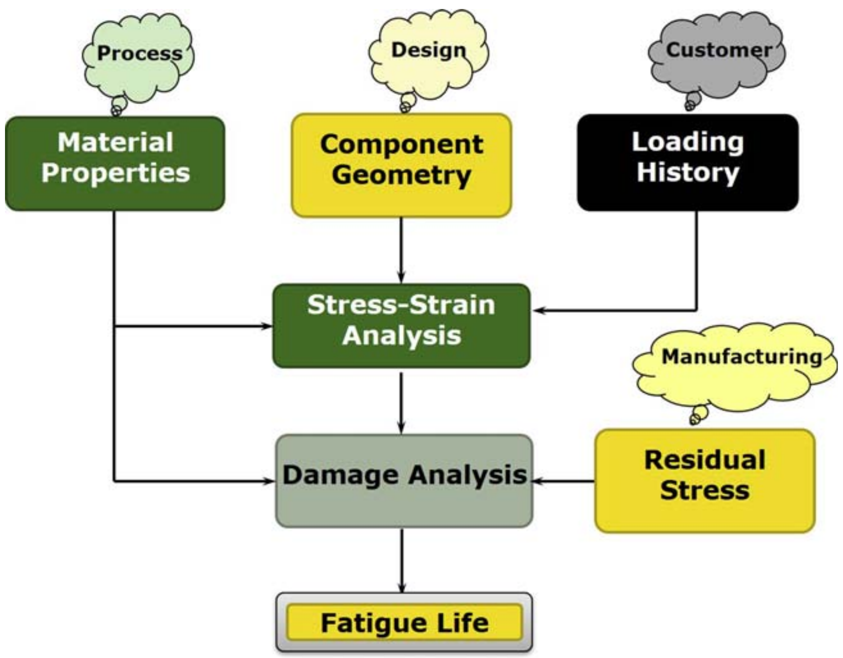

FIG. 3.1 Stress and fatigue analysis flow chart.

are the geometry, load history and material properties. Stress-strain analysis needs to be performed to obtain appropriate stress or strain information as required by the method used for fatigue analysis.

Any fatigue strength and durability analysis follow similar sequence of steps as illustrated in Fig. 3.1. First, the material selection and determination of its properties must be carried out. Secondly, the geometry of the analyzed component or structure must be adequately defined and described. The loading or the stress history is the third segment of the input data necessary of any mechanical fatigue analysis. The content of each segment of the input data varies depending on the fatigue method selected for the analysis. Therefore, the stress analysis and the nature of the stress to be used vary depending on selected fatigue analysis method. The final step in any fatigue analysis is the estimation of the fatigue damage and prediction of the fatigue life. In other words, the content of each input segment and the stress parameter to be used vary depending on the chosen fatigue analysis method.

It is also worth noting that the input data depends on several factors such as the material manufacturing process (material properties), manufacturing method of the object (component geometry and residual stresses) and the loading history. The loading or stress history is the only one being almost the same for various fatigue analysis methods.

There is a vast amount of literature [5–34] on recommendations for the fatigue design of welded components and structures including comprehensive design guide issued by the International Institute of Welding (IIW). Despite this, practical challenge lies in the fact that available theoretical knowledge is not helpful when it comes to implementing the method for real life fatigue design of welded joints in a systematic manner. Another challenge is that different fatigue design procedures requires different stress/strain parameters as input which typically leads to confusion and errors if not applied correctly.

Fatigue strength and durability analyses of welded joints require using several disciplines like mechanics of materials, experimental stress analysis, material science, weld manufacturing process and theory of probability. Therefore, there are several methods of weld fatigue analysis available depending on the country of origin or the engineering field of interest. However, it is possible to identify the three most popular methodologies of fatigue analysis of welded joints which are contemporary used by various industries such as aviation, automotive or the earth moving machinery sector using welded structures. Three dominant fatigue life analysis philosophies being contemporary used can be classified as below:

- The nominal stress approach, denoted often as the S-N method,
- The local notch tip stress-strain method, denoted as the ε-N method and
- The fracture mechanics method denoted as the da/dN-ΔK method.

As shown in Fig. 3.1, stress-strain analysis is the first important step toward fatigue life estimation. Accurate estimation of the fatigue life requires information about the appropriate stress-strain data.

Local peak stress at the weld toe (or root), σ_{peak} is the main stress parameter (Fig. 3.2) which affects the fatigue life of a weldment at the critical location. For conducting the strain-life fatigue analysis (ε - N method) the magnitude of peak stress or peak stress history is required. For conducting crack propagation analysis using the fracture mechanics approach, non-linear through thickness stress distribution (Fig. 3.2) at the critical section is required. This non-linear through thickness stress distribution and the weight function method can be used

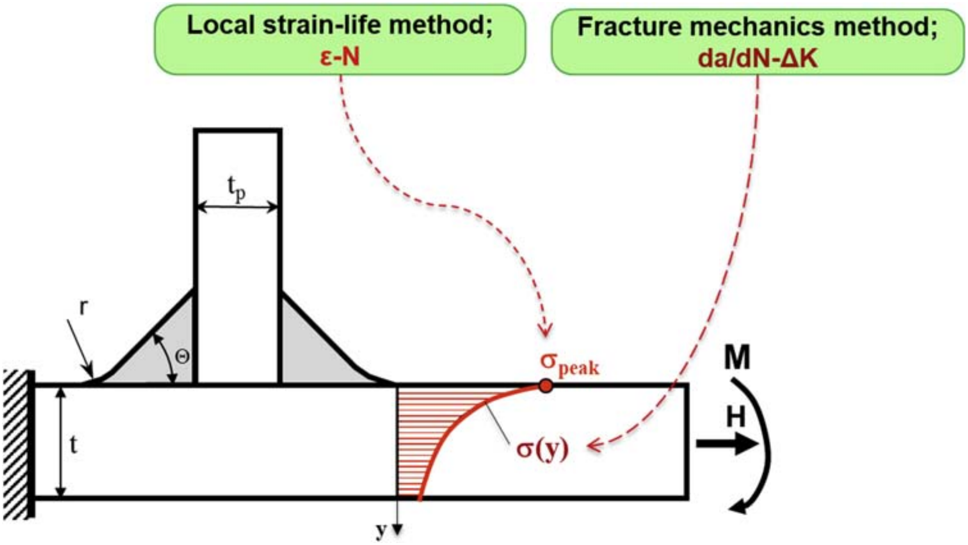

FIG. 3.2 Stress quantities needed for fatigue analysis in a welded joint.

for the determination of stress intensity factors and for the analysis of subsequent fatigue crack growth. Therefore, determination of the stress concentration and stress distribution at the critical locations in the welded structure plays an important role for the fatigue analysis. The strain life approach and the fracture mechanics approach help to determine the fatigue crack initiation life and the fatigue crack propagation life respectively.

Before getting into details of the fatigue analysis methods, Sections 2 and 3 will cover computational weld mechanics and stress parameters needed for weld fatigue analysis respectively. Sections 4–6 provide details of the three main fatigue analysis methods from the point of view of the most important parameter, i.e. the cyclic stress used for the estimation of the fatigue damage and fatigue durability. Sections 7 and 8 are devoted to discussing simplified methodologies developed for obtained the required stress quantities for fatigue analysis of welded joints using shell FE model (GY2 method) and solid model (GR3 model).

2. Computational weld mechanics

The fusion welding processes are widely used for fabrications in many engineering applications such as aerospace, automotive and shipbuilding industries. A metal inert gas welding process consists of heating, melting and solidification of parent metals and a filler material in localized fusion zone by a transient heat source to form a joint between the parent metals. The heat source causes highly non-uniform temperature distributions across the joint and the parent metals. Therefore, the thermal expansion and contraction during heating and subsequently cooling as well as material plastic deformation at elevated temperatures result in inevitable distortions and residual stresses [35,36] in the joint and the parent metals, which greatly affects the fabrication tolerance and quality.

In the current industrial practice, welding processes are developed largely based on trial and error experiments incorporating with engineer's knowledge and experience of previous similar designs. Simulation tools based on finite element (FE) method are very useful to predict welding distortions and residual stresses [37] at the early stage of product design and welding process development. However, the complexity of welding processes and the complex geometry of real engineering components have made the prediction of welding distortions and residual stresses a very difficult task. The engineering field dealing with modeling of welding process is known as computational weld mechanics. Fig. 3.3 shows the variables involved with computational weld mechanics, further emphasizing the complexity involved.

FE methods such as coupled/decoupling thermal and mechanical analysis for local and global models of complex structures [38–40] have been developed to reduce solution time with enough accuracy. The development of effective simulation tools requires an accurate analysis of thermal history during welding and a good understanding of the effect of process parameters on temperature distributions and variations. The research on welding heat source models dates back to early 1940s and Rosenthal [41] first proposed a mathematical model of the moving heat source under the assumptions of quasi-stationary state and concentrated point heating in the 3D analysis. In the late 1960s, Pavelec et al. [42] suggested a circular disc heat source model with Gaussian distribution of heat flux on the surface of the work

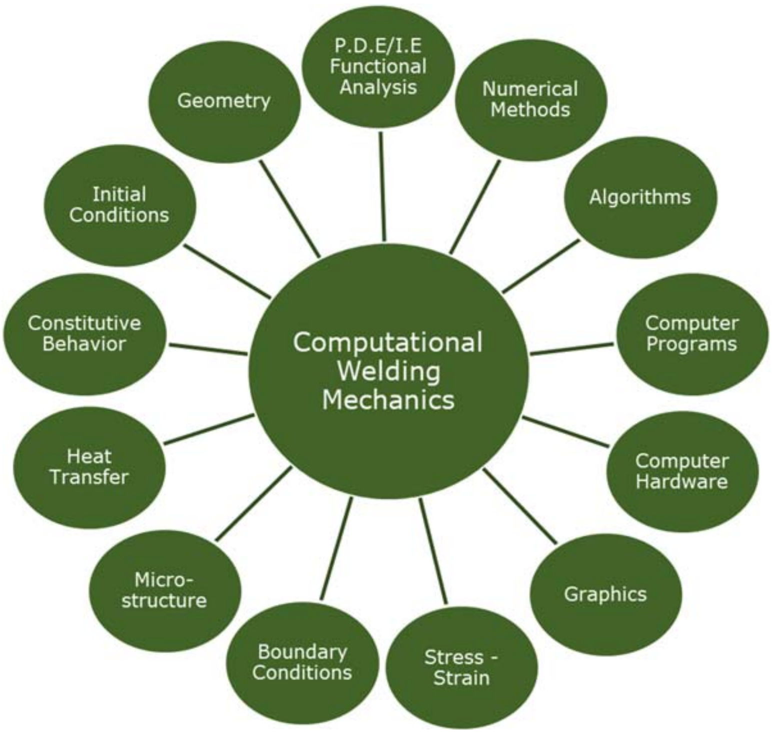

FIG. 3.3 Variables involved with computational weld mechanics.

piece. These heat source models and some simplified models have been widely used in welding simulation for prediction of the distortions and residual stresses [39,43,44].

The first welding numerical simulations made their appearance in the early 1970s, for example, in the work of Ueda et al. [45] and Hibbit et al. [46]. These analyses were greatly simplified relative to the real situations. In particular, the welding simulations were confined to analyses based on two-dimensional cross-sections. The results gave indications of the welding residual stresses evolved in quasi-static, plane strain situations but did not give a picture of the total out-of-plane deformations. Following increases in computer power, more complex aspects of welding have now been successfully investigated in greater detail by many researchers. A detailed literature review of finite element analyses and welding simulations presented between 1976 and 1996 [47] and 1996–2001 [48] has been compiled by Mackerle.

Optimization of the welding sequence and process is one way to limit the use of clamping tools to reduce the cost and facilitate the automation of assembly lines. However, experimental optimization requires prototyping and measurements which are extremely expensive and time consuming and finally, very few solutions can be used. Finite element simulations can be used in that aim, but the difficulty is, on one hand, that welding processes involve complex physical phenomena, and, on the other hand, that where local models are sufficient to predict stresses, only global 3D models can correctly evaluate distortions [49].

Residual stresses were modeled using commercial FEA package such as Ansys for butt welded plate [50]. Similar work was carried out to model residual stresses in weld joint of HQ130 grade high strength steel using Ansys [51]. Viorel developed similar methodology based on a thermo-elastic-plastic FE analysis and simulated simple butt welded joint using the ANSYS computer code [52]. Gery et al. developed a C++ program in order to implement heat inputs into finite element thermal simulation of the simple butt joint, approach used moving heat source model based on Goldak's double-ellipsoid heat flux distribution [53]. An uncoupled thermo-mechanical FE analysis, using the ABAQUS code was carried out to determine the distribution of residual stress at the cylinder-to-nozzle junction weld. Only the axis-symmetric model was simulated due to impractically to run full model [54]. Drawback of these codes is that they do not have the capability to handle complex geometry from real structures and, they do not capture the micro-structural transformations and their effects during welding. Some of these proposed models were not proven against experiment for their capability.

Rong-Hua Yeh et al. investigated the temperature distribution of aluminum plates welded by gas tungsten arc welding; attempt was limited to transient temperature estimation [55]. Simple Laboratory and shipyard Mock-up structures were simulated using 2D and 3D models [56]. Multipass welding of a 316 L stainless steel pipe was simulated by Duranton et al. [57]. Dike et al. [58] carried out three-dimensional finite element simulations of thermal and mechanical response of a 304 L stainless steel pipe subjected to a circumferential autogenous gas tungsten arc weld to predict residual stresses in the pipe. Model used simple geometry and load history, excluded material properties variation and didn't made reference to real boundary conditions.

The work by Camilleri et al. [59] aimed to improve the applicability of computational distortion prediction by providing simple adaptable methodologies with an effort to produce economic and robust distortion simulation strategies. Basic approach involved uncoupled computational methods, whereby the thermal transient, thermo-elastic-plastic and overall structural stages of the thermo-mechanical welding process were treated separately. Also, the transient problem was reduced to a static, single load-step analysis. Three efficient models were identified that reduce the transient analysis to a simple multi-load-step analysis and these were applied to sample butt-welded plates. Less attention was given to simulation of residual stress fields as it was observed that a full transient thermo-elastoplastic analysis is required if such information is required.

Souloumiac et al. [60] developed a local/global approach in order to determine the welding residual distortions of large structures. It is assumed that plastic strains induced by the welding process are located close to the welding path and only depend on local thermal and mechanical conditions. The plastic strains obtained by the local model are then projected to a complete shell of whole structure as initial strain. Drawbacks of this method is that due to many different weld joint configurations in a large welded structure, it requires large number of local models, further how the effects of welding fixture on large structure is transferred from local models is not well understood.

The recently welding simulation models over last 5 years can predict temperature, microstructure, phases, residual stresses and distortion during welding process properly accounting for any variables. Most of these models use the double ellipsoidal power density distribution of heat source model [53] below the welding arc, which can accurately simulate different types of welding processes with shallow and deep penetration. Such analysis accounts for transient thermal effects because of the localized, non-uniform and dynamic nature of the heat input. The heat distribution, heating and cooling rates which affect the microstructure of the weld and the heat-affected-zone are accounted. The thermal and microstructure history which, in turn, affects the stress distribution in the model are also accounted. Microstructures are modeled using the algorithms described in Watt et al. [61] and Henwood et al. [62]. As described by Goldak et al. [63], stress analysis requires that the boundary conditions are prescribed as displacement constraints such as fixtures and tack welds. Suman et al. [64] developed improved version of equivalent load method using transient behavior of plastic strain distribution for analyzing the large welded structures. The welding simulation basically solves the coupled equations for the conservation of energy, mass and momentum for a structure being welded. Complex equations are solved by using the mathematics of transient non-linear FEM and the evolution of microstructure. The welding simulation model set up include accurately defining the material properties, welding parameters, welding sequence and boundary conditions that include tack welds and constraints. The modern weld simulation models allow to create a mesh and define time stepping in a way that can accurately capture the thermal, microstructure and stress history of the welding process. In author's experience, validation of the welding simulation outcome requires carefully captured extensive experimental data. Couple of examples are presented next. Thermal validation involved measuring the full transient temperature field on the backside of base plate of a double fillet T-joint. Thermocouples mounted on the back side of base plate recorded online temperature history during the welding as well as cooling of the weld joint. Same test conditions were simulated, and thermal predictions were found to correlate well with the measurements, Fig. 3.4.

Distortion validation was conducted by measuring distortion during and after the welding on the backside of base plate of a single fillet T-Joint, using ARAMIS camera which is 3D

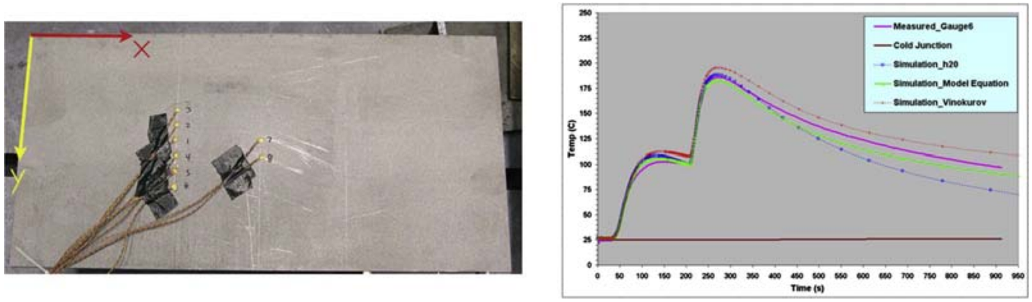

FIG. 3.4 Thermal validation on double fillet T-joint: Transient temp measurement (left) and Comparison of thermal profile - simulation versus measured (right).

optical deformation analysis system. Simulated distortion matched well with the measurements, Fig. 3.5.

The welding simulation can help designers to select appropriate design, welding sequence and welding fixtures at early design stage for robust product design to eliminate the issues which could turn out expensive at later stage. Biggest challenge for doing full 3D transient simulation is the simulation run time. For large welded structures having hundreds of welded joints, it may take around two weeks of simulation time, which could be justified for new product development, but for the production parts, it is not acceptable time. Currently efforts are going on to make the simulation faster by using different strategies such as having the capability to run the simulation with the help of parallel processors. Other challenges include collecting the accurate inputs for running welding simulation. As mentioned earlier, it is required to have temperature dependent material properties, not only for the basic material but also for its different phases at which it exists at different temperatures. Currently such a data base is not available, even for most of the commonly used materials and there is need to develop such types of data bases. Welding simulation has matured from research era to real application stage. In coming years, this will be used as

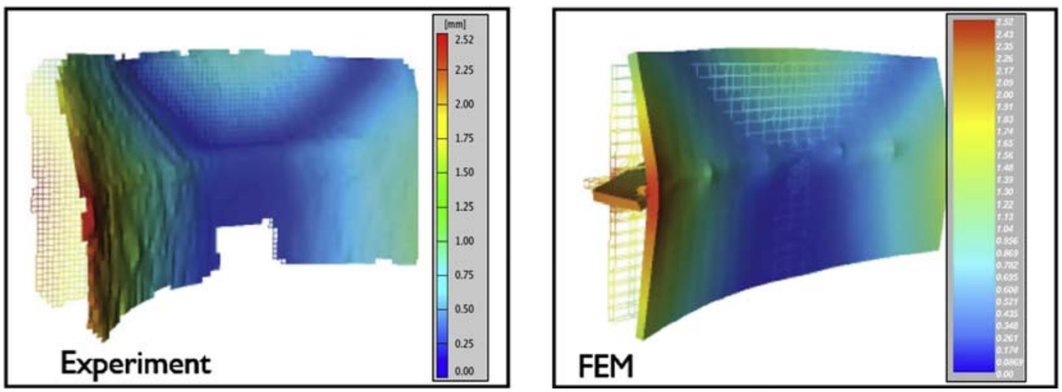

FIG. 3.5 Distortion validation on single fillet T-joint: Comparison of deformation – measured (left) versus simulation (right).

regular tool in industries, during early design cycle due to numerous advantages offered by the technology. Welding simulation is not limited to researchers now, for simulating simple welded joint but this can be used to design large welded structures at the shop floor. It is very helpful for reduction in physical trials and prototypes using virtual designs and hence resulting into savings of energy, money, efforts and accelerated product design. Improvement in quality by distortion reduction can be achieved, minimizing the assembly problems. Wang et al. [65] concluded that presence of residual stress significant affect fatigue life of the component when dealing with loading stress ratio, $R < 0.5$ and negligible for $R \geq 0.5$. Safer and robust designs with better confidence can be built by including residual stress in life-cycle prediction as demonstrated by Deschênes et al. [66]. Hensel et al. [67] tried to understand the influence and treatment of residual stresses in fracture mechanics calculations and the fatigue strength in general as a part of German cluster project IBESS short name for Integrale Bruchmechanische Ermittlung der Schwingfestigkeit von Schweißverbindungen. Welding simulation models provide the possibility of process parameter optimization enabling the feasibility to ascertain optimum processing regime.

3. Various stress definitions used in weld fatigue analysis

All fatigue analysis methods use stresses or strains in critical locations, for assessing fatigue life or durability of structures. Therefore, it is important to discuss various stress or strain parameters used in contemporary fatigue analyses and specific to weld fatigue analysis.

It is well known that the fatigue process is a local phenomenon, i.e. the fatigue damage starts locally from the point of highly stressed material volume associated often with stress concentration regions as indicated in Fig. 3.6.

The simple and most commonly used term in engineering analyses is the nominal stress, σ_n or S_n, obtained by using simple mechanics of material formula for simple load cases of axial, bending and torsion loads. The through the thickness stress is, in most cases, is approximated by the linear stress distribution. However, more detailed stress analysis can be carried out to obtain nonlinear through thickness stress distribution including the high local stress, σ^e_{peak}, at the weld toe (Fig. 3.6). The weld toe is considered in this case as the stress concentrator which due to sudden change of geometry. However, the nominal stress, σ_n, and the local elastic peak stress, σ^e_{peak}, at the weld toe are not the only stress quantities needed to be considered. When the linear-elastic notch tip stress, σ^e_{peak}, exceeds the yield limit, σ_{ys}, of the material the actually induced stress, σ^a_{peak}, will be less than the linearly obtained notch tip stress σ^e_{peak}.

Before getting into the more complicated stress state situation for welded joints, simple notched component is shown in Fig. 3.7 for illustrating the terminology. The necessary stress quantities and stress parameters needed for fatigue analyses are denoted in Fig. 3.7 using a series of generic notched components subjected to most frequent loading modes.

The gross nominal stress S is related to the gross cross section neglecting the existence of the notch while the net nominal stress S_n is obtained for the net cross section, accounting for the decrease of the effective cross section area. The peak stress, σ^e_{peak}, is the stress at the notch tip obtained by solving the linear elastic boundary problem, i.e. accounting for the actual load

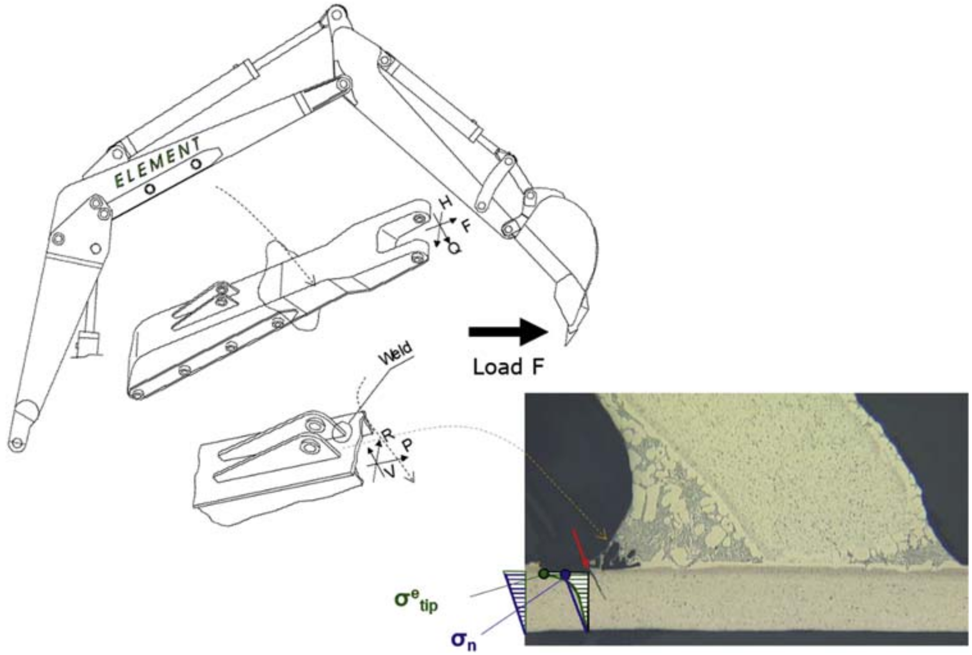

FIG. 3.6 Example of welded structure (excavator arm) and linear stress fields in the critical cross section.

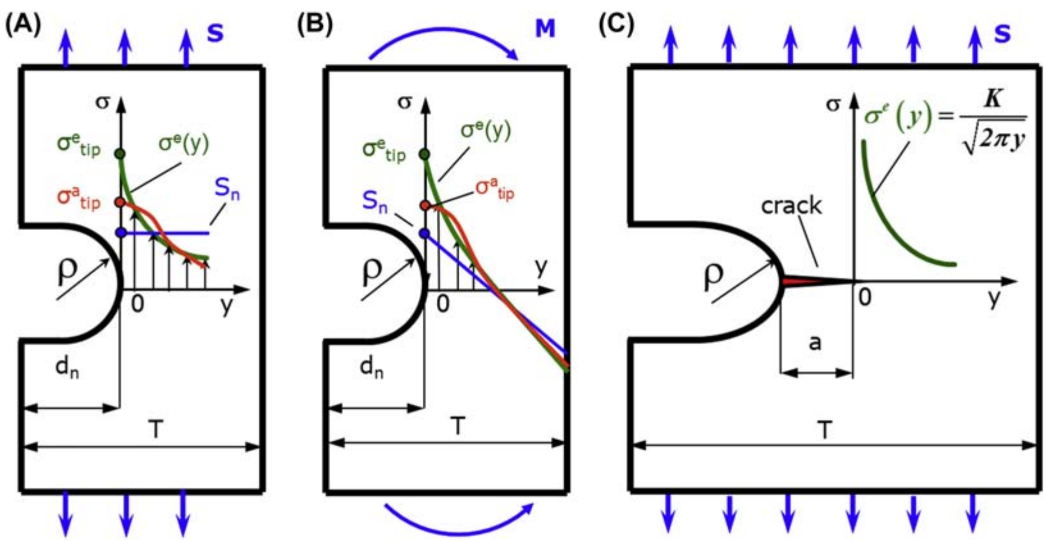

FIG. 3.7 Stress parameters used in fatigue analyses.

and geometry configuration but assuming the linear elastic behavior of the material. The linear elastic peak stress, σ^e_{peak}, and the associated stress distribution are most often obtained by the linear elastic finite element analysis. The nominal, S, and the linear elastic notch tip peak stress, σ^e_{peak}, are related to each other by the stress concentration factor K_t.

$$K_t = \frac{\sigma^e_{peak}}{S_n} \text{ or } K_t = \frac{\sigma^e_{peak}}{S} \tag{3.1}$$

When the linear elastic notch tip stress is less than the material yield limit ($\sigma^e_{peak}<\sigma_{ys}$) the linear elastic notch tip stress is equal to the actual stress at the notch tip, i.e. $\sigma^e_{peak} = \sigma^a_{peak}$. However, when the stress peak obtained from the linear elastic analysis exceed the material yield limit ($\sigma^e_{peak}>\sigma_{ys}$) then the actual stress at the notch tip is less than the linear elastic peak stress, σ^e_{peak}, but greater than the material yield limit, i.e. $\sigma_{ys} < \sigma^a_{peak} < \sigma^e_{peak}$ and more elaborate elastic plastic stress-strain analysis is required for the determination of the actual notch tip stress σ^a_{peak}.

In the case of cracked machine or structural elements (Fig. 3.7C) the crack tip stress can't be used because the linear elastic small deformation analyses provide stresses tending to infinity. Therefore, a more resourceful parameter is used in the case of cracked objects, i.e. the stress intensity factor K being the fundamental parameter of the Linear Fracture Mechanics.

$$K = S\sqrt{\pi a}\cdot Y \tag{3.2}$$

The stress intensity factor K accounts for the type of loading (represented usually by the nominal stress S) applied to the crack component, the crack size a, and the geometrical configuration represented by the parameter Y.

3.1 Stress state at a weld toe

The difficulty, when analyzing fatigue durability of weldments, is in determination of stresses at critical locations. Therefore, it is necessary to discuss possible stress indexes being used [26] in fatigue analyses of weldments and welded joints and methods of their determination. Let analyze a generic T-butt weldment (Fig. 3.8) with denoted characteristic stress distributions and stress indexes used in various fatigue analyses and listed below.

- A − Remote (nominal) through thickness stress, σ_n,
- B − The elastic through-thickness stress distribution in the weld toe cross section, $\sigma^e(x)$,
- C − Statically equivalent linearized through-thickness stress distribution in the weld toe cross section and the hot spot stresses, σ^1_{hs} and σ^2_{hs},
- σ^N, σ^E − the Neuber or the Equivalent strain energy density (ESED) elastic-plastic stress at the weld toe
- σ^a_{tip} − the actual elastic-plastic stress at the weld toe

The most frequent location of fatigue cracks in weldments with full weld penetration is the weld toe region. Therefore, it is important to be aware of various stress fields and stress magnitudes at critical locations being used in various fatigue analyses of weldments. The nominal stress distribution A (Fig. 3.8) and the nominal stress, σ_n, are usually determined in cross

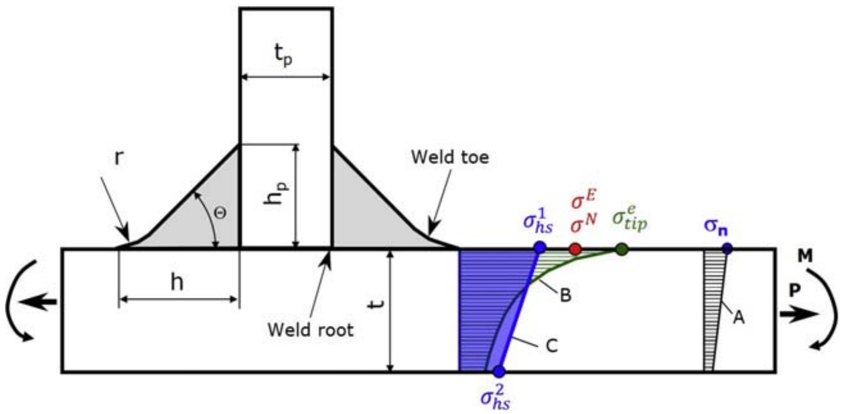

FIG. 3.8 Stress distributions and characteristic stress indexes in a weldment.

sections located away from the weld toe position. This is due to difficulties with obtaining the nominal stress at the required location (i.e. at the weld toe) due to geometrical complexity of welded components and multiple modes of loading. However, the nominal stress in the plane containing the weld toe is needed for fatigue analyses. Those nominal stresses are often termed [26] as hot spot stresses σ_{hs}^1 and σ_{hs}^2 shown in Fig. 3.8. The knowledge of hot spot stresses σ_{hs}^1 and σ_{hs}^2 makes it possible to determine the membrane and bending hot spot stress σ_{hs}^m and σ_{hs}^bwhich, when combined with appropriate stress concentration factors $K_{t,hs}^m$ and $K_{t,hs}^b$ makes it is possible to determine the "linear elastic" notch tip stress.

$$\sigma_{tip}^e = K_{t,hs}^m \cdot \sigma_{hs}^m + K_{t,hs}^b \cdot \sigma_{hs}^b \tag{3.3}$$

The "linear elastic" notch tip stress σ_{tip}^e, is further used to determine the actual elastic-plastic stress (σ_N, σ_E) and strain (ε_N, ε_E) at the weld toe needed for fatigue life estimations.

It is also possible to carry out numerical stress analysis of the entire welded component or structure and determine the linear elastic weld toe stress σ_{tip}^e, directly from the numerical output. Unfortunately, such an analysis even for geometrically simple welded structure, like the tube on plate shown in Fig. 3.9, requires careful meshing of the weld toe region with fine finite elements dependent on the magnitude of the weld toe radius. The magnitude of the weld toe radius "r" is dictated by physical properties of welded metals and the welding process.

In most practical cases the weld toe radius varies in the range of few tens of a millimeter. Therefore, the size of the series of smallest finite elements around the weld toe perimeter should not (see Fig. 3.9B) be greater than 0.2 mm. In the case of large welded structures like an excavator arm or bulldozer chassis it would result in a FE mesh with prohibitively large number of elements. Therefore, it is more practical to use the FE method for the derivation of nominal hot spot stresses σ_{hs}^1 and σ_{hs}^2 rather than directly the weld toe peak stress σ_{tip}^e. When the hot spot stresses are of interest then even simple shell FE model of an analyzed welded structure might be sufficient (Fig. 3.10).

Detailed FE element methods of deriving meaningful hot spot stresses will be discussed in Sections 7 and 8. Let us demonstrate first how the knowledge of hot spot stresses can be used for determining the "elastic" notch tip stress σ_{tip}^{e} (i.e. the linear elastic stress at the weld toe).

The hot spot stresses, σ_{hs}^{1} and σ_{hs}^{2}, enable determination (Fig. 3.10) of the membrane and bending hot spot stress, σ_{hs}^{b} and σ_{hs}^{m}, respectively.

$$\sigma_{hs}^{m} = \frac{\sigma_{hs}^{1} + \sigma_{hs}^{2}}{2} \ and \ \sigma_{hs}^{b} = \frac{\sigma_{hs}^{1} - \sigma_{hs}^{2}}{2} \tag{3.4}$$

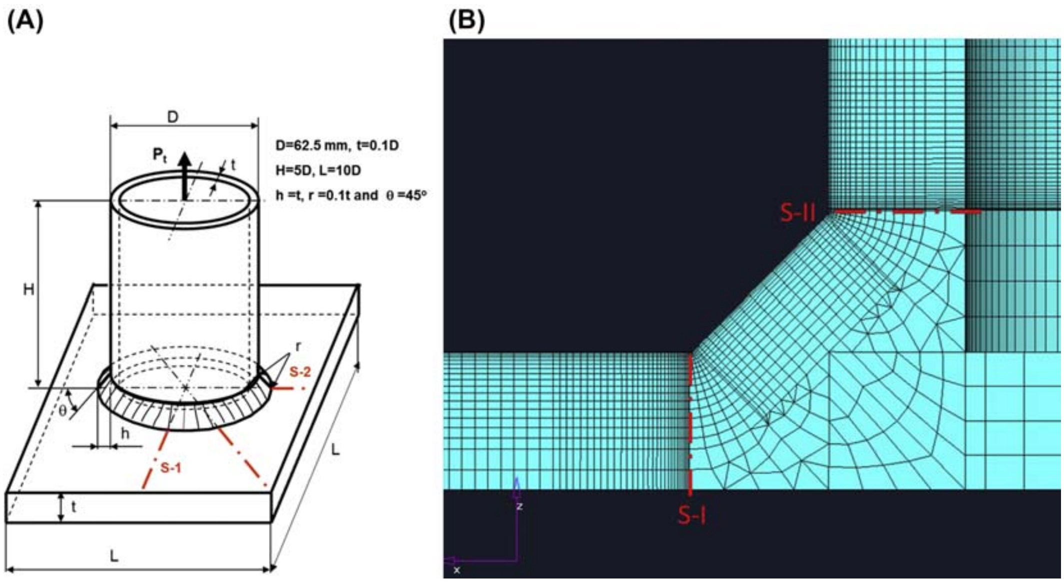

FIG. 3.9 Tube on plate welded joint; (A) Tube welded to a base plate; (B) Finite element mesh of the joint process.

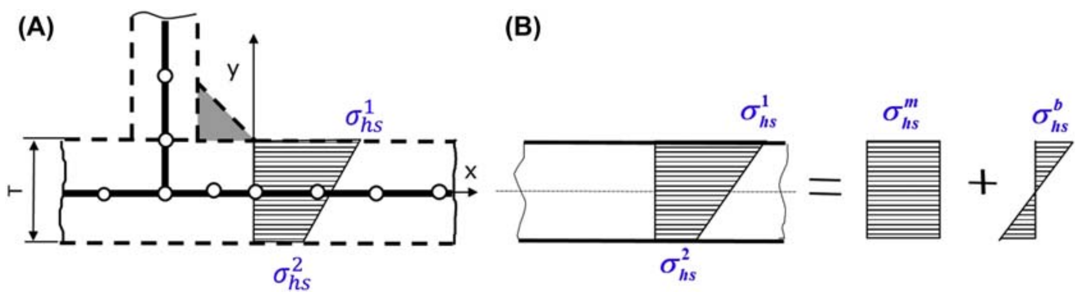

FIG. 3.10 Determination of hot spot stresses; (A) Shell FE model of a weldment and resulting through-the-thickness stress distribution, (B) decomposition of the shell FE stress data found in the weld toe cross section, (C) the hot spot membrane and shell bending stress.

When the membrane σ^m_{hs}, and bending σ^b_{hs}, hot spot stresses are combined with appropriate stress concentration factors $K^m_{t,hs}$ and $K^b_{t,hs}$ it is possible Eq. (3.3) to determine the weld toe "linear elastic" stress at the weld toe σ^e_{tip}.

In the cases of simple geometry and loading mode combination the hot spot and appropriate nominal stress are often the same and they can be determined manually. The necessary stress concentration factors can be found in the literature [68–71] or stress concentration databanks created by individual organization could be used.

Depending on the welding process and technique, there is high variability in weld micro geometrical features. Most of the welding codes require that stress concentration created by the weld micro geometrical features must be accounted for during the design process. Although due to the small size and complex nature of these features, detailed and large size fine mesh FEA models are needed to capture the stress concentration effect.

It is known that stress concentration factors for the weld geometry are highly dependent on the micro geometrical features such as the weld toe radius and angle but also sensitive to the modes of loading. Depending on the welding techniques (manual vs. robotic), process capabilities and the skill level of welding operators, shape and size of these weld micro geometrical features and hence the stress concentration factors could vary significantly, which could significantly impact the fatigue life. So, it is critical to account for this variability of the stress concentration factors while determining the appropriate stress-strain information required for the fatigue life estimation.

4. The nominal (S-N) stress method

The S-N fatigue analysis method, being the oldest one, is based on the use of the nominal stress S or S_n. Depending on the analyst choice the nominal net stress S_n or the nominal gross stress S can be used. However, the chosen nominal stress must be consistently used over the entire fatigue analysis process, i.e. both the material properties and the stress history must be presented either in terms of the gross S or the net nominal stress S_n. Examples of nominal stress distributions induced by pure bending or axial load and the fluctuating notch tip nominal stress are shown in Fig. 3.11. The nominal stress can be sometimes determined manually but it requires later several corrections in order to account for the stress concentration and many other geometrical and material factors. The method is limited to nominal stresses not exceeding the material yield limit.

In order to understand the difference between the three mechanical fatigue analysis methods it is helpful to follow the sequence of basic steps associated with each of the method. First, the analyst needs to identify the critical location as indicated in Fig. 3.12.

Then S-N fatigue life prediction procedure (as well as the other two methods) requires collecting the input data as shown in Fig. 3.12. The load is represented by the loading (force, bending moment) or the nominal stress fluctuations – called as the load/stress history. The load (stress, moment or force) needs to be subsequently translated into the nominal stress history, i.e. the time sequence of nominal stress peaks and valleys. The geometry is most often defined by the stress concentration factor K_t associated with appropriate definition of the nominal stress $S_n$or S. The analyst must make sure that the same definition of the nominal

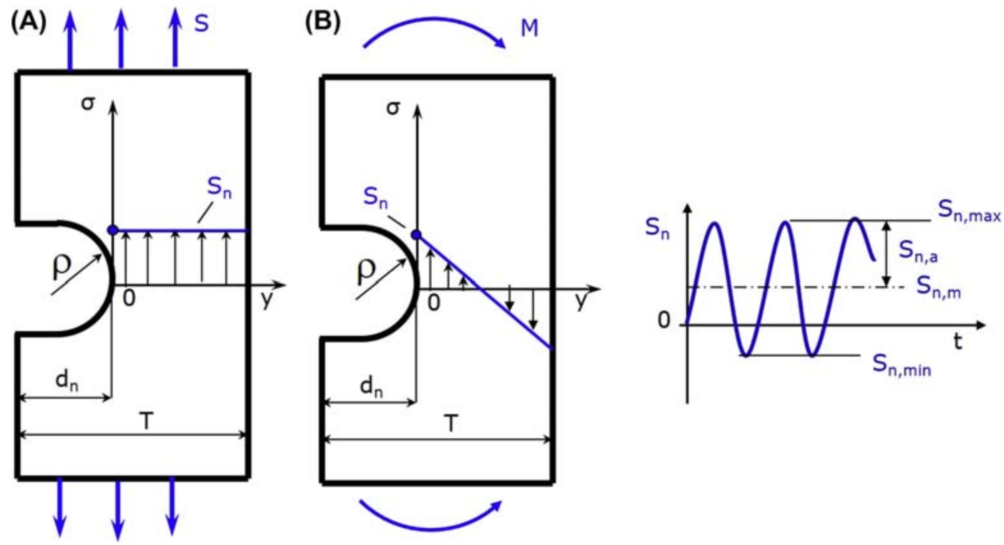

FIG. 3.11 Fluctuating net and gross nominal stresses induced by pure axial or/and bending stresses in notched components.

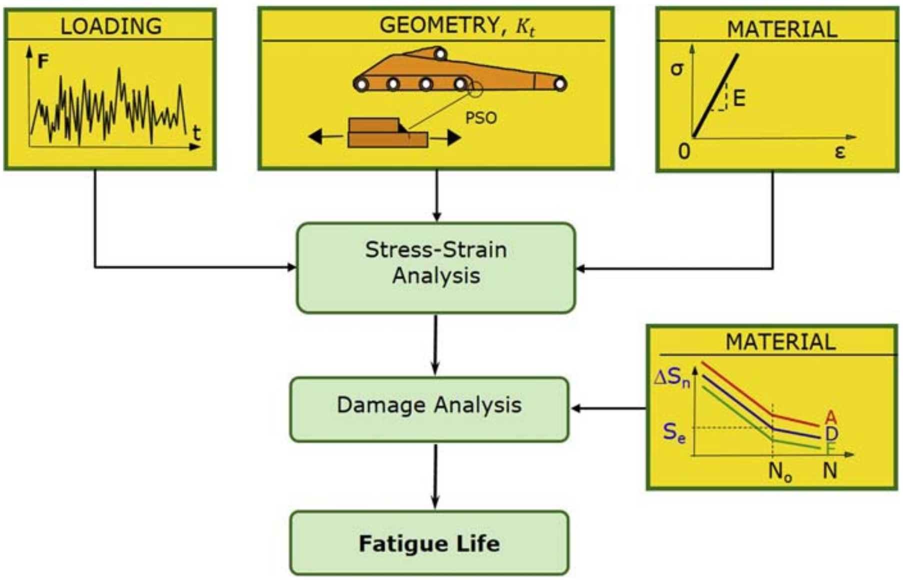

FIG. 3.12 The input data and the sequence of steps in the S-N based fatigue life estimation procedure.

stress applies when defining the ready-made stress concentration factor, K_t, expressions. Material properties are represented by two data sets. The first data set is the linear-elastic material stress-strain curve. Only the linear part of the material stress-strain curve is used in the S-N stress analysis as the method is limited to nominal stresses not exceeding the material yield limit. The second set of material properties represents fatigue properties of the material or the analyzed component. Those material properties are most often given in terms of S_a-N_f curves named often as material S-N curves. They represent the number of cycles to failure N_f under applied nominal stress range ΔS or ΔS_n.

The input data sets representing the Loading, Geometry and Material are used for the determination of the nominal stress history to be combined later with appropriate fatigue (S-N) curve. It is believed that fatigue life of the welded specimen (Fig. 3.13), used to obtain the fatigue S-N curve, will be the same when the stress concentration and the through thickness stress distribution in the specimen are the same as those at the critical location in the analyzed welded structure.

This assumption is often termed as the similitude concept. The term similitude means the same stress distributions in the generic specimen used for determination of the fatigue S-N curve and in the analyzed structure. The family of generic S-N curves obtained by testing a variety of geometrically different specimens and subjected to various levels of the nominal stress can be often found in standards concerned with the S-N fatigue analysis procedures. They are often recommended for fatigue analysis of welded structures. The analysis in such cases is simplified because the stress concentration phenomenon and any other effects such as residual stress are contained in those generic fatigue S-N curves.

Therefore, fatigue analyses of welded components can be limited to the determination of appropriate nominal stress history and selection of appropriate S-N curve. The step-wize procedure for assessing the fatigue life of a welded structure is illustrated in Fig. 3.14 when the welded arm of an excavator is used as an example.

The excavator arm (a) is subjected to the load F applied at the edge of the spoon. Next loadings acting on each segment (b) of the arm need to be determined. Then the nominal stress at the critical cross section (c) needs to be evaluated. It was anticipated in this case

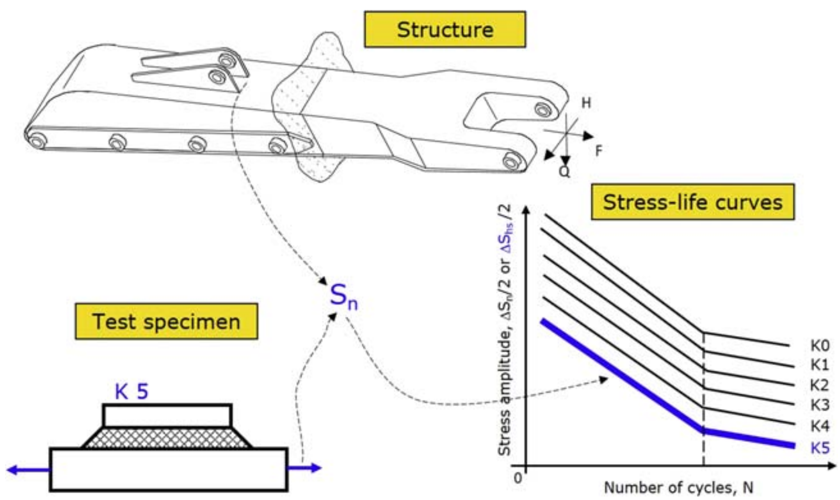

FIG. 3.13 The similitude concept used in fatigue analyses of welded joints based on the set of standard fatigue curves (S-N).

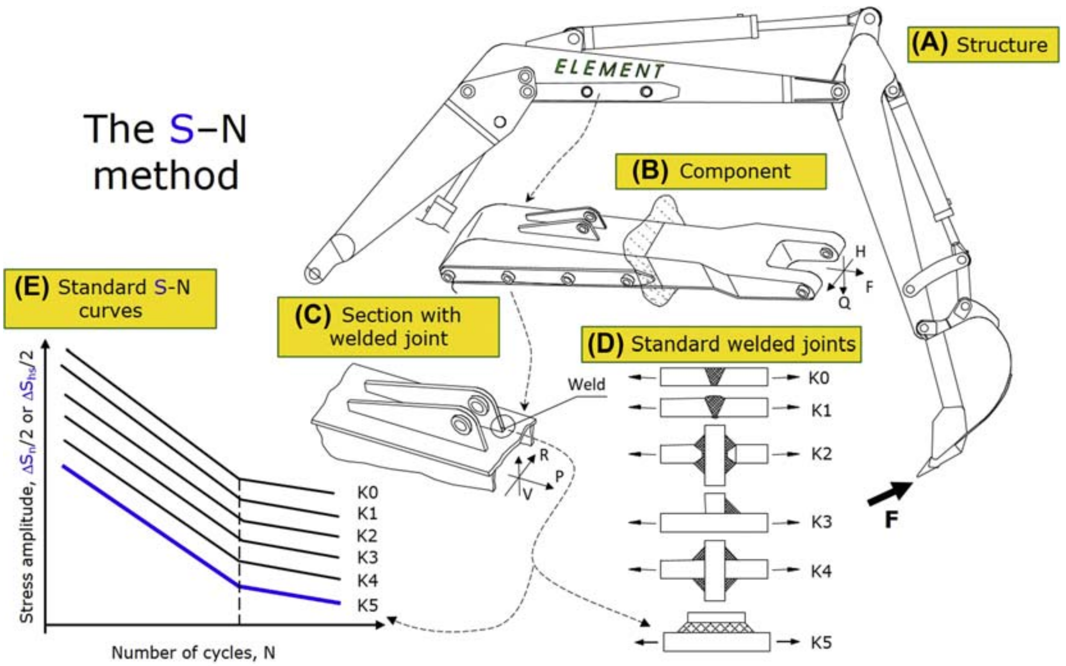

FIG. 3.14 Steps in fatigue life assessment procedure based on standard fatigue S-N curves.

that the cross section adjacent to the bracket was the critical location. Therefore, the nominal stress in the cross section containing the weld holding the bracket needed to be determined. The next step was the selection of the most appropriate S-N curve (d) from the set of standard S-N curves. The curve K5 seems to be the closest one as far as the geometrical features of the analyzed component are concerned. The last step in the procedure is determination of the nominal stress range ΔS or ΔS_n and estimation (e) of the number of cycles to failure N_f based on the standard S-N curve K5 associated with the already determined nominal stress range (or amplitude).

In the case of constant amplitude stress history, the estimation of the number of cycles to failure (the fatigue life) is straight forward because it requires finding (on the S-N curve) the number of cycles N_f associated with given stress range ΔS or ΔS_n. However, in the case of a variable amplitude stress history, occurring most often in practice, the fatigue damage for each stress cycle needs to be determined.

In order to determine the fatigue life of the joint (or the cross section) the fatigue damage D_i induced by each subsequent stress cycle needs to be determined. Then the damages are summed up (Fig. 3.15) and the total number of cycles to failure is estimated. It is assumed that fatigue damages caused by subsequent stress cycles can be added linearly and the analyzed component fails when the total fatigue damage reaches the critical fatigue damage value of $D = 1$.

The meaning of the fatigue damage is given in a mathematical sense, i.e. if the number cycles to failure under constant stress range ΔS_1 is N_1 then the fatigue damage caused by one

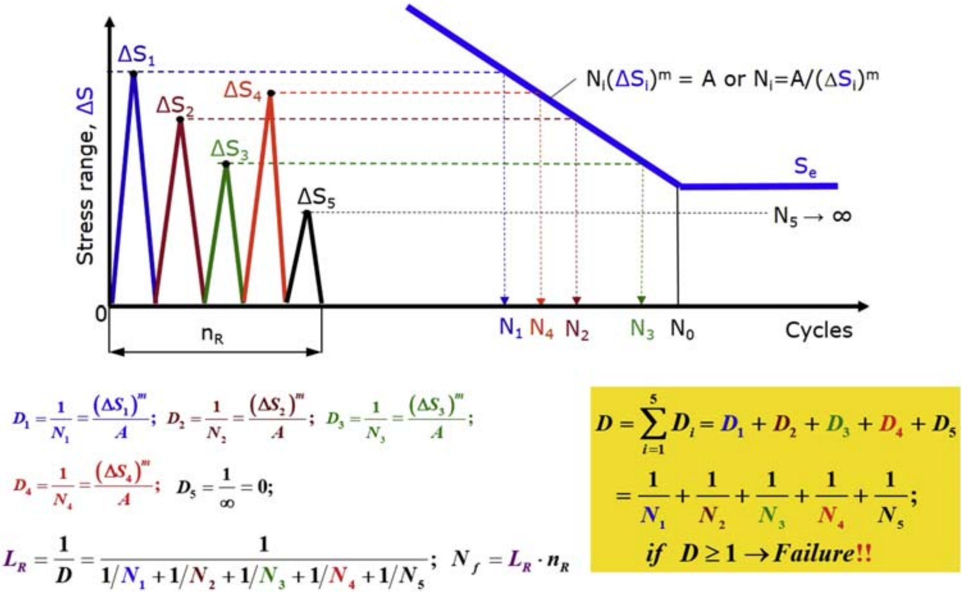

FIG. 3.15 The linear summation of fatigue damages (the Miner rule).

stress cycle of the stress range of ΔS_1 is D_1. Fatigue curves S-N are most often approximated by a power law expression in the form of:

$$N_i = \frac{A}{(\Delta S_i)^m} \tag{3.5}$$

Where: "A" and "m" are material constants.

The fatigue damage caused by a stress cycle ΔS_i of the applied nominal stress history shown in Fig. 3.15 is:

$$D_i = \frac{1}{N_i} = \frac{(\Delta S_i)^m}{A} \tag{3.6a}$$

Fatigue damages induced by the first and subsequent loading cycles (Fig. 3.15) are:

$$D_1 = \frac{1}{N_1} = \frac{(\Delta S_1)^m}{A}; D_2 = \frac{1}{N_2} = \frac{(\Delta S_2)^m}{A}; D_3 = \frac{1}{N_3} = \frac{(\Delta S_3)^m}{A}$$

$$D_4 = \frac{1}{N_4} = \frac{(\Delta S_4)^m}{A}; D_5 = \frac{1}{N_5} = \frac{(\Delta S_5)^m}{A} \tag{3.6b}$$

The total damage induced by one pass of the entire stress history (Fig. 3.15) is:

$$D = D_1 + D_2 + D_3 + D_4 + D_5 \tag{3.7}$$

If the damage caused by one pass of the stress history is less than 1 (i.e. $D < 1$) then the stress history can be repeated until the resultant fatigue damage reaches the critical value of 1. It means that the fatigue failure will occur after L_R applications of the stress history containing n_R cycles (Fig. 3.15).

$$L_R = \frac{1}{D} \tag{3.8}$$

Thus, the number of cycles to failure can be estimated as:

$$N_f = L_R \cdot n_R \tag{3.9}$$

The S-N method has the advantage to be simple and relatively easy to use but it can't account for the effect of several other factors such as the load sequence or actual residual stresses present and it requires several, not very rigorous, adjustments dependent on the available input information. Nevertheless, this is still the most popular method used in practice around the world.

5. The local (ε-N) elastic-plastic strain-stress method

The local strain-life method (ε-N) requires using the actual notch tip stress and strain (Fig. 3.16). Therefore, the notch tip stress analysis is required before appropriate stress-strain information is determined. This is since the initially available input information is the nominal stress S_n and the associated stress concentration factor K_t [72] or the linear elastic notch tip stress σ^e_{tip}. The linear elastic notch tip stress σ^e_{tip} needs to be subsequently transformed into the actual elastic-plastic stress-strain response σ^a_{tip} and ε^a_{tip}. In the case of a cyclic stress history it requires transformation of each subsequent maximum and minimum of the linear elastic input stress into the actual elastic-plastic minimum and maximum stress and strain on the reversal by reversal basis, as shown in Fig. 3.17.

The local stress-strain method (ε-N) has gained significant recognition during the last 40 years period and beside its sound theoretical background is also more convenient to be coded into a computer program. Basic formulations of the contemporary local stress-strain methodology (ε-N) are given in Refs. [73–75]. The method is based on modeling the elastic-plastic stress-strain material behavior. Therefore, the early work concerned with the description of elastic-plastic material behavior under cyclic stresses, reported in Refs. [76–78], has been incorporated. Its main elements are discussed next.

The (ε-N) fatigue life prediction procedure (as well as the other two procedures) requires collecting the input data as shown in Fig. 3.18. The load is represented, similarly to the (S-N) method, by the loading (force, bending moment), the nominal stress fluctuations or the pseudo-elastic stress fluctuations at the notch tip. The applied input load (stress, moment, force, nominal stress or the notch tip linear elastic stress) needs to be translated into the notch tip elastic-plastic stress-strain response/history given as a time series, i.e. the sequence of

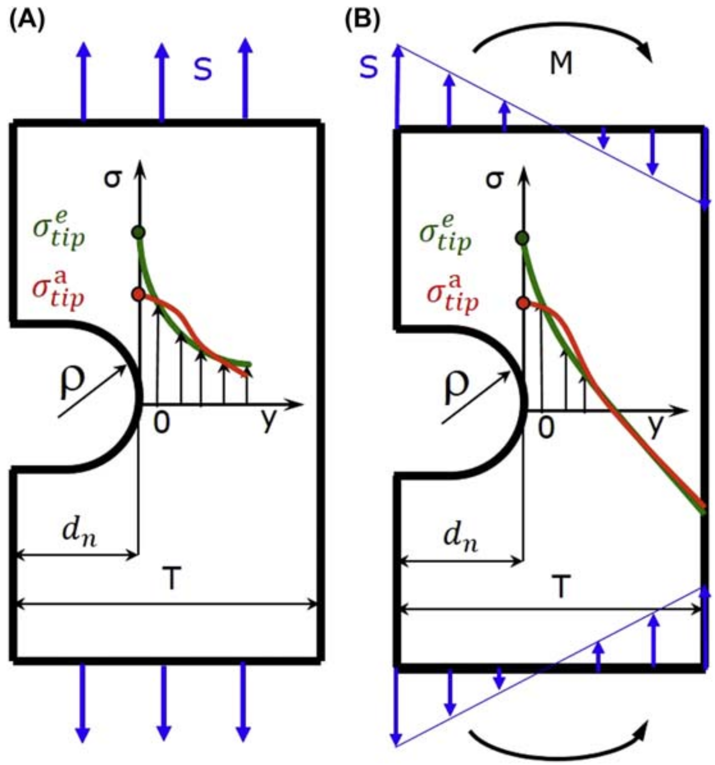

FIG. 3.16 The linear elastic stress at the notch tip σ^e_{peak} and the actual elastic plastic notch tip response σ^a_{peak}.

elastic-plastic notch tip stress-strain peaks and valleys. The geometry is frequently but not always defined by the stress concentration factor K_t associated with appropriate definition of the nominal stress S_n or S. It is also worth to note that the nominal stress S_n and the associated stress concentration factor K_t are often replaced by the local (Fig. 2.5) linear elastic notch tip stress, σ^e_{tip}, obtained with the help of the finite element method. Material properties are represented by two data sets. The first data set is the true nonlinear elastic-plastic stress-strain material (σ-ε) curve linking the stress and the total strain amplitude.

$$\frac{\Delta\varepsilon^a}{2} = \frac{\Delta\sigma^a}{2} + \left(\frac{\Delta\sigma^a}{2K'}\right)^{\frac{1}{n'}} \; or \; \varepsilon^a = \frac{\sigma^a}{E} + \left(\frac{\sigma^a}{K'}\right)^{\frac{1}{n'}} \tag{3.10}$$

The expression above is based on the analytical formula of Ramberg and Osgood [79] who proposed the power law function for relating the plastic strain and stress. Therefore expression (3.10) is often termed as the Ramberg-Osgood cyclic stress-strain material curve.

The fatigue strain-life curve, given in the form of expression Eq. (3.11a), is also connected with two researchers, namely Coffin [77] and Manson [78], who independently proposed the power law relation between the plastic strain amplitude and the number of cycles to failure.

The elastic term was added later [76] and as a result the total strain amplitude was related to the number of cycles to failure.

$$\frac{\Delta\varepsilon^a}{2} = \frac{\sigma_f^{'}}{2}(2N_f)^b + \varepsilon_f^{'}(2N_f)^b \qquad (3.11a)$$

The expression Eq. (3.11a) is frequently called as the Manson-Coffin strain-life fatigue curve.

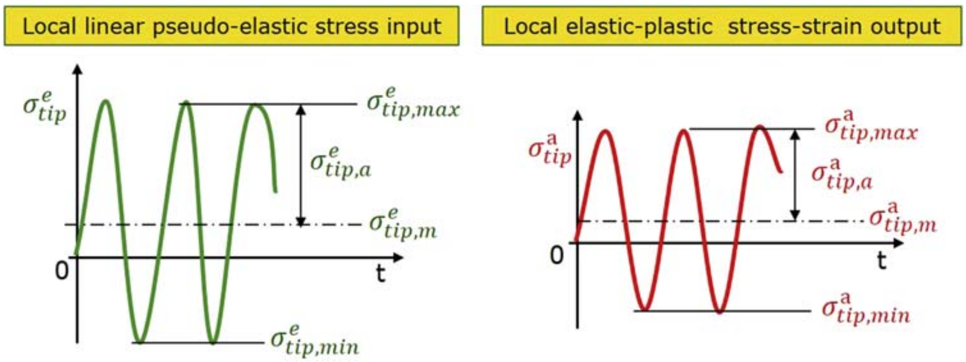

FIG. 3.17 Pseudo-linear notch tip stress history and the actual (elastic-plastic) notch tip stress response.

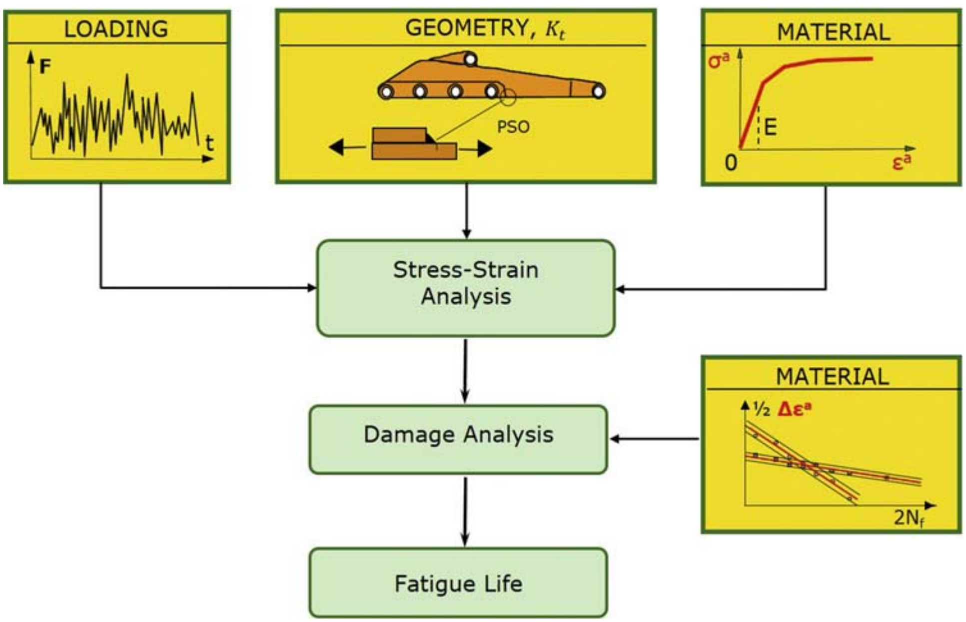

FIG. 3.18 The Information path according to the local stress-strain fatigue durability analysis.

The three groups of the input data (the stress history, the geometry and the stress-strain curve) make it possible to determine the elastic-plastic stress-strain response at the notch tip.

The entire concept of the local stress-strain methodology is based on the similitude concept (Fig. 3.19) enabling to link the material stress-strain properties, obtained from smooth specimens, with the behavior of a real notched element needed to be analyzed.

The fatigue analysis method is based on the Similitude Concept stating that if the local notch-tip strain history at the notch tip and the strain history in the test specimen are the same, then the fatigue response in the notch tip region of the analyzed component and in the specimen will also be the same and can be described by the same material strain-life (ε-N) curve. It also means that the material strain-life fatigue curve Eq. (3.11a) can be obtained from smooth material specimens and used later for fatigue life prediction of real notched mechanical and structural components. It also means that, contrary to the S-N method, only one material fatigue curve is needed. The disadvantage is that the determination of notch tip stresses and elastic-plastic strains requires nonlinear elastic-plastic stress-strain analysis. Such analyses are time consuming and cumbersome in the case of manual computations, but they are relatively easy and efficient when numerical methods and computers are employed.

There are several important steps to be executed (Fig. 3.20) when estimating fatigue life/durability according to the local strain-life methodology.

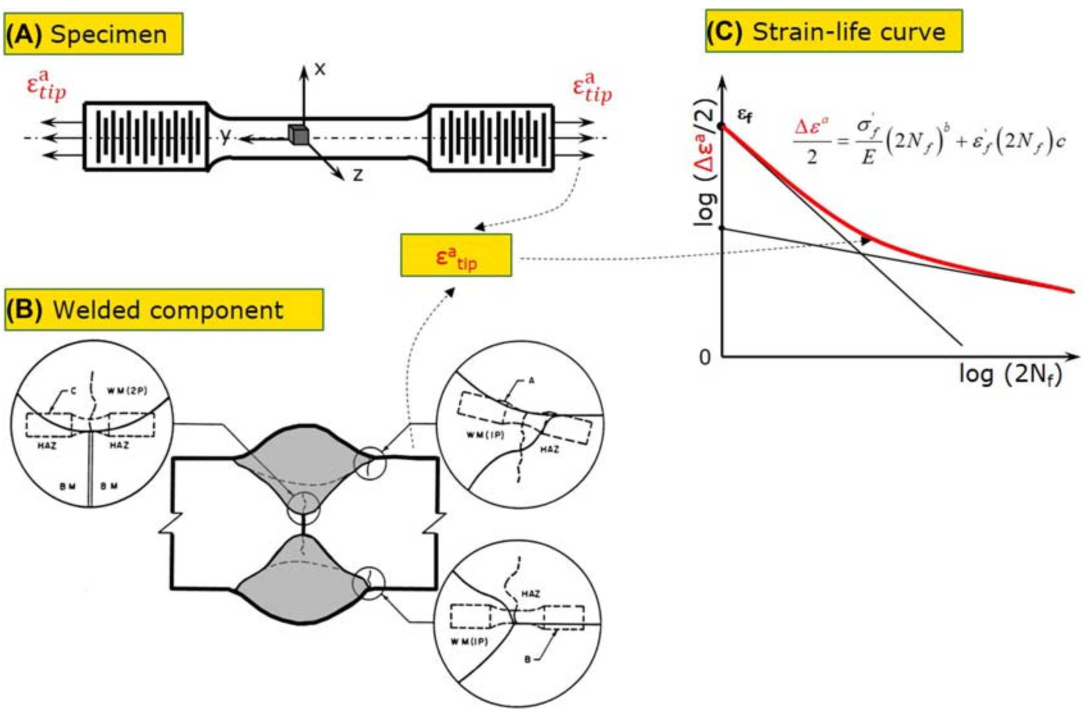

FIG. 3.19 The similitude concept being the base for the local strain-life methodology.

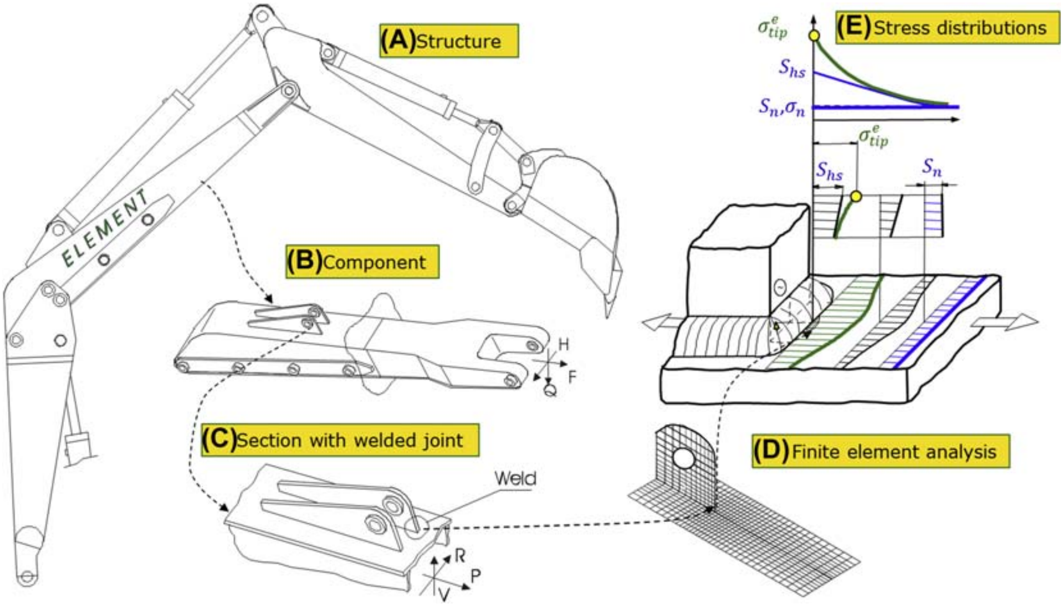

FIG. 3.20A Identification of the cross section and estimation of the linear elastic stress at the critical location.

First the identification of the critical location (steps a, b, c) needs to be carried out and it involves finding the critical cross section (Fig. 3.20A) in the structure, analogously to the previously discussed nominal stress method (S-N). Then the complete linear elastic stress analysis is required (steps d and c, boundary problem solution) in order to determine the linear elastic peak, σ^e_{tip}, stress at the critical point within the critical cross section of the analyzed object.

The so called linear elastic notch tip stress, σ^e_{tip}, at the critical location (at the weld toe in Fig. 3.20a) needs to be subsequently transformed (Fig. 3.20B) into the actual elastic-plastic stress, σ^a_{tip}, and elastic-plastic strain, ε^a_{tip}, at the notch tip with the help of elastic-plastic numerical stress-strain analysis or with the help of simplified methods like the Neuber [80] or the equivalent strain energy density method, ESED [81] rule. The transformation needs to be carried out for the entire pseudo-elastic stress history (Fig. 3.20B–F) accounting for the nonlinearity of the material stress-strain curve (Fig. 3.20B–G) and the sequence of applied loading cycles. The most often used Neuber rule (Fig. 3.20B–H) provides the connection between the pseudo linear elastic input stress, σ^e_{tip}, and the actual stress, σ^a_{tip}, and associated elastic-plastic strain, εatip, response at the notch tip. The resultant actual elastic-plastic notch tip stress-strain response (Fig. 3.20B–I) is usually presented in the form of strain-stress hysteresis loops where each loop represents one loading cycle. The actual strain range, $\Delta\varepsilon^a$, at the notch tip is the stress parameter necessary for the determination of the fatigue damage induced by given stress/load cycle. The fatigue damage D_i induced by a cycle "i" is determined (Fig. 3.20C) in analogous way as in the case of the S-N method.

First, the fatigue damage D_i needs to be determined (Fig. 3.20C) for each stress/load cycle by finding from Eq. (3.11b) the number of cycles to failure, $N_{f,i}$, for given strain range, $\Delta\varepsilon^a_i$.

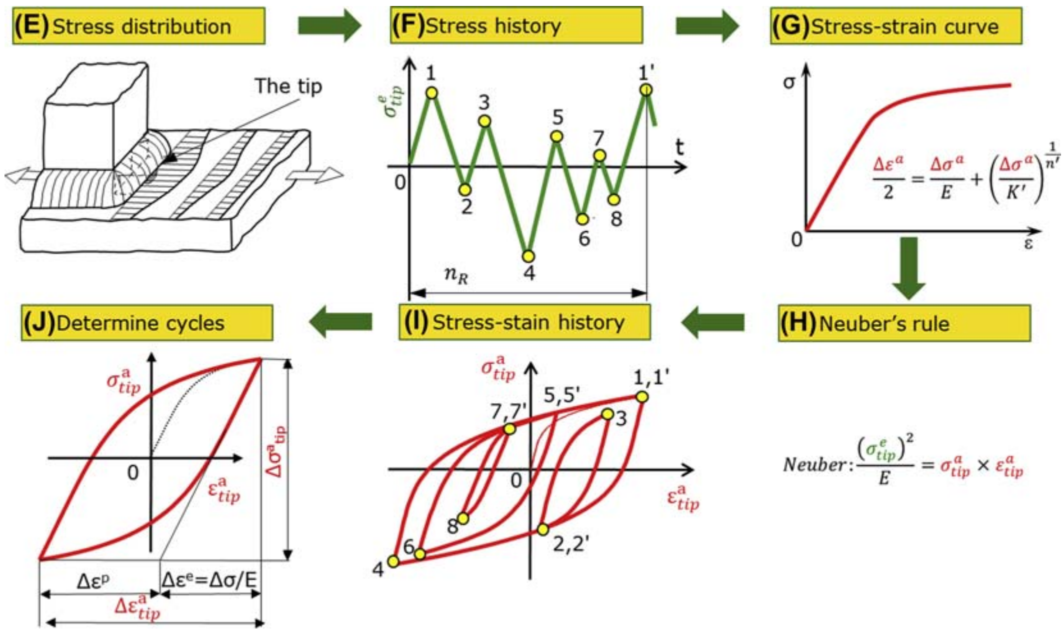

FIG. 3.20B Determination of the cyclic stress-strain response at the notch tip.

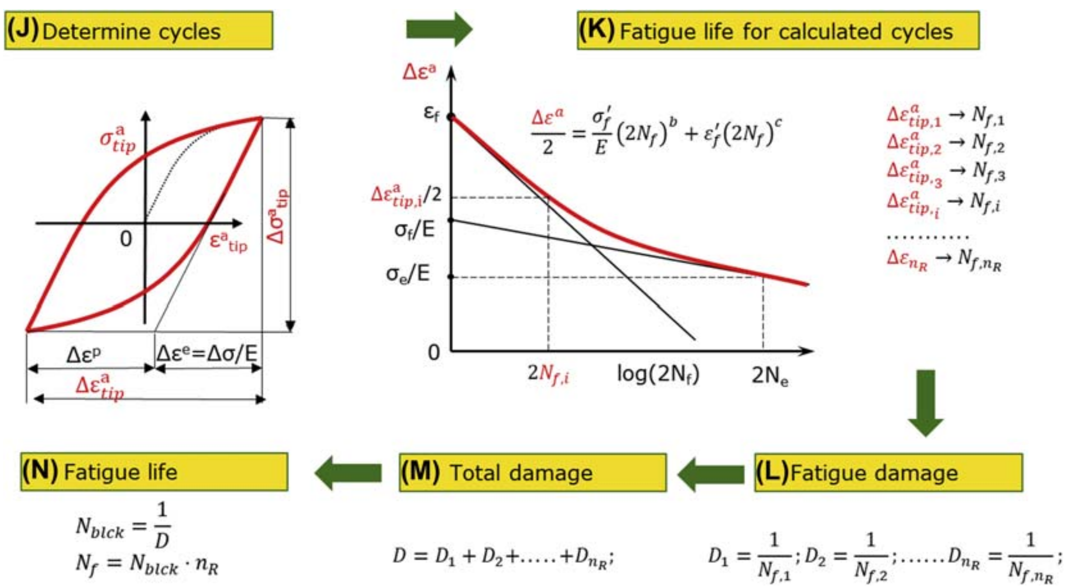

FIG. 3.20C Calculation of fatigue damage and prediction of fatigue life.

$$D_i = \frac{1}{N_{f,i}} \tag{3.11b}$$

Secondly, the total fatigue damage induced by one pass of the applied stress/load history needs to be calculated.

$$D = \sum_{1}^{n_R} D_{i_1} = D_1 + D_2 + \ldots + D_{n_R} = \frac{1}{N_{f,1}} + \frac{1}{N_{f,2}} + \ldots\ldots + \frac{1}{N_{f,n_R}} \tag{3.12}$$

Then the number of repetitions L_{blck} to failure of the applied stress/load history needs to be determined and finally the total number of cycles to failure N_f can estimated.

$$L_{blck} = \frac{1}{D} \tag{3.13}$$

$$N_f = L_{blck} \bullet n_R \tag{3.14}$$

It is important to note that the elastic-plastic stress-strain simulation at the notch tip requires analyzing the notch tip stress-strain fluctuations on reversal by reversal basis. This is due to the fact that the elastic-plastic stress-strain response at the notch tip depends on the previously applied loading/stress cycles, i.e. it is history dependent.

The fatigue damage of the current cycle depends on the previous stress-strain history at the notch tip. This is very important advantageous feature of the local stress-strain method because it accounts for the effect of the history, i.e. the damage of the current cycle and the fatigue life in general depend not only on the strain magnitude of each cycle but also on the sequence of their application.

6. The fracture mechanics (da/dN-ΔK) method

The third fatigue life prediction method used recently in practice is the Fracture Mechanics approach and it is based on the analysis of fatigue crack growth. It is known that each sufficiently large load or stress cycle may extend a pre-existing crack of size "a" by a certain increment "Δa". The fatigue life is in such a case equal to the number of loading or stress cycles necessary to grow the fatigue crack from its initial size "a_i" to its final or critical dimension "a_f". The fundamental parameter used in Fracture Mechanics analyses is the stress intensity factor K. In the case of cracked bodies, the fracture mechanics is used for assessing the crack growth rate and resulting fatigue life. The gross nominal stress S is used in this case (Fig. 3.21) to determine the principal parameter used in the analysis, i.e. the stress intensity factor K. Because the nominal stress fluctuates from its maximum S_{max} to its minimum value S_{min} the minimum and maximum stress intensity factors (K_{max} and K_{min}) need to be determine as well. The difference between the two stress intensity factors, named as the stress intensity range ΔK, is the main parameter for estimating the fatigue crack growth rate and subsequent fatigue life. It is also understood that the stress intensity factor K is the scaling parameter for

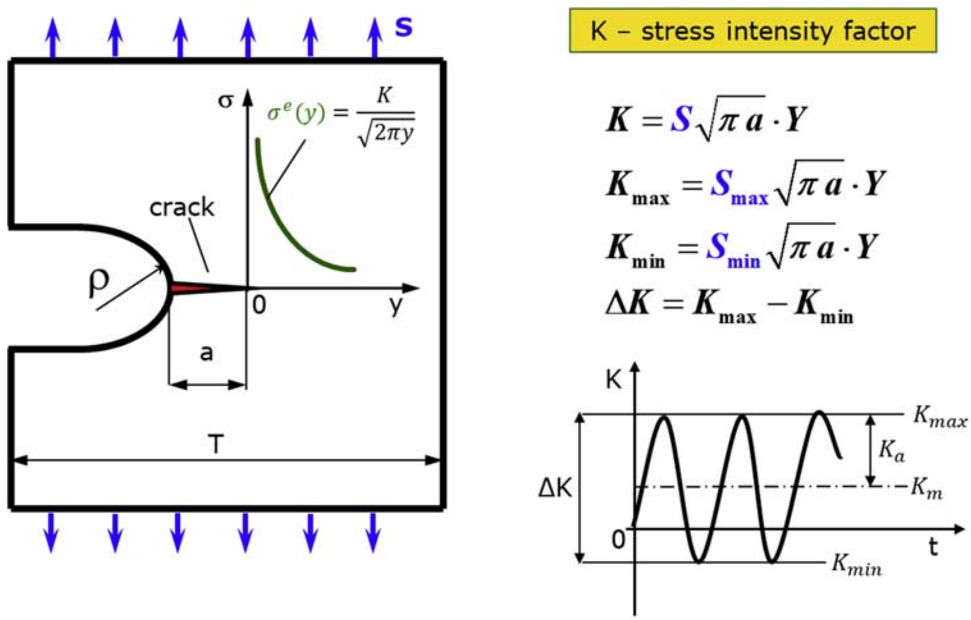

FIG. 3.21 Cracked component and the fluctuating stress intensity factor resulting from fluctuations of the nominal stress S.

the fluctuating stress field ahead of the fatigue crack. It is believed that cracks having the same stress intensity factors propagate with the same rate regardless of their size and geometry.

The stress intensity factor K is a parameter scaling the linear elastic stress distribution ahead of an infinitely sharp crack. It was found [82] that cracks of various geometries and subjected to various loading systems will grow with the same rate if their stress intensity factors are the same. Therefore, the use of only the stress intensity factor K is enough for the description of fatigue cracks behavior.

The Fracture Mechanics based fatigue life estimation methodology $\left(\frac{da}{dN-\Delta K}\right)$, as well as the two other procedures discussed earlier, requires collecting the input data as shown in Fig. 3.22. The load is represented, similarly to the previous two methods, by fluctuations of the loading (force, bending moment) or the nominal stress.

The effect of the geometry is contained in the stress intensity factor expression Eq. (3.15) given in the general form as (see Fig. 3.21):

$$K = S\sqrt{\pi a} \bullet Y \tag{3.15}$$

The geometry effects are accounted for by the Y parameter. Selected reference stress or the nominal stress S and the geometry parameter Y are interconnected, i.e. parameter Y is valid only for the reference stress S for which it has been determined. The determination of the stress intensity factor K is at the end reduced to finding the parameter Y dependent on the definition of the reference or nominal stress S, the crack size "a" and the overall geometry

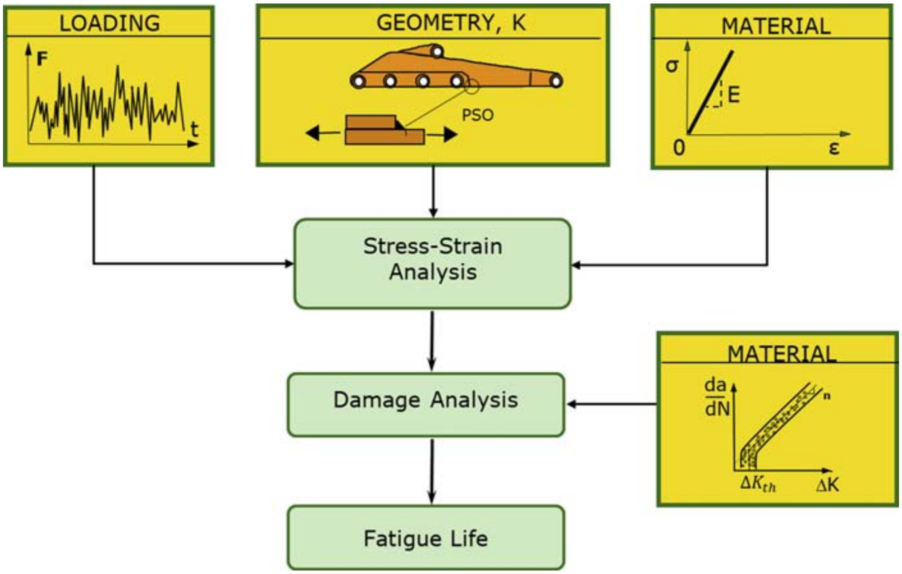

FIG. 3.22 Information path for the fatigue analysis based on the fatigue crack growth phenomenon.

of analyzed cracked body. A large variety of geometrical parameters Y can be found in several electronic and hard copy sources like the Handbook of Stress Intensity Factors [83].

The determination of the stress intensity factor requires knowing the nominal or specific reference stress S and the cracks size "a". The stress analysis is performed using the linear elastic material stress-strain model.

The sequence of steps required for the fatigue life estimation for a welded component based on the Fracture Mechanics approach can be summarized as follows:

First, the standard linear elastic stress analysis of an un-cracked structure/component needs to be carried out with the purpose of determining appropriate reference or nominal stress S (Fig. 3.23A–C).

The purpose of the stress analysis (Fig. 3.23D) is to transform the applied input load (stress, moment, force, nominal stress) into fluctuations of the nominal/reference stress, i.e. the determination of $S_{max,i}$ and $S_{max,i}$ for each stress cycle. Then the initial crack size and its geometry are measured or postulated, and the maximum and minimum stress intensity factors are calculated for each nominal/reference stress cycle and the current crack size. The purpose of the stress intensity factor analysis is determination of the stress intensity range (ΔK) for current stress/load cycle and current crack size a_i.

$$\Delta K_i = K_{max,i} - K_{min,i} = S_{max,i}\sqrt{\pi a_i}Y_i - S_{min,i}\sqrt{\pi a_i}\,Y_i = \Delta S_i\sqrt{\pi a} \tag{3.16}$$

The stress intensity factor formulation given in the form of expression Eq. (3.16) is used when the geometrical factor Y is available. In the case of complex stress distributions (Fig. 3.23F) in analyzed cross sections the weight function technique [84] can be used.

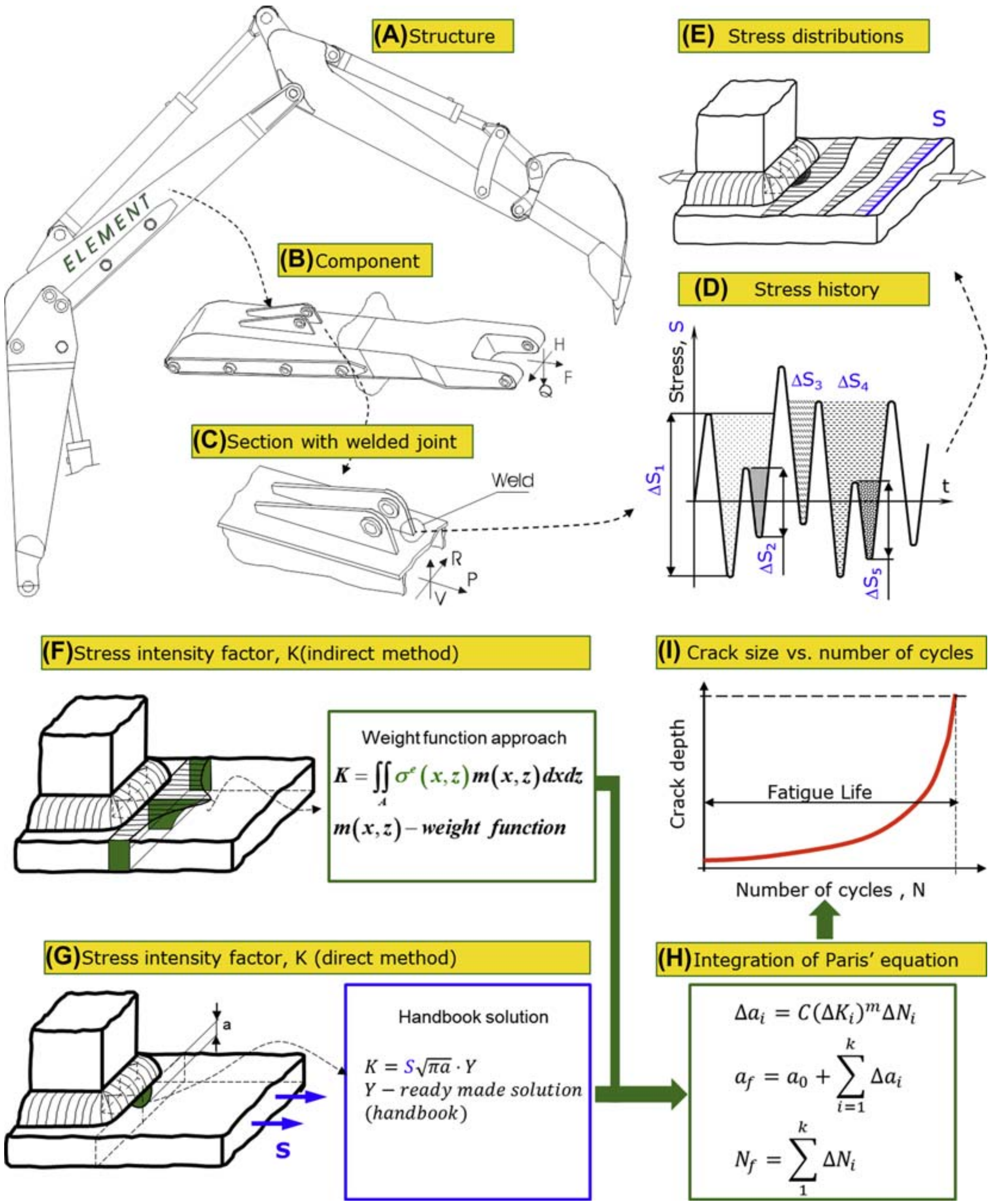

FIG. 3.23 Stepwise procedure for assessing the stress intensity factor and fatigue life of a cracked welded component.

The stress intensity factor range makes it possible to determine the crack growth increment induced by the current loading cycle providing that the material fatigue crack growth properties are given in the form of a fatigue crack growth rate expression such as:

$$\frac{da}{dN} = C(\Delta K)^m \tag{3.17}$$

The crack growth rate is replaced in practice by finite crack increments Δa_i and the number of associated loading cycles ΔK_i. However, the analysis is carried out most often on cycle by cycle basis, i.e. the crack increment is determined for each cycle in the sequence as they occur. Therefore, the crack growth rate used in practice is based on finite increments, i.e.

$$\frac{\Delta a_i}{\Delta N_i} = C(\Delta K_i)^m \tag{3.18}$$

The determination of the fatigue life requires integrating the material crack growth rate expression from the initial crack size a_0 until its final size a_f. The integration is most often carried out numerically or when possible analytically. The number of cycles N_f necessary to reach the final crack size a_f is the fatigue life of the component being analyzed.

$$a_i = a_0 + \sum_{1}^{i} \Delta a_i = a_0 + \sum_{i=1}^{i} C(\Delta K_i)\Delta N_i \; until \; a_i \leq a_f \tag{3.19}$$

$$N_f = \sum_{1}^{i} \Delta N_i \tag{3.20}$$

The fracture mechanics-based fatigue analyses are addressing only the crack growth phase of the entire fatigue process. However, the approach enables in practice the prediction of almost the entire fatigue life of a component when the initial crack is induced during manufacturing processes like welding. Besides that, the FM approach makes it possible to account quantitatively for the residual stress effect, loading sequence effect, fracture toughness of the material and geometry of the initial and the final crack.

7. The GY2 method for shell mesh weld modeling

It has been discussed in earlier sections that direct analytical or numerical determination of the linear elastic weld toe stress peak σ_{tip}^{e}, might be difficult and prohibitively labor intensive in the case of real large-scale welded structures. Therefore, the method involving the nominal, σ_n, or the hot spot stress, σ_{hs}, outlined in Section 4, is preferable when dealing with welded structures. Unfortunately, the nominal or the hot spot stresses are not unique when dealing with complex 3D stress distributions. Therefore, it is necessary to discuss all stress quantities used in fatigue durability analyses when dealing with welded structures and to define a unique non-arbitrary reference stress (similar to the hot spot stress) enabling determination of the linear elastic weld toe peak stress without any ambiguity. Various stress quantities used in strength analyses of welded structures are shown in Fig. 3.8.

The nominal stress σ_n is usually the maximum magnitude of the linearized stress field resulting from superposition of axial and bending stresses. This stress is unique and relatively easy to determine in cross sections away from the weld toe, but it might be more complex when dealing with several elements welded together and subjected to multiple loading modes. The nominal stress at the weld toe cross section might be sometimes coinciding with the hot spot stress σ^1_{hs}, but it may differ depending on its method of determination as pointed out in Refs. [6,26]. Therefore, needed is a definition and method of determination of the hot spot stress σ^1_{hs}, enabling subsequent unambiguous estimation of the weld toe peak stress σ^e_{tip}, regardless of the geometrical complexity of the welded joint and the loading configuration. It is also necessary to combine the unique hot spot stress σ^1_{hs}, with appropriate ready-made stress concentration factors Kt.

The aim of the stress analysis is to determine the "linear elastic" peak stress σ^e_{tip}, being subsequently used for calculations of the weld toe elastic-plastic strains ($\varepsilon^E or\, \varepsilon^N$) and associated stresses (σ^E or σ^N).

7.1 The nominal and the hot spot stress in a welded joint structure

The difficulty with defining and determining the nominal stress in welded structures is illustrated when analyzing stresses in the tubular welded joint shown in Fig. 3.24.

The load was applied (Fig. 3.24) by the hydraulic cylinder visible at the right-hand side upper corner of the photograph. The force generated torque and bending moment in the region where the two rectangular tubes have been welded together (the white colored region).

Therefore, detailed finite element analysis was carried out in order to obtain the reference stress data for comparison with stresses obtained from simplified models by using more efficient stress analysis method. The geometry and dimensions of the analyzed and tested

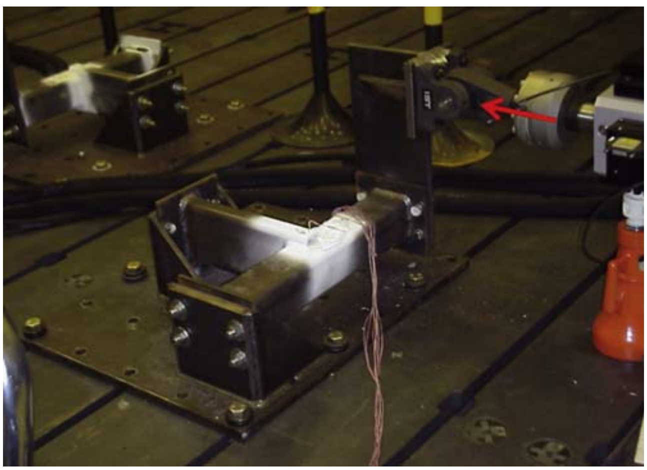

FIG. 3.24 Tubular welded joint subjected to simultaneous bending and torsion loading.

welded structure are given in Fig. 3.25. The weld toe radius of all welds was approximately r = 0.031in and therefore the finite element size modeling the weld toe region was approximately 4 times smaller, i.e. $\Delta r = 0.008$in. The solid and the FE model of the structure are shown in Fig. 3.26. The solid model shows the entire geometry of the analyzed object. The critical position was the end of the fillet weld joining the two tubes. Therefore, this region was modeled with small Finite Elements ($\Delta r = 0.008$in) and then the elements were gradually increased. Two types of elements were used, i.e. the tetrahedral and brick elements as shown Fig. 3.26. Both models provided almost the same stress data. The through the thickness stress distribution at the critical location is presented in Fig. 3.27.

The purpose of the simplified stress analysis method presented below is to recreate this stress distribution (Fig. 3.27) by using less detail and more economical model of the structure obtained by applying relatively large shell finite elements.

The through thickness distribution presented in Fig. 3.27 is the final goal of the simplified procedure described below. It is also worth to note that welded structures are often made of

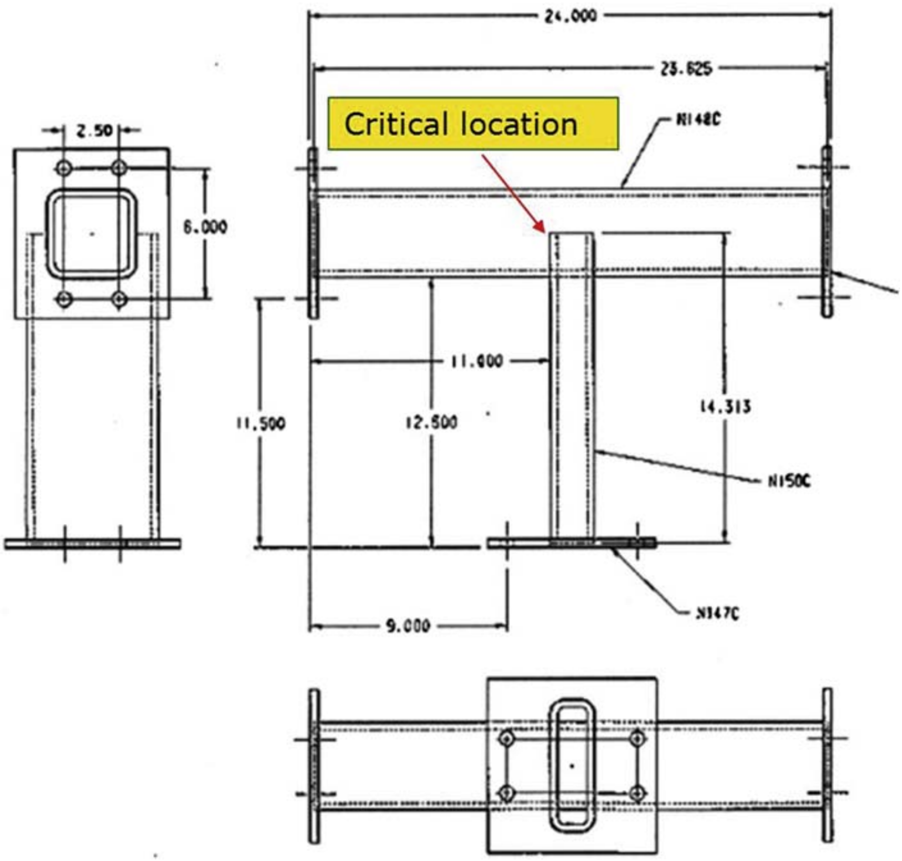

FIG. 3.25 Dimensions of the analyzed welded structure. All dimensions in inches. Tube wall thickness t = 0.312 in, Weld leg length h = 0.312 in, Weld angle $\theta = 45°$, Weld toe radius r = 0.031 in.

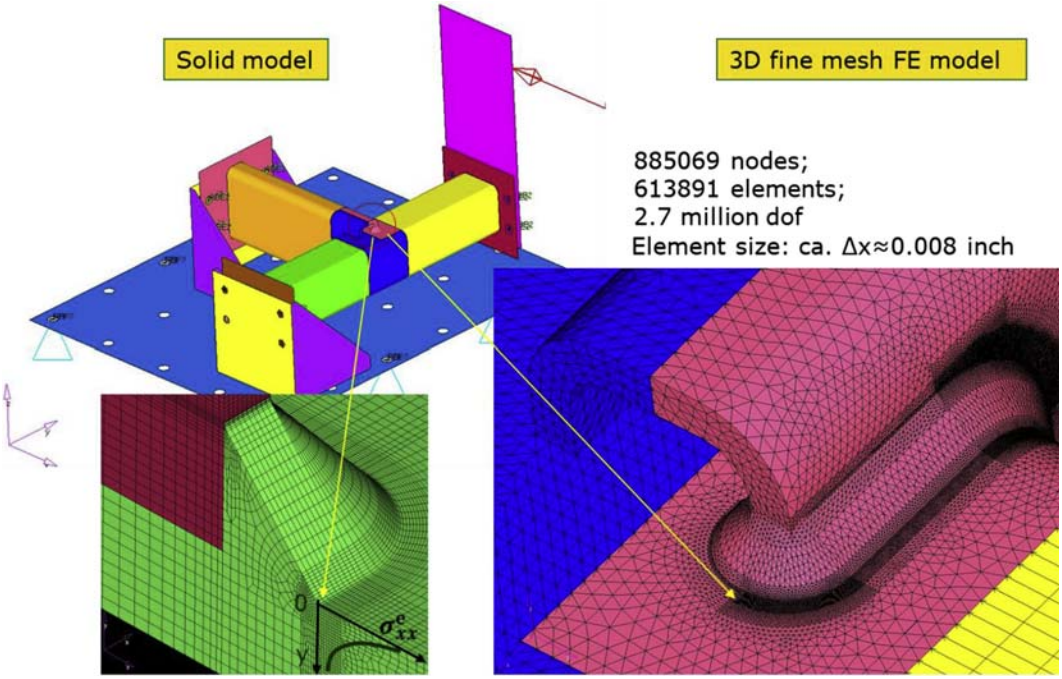

FIG. 3.26 Solid and detailed finite element models of the analyzed welded structure.

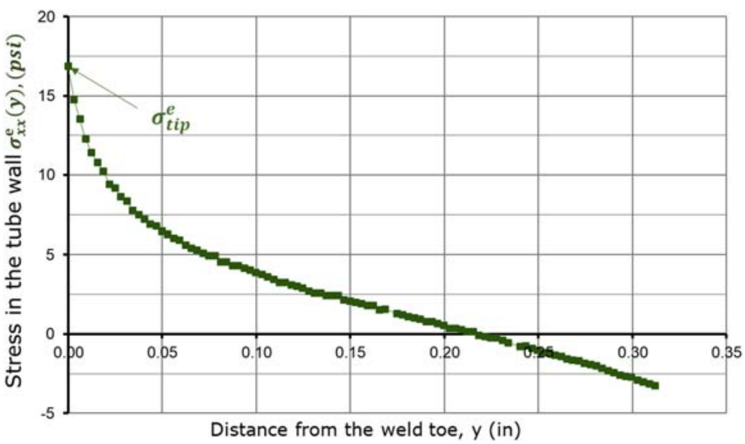

FIG. 3.27 Through the thickness stress distribution at the critical location.

thin walled components like tubes or plates. It means that the thickness dimension is relatively small while comparing with other dimensions of the structure or weldment. Therefore, welded structures are often modeled as so called thin walled structures were justified is the shell finite element technique.

Unfortunately, the information concerning the actual through thickness stress distribution and the magnitude of the weld toe peak stress are lost in such analyses. Therefore, it is necessary to identify stress quantities (or properties of the stress field) which are not lost in the FE shell model and which could be used for subsequent determination of the weld to peak stressσ^e_{tip}, necessary for fatigue analyses. Needed are in other words invariants of the stress field in the plane located at the weld toe position which are independent of the FE mesh size - like the hot spot nominal stress,σ_{hs}, and the slope of the linearized through thickness stress field,$\sigma_{hs}(y)$, or theσ^1_{hs} andσ^2_{hs} hot spot stresses on both sides of the plate thickness.

7.2 Various stress quantities in weldments and stress field invariants

The difficulty with using traditional reference stresses like the nominal stress,σ_n, or the classical [6,26] hot spot stress,σ_{hs}, lies in the fact that those stresses are not unique, and they depend on their method of determination. The simple geometry welded bracket illustrates the ambiguity of the nominal stress term.

It is relatively easy to define the nominal stress in the cross section (x = 0, y, z), denoted by the weld toe point A in Fig. 3.28, because it can be determined as the average stress.

$$\sigma_n = \frac{P}{A} = \frac{P}{t \cdot L} \tag{3.21}$$

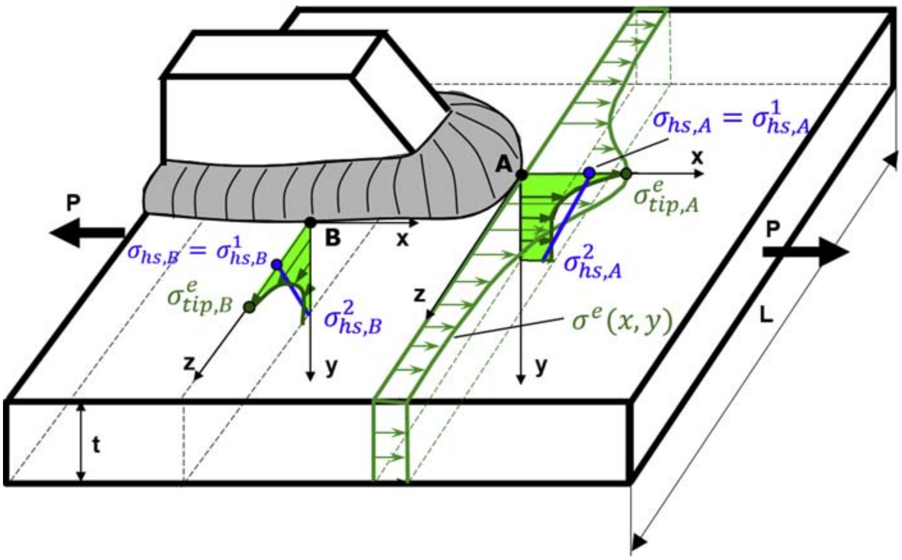

FIG. 3.28 Stress distributions in a welded bracket.

However, it is not obvious what nominal stress should be associated with the weld point B lying in plane denoted by the local coordinates (x, y, z = 0). One can use the same nominal stress as for point A, i.e. the average stress in section (x = 0, y, z) or to determine some kind of average stress in the cross section (x = 0, y, z) containing the weld point B and being strongly dependent on boundary conditions. It means that depending on the definition of the nominal stress being used the stress concentration factor at points A and B will also change in spite of the fact that the weld geometry along the weld length may stay the same. It also means that large library of stress concentration factors might be necessary in practice because they would vary for the same weld depending on the choice of the nominal stress definition.

Therefore, a more unique reference or nominal stress definition is needed in order to avoid confusion and deriving stress concentration factors being dependent on the choice of the nominal stress definition or the reference stress. Therefore, invariants of the stress field are needed based on which the unique definition of the reference/nominal stress can be formulated and used for subsequent determination of the weld toe peak stress,σ^e_{tip}.

Such stress field invariants, being independent of the weld geometry and unique for given location in a welded joint can be obtained in the form of the local hot spot stress achieved by the linearization (Fig. 3.29) of the stress field across the plate thickness. The linearization is understood as a transformation of the as received stress field into the statically equivalent linear stress field.

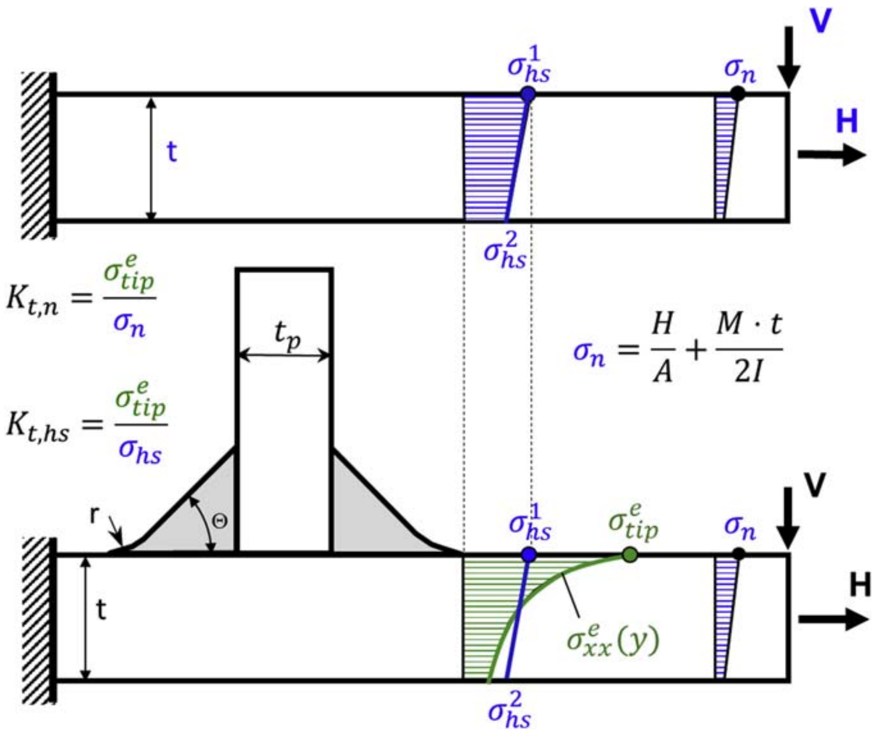

FIG. 3.29 "Linear elastic" stress fields in a plate and welded joint.

Let's analyze stress fields in a flat plate and welded joint (Fig. 3.29) having the same dimensions, the same thicknesses of load carrying plates and subjected to the same loading system. In the case of the flat plate without any welded attachments the stress field in any cross section along the plate length (except near the supporting end) can be determined by using simple membrane and bending stress formula.

$$\sigma_n = \frac{H}{A} + \frac{M \bullet t}{2I} \tag{3.22}$$

This includes the cross section coinciding with the weld toe position. However, in the case of welded joints the presence of the weld makes the through thickness stress distribution, $\sigma^e_{xx}(y)$, a nonlinear one in spite of the same overall geometry and the same load applied - even if this is a non-load carrying welded bracket. Because both objects shown in Fig. 3.29 have the same dimensions and the same loading systems it is obvious that there must be some relationships between the linear through thickness stress field defined by stresses σ^1_{hs} and σ^2_{hs} in the flat plate and the nonlinear stress distribution $\sigma^e_{xx}(y)$, in the weldment cross section. Those are the internal loads, i.e. the axial force and the bending moment equilibrating the external loads V and H must the same in the unwedded and welded plate. It means that when the nonlinear stress distribution $\sigma^e_{xx}(y)$, is replaced by the equivalent linear stress distribution defined by the hot spot stresses σ^1_{hs} andσ^2_{hs}. The equivalence of the linear and nonlinear stress field means that they have the same internal forces, i.e. the same axial force and the same bending moment. This is due to the fact that in both cases the internal loads in both cross sections coinciding with the weld toe position must equilibrate the same external loads. In other words, the internal axial force and the bending moment in the weld cross section must be the same as those in the analogous cross section in the flat plate element. It means that internal forces in the weld toe cross section are invariant and independent of detail geometrical features of the welded attachment. This further means that the nonlinear stress distribution $\sigma^e_{xx}(y)$, depends on the geometry of the welded attachment and it may change when the weld size or the weld geometry vary. However, the statically equivalent linearized stress distribution, characterized by stresses σ^1_{hs} andσ^2_{hs}, remains the same providing that the external loads V and H remain the same in both cases. Therefore the aim of the methodology discussed below is to accurately determine the equivalent linearized stress distribution in the weldment, characterized by the hot spot stresses σ^1_{hs} andσ^2_{hs}, and then to convert it into the equivalent nonlinear stress distribution $\sigma^e_{xx}(y)$. The advantage of such an approach lies in the fact that the accuracy of the non-linear stress distribution $\sigma^e_{xx}(y)$ depends on the FE mesh (i.e. the finite element size) while the equivalent linearized stress distribution is independent of the FE mesh because it always must satisfy the equilibrium conditions − regardless of the size of finite elements being used for modeling the weldment. It means that the accuracy of the equivalent linearized stress field in the weld cross section does not depend on the accuracy of the nonlinear stress field distribution. Therefore, when the purpose of the FE analysis is to determine hot spot stresses σ^1_{hs} andσ^2_{hs} the accuracy of the nonlinear stress distribution is not so important as long as it satisfies necessary equilibrium conditions. The purpose of the method discussed below is to determine first an approximate instead of very accurate through the thickness stress distribution $\sigma^e_{xx}(y)$ from a coarse FE model of the weldment. The approximate nonlinear stress distribution $\sigma^e_{xx}(y)$ is sufficient, regardless of its accuracy, for the determination of hot spot stresses σ_{hs}^1 and σ_{hs}^2. These two hot spot stresses can be subsequently used for the simulation of sufficiently accurate through the thickness stress distribution $\sigma_{xx}^e(x)$ and estimation of the weld toe peak stress σ_{tip}^e. The advantage of such a use of the finite element method lies in the fact that even very approximate coarse FE mesh provides through thickness stress distribution sufficient for accurate estimation of the linear stress distribution and hot spot stresses σ_{hs}^1 and σ_{hs}^2.

However, it is important and helpful to understand well differences between the classical nominal stress and various hot spot stresses used in contemporary engineering practice and that one used in the proposed methodology.

7.3 The nominal stress in welded structures

The nominal stress is usually defined as the average membrane or bending stress in the analyzed cross section resulting from the linearization of the actual nonlinear stress distribution (shown in Fig. 3.30). The average/nominal stress is usually obtained by averaging the actual non-linear stress field over selected part ($A = L \cdot t$) or over the entire cross section area ($A = W \cdot t$) of interest. The average/nominal stress,σ_n, in the case of the weldment shown in Fig. 3.30A does not depend on the dimension L because the stress distribution is one-dimensional, i.e. it depends on only one coordinate y.

$$\sigma_n = \frac{\int_{-t}^{0} \int_{-L/2}^{L/2} \sigma^e(y,z)dxdy}{t \cdot L} = \frac{P}{t \cdot W} \tag{3.23}$$

However, this is not true in the case of the geometry shown in Fig. 3.30B where the stress distribution is two-dimensional, i.e. it depends on coordinates x and z. The average stress in such a case is dependent on coordinate z as well, i.e. the choice of dimension L. The definition of dimension L and the size W might be non-unique in the case of complex 3D geometrical configurations like tubular connections or welded excavator arm.

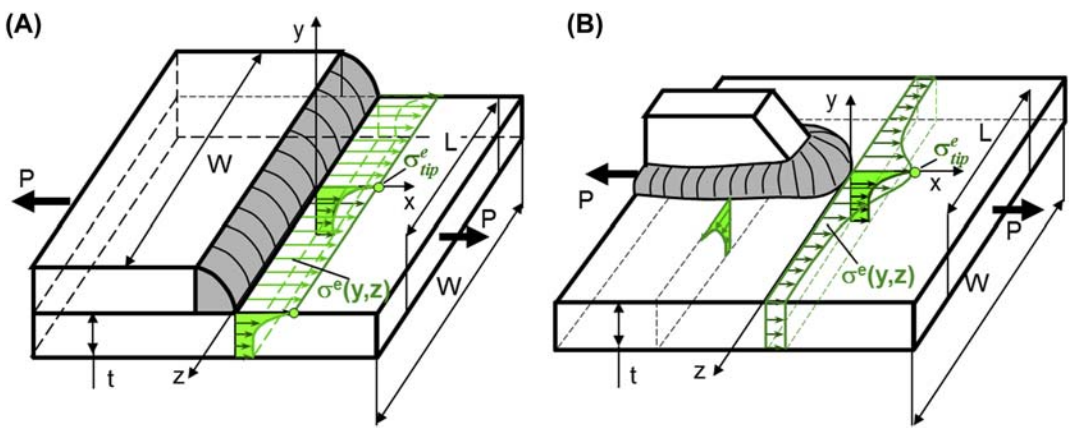

FIG. 3.30 Typical linear elastic stress distributions in weldments.

$$\sigma_n = \frac{\int_{-t}^{0} \int_{-L/2}^{L/2} \sigma^e(y,z)dxdy}{t \bullet L} \neq \frac{P}{t \bullet W} \tag{3.24}$$

The two simple examples illustrate the non-uniqueness of the nominal stress which in practice may lead to inconsistent combination of nominal stresses and stress concentration factors. The non-uniqueness of the nominal stress definition requires using various stress concentration factors depending on the nature of the nominal stress. This in consequence requires using various stress concentration factors for the same geometry depending on the current definition of the nominal stress. Therefore, required is unique and consistent definition of the reference stress and associated stress concentration factors.

7.4 Definition of the local nominal stress or the local hot spot stress

The traditional nominal stress is usually defined for the entire cross section or part of the cross section associated with finite area over which the stress is acting. For this reason, its magnitude may depend on the choice of the averaging surface area. On the other hand, it is known that fatigue process depends strongly on the local stress magnitude where the fatigue crack may get initiated. Therefore, it is proposed to link the definition of the nominal or the hot spot stress with the point (location) at which the fatigue crack initiation life is to be estimated. This can be achieved by linearization of the actual stress distribution at given point on the weld toe line over only the plate thickness and not over the cross section area (Fig. 3.29).

First the hot spot membrane $\sigma^m_{hs,A}$ and bending $\sigma^b_{hs,A}$ stress need to be determined by integration of the stress distribution $\sigma^e(y,z)$ at chosen location A on the weld toe line, i.e. over the thickness dimension, t. Those stresses enable also to determine the local hot spot stresses, $\sigma^1_{hs,A}$ and $\sigma^2_{hs,A}$, which can be used for the S-N fatigue analysis method when needed.

$$\sigma^m_{hs,A} = \frac{\int_{-t}^{0} \sigma^e(y,z=0)dy}{t} \tag{3.25}$$

$$\sigma^b_{hs,A} = \frac{6 \cdot \int_{-t}^{0} \sigma^e(y,z=0)ydy}{t^2} \tag{3.26}$$

$$\sigma^1_{hs,A} = \sigma_{hs,A} = \sigma^m_{hs,A} + \sigma^b_{hs,A} = \frac{\int_{-t}^{0} \sigma^e(y,z=0)dy}{t} + \frac{6 \cdot \int_{-t}^{0} \sigma^e(y,z=0)ydy}{t^2} \tag{3.27}$$

$$\sigma^2_{hs,A} = \sigma^m_{hs,A} - \sigma^b_{hs,A} \tag{3.28}$$

The membrane and bending hot spot stress $\sigma^m_{hs,A}$, and $\sigma^b_{hs,A}$, respectively enable subsequently to determine the linear elastic peak stress $\sigma^e_{tip,A}$, at the point A on the weld toe line, necessary for further fatigue analyses.

Analogous analysis can be carried out for point B on the weld toe line and there is no ambiguity concerning the hot spot stress definition as it would be in the case of the nominal stress definition at this location.

7.5 The composed stress concentration factors for weldments

In order to determine the linear elastic stress $\sigma^e_{tip,A}$, at the weld toe needed are reference/nominal stress,σ_n, and the stress concentration factor K_t, as discussed earlier (3.1). The classical stress concentration factor is defined as the ratio of the nominal stress over the linear elastic peak stress. The classical stress concentration factor is, as shown in Fig. 3.31, analogously defined in the case of welded components.

$$K_t = \frac{\sigma^e_{tip}}{\sigma_n} = \frac{\sigma^e_{tip}}{\sigma_{hs}} = \frac{\sigma^e_{tip}}{\sigma^m_{hs} + \sigma^b_{hs}} \tag{3.29}$$

$$where, \ \sigma^m_{hs} = \frac{\sigma^1_{hs} + \sigma^2_{hs}}{2} \quad and \quad \sigma^b_{hs} = \frac{\sigma^1_{hs} - \sigma^2_{hs}}{2} \tag{3.30}$$

Unfortunately, such stress concentration factors depend not only on the geometrical features of the welded component but also on the ratio of the membrane to bending hot spot stress $\sigma^m_{hs}/\sigma^b_{hs}$.

Hot spot stress, σ_{hs}, may in reality have different stress concentration factors and generate different weld toe stresses σ^e_{tip}, as shown in Fig. 3.32. It means that classical stress concentration factors for those two cases are different ($K^1_{t,hs} \neq K^2_{t,hs}$) in spite of the same geometry and the same hot spot stress.

Therefore, in order to avoid generating stress concentration factors for a variety of loading combinations resulting in various ratios of membrane to bending stress it is proposed to use only two stress concentration factors related to only pure membrane and bending nominal hot spot stresses.

Stress concentration factors for pure axial (membrane stress) and bending loading configurations do not depend on the loading or the nominal stress magnitude. They are functions of

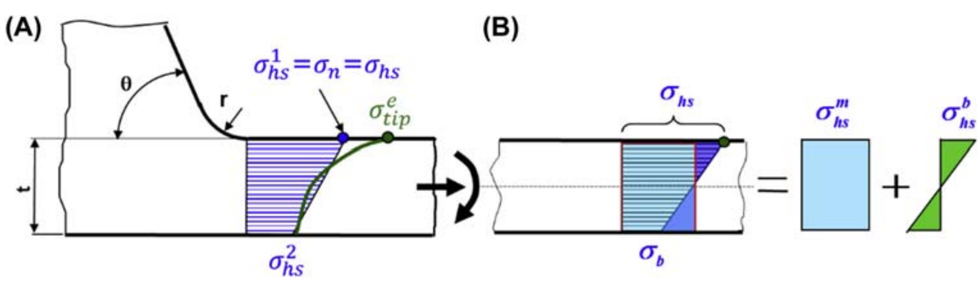

FIG. 3.31 The linearized through thickness stress distribution in a weldment and the membrane and bending hot spot contributions.

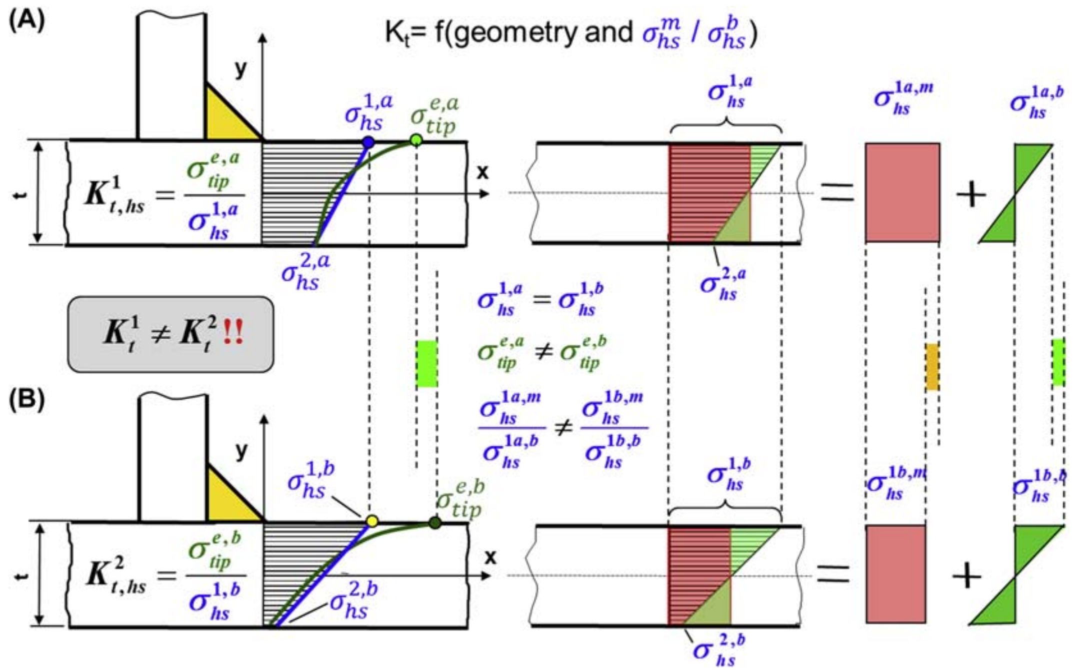

FIG. 3.32 Various weld peak stresses, $\sigma_{tip}^{e,a}$ and $\sigma_{tip}^{e,b}$, generated in the same weldment and subjected to the same hot spot stress $\sigma_{hs}^{1,a} = \sigma_{hs}^{1,b}$.

only geometrical properties of the analyzed weldment. Therefore, the pure membrane and bending stress concentration factors are unique for given geometry as illustrated in Fig. 3.33.

It has been also indicated that the same hot spot stresses produce, similarly to machined notches, different peak stresses at the weld toe (i.e. the notch tip) depending on the type of loading.

The proposed method of calculating the weld toe peak stress σ_{tip}^e, is to use the membrane and bending hot spot stresses (σ_{hs}^m and σ_{hs}^b) and appropriate stress concentration factors derived for only pure axial and bending load configurations ($K_{t,hs}^m$ and $K_{t,hs}^b$).

The weld toe stress peak can be subsequently determined as:

$$\sigma_{tip}^e = K_{t,hs}^m \cdot \sigma_{hs}^m + K_{t,hs}^b \cdot \sigma_{hs}^b \tag{3.31}$$

Expression Eq. (3.31) is valid for any membrane to bending stress ratio. The first advantage of using expression Eq. (3.31) lies in the fact that the two stress concentration factors need to be obtained only once for given geometry and can be used for any combination of membrane and bending stress. The second advantage is the use of hot spot stresses which can be determined from a simplified shell finite element model of the analyzed welded structure.

In summary – determination of the linear weld toe peak stress σ_{tip}^e, requires the knowledge of the membrane and bending hot spot stresses, σ_{hs}^m and σ_{hs}^b, respectively and corresponding stress concentration factors, $K_{t,hs}^m$ and $K_{t,hs}^b$.

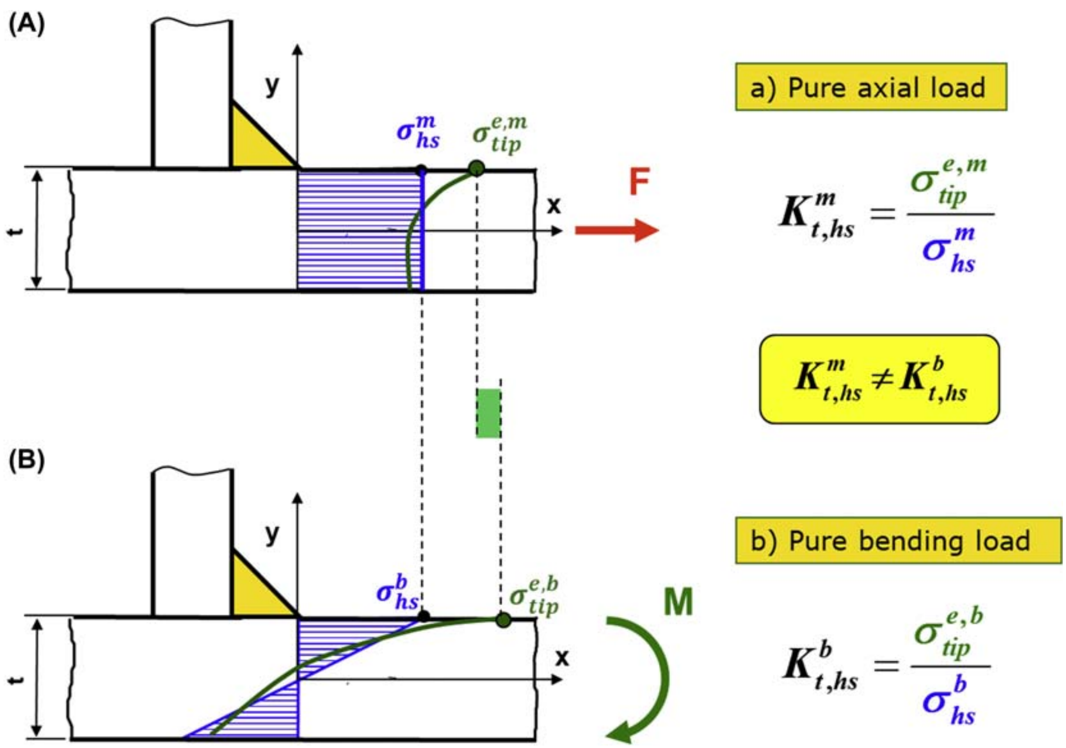

FIG. 3.33 Generic stress concentration factors for pure membrane and bending hot spot stress distributions.

7.6 Determination of the shell hot spot stresses σ^{m}_{hs} and σ^{b}_{hs}

The shell finite element method is a convenient simplification of the stress analysis problem in the case of thin walled structures as welded structures often are.

However, it is important to model it and analyze in a way providing sufficient data for the estimation of necessary stresses. The methodology explained next was initially proposed by Chattopadhyay [71]. Needed is the through thickness stress distribution being the base for determining the membrane and bending hot spot stresses σ^{m}_{hs} and σ^{b}_{hs}, respectively. The through the thickness stress distribution in shell elements is assumed in most cases linear. Therefore, the hot spot stresses σ^{m}_{hs} and σ^{b}_{hs}, are sufficient for the complete description of the stress field. However, due to simplifications made when modeling (Fig. 3.34) the analyzed welded structure with shell finite elements several geometrical details of the actual structure are omitted (like the weld angle and the weld toe radius).

It is important to remember that the cross section of interest is that one located at the weld toe which is the location of the maximum stress. However, the weld toe region is not modeled (Fig. 3.34) in the shell finite element model. On the other hand, even in the shell FE model the hot spot stresses must be obtained at the physical location of the weld toe, i.e. at point A located at the same distance from the axis of symmetry of the bracket plate as it is in reality. Removal of the weld is not always possible because the weld metal changes the stiffness of

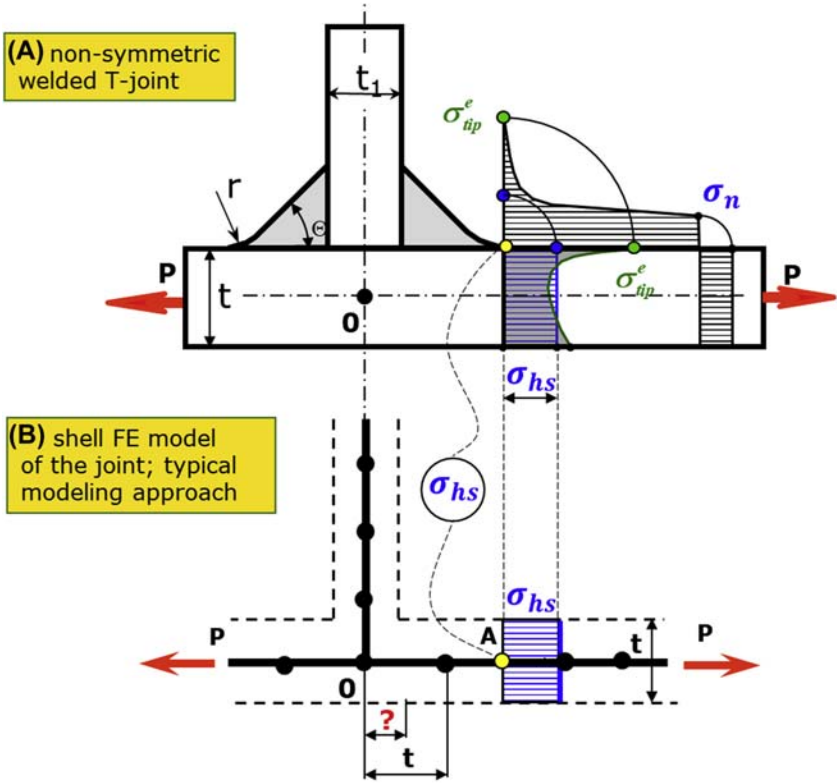

FIG. 3.34 The actual weldment geometry and its shell finite element model.

the weld toe region. Therefore, it was recommended to add the shell element imitating the weld stiffness. It was found that an inclined shell element (Fig. 3.35) with declared thickness equal to the thinner plate should be added in order to account of the weld effect on the hot spot stress in the critical cross section. Such requirements subsequently determine the finite element size and the mesh configuration as shown in Fig. 3.35.

It is recommended that the shell element, imitating the weld, should be attached to both plates at the middle of the leg length of the physical weld. It means that the position of the weld toe is located half weld leg length away from the node/point where the shell weld element is attached to the welded plate. This way stresses are determined at the physical location of the weld toe and they are not perturbed by connection if several finite elements at the same node. It means that the point connecting the weld element and the plate in the FE shell model is located at the distance h/2 (half weld leg length) away from the physical position of the weld toe. It also means that the shell finite element modeling the weld should not be bigger than half of the weld leg length. The finite element mesh size and the shell model of the joint are shown in Fig. 3.35D. The FE shell model presented above has been termed as the GY2 model.

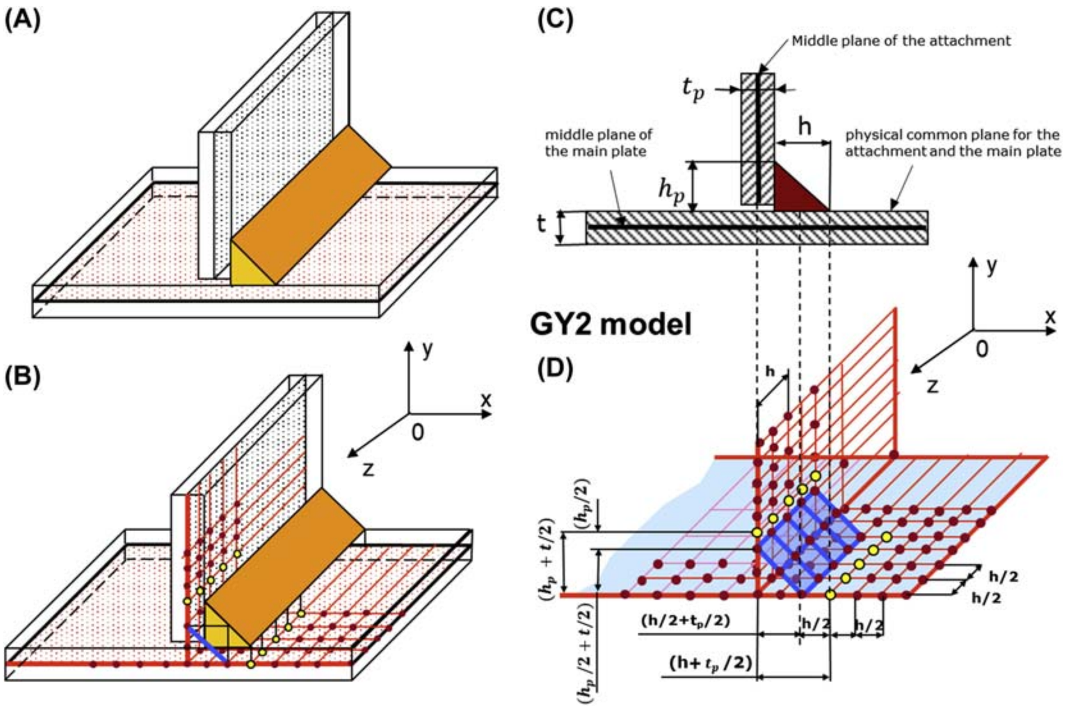

FIG. 3.35 Welded T-joint and its shell FE model; (A) welded joint with a vertical bracket, (B) welded joint with superposed shell finite element mesh, (C) essential dimensions of the weldment; (D) the shell finite element model of the weldment.

Analogous shell finite element model is presented in Fig. 3.36 where the overlap welded joint is used as an example. The weld shell element is joining the main plate at the center of the weld leg length (h/2) and it is located at the distance (h/2) away from the physical location of the weld toe. The required stress should be determined at nodes or Gaussian points (yellow) coinciding with the physical position of the weld toe.

The shell stresses σ_{hs}^1 and σ_{hs}^2 found at weld toe location are the base for finding the membrane and bending hot spot stresses Eq.(3.30) as shown in Fig. 3.31.

The decomposition of shell FE stresses is also shown in Fig. 3.37 where the linearized through thickness shell FE stress distribution relates to the critical location of the tubular welded structure shown in Fig. 3.26. It is noticeable that the bending stress σ_{hs}^b is prevailing at that location and the membrane stress σ_{hs}^m is tensile.

In summary − the method can be carried out using the following stepwise procedure:

- The shell element simulating the stiffens of the weld must be attached to the plate coinciding with the location of the center of the weld leg length,
- The stress reference point must be located at the physical weld toe position,
- The size of the smallest shell element can be of the order of the plate thickness t,

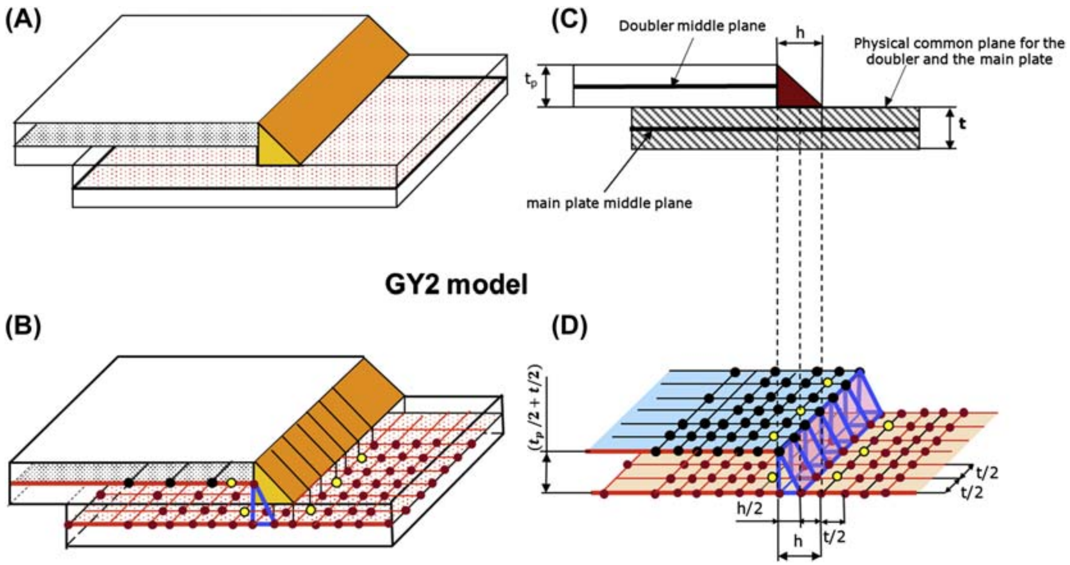

FIG. 3.36 Welded overlap joint and its shell FE model; (A) welded joint with an overlapping welded plate, (B) welded joint with superposed shell finite element mesh, (C) essential dimensions of the overlapping welded joint; (D) the shell finite element model of the weldment.

- It is recommended to locate nodes of finite elements along the weld toe line and read the nodal stress components along this line,
- Shell stresses components (σ^1_{hs} and σ^2_{hs}) located on both side of the plate thickness are needed for the subsequent analysis.

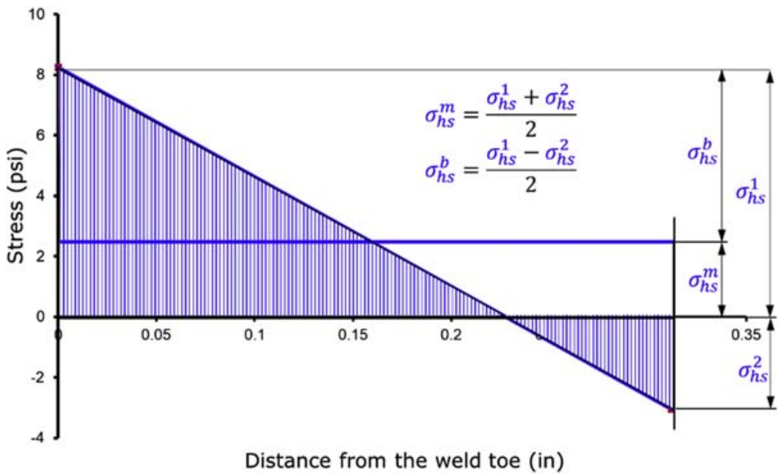

FIG. 3.37 Linearized through thickness stress distribution obtained from the shell FE model.

In order to determine the linear elastic weld toe stressσ^{e}_{tip}, at the weld toe the hot spot membrane and bending stresses need to be combined, according to Eq. (3.31), with appropriate stress concentration factors.

7.7 Stress concentration factors for welds

The advantage of using the hot spot stresses as the reference is the fact that only two stress concentration factors are needed for all butt welds, another two for all one-sided (asymmetric) fillet welds and the third set for all symmetric (double) fillet welds. It means that six ready-made stress concentration factor expressions are sufficient for analysis of most of welded joints encountered in engineering practice.

The Japanese stress concentration factors derived by Uemura and Iida [68] are recommended for obtaining stress concentration factors for analyzed welded joints.

7.7.1 Stress concentration factors for butt welded joints

Stress concentration factor K_t^m for pure tension load (Fig. 3.38)

$$K_t^m = 1 + \frac{1 - exp\left(-0.9\theta\sqrt{\frac{W}{2h}}\right)}{1 - exp\left(-0.45\pi\sqrt{\frac{W}{2h}}\right)} \times 2\left[\frac{1}{2.8\left(\frac{W}{t}\right) - 2} \times \frac{h}{r}\right]^{0.65}; Where: \quad W = t + 2h + 0.6h_p \tag{3.32}$$

Stress concentration factor K_t^b for pure bending load (Fig. 3.38)

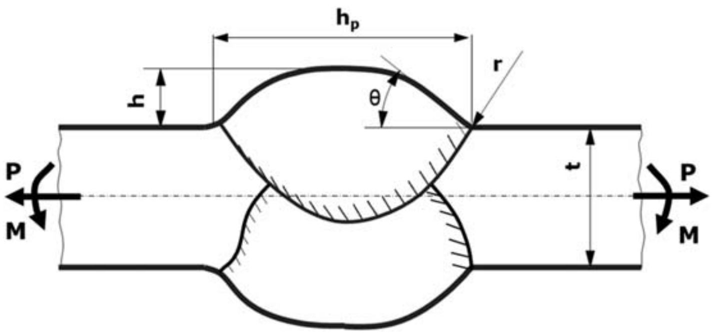

FIG. 3.38 Geometry and notation for calculating stress concentration factor at the weld toe radius location of a butt weld.

$$K_t^b = 1 + \frac{1 - exp\left(-0.9\theta\sqrt{\frac{W}{2h}}\right)}{1 - exp\left(-0.45\pi\sqrt{\frac{W}{2h}}\right)} \times 1.5\sqrt{tanh\left(\frac{2h_p}{t+2h} + \frac{2r}{t}\right)}$$

$$\times\, tanh\left[\frac{\left(\frac{2h}{t}\right)^{0.25}}{1 - \frac{r}{t}}\right] \times \left[\frac{0.13 + 0.65\left(1 - \frac{r}{t}\right)^{4}}{\left(\frac{r}{t}\right)^{\frac{1}{3}}}\right] Where: \quad W = t + 2h + 0.6h_p \tag{3.33}$$

7.7.2 *Stress concentration factors for asymmetric fillet welds* (T-*welded joint*)

Stress concentration factor K_t^m for pure tension load (Fig. 3.39)

$$K_t^m = 1 + \frac{1 - exp\left(-0.9\theta\sqrt{\frac{W}{2h}}\right)}{1 - exp\left(-0.45\pi\sqrt{\frac{W}{2h}}\right)} \times \left[\frac{1}{2.8\left(\frac{W}{t}\right) - 2} \times \frac{h}{r}\right]^{0.65};$$

$$Where: \quad W = (t + 2h) + 0.3(t_p + 2h_p) \tag{3.34}$$

Stress concentration factor K_t^b for pure bending load (Fig. 3.39)

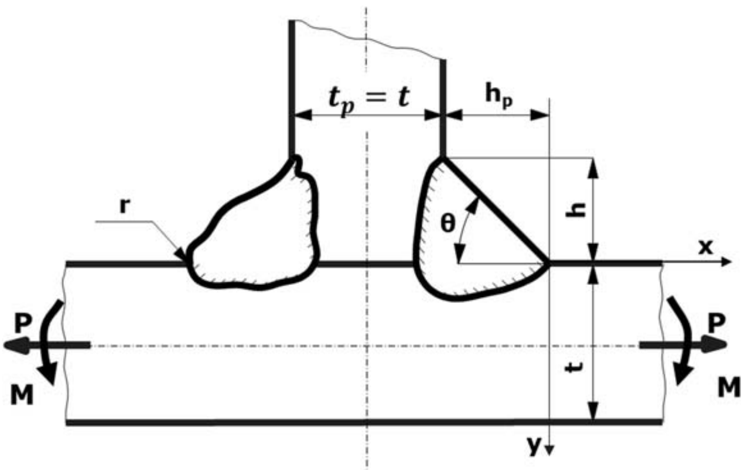

FIG. 3.39 Geometry and notation for calculating stress concentration factor at the weld toe of asymmetric fillet weld in a T-butt welded joint.

$$K_t^b = 1 + \frac{1 - exp\left(-0.9\theta\sqrt{\frac{W}{2h}}\right)}{1 - exp\left(-0.45\pi\sqrt{\frac{W}{2h}}\right)} \times 1.9\sqrt{tanh\left(\frac{2t_p}{t+2h} + \frac{2r}{t}\right)}$$

$$\times\, tanh\left[\frac{\left(\frac{2h}{t}\right)^{0.25}}{1-\frac{r}{t}}\right] \times \left[\frac{0.13 + 0.65\left(1-\frac{r}{t}\right)^4}{\left(\frac{r}{t}\right)^{\frac{1}{3}}}\right] \quad Where: \quad W = (t+2h) + 0.3(t_p + 2h_p) \tag{3.35}$$

7.7.3 Stress concentration factors for symmetric fillet welds (cruciform joint)

Stress concentration factor K_t^m for pure tension load (Fig. 3.40)

$$K_t^m = 1 + \frac{1 - exp\left(-0.9\theta\sqrt{\frac{W}{2h}}\right)}{1 - exp\left(-0.45\pi\sqrt{\frac{W}{2h}}\right)} \times 2.2\left[\frac{1}{2.8\left(\frac{W}{t}\right) - 2} \times \frac{h}{r}\right]^{0.65}$$

$$where: W = (t + 4h) + 0.3(t_p + 2h_p) \tag{3.36}$$

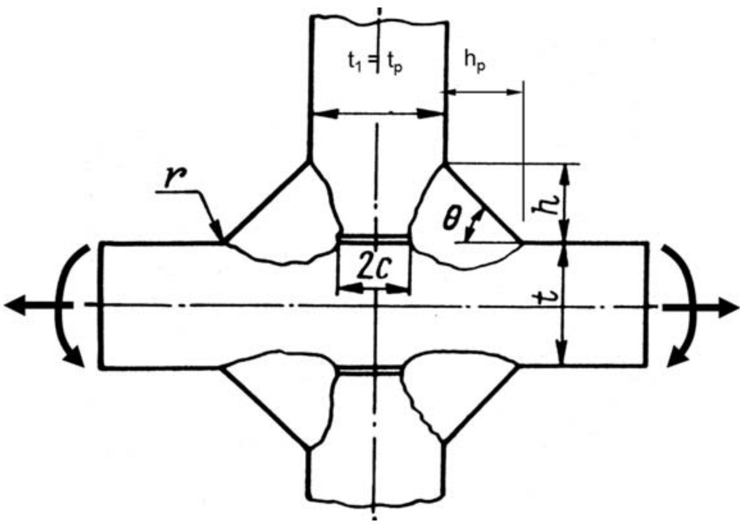

FIG. 3.40 Geometry and notation for calculating stress concentration factor at a symmetric fillet weld toe location in a cruciform joint.

Stress concentration factor K_t^b for pure bending load (Fig. 3.40)

$$K_t^b = 1 + \frac{1 - exp\left(-0.9\theta\sqrt{\frac{W}{2h}}\right)}{1 - exp\left(-0.45\pi\sqrt{\frac{W}{2h}}\right)} \times \sqrt{tanh\left(\frac{2t_p}{t+2h} + \frac{2r}{t}\right)}$$
$$\times\, tanh\left[\frac{\left(\frac{2h}{t}\right)^{0.25}}{1 - \frac{r}{t}}\right] \times \left[\frac{0.13 + 0.65\left(1 - \frac{r}{t}\right)^4}{\left(\frac{r}{t}\right)^{\frac{1}{3}}}\right] Where:\quad W = (t + 4h) + 0.3(t_p + 2h_p) \tag{3.37}$$

7.8 Example — Illustration of GY2 weld model

In order to illustrate the use of shell finite element stress data for the determination of the linear elastic stress at the weld toe σ_{tip}^e, the FE shell analysis was carried out for the geometry presented in Fig. 3.26. The fine mesh 3-D FE model, shown in Fig. 3.27, provided the estimation of the linear elastic peak stress, $\sigma_{tip}^e = 16.9$ ksi, as the reference for the assessment of the accuracy of the weld toe stress based on shell FE stress data. It is to note that the 3-D FE model required 613,891 finite elements to model all geometrical detail of the analyzed structure.

The shell finite element model of the analyzed welded structure, prepared according to the rules described in Section 7.6, is presented in Fig. 3.41. The entire structure required only 18,858 finite elements, i.e. 32 times fewer elements than the 3D FE model. Three locations with high hot spot stresses have been found as indicated in Fig. 3.42.

The hot spot stresses at Location 1 obtained from the shell FE model were:

$$\sigma_{hs}^1 = 8.25\,\text{ksi},\ \sigma_{hs}^2 = -3.05\,\text{ksi}$$

The membrane and bending hot spot stresses were subsequently calculated as:

$$\sigma_{hs}^m = \frac{\sigma_{hs}^1 + \sigma_{hs}^2}{2} = \frac{8.25 + (-3.05)}{2} = 2.60\text{ksi}$$

and

$$\sigma_{hs}^b = \frac{\sigma_{hs}^1 - \sigma_{hs}^2}{2} = \frac{8.25 - (-3.05)}{2} = 5.65\text{ksi}$$

The stress concentration factors for dimensions given in Fig. 3.25 were found using Eqs. (3.34) and (3.35).

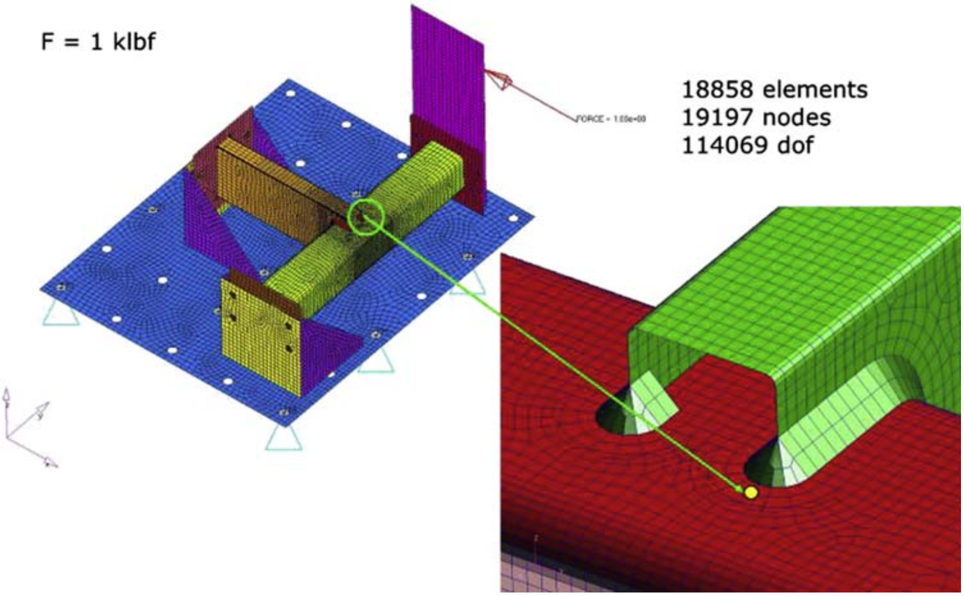

FIG. 3.41 The shell finite element model of analyzed welded structure.

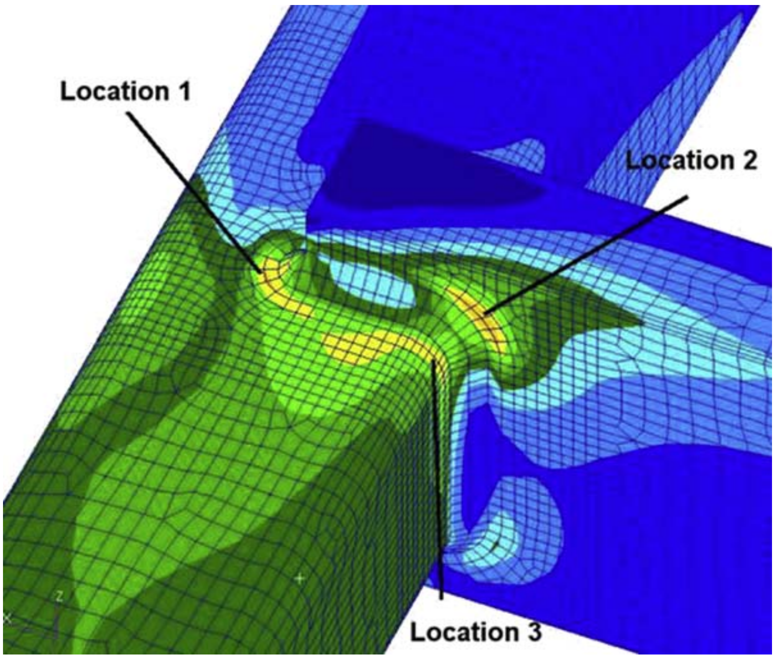

FIG. 3.42 Three regions of high stresses at theoretical weld toe locations.

$$K_{t,hs}^{m} = 1.784 \text{ and } K_{t,hs}^{b} = 2.203$$

The linear elastic peak stress at the weld toe (Location 1) was subsequently determined as:

$$\sigma_{tip}^{e} = \sigma_{hs}^{m} \cdots K_{t,hs}^{m} + \sigma_{hs}^{b} \cdots K_{t,hs}^{b} = 2.6 \times 1.784 + 5.65 \times 2.203 = 17.1 \text{ ksi}$$

Analogous stress obtained from the fine mesh 3D FE model (Fig. 3.27) was:

$$\sigma_{tip}^{e} = 16.9 \text{ ksi}$$

The fine mesh FE data (Fig. 3.27) and those obtained from the simplified large element shell model (Figs. 3.41 and 3.42) are listed in Table 3.1.

It is interesting to note that the weld toe peak stresses σ_{tip}^{e}were almost the same at Locations 1 and 2 where the Location 2 appears to be the most critical one. The fatigue cracks were noticed at both locations while testing the structure.

7.9 Conclusions − GY2 weld model

- The GY2 shell FE method makes it possible to determine local membrane and bending reference or hot spot stresses at any point along the weld toe line.
- The local membrane and reference hot spot stresses enables using pure tension and pure bending stress concentration factors applicable to any point along the weld toe line.
- Therefore, only three sets of two stress concentration factors are required for the most common fillet and butt welds, i.e. needed are only stress concentration factors for pure bending and pure membrane stress.
- When the weld geometry and its size remain constant the readymade stress concentration factors can be used for the determination of the linear elastic peak stress at the weld toe.

8. The GR3 method for solid mesh weld modeling

Welded structures are in most cases made of plates, i.e. structural elements having one dimension (the thickness) smaller than the other two dimensions. Therefore, it is natural,

TABLE 3.1 Comparison of stresses at the weld toe obtained from the 3D fine mesh and the shell coarse mesh FE models.

	σ_{tip}^{e} (via K_t and GY-2)	σ_{tip}^{e} (from 3-D FEA)
Location 1	17.1 ksi	16.9 ksi
Location 2	17.4 ksi	17.4 ksi
Location 3	11.4 ksi	10.6 ksi

as explained in Section 7, to use for the stress analysis of welded structures the shell finite element method. However, the use of shell FE elements requires additional effort associated with appropriate modeling of the weld effect on stiffness of analyzed welded joint. Therefore, more popular becomes modeling of welded structures with brick 3D Finite Elements. The use of brick finite elements enables modeling the weld in global sense except simplifications concerning details of the weld geometry like the weld toe radius or the root radius. Modeling sufficiently accurate the weld toe region would require using large number of small finite elements making the method tedious, time consuming and expensive. Unfortunately, the stress at the weld toe and the weld root are necessary for the strain-life fatigue analysis method. Therefore, the finite element method based on using large brick elements requires special post-processing of the stress data resulting in determination of the stress parameter needed for subsequent fatigue analyses. The method does not provide direct estimation of the weld toe stress peak σ^e_{tip}, but it provides stress data for the estimation of the hot spot stressσ^1_{hs} and σ^2_{hs}. Those stress parameters are the base for estimation of the weld toe stress peakσ^e_{tip}, as described in Section 7.

8.1 Stress quantities obtained from various finite element analyses

It has been discussed earlier that direct analytical or numerical determination of the linear elastic weld toe stress peak σ^e_{tip}, might be difficult and prohibitively labor intensive in the case of real large-scale welded structures. Therefore, the method involving the nominal, σ_n, or the hot spot stress, σ_{hs}, outlined in Section 6, is preferable when dealing with fatigue evaluations of welded structures. Unfortunately, the nominal or the currently used hot spot stresses [6,26] are not unique when dealing with complex 3D stress distributions.

Several stress quantities used in strength and fatigue analyses of welded structures were discussed and shown in Fig. 3.8. The nominal stress σ_n is usually the maximum magnitude of the linearized through thickness stress field resulting from superposition of axial and bending stresses. This stress is unique and relatively easy to determine in cross sections away from the weld toe, but it might be more complex when dealing with several elements welded together and subjected to multiple loading modes. The nominal stress at the weld toe cross section might be sometimes coinciding with the hot spot stress σ^1_{hs}, but it may differ depending on the method of its determination as pointed out in Ref. [6,26]. Therefore, the local hot spot stresses, σ^1_{hs} and σ^2_{hs}, are used again for determination of the required weld toe peak stress σ^e_{tip}. However, special care is required as far as the FE modeling and interpretation of the stress data is concerned because the hot spot stresses, σ^1_{hs} and σ^2_{hs}, are not directly given as the output when analyzing welded joints with 3D finite elements.

The aim of the 3D coarse mesh FE stress analysis is to determine first hot spot stresses, σ^1_{hs} and σ^2_{hs}, and then the "linear elastic" peak stress σ^e_{tip}, being subsequently used for calculations of the weld toe elastic-plastic strains (ε^N orε^E) and associated stresses (σ^N or σ^E) and the fatigue analysis.

It has been mentioned in previous section that the fine mesh finite element method is capable of providing acceptable estimation of the linear elastic' peak stress σ^e_{tip}, at the weld toe but it requires using very small finite elements (ca. 0.2 mm) while constructing the FE model of the analyzed structure. There is also tendency of conveniently modeling the weld toe region as a sharp corner. Therefore, it is necessary to understand what kinds of stresses provided by various finite element models.

Fig. 3.43 shows stress distributions in the upper surface of the welded joint subjected to tensile load. The first analysis (green) was carried out by using 3D fine brick finite elements. Unfortunately, the weld toe region was modeled as a sharp corner therefore the stress at the weld to location (at the corner) is highly inaccurate and its magnitude depends strongly on the averaging technique being used by the FE code. The stress magnitude at the sharp corner tends theoretically to infinity and any finite averaged stress value at this location is erroneous and has a weak connection with the actual weld toe geometry.

The shell FE model (blue) does not provide any information about the stress concentration at the weld toe as discussed in Section 7. Therefore, certain post processing would be needed in order to get the linear elastic stress peak at the weld toe, σ^e_{tip}.

The 3D FE coarse mesh model (black) does have the same deficiency as the fine mesh model discussed above, however the coarse mesh model is easier to construct and cheaper in terms of the operating costs.

It means that none of the FE models discussed above provide sufficiently accurate estimation of the weld toe peak stress, σ^e_{tip}. However, the stress data obtained from those models can be used for the determination of the linearized through thickness stress field and hot spot stresses, σ^1_{hs} and σ^2_{hs}. Therefore one can use the coarse 3D brick finite element model and determine the hot spot stresses σ^1_{hs} and σ^2_{hs} then proceed with evaluation of the weld toe stress σ^e_{tip}, analogously to the method described in Section 7.

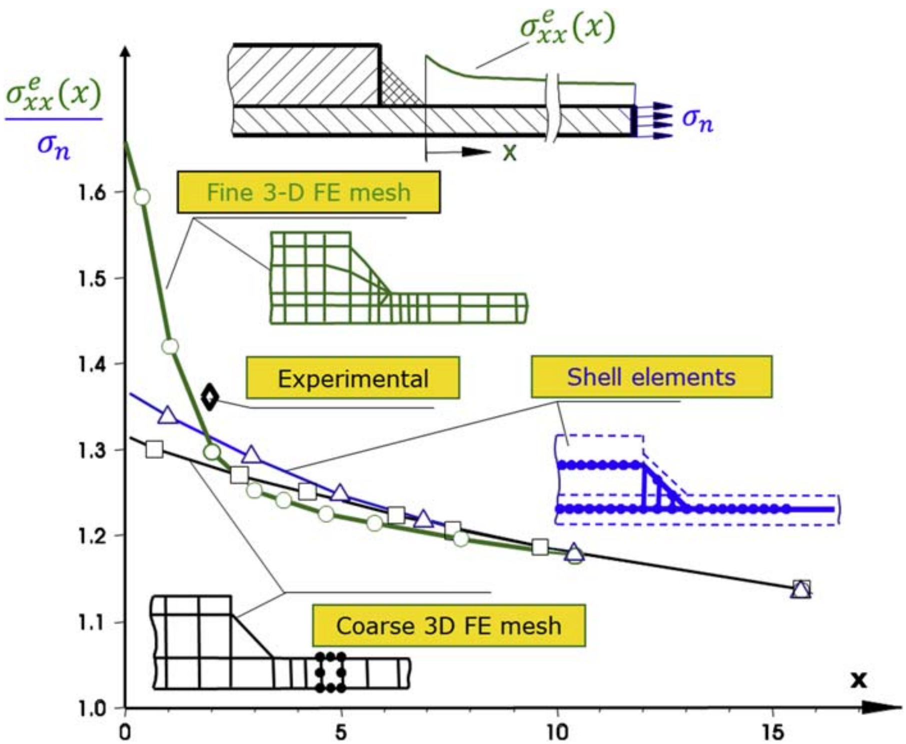

FIG. 3.43 Stress distributions in the upper ligament (top surface) of a lap joint under pure tension loading.

8.2 Determination of hot spot stresses from coarse mesh 3D FE data

The difficult and time-consuming task when analyzing stresses and durability of welded structures is, as mentioned above, adequate modeling of the weld toe region. Modeling welded structures with shell finite elements requires additional effort ensuring that certain effects of the weld geometry are not neglected, i.e. the weld stiffness effect discussed in Section 7. Therefore, the advantage of using 3D Finite Element models of welded structures lies in the fact that the weld itself and its stiffness effect can be naturally included into the analysis. In addition, significant simplification of the 3D FE model can be achieved by omitting geometrical details such as the weld toe and the weld root region. However, the weld stress needed for the fatigue analysis is erroneous in such a case. Fortunately, the meaningful and very useful information obtained from such coarse mesh 3D FE models are the hot spot stresses σ_{hs}^1 and σ_{hs}^2 which can be used for the determination of the linear elastic weld toe peak stress σ_{tip}^e, necessary for fatigue durability evaluations.

8.3 The link between the membrane and bending hot spot stresses and the 3D FE stress data

The nonlinear through thickness stress distribution $\sigma_{xx}^e(y)$, represents results of the 3D Finite Element analysis (Fig. 17.3). The accuracy of this stress distribution depends on the finite elements size used to create the FE mesh. However, regardless of the sophistication of the FE mesh and its accuracy the through thickness stress distribution must always equilibrate the axial force and the bending moment acting in the considered cross section.

It means that integrals Eqs. (3.38) and (3.39) of the stress distribution$\sigma_{xx}^e(y)$, should always be the same regardless of how accurately the FE stress is distributed over the plate thickness. The integrals as explained in Section 7 represent the membrane and through thickness bending stress distribution.

$$\sigma_{hs}^m = \frac{\int_{-t}^{0} \sigma_{xx}^e(x = 0, y, z = z_i)dy}{t} \tag{3.38}$$

$$\sigma_{hs}^b = \frac{6 \cdot \int_{-t}^{0} \sigma_{xx}^e(x - 0, y, z = z_i)ydy}{t^2} \tag{3.39}$$

When appropriate stress concentrations factors are known the peak stress at the weld toe can be calculated using Eq. (3.31).

The two stress concentration factors $K_{t,hs}^m$ and $K_{t,hs}^b$ are independent of the load magnitude and they are unique for given weld geometry. It is recommended to use the Japanese Stress Concentration Factor expressions [68] discussed earlier. Therefore, it is also important to formulate appropriate recommendations addressing the creation of representative coarse 3D FE model of the analyzed welded joint and the procedure for extracting the membrane and bending hot spot stresses σ_{hs}^m and σ_{hs}^b.

8.4 The GR3 method for determination of the local hot spot stresses

The aim of the GR3 method is development of a coarse mesh 3D FE method providing stress information sufficient for the determination of the linearized through thickness stress distribution and hot spot stresses σ_{hs}^1 and σ_{hs}^2. It has been mentioned earlier that the knowledge of the exact through thickness stress distribution is not so important and therefore the inaccurate estimation of the stress σ_{tip}^e, at the sharp corner imitating the weld toe region in the FE model can be dealt with as discussed below. The purpose of the coarse mesh 3D FE analysis is to obtain the hot spot stress σ_{hs}^1 and σ_{hs}^2 (Fig. 3.44) and then the membrane and bending hot spot stresses σ_{hs}^m and σ_{hs}^b.

It has been found, based on multiple FE analyses, that four finite elements per plate thickness are sufficient to get reliable stress data for the determination of the weld toe hot spot stresses [85,86]. A generic 3D FE model of a welded joint which can be used for the determination of required local hot spot stresses is shown in Fig. 3.45.

The purpose of using the coarse FE mesh is the possibility of analyzing entire full-size welded structure because of significant reduction of the number of necessary finite elements. It is recommended to use in the weld toe region not less than four finite elements per plate thickness. The size of finite elements can increase at distances greater than one plate thickness away from the weld toe location. It is also noticeable that weld micro-geometrical features such as the radiused weld toe region do not need to be modeled. The normal nodal stress components $\sigma_{xx}^e(y_i)$, are to be used in the case of the cross section S-I and the normal nodal stress components $\sigma_{yy}^e(x_i)$, in the case of the cross section S-II. The sharp corner at the weld toe location is often (Fig. 3.46) the common node/point for several finite elements and the nodal stress might be averaged at such a node. Therefore, it is recommended to use the element nodal stresses $\sigma_{xx,A}^1$, associated with the element A1, rather than the overall averaged stress at this point. All other nodal stresses along the axis y can be accepted as they stand.

It is recommended to use nodal stresses along the cross section starting at the weld toe (like the cross-section S-I) and determine the membrane and bending stresses as recommended below [85,86].

The first step is to extract the distribution of the normal stress component in the critical cross section S-I or S-II as shown in Fig. 3.46. As normal stress components contribute mainly toward fatigue performance of welded joints, it is rational to extract normal stresses $\sigma_{xx}^e(y_i)$ in

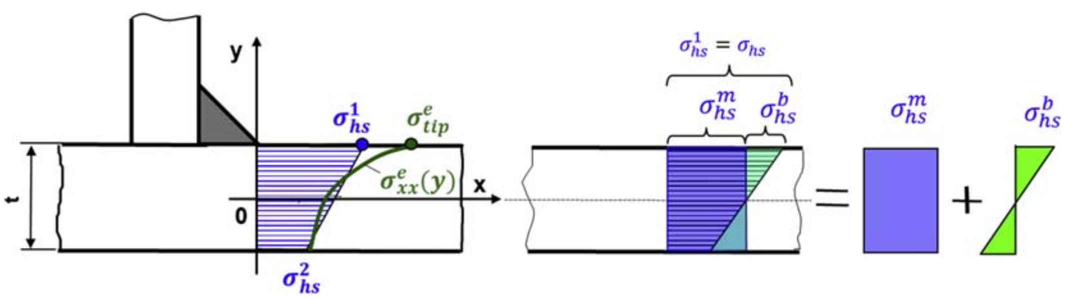

FIG. 3.44 The nonlinear distribution of through thickness stress $\sigma_{xx}^e(y)$, the linearized through thickness stress distribution in a weldment and the membrane and bending hot spot stresses σ_{hs}^1 and σ_{hs}^2.

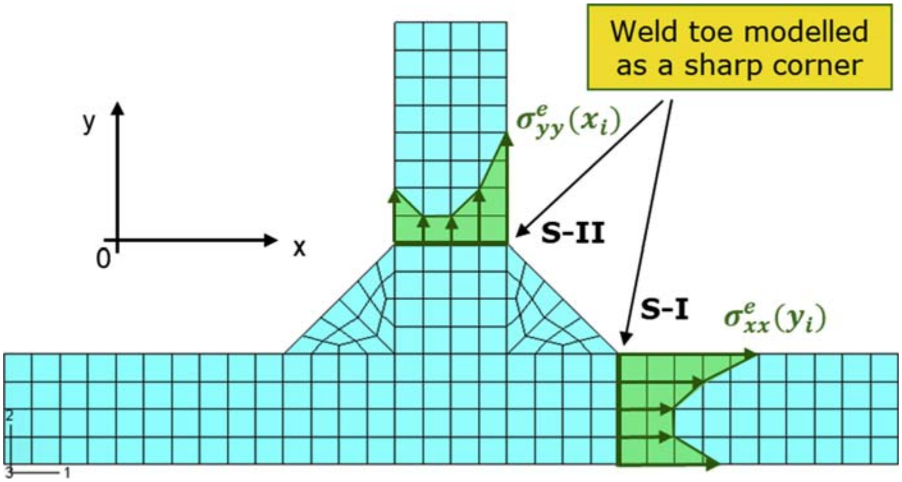

FIG. 3.45 A generic GR3 Finite Element model of a T-butt welded joint.

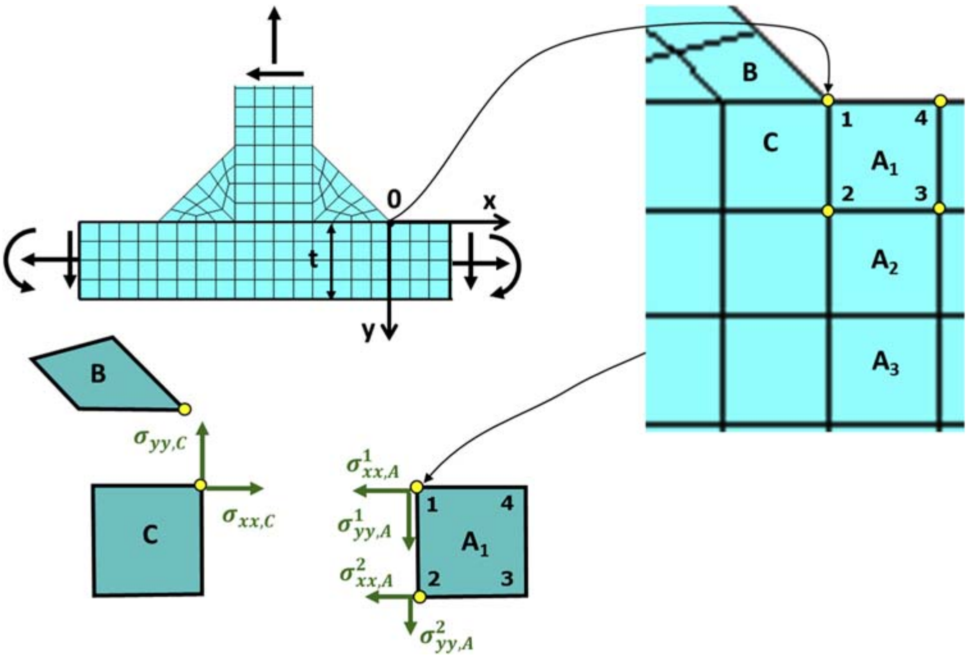

FIG. 3.46 Extraction of nodal stresses at a node common for multiple finite elements joined at a sharp corner.

the cross section S-I for the fatigue analysis of the base plate (Fig. 3.45) and normal stresses $\sigma^e_{yy}(x_i)$, in the cross section S-II for the fatigue analysis of the attachment.

The second step is to determine the hot spot membrane σ^m_{hs} and bending σ^b_{hs} stress at the weld toe by linearization of the discrete stress field (Fig. 3.47) obtained from the coarse

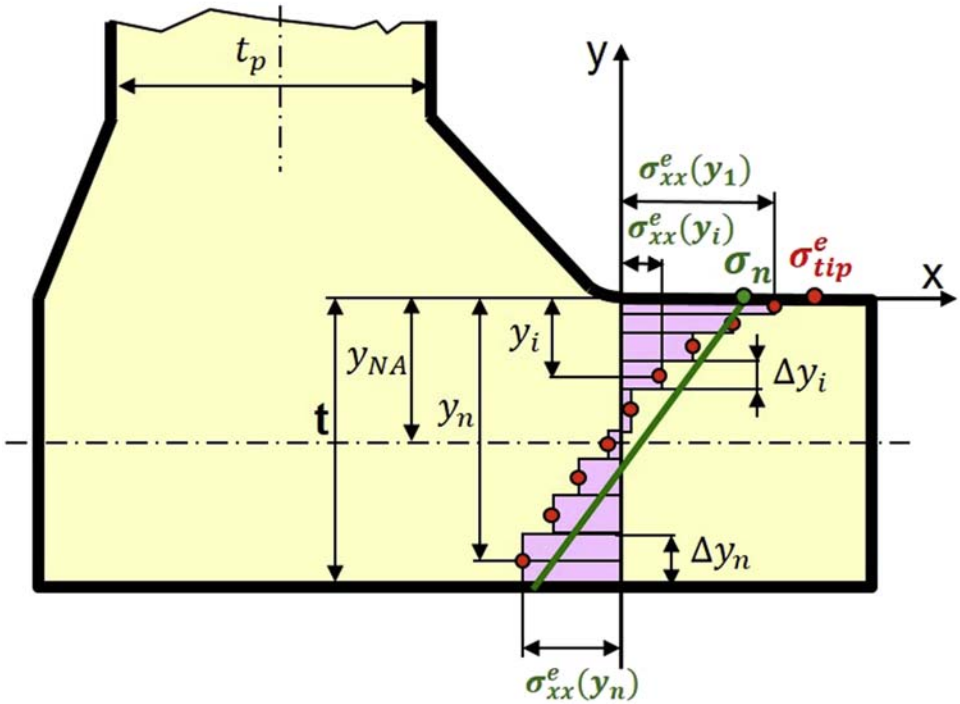

FIG. 3.47 Discrete through thickness stress distribution obtained from the Finite Element analysis.

mesh FE analysis. The linear equivalent stress field characterized by hot spot stresses σ^1_{hs} and σ^2_{hs} is the linear through the thickness stress field having the same axial force and the same bending moment as the FE nonlinear stress field $\sigma^e_{xx}(y)$ obtained from the FE analysis. The linearization is carried out locally over the plate thickness "t" and a small strip of "Δz" wide, i.e. over an area "t ×Δz" starting at the weld toe point identified by coordinates ($x = 0$, $y = 0$, $z = z_i$), where the coordinate $z =$ zi defines the position on the weld toe line. The axial force, P and the bending moment, Mb can be calculated by integrating the stress function $\sigma^e_{xx}(x = 0, y, z)$ acting over the area "t ×Δz".

The linearization of the discrete stress field $\sigma^e_{xx}(y)$ needs to be carried out along the axis y starting at the point on the weld toe (x = 0, y = 0, $z = z_i$). The integration is to be carried over the domain $[x = 0; 0 \leq y \leq t, z = z_i]$. The width "Δz" of the cross-section segment "t×Δz" approaches zero and accordingly the stress $\sigma^e_{xx}(y)$ can be assumed constant over such a small variation of co-ordinate "z". Therefore, it was assumed for convenience that "Δz = 1" and the integration was carried out only with respect to co-ordinate "y".

The stress field in the cross section of interest is usually given (Fig. 17.6) in the form of a series of discrete points [$\sigma(y_i)$,y_i], i.e. nodal stresses and their coordinates. Therefore, a numerical integration method has been developed for the calculation of the axial force and the bending moment at the selected location, z_i on the weld toe line. It was assumed, in the proposed integration method, that simple finite elements with the linear shape function are used.

Therefore, the stress field between two subsequent nodal points can be represented by the linear Eq. (17.4).

$$\sigma^e_{xx}(y) = a_i y + b_i \ \ where: \ y_i \le y \le y_{i+1} and 1 \le i \le n-1 \tag{3.40}$$

Where: ai and bi are the straight-line stress distribution parameters valid within the interval $y_i \le$ y $\le y_{i+1}$, i.e. between two adjacent nodal points and can they be determined by using nodal stresses and their co-ordinates:

$$a_i = \frac{\sigma^e_{xx}(y_i) - \sigma^e_{xx}(y_{i+1})}{y_i - y_{i+1}} \quad and \ \ b_i = \frac{\sigma^e_{xx}(y_{i+1})y_i - \sigma^e_{xx}(y_i)y_{i+1}}{y_i - y_{i+1}} \tag{3.41}$$

$$where: 1 \le i \le n-1$$

So, the force contributed by the stress distribution acting over the interval, $y_i \le y \le y_{i+1}$, can be written as:

$$\begin{aligned} P_i = \Delta z \bullet \int_{y_i}^{y_{i+1}} \sigma^e_{xx}(y_i) \bullet dy &= \Delta z \bullet \int_{y_i}^{y_{i+1}} (a_i y + b_i) \bullet dy = \Delta z \bullet \left| \frac{a_i y^2}{2} + b_i y \right|_{y_i}^{y_{i+1}} \\ &= \Delta z \bullet \frac{\left[\sigma^e_{xx}(y_{i+1}) + \sigma^e_{xx}(y_i)\right](y_{i+1} - y_i)}{2} \\ &= \frac{\left[\sigma^e_{xx}(y_{i+1}) + \sigma^e_{xx}(y_i)\right](y_{i+1} - y_i)}{2} \end{aligned}$$

$$P_i = \frac{\left[\sigma^e_{xx}(y_{i+1}) + \sigma^e_{xx}(y_i)\right](y_{i+1} - y_i)}{2} where: \Delta z = 1 \tag{3.42}$$

In order to determine the resultant force P acting over the entire plate thickness all force contributions P_i need to be summed up all together:

$$P = \sum_1^{n-1} P_i = \sum_1^{n-1} \frac{\left[\sigma^e_{xx}(y_{i+1}) + \sigma^e_{xx}(y_i)\right](y_{i+1} - y_i)}{2} \tag{3.43}$$

Similarly, the bending moment $M_{b,i}$ contributed by the stress distribution segment $[y_i, y_{i+1}]$ can be calculated as:

$$M_{b,i} = \Delta z \bullet \int_{y_i}^{y_{i+1}} \sigma^e_{xx}(y)(y_{NA} - y) \bullet dy = \Delta z \bullet \int_{y_i}^{y_{i+1}} (a_i y + b_i) \bullet (y_{NA} - y) \bullet dy$$

$$M_{b,i} = a_i \left(\frac{y_i^3 - y_{i+1}^3}{3}\right) - (a_i y_{NA} - b_i)\left(\frac{y_i^2 - y_{i+1}^2}{3}\right) - b_i y_{NA}\ (y_i - y_{i+1}) where: \Delta z = 1 \tag{3.44}$$

After substitution of Eq. (3.40) into Eq. (3.44) and rearrangement the bending moment can be written in terms of nodal stresses:

$$M_{b,i} = \frac{\sigma^e_{xx}(y_i) - \sigma^e_{xx}(y_{i+1})}{(y_i - y_{i+1})} \bullet \frac{(y_i^3 - y_{i+1}^3)}{3} + \{$$
$$\times \left[\sigma^e_{xx}(y_i) - \sigma^e_{xx}(y_{i+1})\right] y_{NA} - \sigma^e_{xx}(y_{i+1}) y_i + \sigma^e_{xx}(y_i) y_{i+1}\} \frac{(y_i + y_{i+1})}{2}$$
$$- \left[\sigma^e_{xx}(y_{i+1}) y_i + \sigma^e_{xx}(y_i) y_{i+1}\right] y_{NA} \tag{3.45}$$

The resultant bending moment M_b acting over the entire thickness, t, can be calculated as:

$$M_b = \sum_1^{n-1} M_{b,i} \tag{3.46}$$

The membrane and bending hot spot stresses σ^m_{hs} and σ^b_{hs} at the specified point on the weld toe line can be determined from the membrane and bending stress formulae.

$$\sigma^m_{hs} = \frac{P}{\Delta z \bullet t} = \frac{1}{t} \sum_1^n \frac{\left[\sigma^e_{xx}(y_{i+1}) + \sigma^e_{xx}(y_i)\right](y_{i+1} - y_i)}{2} \tag{3.47}$$

$$\sigma^b_{hs} = \frac{c \bullet M_b}{I} = \frac{\frac{t}{2} \bullet M_b}{\frac{\Delta z \bullet t^3}{12}} = \frac{6 \bullet M_b}{t^2} \quad where: \ \Delta z = 1 \tag{3.48}$$

It has been found that the average membrane stress determined from Eq. (3.47) resulted in a very close approximation of the actual membrane stress and therefore the procedure described above is recommended for both fine and coarse finite element mesh.

Unfortunately, the bending moment obtained by integrating Eq. (3.45) the coarse mesh stress field over the entire domain (-t ≤ y ≤ 0) was found to be inaccurate due to strong effect of the highest and inaccurate stress magnitude at the sharp corner representing the weld toe line. Investigations led to finding that the mid-thickness segment (-0.75t ≤ x ≤ -0.25t) of the through thickness stress distribution was found to be fairly independent of the FE mesh resolution (fine or coarse finite element).

Numerical studies have shown (Fig. 3.48 and 3.49) that the mid-thickness stress distribution, i.e. over the segment 0.25t ≤ t ≤ 0.75t was very little dependent on the size finite elements.

Therefore, it is suggested to use only the interior fragment of the through thickness stress distribution (from 0.25t to 0.75t) for the estimation of the bending moment M_b.

The linear through thickness stress distribution induced by pure bending load is shown in Fig. 3.49. The shaded mid-thickness fragments of the stress are the base for the estimation of the bending moment M_b generating the entire stress field.

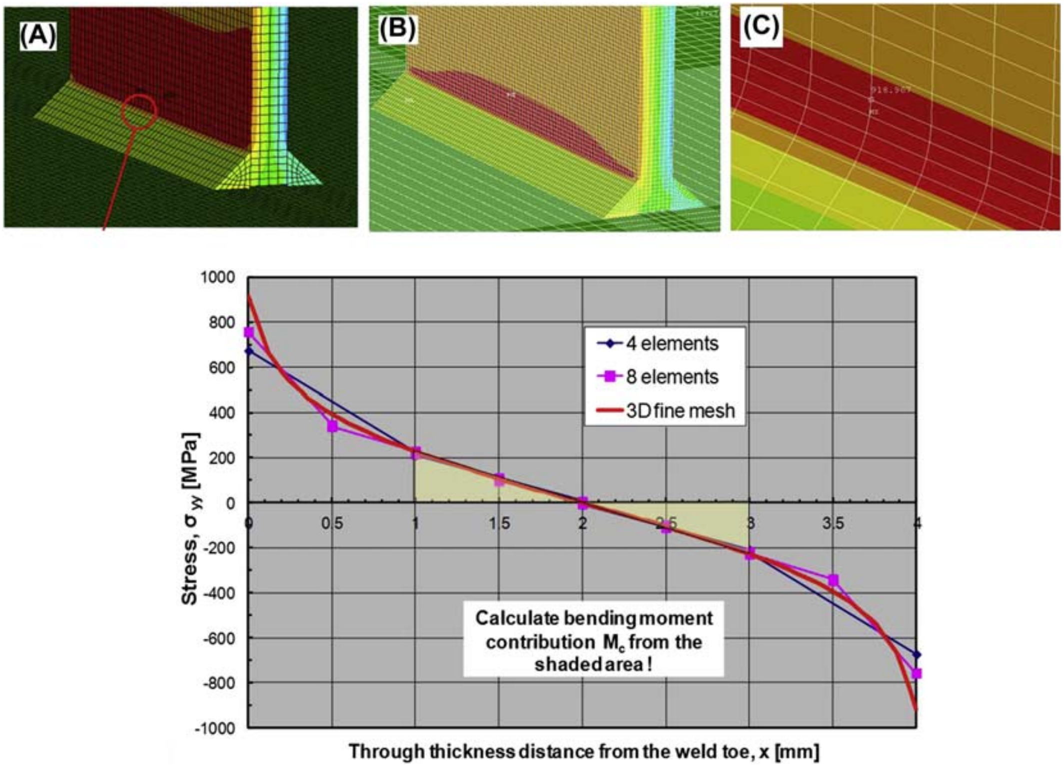

FIG. 3.48 Finite element size effect on the through thickness stress distribution.

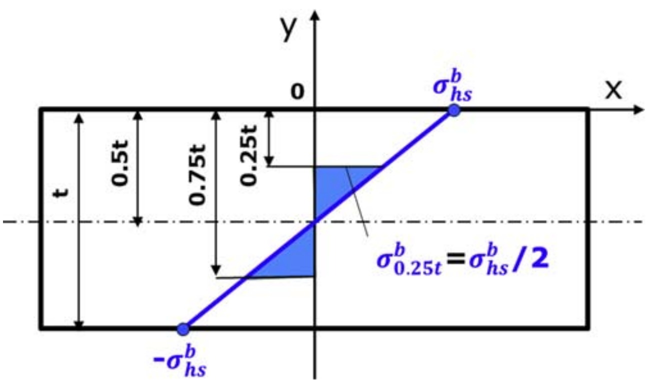

FIG. 3.49 The linear through thickness bending stress distribution in a plate.

The central part of the mid-thickness bending stress distribution is defined by the stress magnitude at position 0.25t and 0.75t, i.e. $\sigma^b_{0.25t} = 0.5\sigma^b_{hs}$ and at the position 0.75t the bending stress is $\sigma^b_{0.75t} = -0.5\sigma^b_{hs}$.

The bending moment inducing the hot spot stress σ^b_{hs} at the furthest ligament from the neutral axis is:

$$M_b = \frac{\sigma^b_{hs} t^2 \Delta z}{6} = \frac{\sigma^b_{hs} t^2}{6} \quad where: \Delta z = 1 \tag{3.49}$$

The contribution of the bending moment generated by the mid-thickness part of the stress distribution is:

$$M_c = \frac{\sigma^b_{0.25t} \bullet t^2 \Delta z}{24} = \frac{\sigma^b_{hs} t^2}{48} \quad where: \Delta z = 1 \tag{3.50}$$

Thus, the total bending moment M_b is:

$$M_b = 8M_c \; because \frac{M_b}{M_c} = \frac{\dfrac{\sigma^b_{hs} t^2}{6}}{\dfrac{\sigma^b_{hs} t^2}{48}} = 8$$

or

$$M_b = 8M_c = \frac{\sigma^b_{0.25t} \bullet t^2}{3}$$

Thus, the knowledge of the bending stress at the position y = -t/4 makes it possible to determine the total bending moment applied in the analyzed cross section. In spite of the fact that the stress distribution over the mid-thickness region of the plate is very close to a linear one it unfortunately does not follow exactly the linear stress distribution of a flat plate as shown in Fig. 3.49. The mid-thickness stress distribution in the weldment remains linear (Fig. 3.50) but it is lower than in the case of flat plate of the same thickness and subjected to the same bending moment.

It has been found that the decrease of the mid-thickness linear stress in the weldment at locations 0.25t and 0.75t was of the range of 0.1 σ^b_{hs}. Therefore, the actual bending moment at the selected cross section should be increased by 25% when estimated based on the FE stress data obtained for the actual weldment geometry (not a plate). It means that the bending moment at the critical cross section based on the FE stress data should be increased by 25%.

$$M_b = 1.25 \times 8M_c = 10M_c = \frac{1.25\sigma^b_{0.25} t^2}{3} \tag{3.51}$$

Expression Eq. (3.50) has been recommended for the determination of the bending moment and bending stresses in weldments based on the coarse mesh 3D FE stress data taken from

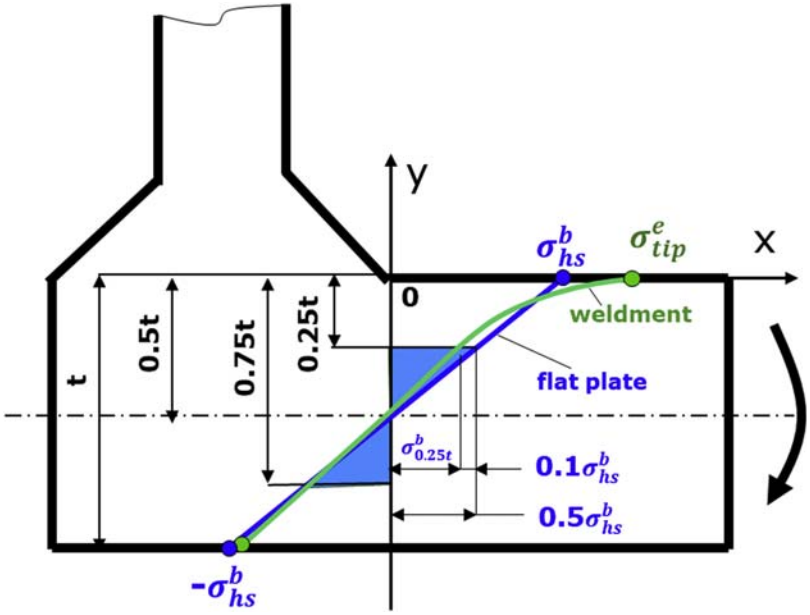

FIG. 3.50 The decrease of the mid-thickness stress field due to high stress concentration around the weld toe.

the mid-thickness of the analyzed welded plate. Thus, the final estimation of the bending stress based on the coarse 3D FE stress data at the location 0.25t is:

$$\sigma^b_{hs} = \frac{c \bullet M_b}{I} = \frac{\frac{t}{2} 10M_c}{\frac{t^3}{12}} = \frac{60M_c}{t^2} = \frac{60\frac{\sigma^b_{0.25t} \bullet t^2}{24}}{t^2} = 2.5\sigma^b_{0.25t} \tag{3.52}$$

The stress $\sigma^b_{0.25t}$ is that one at location t/4 away from the weld toe and determined from coarse mesh 3D FE analysis.

In the case of the FE mesh constructed with four (the same size) elements per plate thickness (Fig. 3.51) the estimation of the membrane and bending stress can be based on expressions Eqs. (3.53) and (3.54) respectively.

The nodal stresses obtained from the FE analysis are $\sigma^e_{xx}(y_1)$, σ^e_{xx} (y_2), σ^e_{xx} (y_3), σ^e_{xx} (y_4) and σ^e_{xx} (y_5). The membrane stress based on these FE data can be obtained as the average stress calculated according to Eq. (3.47) discussed above.

$$\sigma^m_{hs} = \frac{1}{t}\sum_{1}^{4} \frac{\left[\sigma^e_{xx}(y_{i+1}) + \sigma^e_{xx}(y_i)\right](y_{i+1} - y_i)}{2} \tag{3.53}$$

While the bending hot spot stress can be subsequently calculated from expression Eq. (3.52).

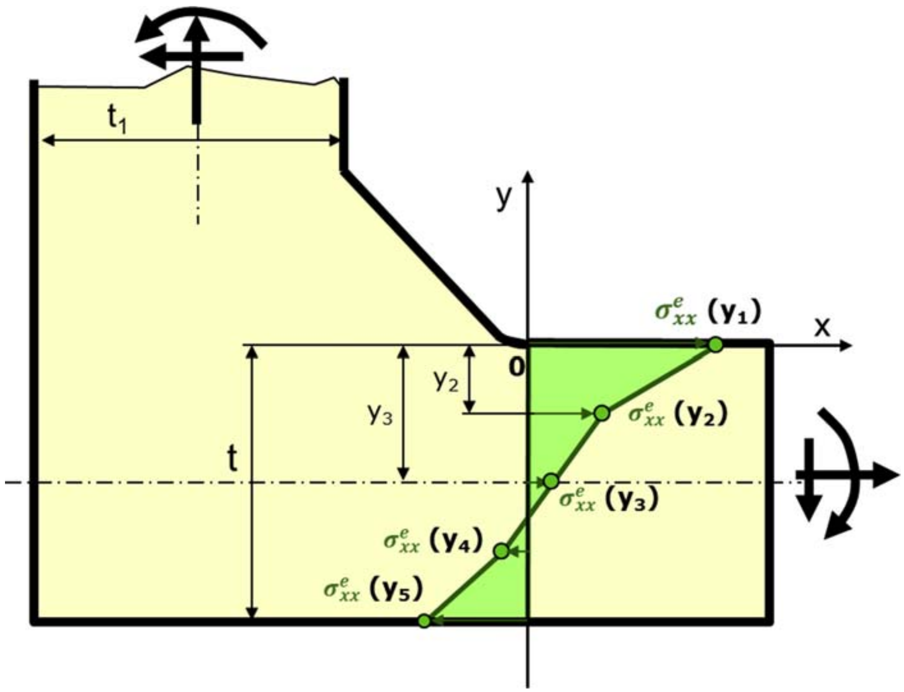

FIG. 3.51 Stress data obtained from a coarse FE mesh having only 4 elements per plate thickness.

$$\sigma^b_{hs} = \frac{60M_c}{t^2} = 2.5 \times \sigma_{xx}(y_2) \tag{3.54}$$

When the nodes are not located exactly at locations 0.25t and 0.75t the FE stresses need to be extrapolated to those locations or the bending moment M_c needs to be determined based on the stress field within the sector $0.25t \le y \le 0.75t$.

8.5 Example— Illustration of GR3 weld model

The vertical bracket (Fig. 3.52) has been welded to the base plate and subjected to out of plane loading/force P. The dimensions and location of the bracket are also shown in Fig. 3.52. The thickness of both plates was 4 mm. The bracket was welded to the base plate by two 50 mm fillet welds having the weld leg length of 4 mm. All other dimensions are shown in Fig. 3.52B.

The applied force was P = 1000N. The task of the analyst is to determine the local membrane and bending hot spot stresses by using coarse mesh finite element method supplemented for comparison by manual analytical stress analysis.

The coarse mesh finite element model of the structure is shown in Fig. 3.53. Four finite elements (Δy = 1 mm) per plate thickness were used to model the welded joint. The weld toe

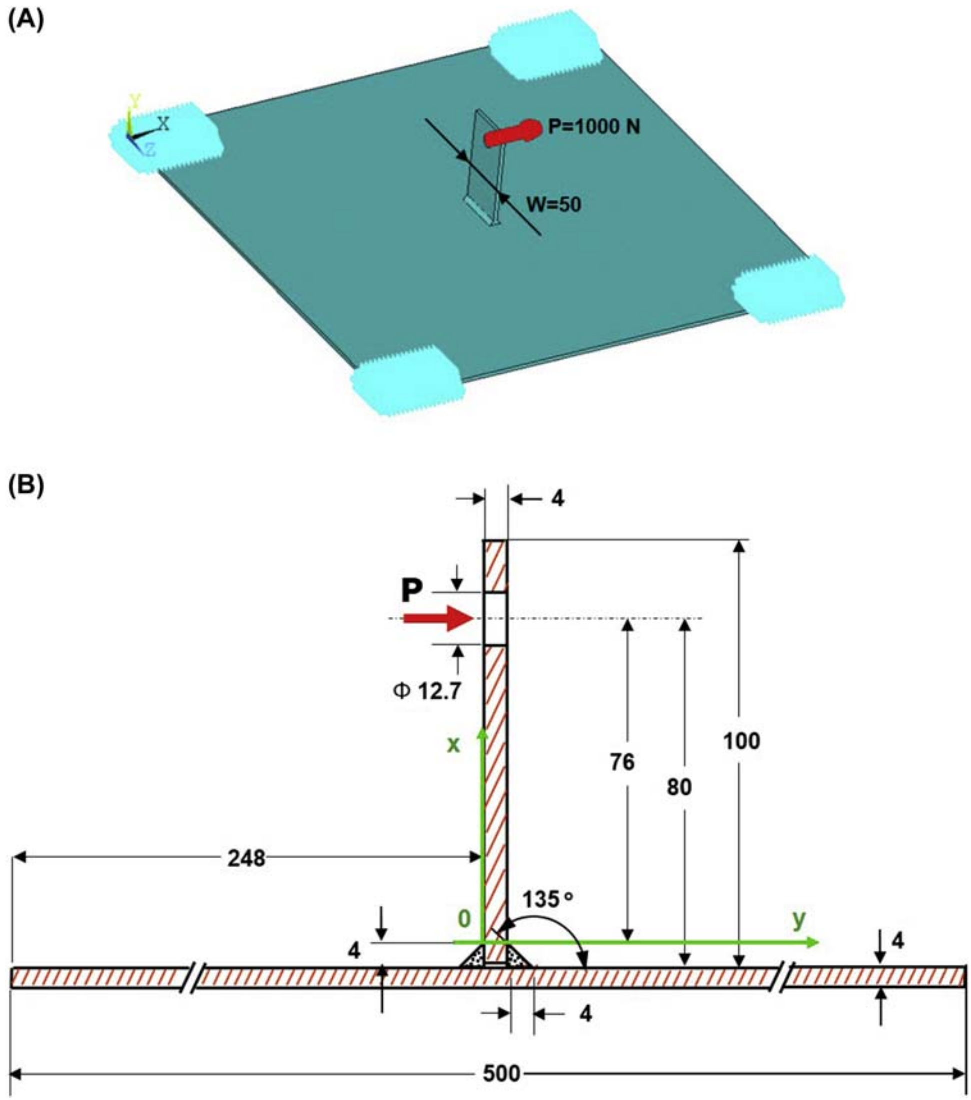

FIG. 3.52 Geometry of the welded structure and dimensions. All dimensions are in mm.

region was modeled as a sharp corner. The FE modeling included also the lack of penetration region ($2c = 3$ mm), i.e. the bracket did not have full contact with the base plate.

The stress data obtained from the FE model was given as stress magnitudes at nodal points:

$\sigma_{xx}(y_1 = 0) = 509.14$ MPa
$\sigma_{xx}(y_2 = 1) = 230.84$ MPa
$\sigma_{xx}(y_2 = 2) = 0.0$ MPa

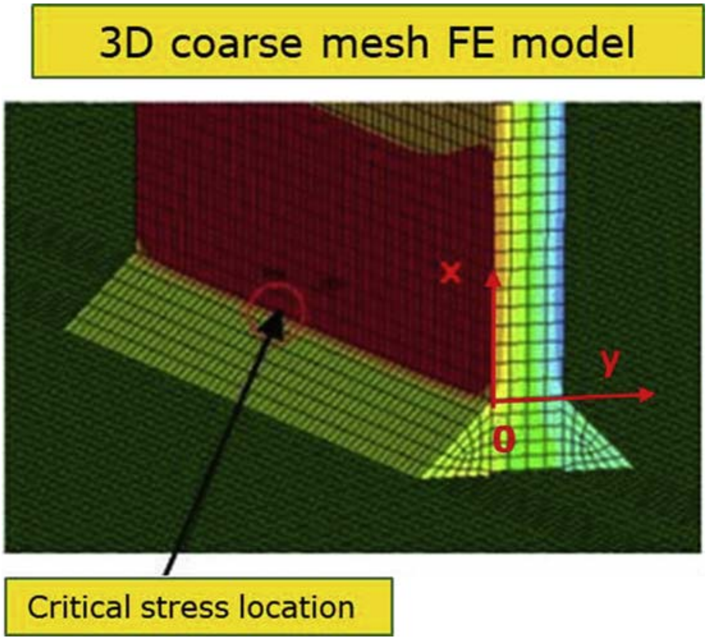

FIG. 3.53 Finite element mesh and model of the analyzed welded joint/structure.

$\sigma_{xx}(y_2 = 3) = -\ 230.84$ MPa
$\sigma_{xx}(y_2 = 4) = -\ 509.14$ MPa

The membrane hot spot stressσ_{hs}^{m}, estimated by using the nodal stresses Eq. (3.47):

$$\sigma_{hs}^{m} = \frac{1}{t}\sum_{1}^{4}\frac{\sigma_{xx}(y_i)+\sigma_{xx}(y_{i+1})}{2}|y_{i+1}-y_i| = \frac{1}{4}\left[\frac{509.14+230.84}{2}|1-0|+\frac{230.84+0}{2}|2-1|\right] + \frac{1}{4}\left[\frac{0-230.84}{2}|3-2|+\frac{-509.14-230.84}{2}|4-3|\right] = 0$$

The bending hot spot stress σ_{hs}^{b}, estimated according to Eq. (3.48) was:

$$M_c = \sum_{2}^{3}\sigma_{xx}(y_{i+1})\bullet(y_{i+1}-y_i)\bullet\left(\frac{t}{2}-\frac{y_i+y_{i+1}}{2}\right) + \frac{1}{2}\sum_{2}^{3}[\sigma_{xx}(y_i)-\sigma_{xx}(y_{i+1})]\bullet(y_{i+1}-y_i)\bullet\left(\frac{t}{2}-\frac{2y_i+y_{i+1}}{3}\right)$$

$$= 0\cdot(2-1)\left(\frac{4}{2}-\frac{1+2}{2}\right)+\frac{1}{2}[230.84-0](2-1)\left(\frac{4}{2}-\frac{2\cdot 1+2}{3}\right)-230.84(3-2)\left(\frac{4}{2}-\frac{2+3}{2}\right)$$
$$+\frac{1}{2}[0-(-230.84)](3-2)\left(\frac{4}{2}-\frac{2\cdot 2+3}{3}\right)$$

$$= 0+\frac{1}{3}230.84+\frac{1}{2}230.84-\frac{1}{6}230.84 = \frac{2}{3}230.84N\cdot\text{mm and } \sigma_{hs}^{b} = \frac{60M_c}{t^2} = \frac{60\cdot\frac{2}{3}\cdot 230.84}{4^2}$$
$$= 577.1\text{MPa} - GR3;$$

In the case of using four finite elements of the same size per plate thickness the bending hot spot stress σ_{hs}^{b}, can be estimated based on the bending stress either at location $y = 0.25t$ or $y = 0.75t$, i.e.

$$\sigma_{hs}^{b} = 2.5\times\sigma_{xx}^{b}(y_2 = 1) = 2.5\times 230.84 = 577.1\text{MPa} - GR3;$$

In order to verify whether the coarse 3D FE method provided sufficiently accurate estimation of hot spot stresses another FE analysis was carried out for comparison by employing the fine mesh FE model shown in Fig. 3.54.

The weld toe radius of the weld was $r = 1$ mm and the finite element size around the weld toe location was $\Delta y = 0.25$ mm. The finite element mesh is shown in Fig. 3.54 and the through thickness stress distribution obtained in the cross-section $x = 0$ is presented in Fig. 3.55. The

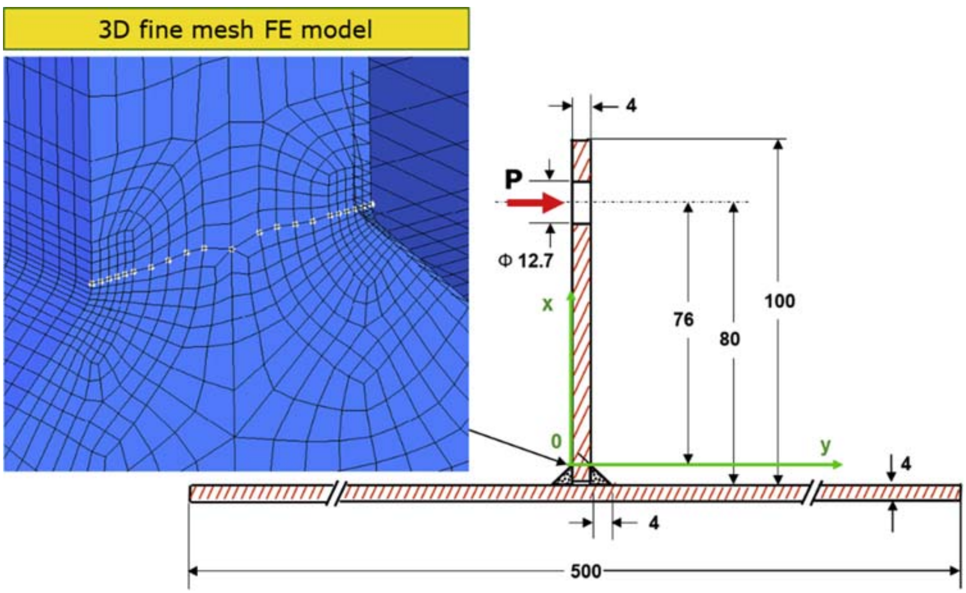

FIG. 3.54 The fine mesh 3D FE model of the analyzed welded joint.

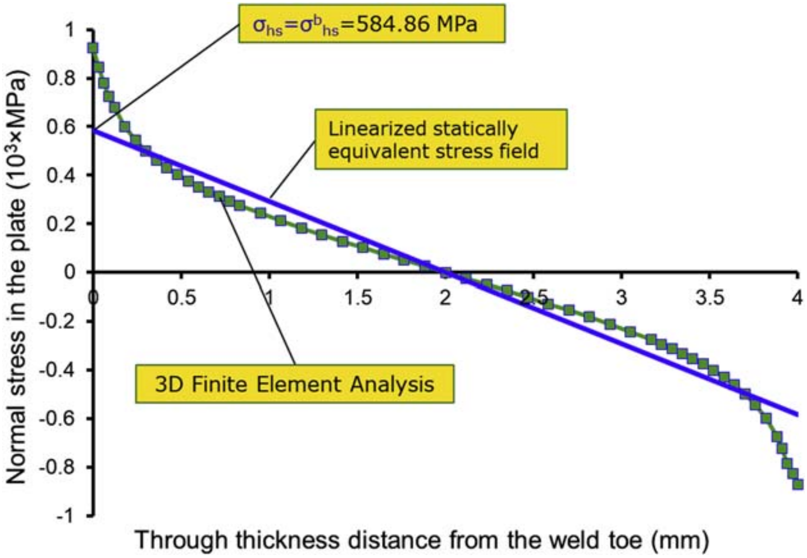

FIG. 3.55 Through thickness stress distribution obtained from the fine 3D FE model and the statically equivalent linearized stress field.

actual fine mesh stress distribution was subsequently linearized, and the hot spot bending stress was determined as $\sigma_{hs}^{b} = 584.86$ MPa (Fig. 3.55).

The coarse mesh 3D FE model used earlier (Fig. 3.53) provided the hot spot stress $\sigma_{hs}^{b} = 577.1$ MPa, i.e. the coarse mesh 3D FE model provided the hot spot stress smaller by only 1.3% when compared with the fine mesh 3D FE model.

A manual stress analysis is also possible in this load and geometry configuration. The bending moment at the $x = 0$ cross section (Fig. 3.54) can be calculated as:

$$M = P \cdot l = 1000 \cdot 76 = 76000\text{Nmm}$$

Where: l – the distance of the point of application of the force P to the weld toe of the bracket weld.

The bracket moment of inertia of the cross section at location ($x = 0$) is:

$$I = \frac{L \cdot t^3}{12} = \frac{50 \cdot 4^3}{12} = 266.66\text{mm}^4$$

Where: L – the width of the bracket.

The bending stress can be finally calculated from the well-known bending formula.

$$\sigma_{hs} = \sigma_{hs}^{b} = \frac{Mc}{I} = \frac{M\frac{t}{2}}{\frac{Lt^3}{12}} = \frac{76000 \cdot \frac{4}{2}}{\frac{50 \cdot 4^3}{12}} = 570.0\text{MPa}$$

All three stress analysis results are listed below, i.e.

$$\sigma_{hs} = \sigma_{hs}^{b} = 584.86\text{MPa}(\textit{fine 3D finite element mesh})$$

$$\sigma_{hs} = \sigma_{hs}^{b} = 571.10\text{MPa}(\textit{coarse 3D finite element mesh})$$

$$\sigma_{hs} = \sigma_{hs}^{b} = 570.0\text{MPa}(\textit{manual stress analysis})$$

The lowest hot spot stress was obtained from the manual analysis. This is due to the fact that the manual one was in fact a 2D stress analysis where it was assumed that the stress was constant along the entire weld toe line. In the case of both 3D FE stress analyses the stress was varying along the weld toe line and reaching the maximum in the middle of the bracket width L (Fig. 3.53). However, the stress data obtained from the coarse mesh 3D FE model seem to be sufficiently accurate for the determination of the hot spot stress.

8.6 Conclusions – GR3 weld model

- The GR3 coarse mesh 3-D FE method makes it possible to determine local membrane and bending reference or hot spot stresses at any point along the weld toe line.
- The local membrane and bending hot spot stresses enable using pure tension and pure bending stress concentration factors and making them applicable at any point along the weld toe line
- Therefore, only two stress concentration factors are required for fillet and butt welds (different sets for each), i.e. the stress concentration factor for pure bending and pure axial stress.
- When the weld geometry and size remain constant the same set of stress concentration factors can be used for the determination of the linear elastic peak stress at any point along the weld toe line providing that the membrane and bending hot spot stresses have been determined.
- The advantage of the GR3 method is coming from the fact that the weld is globally modeled as it stands in reality. The weld stiffness effect is accounted for without the necessity of exact modeling of the local weld toe geometry and therefore it enables using relatively large Finite Elements (~0.25t).

References

[1] J. Bannantine, Corner, Handrock, Fundamentals of Metal Fatigue Analysis, Prentice-Hall, 1990.
[2] N. Dowling, Mechanical Behavior of Materials, third ed., Prentice Hall, 2011.
[3] R.I. Stephens, A. Fatemi, A.A. Stephens, H.O. Fuchs, Metal Fatigue in Engineering, John Wiley, 2001.
[4] M. Janssen, J. Zudeima, R.J.H. Wanhill, Fracture Mechanics, VSSD, The Netherlands, 2006.
[5] D. Radaj, Design and Analysis of Fatigue-Resistant Welded Structures, Abington Publishers, Cambridge, 1990.
[6] E. Niemi, Stress determination for fatigue analysis of welded components, in: IIS/IIW -1221-93 (Ex Doc XIII-1458-92, XV-797-92), 1993.
[7] E. Niemi, Recommendations Concerning Stress Determination for Fatigue Analysis of Welded Components, IIW Document Abington Publishers, Cambridge, UK, 1995, pp. 1221–1293.

[8] D. Radaj, Review of fatigue strength assessment of nonwelded and welded structures based on local parameters, International Journal of Fatigue 18 (1996) 153−170.
[9] A. Hobbacher, Recommendations for Fatigue Strength of Welded Components, Abington Publishers, Cambridge, 1996.
[10] D. Radaj, C.M. Sonsino, Fatigue Assessment of Welded Joints by Local Approaches, Abington Publishers, Cambridge, 1998.
[11] E. Niemi, P. Tanskanen, Hot spot stress determination for welded edge gussets, Welding in the World 5 (44) (2000) 31−37.
[12] S. Maddox, Recommended design S−N curves for fatigue assessment of FPSO, in: Proceedings of the ISOPE, Stavanger, 2001.
[13] E. Niemi, Structural stress approach to fatigue analysis of welded components—designer's guide, in: IIW-Doc. XIII-1819-00/XV-1090-01, International Institute of Welding, Paris, 2001.
[14] P. Dong, A structural stress definition and numerical implementation for fatigue analyses, International Journal of Fatigue 10 (23) (2001) 865−876.
[15] W. Fricke, R. Bogdan, Determination of hot spot stress in structural members with in-plane notches using a coarse element mesh, in: IIW-Doc. XIII-1870-01, international Institute of Welding, 2001.
[16] S.J. Maddox, Hot-spot stress design curves for fatigue assessment of welded structures, International Journal of Offshore and Polar Engineering 12 (2002) 134−141.
[17] P. Dong, J.K. Hong, Z. Cao, Structural stress-based master S−N curve for welded joints, in: IIW Doc XIII-1930-02/XV-1119-02, Int Inst Welding, 2002.
[18] W. Fricke, Recommended hot-spot analysis procedure for structural details of ships and FPSOs based on round-robin FE analysis, International Journal of Offshore and Polar Engineering 12 (1) (2002) 40−48.
[19] W. Fricke, Fatigue analysis of welded joints: state of development, Marine Structures 16 (2003) 185−200.
[20] O. Doerk, W. Fricke, C. Weißenborn, Comparison of different calculation methods for structural stresses at welded joints, International Journal of Fatigue 25 (2003) 359−369.
[21] Z.G. Xiao, K. Yamada, A method of determining geometric stress for fatigue strength evaluation of steel welded joints, International Journal of Fatigue 26 (2004) 1277−1293.
[22] W. Fricke, A. Kahl, Comparison of different structural stress approaches for fatigue assessment of welded ship structures, Marine Structures 18 (2005) 473−488.
[23] D. Radaj, C.M. Sonsino, W. Fricke, Fatigue Assessment of Welded Joints by Local Approaches, second ed., Woodhead Publishing and Boca Raton CRC Press, Cambridge, 2006.
[24] B. Noh, J. Song, S. Bae, Fatigue strength evaluation of the load-carrying cruciform fillet-welded joints using hot spot stress, Key Engineering Materials (2006) 324−325.
[25] I. Poutiainen, G. Marquis, A fatigue assessment method based on weld stress, International Journal of Fatigue 28 (2006) 1037−1046.
[26] E. Niemi, W. Fricke, S.J. Maddox, Fatigue Analysis of Welded Components, Designer's Guide to the Structural Hot-Spot Stress Approach, Woodhead Publishing Limited, Cambridge, England, September 27, 2006.
[27] A.F. Hobbacher, The new IIW recommendations for fatigue assessment of welded joints and components - a comprehensive code recently updated, International Journal of Fatigue 31 (2009) 50−58.
[28] D. Radaj, C.M. Sonsino, W. Fricke, Recent developments in local concepts of fatigue assessment of welded joints, International Journal of Fatigue 31 (2009) 2−11.
[29] J. Schijve, Fatigue predictions of welded joints and the effective notch stress concept, International Journal of Fatigue 45 (2012) 31−38.
[30] H. Remes, W. Fricke, Influencing factors on fatigue strength of welded thin plates based on structural stress assessment, Welding in the World 58 (2014) 915−923.
[31] G. Meneghetti, D. Marini, V. Babini, Fatigue assessment of weld toe and weld root failures in steel welded joints according to the peak stress method, Welding in the World 60 (2016) 559−572.
[32] J. Baumgartner, Review and considerations on the fatigue assessment of welded joints using reference radii, published in special Issue: fatigue Assessment of Welded Joints by Modern Concepts, International Journal of Fatigue 101 (2017) 459−468.
[33] L. Bertini, F. Frendo, G. Marulo, Fatigue life assessment of welded joints by two local stress approaches: the notch stress approach and the peak stress method, International Journal of Fatigue 110 (2018) 246−253.
[34] P. Xianjun, D. Pingsha, X. Shizhu, A structural strain parameter for a unified treatment of fatigue behaviors of welded components, International Journal of Fatigue 124 (2019) 444−460.
[35] L.M. Gourd, Principles of Welding Technology, third ed., Edward Arnold, 1995.
[36] J. Puchaicela, Control of distortion of welded steel structures, Welding Journal (77) (1998) 49−52.

[37] J. Mackerle, Finite element analysis and simulation of welding—a bibliography (1976—1996), Modelling and Simulation in Materials Science and Engineering 4 (1996) 501—533.
[38] C. Hackmair, E. Werner, M. Ponisch, Application of welding simulation for chassis components within the development of manufacturing methods, Computational Materials Science 28 (2003) 540—547.
[39] A. Bachorski, M.J. Painter, A.J. Smailes, M.A. Wahab, Finite element prediction of distortion during gas metal arc welding using the shrinkage volume approach, Journal of Materials Processing Technology 92 (1999) 405—409.
[40] P. Michaleris, A. DeBiccari, Prediction of welding distortion, Welding Research Supplement 76 (1997) 172—181.
[41] D. Rosenthal, Mathematical theory of heat distribution during welding and cutting, Welding Journal 5 (1941) 220—234.
[42] V. Pavelec, R. Tanbakuchi, O.A. Uyehara, P.S. Myers, Welding Journal Research Supplement 48 (1969) 295—305.
[43] G.H. Little, A.G. Kamtekar, The effect of thermal properties and welding efficiency on transient temperatures during welding, Computers and Structures 68 (1998) 157—165.
[44] T.L. Teng, C.P. Fung, P.-H. Chang, W.C. Yang, Analysis of residual stresses and distortions in T-joint fillet welds, International Journal of Pressure Vessels and Piping 78 (2001) 523—538.
[45] Y. Ueda, T. Yamakawa, Analysis of thermal elastic-plastic stress and strain during welding by finite element method, JWRI 2 (1971) 90—100.
[46] H.D. Hibbitt, P.V. Marcal, A numerical thermo-mechanical model for the welding and subsequent loading of a fabricated structure, Computers and Structures 3 (1973) 1145—1174.
[47] J. Mackerle, Finite element analysis and simulation of welding: a bibliography (1976—1996), Modelling and Simulation in Materials Science and Engineering 4 (1996) 501—503.
[48] J. Mackerle, Finite element analysis and simulation of welding—an addendum: a bibliography (1996—2001), Modelling and Simulation in Materials Science and Engineering 10 (2002) 295—318.
[49] Y.G. Duan, J.M. Bergheau, Determination of welding residual distortions of large structures, in: 8th. World Congress on Computational Mechanics (WCCM8), Venice, Italy, June 30—July 5, 2008, 2008.
[50] F.V. Tahami, A.H. Sorkhabi, Finite element analysis of thickness effect on the residual stresses in butt welded 2.25Cr1Mo steel plates, Journal of Applied Sciences 9 (2009) 1331—1337.
[51] L. Yajiang, W. Juan, C. Maoai, S. Xiaoqin, Finite element analysis of residual stress in the welded zone of a high strength steel, Bulletin of Materials Science 27 (2) (2004) 127—132.
[52] V. Deaconu, Finite element modelling of residual stress - a powerful tool in the aid of structural integrity assessment of welded structures, in: 5th Int. Conference Structural Integrity of Welded Structures (ISCS2007), Timisora, Romania, 20—21 Nov 2007, 2007.
[53] D. Gery, H. Long, P. Maropoulos, Effects of welding speed, energy input and heat source distribution on temperature variations in butt joint welding, Journal of Materials Processing Technology 167 (2005) 393—401.
[54] D.J. Smith, P.J. Bouchard, D. Geoge, Measurement and prediction of residual stresses in thick-section steel welds, Journal of Strain analysis 35 (4) (2000) 287—305.
[55] R.,H. Yeh, S.P. Liaw, H.B. Yu, Thermal analysis of welding on Al plates, Journal of Marine Science and Technology 11 (4) (2003) 213—220.
[56] P. Michaleris, A. Debiccari, A two-step numerical analysis technique was developed to predict welding induced distortion and the structural integrity of large and complex structures, AWS Welding Journal (1997) 172—180.
[57] D.J. Duranton, V. Robin, P. Gilles, J.M. Bergheau, 3D modelling of multipass welding of a 316L stainless steel pipe, Journal of Materials Processing Technology 153 (2004) 457—463.
[58] J.J. Dike, A.R. Ortega, C.H. Cadden, Finite element modeling and validation of residual stresses in 304L Girth welds, in: 5th International Conference on Trends in Welding Research, Pine Mountain, GA, June 1—5, 1998, 1998.
[59] D. Camilleri, T.G.F. Gray, Computationally efficient welding distortion simulation techniques, Modelling and Simulation in Materials Science and Engineering 13 (2005) 1365—1382.
[60] B. Souloumiac, F. Boitout, J.M. Bergheau, A new local global approach for the modelling of welded steel component distortions, in: P.H. Cerjak (Ed.), Mathematical Modelling of Weld Phenomena 6, Maney Publishing, London, 2002, pp. 573—590. ISBN 1-902653-56-4.
[61] D.F. Watt, L. Coon, M.J. Bibby, J. Goldak, C. Henwood, Modeling microstructural development in weld heat-affected zones, Acta Metallurgica 36 (1988) 3029.
[62] C. Henwood, M.J. Bibby, J.A. Goldak, D.F. Watt, Coupled transient heat transfer-microstructure weld computations, Acta Metallurgica 36 (1988) 3037.

[63] J. Goldak, J. Zhou, S. Tchernov, D. Downey, S. Wang, B. He, Predicting distortion and residual stress in complex welded structures by designers, in: 7th International Trends in Welding Research, Callaway Gardens Resort, Pine Mountain, Georgia, USA, 2005.
[64] S. Suman, P.V.S.S. Sridhar, P. Biswas, D. Das, Prediction of welding-induced distortions in large weld structure through improved equivalent load method based on average plastic strains, Welding in the World 64 (2020) 179−200.
[65] D. Wang, H. Zhang, B. Gong, C. Deng, Residual stress effects on fatigue behavior of welded T-joint: a finite fracture mechanics approach, Materials and Design 91 (2016) 211−217.
[66] P.A. Deschênes, J. Lanteigne, Y. Verreman, D. Paquet, J.B. Lévesque, M. Brochu, A new experimental method to study the influence of welding residual stresses on fatigue crack propagation, International Journal of Fatigue 100 (2017) 444−452.
[67] J. Hensel, P.T. Nitschke, D.T. Ngoula, H.T. Beier, D. Tchuindjang, U. Zerbst, Welding residual stresses as needed for the prediction of fatigue crack propagation and fatigue strength, Engineering Fracture Mechanics 198 (2018) 123−141.
[68] K. Iida, T. Uemura, Stress concentration factor formulas widely used in Japan, Fatigue Fatigue and Fracture of Engineering Materials and Structures 19 (6) (1996) 779−786.
[69] H. Neuber, Kerbspannungslehre, third ed., Springer-Verlag, Berlin, 1985.
[70] W.D. Pilkey, D.F. Pilkey, Peterson's Stress Concentration Factors, John Wiley & Sons, Inc., Hoboken, New Jersey, USA, 2008.
[71] A. Chattopadhyay, G. Glinka, M. El-Zein, J. Qian, R. Formas, Stress analysis and fatigue of welded structures, Welding in the World, (IIW) 55 (7−8) (2011) 2−21.
[72] W.J.M. Rankine, On the causes of the unexpected breakage of the journals of railway axles, and on the means of preventing such accidents by observing the law of continuity in their construction, Minutes of the Proceedings of the Institution of Civil Engineers 2 (1843) 105−107.
[73] T.H. Topper, B.I. Sandor, J.D. Morrow, Cumulative fatigue damage under cyclic strain control, Journal of Materials 4 (1969) 189.
[74] T.M. Topper, R.M. Wetzel, J. Morrow, Neuber's rule applied to fatigue of notched specimens, Journal of Materials 4 (1969) 200−209.
[75] J.D. Morrow, J.F. Martin, N.E. Dowling, Local Stress-Strain Approach to Cumulative Damage Analysis, Report 379, University of Illinois, Dept. Theoretical and Applied Mechanics, Urbana, Illinois, USA, 1974.
[76] O.H. Basquin, The exponential law of endurance test, Proceedings of the American Society for Testing and Materials 10 (1910) 625−630.
[77] L.F. Coffin Jr., A study of the effects of cyclic thermal stresses on a ductile metal, Transactions of the ASME 76 (1954) 931−950.
[78] S.S. Manson, Behavior of Materials under Conditions of Thermal Stress, National Advisory Committee for Aeronautics, 1953. NACA TN-2933.
[79] W. Ramberg, W.R. Osgood, Description of Stress−Strain Curves by Three Parameters, Technical Note No. 902, National Advisory Committee for Aeronautics, Washington DC, 1943.
[80] H. Neuber, Theory of stress concentration for shear-strained prismatic bodies with arbitrary nonlinear stress strain law, Journal of Applied Mechanics 28 (1961) 544−551.
[81] K. Molski, G. Glinka, A method of elastic-plastic stress and strain calculation at a notch root, Materials Science Engineering 50 (1981) 93−100.
[82] G.R. Irwin, J.A. Kies, H.L. Smith, Fracture strength relative to onset and arrest of crack propagation, Proceedings of the American Society for Testing Materials 58 (1958) 640−657.
[83] Y. Murakami, et al., Stress Intensity Factors Handbook, in: The Society of Materials Science, vols. 1−5, Pergamon Press, Japan, 1987-2001.
[84] H.F. Bueckner, A novel principle for the computation of stress intensity factors, Zeitschrift für Angewandte Mathematik und Mechanik 50 (1970) 529−546.
[85] R. Goyal, Fatigue Evaluation of Welded Structures, PhD Thesis, Department Mechanical and Mechatronics Engineering, University of Waterloo, Waterloo, Ontario, Canada, 2015.
[86] R. Goyal, M. El-Zein, G. Glinka, A Robust Stress Analysis Method for Fatigue Life Prediction of Welded Structures, International Institute of Welding, 2015. Paper No. XIII-2539-14.

PART B

Deformation assisted joining

This page intentionally left blank

CHAPTER

4

Deformation assisted joining

N. Bay[a], L.M. Alves[b], C.V. Nielsen[a], C.M.A. Silva[b], P.A.F. Martins[b]

[a]Department of Mechanical Engineering, Technical University of Denmark, Lyngby, Denmark; [b]IDMEC, Instituto Superior Tecnico, Universidade de Lisboa, Lisboa, Portugal

1. Introduction

The increasing demands for weight savings in automotive, aerospace and rail industry have stimulated the development and application of new materials, e.g. Advanced High Strength Steels (AHSS), aluminum alloys, magnesium alloys, titanium alloys and carbon fiber reinforced polymers [1]. The new materials imply severe challenges to assembly operations. Fusion welding may be difficult or impossible when joining dissimilar material combinations and in several cases even when joining to themselves. This calls for alternative joining methods such as deformation assisted joining. Comprehensive reviews on these joining methods including mechanical joining and solid-phase welding are given by Refs. [2,3].

Mechanical joining may be either form-fit joints or force-fit joints [3], the latter also named interference-fit joints [4] (Fig. 4.1).

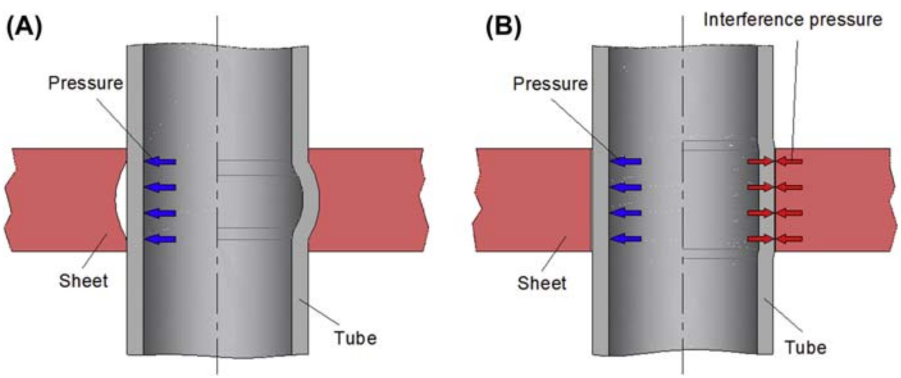

FIG. 4.1 Mechanical joining using (A) form-fit and (B) force-fit joints.

Advanced Joining Processes
https://doi.org/10.1016/B978-0-12-820787-1.00004-8

Form-fit joints are built upon combination of plastic material flow with the utilization of different types of features such as bends, curls, beads and undercuts to produce a mechanical interlock between the components to be joined. Examples of deformation assisted form-fit joining are hemming, clinching, riveting and self-pierce riveting (Fig. 4.2A), which are used for joining sheets of similar as well as dissimilar materials.

Hemming (Fig. 4.2A) is a forming operation in which sheet edges are folded over themselves to reinforce or improve appearance or folded over another sheet (or, part) to connect two sheets (or, parts) together. The process is used in the automotive industry to assemble hoods, doors and fenders and in canned drinks and food of the agro-industry. A variant of conventional hemming is roll hemming in which the operation is carried out incrementally along a pre-defined path.

Clinching (Fig. 4.2A) is a deformation assisted joining process aimed at fixing thin sheets without additional consumables or pre-drilled holes by means of dedicated punches and dies that plastically deform the sheets to achieve a form-fit based mechanical interlock.

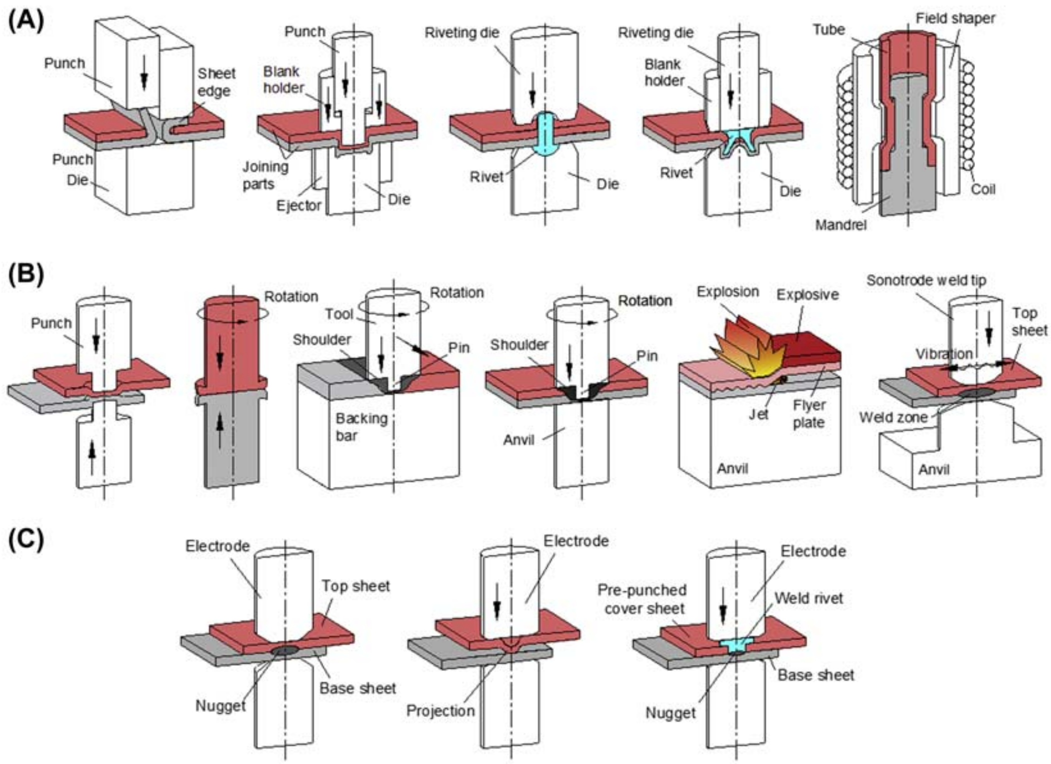

FIG. 4.2 Examples of deformation assisted joining by (A) mechanical joining (hemming, clinching, riveting, self-pierce riveting and electro-magnetic forming), (B) solid-phase welding (cold pressure welding, friction welding, friction stir welding, friction stir spot welding, explosive welding and ultrasonic welding) and (C) fusion welding combined with plastic deformation (resistance welding, resistance projection welding, and resistance element welding).

The process is generally performed at room temperature and can join sheets made from dissimilar materials as well as pre-coated and pre-painted sheets without damaging their surfaces. The main limitation of clinching is sheet formability, which needs to be good in order to avoid failure by cracking. Clinching is commonly used in high-speed production of automotive, white goods and electronic components, where it often replaces riveting and spot welding. In contrast to spot welding, clinching can easily assemble polymer sheets and polymer-metal sandwich composite sheets.

Self-pierce riveting is another high-speed deformation assisted joining process that makes use of a semi-tubular (or, solid) rivet to produce a form-fit based mechanical interlock between two or more sheets. The process is generally performed at room temperature and makes use of dedicated punches and dies. The main advantage is its capability of fixing sheets made from dissimilar materials that are difficult or impossible to weld. Self-pierce riveting, like clinching, can also be used with pre-coated or pre-painted sheets without damaging their surfaces. The process is widely applied in automotive industry for joining dissimilar materials, which are difficult or impossible to spot weld, such as AHSS to mild steel and aluminum alloys.

Comprehensive reviews are given by Refs. [5,6]. Examples of form-fit tube-tube joining and tube-sheet joining are given by Refs. [7–9].

Interference-fit joints are based on an elastic-plastic deformation of the two components establishing residual normal stresses at the interface, which prevents tangential movement due to friction. Examples of applications are camshaft production by expansion of tubular axles and cams using either hydroforming or internal rolling [10]. In hydroforming liquid is used as a flexible tool.

Deformation assisted joining using electro-magnetic forming (Chapter 5) (Fig. 4.2A) has found increasing applications since the 1960s [4]. Similar as well as dissimilar materials can be mechanically joined as either form-fit or interference-fit joints. Tubes can be connected to bars or cables by electro-magnetic compression in a form-fit or an interference-fit mechanical joint.

Deformation assisted joining by solid-phase welding includes cold pressure welding, friction welding, friction stir welding (Chapter 6), friction stir spot welding, magnetic pulse welding, explosive welding (Chapter 7) and ultrasonic welding (Chapter 8) (Fig. 4.2B). In cold pressure welding, the mating surfaces are normally prepared by scratch brushing, which creates a brittle surface layer that is fractured by joint plastic deformation of the two metals. When a threshold surface expansion is reached, the exposed virgin material is extruded through cracks of the brittle cover layer meeting similarly exposed and extruded material from the opposing metal. Joining of sheet metals may be done by rolling or local indentation with small tools. Roll bonding is used for manufacturing of precious metal contacts combining Ag or Au with Cu or Al. Extrusion is applied for cold pressure welding of tube transition joints, e.g. Al-stainless steel and Al-Ti, and butt welding is applied for manufacturing of electric bus bars combining Cu and Al. A review on cold pressure welding describing the main process parameters and the mechanisms of bonding is given in Ref. [11] and the same author has listed process variants and industrial applications in Ref. [12].

Conventional friction welding is used to join rotational symmetric bars and tubes. A small load is established between the two components of which one is rotating, while the other is stationary. Friction heating causes local softening and radial expansion of the components at the interface thereby creating a clean interface. After stopping the rotation, an increased load is applied forming metallic bonding between the two mating surfaces. In linear friction welding, the relative motion is limited to oscillations with small linear amplitude. This makes it possible to join bars with rectangular cross section. In both cases similar as well as dissimilar metals can be joined, e.g. Al-Cu and Al-steel.

A more recently developed friction welding process is friction stir welding (Chapter 6), where a rotating, threaded pin tool provided with a shoulder for control of the penetration and for creating additional frictional heat is traversing along the joint line between the butted ends of two plates. The heat lowers the flow stress of the two materials locally and together with plastic deformation, which kneads the two mating materials together, a solid-state weld is formed. The two plates may be of similar as well as dissimilar material. Friction stir welding is primarily used to join aluminum alloys but other metal combinations including dissimilar ones are also noted. Extruded Al-profiles are friction stir welded in shipbuilding, aerospace and rail industries. A comprehensive review on the different types of friction welding, bonding mechanisms and microstructures in a large number of metal combinations is given in Ref. [13]. Focus on friction stir welding of similar as well as dissimilar metals is presented in the detailed review [14].

Friction stir spot welding is a solid-state welding process applied for lap joining of two sheets. A rotating, threaded pin tool with a convex shaped shoulder rather similar to the one used in friction stir welding is plunged into the two overlapping sheets supported by a backing plate. The shoulder ensures only partly penetration of the lower sheet by the pin tool. Friction between the tool and the two sheets heats them locally and the plastic deformation creates a solid-state bond. The process is applied in automotive and aerospace industry for joining of aluminum [15].

If the initial clearance between the parts in electro-magnetic joining is appropriately adjusted and the moving part is accelerated to high velocity, high-energy impact and large shear strains are developed in the two mating surfaces causing an outgoing jet of softened metal to form at the collision front. This cleans the surfaces permitting subsequent solid-state bonding to occur. This process variant is called magnetic pulse welding, which enables welding of similar as well as dissimilar metal combinations. Kang [16] shows examples of joining Al-tubes to Cu-tubes for refrigerators and Al-tubes to steel-cardan joints for automotive drive shafts.

Explosive welding (Chapter 7) is a solid-state welding process operating at room temperature with only minor temperature development. Fig. 4.2B shows a schematic outline of the process. A description of the bonding mechanisms is presented in Ref. [17]. An explosive material is placed upon the flyer plate or cladding layer and ignited to accelerate the flyer plate locally. This results in an oblique collision with the underlying base plate and a high-pressure zone at the collision line. To obtain a good bond it is necessary that the velocity of the collision point is below the speed of sound of the materials. Similar to magnetic pulse welding, a jet of metal is formed at the apex of the collision and is forced outward between the colliding metals at high velocity. This mechanism cleans the two facing metal surfaces, which are then metallurgically bonded together under high pressure.

Industrial applications of explosive welding include the manufacture of large clad plates combining stainless steel to mild steel and titanium to mild steel, which are used for pressure vessels, heat exchangers and containers for electrochemical processing. Al-steel, Ti-steel, Ti-Al and Al-CuNi are applied in marine industry, Al-stainless steel is used for cryogenic pipe couplings and Ti-stainless steel is applied in aerospace industry [18].

Ultrasonic welding (Chapter 8) is a solid-state welding process, which creates a metallurgical bond by simultaneous application of localized high-frequency vibratory energy and moderate normal pressures [19]. Friction and plastic deformation at the interface deform the surface asperities and break up contaminant films and oxides resulting in direct contact between virgin surfaces and formation of a metallurgical bond. Although most metals can be ultrasonically welded, the widest use is found among softer metals such as Al, Cu, Mg, Au and Ag. Dissimilar metal combinations are readily welded and joints between metal plates, sheets, foils and wires are possible [20]. Application of ultrasonic welding includes joining of stranded cables of Cu- or Al-wires to terminals in automotive industry, encapsulation of temperature-sensitive electrical, chemical or pyrotechnical material, and bonding of micro-wire is widely used in semiconductor and microelectronics industry.

Deformation assisted joining combined with fusion welding includes resistance welding, resistance projection welding and resistance element welding (Fig. 4.2C). Electric current is utilized to heat the metals locally at the contacting interface. The heat softens and melt the materials locally. In resistance projection welding, where the current is locally confined to a narrow cross section, local melt is often expelled from the interface in which case a solid-state bond may be formed. It is thus possible to join metal combinations, which cannot be fusion welded. The introduction of new sheet materials in automotive industry and resulting requirements for joining dissimilar metals put limits to the application of resistance spot welding. In order to solve this problem, resistance element welding was developed [21,22]. In contrast to conventional resistance spot welding, an auxiliary element made of for example steel, a so-called weld rivet is used to ensure metallurgical compatibility. The weld decoupling of the cover plate (lightweight part) allows spot weld joints between weldable and non-weldable materials. Reviews on resistance welding processes may be found in Refs. [23,24].

As regards deformation assisted joining the present authors have especially been working in the fields of mechanical joining, cold pressure welding and resistance welding. In the following, examples of their development of joining solutions with these assembly methods are presented.

2. Mechanical joining

2.1 Form-fit joints

Mechanical joining of thin-walled tubes to sheets by form-fit joints at room temperature is based on local buckling [25], combination of local buckling and flaring [26], or combination of sheet-bulk forming and flaring [27,28], see (Fig. 4.3A—C).

Plastic instability of thin-walled tubes under axial compression is characterized by two fundamental modes of deformation: global and local buckling. Global buckling takes place when a tube fails as a whole (that is, like a column), and is expected to occur when the tube is long and has relatively thick walls. Local buckling involves the development of plastic

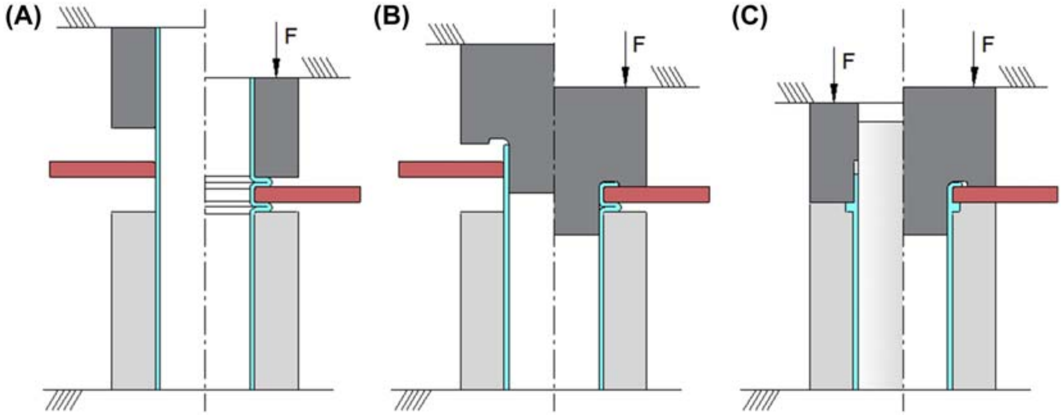

FIG. 4.3 Mechanical joining of thin-walled tubes to sheets using form-fit joints produced by (A) local buckling, (B) combination of local buckling and flaring and (C) combination of sheet-bulk forming and flaring.

instability waves (or wrinkles) usually taking place when a tube, either short or long, has thin walls.

Mechanical joining of tubes to sheets by local buckling is based on the formation of compression beads from the development and propagation of plastic instability waves. Plastic waves can be formed naturally to provide axisymmetric compression beads, or they may be forced to propagate along inclined planes with respect to the tube axis to form inclined compression beads. In both cases, two compression beads are needed to fix the sheet in position by means of a form-fit joint.

Fig. 4.4A presents the active tool components for producing inclined compression beads in tubes in the open and closed positions. They consist of two (upper and lower) inclined dies and an inner mandrel. The inclined dies, which are dedicated to a specific reference radius r_0 of the tube and its geometry, together with the initial gap opening l_{gap} between them, are responsible for defining the angle α and the position of the compression beads.

As seen in the figure, inclined compression beads are formed by forcing one tube end toward the other while leaving a gap opening in-between the dies that support and hold the tube. As the upper die compresses the tube, a plastic instability wave is triggered within the gap opening and an inclined compression bead is formed (Fig. 4.4B). By producing a second inclined compression bead it is possible to connect a tube to a sheet along an inclined plane with respect to the tube axis (Fig. 4.4C).

The utilization of a mandrel inside the tube is mandatory because development and propagation of plastic waves without a mandrel will allow material to flow both inward and outward. This gives rise to defects (geometrical depression) on the tube surfaces located above and below the inclined compression bead. The defect is shown in the predicted finite element geometry and photograph of the tube that are included in Fig. 4.5 (refer to the figures with red circular marks).

The utilization of a mandrel inside the tube not only avoids defects along its surface but also guarantees the dimension of the inner diameter, which in many applications is a critical value to stay within tolerances. In practical terms, the use of a mandrel eliminates inward

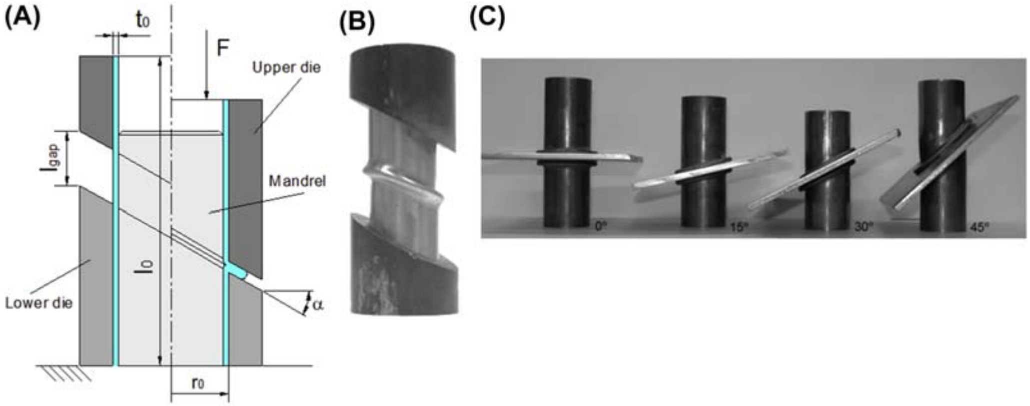

FIG. 4.4 Mechanical joining of tubes to sheets by local buckling along inclined planes. (A) Schematic representation of the process and identification of the main process parameters, (B) tube showing a partially formed compression bead along an inclined plane and (C) application of the process for joining tubes to sheets along planes with different inclinations. *Adapted from L.M. Alves, P.A.F. Martins. Mechanical joining of tubes to sheets along inclined planes. Steel Research International 83 (12) (2012) 1135–1140. https://doi.org/10.1002/srin.201200035; A. Gonçalves, L.M. Alves, P.A.F. Martins. Inclined tube-sheet plastically deformed joints. Steel Research International 85 (1) (2014) 67–75. https://doi.org/10.1002/srin.201300078.*

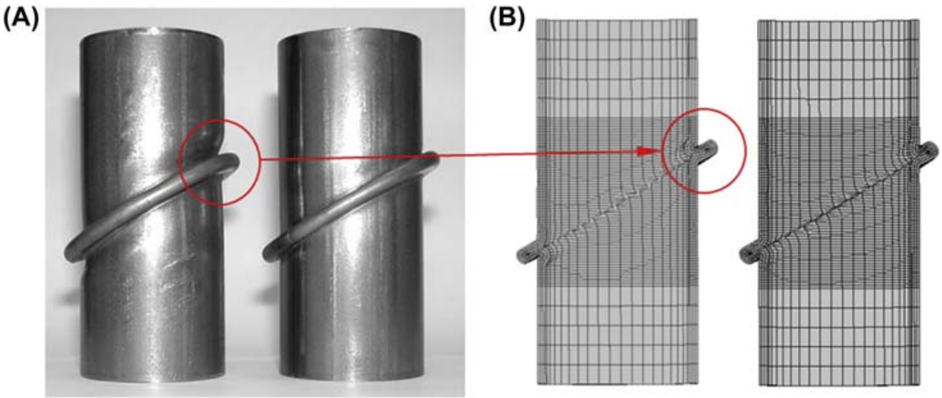

FIG. 4.5 Influence of the internal mandrel on the formation of inclined compression beads. (A) Photographs of tubes that are subjected to axial compression without (left) and with (right) internal mandrel and (B) finite element predicted geometries of the axial cross-sections of the tubes shown in (A). *Adapted from L.M. Alves, P.A.F. Martins. Mechanical joining of tubes to sheets along inclined planes. Steel Research International 83 (12) (2012) 1135–1140. https://doi.org/10.1002/srin.201200035.*

material flow and forces the inclined compression beads to develop exclusively outwards (refer to the tubes without circular red marks in Fig. 4.5).

The combination of compression beads produced by local buckling with flaring allows producing tube-sheet connections at the tube ends. Flaring consists in the compression of the upper tube end against a rounded die (Fig. 4.6A) to expand material outwards and form a single-lap flange. The process allows producing mechanical joints in dissimilar materials as shown in Fig. 4.6B, which presents the connection of a commercial S460MC (carbon steel) welded tube in the "as-received" condition to a polycarbonate sheet. The other photograph included Fig. 4.6C shows the application of mechanical joining by combination of local buckling and flaring to the fabrication of the metallic structure of a train passenger seat.

Mechanical joining by combination of sheet-bulk forming and flaring is an alternative solution for producing tube-sheet connections at the tube ends. The process combines partial sheet-bulk compression of the tube wall thickness (also designated as "boss forming") and locking by upsetting the free tube end against the sheet panel with a flaring die. The process

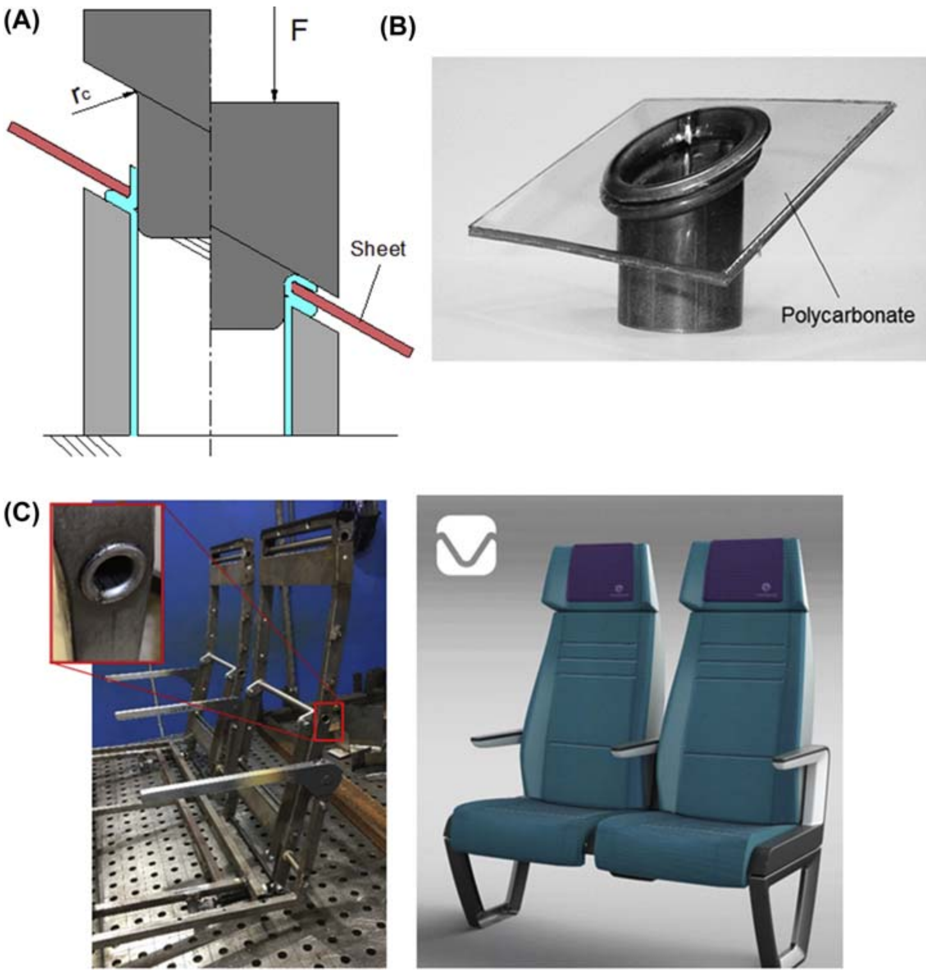

FIG. 4.6 Mechanical joining of tubes to sheets along inclined planes by combination of local buckling and flaring. (A) Schematic representation of the process, (B) application of the process for joining dissimilar materials and (C) application of the process to fabricate the metallic structure of a train passenger seat [31].

is schematically shown in Fig. 4.7 and the example concerns the connection of a tube to a sandwich composite panel [28].

As seen in Fig. 4.7A, material from the outward tube wall thickness is piled-up into a die cavity with rectangular cross section in order to obtain an annular flange with tight dimensional control. The sandwich composite panel is subsequently placed upon the annular flange and the free tube end is compressed against it with a flaring die to obtain the required mechanical interlock (Fig. 4.7B). The process avoids bending the sandwich composite panels and, therefore, prevents the risk of delamination.

Table 4.1 offers a complete overview of the experimental results obtained when fixing aluminum AA6063-T6 tubes to sandwich composite panels with 2 mm thickness consisting of a polymer core layer (1 mm) made of a mixture of polyamide and polyethylene and two thin metal sheets (0.5 mm) made of an interstitial free steel. By changing the length l_f of the free tube end and the fillet radius r_f of the flaring die it is possible to identify four different modes of deformation. Three of these modes, labeled as "I", "II" and "IV" give rise to unacceptable joints while a fourth mode labeled as "III" allows producing sound joints.

Mode I contain one or more horizontal folds due to plastic instability of the free tube end. This mode of deformation is typical of slender free tube ends and occurs for sharp fillet radius r_f of the flaring punch, whenever $l_f > l_{buckling}$. Fig. 4.8A provides an example showing the finite element predicted cross section before and after flaring with a die having $r_f = 0$ mm.

Mode II is characterized by a tube flare that is too small to ensure a robust mechanical interlocking between the sandwich composite panel and the tube. This mode of deformation takes place when the length l_f of the free tube end is shorter than needed, as shown in Fig. 4.8B.

The problem with mode IV is the in-plane instability of the sandwich composite panels. This phenomenon occurs when there is substantial outward material flow originated by the large fillet radius r_f of the flaring die. Fig. 4.8D provides an example showing the finite element predicted cross section before and after flaring with a die having $r_f = 6$ mm.

Finally, mode III corresponds to a sound joint without signs of plastic instability. The development of mode III requires the length of the free tube end $1.2 < l_f < 4$ mm in case the filet radius $r_f = 2$ and the length of the free tube end $2.5 < l_f < 4$ mm in case the filet radius $r_f = 1$ mm. In such cases, the geometry and size of the flare are adequate to ensure a robust

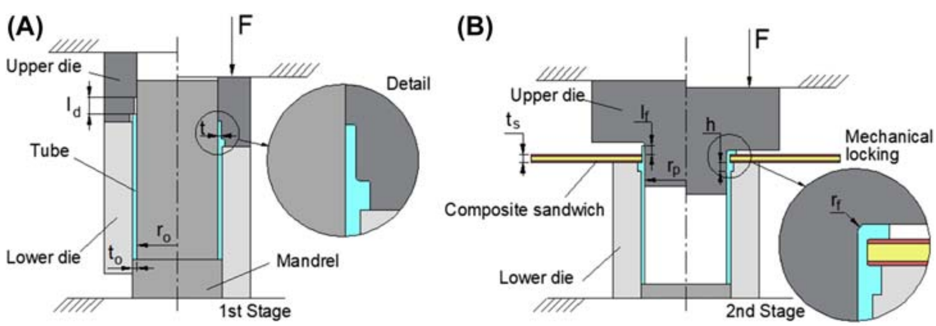

FIG. 4.7 Mechanical joining of tubes to composite sandwich sheets panels by combination of (A) partial sheet-bulk compression of the tube wall and (B) flaring.

TABLE 4.1 Summary of the experimental results obtained in the mechanical joining of aluminum AA6063-T6 tubes to sandwich composite panels with 2 mm thickness. The symbols are self-explanatory and correspond to the different modes of deformation that give rise to successful and unsuccessful form-fit joints.

		r_f (mm)			
		0	1	2	6
l_f (mm)	4	 Mode I	 Mode III	 Mode III	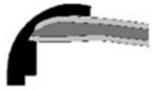 Mode IV
	2.5	 Mode II	 Mode III	 Mode III	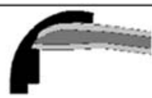 Mode IV
	1.2	 Mode II	 Mode II	 Mode III	 Mode IV

mechanical interlocking between the tube and the sandwich composite panel. Fig. 4.8C includes a typical finite element and experimental cross section.

2.2 Interference-fit joints

Proof coins for collection purposes make use of a very restricted set of metals that are mainly taken from groups 10 and 11 of the periodic table, excluding the radioactive (Ds and Rg) metals. The first attempt to use polymers as alternative coining materials was made in 2015 by the German central bank who issued the 5 Euro "Planet Earth" coin (Fig. 4.9A). Although "Planet Earth" may be considered the first polymer-metal coin, the use of polymer is marginal and limited to a relatively thin blue ring. This first utilization of polymers in coin minting is entirely different from that employed in tokens for shopping trolleys, which are produced by plastic injection molding.

The step forward in polymer-metal coins consisted of using mechanical joining by interference fitting to produce coins having a large area ratio between the polymer center and the outer metal ring, with high reliefs imparted on the surfaces of the polymer center (Fig. 4.9B) [33]. The design of the interference-fit joint was based on an analytical model for selecting the appropriate geometries of the polymer and metal blanks. The reliability of

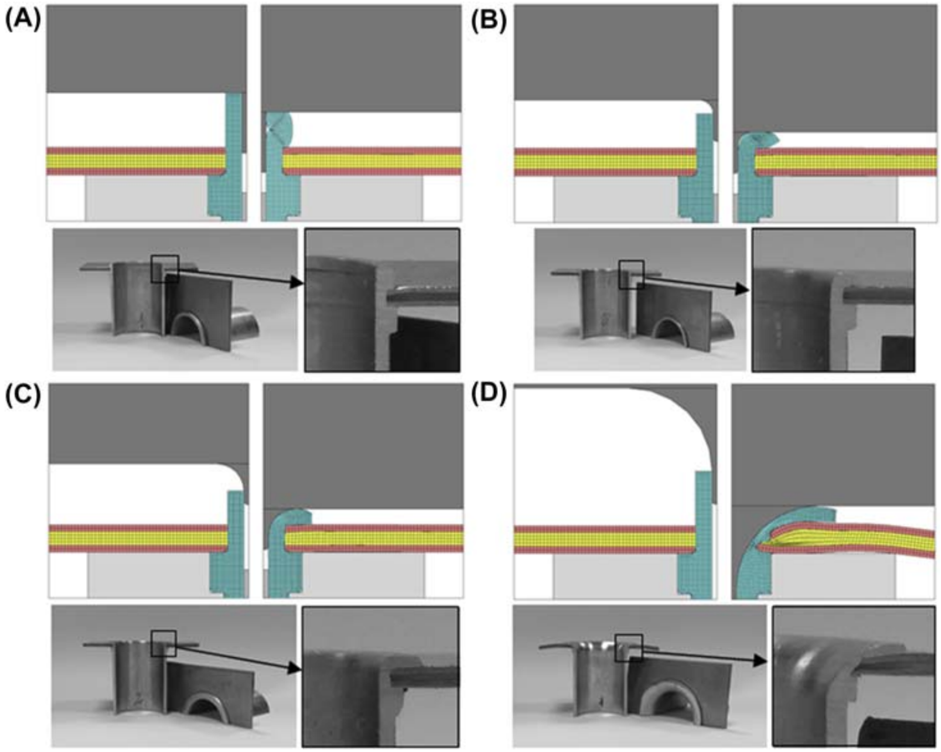

FIG. 4.8 Finite element predicted cross sections and photographs of deformation modes (A) I, (B) II, (C) III and (D) IV before and after performing the mechanical joining.

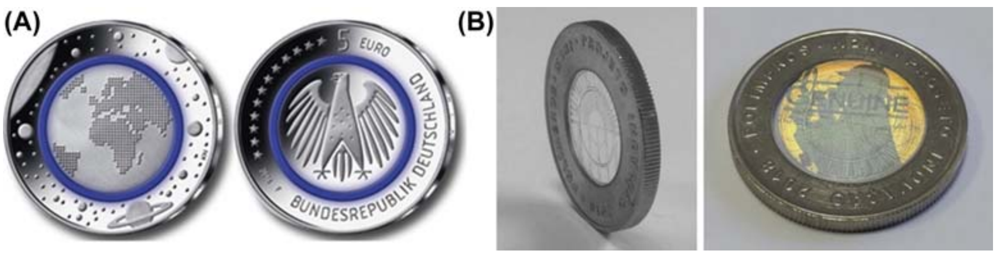

FIG. 4.9 New polymer-metal collection coins. (A) "Planet Earth" coin [32] and (B) prototype coins showing polymer centers with reliefs and holographic images for advanced security.

the analytical model and the overall feasibility of the polymer-metal coin concept was validated by means of finite elements and experimentation.

The mechanical joining is carried out simultaneously with coin minting in a single die stroke to produce an interference-fit joint *i* between the polymer center and the metal ring that is based on the residual normal stresses acting at the contact interface after unloading (Fig. 4.10).

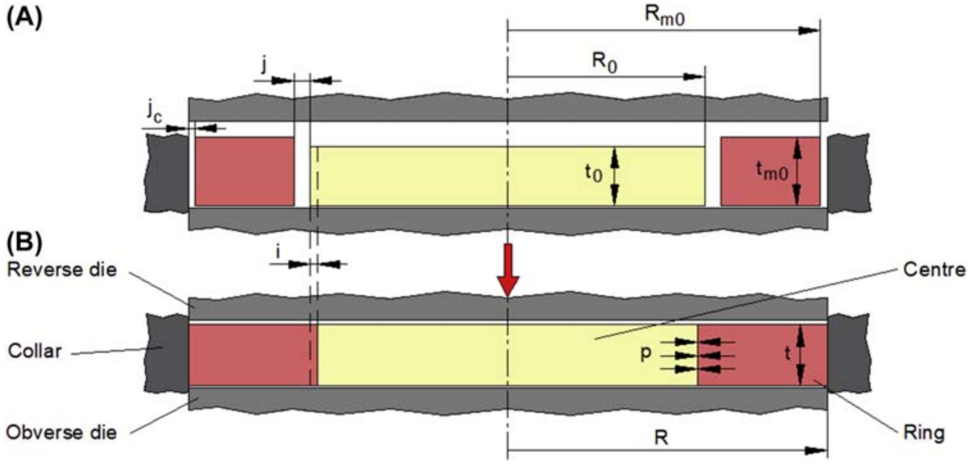

FIG. 4.10 Coining polymer-metal coins by interference joining at the beginning (A) and at the end (B) of the die stroke.

The process is schematically shown in Fig. 4.10, where R_0 is the radius of the polymer center blank with thickness t_0, R_{m0} is the outer radius of the metal ring blank with thickness t_{m0}, j is the clearance between the polymer center and the metal ring, and j_c is the clearance between the metal ring and the collar. Fig. 4.10B shows the thickness t and the radius R of the coin as well as the interference i between the polymer center and the metal ring at the end of the die stroke.

The analytical model for designing the interference-fit joint considers plastic deformation of the polymer center and of the metal ring to be homogenous (i.e. plane sections remain plane) and isotropic under axisymmetric material flow conditions. The surface of the ring blank is assumed to be flat without rimmed edges. Volume incompressibility during plastic deformation of the metal ring and of the polymer center allows writing the following relation between the clearance j and the interference i,

$$j^2 + 2R_0 j + \left(R_0^2 - R_{m0}^2\right) + R_0^2 \frac{\left(R_{m0} + j_c\right)^2 - \left(R_0 - i\right)^2}{\left(R_0 - i\right)^2} \frac{t_0}{t_{m0}} = 0 \tag{4.1}$$

The above equation gives rise to a process curve, which is plotted as a black solid curve in Fig. 4.11. The vertical-axis interception i_{max} of the process curve is the maximum achievable interference and the horizontal-axis interception corresponds to the maximum clearance j_{max} that can ensure a mechanical locking by interface contact pressure between the polymer center and the metal ring.

The process curve provides the design values for interference-fit joint and the gray bounded area accounts for the variations of R_0 of the four test cases from which measurements are plotted as open markers. The process curve will move upwards or downwards by decreasing or increasing the initial radius R_0 of the polymer center blank or the ratio t_0/t_{m0} between the thickness of the polymer and the thickness of the metal blanks.

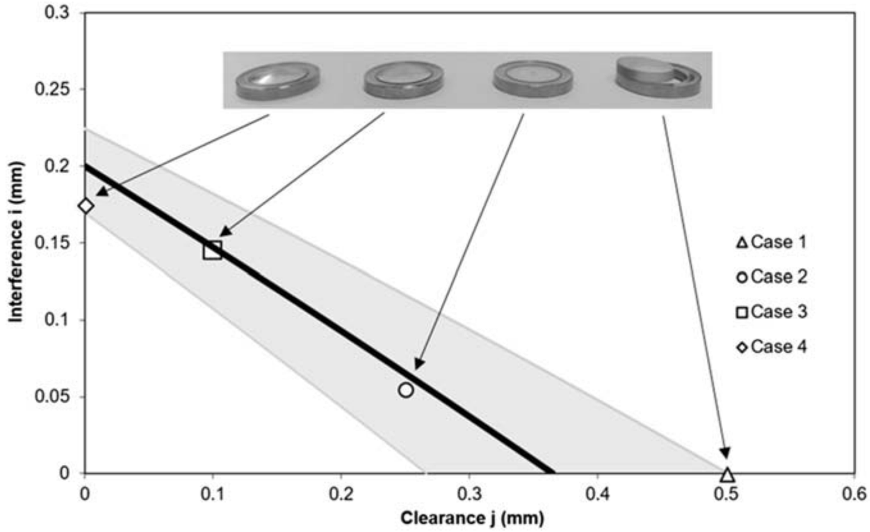

FIG. 4.11 Process curve showing the interference i as a function of the clearance j between the polymer center and the metal ring blank and results obtained from experiments with four different test cases.

As seen, there are three different modes of deformation. When the clearance j between the polymer center and the metal ring is larger than the maximum allowable clearance j_{max} there is no locking by interface contact pressure between the two parts. The resulting mode of deformation is designated as "mode I" and the polymer center remains separated from the metal ring after coin minting (refer to the rightmost coin sample of Fig. 4.11).

The main reason behind the occurrence of deformation mode I for $j > j_{max}$ is the contact between the reverse die and the polymer center taking place before the contact between the metal ring and the polymer center. Such inadequate contact sequence promotes elastic recovery of the polymer center toward the inner radius and, therefore, leads to separation of the two parts, after unloading. A similar result occurs when the initial thickness t_0 of the polymer center is larger than the initial thickness t_{m0} of the metal ring because contact between the reverse die and the polymer center will start before contact with the metal ring. As a result of this, the polymer center will be forced to move outwards, which implied that during unloading it will reduce its diameter due to elastic recovery up to a point of separation from the metal ring.

Sound polymer-metal coins are produced under deformation "mode II", which requires the clearance j between the polymer center and the metal ring to be within the range $j_{cr} < j < j_{max}$, where j_{cr} is the critical clearance below which the polymer center will buckle under uniform radial edge compression. In mode II, the contact pressure p between the two parts after unloading is appropriate and the resulting interference i is in the region of the process curve placed below the onset of plastic instability. The second- and third-coin samples included in Fig. 4.11 are examples of sound polymer-metal coins with interference-fit joints.

An unacceptable concave shape is triggered when the clearance j between the polymer center and the metal ring is smaller than the critical clearance j_{cr} due to excessive interference

i. This deformation mode is designated as "mode III" and corresponds to the leftmost coin sample in Fig. 4.11.

From a manufacturing point of view the optimum design conditions requires a clearance j between the metal ring and the collar that corresponds to the critical value of interference i above which buckling will occur. This will ensure the maximum separation force between the polymer center and the metal ring. Destructive tests performed under these conditions and aimed at pushing the polymer center out of the metal ring provided a force of approximately 0.4 kN, which is adequate for the fabrication of collection coins.

2.3 Resistance heated interference joining of micro fork and wire

This section presents an industrial example of micro joining based on [34]. The industrial case refers to collaboration with a German company in the electronics industry. The application is micro fork-to-wire connection shown in Fig. 4.12 before joining. The wire (1) is pure copper of diameter Ø 0.73 mm coated by a 5 μm thick polyimide plastic (2). It is joined to a copper alloy fork (3) between two tungsten electrodes (4) and (5). The joint is formed by closing the fork legs around the wire by an applied force through the tungsten electrodes, which creates a force-fit joint. An electric current is simultaneously applied for two reasons. The resistance heating facilitates the closing of the fork around the wire due to softening of the fork material. At the same time, the induced temperature melts the polymer coating locally on the wire to create electrical connection between the wire and the fork, which is required for the given application while the polymer keeps the remaining wire isolated.

There is no fusion weld because there is no melting of the metals, only local melting of the coating. The joining is therefore a mechanical joint facilitated by resistance heating. Numerical simulation, based on the principles described in Ref. [34], is applied to analyze the micro joining process. Two symmetry planes are utilized to reduce the finite element model, such that the finite element mesh in Fig. 4.13A represents the overall geometry. The process conditions shown in Fig. 4.13B are applied in the simulation. The force is kept constant at 120 N during the first current pulse, which has an up-slope time of 80 ms reaching 0.75 kA for additionally 80 ms. The force is raised to 150 N before the second current pulse, which is applied as a constant current of 1.2 kA during 50 ms.

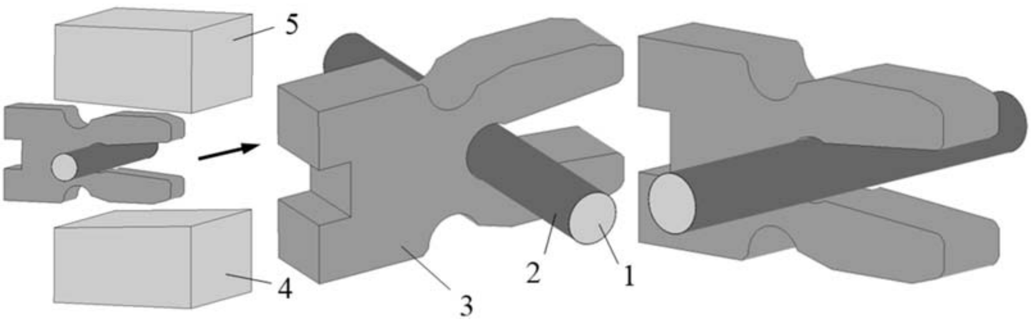

FIG. 4.12 Initial configuration of micro joining process of copper wire (1) coated by polyimide plastic (2) to a copper alloy fork (3) between two tungsten electrodes (4) and (5).

The effect of the two current pulses is shown by simulation results in Fig. 4.14. Fig. 4.14A shows the moment where the tungsten electrodes just touch the legs of the fork, corresponding to time 0 in Fig. 4.13B. After 80 ms, the applied force has been kept constant for 30 ms and the first current pulse is applied. At this stage (Fig. 4.14B) the deformation of the fork is

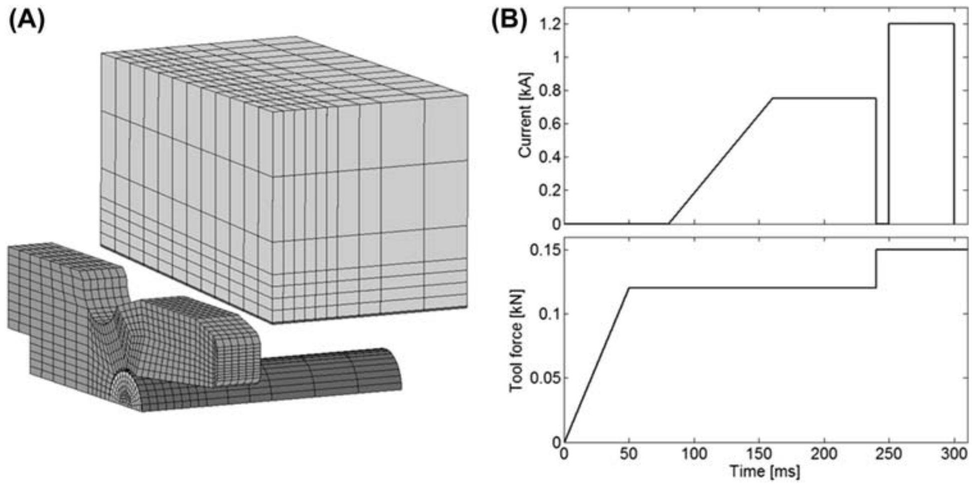

FIG. 4.13 Simulation of micro joining of fork to wire represented by (A) initial mesh utilizing two symmetry planes and (B) the applied electric current and electrode force as function of process time.

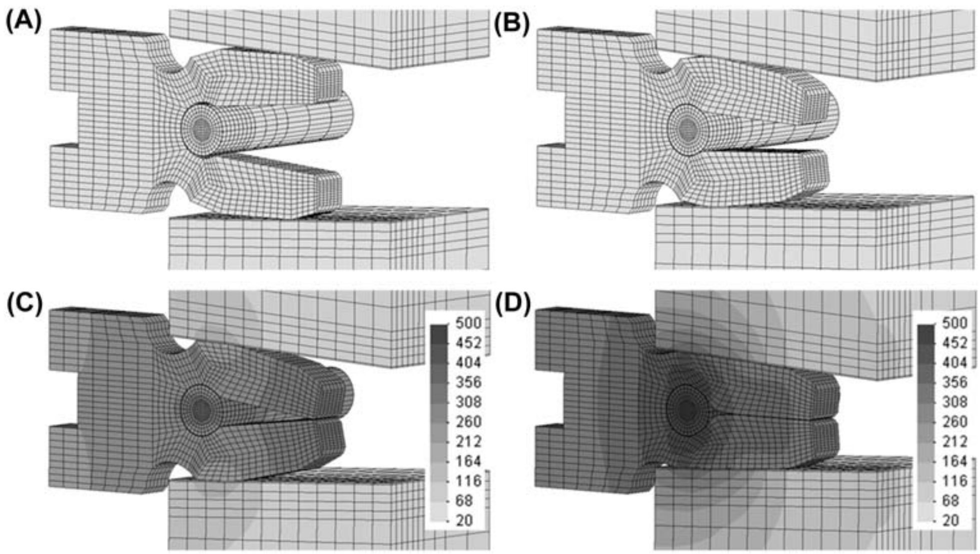

FIG. 4.14 Numerically simulated temperature at (A) the start of the joining process, where the electrodes just touch the fork, (B) the onset of the first current pulse after 80 ms, (C) the end of first current pulse at time 250 ms with maximum temperature 334°C, and (D) after completing the joining process including the two current pulses at time 300 ms with maximum temperature 507°C.

enough to close the initial gap toward the wire such that a sound contact is established before applying the electric current. At the end of the first current pulse, the tips of the fork legs are closed (Fig. 4.14C). This deformation happens under the same applied force due to softening of the material. The temperature field after the first current pulse is shown in Fig. 4.14C with a maximum reached temperature of 334°C. In order to perform the final closing of the fork, the second pulse is applied under increased electrode force. This results in the final geometry shown in Fig. 4.14D. The figure also shows the temperature field with a maximum reached temperature of 507°C, which is sufficient to melt the polymer coating to create electrical contact between the fork and the wire of importance to the final component.

The final geometry is compared to the real component in Fig. 4.15. The overall deformation is compared in the left figures, showing that both the simulation and the real joint result in closing of the fork to a degree where the fork legs touch each other along most of their length. A detailed view of the region near the wire is shown in the right figures, where it is seen that the fork is closed around the wire with almost no deformation of the wire, which has part of

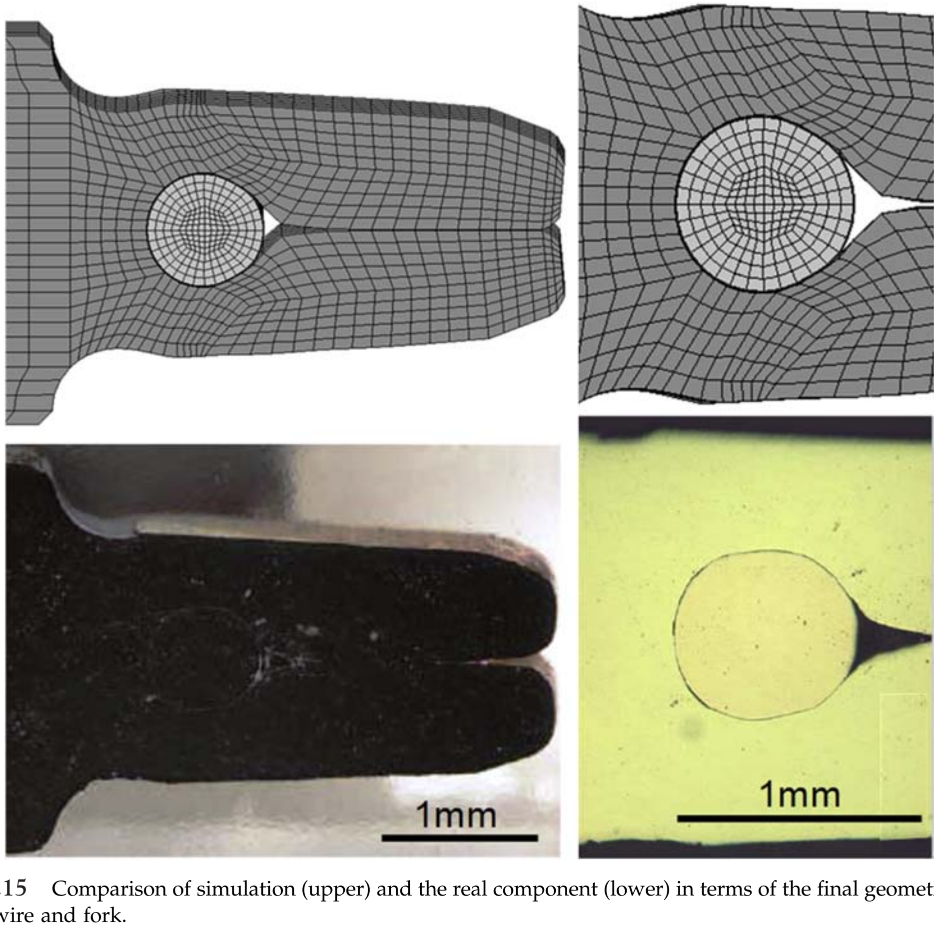

FIG. 4.15 Comparison of simulation (upper) and the real component (lower) in terms of the final geometry of the joined wire and fork.

its stiffness from the wire outside the contact area to the fork. The right figures also show that the amount of simulated closing of the fork near the wire agrees with the real micro fork-to-wire connection.

3. Joining by solid-phase welding

3.1 Cold pressure welding of Al-Steel slide bearing

Roll bonding of two metal sheets with similar flow stress may be carried out by conventional rolling with two equal sized rolls running with the same speed. Bonding is obtained by uniform deformation of the two sheets leading to uniform breakup of the brittle cover layer. When two dissimilar metals with rather large difference in flow stress are to be roll bonded the deformation pattern and the mechanisms governing bonding is more complex due to inhomogeneous deformation and superimposed sliding between the two sheets. Due to this a number of variants of the roll bonding process have been developed like roll bonding in a 3-high mill with a large roll in contact with the harder metal and a much smaller roll in contact with the softer metal, Fig. 4.16A [35]. The smaller roll is supported by a larger one, and the result of this asymmetric rolling in a 3-high mill is, that the softer metal is smeared out over the harder metal with little deformation of the latter. This process has been developed for roll bonding of AlSn-alloys to mild C-steel used for automotive slide bearings.

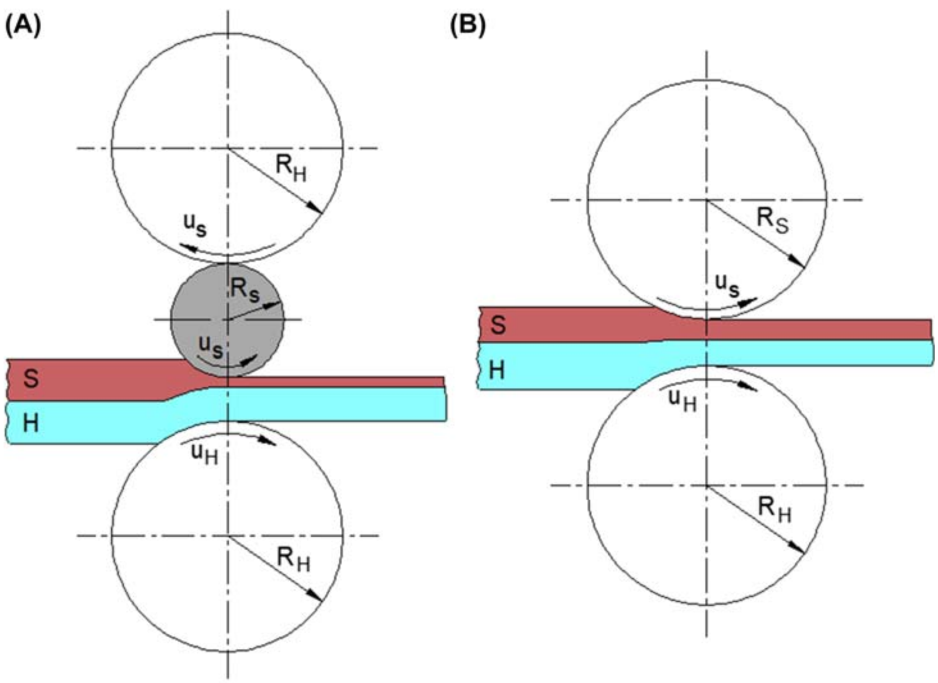

FIG. 4.16 Schematic outline of (A) asymmetric roll bonding, (B) cross shear roll bonding [35].

The development within slide bearings, however, has tended toward application of harder Al-alloys such as AlZn instead of AlSn, so when the same asymmetrical roll bonding technique is adopted this implies more uniform deformation and poorer bond strength. In collaboration with a Brazilian company [35] have studied the cross shear rolling principle as an alternative joining technique, see Fig. 4.16B. In this process, the harder metal contacts the faster of the two equal sized rolls running with different speed of rotation.

The resulting difference in peripheral speed of the two work rolls in cross shear rolling causes a change of the friction stress distribution compared to conventional rolling, see Fig. 4.17. In conventional rolling, Fig. 4.17A, the deformation zone is divided into two zones, an entry zone, where the workpiece is running slower than the roll surface and an exit zone where it runs faster. Friction on the upper and lower roll is thus directed toward the intermediate neutral points, which are positioned on the same vertical line. In cross shear rolling, with the lower roll running faster than the upper one, Fig. 4.17B, the neutral point on the lower roll moves toward the exit and on the upper one toward the entry creating thereby an intermediate "cross shear" zone, where friction on the two rolls has opposite directions. The opposing friction stresses on upper and lower roll in this zone promotes homogeneous deformation.

Cross shear rolling facility was established on DTU's 2-high STANAT rolling mill with a load capacity of 500 kN by combining the two shafts driving the Ø 131.8 mm rolls with new sets of bevel gears resulting in three different speed ratios: $i = 1.09$; 1.21 and 1.30. Experiments were done with these three speed ratios and compared with conventional roll bonding with speed ratio $i = 1.00$. The bond strengths were measured in shear tests as well as peel tests. Fig. 4.18A shows the resulting bond shear strength versus the total thickness reduction running with the four different speed ratios: $i = 1.00$, 1.09, 1.21 and 1.30. It is noticed that the strength for $i = 1.09$ exceeds those of the other speed ratios in the major part of the reduction range. Fig. 4.18B shows the peel strength obtained for the speed ratios $i = 1.00$, 1.09 and 1.21, where it is evident that the best results are obtained with $i = 1.09$.

3.2 Cold pressure welding of a valve floater

Sealing of containers where heating is prohibited, e.g. containers for electronic devices and nuclear fuel elements, may be encapsulated by cold pressure welding using an ironing

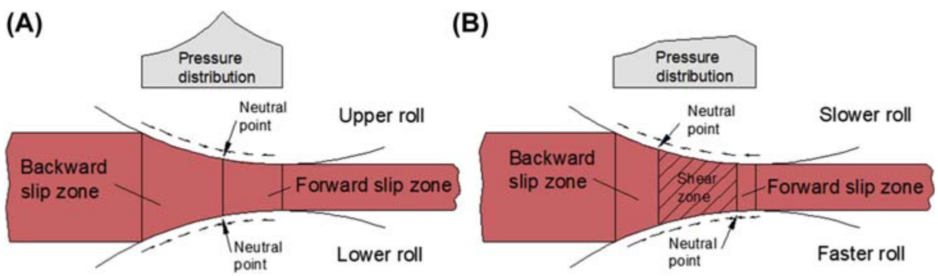

FIG. 4.17 Direction of friction stresses and distribution of normal stress in: (A) Conventional rolling, (B) Cross shear rolling [35].

operation [36]. Fig. 4.19 shows the principle. A deep drawn (red) can provided with a conical collar is joined to a (blue) end cap with a matching, conical collar after preparing the two mating, conical surfaces by degreasing and scratch brushing. The two components are cold pressure welded by ironing through a die with slightly larger bore than the outer diameter of the can, which is pushed through the die by the light blue, stepped punch thereby reducing the joint thickness of the two collars sufficient to obtain a vacuum leak tight joint.

In collaboration with a Danish company producing equipment for gas technology, the same technique has been developed by the authors at DTU for manufacturing of Ø 28 mm

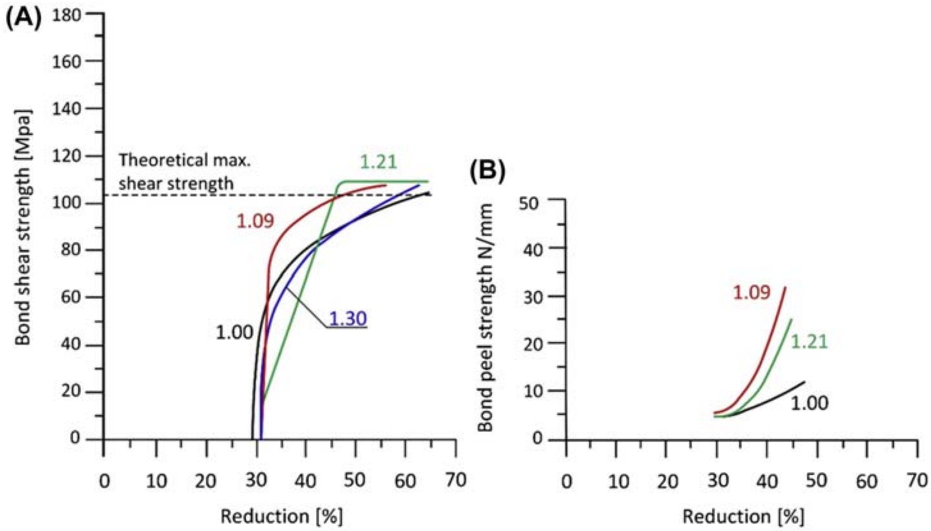

FIG. 4.18 (A) Bond shear strength as a function of reduction and speed ratio, (B) Bond peel strength as a function of reduction and speed ratio [35].

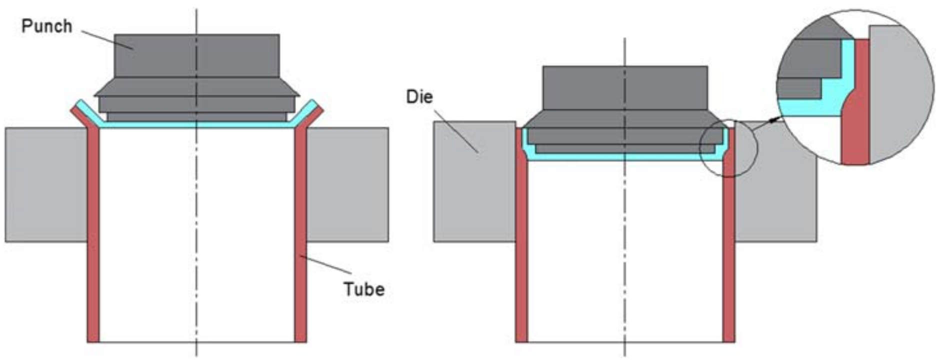

FIG. 4.19 Schematic outline of encapsulation by ironing. *Adapted from K.-I. Mori, N. Bay, L. Fratini, F. Micari, A.E. Tekkaya. Joining by plastic deformation. CIRP Annals — Manufacturing Technology 62 (2) (2013). https://doi.org/10.1016/j.cirp.2013.05.004.*

FIG. 4.20 Left: Deep drawn housing and cold forged lid. Right: Cold pressure welded floater.

floaters for liquid gas valves. Fig. 4.20 shows the two components and the assembled floater. The lid provided with two rectangular pins connecting the floater to the valve is made by cold forging.

4. Joining by combined fusion and solid-state welding

4.1 Resistance welding of a thermostat valve

Fig. 4.21 shows a thermostat valve together with selected process steps manufactured by a Danish company. An Ø 8 mm, thin-walled (0.14 mm) bellow tube of tin-bronze (CuSn6) with a conical collar (2) is resistance projection welded to a 1 mm thick ring (with inner diameter Ø 8.3 mm and outer diameter Ø 29 mm) of mild C-steel (3) between electrodes (1) and (4).

The projection is natural, included in the joint design as the upper, inner edge of the steel ring. After this joining operation the bellow is hydro-mechanically formed and subsequently the joined bellow and steel flange is projection welded to a deep drawn housing of steel in a similar joint design, where the housing is provided with a conical collar contacting the lower, outer edge of the steel ring acting as the projection. Defective components, which were not helium leak tight, appeared, especially when the electrodes were worn. In collaboration with DTU a study was carried out to explain and predict harmful metallurgical phase transformations caused by electrode wear, which would influence the weld quality, [37].

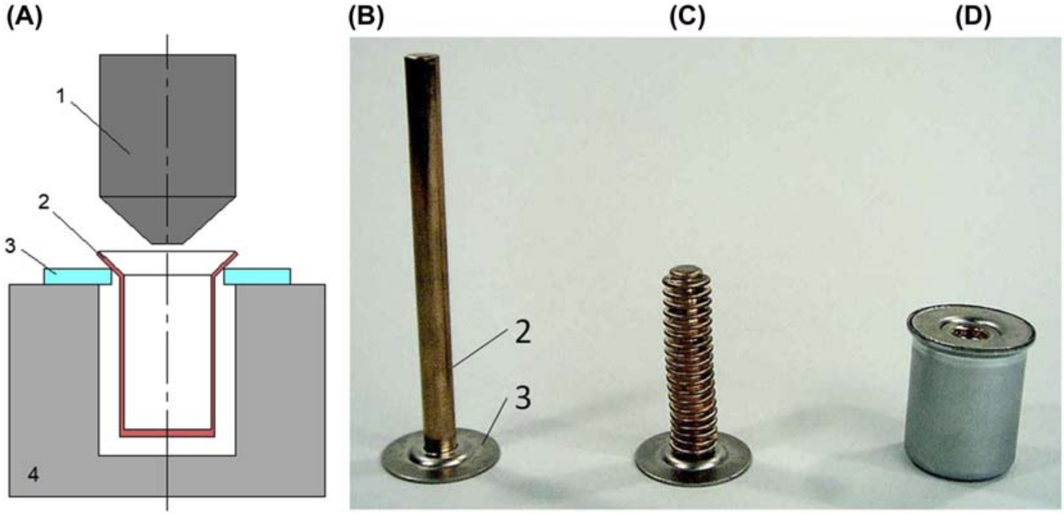

FIG. 4.21 Selected process steps in manufacturing of a thermostat valve. (A) Resistance projection welding of tin-bronze bellow tube to steel ring. (B) Joined bellow tube and steel ring. (C) Formed bellow. (D) Bellow mounted in steel housing [37].

To facilitate the joining of steel to tin-bronze, the ring is coated with a 2–6 μm thick layer of electro-less deposited Ni-P alloy (8–12 wt% P). Metallographic studies of the microstructure in the weld zone of joints made with new and worn electrodes showed a distinct difference; see Fig. 4.22A and C.

The low melting point (870°C) of the coating has ensured that this is melted by resistance heating of the steel ring and subsequently forced out of the joint interface after which a solid-state bond is established between the steel and the tin-bronze. After welding with a new electrode, an investigation of the microstructure (Fig. 4.22A) shows that the steel adjacent to the weld interface has a coarse, ferritic grain structure, which is observed as a thin, bright zone. Apparently, the steel in this zone has been heated close to but not over 900°C, leading to grain growth in the ferrite. Below this zone the microstructure appears to be dark indicating that the steel at the peak temperature of the process has been heated beyond 900°C causing a phase transformation to fine-grained austenite. During the subsequent rapid cooling this austenite transformed to fine-grained ferrite, which appears dark on the micrograph.

The microstructure of Fig. 4.22A indicates that the highest temperature during the welding process was reached inside the steel at a certain distance from the weld interface, and not at the interface itself. This is due to the large difference in electric resistivity of the two workpiece materials, steel having a much higher resistivity than tin-bronze implying large heat generation in the steel. No phase transformations are observed in the tin-bronze. The corresponding numerical simulation in Fig. 4.22B confirms this, where the white isothermal line corresponds to 900°C peak temperature. This isothermal line is seen to leave a small gap to the interface confirming the above hypothesis.

Welding with a heavily worn electrode results in a microstructure (Fig. 4.22C), which as regards the steel contains the same microstructural elements as those seen in Fig. 4.22A.

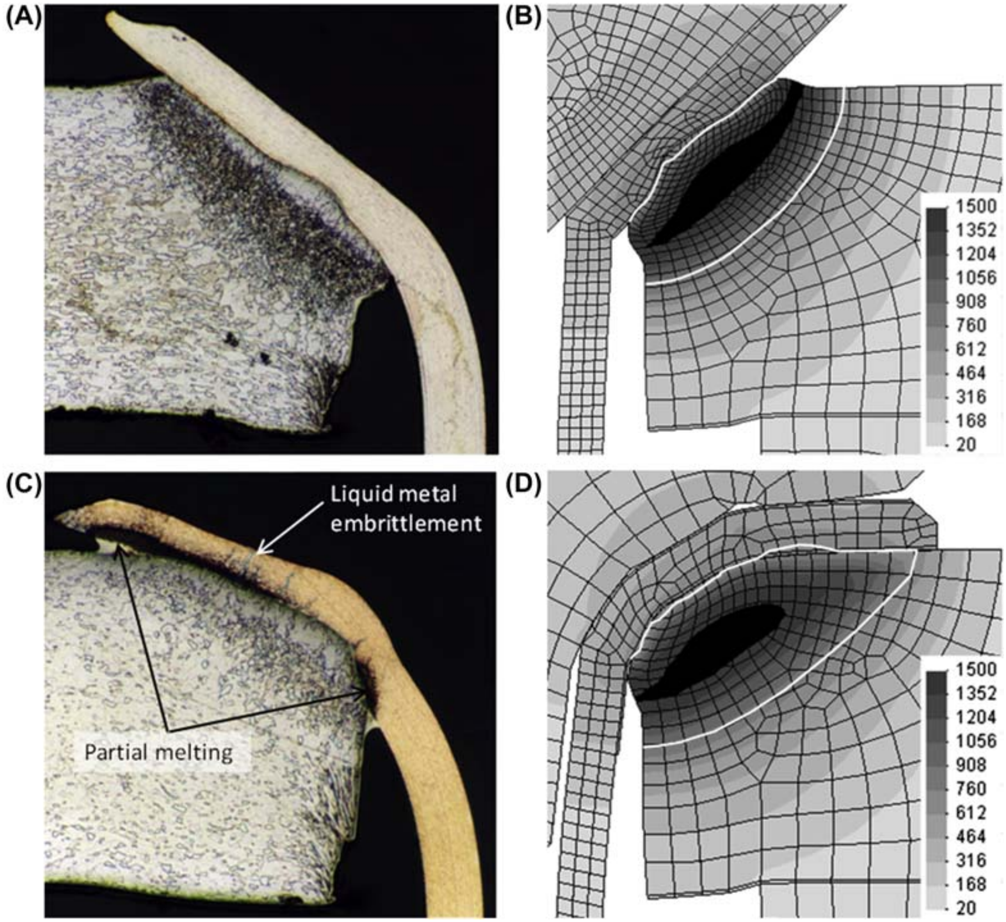

FIG. 4.22 (A) Cross section of welded bellow tube to steel ring. (A) Weld performed with a new electrode. (B) Simulation of temperature distribution with new electrode. (C) Weld performed with worn electrode. (D) Simulation with worn electrode [34,37].

Due to the poor contact between the upper electrode and the tin-bronze tube in the first phase of welding, the tube experiences higher temperatures than with a new electrode. The dark areas in the tin-bronze represent areas of partial melting and hot cracking. This occurs for the bellow tube material when the temperature is above approximately 900°C, cf. the Cu-Sn phase diagram provided in Fig. 4.23, where the actual tin-bronze alloy (CuSn6) is marked by the dashed line.

The simulated weld by the worn electrode (Fig. 4.22D) also reveals peak temperatures above 900 °C in the tin-bronze by the white isothermal line. The real weld is seen to have experienced heavier partial melting than the simulation shows. This can stem from asymmetric wear of the electrode, which will result in further localization of the heat along the circumference, whereas the axisymmetric simulation distributes the heat evenly along the circumference.

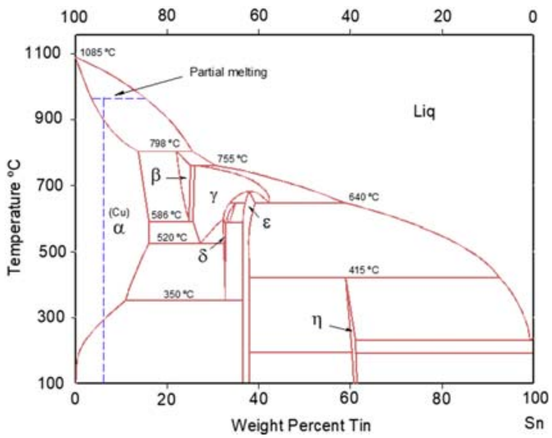

FIG. 4.23 Phase diagram of copper (Cu) and tin (Sn) with the actual tin-bronze alloy marked by the dashed line at 6 weight-% tin. The specific alloy experiences partial melting in the region above approximately 900°C. *Adapted from ASM International. Alloy phase diagrams. in: ASM Handbook, vol. 3, 1992. https://doi.org/10.31399/asm.hb.v03.9781627081634.*

Besides the partial melting, liquid metal embrittlement in the tin-bronze is noticed in Fig. 4.22C. This is caused by penetration of melted Ni-P coating into the grain boundaries of the tin-bronze. These phase transformations are explained by the elevated temperatures reached when welding with a worn electrode.

4.2 Resistance spot welding of three sheets

Resistance spot welding is a key technology in automotive assembly production, and it is by number the most used welding process. According to Ref. [39] more than 200 sheet metal parts are spot welded together resulting in 4000−7000 spot welds of two and three sheet combinations in a modern car. Mostly steel sheets are spot welded, and the development of new steel grades such as advanced high strength steels (AHSS) and ultrahigh strength steels (UHSS) presents challenges to the resistance spot welding process when combined with other materials. These new steel types are often used in structural parts of the car and in safety parts that are designed to absorb the impact of a crash. These parts are typically joined to considerably thinner and softer low carbon steel sheets that act as the outer panels of the car. Joining of three sheets by spot welding is therefore common in automotive assembly and typically involves two thicker, high strength steels and one, thin mild steel as one of the outer sheets. This combination has attracted a lot of attention because of the difficulties in attaining a weld nugget at both interfaces as shown by Ref. [40] and discussed in this section.

A specific three-sheet combination is selected from Ref. [40] to be presented here. The lap joint is schematically shown in Fig. 4.24. It consists of a 1.2 mm TRIP 700 steel with 7 μm zinc coating on each side as the bottom sheet, a 0.8 mm HSLA 340 steel sheet as the middle sheet, and a 0.6 mm DC06 low carbon steel at the top sheet. With this combination, which is common in automotive industry, it is particularly difficult to achieve a weld nugget across both

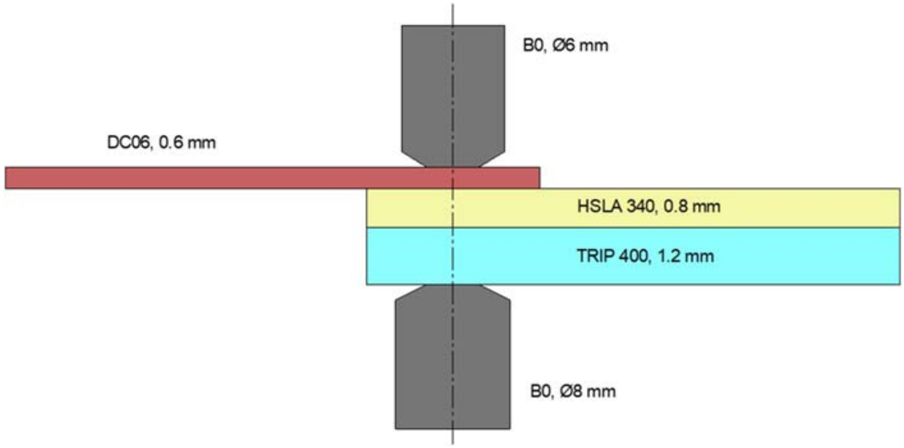

FIG. 4.24 Three-sheet combination to be spot welded.

interfaces. Furthermore, it shows a remarkably high tensile-shear strength and plug failure between the DC06 and the HSLA 340 even without a fusion weld.

The three sheets were spot welded between two ISO type B0 CuCrZr electrodes with tip diameters Ø6mm at the top (in contact with the DC06) and Ø8mm at the bottom (in contact with the TRIP 700). The difference in electrode tip diameters was chosen to increase the current density at the upper interface. Two levels of electrode force, 3 kN and 4 kN, were tested. The electric current was applied as an alternating current at 50 Hz and an approximate conduction angle of 75% over a constant welding time corresponding to 16 cycles.

Fig. 4.25 shows the resulting weld nugget diameters and tensile-shear strengths obtained as function of the applied welding current (RMS value). Fig. 4.25A shows that a good nugget size is obtained at the lower interface over a broad range of welding parameters, while the upper interface (between the thin DC06 and the HSLA 340) is more difficult to weld. With a welding force at 3 kN, the nugget did not develop into the upper sheet. At 4 kN, it is possible to get a welded upper interface, but in a narrower range of welding current as compared to the lower interface.

Another issue is the amount of nugget penetration into the upper sheet, which is often limited. The narrow process window for the upper interface has a number of causes: i) the electrical resistance is higher in the two lower sheets with corresponding higher heat generation, ii) the poorer contact between the two stiffer sheets at the bottom results in more heat generation at the lower interface, iii) the distance between the upper interface and the neighboring electrode is shorter than for the lower interface, which leads to more heat conduction away from the upper interface, and finally iv) splash will occur at the lower interface if the heat input is increased to penetrate the nugget into the upper sheet. The narrow process window has led to innovative solutions mentioned by Ref. [40].

Tensile-shear strength testing by pulling the upper sheet from the two lower sheets has revealed a proper strength; see Fig. 4.25B, for all the welding parameters included in Fig. 4.25. Moreover, all the tests shown in Fig. 4.25B resulted in plug failure. Fig. 4.26 shows an example of a plug failure obtained without nugget penetration across the upper interface.

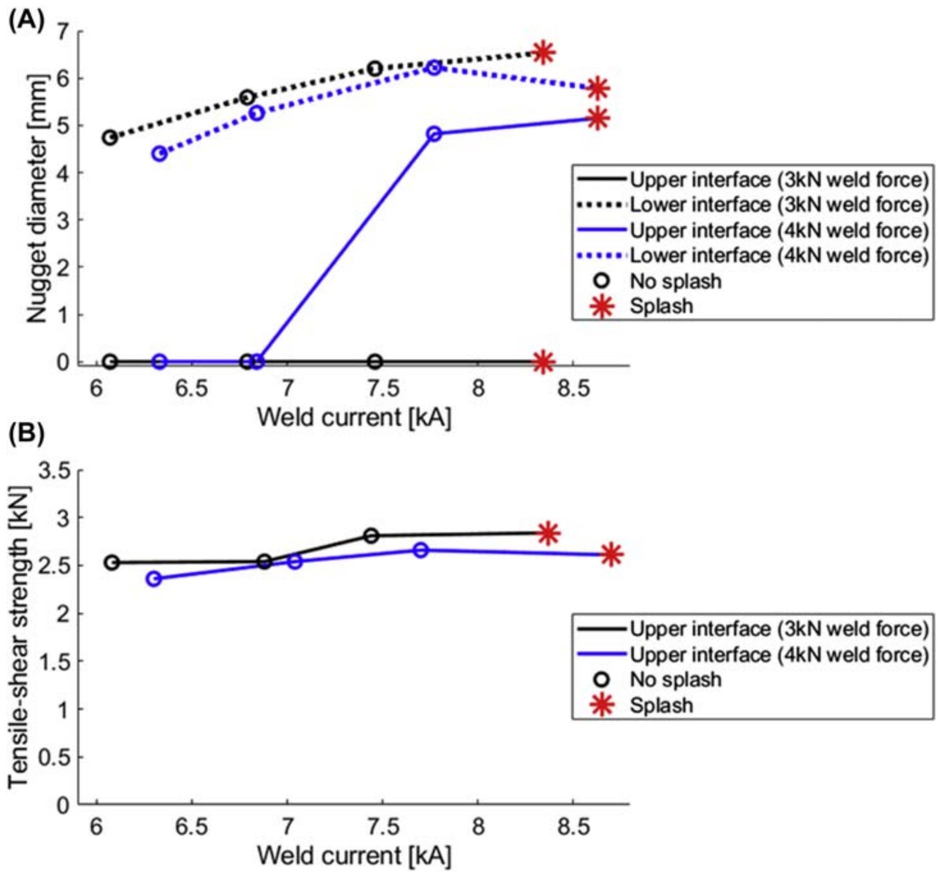

FIG. 4.25 Resulting (A) nugget diameters at the two interfaces and (B) tensile-shear strength as function of welding current at two levels of electrode force and constant welding time (16 cycles at 50 Hz).

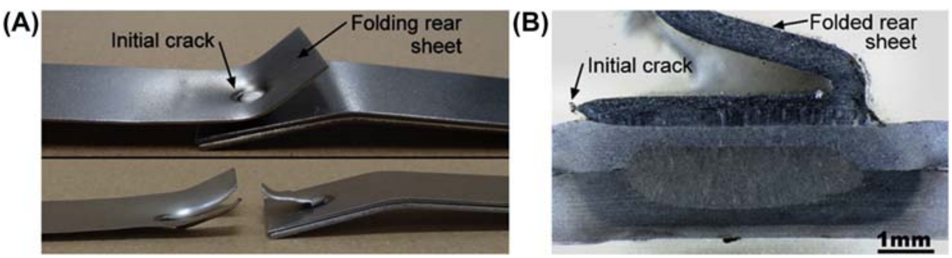

FIG. 4.26 Result of tensile shear testing showing (A) the initial crack and folding of the rear of the thinner sheet (upper) and full separation (lower), and (B) cross-section after full separation. Welding parameters are 6.3 kA welding current during 16 cycles at 50 Hz under an electrode force of 4 kN.

The bonding mechanism at this interface is a solid-state bond facilitated by the high normal pressure and the elevated temperature. The bonding mechanisms were studied further in Ref. [41], where an additional, secondary bonding mechanism was observed due to formation of new grains across the interface. Moghadam et al. [41] also shows high strength and plug failure in tensile-shear testing of spot welds without nugget penetration and note that these bonding mechanisms exist in the corona band around normal weld nuggets and therefore contribute to the overall strength of regular spot welds.

While tensile-shear testing indicates high quality of the spot welds relying on solid-state bonding, it is still necessary to test the welds in other loading conditions, e.g. by cross-tension testing and peel testing, and under cyclic loading by fatigue testing.

4.3 Joining of two perpendicular sheets by resistance projection welding

Resistance projection welding of two sheets perpendicular to each other is e.g. used in fabrication of housings and containers that are not required to be water or airtight and to the addition of perpendicular stiffeners to sheet panels. This section presents an industrial example from Ref. [34], which is based on an application by a Japanese company, see Fig. 4.27.

In order to facilitate joining of the two sheets perpendicular to each other by projection welding, one of the sheets is embossed as shown in Fig. 4.27A. When the other sheet is positioned as shown in Fig. 4.27B, the longitudinal embossments ensure current concentration between the two sheets during resistance projection welding, which is here done under constant weld force and DC current. The resulting joint is shown in Fig. 4.27C, and a close up of one of the projection welds is shown in Fig. 4.27D and a cross-section is shown in Fig. 4.27E. The two sheets are 0.8 mm thick high strength low alloy steel sheets (grade similar to HSLA 340). The welding parameters are 700 N weld force and 3.5 kA DC weld current applied during 30 ms.

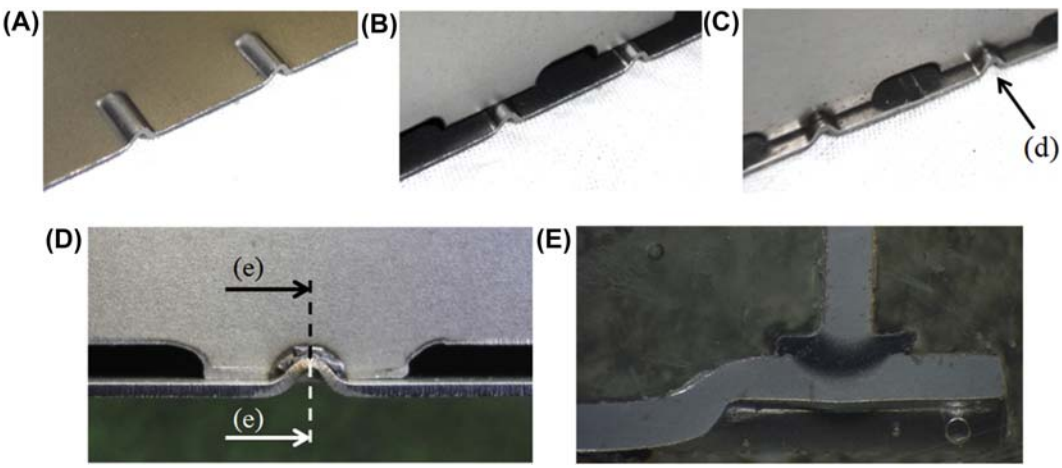

FIG. 4.27 Industrial example of projection welding of two sheets perpendicular to each other. (A) Sheet with embossed longitudinal projections. (B) Positioned perpendicular sheets before welding and (C) after welding. (D) Side view after welding (view indicated in (C)). (E) Cross-section as defined in (D).

Numerical simulation of the projection welding process is carried out to obtain knowledge on the temperature distributions and to optimize welding parameters. The simulation is based on the FEM program described in Ref. [34]. Fig. 4.28A shows the finite element discretization of one of the projection welds in the particular case. It utilizes a natural symmetry plane along the longitudinal projection (that is the cutting plane utilized to show the cross-section in Fig. 4.27E). An additional symmetry plane is assumed in the simulation to reduce the model size. It is introduced in the center of the vertical sheet in Fig. 4.27E, such that the final model utilizing both symmetry planes is the one shown in Fig. 4.28A. The round periphery of the lower sheet is only to make structured meshing of the round end of the projection easier. It does not influence the simulation due to the distance from the weld.

The second symmetry plane is justified as follows with reference to Fig. 4.27E. The differences on each side of the vertical sheet in terms of the electrical and thermal fields are considered negligible due to the short process time (weld time is 30 ms) and the distance to the end of the embossment on one side and to the end of the bottom sheet on the other side. As regards the mechanical aspects of the assumed symmetry plane, the geometry after welding (Fig. 4.27E) is symmetric around the vertical sheet. The longitudinal embossment does not bend toward the free end, and the free end can therefore be omitted from the simulation. The side including the rounded end of the embossment is included to prevent the embossment from flattening, and the mirroring of that does not affect the overall deformation.

The simulated weld is shown in Fig. 4.28B with its peak temperature distribution. In the interface of the two sheets, the material melts and squeezes out as in the real case (compare detail in Fig. 4.28B to the cross-section in Fig. 4.27E) while the upper sheet closes toward the bottom sheet (compare Fig. 4.28B to the side-view in Fig. 4.27D).

A detailed comparison of the real example (Fig. 4.27) and the simulated projection weld (Fig. 4.28) is presented in Fig. 4.29 in the cross-section similar to Fig. 4.27E. The comparison covers the final geometry as well as the peak temperature field. As regards the geometry, the main difference is the shape of the metal that is squeezed out between the two sheets in a molten or mushy state. The exact shape might be of less importance compared to the volume squeezed out and the formed contact area during welding as it relates to the heat generation. In the specific example, more elements would be required in the volume that is squeezed out if the details of the squeeze out are of importance.

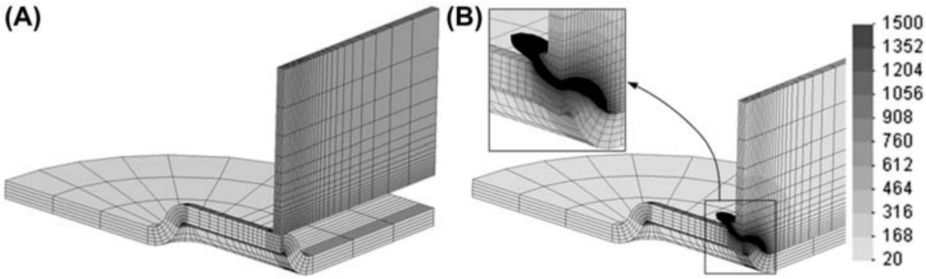

FIG. 4.28 Projection welding of two perpendicular sheets. (A) Initial finite element mesh and (B) predicted peak temperature field (degrees Celsius) at the end of welding showing molten volume squeezed out between the two sheets.

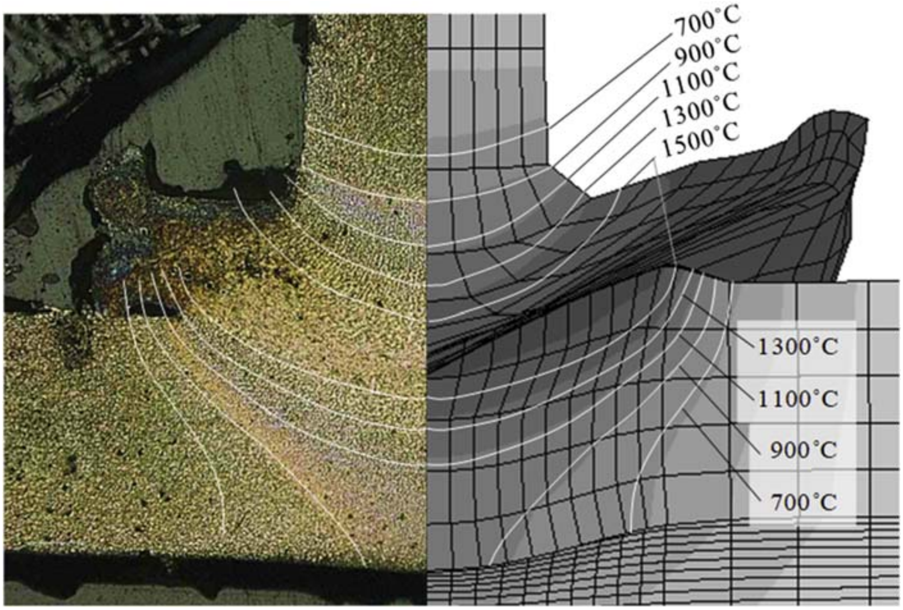

FIG. 4.29 Comparison of cross-section of the real component and simulated peak temperature distribution in the cross-section view similar to Fig. 4.27E. The simulated peak temperature field is shown on a 20–2000°C scale with selected isothermal lines. These lines are mirrored onto the actual cross-section.

The heat development and the heat balance were of more importance when doing the presented simulation in collaboration with the company. The simulated peak temperature field and the resulting microstructure of the real case are compared. The selected isothermal lines in the simulated temperature field are mirrored onto the cross-section of the real case, revealing that the temperature gradients are simulated correctly as the isothermal lines of the simulated temperature field match the shape of the borderlines between the different microstructures.

4.4 Joining of a new lightweight sandwich material by spot welding

This section presents resistance spot welding of three layers involving a lightweight sandwich material with a polymer core. The sandwich material is LITECOR® introduced by Ref. [42] for weight saving purposes. The existence of a polymer layer adds obvious challenges to the resistance spot welding process, and is here only feasible by the aid of a shunt tool as utilized in Ref. [43], which this section is based upon. Fig. 4.30 shows the combination that is being welding. The middle sheet is LITECOR® consisting of a 0.4 mm PE/PA polymer core and two 0.2 mm BH220 steel skin layers. The two outer sheets are 1.5 mm DC06 steel. The electrodes are ISO type B0 with 6 mm tip diameter. A copper shunt tool is introduced to bypass the polymer layer and initiate the welding process. Fig. 4.31 shows the experimental setup.

The role of the shunt tool is schematically shown in Fig. 4.32. At the beginning of the process, the current cannot pass through the stack-up because of the polymer layer in the

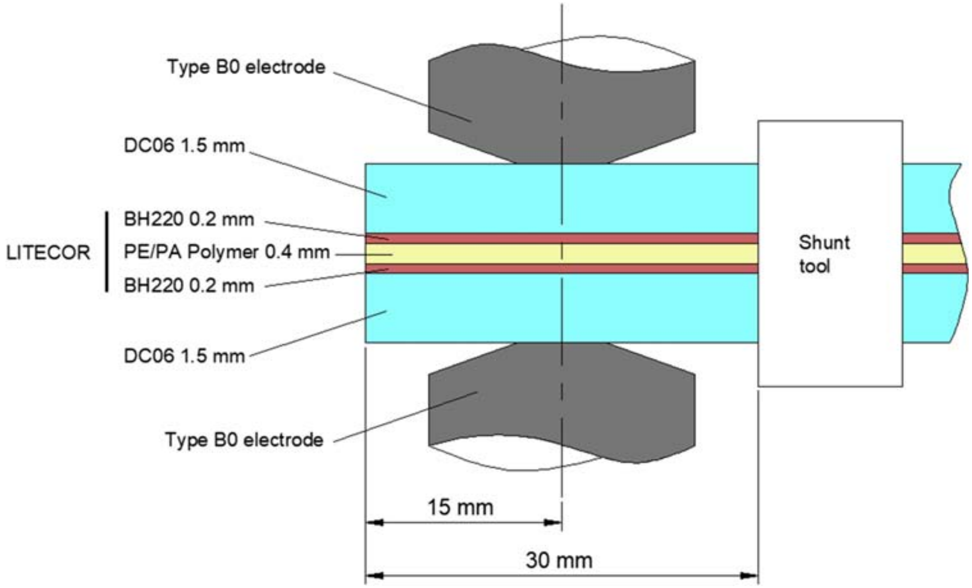

FIG. 4.30 Weld configuration of three sheets, of which the middle sheet is a lightweight sandwich material with a polymer core.

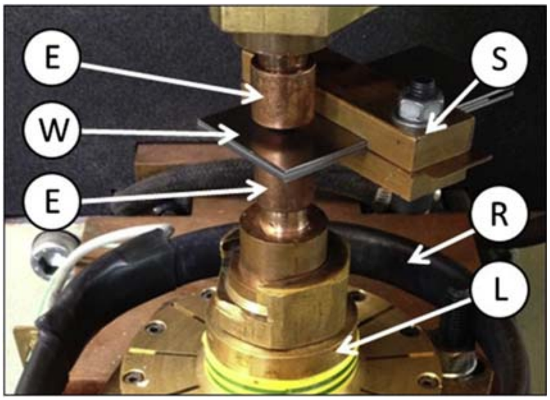

FIG. 4.31 Experimental setup showing the weld stack-up (W) between the electrodes (E). The shunt tool is marked (S), and process parameters are measured by a Rogowski coil (R) and a load cell (L).

sandwich material. The shunt tool is therefore needed to allow a current flowing between then electrodes as illustrated in Fig. 4.32A. Heat is generated due to Joule heating, especially in the DC06 and the skin layers of the sandwich near the electrodes due to high current density. This heat results in softening of the polymer layer, which is then squeezed out to allow metal-metal contact between the skin layers as shown in Fig. 4.32B. When the metal-metal contact appears in the sandwich, the current starts flowing through the weld spot, but since the shunt tool is still mounted, the current will also partly flow through the shunt tool.

Numerical simulation of the spot welding process involving the sandwich material has been performed with the software SORPAS® 3D; see Ref. [34] for further explanations of the numerical methods. The simulated current density is shown in Fig. 4.33. The result in Fig. 4.33A represents a situation before metal-metal contact, and hence all the current flows through the shunt tool. It is seen in the simulation that the current density is high around the

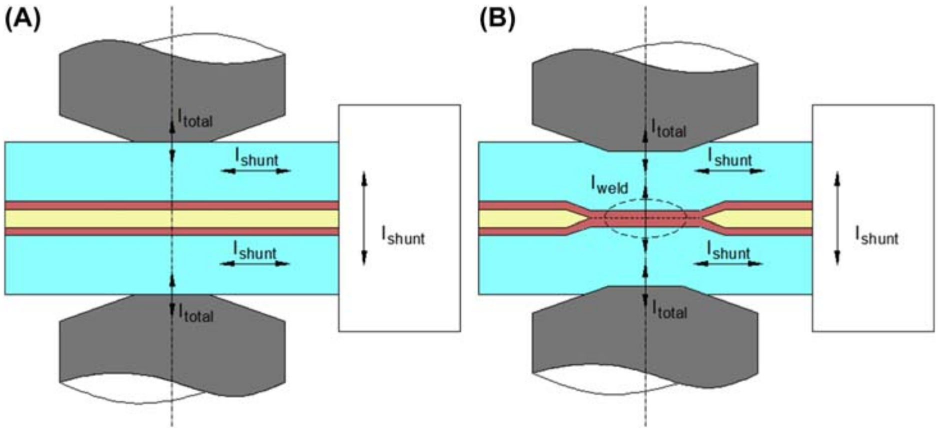

FIG. 4.32 Schematic current flow (A) in the beginning of the process and (B) after metal-metal contact in the sandwich layer.

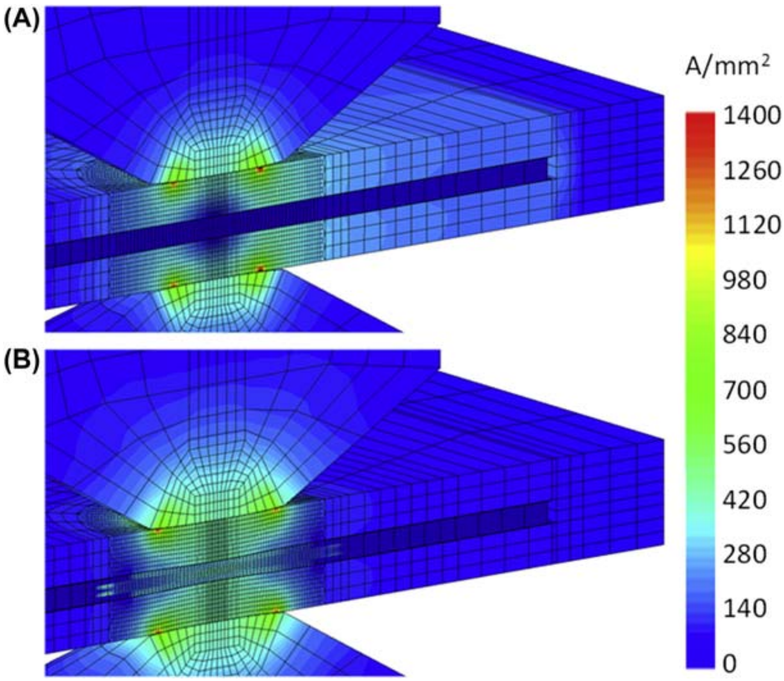

FIG. 4.33 Numerically simulated current density during (A) the beginning of the process corresponding to Fig. 4.32A and (B) after the current can pass through the weld spot corresponding to Fig. 4.32B.

electrodes, where the heat is needed for softening the polymer to obtain metal-metal contact, which has been obtained at the situation shown in Fig. 4.33B. Here, most of the current flows through the weld spot, while only a minor part of the current still flows through the shunt tool.

The actual welding took place in an AC resistance spot welding machine with an estimated conduction angle of 75 %. It was found that a constant electrode force of 3.6 kN was an appropriate balance between having enough force to squeeze out the polymer as explained above and to avoid a too high force resulting in excessive electrode indentation and bending of the sheets. The electric current was delivered in two pulses, where the first pulse was adjusted to obtain a stable metal-metal contact in the sandwich layer. The second pulse was used for the actual spot welding and analyzed by creating a weldability lobe.

The first electrical pulse consisted of 14 cycles. A typical current level would be 6.7 kA RMS during the first 12 cycles, while it could raise to 8.9 kA RMS in the last two cycles. The jump in current would mean that the metal-metal contact occurred after the first 12 cycles. The increase in current is due to the machine dependence on the electrical resistance in the secondary circuit. See Ref. [43] for more details.

The second pulse was varied in terms of welding time and current with the electrode force being constant at 3.6 kN. Fig. 4.34 shows the experimentally obtained weldability lobe considering the second pulse. Experiments and numerical simulations were compared on a weld growth curve level in Ref. [43]. The weldability lobe in Fig. 4.34 reveals a process window of more than 2 kA in width over the tested range of welding time from 8 cycles to 20 cycles.

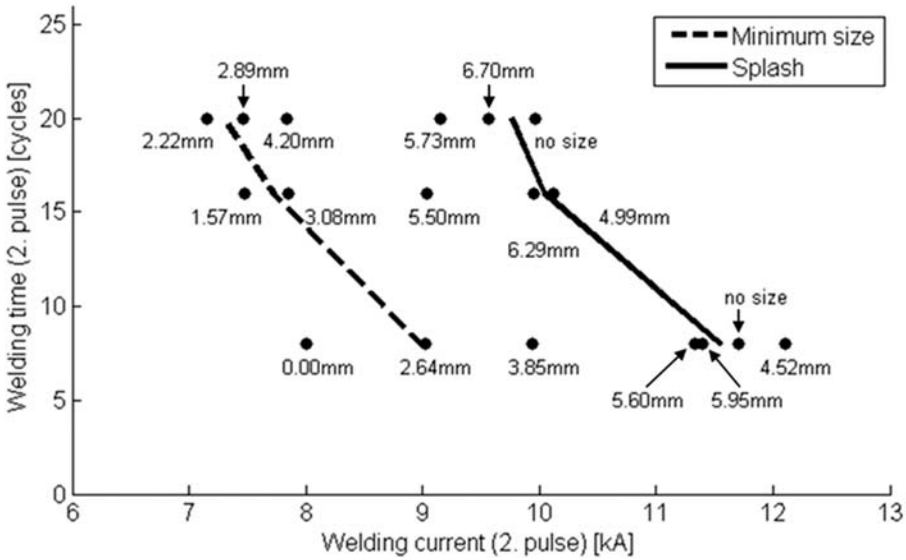

FIG. 4.34 Weldability lobe obtained by variation of the welding time and current (in RMS) of the second pulse while keeping the first pulse constant.

5. Conclusions

The increasing focus on weight saving in the automotive, rail and aerospace industries resulting in the introduction of new materials, e.g. AHSS, Al-, Mg- and Ti-alloys as well as polymers and sandwich sheets, requires new assembly methods replacing traditional welding techniques. This has resulted in renewal of mechanical assembly methods such as clinching and self-pierce riveting and new applications of cold pressure welding and friction welding as well as development of friction stir welding, friction stir spot welding, explosive welding and magnetic pulse welding. After a short introductory review of the trend in new assembly methods, the paper presents examples of the authors' own developments of industrial joining methods, including:

- mechanical joining of tube to sheet by controlled plastic instability applied for fabrication of the metallic structure of a train passenger seat
- coining with interference fit joining of polymer and metal for collection coins
- resistance heated interference joining of micro components for electronics
- cold roll bonding of AlZn to mild steel for automotive slide bearings
- cold pressure welding of floater for liquid gas valve
- resistance spot welding of three sheets
- resistance projection welding of tin-bronze to mild steel for a thermostat valve
- resistance projection welding of perpendicular sheets
- spot welding of mild steel to lightweight sandwich material

Acknowledgments

The authors would like to acknowledge the support provided by Fundação para a Ciência e a Tecnologia of Portugal and IDMEC under LAETA-UIDB/50022/2020.

References

[1] H. Tang, Comprehensive considerations on material selection for lightweighting vehicle bodies based on material costs and assembly joining technologies, International Journal of Manufacturing, Materials, and Mechanical Engineering 7 (4) (2017) 1–14, https://doi.org/10.4018/ijmmme.2017100101.

[2] K.-I. Mori, N. Bay, L. Fratini, F. Micari, A.E. Tekkaya, Joining by plastic deformation, CIRP Annals – Manufacturing Technology 62 (2) (2013), https://doi.org/10.1016/j.cirp.2013.05.004.

[3] P. Groche, S. Wohletz, M. Brenneis, C. Pabst, F. Resch, Joining by forming – a review on joint mechanisms, applications and future trends, Journal of Materials Processing Technology 214 (10) (2014) 1972–1994, https://doi.org/10.1016/j.jmatprotec.2013.12.022.

[4] V. Psyk, D. Risch, B.L. Kinsey, A.E. Tekkaya, M. Kleiner, Electromagnetic forming – a review, Journal of Materials Processing Technology 211 (5) (2011) 787–829, https://doi.org/10.1016/j.jmatprotec.2010.12.012.

[5] M.M. Eshtayeh, M. Hrairi, A.K.M. Mohiuddin, Clinching process for joining dissimilar materials: state of the art, International Journal of Advanced Manufacturing Technology 82 (1–4) (2016) 179–195, https://doi.org/10.1007/s00170-015-7363-0.

[6] K. Mori, Y. Abe, A review on mechanical joining of aluminium and high strength steel sheets by plastic deformation, International Journal of Lightweight Materials and Manufacture 1 (1) (2018) 1–11, https://doi.org/10.1016/j.ijlmm.2018.02.002.

[7] H.Y. Yu, J.i. Li, Z. He, Formability assessment of plastic joining by compression instability for thin-walled tubes, International Journal of Advanced Manufacturing Technology 97 (9−12) (2018) 3423−3430, https://doi.org/10.1007/s00170-018-2128-1.
[8] B. Viehweger, A. Sviridov, P. Grützner, B.-A. Behrens, A. Bouguecha, A. Almohallami, Ermittlung von Verfahrensgrenzen für das Fügen durch Knickbauchen anhand des Werkstoffes E235+N, Materialwissenschaft und Werkstofftechnik 46 (8) (2015) 804−812, https://doi.org/10.1002/mawe.201500383.
[9] A. Sviridov, M. Rusch, A. Almohallami, C. Bonk, A. Bouguecha, M. Bambach, B.A. Behrens, Creating load-adapted mechanical joints between tubes and sheets by controlling the material flow under plastically unstable tube upsetting, Procedia Engineering 207 (September) (2017) 968−973, https://doi.org/10.1016/j.proeng.2017.10.860.
[10] W. Homberg, M. Marré, C. Beerwald, M. Kleiner, Joining by forming of lightweight frame structures, Advanced Materials Research 10 (2009) 89−100, https://doi.org/10.4028/www.scientific.net/amr.10.89.
[11] N. Bay, Cold Welding. ASM Handbook, vol. 6A, 1991, pp. 711−716.
[12] N. Bay, Cold welding: part 2 process variants and applications, Metal Construction 18 (8) (1986) 486−490.
[13] M.B. Uday, M.N. Ahmad Fauzi, H. Zuhailawati, A.B. Ismail, Advances in friction welding process: a review, Science and Technology of Welding and Joining 15 (7) (2010) 534−558, https://doi.org/10.1179/136217110X12785889550064.
[14] T. Khaled, An Outsider Looks at Friction Stir Welding. Report, Federal Aviation Administration, CA, USA, July 2005. ANM-112N-05-06.
[15] M. Fujimoto, M. Inuzuka, S. Koga, Y. Seta, Development of friction spot joining, Welding in the World 49 (3−4) (2005) 18−21, https://doi.org/10.1007/BF03266470.
[16] B.-Y. Kang, Review of magnetic pulse welding, Journal of Welding and Joining 33 (1) (2015) 7−13.
[17] D. Meuken, E.P. Carton, Explosive welding and cladding, AIP Conference Proceedings 706 (2004) 1110−1113, https://doi.org/10.1063/1.1780433.
[18] S. Liu, J. Banker, C. Prothe, Explosion welding.pdf, in: ASM Handbook, vol. 6A, 2011, pp. 690−700.
[19] J. Devine, Ultrasonic welding, in: ASM Handbook, vol. 6A, 2011, pp. 725−730.
[20] M.P. Matheny, K.F. Graff, Ultrasonic welding of metals, in: Power Ultrasonics: Applications of High-Intensity Ultrasound, 2014, https://doi.org/10.1016/b978-1-78242-028-6.00011-9.
[21] G. Meschut, O. Hahn, V. Janzen, T. Olfermann, Innovative joining technologies for multi-material structures, Welding in the World 58 (1) (2014) 65−75, https://doi.org/10.1007/s40194-013-0098-3.
[22] N. Holtschke, S. Jüttner, Joining lightweight components by short-time resistance spot welding, Welding in the World 61 (2) (2017) 413−421, https://doi.org/10.1007/s40194-016-0398-5.
[23] RWMA, Resistance Welding Manual, fourth ed., Resistance Welder Manufacturers' Assoc, Philadelphia, PA, 2003.
[24] H. Zhang, J. Senkara, Resistance Welding − Fundamentals and Applications, second ed., CRC Press, Taylor & Francis, Boca Raton, FL, USA, 2011.
[25] L.M. Alves, E.J. Dias, P.A.F. Martins, Joining sheet panels to thin-walled tubular profiles by tube end forming, Journal of Cleaner Production 19 (6−7) (2011) 712−719, https://doi.org/10.1016/j.jclepro.2010.12.014.
[26] L.M. Alves, P.A.F. Martins, Single-stroke mechanical joining of sheet panels to tubular profiles, Journal of Manufacturing Processes 15 (1) (2013) 151−157, https://doi.org/10.1016/j.jmapro.2012.12.001.
[27] L.M. Alves, R.M. Afonso, C.M.A. Silva, P.A.F. Martins, Boss forming of annular flanges in thin-walled tubes, Journal of Materials Processing Technology 250 (July) (2017) 182−189, https://doi.org/10.1016/j.jmatprotec.2017.07.011.
[28] L.M. Alves, R.M. Afonso, C.M.A. Silva, P.A.F. Martins, Joining sandwich composite panels to tubes, Proceedings of the Institution of Mechanical Engineers, Part L: Journal of Materials: Design and Applications 233 (7) (2018) 1472−1481, https://doi.org/10.1177/1464420718763463.
[29] L.M. Alves, P.A.F. Martins, Mechanical joining of tubes to sheets along inclined planes, Steel Research International 83 (12) (2012) 1135−1140, https://doi.org/10.1002/srin.201200035.
[30] A. Gonçalves, L.M. Alves, P.A.F. Martins, Inclined tube-sheet plastically deformed joints, Steel Research International 85 (1) (2014) 67−75, https://doi.org/10.1002/srin.201300078.
[31] Modseat, Modular Light-Rail Seat, 2017. Retrieved from, http://modseat.pt/en/home_en/.
[32] D. Bundesbank, Sammlermünzen, 2019. Retrieved from, www.bundesbank.de/de/aufgaben/bargeld/euro-muenzen/sammlermuenzen.

[33] R.M. Afonso, P. Alexandrino, F.M. Silva, P.J. Leitão, L.M. Alves, P.A.F. Martins, A new type of bi-material coin, Proceedings of the Institution of Mechanical Engineers, Part B: Journal of Engineering Manufacture (2019) 1−10, https://doi.org/10.1177/0954405419840566.
[34] C.V. Nielsen, W. Zhang, L.M. Alves, N. Bay, P.A.F. Martins, Modeling of Thermo-Electro-Mechanical Manufacturing Processes, Springer, London, 2013, https://doi.org/10.1007/978-1-4471-4643-8.
[35] N. Bay, H. Bjerregaard, S.B. Petersen, C.H.G. dos Santos, Cross shear roll bonding, Journal of Materials Processing Technology 45 (1994) 1−6, https://doi.org/10.1016/0924-0136(94)90309-3.
[36] I.M. Stroiman, G.A. Mitrukov, Cold-welding of aluminium and copper, Welding International 16 (6) (2002) 488−490, https://doi.org/10.1080/09507110209549564.
[37] N. Bay, W. Zhang, M.H. Rasmussen, K.A. Thorsen, Resistance welding: numerical modelling of thermomechanical and metallurgical conditions, in: Proceed. Dansk Metalurgisk Selskabs Vintermøde, 2003.
[38] ASM International, Alloy phase diagrams, in: ASM Handbook, vol. 3, 1992, https://doi.org/10.31399/asm.hb.v03.9781627081634.
[39] W.-F. Zhu, Z.-Q. Lin, X.-M. Lai, a.-H. Luo, Numerical analysis of projection welding on auto-body sheet metal using a coupled finite element method, The International Journal of Advanced Manufacturing Technology 28 (2006) 45−52, https://doi.org/10.1007/s00170-004-2336-8.
[40] C.V. Nielsen, K.S. Friis, W. Zhang, N. Bay, Three-sheet spot welding of advanced high-strength steels, Welding Journal (Miami, Fla) 90 (2) (2011) 32s−40s.
[41] M. Moghadam, N.S. Tiedje, M. Seyyedian Choobi, C.V. Nielsen, K. Pantleon, N. Bay, Bonding mechanisms in spot welded three layer combinations, in: Proceedings of 9th International Seminar & Conference on Advances in Resistance Welding. Miami, Florida, 2016.
[42] O. Hoffmann, Environment Oriented Light Weight Design in Steel, Ökologischer Leichtbau in Stahl, Hannovermesse Werkstoff-Forum, Hannover, Germany, 2012.
[43] J. Sagüés Tanco, C.V. Nielsen, A. Chergui, W. Zhang, N. Bay, Weld nugget formation in resistance spot welding of new lightweight sandwich material, International Journal of Advanced Manufacturing Technology 80 (5−8) (2015) 1137−1147, https://doi.org/10.1007/s00170-015-7108-0.

CHAPTER

5

Friction stir welding

Daniel F.O. Braga[a], *Shayan Eslami*[b], *P.M.G.P. Moreira*[b]

[a]LAETA, IDMEC, Instituto Superior Técnico, Universidade de Lisboa, Av. Rovisco Pais, 1, Lisbon, Portugal; [b]INEGI, University of Porto, Rua Dr. Roberto Frias, 400, Porto, Portugal

Nomenclature

AHSS Advanced High Strength Steel
AS Advancing Side
BM Base Metal
EBSD Electron Back-Scattered Diffraction
FSC Friction Stir Channeling
FSD Friction Stir Deposition
FSP Friction Stir Processing
FSSW Friction Stir Spot Welding
FSW Friction Stir Welding
HAZ Heat Affected Zone
HDPE High Density Polyethylene
HSLA High Strength Low Alloy
IMC Intermetallic Compounds
MIG Metal Inert Gas
NVH Noise Vibration and Harshness
ODS Oxide Dispersion Strengthened
PCBN Poly Cubic Boron Nitride
PWHT PostWeld Heat Treatment
rFSSW Refill Friction Stir Spot Welding
RS Retreating Side
SHM Structural Health Monitoring
SZ Stir zone
TIG Tungsten Inert Gas
TMAZ Thermo-mechanically affected zone
TWI The Welding Institute

Advanced Joining Processes
https://doi.org/10.1016/B978-0-12-820787-1.00005-X

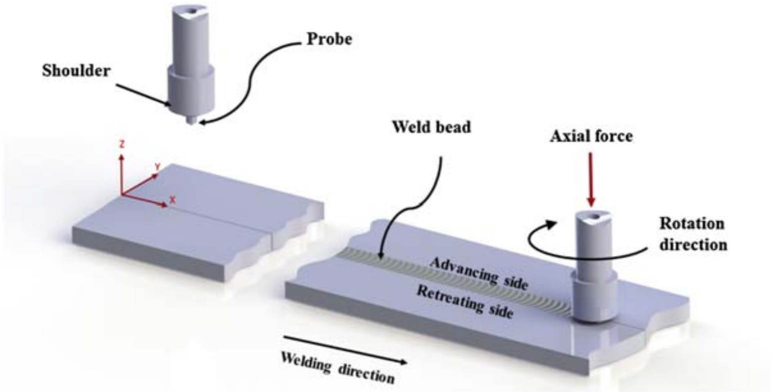

FIG. 5.1 FSW scheme.

1. Introduction

Friction Stir Welding (FSW) is a solid-state welding process invented at The Welding Institute (TWI) in 1991 [1]. Unlike conventional fusion welding processes, in solid-state welding processes, joining occurs at temperatures below the base metal (BM) melting point. Therefore, there is generally no need for an inert ambience to inhibit the formation of oxide phases, with the exception of metals that form oxides below melting temperature (i.e. Titanium alloys). Given the solid-state nature of the welding process there is also no need for filler material, as the existing volume of material in both workpieces in the vicinity of the abutting faces to be joined will be stirred and form the weldment. Along with FSW, other examples of solid-state welding processes are for example, friction welding and its derivatives, ultrasonic welding, explosion welding, forge welding. The lower heat input of FSW when compared to conventional fusion welding methods results in smaller heat affected zone (HAZ), lower distortions and residual stress, and overall excellent mechanical properties.

In its most basic configuration, FSW is achieved by having a tool composed of a shoulder and pin made of a harden alloy that rotates, plunges, and moves along the abutting faces of two workpieces to be joined. The rotation generates friction heat between the tool and the workpieces, which softens the material to join. The constant relative movement of the tool regarding the workpieces, see Fig. 5.1, causes mixing of the two materials to weld. The relative tool movement may be achieved either by moving the tool along an axis while the workpieces remain stationary, or by having the tool axially stationary while the table containing the workpieces moves.

The stirred material around the pin experiences severe plastic deformation, as material flows from the front of the tool to the trailing edge. Given the simultaneous axial movement and rotation, the velocity profile in a cross-section of the weld is not symmetric. This asymmetry is replicated on the heat transfer and material flow, leading to asymmetry in the microstructure.

The combination of heat input and severe plastic deformation, results in 4 distinct microstructural zones in FSW joints (as shown in Fig. 5.2):

- Unaffected parent material;
- Heat affected zone (HAZ);
- Thermo-mechanically affected zone (TMAZ);
- Stir zone (SZ).

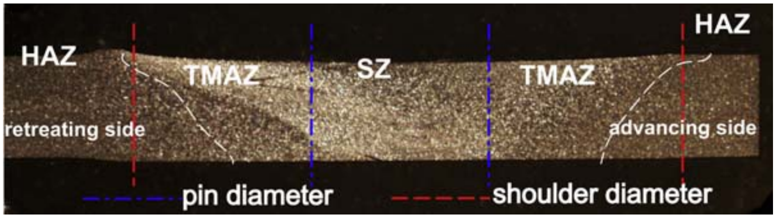

FIG. 5.2 Cross-section of an aluminum AA6082 FSW joint.

Also, given the aforementioned asymmetry, the width of each zone in the cross-section is different between advancing side (AS) and retreating side (RS). In the heat affected zone, as the name implies the material is only affected by the heat generated during the welding process, and as there is no plastic deformation, the grain structure remains similar to the parent material. Closer to the center of the weld, the TMAZ besides heating, undergoes plastic deformation, but shows no signs of recrystallization. At the center of the weld is the SZ where the deformation strain and temperatures are enough to cause dynamic recrystallization. The resulting microstructure in this area is composed of fine equiaxed grains.

The potential of FSW arises from the advantages it presents regarding conventional fusion welding processes. Bellow it is listed some of these advantages:

- High strength, ductility, fatigue strength and other mechanical properties in as welded condition;
- Large array of weldable materials;
- Ability to weld dissimilar materials;
- Non-consumable tools,[1] no filler metals or shielding gas required;
- Higher energy efficiency;
- Relatively good surface finish with no significant changes in joint thickness, especially in the case of stationary shoulder welding;
- Lower residual stresses and distortion levels.

Along with these advantages some limitations and drawbacks should be noted:

- Keyhole resulting from the tool exit at the weld exit;
- Specialized equipment and clamping required due to the large plunging forces involved;
- Slower weld speeds when compared to single pass fusion welding processes;
- Requires special care when welding joints with variations in thickness or with non-linear weld paths;
- Requires strict geometric tolerance management as small misalignments reduce joint strength.

Along with the advancements in joining with FSW, some variants of the process have been adapted to other applications. Examples of this are Friction Stir Processing (FSP), Friction Stir Channeling (FSC) and Friction Stir Deposition (FSD).

[1]Disregarding tool wear during service.

FSP is a process used to improve the mechanical properties of metallic materials based on the functioning mechanism of FSW. Through FSP it is possible to locally refine the microstructure of the material, similarly to what occurs in the stir zone of an FSW joint [2]. FSP may also be used to create surface composites by stirring reinforcement particles into a base material.

FSC is also variant of FSW, but in this case it is used to produce integral channels in a base material. The main application for this technique is heat exchangers [3], although other applications have been identified such as networks for lubrication or hydraulics or structural health monitoring (SHM), through instrumentation of the cavities formed with FSC [4].

As for FSD it is an additive manufacturing method based on FSW. This process as FSW is a solid-state process which contrasts with more common fusion additive processes. This way, drawbacks of fusion additive processes, such as, hot cracking, porosity, and columnar grain structures are avoided and secondary densification post processing steps are not required [5]. In FSD, a rotating hollow non-consumable tool plunges onto a base plate, while a feedstock is plunged through the hole of the tool. Metallurgical bonding is achieved by the combination of friction heat and shear extrusion.

2. FSW of aluminum alloys

FSW was first applied to the joining of aluminum alloys, as given the solid-state nature of the process, it led to significant improvements in joints mechanical performance over conventional fusion processes. The welding of these alloys through FSW has been further studied than others and their industrial application has also been more widespread than others. This relates to the aforementioned mechanical performance improvement, but also to the lower requirements in terms of special tooling (when compared to FSW of harder alloys), and increased feed rates which improve economic feasibility of the process.

There are two main groups of aluminum alloys which will result in different microstructure and mechanical behavior when friction stir welded. These are heat treatable and non-heat treatable aluminum alloys. Non-heat treatable alloys (series AA1XXX, AA3XXX, some of AA4XXX and AA5XXX) are strengthened by alloying the aluminum with additions of other elements. Besides this, they are usually subjected to cold working or strain hardening. Meanwhile heat treatable aluminum (series AA2XXX, some of AA4XXX, AA6XXX and AA7XXX) alloys are strengthened by second-phase particles, as the alloying elements and their combinations improve their solubility in aluminum with temperature increase. As such these alloys are usually subjected to thermal treatment, quenching, and artificial aging. Given the combination of thermal input and induced plasticity in FSW, the resulting microstructure and mechanical behavior of these alloys will vary accordingly.

Given that non-heat treatable aluminum alloys are not strengthened by second-phase particles and the only appropriate heat treatment is annealing to gain further capacity for deformation, the heat input of FSW will only result in annealing of distinct zones within the joint cross-section. The condition of the base material will define the microstructural features of the welded joint. If the material is completely annealed (O temper), the resulting temperature transient may lead to grain growth in the HAZ. In case there is some cold working in the BM (Hxxx condition), there may be recrystallization in the HAZ [6]. The combined effect of deformation and heat during FSW of non-heat-treatable aluminum alloys in O or Hxxx condition was studied by Etter et al. [7]. Through electron back-scattered diffraction (EBSD), the authors studied the microstructure of a AA5251 in O and H14 condition. While the cold worked joint showed changes to grain size and shape starting in the HAZ, with new equiaxed grains, the fully annealed only showed obvious deformation of the grains starting at the TMAZ. The resulting hardness profile also differs very significantly, as the loss of cold working in the H14 joint leads to a decrease in hardness in the HAZ and TMAZ followed by an increase (still lower than BM) in the SZ due to aging, while in the O joint the BM hardness is maintained with small peaks in the TMAZ. Çam et al. [8] welded a 3 mm thick plate of aluminum AA5082-H32, which is a non-heat-treatable cold worked alloy. The heat input from FSW resulted in a decrease of hardness in the TMAZ due to the loss of cold working. The location of this hardness decrease coincides with the failure location in tensile tests of the joints, which showed an undermatching strength (65%—75% of BM). The reduction in ductility of the joints are even more significant than the reduction in strength with the best joint achieving 25% of the final elongation of BM. For non-heat-treatable aluminum alloys it can be generally stated that fully annealed BM will have smaller changes in terms of microstructure and mechanical properties while cold worked alloys will face more significant microstructural changes and will have undermatching mechanical properties due to the loss of cold working.

In heat-treatable alloys FSW will result in annealing as well as aging, over-aging, precipitation growth or dissolution [6]. These alloys when subjected to FSW will have a loss of strength in the weld region, although smaller than in conventional fusion welding processes, particularly in age-hardened materials. In these alloys the strength loss may be recovered through postweld heat treatment (PWHT). Sato and Kokawa [9] reported that postweld aging and postweld solution heat-treatment and aging restored yield and ultimate tensile strengths of FSWed aluminum alloy AA6063-T5 joints to BM levels. Ductility was also recovered with PWHT. The effects of PWHT on strength and ductility of heat-treatable alloys may be observed in Fig. 5.3, where aluminum AA6061-T6 was friction stir welded and submitted to PWHT.

The softening that occurs in the weld region was also eliminated with the PWHT joints having a relatively homogeneous distributions of high hardness. Similar observations were made for other alloys, such as AA2024-T4 [11,12], AA2219-O [13], AA6061-O/T6 [14,15], AA6082-T6/T651 [16,17] and AA7070-O/T6 [18,19]. Dissimilar heat-treatable alloys may also be welded and PWHT. İpekoğlu and Çam [20] studied the effect of initial temper condition and PWHT of dissimilar FSW joints of AA6061 and AA7075 aluminum in O and T6 initial temper condition. Joints in the O condition showed strength overmatching while T6 undermatching. The overmatching of unaged joints (O condition) led to consistent failure location in the weaker base material (AA6061), regardless of the presence or absence of defects. The PWHT of these joints (O condition joints) resulted in a more homogeneous hardness distribution and made the presence of weld defects more significant in the failure location. Generally, PWHT resulted in an increase in strength in joints of both initial temper conditions. Ductility was however less recovered due to confined plasticity.

FSW of aluminum alloys has been proposed for applications such as aeronautical or automotive structures where fatigue is a serious consideration. As such several authors have studied FSW joints under cyclic loading. S-N fatigue behavior of several aluminum alloys FSW

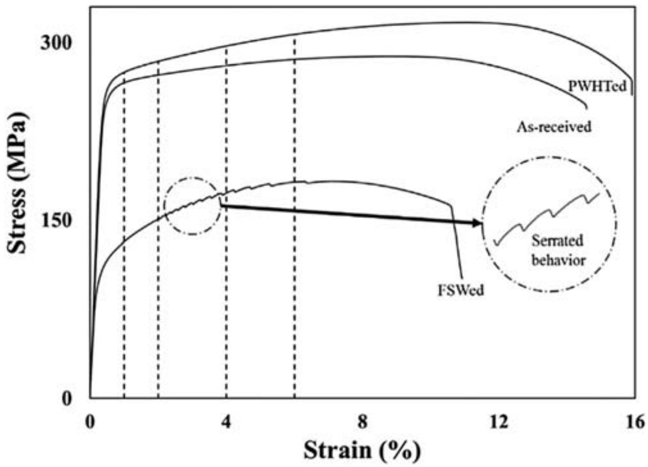

FIG. 5.3 Effect of PWHT on the mechanical properties of FSW AA6061-T6 [10].

joints (AA6006-T5, AA2024-T351, AA2024-T3, AA2024-T3, AA6013-T6, AA7475-T76, AA2219-T8751 and AA2519-T87) is reviewed in Ref. [6]. Generally, FSW leads to a decrease in fatigue strength when compared to BM. The fatigue strength of welds is dependent on loading direction, with specimens loaded transversely to the weld bead having lower strength than when loaded longitudinally. Fatigue strength is also much more dependent on the resulting surface quality of welds than on the weld speed/rotation speed ratio.

Although FSW results in lower fatigue strength when compared to base material, when compared to conventional fusion welding processes, it shows an improvement. Several authors compared FSW to other joining processes in order to showcase the potential applicability of FSW. Moreira et al. [21] compared FSW and metal inert gas (MIG) in constant amplitude cyclic loading at $R = 0.1$. FSW AA6061-T6 joints achieved an infinite life (10^7 cycles) with a fatigue strength of 65% of BM yield strength. FSW joints of aluminum AA6061-T6 achieved lower fatigue life than AA6082-T6 joints for stresses lower than 130 MPa, as the fatigue strength for FSW joints of this alloy reduced more sharply than AA6082, as shown in Fig. 5.4. When MIG welded both alloys presented similar S-N curves. Fatigue strength and lives were higher for both alloys when FS welded than MIG welded.

In [22], FSW, MIG and TIG were compared when welding in AA6082 plates and cyclic loading at $R = 0.5$. It was shown that FSW joints have higher fatigue strength than both techniques and also that for this alloy the fatigue strength is insensitive to the welding speed.

Along with fatigue strength and life analysis, fracture propagation studies have also been performed to enable a damage tolerance approach. Compact tension specimens were used to assess fatigue crack propagation in FSW AA2024-T3 and AA6013-T6 and at lower loads and lower R-ratio of 0.1 showed superior properties than base material [23]. At higher loads and higher R-ratios (0.7–0.8), both base material and FSW joints showed similar fatigue crack propagation behavior. This varying behavior with load level and R-ratio was attributed to the residual stress field resultant from the FSW process. The existence of compressive residual stress at the crack front results in a decrease of the effective stress intensity factor. However,

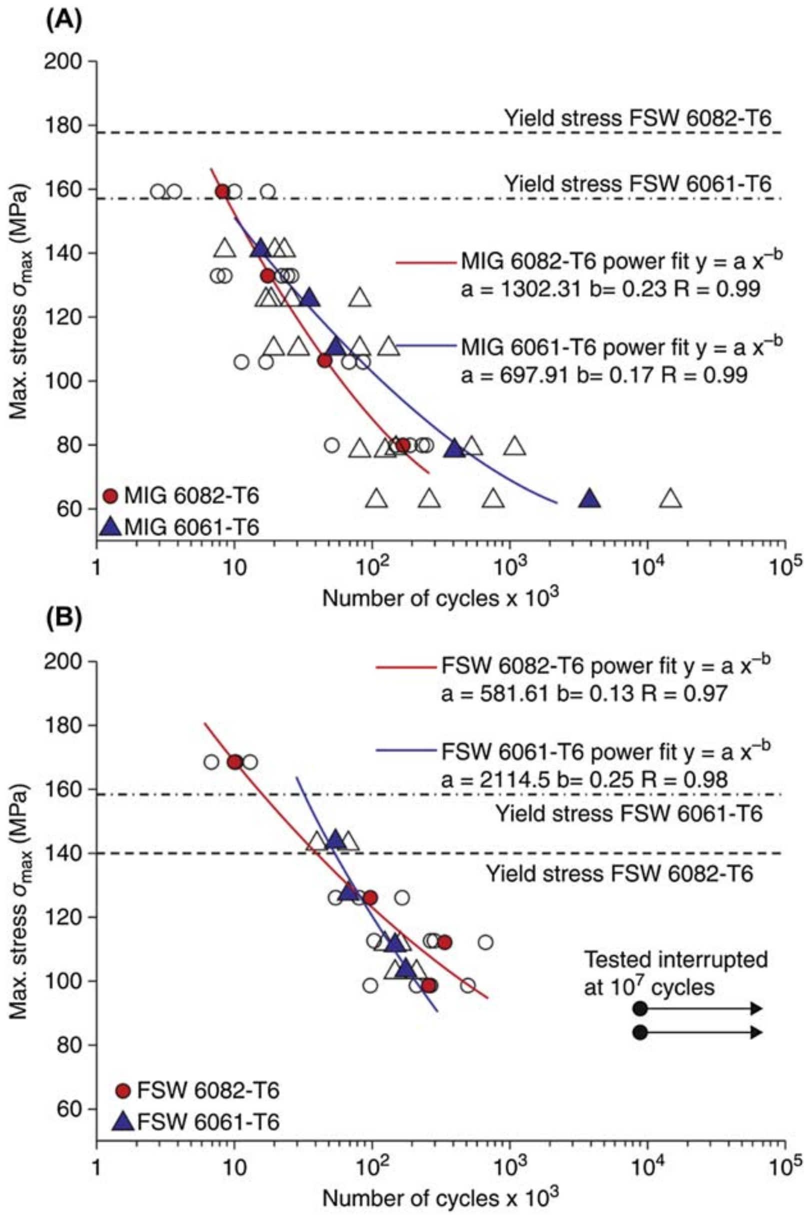

FIG. 5.4 AA6061-T6 and AA6082-T6 $R = 0.1$ S-N curves of (A) MIG and (B) FSW [21].

with the increase of load level and *R*-ratio this compressive residual stress becomes less relevant in the overall loading of the crack front.

The effect of residual stress in the fatigue crack behavior is further reported by other authors. In Ref. [24], the fatigue crack growth behavior of AA2024-T351 FSW joints depending

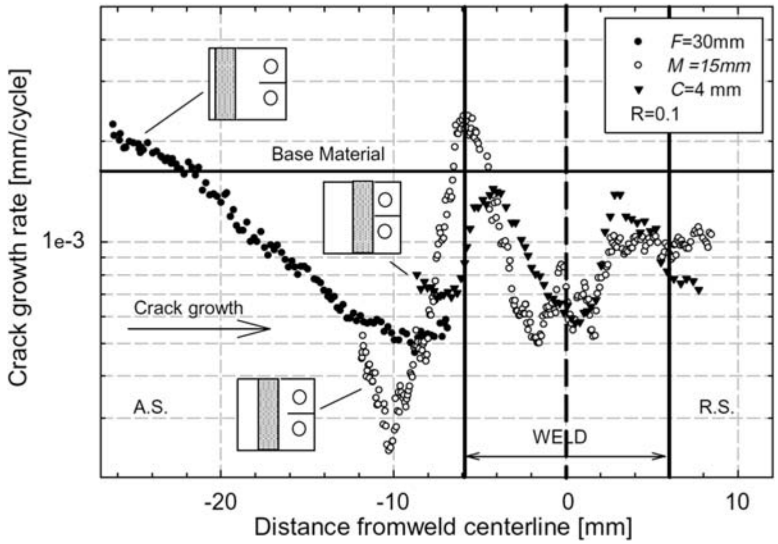

FIG. 5.5 Crack growth rate as a function of distance from weld centerline [24].

on distance to the weld line was studied. The results were complemented with residual stress measurements using the cut-compliance method. It was found that outside of the weld zone, residual stress led to low crack growth rates, while in the weld zone, microstructural and hardness changes affect the crack growth. The lower fatigue crack growth away from the weld centerline, as shown in Fig. 5.5, was coincident with the lowest residual stress intensity factor. The lower hardness in the weld region was shown to be predominantly responsible for the increased fatigue crack growth, as tests were made with specimens as welded and stress-relieved, showing always an increased fatigue crack growth rate in this region.

In Ref. [25], the fatigue crack propagation in two Al-Mg alloys, AA6082-T6 and AA6061-T6, was studied taking into consideration the location of the crack (BM, HAZ, SZ, as well as transverse to the weld) and rolling direction. Even though welding resulted in lower strength and ductility than base material, the welded material exhibits superior crack propagation resistance. Both alloys displayed a reduction in fatigue crack growth after FSW and compressive residual stresses were pointed out as possible explanation for this. The presence of compressive residual stress at the edges of the weld is shown in Ref. [26], where Contour Method residual stress measurements are made on FSW AA6082-T6 joints. Using this technique, the authors were able to create a full 2D weld cross section map of the longitudinal residual stress. Prime et al. [27], also studied the residual stress field of FSW joints with the Contour Method, comparing it to Neutron Diffraction, but in this case for a dissimilar AA2024-T351 AA7050-T7451 joint. An M shaped residual stress profile was observed with compressive stress within the welded material, as shown in Fig. 5.6.

The beneficial effect of FSW induced compressive residual stress in fatigue crack growth was also verified in Ref. [28], where a stiffened panel (see Fig. 5.7A) with skin through crack was fatigue tested. Two alloys, AA2024 and AA6056 in different heat treatment conditions were used in these specimens. The specimens were either high speed milled, or had their

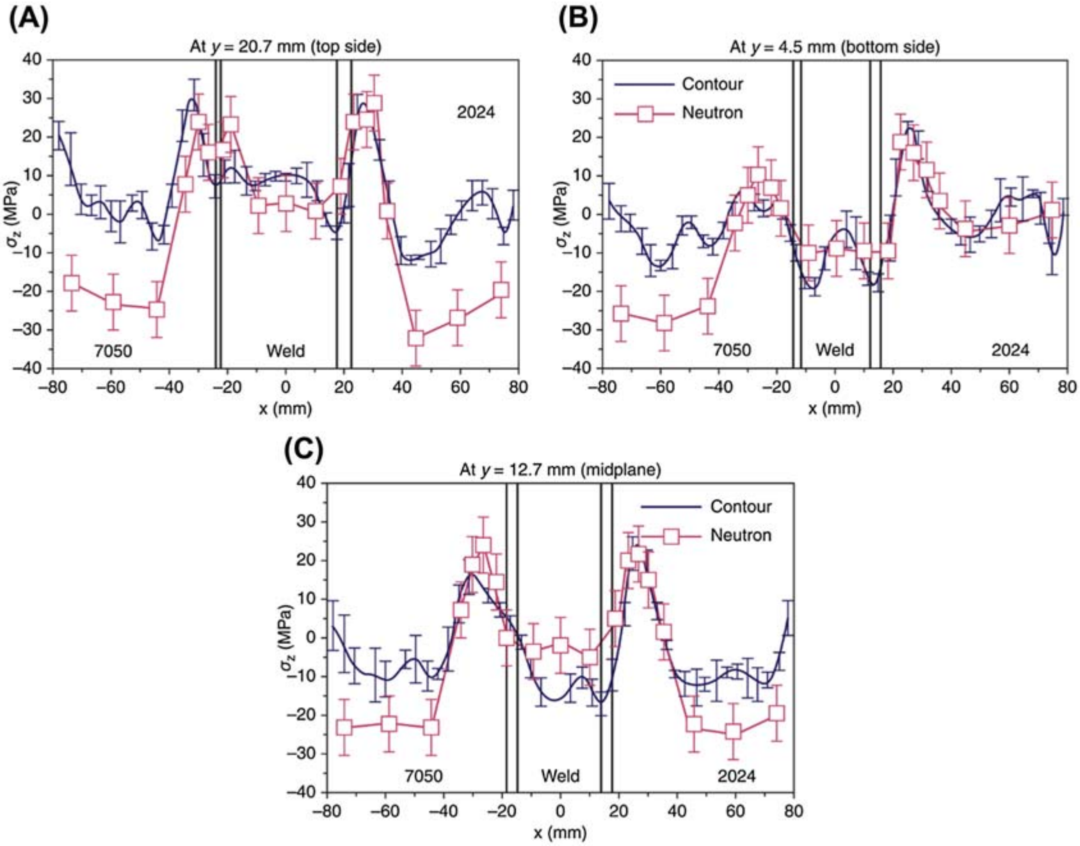

FIG. 5.6 Residual stress measurement of dissimilar FSW AA2024 AA7050 at (A) top side, (B) bottom side and (C) midplane [27].

stringers joined by either laser beam welding or FSW. As shown in Fig. 5.7B), FSW consistently resulted in lower fatigue crack growths which were justified by the compressive residual stress resultant of the welding process.

3. Harder metal alloys FSW

Friction stir welding was initially developed to weld aluminum alloys, but technological developments in terms of welding tools, clamping apparatus, process control and FSW variants have expanded the materials that may be welded by this process.

FSW of steels as generated significant interest in research and potential applicability, however welding these materials is significantly more difficult than welding aluminum. This difficulty stems from the fact that in order to friction stir weld steels the temperatures the material and as consequence tool achieve are very high (up to 1300 °C) [30]. Besides the elevated

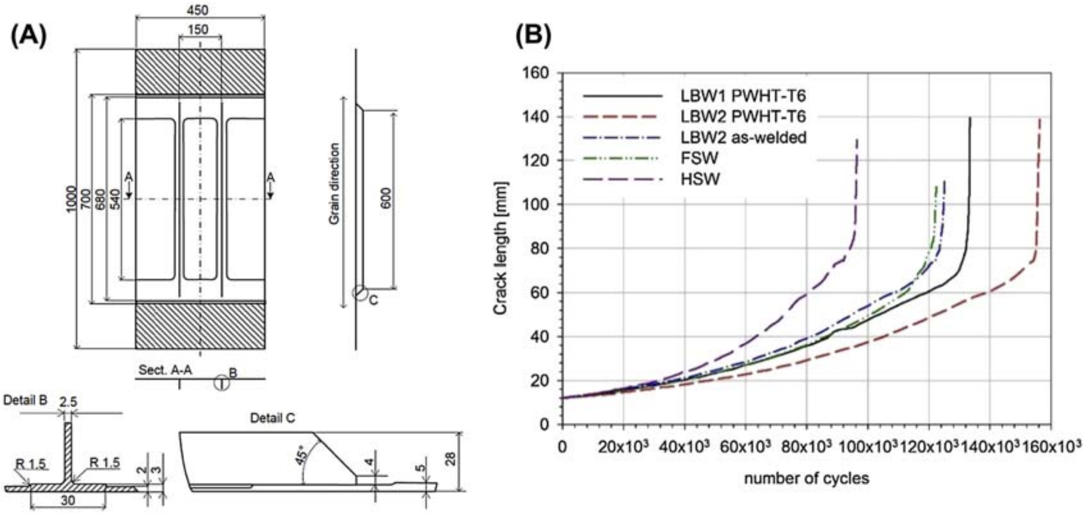

FIG. 5.7 Stiffened panel design (A) and crack growth at R = 0.1 depending on joining method (B) [29].

temperatures, hot steel retains a considerable flow stress countering the weld tool as it moves through the workpiece. The elevated temperatures are result of lower temperature diffusivity than aluminum alloy, which in austenitic stainless steels is compounded by the high elevated temperature flow stress and low thermal diffusivity even compared with carbon steels [31]. This leads to high contact stresses and abrasion of the welding tool. Given this, the tool requirements to weld steel are much higher than the ones to weld aluminum and other softer alloys. While for FSW of aluminum tool steel has been successfully employed in FSW tools, to weld steel the tool materials must exhibit excellent properties at temperatures in excess of 900 °C, as well as fatigue strength, fracture toughness and resistance to mechanical and chemical wear [32]. The two classes of materials that have been employed in FSW tools for steel are poly crystalline cubic boron nitride (PCBN) and refractory metals. PCBN is a very hard material, only less hard than diamond, but with improved chemical and thermal stability. However, this high hardness makes machining very hard and as such early FSW tools had very simple designs. Continuous research in the field of steel FSW led to the introduction of grooved PCBN tools, which improved process productivity, eliminated adverse microstructures and defects. Refractory metals like tungsten and molybdenum have also been applied in FSW tools for steel. However, their high ductile-to-brittle transition temperatures lead to tool fracture. In the class of refractory metals, several alloys have been used, such as Tungsten–Rhenium (W-25%Re) [33], Tungsten Carbide (WC) [34] and Tungsten Lanthanide (W-La) [35].

The elevated temperatures in FSW of steels, result in transformation, recrystallization and grain growth. As such, these alloys undergo more complex microstructural evolution than aluminum alloys when FS welded [6,32]. In FSW of steels the TMAZ is sometimes not readily clear in the microstructure of the weld, due to allotropic transformation on cooling [36]. As allotropic phase transformation occurs, the austenitic phase at elevated temperatures is consumed by the room temperature phase. The phase transformation alters or obscures the

FIG. 5.8 Cross section of an austenitic stainless steel FSW joint.

deformation history, texture and grain structure of the austenitic phase [32]. An example of a steel FS weld cross section is show in Fig. 5.8, where TMAZ is not clearly distinguishable. FSW was found to result in a finer microstructure in the SZ, consisting of ferrite, grain boundary ferrite and fine perlite. The grains were also shown to be finer closer to the shoulder.

Within steels, carbon steels are the most frequently used. These steels can generally be successfully welded using tradition fusion welding processes. However, FSW can weld these steels at lower temperatures, which lead to lower residual stress and distortion [37]. Also, with optimized process parameters, welding may be done at temperatures even below A_1 avoiding phase transformations. This will lead to refined microstructure and improved mechanical properties. Hydrogen damage in low carbon steel may also be suppressed by grain refinement [32].

Reynolds et al. [38] successfully FS welded DH36 steel using a Tungsten alloy tool and studied the relationship between weld parameters and joint properties. The SZ was found to be composed of bainite and martensite while ferrite and pearlite compose the base material. The joints were found to be in overmatching in hardness and tensile strength. Failure in tensile testing was in the base material with it governing the joint failure. Increasing weld speed decreases specific weld energy, as less revolutions of the tool are made by mm of weld and cooling rates are increased, resulting in increased hardness overmatching. The effect of carbon content and the transformation on carbon steel FSW joints mechanical properties and microstructures was studied in Ref. [39]. When welding 1.6 mm thick ultralow-carbon interstitial free steel, FSW temperatures were bellow A_3 temperature (about 910 °C). This way, it was possible to weld interstitial free steel in the ferrite single phase range. A refined microstructure is achieved in the SZ and increased strength and hardness is attained. The refined ferrite single phase microstructure is expected to result in significant formability, enabling the use of FSW in tailor welded blanks [32]. Welding higher thickness steel may however lead to temperatures leading to phase transformation. In Ref. [39], S12C steel, a low carbon steel with a small portion of pearlite, was also FS welded. The resulting microstructure was shown to be dependent on the weld temperature and cooling rate. In the case where weld temperatures are above A_3 and as such, FSW is done in the austenite single-phase region, grain coarsening occurs rapidly after recrystallization as no second phase exists to impede grain growth. In the case where welding is done in the two-phase $\alpha + \gamma$ region, grain coarsening rate is reduced, as recrystallized α and γ grains work as the second phase. This leads to fine ferrite grains. For higher carbon content steels, such as S35C, more phase transformations occur during cooling in FSW, resulting in more complex microstructures. When welding above A_1 temperature, part of the austenite that is formed during welding may become martensite, which will increase hardness. Sato et al. [40] studied the microstructure of FSW joints of a duplex (ferrite + cementite) ultrahigh carbon steel. Welding was performed with a PCBN tool on 2.3 mm thick plates. Argon gas was also used to shield the weld, minimizing surface oxidation. Given the high hardenability of ultrahigh carbon

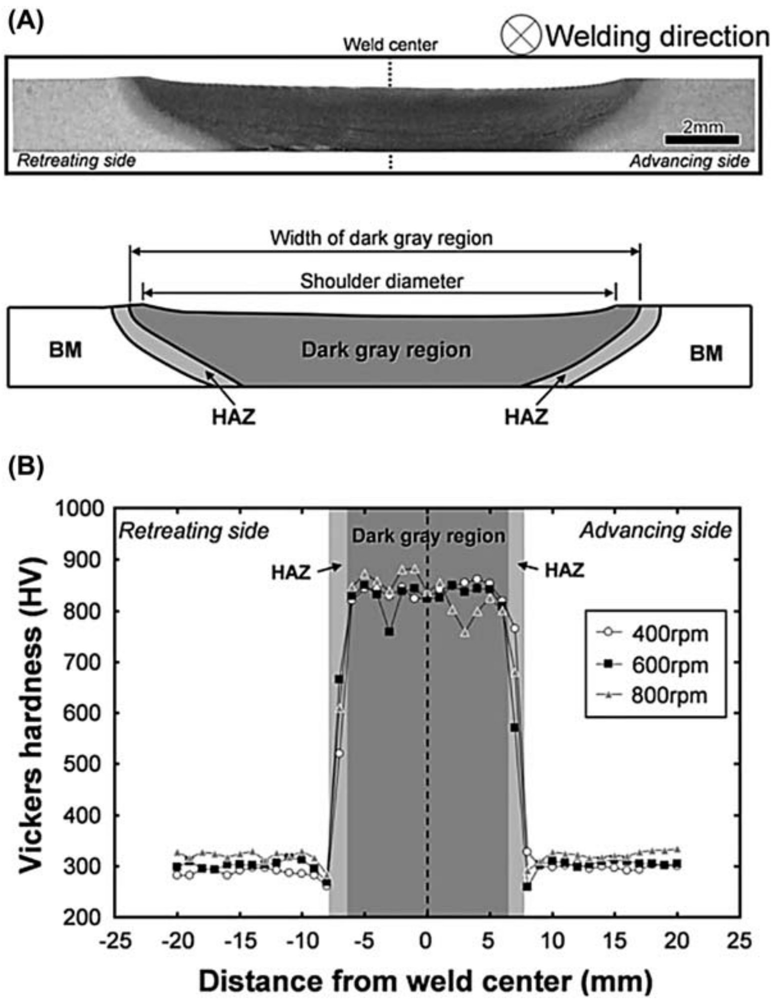

FIG. 5.9 Ultrahigh carbon steel FSW microstructure (A) and hardness profile (B) [40].

steels, the central region of the weld undergoes transformation during cooling from single-phase austenite structure (formed during material stirring) to martensite. Some austenite is still retained in this region as the martensite finish temperature is bellow room temperature for these steels. The HAZ also showed some martensite along with some undissolved cementite particles. This microstructure explains the significant increase in hardness in the weld region as show in Fig. 5.9.

The transformation into martensite resultant from FSW, increases hardness and strength but reduces ductility and toughness. Selecting proper process parameters can however mitigate the formation of martensite, by welding at temperatures below A_1. As example a hyper-eutectoid steel (0.85 mass% C, AISI-1080) was FS welded with varying process parameters, resulting in welds above and below A_1. Toughness was measured through Charpy impact test, resulting in impact energies of 67.62 N mm (74.8% of base material) and 24.2 N mm (26.8% of base material), respectively [41].

Beyond carbon steels, FSW of stainless steels [31,42–45], advanced high strength steels (AHSSs) [46,47], high strength low alloy (HSLA) steels [48,49] and oxide dispersion strengthened (ODS) steels [50,51], have also been studied. Similarly, to the previously discussed steels, the high strength, high flow stress is a challenge to overcome in FSW. The process parameters affect significantly the heat generated during the process and the temperatures achieved in the material to be welded. The welding temperatures in relation to allotropic transformation temperatures, greatly affects the mechanical properties of the joint. In austenitic stainless steels, which are the most common, the FSW process may affect the corrosion resistance, which is a key property of these alloys. In cases where the cooling rate after FSW is relatively low (thick welds with lower welding speed), the delta ferrite formed at high temperatures decomposes rapidly into sigma and austenitic phases [44]. The sigma particles contain a high fraction of Cr and if they are present in the grain boundaries, they impede the formation of the protective chromium oxide layer, resulting in lower corrosion resistance [45]. AHSS have been mainly developed for application in automotive manufacturing, due to their high strength and good formability, allowing for lighter vehicles. The interest in FSW of these alloys is mainly for tailored blanks. However the challenge to the adoption of FSW for this purposes is the longevity of the tools and the very high spindle load required to create a joint [32]. The latter is a limitation on the use of robot arms which are common in automotive manufacturing.

FSW of titanium alloys, namely Ti-6Al-4V, has also been studied in order to overcome the limitations of conventional fusion processes, such as high residual stress, large distortions and the formation of brittle solidification microstructures. As in FSW of steel, tool design and material are crucial. The relatively high strength and flow stress, combined with the low thermal conductivity and reactivity to oxygen, requires a tool material that will not wear excessively at high temperatures and that does not interact chemically with the material to weld. Even though PCBN tools have been used successfully to weld steel alloys as discussed before, these tools will wear excessively when welding titanium. The contact between PCBN tool and the titanium alloy results in the formation of TiB [52]. Given the demanding requirements most tools used in welding of titanium alloys are made of refractory materials. Tungsten-based tools, especially tungsten carbide, are the most used tools in studies regarding FSW of titanium alloys [53]. These tools are chemically stable, not reacting with Ti-6Al-4V, hard and cost-effective [54]. Some studies have also been made on tools made from tungsten-rhenium. These materials are capable of operating at elevated temperatures, but are more difficult and costly to manufacture [55]. Besides the material tool, the tool design must also be taken into consideration to assure sound titanium welds. Given the relatively low thermal conductivity of titanium alloys, larger diameter pins with high ratio of pin to shoulder diameter are required to assure proper heating at the weld root and prevent tool breakage [56]. The low thermal conductivity and high hardness makes the plunging phase of the FSW process dangerous in terms of tool damage. As such, it is recommended to use a pilot hole in the workpiece to weld [57].

To achieve sound titanium welds, beyond a properly chosen tool, the correct process parameters must be selected. It has been shown that the process window for titanium FSW is very narrow, with Edwards et al. [58] showing that sound welds were achievable for a combination of thickness and tooling design only in a range of 25 rpm and 25 mm/min. With the low thermal conductivity of titanium, large temperature gradients may be found between the top surface and the weld root. This effect is more significant the thicker the plate to weld is. As such, the majority of the weld defects will originate in the weld root [55,59,60]. Heated back plate has been proposed to overcome this challenge [59,61], resulting in more uniform temperature field, which reduced tearing defect and achieved a more uniform microstructure and higher hardness. Tool wear was also shown to be reduced [61]. However, some authors have also proposed back plate cooling to prevent the workpiece from adhering to the backing plate [60,62]. The solution proposed in Fig. 5.10 is claimed to improve the thermal flow through the titanium sheets thickness, improving the joint quality. Also, it makes use of a tungsten insert in order to avoid contact between high temperature titanium and steel, leading to carbon contamination of the workpiece.

Beyond special heat or cooled fixtures and specially designed tools made from specific materials, some authors have also employed argon shielding gas in order to prevent the workpiece from reacting with the environment and forming titanium oxide formation [62–66].

The resulting microstructure from titanium FSW is composed by the common 4 distinct zones, HAZ, TMAZ, BM and SZ. However, HAZ and TMAZ is narrower than in aluminum alloy welds [57,60,61,67,68]. The width of the HAZ has been reported to be ~400 μm [67,69] and the TMAZ, similarly to FSW of steels is sometimes not clearly visible [66–68]. The low thermal conductivity of these alloys leads to significant temperature gradients, which may explain the narrow width of these microstructural zones. The higher the rotation speed, the larger the SZ, as the thermal input is higher [70].

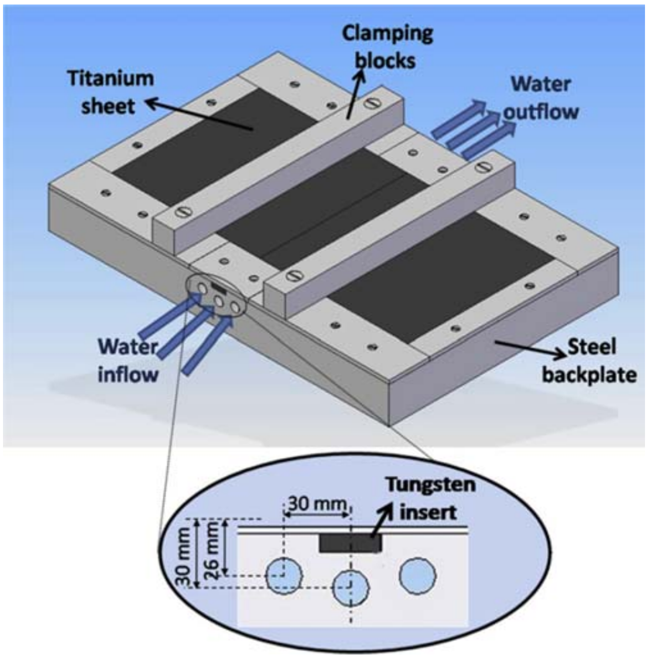

FIG. 5.10 Schematic of back cooled fixture for titanium FSW [62].

Pure titanium has 2 allotropic forms, a compact hexagonal structure α, stable at room temperature up to 880 °C (in the case of pure titanium) and a body-centered cubic structure β, stable between 880 °C and melting temperature. In the case of grade 5, Ti-6Al-4V, which is the most used alloy, the metallurgical composition is a biphasic α-β. Given the existence of multiple allotropic forms and the relatively low allotropic transformation temperature, FSW will lead to recrystallization in the SZ, in addition to the dynamic recrystallization caused by the stirring [53,60]. These microstructural changes result in changes in the local mechanical properties. The heat input will usually lead to softening in the HAZ, with this effect being more pronounced with higher rotation speeds [66]. The β microstructure formed at higher temperature normally has lower hardness than the globular microstructure that is formed at lower temperatures [62]. Beyond temperatures achieved during welding, cooling rate also affects the hardness of titanium FSW joints and is mainly controlled by the welding speed. The formation of basket-weave microstructure and precipitation of the α′ martensite in the β processed material may increase hardness [71]. The competing effects of softening due to the primary α recrystallization and hardening due to precipitation of the β phase, leads to some variation within results, with some authors reporting increase in local hardness, while other report lowering or no change at all [53].

Microhardness is typically in good agreement with tensile strength, with the lower hardness β transformed phase resulting lower strength than base material or the globular microstructure [68]. The relation with joint ductility is inversed. In the case of defect free joints, failure in tensile testing usually occurs in the HAZ with high joint efficiencies. In Ref. [68] an ultimate tensile strength of 953 MPa was reported, which was equivalent to 92% of the base material. Ji et al. in Ref. [61] achieved 1014 MPa ultimate tensile strength (98.9% of base material) and 6.8% elongation at failure (54.4%), with a heated back plate and a W-Re tool. These results were achieved for the combination of parameters 100 rpm, 30 mm/min, 2.5° tool tilt and 0.2 mm plunge depth. This parameter combination was found to result in welding temperatures below β−transus temperature.

Fatigue performance is of great relevancy for most of the applications FSW of titanium alloys is being proposed and as such has been studied by some authors. Weld defects, namely root defects, that as discussed above may arise in FSW of titanium alloys due to their low thermal conductivity, greatly limit the fatigue strength of joints and are the failure location if they exist in the joint [60]. In the case where proper process parameters have been selected and the workpiece has been milled after welding (to remove surface roughness due to FSW), fatigue life is similar to base material [60,72]. In Ref. [73] a 25% increase in fatigue life has been reported for $R = -0.2$ and a load of 620 MPa, although the results showed some scatter. This result was obtained in 24 mm thick welds, which is relatively thick, and using 150 RPM and 75 mm/min process parameters, with a tungsten lanthanum tool. However, thinner welds (3−6 mm) have reported lower fatigue endurances than base material (60−20%) [72]. Post weld heat treatment stress relief has shown to improve fatigue life of titanium FSW joints. In Ref. [72], fatigue life of as welded joints was reported to be 50% lower than base material, while an 871 °C post weld treatment resulted in 80% of base material.

Fatigue crack growth was studied in Ref. [74], and showed that fatigue crack growth rate was lower than in the base material due to the compressive residual stress in the HAZ. This compressive residual stress originates a negative residual stress intensity factor, which leads to slower crack growth. In this study the authors employed a CT specimen with a weld parallel to the loading direction and loaded in $R = 0.1$. In Ref. [73] the authors assess fatigue crack growth of 24 mm thick titanium FSW welds, using 19 mm thick CT specimens. The crack growth curve in both *L-T* and *T-L* directions showed similar behavior to the base material, differing mostly in the threshold region.

4. Polymers and composites FSW

The numerous advantages of FSW, as well as the increase of industrial demand for lightweight designed structures, naturally led to studying the possibility of using FSW for welding non-metallic materials [75], and recently new studies investigated the possibility of joining polymer-polymer [76], polymer-aluminum [77] and composites [78]. The commercially available joining techniques for polymers are usually limited to materials' thicknesses and configurations, and usually require third party filler materials, expensive equipment, physical changes in the parent materials, or produce weak joints. For instance:

- Mechanical fasteners such as rivets, screws and blots are usually limited to overlapped joints, and lead to substantial weight increase of the final product [79];
- Welding methods such as heat sealing and hot gas are required for filler rods to melt and weld the materials together, along with welding position limitation due to the gravitation effect [80];
- Ultrasonic welding needs parent material design modification, surface preparation and large joints cannot be welded in a single operation [81];
- Adhesive bonding requires careful surface preparation due to low surface energy of polymers, and environmental conditions can affect the joint quality [82].

Considering the established reliability of using FSW for welding metallic structures, researchers attempted to study and propose a systemic solution to overcome the limitations regarding polymer joining using FSW technology [83]. However, polymeric materials behave differently than metallic ones, due to their low melting point, thermal conductivity and hardness [84]. The welding tool plays an essential role to achieve sound welds with good surface quality, and the main difference between FSW of polymeric and metallic materials is due to the tool design concept [85]. For polymer FSW there are three main categories regarding the tool design and joint configurations:

1. Friction Stir Spot Welding (FSSW)
2. Friction Stir Welding (FSW)
3. Stationary Shoulder Friction Stir Welding (SSFSW)

All the mentioned categories benefit from the FSW concept, which refers to generating heat using friction, and stirring the plasticized material under an axial force. With respect to the parent material's characteristics and geometrical properties of the final components, different researchers investigated different approaches and attempted to optimize the welding process and compare with other joining methods.

4.1 Friction stir spot welding (FFSW)

FSSW is one of the techniques that branched from FSW, which benefits from the same concept as FSW but without a linear motion. This joining method was developed for overlapped configurations to replace mechanical fastening such as screws and rivets. Originally, FSSW was developed by Mazda Motor Corporation and Kawasaki Heavy Industry, to replace Resistance Spot Welding (RSW) for aluminum plates [86]. The FSSW starts with plunging of the welding tool into the base materials under an axial force, then after dwelling, the tool retracts when the desired temperature is reached, aborting the traversing part of the process. The main benefits of FSSW compared to the other similar techniques are: environmentally friendly, low energy consumption and cost-efficient process [87]. However, for polymeric materials, obtaining quality welds is challenging using FSSW due to the mechanical characteristics of polymers.

As presented in Fig. 5.11, in FSSW process, the rotating probe plunges partially into the parent material surface to increase the temperature to the desired value. After, the tool plunges more until the shoulder contacts the top of the base material to the pre-defined plunge depth or axial force, depending on the welding method and available equipment. At this stage, the tool stops the vertical movement and just dwells and stirs the plasticized material under shoulder's axial force. After dwelling stage, the tool suddenly stops, and remains in that position to consolidate the materials, followed by a retracting phase [88].

Several researchers investigated welding polymers using FSSW, such as High Density Polyethylene (HDPE) [89], Acrylonitrile Butadiene Styrene (ABS) [90], Polypropylene (PP) [91], Polyethylene (PE) [6], Polymethyl Methacrylate (PMMA) [92] and even dissimilar materials such as PMMA/ABS materials [93]. Generally, it was stated that all the welding parameters related to the welding tool have a significant effect on the weld quality, as it is responsible for heat generation, forging and stirring [94]. There are two approaches regarding the welding tool for FSSW process, which are common welding tool with rotary shoulder, and stationary shoulder welding tool. Hira et al. [6] investigated the FSW behavior for several polymeric materials using the conventional welding tool. It was concluded that among the tested thermoplastics, PE is the only polymer suitable for welding at ambient temperature, while the rest required additional heating source to compensate lack of the generated heat due to polymers mechanical properties. In order to have a proper material flow, a 50 °C additional heating is needed for PA6 (Nylon6) and PA66, and for Polyphenylene Sulfide (PPS) 70 °C additional heat. However, the results showed that joint strength was relatively low

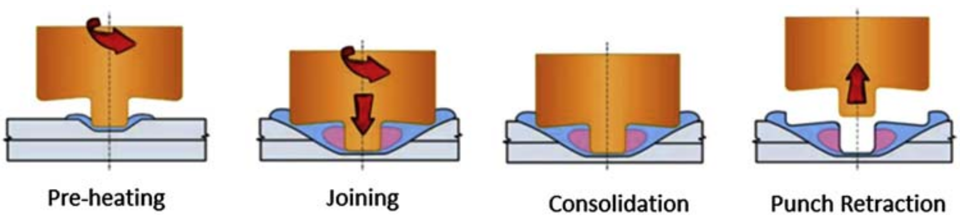

FIG. 5.11 Schematic representation of the FSSW [88].

compared to the base materials due to the polymers high expansion coefficient, which led to large shrinkage in the weld beads.

Using a conventional tool for polymers, the soft material tends to eject from the weld zone, leading to material loss in the stir zone. In order to solve this problem, an improved stationary shoulder welding tool was developed to spot weld dissimilar polymers [93]. The stationary shoulder forges the nearly molten material inside the stirring zone under the axial force, avoiding flash defect and blisters formation. However, it is important to choose the right material with low thermal conductivity for stationary shoulder to avoid the heat loss on the stirring zone. The effective welding parameters on the weld quality are plunge rate, rotational speed and dwell time.

A new spot joining method was developed and patented by Helmholtz Zentrum Geesthacht (HZG) in Germany [95] called FricRiveting. This innovative joining technique initially developed for polymer-metal hybrid structures. The process is based on combination of friction welding and riveting principals, which works by mechanical interference and adhesion between the parent materials [96]. The process consists of a high-speed rotating cylindrical rivet by plunging in a polymeric base material under an axial force, Fig. 5.12 [97]. The frictional heat generated by the rotating rivet melts the polymeric material and forms polymeric layers around the rivet tip. Then, the temperature increases, which leads to the plasticizing of the rivet, and under more pressure the tip deforms and locks into the material [98]. The FricRiveting method was investigated for a variety of dissimilar materials. For example, Polyethylenimine (PEI) and aluminum AA2024-T351 [96], and in another study short carbon fiber Polyether Ether Ketone (PEEK) composite and grade-3 Titanium [98] were successfully joined. The FricRiveting joining technique proved to be an interesting alternative joining technique for dissimilar composite-metal joints, with high mechanical performance under tensile and shear loading with high flexibility and short processing time.

In another approach, in order to increase the joint quality, laser texturing surface treatment was applied to increase the mechanical fastening between Titanium and PEEK using FSSW method [99]. Specimens tested without the laser texturing treatment on the metallic partner failed to achieve the strength of those with laser texturing surface treatment. The laser texturing creates micro-teeth on the metallic material, consequently improving the mechanical bonding between the substrates. Polyvinyl Chloride (PVC) and aluminum materials were joined using the same technique, which pre-treated metallic material locates on the top and polymeric material on the bottom position. After the optimizing process, a maximum shear strength of 75% was achieved if compared to PVC base material [100].

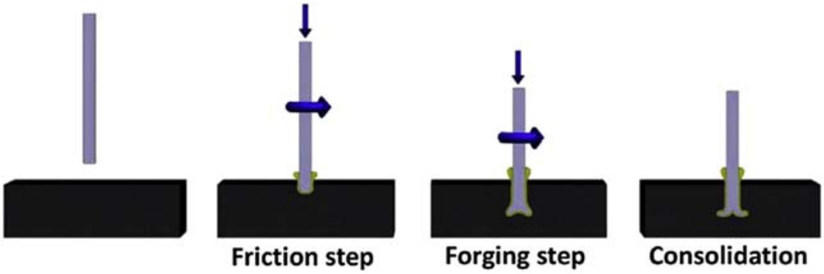

FIG. 5.12 Friction Riveting process [97].

In general, FSSW is limited for specific applications, geometries and necessity of overlapped positioning. With all this in mind, a new systematic tool design is required to produce sound welds for different polymeric materials, thicknesses and configurations.

4.2 Friction stir welding (FSW)

As mentioned earlier in this chapter, the conventional FSW tool consists of a rotating probe attached to a cylindrical shoulder with a larger diameter. Using this tool, most of the frictional heat is generated by the rotating shoulder on top of the plate's surface, while the probe stirs the plasticized materials under the applied axial force. In order to analyze the weld strength using a conventional welding tool, different polymers were tested and analyzed. Some of the tested materials using conventional friction stir welding tools are: PP [101,102], PE [103], PA6 [6,104], PVC [6,105], Polycarbonate (PC) [106] and PMMA [107].

One of the main conclusions from the preliminary experiments using conventional FSW tool is the importance of the probe geometry on the heat generation, material flow and weld strength. It was verified that the probe geometry and length have significant effect on the weld quality, and compensating the shortness of the probe by applying more axial force, leads to formation of flash defects [108]. Another aspect of the probe design that needs to be considered is the probe tip geometry, which is preferred to be threaded [108] or grooved [109] in order to stir the materials properly. However, using a FSW conventional tool for welding polymers showed some difficulties. To avoid the flash defect, the soft materials cannot be subjected to an adequate axial force, consequently, lack of frictional heat occurs, and low thermal conductivity and the friction coefficient of polymers magnifies this issue.

To solve the insufficient heat generation using rotating shoulder, some researchers attempted to weld polymers by adding an auxiliary heating source to compensate lack of heat [110]. It was stated that in order to reach to the desired temperature, it is necessary to heat up the parent materials, rather than heating the welding tool directly. Using a hot plate at the bottom of the parent materials as an additional heat source created very strong welds, yet the lack of repeatability was the main drawback of using this tool and method. From the initial experimental test, it was concluded that the conventional FSW tools may not be suitable for welding polymeric materials due to the flash defect formation and inadequate frictional heat [111]. Tensile strength of the joints is normally low and mostly affected by the probe geometry, welding speed and axial force, which causes the formation of defects in weld seams.

Applying FSW for joining thermoplastic composites requires even further studies and tool developments. FSW is not suitable to join long fiber composites as the fibers will be damaged or cut during this process, which affects the structural integrity of the joint. On the other hand, short fiber thermoplastics are a good option to use FSW as a joining method. In Ref. [112] a technical solution to weld short fiber thermoplastics was patented. It was verified that randomly distributed short fibers composites can be welded such that an average volume fraction of the reinforcing fibers within the joint path is substantially the same as an average volume fraction thereof in remainder of the members [112].

In a different approach, the possibility of manufacturing Carbon Fiber Reinforced Plastic (CFRP) and PC hybrid joints was studied [113]. In this method, the probe fully penetrates the top plate, which is PC and small penetration occurs on the CFRP plate to remove a thin ply of the CFRP and replace the epoxy with the plasticized polymer under the axial force. It is stated that the joint quality significantly is influenced by the tool's plunging depth, which is responsible for a good adhesion between the PC and the first ply of fibers. This method showed promising results and further investigations is required regarding the tool design and optimize parameters.

As the previous studies have shown, for welding polymeric materials, the most effective welding parameters are dependent on the tool design and geometry. Using the conventional FSW tool limits the effective welding parameters that can be used in order to generate enough heat and avoid the flash defect. However, it is hard to obtain quality welds with a great repeatability using conventional FSW tool, due to ejection of the plasticized material out of the stir zone. To avoid this unwanted behavior, stationary shoulder is a good alternative to push the material down, avoiding formation of flash defect [93], however, with absence of a rotating shoulder, heat generation is reduced drastically.

4.3 Stationary shoulder friction stir welding (SSFSW)

Since the tool plays a fundamental role in the FSW process, the development of a new systematic tool design for polymeric materials is considered a topic that must be addressed with great care. As mentioned earlier, it is difficult to weld polymers with good surface quality and mechanical properties [111]. Several studies concluded that the conventional rotating shoulder FSW tool pushes the soft material out of the stirring zone [83,109]. This material loss is responsible for poor material flow and produces weak joints compared to the parent material's tensile strength.

With absence of a rotary shoulder, the probe generates all the frictional heat, which is unable to generate adequate heat alone. To compensate the lack of the heat generation, a different approach regarding the tool design is required. Nelson developed and patented a stationary shoulder welding tool called "hot shoe" [83]. The patented schematic of the welding tool is presented in Fig. 5.13A, and consists of a stationary shoulder made of aluminum and coated with Polytetrafluoroethylene (PTFE), in order to avoid flash defect by blocking the material flow out of the stirring zone. The static shoulder equipped with a ball bearing, forces the soft materials into the weld nugget under the shoe's axial force. A heater and a thermocouple were placed inside the aluminum shoe with the intention of measuring and controlling the applied additional heat. The "shoe" is mainly responsible for trapping the soft material inside the stirring zone and holding under the axial force, as it begins to cool down.

After the hot shoe patent, several researchers investigated different polymers and configurations using the hot shoe concept in order to optimize and evaluate the effect of this tool on the weld quality [103,114,115]. An example of a customized version of hot shoe tool is presented Fig. 5.13B. This tool creates strong welds with excellent surface quality and repeatability. The input temperature and probe geometry of the tool can be modified regarding the base material's melting point, thickness and joint configurations. As mentioned above, different materials (HDPE, PP and ABS) successfully welded together with the joint characteristics close to the parent materials.

There are different approaches regarding the tool design in the literature, using stationary shoulder equipped with an external heat source. Those tools were able to produce sound welds, however they have complex geometries, which require thermocouples to monitor and control the additional heat applied during the process. This is a drawback for FSW, as one of the most significant factors of this technology is being a simple, cost-effective and green process.

A new tool concept (Fig. 5.14) was developed and tested, with the purpose of developing a new welding tool, capable of producing quality welds without an additional heat source [109]. It stated that for welding polymers, a stationary shoulder proved to be an essential factor, and to compensate the lack of frictional heat due to the absence of a rotary shoulder, a copper sleeve was added around the rotating probe. The probe's rotation and its axial force inside the copper sleeve generated enough heat to plasticize the base material. Similar and dissimilar polymers were tested using this tool concept [116]. Using this tool, the dwell time is critical to heat up the copper sleeve before advancing. After testing several shoulder

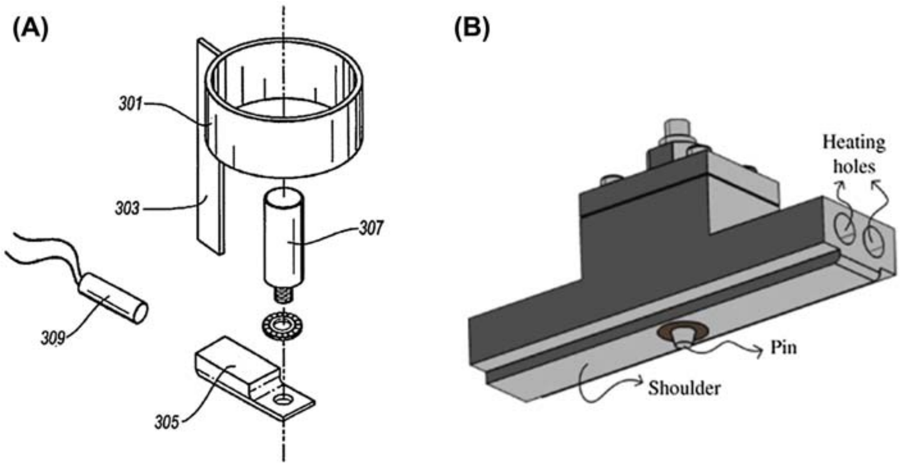

FIG. 5.13 Welding tool for thermoplastics. (A) the patented "hot shoe" [83], (B) the modified welding tool using the same concept [105].

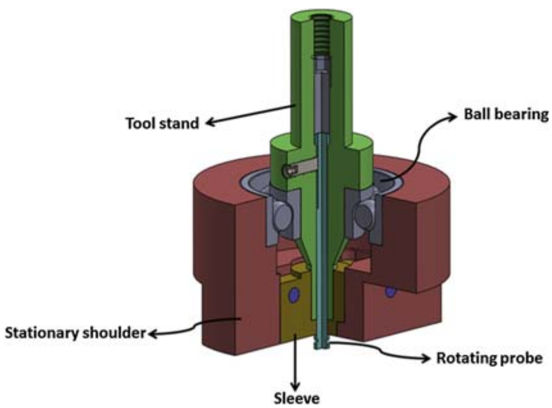

FIG. 5.14 FSW tool without an external heat source [118].

materials, it claimed that PTFE and PEEK are the best options for stationary shoulder as they produce excellent surface quality. The tool shows in Fig. 5.14 is able to generate frictional heat up to 400 °C and produce joints with a tensile strength within 97% of the base material's UTS.

The fatigue life of FSW lap-jointed specimens was compared to the riveted joints using the same tool concept as shown in Fig. 5.14. Although the double-riveted specimens presented the highest shear strength when compared to the FS welded specimens, its fatigue life found to be similar to the FSW produced joints, due to the thermal fatigue failure of double riveting. Using the same testing frequency (25 Hz), the FS joints failed on the retreating side and were not subjected to thermal damage [117].

Regardless of the tool design, the main difference between FSW of polymers and metallic ones is the welding states and necessary welding temperature. Unlike metallic materials, polymer FSW is not an absolute solid-state welding process, since for obtaining sound welds the welding temperature must reach above the parent materials' melting points [115,119].

With the appropriate tool design and judicious parameters, FSW can produce strong welds with good mechanical properties to weld a wide range of similar/dissimilar polymeric materials in different configurations [85]. The most effective parameters on the weld quality are mainly those related to the tool design and their interactions. After the tool design, rotational speed and welding speed are the most influential factors to generate adequate frictional heat. The ratio of rotational speed and welding speed should be chosen in a way that the welding tool is able to generate enough heat to plasticize the material, as well as having enough time for the probe to stir the materials while the tool is advancing. In addition, the axial force is an essential element during this welding process, which is responsible for the heat generation and forging. Mainly, the rotational and welding speeds have the main effect on the lateral and traversing forces, respectively.

FSW technology is a highly adaptable welding technique with ability to weld dissimilar materials in different configurations without the limitations of traditional welding methods. By selecting the right tool and suitable welding parameters, FSW is capable of producing sound welds for composites and polymeric materials.

5. FSW hybridization

As a way of incorporating the advantages brought forward by adhesive bonding and to overcome their limitations, adhesive bonding has been applied in conjunction with other joining methods, resulting in hybrid joining techniques. The broad range of mechanical and chemical characteristics of structural adhesives as well as their ability to bond dissimilar materials as allowed the combination of adhesive bonding with various other joining technologies.

Combining welding methods with adhesive bonding (weld-bonding) has been a more promising field of technology from industrial application perspective as well as from research point of view, with higher number and more recent research performed in this field. The original development of weld-bonding is reported to have been done in the USSR for the type AN-24 aircraft [120]. The method developed, relied in performing resistance spot welding first and then applying a low viscosity adhesive in the overlap interface. This approach is called "flow-in" method. By combining welding and adhesive bonding, structural designers

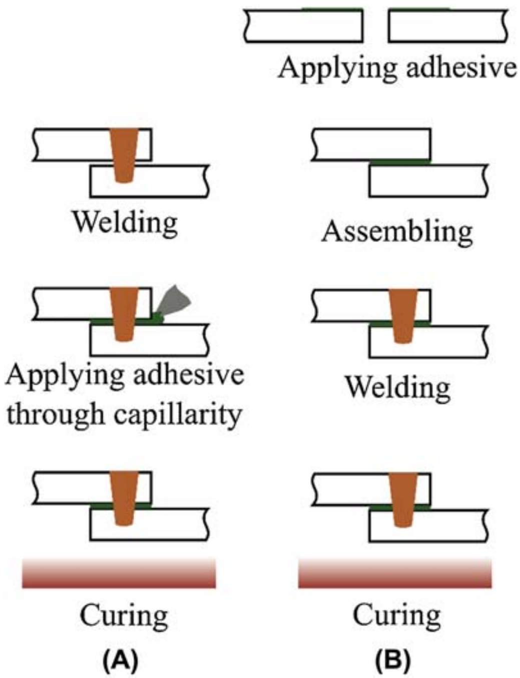

FIG. 5.15 Weld-bonding in (A) flow-in method and (B) weld-through technique.

achieved the following benefits when compared to conventional fastening techniques: (i) reduced manufacturing costs and adaptability to mechanization; (ii) high static strength; (iii) improved fatigue strength; (iv) improved corrosion resistance; (v) the elimination of sealing operations; and (vi) the elimination of the shop noise of riveting. The "flow-in" method is highly laborious and as such not suitable for mass production. As such, an alternative approach was developed where the adhesive bonding was performed first followed by the welding procedure. This approach is called the "weld-through" method. Both techniques are schematically presented in Fig. 5.15.

The general reasons behind the addition of adhesive bonding to welding processes are the following:

- Combining different mechanical properties in one joint (e.g. high ductility and strength);
- Capability of carrying different simultaneous loads in the joint (e.g. shear and peel);
- Damage tolerance (ability to carry load and not fail catastrophically even if part of the joint fails);
- Improved fatigue strength and life;
- Reduced noise and vibration dampening (improving noise vibration and harshness (NVH) in vehicles);
- Corrosion resistance (the adhesive serving as a sealant).

Friction stir welding, is a relatively more recent joining technology, and as such the combination of it with adhesive has not yet been as extensively studied as other fusion welding techniques. Studies on friction stir weld-bonding (hybrid friction stir welding and adhesive bonding) are scarce and recent. Chowdhury et al. in Ref. [121] studied friction stir spot welding (FSSW) with adhesive to joint dissimilar magnesium aluminum joints. Two millimeter AZ31B-H24 and AA5754-O were joined together using FSSW in three different combinations, (top)Al/Mg (bottom), Al/Mg with an adhesive interlayer, and Mg/Al with an adhesive interlayer. The adhesive used (Terokal® 5089) was an epoxy based one component adhesive and was cured at 170 °C for 20 min before welding. Welding these dissimilar materials resulted in the formation of hard intermetallic compounds (IMCs), such as Al, Mg and AlMg.

In the case of the Al/Mg weld these IMC covered most of the boundary but the thickness of the interfacial layer varied, while in the Mg/Al with adhesive weld the adhesive was present in the interfacial layer with IMC remnants. The larger presence of these IMC and the increased bonded area from the addition of the adhesive resulted in significantly improved mechanical performance, both in quasi-static lap joint tensile testing as well as in cyclic loading ($R = 0.2$), as shown in Fig. 5.16. The improvement in mechanical performance between Al/Mg with adhesive and Mg/Al with adhesive were due to lower melting point of the Mg when compared to the Al which resulted in the former softening more with the process temperature and as such penetrating further in the lower plate, causing more interlocking. The failure mode also varied between welds without adhesive with nugget debonding and welds with adhesive with nugget pull-out failure. This difference in failure mode was attributed to the IMC layer as it is much more fragile than the base materials. The same trend observed in quasi-static loading was observed in the cyclic loading tests, with the adhesive layer eliminating the stress concentration surrounding the weld along with the less predominant presence of IMC mentioned before. The failure mode was mainly similar to the one observed in quasi-static but some specimens failed perpendicular to the loading direction.

The use of polymer films as adhesives has also been studied in refill friction stir spot welding (rFSSW) in Ref. [122]. A PPS film interlayer was used in rFSSW of 2 mm thick aluminum

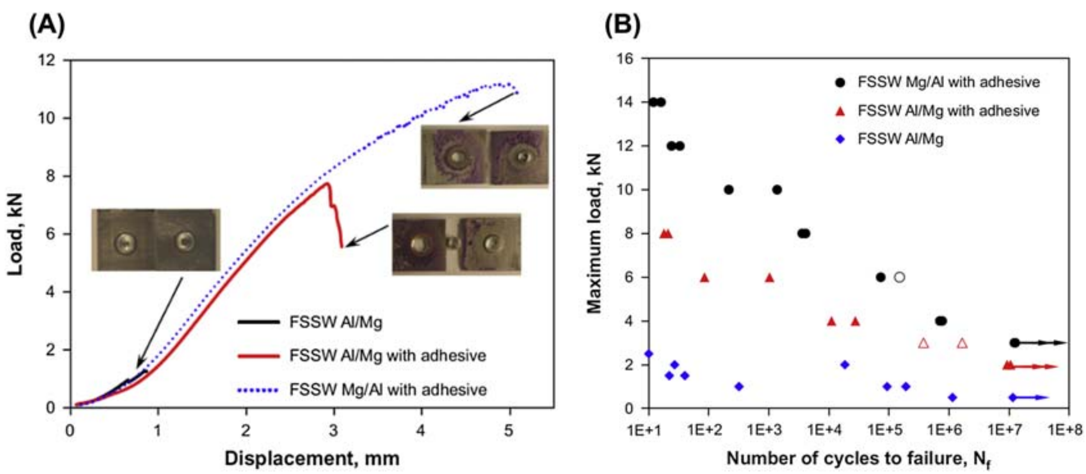

FIG. 5.16 Comparison of quasi-static lap joint tensile (A) and cyclic lap joint tensile (B) between dissimilar aluminum and magnesium joints with and without adhesive [121].

alloy AA2024-T3 and 2.17 mm thick carbon-fiber-reinforced poly (phenylene sulfide) laminate. Two parameters set were used, designated as low heat input and high heat input, relating to energy generated in the joint from the friction joining process. The use of the PPS film resulted in an increase of ultimate lap shear strength of about 55% for the low heat input condition. The higher heat input condition resulted in a decrease of the PPS film viscosity and as such allowed the film to be squeezed out as flash and as such not contributing as much to the mechanical performance of the joint. In this case the improvement in strength was of about 20%. The improvements in mechanical performance with the addition of the PPS film were due to larger bonding area (59,0 $\pm$ 50 mm^2 compared to 355 $\pm$ 10 mm^2 with low heat input condition), as well as better load distribution from the hybrid joining mechanism. The failure surfaces also demonstrated improved micromechanical interlocking between the CFRP and the aluminum when using a PPS film interlayer.

A different approach to friction stir weld-bonding was presented in Ref. [123]. In this study friction stir welding was used to improve mechanical interlocking between adhesive bonded aluminum and carbon fiber reinforced polymer. This approach varies from conventional weld-bonding techniques as in these the goal usually is to improve the mechanical properties of the welded joint by adding adhesive bonding. Joining aluminum sheets and CFRP is challenging as they have very different physical-chemical properties, and as mainly been achieved through adhesive bonding and fastening. As alternative to these joining methods some welding processes were proposed and was found that achieving significant infiltration of aluminum around the fibers in these processes would result in improved mechanical performance. As such, the authors proposed using an FSW tool to promote heating of the bond area and promote softening of the aluminum. With varying parameters (spindle speed, welding speed and pin penetration) the authors found that just outside the destructive zone of stirring there lies a region where plasticized aluminum will infiltrate the carbon fibers yet leave them intact. Carbon fibers processed in such a region and remaining in the direction they were processed. The resin of the CFRP and the softened aluminum act as an adhesive layer in the interface of the two sheets. An infiltration of about 3 layers of carbon filaments (17 μm) was achieved and correlated well with the resin transfer molding model used to predict it.

Even though studies on friction stir weld-bonding (continuous welding instead of spot joining) are scarce, industrial entities have demonstrated interest in the process, which shows in patent applications. Christner in Ref. [124] proposed using a sealant/adhesive within surfaces of components to be friction stir welded, as seen in Fig. 5.17. In this invention the main purpose of the polymer material added in the welding is to protect the welded joints from corrosion. The example of welding stringer to skin using this invention is given in the patent. The effect of sealants in FSSW was also studied in Ref. [125]. Mechanical properties and corrosion resistance of joints performed with this technology were evaluated. The PRC-DeSoto PR-1432 GP sealant, a 2 part dichromate polysulfide compound was used in FSSW of 1 mm thick AA2024-T3. The use of sealants was found to increase the joint strength but at the cost of increased scatter in the results. An improvement in joint strength was also found when compared with riveted coupons, as these only showed to have 44% of the strength of the FSSW with adhesive coupons. Corrosion resistance was also tested with exposure to a controlled environment followed by lap joint tensile testing. The sealant within the FSSW showed to protect the joint by maintaining the same ultimate strength after corrosion exposure, especially when appropriate surface treatment processes were used.

Talwar in Ref. [126], proposed a method to join work-pieced by friction stir welding with and adhesive between at least two workpieces, see Fig. 5.18. The invention comprises both continuous FSW as well as friction stir spot welding with adhesive.

In Ref. [127] a method for weld-bonding together metal sheets with an adhesive in between the sheets and with a cooling apparatus to avoid degrading the adhesive bond was developed. An example proposed in the patent, where it is possible to see the welding and adhesive bonding along with the tool with the cooling apparatus, is shown in Fig. 5.19. The invention proposes a cooling solution implemented in the tool that cools the surrounding material to the weld. This way the high temperatures required for sound welding are contained in the weld region and avoid degradation of the adhesive. Through this method the authors intend to avoid the need for distancing the welds or the increase of adhesive that is used to compensate the effect of the degraded adhesive.

The combination of friction stir welding and adhesive bonding into friction stir weld-bonding was studied for alloys AA6082-T6 [128,129] and AA2024-T3 [130]. In these studies, a two-part epoxy adhesive was used, and quasi-static and fatigue strength were assessed. Joint efficiency in quasi-static loading was significantly improved, with overlap FSW having a maximum of ≈62.8% for AA6082-T6 and ≈76.2% for AA2024-T3, while FS weld-bonding joints had ≈95% for AA6082-T6 and ≈90% for AA2024-T3. Beyond the improvement in joint

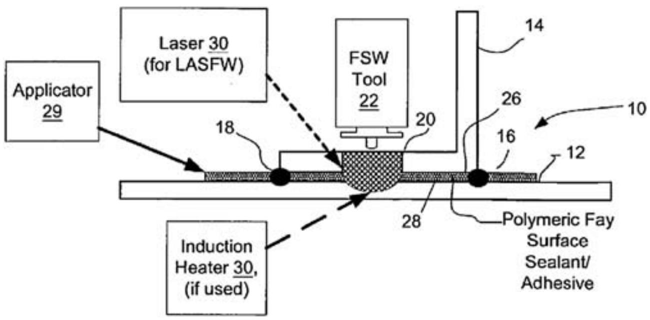

FIG. 5.17 Scheme of FSW with sealant proposed in the invention [124].

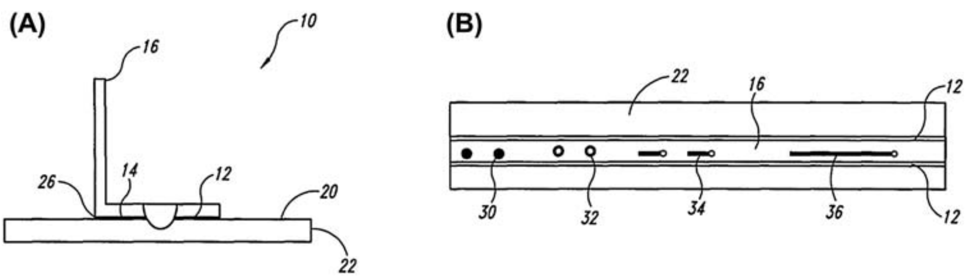

FIG. 5.18 Cross sectional (A) and top view (B) of join described in the invention [126].

strength and ductility it was also found that joint performance of overlap FSW joints was very dependent on FSW process parameters while FS weld-bonded joints mechanical performance was more dependent on bonding strength, especially surface quality, as seen in Fig. 5.20.

Similar improvement was found regarding fatigue strength with FS weld-bonding joints outperforming overlap FSW joints.

Beyond metal alloys, FS weld-bonding has been used to joint polymer materials, namely high density polyethylene (HDPE) [131]. It was found that by adding the adhesive layer

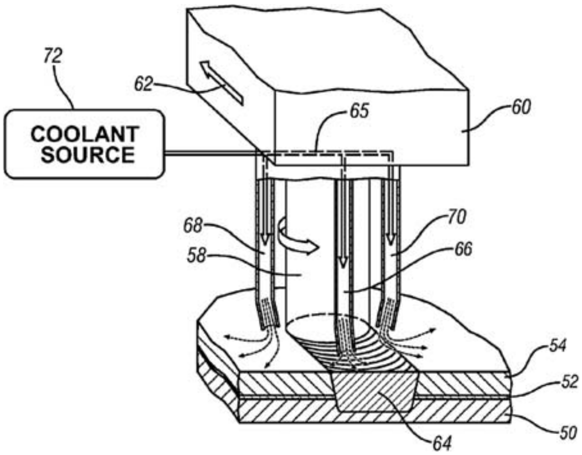

FIG. 5.19 Example of weld-bonding as described in the invention [127].

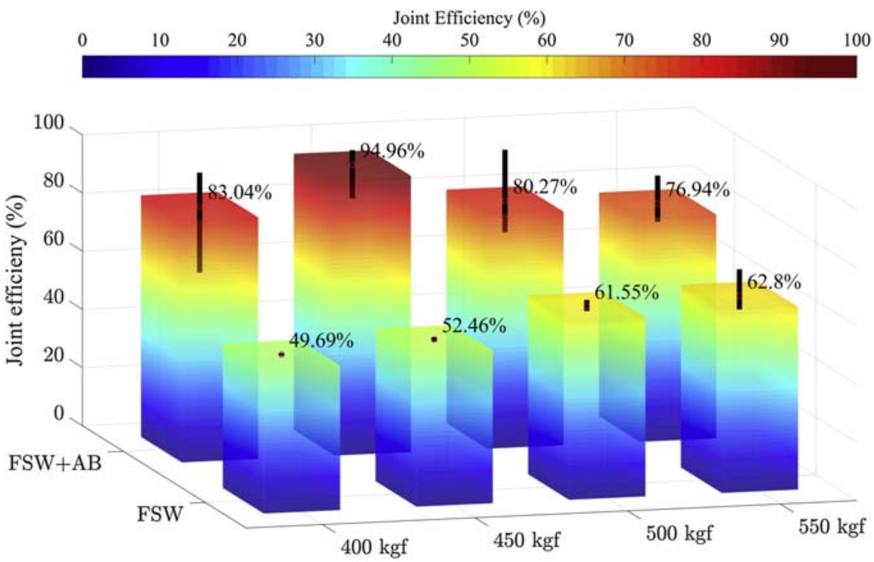

FIG. 5.20 Quasi-static joint efficiency with varying plunging force for FSW overlap and FS weld-bonded joints [129].

onto the overlap FSSW, stress gradients around the weld zone were reduced, which increases the load carrying capacity of the joint. This effect was verified through numerical modeling of the joints. Failure load in quasi-static loading was improved by 34%.

6. Conclusions

FSW has developed significantly, since its introduction in the early 1990's, being now capable of joining evermore materials and its combinations. The solid-state nature of the joining process is the driver of its advantages; as the joining process occurs at lower temperatures, there is less heat input so the process is generally energy efficient and generates high strength joints with low levels of distortion and residual stresses. Microstructural changes occur as a combined effect of the heat input and plastic deformation. Fatigue strength and life is also shown to be higher than other conventional fusion processes, given the lower level of defects and smaller affected zones. The development of FSW for other materials has required the development of new tools, clamping devices and has put other requirements onto to the machines themselves. In some of these cases the parameters process window is relatively narrow and requires significant research effort to assure consistent defect free welds.

References

[1] W.M. Thomas, E.D. Nicholas, J.C. Needham, M.G. Murch, P. Temple-Smith, C.J. Dawes, Friction Welding, Google Patents, 1995.
[2] R.S. Mishra, M.W. Mahoney, S.X. McFadden, N.A. Mara, A.K. Mukherjee, High strain rate superplasticity in a friction stir processed 7075 Al alloy, Scripta Materialia 42 (2) (1999) 163−168, https://doi.org/10.1016/S1359-6462(99)00329-2.
[3] N. Balasubramanian, R.S. Mishra, K. Krishnamurthy, Friction stir channeling: characterization of the channels, Journal of Materials Processing Technology 209 (8) (2009) 3696−3704, https://doi.org/10.1016/j.jmatprotec.2008.08.036.
[4] TWI, Structural Thermal Management by Friction Stir Channeling, 2019.
[5] B.J. Phillips, et al., Microstructure-deformation relationship of additive friction stir-deposition Al−Mg−Si, Materialia 7 (2019) 100387, https://doi.org/10.1016/j.mtla.2019.100387.
[6] R.S. Mishra, Z.Y. Ma, Friction stir welding and processing, Materials Science and Engineering: R: Reports 50 (1) (2005) 1−78, https://doi.org/10.1016/j.mser.2005.07.001.
[7] A.L. Etter, T. Baudin, N. Fredj, R. Penelle, Recrystallization mechanisms in 5251 H14 and 5251 O aluminum friction stir welds, Materials Science and Engineering: A 445−446 (2007) 94−99, https://doi.org/10.1016/j.msea.2006.09.036.
[8] G. Çam, S. Güçlüer, A. Çakan, H.T. Serindag, Mechanical properties of friction stir butt-welded Al-5086 H32 plate, Materialwissenschaft und Werkstofftechnik 40 (8) (2009) 638−642, https://doi.org/10.1002/mawe.200800455.
[9] Y.S. Sato, H. Kokawa, Distribution of tensile property and microstructure in friction stir weld of 6063 aluminum, Metallurgical and Materials Transactions A 32 (12) (2001) 3023−3031, https://doi.org/10.1007/s11661-001-0177-8.
[10] A.H. Baghdadi, A. Rajabi, N.F.M. Selamat, Z. Sajuri, M.Z. Omar, Effect of post-weld heat treatment on the mechanical behavior and dislocation density of friction stir welded Al6061, Materials Science and Engineering: A 754 (2019) 728−734, https://doi.org/10.1016/j.msea.2019.03.017.
[11] M.A. Safarkhanian, M. Goodarzi, S.M.A. Boutorabi, Effect of abnormal grain growth on tensile strength of Al−Cu−Mg alloy friction stir welded joints, Journal of Materials Science 44 (20) (2009) 5452−5458, https://doi.org/10.1007/s10853-009-3735-x.

[12] H. Aydın, A. Bayram, İ. Durgun, The effect of post-weld heat treatment on the mechanical properties of 2024-T4 friction stir-welded joints, Materials & Design (1980-2015) 31 (5) (2010) 2568−2577, https://doi.org/10.1016/j.matdes.2009.11.030.

[13] Y. Chen, H. Liu, J. Feng, Effect of post-weld heat treatment on the mechanical properties of 2219-O friction stir welded joints, Journal of Materials Science 41 (1) (2006) 297−299.

[14] K. Elangovan, V. Balasubramanian, Influences of post-weld heat treatment on tensile properties of friction stir-welded AA6061 aluminum alloy joints, Materials Characterization 59 (9) (2008) 1168−1177, https://doi.org/10.1016/j.matchar.2007.09.006.

[15] G. İpekoğlu, S. Erim, G. Çam, Investigation into the influence of post-weld heat treatment on the friction stir welded AA6061 Al-alloy plates with different temper conditions, Metallurgical and Materials Transactions A 45 (2) (2014) 864−877, https://doi.org/10.1007/s11661-013-2026-y.

[16] E.A. El-Danaf, M.M. El-Rayes, Microstructure and mechanical properties of friction stir welded 6082 AA in as welded and post weld heat treated conditions, Materials & Design 46 (2013) 561−572, https://doi.org/10.1016/j.matdes.2012.10.047.

[17] M.I. Costa, C. Leitão, D.M. Rodrigues, Influence of post-welding heat-treatment on the monotonic and fatigue strength of 6082-T6 friction stir lap welds, Journal of Materials Processing Technology 250 (2017) 289−296, https://doi.org/10.1016/j.jmatprotec.2017.07.030.

[18] G. İpekoğlu, S. Erim, G. Çam, Effects of temper condition and post weld heat treatment on the microstructure and mechanical properties of friction stir butt-welded AA7075 Al alloy plates, The International Journal of Advanced Manufacturing Technology 70 (1) (2014) 201−213, https://doi.org/10.1007/s00170-013-5255-8.

[19] S.M. Bayazid, H. Farhangi, H. Asgharzadeh, L. Radan, A. Ghahramani, A. Mirhaji, Effect of cyclic solution treatment on microstructure and mechanical properties of friction stir welded 7075 Al alloy, Materials Science and Engineering: A 649 (2016) 293−300, https://doi.org/10.1016/j.msea.2015.10.010.

[20] G. İpekoğlu, G. Çam, Effects of initial temper condition and postweld heat treatment on the properties of dissimilar friction-stir-welded joints between AA7075 and AA6061 aluminum alloys, Metallurgical and Materials Transactions A 45 (7) (2014) 3074−3087, https://doi.org/10.1007/s11661-014-2248-7.

[21] P.M.G.P. Moreira, M.A.V. de Figueiredo, P.M.S.T. de Castro, Fatigue behaviour of FSW and MIG weldments for two aluminium alloys, Theoretical and Applied Fracture Mechanics 48 (2) (2007) 169−177, https://doi.org/10.1016/j.tafmec.2007.06.001.

[22] M. Ericsson, R. Sandström, Influence of welding speed on the fatigue of friction stir welds, and comparison with MIG and TIG, International Journal of Fatigue 25 (12) (2003) 1379−1387, https://doi.org/10.1016/S0142-1123(03)00059-8.

[23] C.D. Donne, G. Biallas, T. Ghidini, G. Raimbeaux, in: Proceedings of the International Conference on Jointing of Advanced and Specialty Materials III, ASM International, 2000.

[24] L. Fratini, S. Pasta, A.P. Reynolds, Fatigue crack growth in 2024-T351 friction stir welded joints: longitudinal residual stress and microstructural effects, International Journal of Fatigue 31 (3) (2009) 495−500, https://doi.org/10.1016/j.ijfatigue.2008.05.004.

[25] P.M.G.P. Moreira, A.M.P. de Jesus, A.S. Ribeiro, P.M.S.T. de Castro, Fatigue crack growth in friction stir welds of 6082-T6 and 6061-T6 aluminium alloys: a comparison, Theoretical and Applied Fracture Mechanics 50 (2) (2008) 81−91, https://doi.org/10.1016/j.tafmec.2008.07.007.

[26] V. Richter-Trummer, P.M.G.P. Moreira, J. Ribeiro, P.M.S.T. de Castro, The contour method for residual stress determination applied to an AA6082-T6 friction stir butt weld, in: Materials Science Forum, vol. 681, Trans. Tech. Publ., 2011, pp. 177−181.

[27] M.B. Prime, T. Gnäupel-Herold, J.A. Baumann, R.J. Lederich, D.M. Bowden, R.J. Sebring, Residual stress measurements in a thick, dissimilar aluminum alloy friction stir weld, Acta Materialia 54 (15) (2006) 4013−4021, https://doi.org/10.1016/j.actamat.2006.04.034.

[28] A. Lanciotti, et al., Fatigue crack growth in stiffened panels, integrally machined or welded(LBW or FSW): the DaToN project common testing program, Structural Durability & Health Monitoring 7 (3) (2011) 211−229.

[29] P.M.G.P. Moreira, Lightweight Stiffened Panels: Mechanical Characterization of Emerging Fabrication Technologies, Doctoral Degree in Mechanical Engineering PhD, Departamento de Engenharia Mecânica e Gestão Industrial, Faculdade de Engenharia da Universidade do Porto, 2008.

[30] K.M. Venkatesh, M. Arivarsu, M. Manikandan, N. Arivazhagan, Review on friction stir welding of steels, Materials Today: Proceedings 5 (5, Part 2) (2018) 13227−13235, https://doi.org/10.1016/j.matpr.2018.02.313.

[31] A.P. Reynolds, W. Tang, T. Gnaupel-Herold, H. Prask, Structure, properties, and residual stress of 304L stainless steel friction stir welds, Scripta Materialia 48 (9) (2003) 1289–1294, https://doi.org/10.1016/S1359-6462(03)00024-1.
[32] F.C. Liu, Y. Hovanski, M.P. Miles, C.D. Sorensen, T.W. Nelson, A review of friction stir welding of steels: tool, material flow, microstructure, and properties, Journal of Materials Science & Technology 34 (1) (2018) 39–57, https://doi.org/10.1016/j.jmst.2017.10.024.
[33] A. Kumar, et al., Research Progress on Friction Stir Welding of Pipeline Steels, 2010, https://doi.org/10.1115/IPC2010-31520. Available from:.
[34] C. Meran, V. Kovan, A. Alptekin, Friction stir welding of AISI 304 austenitic stainless steel, Materialwissenschaft und Werkstofftechnik 38 (10) (2007) 829–835, https://doi.org/10.1002/mawe.200700214.
[35] P.D. Edwards, M. Ramulu, Investigation of microstructure, surface and subsurface characteristics in titanium alloy friction stir welds of varied thicknesses, Science and Technology of Welding & Joining 14 (5) (2009) 476–483, https://doi.org/10.1179/136217109X425838.
[36] A. Heidarzadeh, P. Asadi, Microstructural evolution, in: M.-K. Besharati-Givi, P. Asadi (Eds.), Advances in Friction-Stir Welding and Processing, Elsevier, 2014.
[37] P. Baillie, S.W. Campbell, A.M. Galloway, S.R. Cater, N.A. McPherson, Friction stir welding of 6 mm thick carbon steel underwater and in air, Science and Technology of Welding & Joining 20 (7) (2015) 585–593, https://doi.org/10.1179/1362171815Y.0000000042.
[38] A.P. Reynolds, W. Tang, M. Posada, J. Deloach, Friction stir welding of DH36 steel, Science and Technology of Welding & Joining 8 (6) (2003) 455–460, https://doi.org/10.1179/136217103225009125.
[39] H. Fujii, L. Cui, N. Tsuji, M. Maeda, K. Nakata, K. Nogi, Friction stir welding of carbon steels, Materials Science and Engineering: A 429 (1) (2006) 50–57, https://doi.org/10.1016/j.msea.2006.04.118.
[40] Y.S. Sato, H. Yamanoi, H. Kokawa, T. Furuhara, Microstructural evolution of ultrahigh carbon steel during friction stir welding, Scripta Materialia 57 (6) (2007) 557–560, https://doi.org/10.1016/j.scriptamat.2007.04.050.
[41] Y.D. Chung, H. Fujii, R. Ueji, N. Tsuji, Friction stir welding of high carbon steel with excellent toughness and ductility, Scripta Materialia 63 (2) (2010) 223–226, https://doi.org/10.1016/j.scriptamat.2010.03.060.
[42] S. Emami, T. Saeid, A. Abdollah-zadeh, Effect of friction stir welding parameters on the microstructure and microtexture evolution of SAF 2205 stainless steel, Journal of Alloys and Compounds 810 (2019) 151797, https://doi.org/10.1016/j.jallcom.2019.151797.
[43] A.K. Lakshminarayanan, V. Balasubramanian, An assessment of microstructure, hardness, tensile and impact strength of friction stir welded ferritic stainless steel joints, Materials & Design 31 (10) (2010) 4592–4600, https://doi.org/10.1016/j.matdes.2010.05.049.
[44] S.H.C. Park, Y.S. Sato, H. Kokawa, K. Okamoto, S. Hirano, M. Inagaki, Rapid formation of the sigma phase in 304 stainless steel during friction stir welding, Scripta Materialia 49 (12) (2003) 1175–1180, https://doi.org/10.1016/j.scriptamat.2003.08.022.
[45] S.H.C. Park, Y.S. Sato, H. Kokawa, K. Okamoto, S. Hirano, M. Inagaki, Corrosion resistance of friction stir welded 304 stainless steel, Scripta Materialia 51 (2) (2004) 101–105, https://doi.org/10.1016/j.scriptamat.2004.04.001.
[46] M. Ghosh, K. Kumar, R.S. Mishra, Analysis of microstructural evolution during friction stir welding of ultrahigh-strength steel, Scripta Materialia 63 (8) (2010) 851–854, https://doi.org/10.1016/j.scriptamat.2010.06.032.
[47] Y. Hovanski, M.L. Santella, G.J. Grant, Friction stir spot welding of hot-stamped boron steel, Scripta Materialia 57 (9) (2007) 873–876, https://doi.org/10.1016/j.scriptamat.2007.06.060.
[48] S. Ragu Nathan, V. Balasubramanian, S. Malarvizhi, A.G. Rao, Effect of welding processes on mechanical and microstructural characteristics of high strength low alloy naval grade steel joints, Defence Technology 11 (3) (2015) 308–317, https://doi.org/10.1016/j.dt.2015.06.001.
[49] T.W. Nelson, S.A. Rose, Controlling hard zone formation in friction stir processed HSLA steel, Journal of Materials Processing Technology 231 (2016) 66–74, https://doi.org/10.1016/j.jmatprotec.2015.12.013.
[50] J. Wang, W. Yuan, R.S. Mishra, I. Charit, An evaluation of creep behaviour in friction stir welded MA754 alloy, Journal of Materials Engineering and Performance 23 (9) (2014) 3159–3164, https://doi.org/10.1007/s11665-014-1092-7.
[51] B.W. Baker, T.R. McNelley, L.N. Brewer, Grain size and particle dispersion effects on the tensile behavior of friction stir welded MA956 oxide dispersion strengthened steel from low to elevated temperatures, Materials Science and Engineering: A 589 (2014) 217–227, https://doi.org/10.1016/j.msea.2013.09.092.

[52] L.H. Wu, D. Wang, B.L. Xiao, Z.Y. Ma, Tool wear and its effect on microstructure and properties of friction stir processed Ti−6Al−4V, Materials Chemistry and Physics 146 (3) (2014) 512−522, https://doi.org/10.1016/j.matchemphys.2014.04.002.
[53] S. Mironov, Y.S. Sato, H. Kokawa, Friction-stir welding and processing of Ti-6Al-4V titanium alloy: a review, Journal of Materials Science & Technology 34 (1) (2018) 58−72, https://doi.org/10.1016/j.jmst.2017.10.018.
[54] A. Fall, M.H. Fesharaki, A.R. Khodabandeh, M. Jahazi, Tool wear characteristics and effect on microstructure in Ti-6Al-4V friction stir welded joints, Metals 6 (11) (2016) 275.
[55] A. Farias, G.F. Batalha, E.F. Prados, R. Magnabosco, S. Delijaicov, Tool wear evaluations in friction stir processing of commercial titanium Ti−6Al−4V, Wear 302 (1) (2013) 1327−1333, https://doi.org/10.1016/j.wear.2012.10.025.
[56] P. Edwards, M. Ramulu, Effect of process conditions on superplastic forming behaviour in Ti−6Al−4V friction stir welds, Science and Technology of Welding & Joining 14 (7) (2009) 669−680, https://doi.org/10.1179/136217109X12464549883330.
[57] A. Steuwer, D.G. Hattingh, M.N. James, U. Singh, T. Buslaps, Residual stresses, microstructure and tensile properties in Ti−6Al−4V friction stir welds, Science and Technology of Welding & Joining 17 (7) (2012) 525−533, https://doi.org/10.1179/136217112X13439160184196.
[58] P. Edwards, M. Ramulu, Identification of process parameters for friction stir welding Ti−6Al−4V, Journal of Engineering Materials and Technology 132 (3) (2010), https://doi.org/10.1115/1.4001302.
[59] S. Ji, Z. Li, L. Zhang, Y. Wang, Eliminating the tearing defect in Ti-6Al-4V alloy joint by back heating assisted friction stir welding, Materials Letters 188 (2017) 21−24, https://doi.org/10.1016/j.matlet.2016.10.032.
[60] A. Lauro, Friction stir welding of titanium alloys, Welding International 26 (1) (2012) 8−21, https://doi.org/10.1080/09507116.2011.581351.
[61] S. Ji, Z. Li, Y. Wang, L. Ma, Joint formation and mechanical properties of back heating assisted friction stir welded Ti−6Al−4V alloy, Materials & Design 113 (2017) 37−46, https://doi.org/10.1016/j.matdes.2016.10.012.
[62] L. Fratini, F. Micari, G. Buffa, V.F. Ruisi, A new fixture for FSW processes of titanium alloys, CIRP Annals 59 (1) (2010) 271−274, https://doi.org/10.1016/j.cirp.2010.03.003.
[63] D.G. Sanders, M. Ramulu, P.D. Edwards, A. Cantrell, Effects on the surface texture, superplastic forming, and fatigue performance of titanium 6AL-4V friction stir welds, Journal of Materials Engineering and Performance 19 (4) (2010) 503−509, https://doi.org/10.1007/s11665-010-9614-4.
[64] K. Reshad Seighalani, M.K. Besharati Givi, A.M. Nasiri, P. Bahemmat, Investigations on the effects of the tool material, geometry, and tilt angle on friction stir welding of pure titanium, Journal of Materials Engineering and Performance 19 (7) (2010) 955−962, https://doi.org/10.1007/s11665-009-9582-8.
[65] M.J. Fu, X.H. Li, X.Q. Han, H.Y. Xu, Research on work hardening type superplastic deformation behavior of FSW titanium alloy, in: Materials Science Forum, vol. 838, Trans. Tech. Publ., 2016, pp. 506−511.
[66] L. Zhou, H.J. Liu, Q.W. Liu, Effect of rotation speed on microstructure and mechanical properties of Ti−6Al−4 V friction stir welded joints, Materials & Design (1980−2015) 31 (5) (2010) 2631−2636, https://doi.org/10.1016/j.matdes.2009.12.014.
[67] P. Edwards, M. Ramulu, Surface residual stresses in Ti-6Al-4V friction stir welds: pre- and post-thermal stress relief, Journal of Materials Engineering and Performance 24 (9) (2015) 3263−3270, https://doi.org/10.1007/s11665-015-1610-2.
[68] H.-j. Liu, L. Zhou, Microstructural zones and tensile characteristics of friction stir welded joint of TC4 titanium alloy, Transactions of Nonferrous Metals Society of China 20 (10) (2010) 1873−1878, https://doi.org/10.1016/S1003-6326(09)60388-5.
[69] P.D. Edwards, Friction Stir Welding of Titanium-Aluminum-Vanadium Alloy Sheet and Plate for Aerospace Structures, University of Washington, 2010.
[70] G. Buffa, L. Fratini, M. Schneider, M. Merklein, Micro and macro mechanical characterization of friction stir welded Ti−6Al−4V lap joints through experiments and numerical simulation, Journal of Materials Processing Technology 213 (12) (2013) 2312−2322, https://doi.org/10.1016/j.jmatprotec.2013.07.003.
[71] M. Esmaily, S. Nooshin Mortazavi, P. Todehfalah, M. Rashidi, Microstructural characterization and formation of α′ martensite phase in Ti−6Al−4V alloy butt joints produced by friction stir and gas tungsten arc welding processes, Materials & Design 47 (2013) 143−150, https://doi.org/10.1016/j.matdes.2012.12.024.
[72] P. Edwards, M. Ramulu, Fatigue performance of Friction Stir Welded Ti−6Al−4V subjected to various post weld heat treatment temperatures, International Journal of Fatigue 75 (2015) 19−27, https://doi.org/10.1016/j.ijfatigue.2015.01.012.

[73] P.D. Edwards, M. Ramulu, Comparative study of fatigue and fracture in friction stir and electron beam welds of 24 mm thick titanium alloy Ti-6Al-4 V, Fatigue and Fracture of Engineering Materials and Structures 39 (10) (2016) 1226−1240, https://doi.org/10.1111/ffe.12434.
[74] S. Pasta, A.P. Reynolds, Residual stress effects on fatigue crack growth in a Ti-6Al-4V friction stir weld, Fatigue and Fracture of Engineering Materials and Structures 31 (7) (2008) 569−580, https://doi.org/10.1111/j.1460-2695.2008.01258.x.
[75] T.W. Nelson, C.D. Sorenson, C.J. Johns, Friction Stir Welding of Polymeric Materials, Google Patents, 2004.
[76] Y. Bozkurt, The optimization of friction stir welding process parameters to achieve maximum tensile strength in polyethylene sheets, Materials & Design 35 (2012) 440−445.
[77] F. Liu, J. Liao, K. Nakata, Joining of metal to plastic using friction lap welding, Materials & Design (1980-2015) 54 (2014) 236−244.
[78] S. Kumar, T. Medhi, B.S. Roy, Friction stir welding of thermoplastic composites, in: Advances in Industrial and Production Engineering, Springer, 2019, pp. 221−235.
[79] S.D. Thoppul, J. Finegan, R.F. Gibson, Mechanics of mechanically fastened joints in polymer−matrix composite structures−a review, Composites Science and Technology 69 (3-4) (2019) 301−329.
[80] R.C. Reinhardt, Method of Welding Thermoplastic Materials, Google Patents, 1940.
[81] M.J. Troughton, Handbook of Plastics Joining: A Practical Guide, William Andrew, 2008.
[82] P. Kah, R. Suoranta, J. Martikainen, C. Magnus, Techniques for joining dissimilar materials: metals and polymers, Reviews on Advanced Materials Science 36 (2) (2014).
[83] T.W. Nelson, C.D. Sorenson, C.J. Johns, Friction Stir Welding of Polymeric Materials, Patent 6,811,632, 2 Nov. 2004, 2004. Available from: https://www.google.pt./patents/US6811632.
[84] D.A. Grewell, A. Benatar, J.B. Park, Plastics and Composites Welding Handbook, München, 2003.
[85] S. Eslami, Friction Stir Welding of Polymers: An Innovative Technological Approach, 2019.
[86] R. Sakano, Development of spot FSW robo system for automobile body members, in: Proc. 3rd Int. Conf. Friction Stir Welding, Japan, TWI, 2001, 2001.
[87] Y.F. Sun, J.M. Shen, Y. Morisada, H. Fujii, Spot friction stir welding of low carbon steel plates preheated by high frequency induction, Materials & Design (1980-2015) 54 (2014) 450−457, https://doi.org/10.1016/j.matdes.2013.08.071.
[88] A. Paoletti, F. Lambiase, A. Di Ilio, Optimization of friction stir welding of thermoplastics, Procedia CIRP 33 (2015) 562−567, https://doi.org/10.1016/j.procir.2015.06.078.
[89] M.K. Bilici, A.İ. Yükler, Influence of tool geometry and process parameters on macrostructure and static strength in friction stir spot welded polyethylene sheets, Materials & Design 33 (2012) 145−152, https://doi.org/10.1016/j.matdes.2011.06.059.
[90] A. Bagheri, T. Azdast, A. Doniavi, An experimental study on mechanical properties of friction stir welded ABS sheets, Materials & Design 43 (2013) 402−409, https://doi.org/10.1016/j.matdes.2012.06.059.
[91] M.K. Bilici, Application of Taguchi approach to optimize friction stir spot welding parameters of polypropylene, Materials & Design 35 (2012) 113−119.
[92] P.H.F. Oliveira, S.T. Amancio, J.F. dos Santos, E. Hage, Preliminary study on the feasibility of friction spot welding in PMMA, Materials Letters 64 (19)) (2010) 2098−2101, https://doi.org/10.1016/j.matlet.2010.06.050.
[93] S.H. Dashatan, T. Azdast, S.R. Ahmadi, A. Bagheri, Friction stir spot welding of dissimilar polymethyl methacrylate and acrylonitrile butadiene styrene sheets, Materials & Design 45 (2013) 135−141, https://doi.org/10.1016/j.matdes.2012.08.071.
[94] R. Rai, A. De, H.K.D.H. Bhadeshia, T. DebRoy, Review: friction stir welding tools, Science and Technology of Welding & Joining 16 (4) (2011) 325−342, https://doi.org/10.1179/1362171811Y.0000000023.
[95] S. Amancio-Filho, M. Beyer, J. dos Santos, US 7.575. 149 B2: Method for Connecting a Metallic Bolt to a Plastic Piece, US patent, 2009.
[96] S. Amancio, Friction Riveting: Development and Analysis of a New Joining Technique for Polymer-Metal Multi-Materials Structures, GKSS-Forschungszentrum, 2007.
[97] J. Altmeyer, U. Suhuddin, J. Dos Santos, S. Amancio-Filho, Microstructure and mechanical performance of metal-composite hybrid joints produced by FricRiveting, Composites Part B: Engineering 81 (2015) 130−140.
[98] L. Blaga, R. Bancilă, J. dos Santos, S. Amancio-Filho, Friction Riveting of glass−fibre-reinforced polyetherimide composite and titanium grade 2 hybrid joints, Materials & Design 50 (2013) 825−829.
[99] F. Lambiase, A. Paoletti, Friction Assisted Joining of titanium and polyetheretherketone (PEEK) sheets, Thin-Walled Structures 130 (2018) 254−261.

[100] F. Lambiase, A. Paoletti, V. Grossi, A. Di Ilio, Friction assisted joining of aluminum and PVC sheets, Journal of Manufacturing Processes 29 (2017) 221–231.
[101] K. Panneerselvam, K. Lenin, Effects and defects of the polypropylene plate for different parameters in friction stir welding process, Taper 40 (2013) 1500.
[102] Z.C. Kiss, T. Czigány, Microscopic analysis of the morphology of seams in friction stir welded polypropylene, Express Polymer Letters 6 (1) (2012) 54–62, https://doi.org/10.3144/expresspolymlett.2012.6.
[103] E. Azarsa, A. Mostafapour, Experimental investigation on flexural behavior of friction stir welded high density polyethylene sheets, Journal of Manufacturing Processes 16 (1) (2014) 149–155, https://doi.org/10.1016/j.jmapro.2013.12.003.
[104] K. Panneerselvam, K. Lenin, Joining of Nylon 6 plate by friction stir welding process using threaded pin profile, Materials & Design 53 (2014) 302–307, https://doi.org/10.1016/j.matdes.2013.07.017.
[105] N. Mendes, A. Loureiro, C. Martins, P. Neto, J.N. Pires, Morphology and strength of acrylonitrile butadiene styrene welds performed by robotic friction stir welding, Materials & Design 64 (2014) 81–90, https://doi.org/10.1016/j.matdes.2014.07.047.
[106] M. Shazly, M. Ahmed, M. El-Raey, Friction stir welding of polycarbonate sheets, Characterization of Minerals, Metals, and Materials (2014) 555–563.
[107] F. Simões, D.M. Rodrigues, Material flow and thermo-mechanical conditions during Friction Stir Welding of polymers: literature review, experimental results and empirical analysis, Materials & Design 59 (2014) 344–351, https://doi.org/10.1016/j.matdes.2013.12.038.
[108] H. Ahmadi, N.B.M. Arab, F.A. Ghasemi, R.E. Farsani, Influence of pin profile on quality of friction stir lap welds in carbon fiber reinforced polypropylene composite, International Journal of Mechanics and Applications 2 (3) (2012) 24–28, https://doi.org/10.5923/j.mechanics.20120203.01.
[109] S. Eslami, T. Ramos, P.J. Tavares, P.M.G.P. Moreira, Shoulder design developments for FSW lap joints of dissimilar polymers, Journal of Manufacturing Processes 20 (Part 1) (2015) 15–23, https://doi.org/10.1016/j.jmapro.2015.09.013.
[110] E.A. Squeo, G. Bruno, A. Guglielmotti, F. Quadrini, Friction stir welding of polyethylene sheets, The Annals of Dunarea de Jos University of Galati, Technol. Machine Building 5 (2009) 241–246.
[111] A. Scialpi, M. Troughton, S. Andrews, L.A.C. De Filippis, Viblade™: friction stir welding for plastics, Welding International 23 (11) (2009) 46–855, https://doi.org/10.1080/09507110902843271.
[112] P.S. Manicke, E.C. Helder, Friction Stir Welding of Fiber Reinforced Thermoplastics, Google Patents, 2011.
[113] F. Lambiase, V. Grossi, A. Di Ilio, A. Paoletti, Feasibility of friction stir joining of polycarbonate to CFRP with thermosetting matrix, The International Journal of Advanced Manufacturing Technology (2019), https://doi.org/10.1007/s00170-019-04814-8.
[114] N. Mendes, P. Neto, M.A. Simão, A. Loureiro, J.N. Pires, A novel friction stir welding robotic platform: welding polymeric materials, The International Journal of Advanced Manufacturing Technology (2014), https://doi.org/10.1007/s00170-014-6024-z.
[115] S. R. Strand, Effects of friction stir welding on polymer microstructure.
[116] S. Eslami, M. de Figueiredo, P.J. Tavares, P. Moreira, Parameter optimisation of friction stir welded dissimilar polymers joints, The International Journal of Advanced Manufacturing Technology (2017) 1–12, https://doi.org/10.1007/s00170-017-0043-5.
[117] S. Eslami, B.V. Farahani, P.J. Tavares, P.M.G.P. Moreira, Fatigue behaviour evaluation of dissimilar polymer joints: friction stir welded, single and double-rivets, International Journal of Fatigue 113 (2018) 351–358, https://doi.org/10.1016/j.ijfatigue.2018.04.024.
[118] S. Eslami, L. Mourão, N. Viriato, P.J. Tavares, P.M.G.P. Moreira, Multi-axis force measurements of polymer friction stir welding, Journal of Materials Processing Technology 256 (2018) 51–56, https://doi.org/10.1016/j.jmatprotec.2018.01.044.
[119] S. Eslami, J. Francisco Miranda, L. Mourão, P.J. Tavares, P.M.G.P. Moreira, Polyethylene friction stir welding parameter optimization and temperature characterization, The International Journal of Advanced Manufacturing Technology (2018), https://doi.org/10.1007/s00170-018-2504-x.
[120] M.M. Schwartz, Metals Joining Manual (Book), McGraw-Hill Book Co., Chapters paged separately, 1979, p. 1979.
[121] S.H. Chowdhury, D.L. Chen, S.D. Bhole, X. Cao, P. Wanjara, Lap shear strength and fatigue behavior of friction stir spot welded dissimilar magnesium-to-aluminum joints with adhesive, Materials Science and Engineering: A 562 (2013) 53–60, https://doi.org/10.1016/j.msea.2012.11.039.

[122] N.M. André, S.M. Goushegir, J.F. dos Santos, L.B. Canto, S.T. Amancio-Filho, Friction Spot Joining of aluminum alloy 2024-T3 and carbon-fiber-reinforced poly(phenylene sulfide) laminate with additional PPS film interlayer: microstructure, mechanical strength and failure mechanisms, Composites Part B: Engineering 94 (2016) 197−208, https://doi.org/10.1016/j.compositesb.2016.03.011.
[123] D.J. Franke, J.D. Morrow, N.A. Duffie, M. Zinn, F.E. Pfefferkorn, Towards Improved Hybrid Joining of Aluminum Alloys to Carbon Fiber Composites with Friction Stir Welding, 2016, https://doi.org/10.1115/MSEC2016-8747. Available from:.
[124] B. Christner, Welded Joints with Polymer Sealant, Google Patents, 2007.
[125] J.M. Brown, The Effects of Sealants and Surface Treatments on the Faying Surface of Swept Friction Stir Spot Welds, Wichita State University, 2008.
[126] R. Talwar, Method for Joining at Least Two Adjoining Work-Pieces by Friction Stir And/or Friction Stir Spot Welding, Google Patents, 2007.
[127] P.-C. Wang, S.P. Marin, S.A. Marin, P.C. Sun, Method to Reduce Thermal Degradation of Adhesive in Weld-bonding, Google Patents, 2011.
[128] R.L. Maciel, V. Infante, D. Braga, P. Moreira, T. Bento, L. da Silva, Development of hybrid friction stir welding and adhesive bonding single lap joints in aluminium alloys, Frattura Ed Integrità Strutturale 13 (48) (03/05 2019) 269−285, https://doi.org/10.3221/IGF-ESIS.48.28.
[129] R. Maciel, T. Bento, D.F.O. Braga, L.F.M. da Silva, P.M.G.P. Moreira, V. Infante, Fatigue performance of friction stir weld-bonded Al-Mg joints, Procedia Structural Integrity 17 (2019) 949−956, https://doi.org/10.1016/j.prostr.2019.08.126.
[130] D.F.O. Braga, et al., Fatigue performance of hybrid overlap friction stir welding and adhesive bonding of an Al-Mg-Cu alloy, Fatigue and Fracture of Engineering Materials and Structures 42 (6) (2019) 1262−1270, https://doi.org/10.1111/ffe.12933.
[131] M.R. Adibeig, G. Marami, M.A. Saeimi-Sadigh, L.F.M. da Silva, Experimental and numerical study of polyethylene hybrid joints: friction stir spot welded joints reinforced with adhesive, International Journal of Adhesion and Adhesives 98 (2020) 102555, https://doi.org/10.1016/j.ijadhadh.2020.102555.

CHAPTER

6

Explosive welding

A. Loureiro[a], G.H.S.F.L. Carvalho[a], I. Galvão[a,b], R.M. Leal[a,c], R. Mendes[d]

[a]Universidade de Coimbra, CEMMPRE, Departamento de Engenharia Mecânica, Coimbra, Portugal; [b]ISEL, Department of Mechanical Engineering, Polytechnic Institute of Lisbon, Lisbon, Portugal; [c]LIDA-ESAD.CR, Polytechnic Institute of Leiria, Caldas da Rainha, Portugal; [d]Universidade de Coimbra, ADAI/LEDAP, Departamento de Engenharia Mecânica, Coimbra, Portugal

1. Introduction

The field of engineering has been confronted by many challenges regarding the selection of materials and the manufacturing of components. The requirements sought for components manufactured for engineering applications, whether mechanical, corrosive or physical, are continuously becoming stricter, and the need to manufacture components that can provide many different properties simultaneously is pressing. Nevertheless, the pursuit of materials that can have several properties at once may be extremely challenging and leads to two problematic situations: the non-existence of a material that possesses all the properties required, or the material is too expensive for the application. That said, the possibility of combining alloys with different properties that together provide all the requirements needed is very important in manufacturing industries.

Among all the families of metal alloys in engineering, three can be easily highlighted: steels, aluminum alloys and copper alloys. They are three of the most used metals on the planet and represent the majority of applications in engineering. They have very particular physical and mechanical properties, which, if combined, could produce components of unique hybrid properties and countless potential applications in the automotive, shipbuilding, power distribution and chemical industries.

The combination of the low density of aluminum and the high strength and low cost of carbon or low-alloy steels have been discussed for years, but the welding of these two most used metals still represents a serious obstacle. The same thing occurs concerning the welding of aluminum to copper, in which there is also a strong need for scientific support

Advanced Joining Processes
https://doi.org/10.1016/B978-0-12-820787-1.00006-1

to lever an increase in its industrial applications. To this day, there is still no easy and straightforward way to join these materials through welding.

The major challenge in the welding of aluminum to copper and aluminum to steels lies in their discrepancies in physical properties, such as: melting temperature, density, thermal conductivity and thermal expansion, making them incompatible materials to join with the well-known conventional fusion welding processes. Moreover, these combinations easily form brittle intermetallic compounds that harm the mechanical properties.

As a solution to the problems associated with the use of connectors and these welding concerns, solid-state welding processes are the most promising because they do not require bulk melting of the materials [1]. Several solid-state processes can be used for dissimilar welding such as friction welding (FW), magnetic pulse welding (MPW), cold roll bonding, ultrasonic welding, diffusion bonding and explosive welding (EXW). Nevertheless, even using solid-state processes, the welding of aluminum to copper and aluminum to steel is complicated. The temperature of the process and the time that the material remains at that temperature is very important. The influence of the unfavorable effect of the difference in the physical properties and the amount of intermetallic compounds formed are directly proportional to the increase in these two factors (temperature and time of interaction). Thus, welding processes that are carried out under lower temperatures, and that remain less time at these temperatures, are preferred for dissimilar welding.

For this reason, explosive welding has been gaining much attention for welding aluminum, copper and steel to each other [2–7]. The thermal cycle in explosive welding is extremely fast, which avoids the excessive formation of intermetallic compounds and other deleterious phenomena that occur at a high temperature The low cost of the process and the ability to weld large areas in a very short time also increase the interest in this process for dissimilar joining [8].

However, there are still several gaps in the existing knowledge concerning the explosive welding process, especially regarding the dissimilar joining using these three materials. The complex physical and chemical interaction, as well as the thermal phenomena occurring in the weld region and surroundings, are far from being thoroughly understood. Recent studies and findings have boosted the use of EXW process and helped to answer some of these questions regarding weldability, parameter selection, and microstructure.

The current chapter aims to present an overview on the explosive welding process and to show the most recent developments in the last three years (from 2017 to 2019) concerning the explosive joining of aluminum to copper, aluminum to carbon steel and aluminum to stainless steel.

It will be addressed topics based on metallurgical development and topics regarding process development. Regarding the metallurgical development, it will be discussed the accomplishment of good quality dissimilar welds for these three low weldability and complex alloy pairs, the prediction of the morphology and microstructure of the welding interface, and the definition of the fundamental weld features that dictate the quality of the weld (physical properties, presence of intermetallic compounds, welding interfaces and microstructure). The topics related to the development of the welding process address improvements concerning the development of the welding process itself, i.e. better methods for the selection of the welding parameters and their optimization; identifying the features that affect the weldability.

2. The explosive welding process

In order to join two parts, it is necessary to bring the surfaces exceptionally close, at an interatomic level. To achieve this level of interaction, the surfaces of the materials need to be free from any oxide or contaminant. The welding process must be able to provide this type of "cleanness" and permit an interatomic interaction between the materials being welded [9]. Through fusion processes, the materials are melted and mixed. Thus, oxides and contaminants on the surfaces will be dissolved or emerge at the surface of the molten weld pool and the materials can easily interact. In solid-state welding processes, in which no bulk melting is present, this condition must be supplied in different forms such as heat, impact energy, pressure or plastic deformation.

Explosive welding or explosion welding (the nomenclature more used in the USA) is a solid-state welding process characterized by the joining of materials through a high-velocity impact caused by a controlled detonation of an explosive [10,11]. In this process, the detonation of explosives is used to accelerate the workpiece that will collide with a stationary component in an oblique impact. The fascination of the process is its multidisciplinarity owing to the various phenomena associated with the welding process that come from the most diverse fields of engineering and physics [12]. This characteristic also leads to a specific challenge, which is the difficulty to completely characterize the technique and achieve a comprehensive understanding of the process, the phenomena at the interface and the selection of parameters. There has been an effort to extend the scientific knowledge about the explosive bonding process in the last decade, although many theories are still not consensual. These gaps in knowledge are mostly because the process has not been as widely investigated as other processes of solid-state welding technologies.

In EXW, the high-velocity oblique collision between the workpieces causes the metals to behave similarly to fluids. The strong impact leads to the formation of a metallic jet between the surfaces, which leaves clean virgin surfaces [9]. The fact that both surfaces are virgin and free from oxides allows the atoms of the materials to interact at interatomic levels in the aftermath of the impact. It produces a condition which "opens up" the electron media of the welded metals and leads to interatomic/metallurgical bonding across the interface [12].

Fig. 6.1 exemplifies the basic parallel configuration of EXW. The conventional set-up is composed by a baseplate (or stationary plate), the flyer plate and the explosive (or explosive mixture) (Fig. 6.1A). The baseplate is at rest and receives the impact of the flyer plate, which

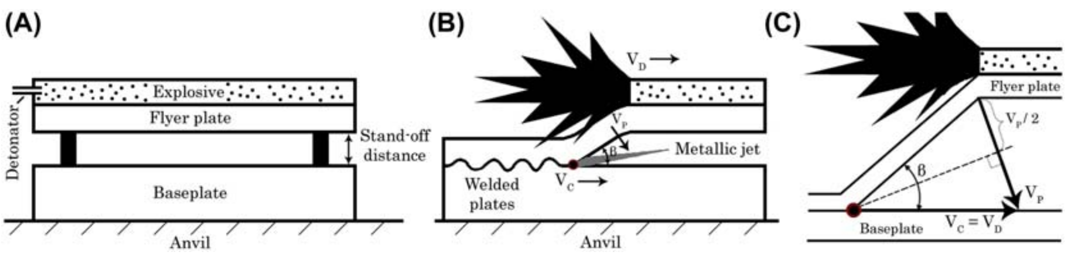

FIG. 6.1 The basic set-up of explosive welding in a parallel configuration before welding (A) and during the welding (B). Geometric relationship between the velocities and the β angle (C).

has been accelerated by the energy coming from the detonation of the explosive mixture [10]. The main welding parameters (displayed in Fig. 6.1B and C) are: the detonation velocity (V_D), the collision point velocity (V_C), the impact velocity or flyer plate velocity (V_P), the dynamic angle (β) and the stand-off distance (STD) [13]. The detonation velocity is the velocity at which the detonation progresses. The collision point velocity is essentially the welding velocity, i.e. the velocity at which the bonding occurs. For parallel configurations, the collision point velocity is equal to the detonation velocity. The impact velocity is the velocity at which the flyer plate collides with the baseplate. Also, the explosive ratio (R), which is the ratio of the mass of the explosive mixture to the mass of the flyer, is very important to the process. In addition to the parallel configuration, there are other types of configuration such as the inclined arrangement and the cylindrical configuration. These other settings require more mathematical processing to characterize the velocities than the parallel configuration.

2.1 The mechanism of explosive welding

Owing to the extremely high velocity at which the process occurs and the complex phenomena of different natures that are sometimes independent of each other, it is not possible to affirm with absolute certainty everything that occurs at the interface. However, it is known that three critical conditions must exist for the welding to occur, which will be discussed below: jetting, sufficient impact pressure and a distance between the workpieces.

(1) Jetting: one of the fundamental concepts for any welding process is the establishment of conditions that allow the materials to be in an interatomic contact. In EXW, this is achieved through the metallic jet. Therefore, the occurrence of jetting is indispensable for all EXW joints. Its formation is related to the dynamic angle of collision [14] and the collision point velocity [12].

(2) Impact pressure: after obtaining a clean surface, the materials must be thrust toward each other to allow and enhance the interatomic contact between them. There is a minimum collision pressure (a minimum impact velocity) that needs to be exceeded, which is related to the dynamic yield strength of the materials [12].

(3) Stand-off distance: for the two previous conditions to occur, the existence of a distance between the plates to be welded is indispensable. The stand-off distance is necessary to provide the space required for the metallic jet to occur, and to provide an unobstructed path to free it from the space between the plates [13]. Also, the STD is indispensable for the flyer to accelerate and reach the impact velocity required to obtain the minimum impact pressure for welding [12].

2.2 Characteristics of the interface and wave formation

From the very first publication regarding EXW by Carl, in 1944, interfacial waves have been detected [15]. Since then, they have been one of the most distinctive peculiarities of EXW and have inspired much curiosity from the phenomenological point of view [9]. The morphology of the interface depends on the materials welded and welding parameters [16]. Essentially, there are two typical types of interfacial morphologies in EXW: a flat interface (or laminar interface) and a wavy interface, as shown in Fig. 6.2. There are also other

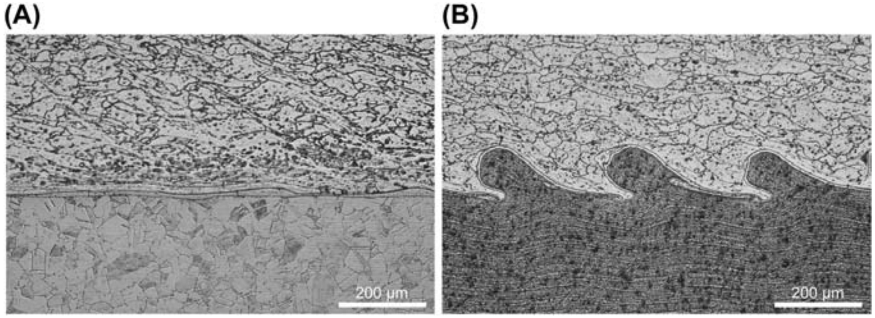

FIG. 6.2 The two typical types of explosive welded interfaces: flat (A) and wavy (B).

variations of these two types, such as a molten layered interface and singular shapes of waves (symmetrical, curled, and so on). Flat interfaces and molten layered interfaces are somewhat similar from the morphological point of view. In turn, the wavy interface is very particular and must be highlighted.

Although numerous scientists have addressed wave formation over the years [16–23], there is still no totally accepted theory about what happens at the interface and all the specific factors that lead to the formation of waves. Nevertheless, there are some widely accepted theories that explain much of what is found microstructurally at the interface. Bahrani et al. [18] presented one of the first well-accepted theories about the formation of waves, which is still today referred to. Patterson [24] analyzed this theory and gave a more concise interpretation of it. According to this author, because of the shear deformation promoted by the impact in the baseplate, a concavity is formed in the apex of the collision and a protuberance arises ahead of it, promoting the formation of the main structure of the wave. The interaction of the protuberance with the jet flow promotes the entrapment of the molten material and the formation of rear and front vortexes.

Several authors [25–27] have achieved numerical simulations or empirical results similar to those proposed by Bahrani et al. [18]. Nonetheless, as highlighted by Carpenter and Wittman [13], Bahrani et al. thought that the metallic jet was composed of flyer material only and did not identify that it was composed of both the flyer and baseplate alloys.

The mechanism proposed by Bahrani et al. [18] is mainly qualitative, describing the formation of the waves from a morphological perspective. It does not present the factors necessary to predict (or the properties that cause) their formation. This type of more complex approaches only began to be considered when similarities between the waves in EXW and the waves in liquid flow situations were identified. Cowan and Holtzman [17] were two of the first to understand and describe this similarity using ideas that are still widely applied today. They proposed that, just as fluids pass from laminar to turbulent flows, the transition from a flat interface to a wavy interface occurs above a critical value of the Reynolds number.

Carton [26] compared the wave forming mechanism to some phenomena of fluid mechanics. The author compared the morphology of the waves to the Von Kármán vortex and to the Kelvin-Helmholtz instability.

Plaksin et al. [28] also addressed the wave formation in EXW. They stated that the reaction zone of the detonation wave presents localized reactions, which results in spots on the surface of the flyer after welding. These localized reactions may cross the flyer and produce disturbances in the development of the Kelvin-Helmholtz instability and, consequently, at the interface. In accordance with this statement, Mendes et al. [29] showed that the wavelength and wave amplitude depend not only on welding parameters but also on the type of explosive because each explosive may cause different disturbances in the interfacial morphology.

More recently, Bataev et al. [27] investigated the wave formation theory presented by Bahrani et al. in detail through numerical simulation and obtained additional details of the transformations occurring inside the weld zones and vortexes, such as phase transformations and solidification.

2.3 Parameter selection: the weldability window

The parameter selection in EXW is very complex. The technology itself has an extremely empirical basis so that most of the discoveries are the result of practical experimentation. Pure experimentation based on trial and error is still widely used, but one of the most important theoretical methods for parameter examination is the weldability window.

The weldability window is a theoretical tool based on equations proposed by different authors, that relates the dynamic angle of collision (β) to the collision point velocity (V_C) [30]. The window consists of 4 boundaries that limit the values for the collision angle and collision point velocity, which will lead (in theory) to good quality welds. Each of the four limits relates an interfacial phenomenon to the dynamic angle of collision or the collision point velocity. The phenomena addressed by the four limits are: jetting, interface morphology, melting and impact pressure.

Most of the equations for the weldability window calculation are independent of each other, i.e. they have been developed by different authors. Several of these equations have variables, constants or units that are not clearly defined. The study undertaken by Ribeiro et al. [30] helped to clarify missing or contradictory information by defining the variables and units for some of these equations. There are several equations for each limit, but only the most accepted and commonly used will be discussed. For the calculation of the window, all equations must be formulated as a function of β or V_C. Fig. 6.3 illustrates a typical weldability window. Each of the equations to calculate the four limits are explained next (the "f" and "b" indexes in the equations indicate that the property refers to the flyer and baseplate, respectively).

1. The minimum impact pressure (lower limit − the blue line in Fig. 6.3)

For a consistent weld to occur, a minimum pressure between the workpieces is required [12,13]. The pressure at the interface is dictated mainly by the impact velocity, which must be sufficient to considerably exceed the dynamic yield stress of the material [13]. The equation from Deribas and Zakharenko's work [31] for the lower limit is calculated using Eq. (6.1).

$$\beta = k\sqrt{\frac{H_H}{\rho_{fb} \cdot V_C^2}} \tag{6.1}$$

Where k is a constant related to roughness and cleanliness of the surface, H_H is the hardness of the harder material (Pa), and ρ_{fb} is the average density between the flyer and baseplate (kg/m^3), and V_C is the collision point velocity (m/s).

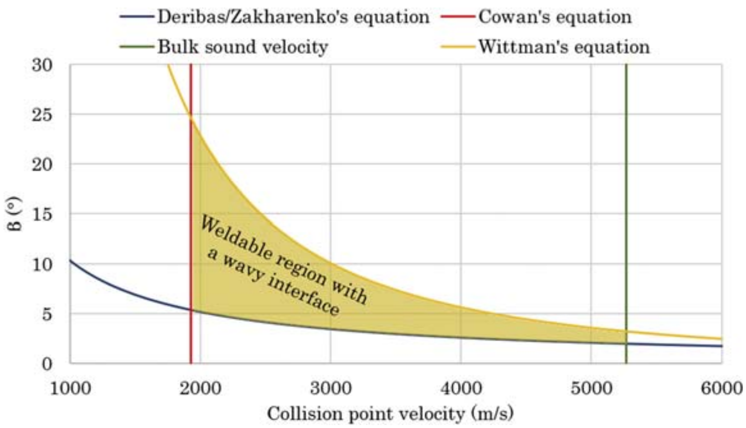

FIG. 6.3 Typical weldability window.

2. **Maximum kinetic energy to avoid excessive melting** (upper limit – the yellow line in Fig. 6.3)

The upper limit is related to the maximum energy permissible at the interface to avoid excessive melting of the materials. After the detonation of the explosive accelerates the flyer, the impact will induce kinetic energy within the system. According to Carpenter and Wittman [13], this energy will be converted into heat by deformation and friction, which will raise the temperature locally. For a good weld, the interface in the vicinity of the collision point must be sufficiently cooled to be free from excessive melting that would not withstand the passage of the shock traction waves. This limit is absolutely critical, particularly in dissimilar welding, where melting leads to the appearance of intermetallic compounds and other issues. Based on that theory, Carpenter and Wittman [13] equated the thermophysical properties of the metal to the impact velocity that could lead to heat dissipation without bulk melting. This formulation is according to Eq. (6.2). To formulate the equation as a function of β or $V_{C,}$ the relation in Eq. (6.3) must be used, according to Fig. 6.1C.

$$V_P = \frac{1}{N} \frac{(T_{mf} \cdot C_{Bf})^{1/2}}{V_c} \frac{(\lambda_f \cdot c_f \cdot C_{Bf})^{1/4}}{(\rho_f \cdot \delta_f)^{1/4}} \tag{6.2}$$

$$V_P = 2V_C \cdot \sin\left(\frac{\beta}{2}\right) \tag{6.3}$$

Where N is a constant, T_m is the melting temperature (°C), C_B is the bulk sound velocity (m/s), λ is the thermal conductivity (W/m•K), c is the specific heat (J/kg•K), ρ is the density (kg/m^3), δ is the thickness (m), and V_C is the collision point velocity (m/s). N is a constant that may assume different values. Rosset [32] is one of the authors who discuss its value.

3. The jet formation (right limit − the green line in Fig. 6.3)

According to the jetting theory, a minimum collision angle must be satisfied for the metallic jet to occur. The critical collision angle depends on the collision point velocity and the material being welded. Walsh et al. [33] and Cowan and Holtzman [17] examined the limiting conditions for the jet formation and established equations to calculate this angle. However, Cowan and Holtzman [17] stated that when the collision point velocity is subsonic, the bond is accomplished if the elastic strength of the material is exceeded (which essentially represents the lower limit). Thus, the collision point velocity must be lower than the bulk sound velocity in the material [12,14,34]. Considering this fact and also that the right limit of the window is rarely a concern (EXW is often conducted at collision point velocities considerably below this level) [35], the right limit can be simplified as the bulk sound velocity in the flyer plate (Eq. 6.4). The bulk sound velocity is calculated using Eq. (6.5) [36].

$$V_C < C_{Bf} \tag{6.4}$$

$$C_{Bf} = \sqrt{V_{Lf}^2 - \frac{4V_{Sf}^2}{3}} \tag{6.5}$$

Where V_C is the collision point velocity (m/s), C_B is the bulk sound velocity (m/s) and V_L and V_S are the longitudinal and shear sound wave velocities in the material (m/s), respectively.

4. Minimum velocity to obtain a wavy interface (left limit − the red line in Fig. 6.3)

The weldability window theory considers that a wavy formation is an indication of a good quality weld. Nevertheless, it is now well known that, although it usually leads to better quality welds, the presence of waves is not fundamental, i.e. it is not a limiting factor or a failure criterion [12]. Cowan et al. [16] affirmed that the parameter related to wave formation is the collision point velocity, which needs to exceed a critical value. They claim that despite the differences in density and hardness, the transition from a smooth to a wavy interface occurs at nearly the same Reynolds values for many materials. That is, the transition is almost constant, and 10.6 is the average critical Reynolds number (R_T) for the transition from a flat to a wavy interface for all the systems they studied. Cowan's [16] equation for the left limit is calculated according to Eq. (6.6).

$$R_T = \frac{(\rho_f + \rho_b) \cdot V_C^2}{2 \cdot (H_f + H_b)} \tag{6.6}$$

Where R_T is the critical Reynolds number, ρ is the density (kg/m^3), V_C is the collision point velocity (m/s), and H is the hardness (Pa).

2.4 Advantages and limitations

The EXW process is not a conventional process. So, its advantages and limitations must be understood in order to select suitable applications for this welding technique. Some advantages and limitations of the process must be highlighted [8,10,11,37]:

Advantages:

- Possibility of welding almost any metal that is capable of withstanding impact;
- Very low-cost welding process;
- Possibility of joining very large areas very quickly and at one step;
- Permitting the joining of materials with very distinct physical properties or materials that are incompatible by conventional processes;
- Essentially not having a heat-affected zone;
- The alloys keep their properties after welding, preserving their microstructure, mechanical properties, and corrosion properties;
- Avoids extensive interaction at high temperatures;
- The welding region is typically stronger than the weaker parent material;
- Very high reliability and reproducibility when conducted by specialized personnel/manufacturers.

Limitations:

- Suitable only for simple geometries in which the detonation can propagate;
- Requires an appropriate environment due to safety and noise issues;
- Needs specialized personnel to handle the hazardous materials;
- The welded materials need to be ductile enough to withstand the impact (usually at least 5%–10% elongation and 14–30J Charpy V impact toughness at room temperature).

2.5 Applications of explosive welded joints

The most common commercial use of explosive welding is the cladding of steel plates with corrosion resistance alloys, especially stainless steel. The possibility of joining large areas quickly has stimulated the use of this process in cases where there is a need for large coatings. Pressure vessels, heat exchangers or pipelines with corrosion resistance clads are regularly manufactured by explosive welding [8,10,11,37].

Regarding the use of more complex dissimilar combinations, the process can be used in the supply of electricity: earthing strip copper-aluminum connections; in the transport industry: rail-to-rail copper-steel current-carrying joints; in chemical plants: copper-aluminum bus bar connections [38]; among others. Due to the ease of joining dissimilar materials (one of the major advantages of the process), EXW is also used for transition joints in the form of blocks, strips, or tubular couplings [8,11]. Transition joints are used in many welded structures to connect different metals that cannot be routinely welded satisfactorily. EXW is used to manufacture the transition joints, i.e. the exact transition region from one material to the other and then the ends of these joints can be easily welded by conventional processes (as they will be similar welds). A few examples of explosive welded transition joints are [8,38]: aluminum-copper for electrical contacts and busbar connections; aluminum-steel, aluminum-titanium, and aluminum-copper-nickel in shipbuilding; aluminum-stainless steel for cryogenic pipe couplings; and titanium-stainless steel for use in the aerospace industry [8].

2.5.1 Applications of aluminum to copper and aluminum to steel joints

Aluminum and copper are the most used metals after iron. The joining of aluminum alloys to copper alloys (Al-Cu) is very strategic due to the possibility of combining their properties and its many industrial applications. This combination is used in many applications, especially the ones that benefit from the high thermal and electrical conductivity of these metals. The low density of aluminum helps to reduce the total weight of the structures. There is high demand for Al-Cu pairs that could be produced by explosive welding in plenty of industries and fields, such as electric power, refrigeration, automobiles, electronics, hydrometallurgy, aeronautics and also cookware [6,7,39–41]. The batteries of electric vehicles require a large number of Al-Cu connections [6,7]; busbar connections, cathode conductive heads, armored cables, earthing strips, yoke coils in TV sets, air-cooling fans are also other examples of the employment of Al-Cu joints [37,38,41–43].

Among the numerous applications for aluminum to carbon/low-alloy steel joining (Al-CS), shipboard and offshore construction should be highlighted. The use of aluminum alloys above the waterline provides a minimization of the topside weight [44,45], which lowers the structure's center of gravity and significantly improves the stability of ships and offshore constructions [38,44]. The Al-CS joints are applied to connect components such as deckhouses, masts and antennae to the steel hulls of ships [38]. The further development of the shipbuilding and offshore industries requires lightweight and fast vessels, which need a high number of Al-CS structural transition joints to attach the aluminum superstructure to the steel hull [2–4]. Gullino et al. [46] also expressed the possibility of using explosive welded joints for car-body applications in the automotive industry. All transport industries use a large amount of steel in their structures. Nonetheless, the low weight of aluminum alloys represents a major advantage in the pursuit of a lighter final component that leads to economies in fuel and energy.

Aluminum to stainless steel joints (Al-SS), due to their good resistance to corrosion and excellent properties at low temperatures, are used for cryogenic pipe couplings [37], both for pipe-work and connections to liquefied gas storage vessels [38]; for nuclear fusion engineering applications [47] and also for cryogenic pressurized hydrogen storage in hydrogen vehicles which are currently being developed and improved [5,48].

However, despite all the advances achieved in recent years and the process currently being used for some applications, some of these applications are still limited by the mechanical properties of the joints that are not optimized yet. The improvement of mechanical properties could significantly expand the use of the EXW process for these combinations. Fig. 6.4 shows different types of application of Al-SS and Al-CS explosive welded joints.

3. Explosive welding of aluminum to copper

Aluminum and copper are incompatible elements from the welding point of view. This is justified by the high affinity to form intermetallic phases [50] and their extremely different physical properties. These facts hinder the joining of these metals, especially by traditional fusion processes. Consequently, the welding between these metals proves to be extremely challenging.

In addition to the concerns caused by the different physical properties, the formation of intermetallic compounds is problematic because it is a thermally activated process, i.e. increasing the temperature will accelerate the nucleation and growth of these compounds [51]. The brittle nature of the Al-Cu intermetallic phases [52] is reported to cause harmful

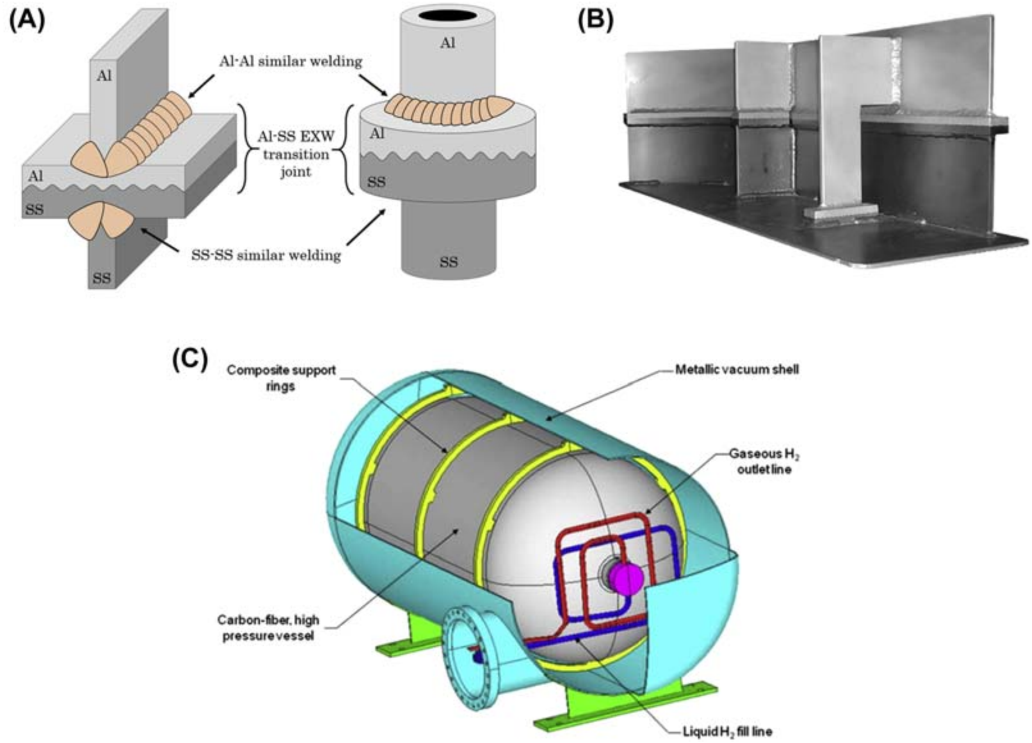

FIG. 6.4 Schematic drawings of two typical transition joint configurations (A), example of an Al-Steel transition connection used in ships [49] (B), cryogenic pressure vessel with Al-SS joints [5,48] (C).

effects in the joint and hinder the welding. The Al-Cu binary phase diagram shows that many intermetallic compounds form under equilibrium conditions [50]. Furthermore, due to the drastic nature of the thermal cycles in the welding processes, metastable and phases far from equilibrium may also appear, giving rise to complex microstructures. The phase diagram also reveals that the Al-Cu system results in a eutectic (33 wt% Cu), that inevitably presents a lower melting temperature (548 °C) than the pure elements. This raises the possibility of melting at temperatures below the melting temperatures of the pure elements, which also increases the probability of the occurrence of intermetallic compounds and welding defects. Table 6.1 shows the main phases found for the Al-Cu system.

Solid-state welding processes help to overcome or lessen most of the abovementioned concerns. On the other hand, they trigger other issues that need to be solved. Al-Cu explosive joints have been manufactured throughout the years, but due to problems related to their physical properties and interfacial phenomena, they have limited application. The welding of aluminum alloys to copper alloys by explosive welding has gained more importance since the mid-90s. Yet, only from 2012 has research about this metallic pair been published more frequently. A chronological literature review regarding the works addressing the explosive welding of aluminum to copper is presented below. Many articles in the past 20 years help to improve the knowledge regarding the welding of this dissimilar combination.

TABLE 6.1 Al-Cu phases.

Phase	At.% Cu	Pearson symbol
Al	0–2.84	cF4 [53]
$CuAl_2(\theta)$	31.9–33.0	tI12 [53]
CuAl (η_2)	49.8–52.3	mC20 [53]
Cu_4Al_3 (ζ_2)	55.2–56.3	oI24–3.5 [54]
$Cu_3Al_2(\delta)$	59.3–61.9	hR52 [55]
Cu_9Al_4 (γ1)	62.5–69	cP52 [53]
Cu	80.3–100	cF4 [53]

One of the earliest articles addressing the subject more scientifically rather than only from an empirical view of the process was published by Izuma et al. [56], in 1994. Aware of the difficulties of combining aluminum to copper, the authors attempt an unconventional configuration using an intermediate plate (interlayer). The authors obtained consistent welds for some configurations, but there was not a deep microstructural examination of the interface to characterize the joint.

Veerkamp [57], in 2002, was one of the first to introduce EXW as a viable process to weld aluminum to copper for a specific industrial application. The author demonstrated the potential to use EXW to fabricate an Al-Cu transition for high direct-current bus system components that were initially made with a bolted joint.

In the works of Dyja et al. [58] and Berski et al. [59], more detailed results about the interface began to emerge. New compounds formed at the interface with high hardness were identified as Al–Cu intermetallic compounds. However, only in 2008 with Gülenç's investigation [60], did the publications start to have more information about the welding parameters and the relation between parameters and microstructure. The author observed the effect of the explosive ratio on the morphology of the interface, that was flat for low ratios and wavy for higher ratios. Then, in 2009, Ashani and Bagheri [61] produced a scarf weld changing the explosive thickness but did not evaluate the microstructure.

From 2012 on, the studies became more comprehensive. Asemabadi et al. [62] and Honarpisheh et al. [42] produced a consistent three-layer Al-Cu-Al joint. The authors draw our attention to the processing of the explosive welded joints by cold-rolling and annealing heat treatment, evaluating mechanical properties and microstructure. The morphology of the waves was coiled, with the curled waves composed by the copper alloy. They suggest the formation of brittle intermetallics and affirm that the fractures from the tensile tests originated from the intermetallic compounds. In the same year, Sedighi and Honarpisheh [63] studied the distribution of residual stresses on three-layer Al-Cu-Al explosive welded joints. They found that the properties of the materials, in particular, the coefficient of expansion, generates some residual stresses inside the joint.

In 2013, Paul et al. [64] undertook one of the first in-depth studies on the interface microstructure of Al-Cu welds. They detected the Cu_9Al_4, CuAl and $CuAl_2$ equilibrium phases, metastable intermetallic phases and also Cu_mAl_n-type phases that do not appear in the equilibrium Al-Cu phase diagram. This work proved the difficulty in identifying the intermetallic compounds at the interface and helped to distinguish the most probable compounds formed in Al-Cu welding.

Similarly, in the same year, Chen et al. [65] observed the diffusivities in Al-Cu explosive welds, finding an influence of the welding parameters on the diffusivities of Cu and Al atoms inside each other. This proved that the occurrence of intermetallic compounds (IMCs) is, indeed, affected by the welding parameters. This conclusion caused a fundamental rethink in explosive welding since the conventional equations for determining the parameters did not consider the formation of intermetallic compounds. Amani and Soltanieh [40] went further and established energetic activation energies for the nucleation of intermetallic compounds at the interface of an Al-Cu explosive weld through an annealing heat treatment, forming $CuAl_2$, CuAl, Cu_4Al_3, and Cu_9Al_4 phases. Nevertheless, the authors indicated that the chemical composition of the intermetallic compounds in the "as-welded" condition did not match a specific phase on the Al-Cu phase diagram. Therefore, the annealing heat treatment cannot be used to predict the exact phases formed during welding. This is further evidence that some compounds are formed under non-equilibrium conditions.

In 2015, Mróz et al. [66] characterized the interface and the intermetallic compounds, evaluating explosive welded bars and the rolling process. They achieved a consistent component. Hoseini-Athar and Tolaminejad [43] made a similar study in 2016, but they examined the interface more carefully, also addressing the effect of the ratio and the effect of the intermetallic compounds on the quality of the rolling. The brittle IMCs formed at the interface were fragmented due to the reduction in thickness during the rolling process. Their most intriguing finding was the fact that a better performance was found for the weld with an intermediate quantity of intermetallic compounds instead of the lowest amount. This fact raised doubts regarding the usual idea that the total absence of intermetallic compounds would always result in better mechanical properties. However, they did not draw attention to this finding, and there was no discussion concerning the reason for this phenomenon.

Also in 2016, Loureiro et al. [67] related the parameters and the explosive mixture to the morphology of the interface and the mechanical behavior of partially overlapping welds. The importance of this research is related to the fact that the authors achieved consistent joints that may be used for load transfer instead of the traditional cladding use.

In the same year, Saravanan et al. [68] studied three types of interlayer plates (aluminum, copper and stainless steel) in an attempt to improve the mechanical properties of Al-Cu EXW joints. They argue that all the three interlayers provided stronger joints compared to the direct welding and that wavy interfaces are formed at the interface when a higher ductile metal is used as the interlayer.

Concerning the weldability window, Loureiro et al. [67], and Hoseini-Athar and Tolaminejad [69] investigated its utilization for Al-Cu welds. While Hoseini-Athar and Tolaminejad [69] tested many equations for the weldability window limits, Loureiro et al. [67] calculated the window using the most conventional equations. Nevertheless, regardless of the equations used in both works, it was possible to realize that the weldability window has considerable limitations in reproducing practical results and, in these studies, it was not able to replicate the practical results.

3.1 Remarks

The investigations mentioned here show that much work concerning the potential of Al-Cu EXW has been carried out, yet there are still some critical questions to be answered in order to encourage the development of components using this combination. In this sense, some topics that still need to be explored are highlighted below.

- **Parameter optimization and weldability analysis:** these analyses should address the configuration in which the materials are positioned (flyer or baseplate), the intermetallic phase formation and their physical properties, which significantly influence the weldability and parameter selection.
- **The morphology of the interface**: the main properties that dictate the morphology need to be evaluated in order to predict it better.
- **The weldability window:** the difficulty in reproducing the experimental results by using the weldability window should be investigated.
- **The welding viability:** it should be investigated whether non-conventional welding is strictly necessary and if the intermetallic compounds are, in fact, the main problem in Al-Cu EXW.

3.2 Recent developments

Recently, several topics have been addressed to increase knowledge about the joining between aluminum and copper by explosive welding. From 2017 to 2019, Carvalho et al. [70–73] undertook a series of works addressing this combination in order to obtain a more comprehensive study from the point of view of the weldability, morphology of the interface and parameter selection. In the same period, Wei et al. [6,41], Tajyar and Masoumi [74], Denisov et al. [75], Saravanan and Raghukandan [39] and Kaya [7] gave also a strong contribution to the study of the union between these materials addressing topics such as parameter optimization and analyzing more practical topics like corrosion resistance, electrical conductivity measurements, effects of shape-rolling process after welding among others.

One of the most important topics to discuss is the regular achievement of good quality Al-Cu welds. Carvalho et al. show that good quality joints can be obtained both with the aluminum alloy positioned as the baseplate [70,72,73] or as the flyer plate [71,73]. Regardless of the welding parameters or position of the aluminum and the copper plates, a transition layer with an Al-Cu intermetallic composition was reported to be always present. Despite the effort to avoid the formation of IMCs due to their brittle nature and supposed harmful effect on the mechanical properties, they were always present in the consistent welds of these authors. Wei et al. [6,41] and Kaya [7] also detected the presence of intermetallic phases at the interface of the welds.

According to some authors [70–72], the quality of the weld is always better when the intermetallic volume is not linear and continuous throughout the interface. Tajyar and Masoumi [74] corroborated this result, stating that the final mechanical properties depend on the intermetallic layer thickness and its continuity. They found that for Al-Cu joints that have a thick intermetallic layer the crack propagation is more intense in the rolling process. In terms of weldability, a continuous and thick layer of intermetallic compounds leads to failure and separation of the plates during the welding process [71]. Although a continuous layer comes from excessive interfacial melting, it was reported [73] that this type of failure occurred mostly when the aluminum alloy was used as the flyer plate because of its low melting temperature. This fact raises important questions about the weldability of this combination of materials related to what the best possible configuration would be.

Wei et al. [6] also detected that compared with copper and aluminum, the intermetallic phases had a high electrical resistivity. This is very important because Al-Cu joints are largely selected for electrical applications. So, processes that avoid large volumes of IMCs will favor the performance for electrical use.

It was shown that using the aluminum alloys as the flyer plate narrows the range of energy that can be used, i.e. the weldability is significantly decreased by positioning the aluminum as the flyer plate and the copper alloy as the baseplate [73]. The interaction of the materials is entirely different, depending on how they are positioned. Therefore, when aluminum is being welded as the flyer plate in dissimilar welding, joining will be preferentially achieved under lower collision point velocities.

The most conventional weldability theories have some limitations to predict the experimental results in Al-Cu welding. The weldability window (in particular the upper limit) presented in Fig. 6.5, for instance, shows that the weldability of Al-Cu welding is better if the aluminum is placed as the flyer plate, which is exactly the opposite to what was observed in the experimental trials conducted by Carvalho et al. [73]. The upper limit is very important because it is the limit that is related to the explosive ratio and impact velocity (or flyer plate velocity). Kaya [7] showed the influence of the explosive ratio both mechanically and microstructurally. This fact shows how important it is to better understand the upper limit of the weldability window.

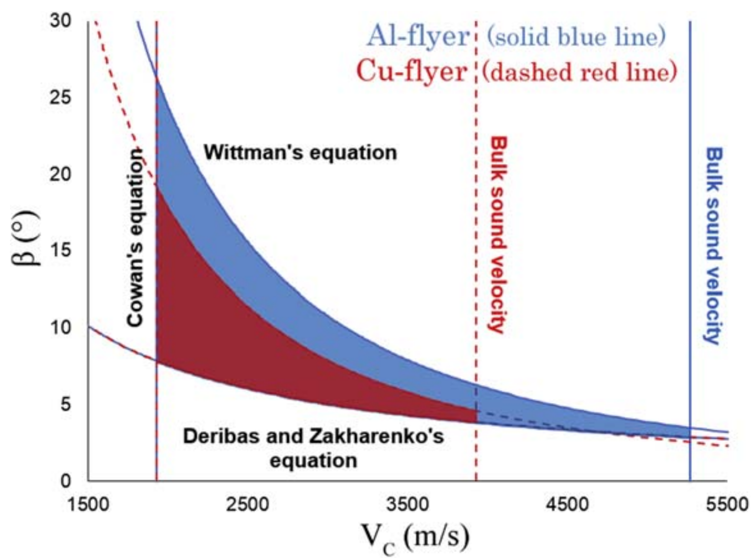

FIG. 6.5 Comparison of the weldability windows of the two configurations of the Al-Cu welding: the aluminum as the flyer (*solid blue line*) and the copper as the flyer (*dashed red line*).

One of the issues of the weldability window is that it mainly considers the properties of the flyer plate, which is not sufficient. Two noteworthy equations, developed by Zakharenko [76] and Efremov and Zakharenko [77], are rarely mentioned today. The equations are more comprehensive than the conventional theories and, besides including many physical properties, have the advantage of considering the influence of the thickness of both the flyer and the baseplate. However, even with better results from the two abovementioned equations, as reported in Carvalho et al. [73], no theory or equation regarding the requirements for achieving consistent dissimilar welds proved to be able to reflect the Al-Cu welding experiments completely. There is a significant mismatch between theory and experiments. New approaches considering the properties of both welded alloys, and their differences, and the occurrence of intermetallic compounds at the weld interface must be developed.

Another detected inconsistency between the EXW theory and experimental welds concerns the bond zone: the Al-Cu welds using copper as the flyer plate [70,72,73] displayed an essentially flat interface even though they were supposed to be wavy according to Cowan's equation. On the other hand, using aluminum as the flyer plate [71,73], waves formed very easily. From Cowan's equation, the transition collision point velocity from a flat to a wavy interface would be precisely the same regardless of the order of the materials, i.e. the equation predicts that Al-Cu and Cu-Al welds (changing the positions) would have the same transition velocity. However, the experiments show that this does not happen in practice. Fig. 6.6 compares the welding of aluminum to copper with the same parameters but changing the positions of the flyer and baseplate. Despite using the same parameters, the interface is completely different.

Carvalho et al. [70] conducted an in-depth examination of many experiments in the literature, concluding that if the flyer is denser than the baseplate, and there is a substantial density disparity between the plates, the waves are not formed regardless of the welding parameters. The same happens if the melting temperature of the flyer is substantially higher than the baseplate. This proved that both properties have a significant influence on wave formation, but Cowan's equation does not consider the melting temperature nor the difference between the flyer and the baseplate for any of the properties. One of the most important findings is the perception that there is a profound influence of the positioning of the materials and there is a direct relationship between the density and melting temperature to the formation of

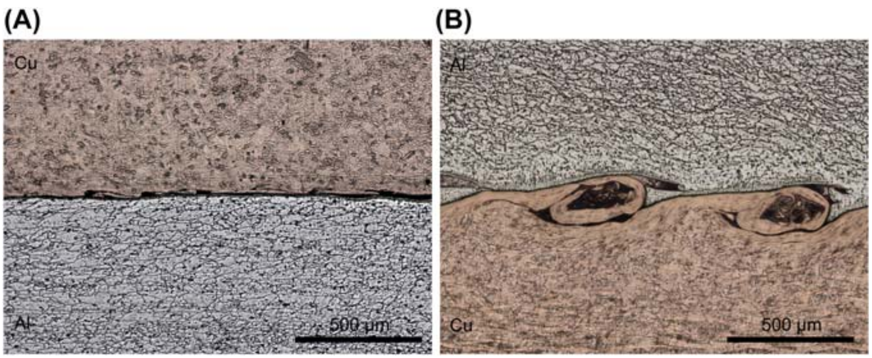

FIG. 6.6 Comparison of the interfacial microstructure of the two configurations of the Al-Cu welding: the copper alloy as the flyer plate (A), and the aluminum alloy as the flyer plate (B).

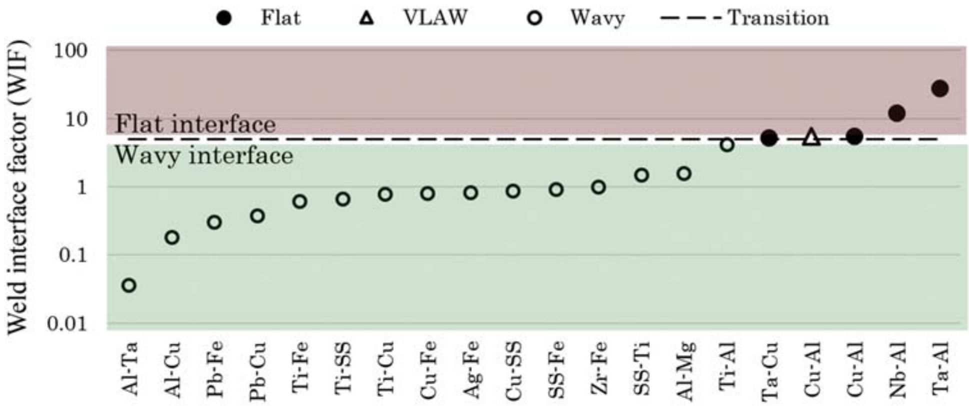

FIG. 6.7 Diagram presenting the WIF calculated for dissimilar explosive welds in the literature. *Adapted from G.H.S.F.L. Carvalho, R. Mendes, R.M. Leal, I. Galvão, A. Loureiro, Effect of the flyer material on the interface phenomena in aluminum and copper explosive welds, Materials and Design 122 (2017) 172–183. https://doi.org/10.1016/j.matdes.2017.02.087.*

the waves. Based on this discovery, an equation was created combining the density and melting temperature ratio of the flyer to the baseplate (flyer property/baseplate property), which was called "wave interface factor" (WIF), Eq. (6.7) [70]. This equation directly considers the positioning of the materials.

$$\mathrm{WIF} = \frac{\rho_{\mathrm{flyer}}}{\rho_{\mathrm{baseplate}}} \times \frac{T_{\mathrm{mflyer}}}{T_{\mathrm{mbaseplate}}} = \rho_R \times T_{mR} \tag{6.7}$$

Where ρ is the density (kg/m^3), T_m the melting temperature (°C), ρ_R is the density ratio, and T_{mR} is the melting temperature ratio.

The WIF indicates the possibility of obtaining a wavy interface (Fig. 6.7), i.e. above a specific WIF value the weld interface will not be wavy regardless of the welding parameters. Below that value, the weld interface may be wavy depending on the welding parameters. Kaya [7], for instance, showed that the explosive ratio and impact velocity affect the interface and wavy morphology of the Al-Cu weld. However, the WIF shows that for some other metallic combinations, the interface transition from flat to wavy may never occur.

In the last years, much attention has also been paid to studies focusing on the application of the EXW to engineering components. This is important because besides the process development, it is necessary to study the specific applications to improve and promote the application of the process.

Tajyar and Masoumi [74] manufactured a cylindrical Al-Cu weld joint, which is a less common but important application. The authors undertook a metallurgical characterization of the EXW pipes and the components after rolling at various stages through shear and hardness testing and optical microscopy. They were able to produce good quality bimetallic circular and square tubes, but the presence of intermetallic compounds impaired the performance proportionally to the roll gap reduction for the square tube. These results showed that thick intermetallic layers must be avoided in order to achieve a good quality joint.

Denisov et al. [75] studied the manufacturing of Al-Cu for electrical contacts. They found that after welding the joint possesses an electrical conductivity similar to the aluminum, i.e. the EXW can be used for this combination of materials without losing the good electrical conductivity. They also studied the use of different “damping layers” in order to avoid the damage of the surface of the flyer during explosion. They used bituminous mastic (1.5 mm thickness) and milled ammonium nitrate (2 mm thickness). The best quality of the welded joint was achieved using the bituminous mastic damping layer. However, regarding the surface quality, the damping layer produced from milled nitrate presented the best results.

Wei et al. [6,41] characterized conductive heads manufactured by EXW. Wei et al. [6] compared conductive heads made by explosive welding, cold pressure welding, and solid-liquid casting in order to identify the best manufacturing process for this type of component. They concluded that not only the conductivity but the interfacial bonding strength and corrosion resistance of the conductive heads prepared by EXW were superior to the other processes. Further, Wei et al. [41] studied distinct usage times of the component in an environment that included high temperatures, hot and cold thermal cycles, the passage of electric current and a corrosive atmosphere. After long hours of service, the failure of the component occurred at the interface, attributed to the deterioration of the interfacial microstructure and corrosion. The authors proved that EXW is a viable and advantageous process for the manufacturing of Al-Cu conductive heads.

Saravanan and Raghukandan [39] addressed a less common technique. They produced an Al-Cu explosive cladding using a stainless steel wire-mesh at the interface. They found that the wire-mesh reinforced clad was stronger than the weaker aluminum parent plate. Moreover, the corrosion tests results showed that the application of a stainless steel wire-mesh can be used in corrosive environments.

4. Explosive welding of aluminum to steel

The joining of aluminum alloys to steels is not compatible with conventional fusion welding [78]. The difference between the melting temperatures of pure iron and pure aluminum is 878 °C, which makes the welding of these materials very complex. Each one has almost no solubility for the other element and the nucleation of IMCs is very likely [78]. The Al-Fe phase diagram shows that many intermetallic phases appear with the mixture of these two metals [79]. The most common phases in the Al-Fe system are listed in Table 6.2. The Al-Fe eutectic does not represent a major concern in aluminum to steel welding because its melting temperature (652 °C) is not significantly different from pure aluminum (660 °C).

The issue of the appearance of intermetallic compounds is more complicated when aluminum is welded to stainless steel than when it is welded to carbon steels. Stainless steels are Fe-Cr-Ni alloys (although there are other alloying elements) with more than 10.5% of Cr, and each of these three elements can also form intermetallic compounds with aluminum. Thus, it is possible that three or more of these elements combine, forming complex ternary or quaternary intermetallic compounds. The Al-Cr [80] and Al-Ni [81] binary phase diagrams show that many IMCs are likely to be formed and they could profoundly affect the welding. Besides all the possible IMCs predicted by the phase diagrams, there will always be the possibility of the formation of metastable phases and phases far from equilibrium in welding.

TABLE 6.2 Al-Fe phases.

Phase	wt.% Al	Pearson symbol
α-Fe	0–28	cI2 [82]
γ-Fe	0–0.6	cF4 [82]
FeAl	12.8–37	cP2 [83]
Fe_3Al	13–20	cF16 [82]
$FeAl_2$	48–49.4	aP19 [83,84]
Fe_2Al_5	53–57	oC24 [83,84]
$FeAl_3$	58.5–61.3	mC102 [82]
Al	100	cF4 [82]

4.1 Explosive welding of aluminum to carbon/low-alloy steel

Explosive welding of aluminum alloys to steels (covering mild steels, carbon steels, low-alloy steels) has been investigated regularly over the years due to its industrial importance. But, due to the growing need to join aluminum to steels, research has been considerably intensified from 2014 when papers were published in a short period. A chronological literature review will now be presented that includes most of the works (in English) available in the main international journals regarding the explosive welding of aluminum to carbon/low-alloy steel. The evolution of the discoveries over time is discussed.

Szecket et al. [85], in 1985, published one of the first noteworthy references about the explosive welding of aluminum to mild steel. They did a broad study, comparing the mechanical behavior of welds with a flat to a wavy interface morphology. The authors show that the flat interfaces had better mechanical behavior in the tensile tests, which was not expected.

In 1992, Leszczynski [86] welded these two alloys and recorded the evolution of the microstructures and properties under several heat treatments. The results revealed the detrimental effect of a long permanence under high temperatures for materials with an affinity to form intermetallic compounds. They concluded that the intermetallic layer increases with a temperature increase of the heat treatment. This proved that Al-CS explosive welds cannot be used for high-temperature applications.

In the late 90s, Chao et al. [2] analyzed the toughness of the aluminum to carbon steel joint for shipboard employment. They attempted different configurations of joints and showed out that the joint with three layers (with a titanium interlayer) presented the best mechanical properties. The authors verified that above 400 °C, the mechanical properties of the joint dropped.

Li et al. [87], in 2000, observed the morphology of an Al-CS joint. The authors sought a more exhaustive characterization of the Al-CS welded interfaces, providing new insight and knowledge about what is likely to be found in terms of microstructure after the welding process. They obtained consistent welds, with a curled wave morphology (formed by the steel), with the presence of the FeAl, $FeAl_2$, $FeAl_3$ and $FeAl_6$ phases.

A few years later, Han et al. [88] examined the effect of the thickness of an aluminum interlayer on the welding of aluminum to mild steel. The authors used several thicknesses of the interlayer and found that by raising the thickness of the interlayer, the interfacial zone grew, and the shear strength decreased. Nonetheless, the growth of the interfacial zone with the interlayer thickness is not expected since by increasing the thickness of the interlayer, kinetic energy decreases.

Acarer and Demir [89] evaluated an aluminum flyer plate directly welded to a low-alloy steel and a dual-phase steel. They reported good quality joints with a flat interface for both welds, but the microstructural analysis was not very profound.

Tricarico et al. [4], in 2009, examined the effect of heat treatments on the explosive welded Al-CS joint. They found a curly wave morphology and concluded that there was an increase of the intermetallic layer (and a deterioration of the mechanical properties) proportional to the temperature. Further, they also noted that the influence of the time of heat treatments was less significant. Later, Tricarico and Spina [3] examined the effect of thermal loads on the same type of transition joint. The authors stated that only above 300 °C did the mechanical properties begin to be significantly damaged. These investigations are necessary because when explosive weld joints are used for transition joints, it is very likely that they will be welded again at a later step.

From 2014, due to the critical need for more definitive solutions concerning the welding of aluminum to steel, the studies have become more frequent. Mal'tseva et al. [90] welded a three and a five-layer aluminum to maraging steel and examined the interface. They found a flat interface and an interfacial layer with a mixture of elements at the interface.

In 2015, Li et al. [91] tried a new approach to improve the bonding strength of the Al-CS welding by machining the steel baseplate with small dovetail grooves. They reported the achievement of good quality welds, and despite the unusual interface morphology caused by the presence of the grooves, an intermetallic layer was still formed ($FeAl_2$ and Fe_2Al_5).

Costanza et al. [92] characterized Al-CS welds (with an aluminum interlayer) for transition joints, in 2016. The authors reported that despite the presence of IMCs, they got a good quality weld with a tensile test with a ductile rupture in the weaker material (aluminum interlayer) but did not discuss the matter in depth. These results draw attention to the fact that the absence of intermetallic compounds may not be absolutely indispensable to achieve a good quality welded joint.

In the same year, Aizawa et al. [93] compared experiments and numerical analyses in order to observe the interfacial layer that is formed in Al-CS welds. The experiments revealed that an Al-Fe mixed layer appeared both at the tail side and the front side of the wave. The microstructural inspection suggested the occurrence of melting in the tail side layer. The morphology of the interface found through the numerical simulation was similar to the empirical tests. It indicated that the tail side layer presented a higher temperature increase than the front side.

4.2 Explosive welding of aluminum to stainless steel

Regarding the welding between aluminum alloys and stainless steel, the quantity of papers is much smaller and more incipient than aluminum to carbon/low-alloy steel. The complexity in successfully manufacturing this combination discouraged research addressing these alloys for a long time. Most articles began to be published after 2013. As in the previous chapters, a chronological literature review regarding the explosive welding of aluminum to stainless steel is presented. The review shows the chronological development of the study.

In 1992, Izuma et al. [94] evaluated an Al-SS joint. The authors identified the difficulty in joining these alloys and proposed the use of a stainless steel interlayer to affect the distribution of energy at the interface. The work addresses crucial issues like the weldability window and the formation of intermetallic compounds. The authors showed that it is possible to weld these materials.

The year next, Hokamoto et al. [95] published one of the first great references for Al-SS joining by explosive welding. Like the previous article, the authors used a stainless steel interlayer to improve the weldability of the joint, arguing that it was not possible by conventional direct welding. Discussions about the quantification of the energy at the interface, parameter variation and the use of interlayers were very rare at the time.

In 2000, Kakimoto [96] studied the welding of these two alloys focusing mainly on practical results. The author sought the fabrication of a dissimilar transition joint for cryogenic uses, showing the promising industrial relevance that this union could have.

After that, studies addressing this combination were very scarce, and only from 2013 on did it become a more frequent subject. In that year, Guo et al. [97] showed that a direct joining of Al-SS in a cylindrical configuration is possible, which is a considerable advance since pipe transitions are an essential application for this combination. Owing to the difficulty in direct welding aluminum to stainless steel, several defects and IMCs were present at the interface, leading to a poor-quality bond.

Because of the development of hydrogen vehicles with cryogenic pressure vessels [48], Aceves et al. [5] highlight the critical need for a reliable Al-SS weld for a transition joint in order to manufacture a structurally efficient and well-insulated cryogenic pressure vessel. Such as most of the previous works, the authors chose to use interlayers between the aluminum and stainless steel. They used two layers as interlayers: one of aluminum and tried three different alloys to be used together with the aluminum (copper, titanium and tantalum). So, they tested three bimetallic interlayer configurations: Al-Cu, Al-Ti and Al-Ta. The authors got consistent welds for all three types of interlayers.

In 2016, Guo et al. [98] directly welded aluminum to stainless steel. Consistent joints were obtained, but an intermetallic layer was formed at the interface leading to poor mechanical behavior. They report that the interface waves decreased gradually along the detonation direction.

4.3 Remarks

What is known about aluminum to steel explosive welding is mostly based on the studies commented on in the literature reviews presented above. Although there are many studies in the area, the total number of articles is very limited considering the importance of the aluminum and the steels for engineering. This fact suggests that the study of welding aluminum to steel, especially to stainless steel is still incipient.

More recent works help to address some important gaps in the knowledge of this combination. These works address:

- **Feasibility of welding these materials directly**: it is necessary to define the feasibility of directly welding these materials regularly and with a practicable range of parameters.
- **Interlayer**: if it is not possible to join these materials directly with a high quality, the use of more economical interlayers to lower the final cost of the component should be investigated, since the joining of stainless steel to aluminum is sometimes done with costly materials such as nickel, titanium and silver.
- **The weldability window:** the weldability window is rarely studied in aluminum to steel welding and it needs to be addressed. If this tool does not work, it is fundamental to provide other theoretical alternatives for the selection of the parameters.
- **Direct comparison of diverse configurations:** it is necessary to compare different positioning configurations directly, to search for improvements in the mechanical properties.
- **Parameter optimization and weldability analysis:** experiments and discussions for the development of methodologies for parameter optimization and weldability analysis need to be performed to help with the selection of parameters and the choice of the best configuration.

4.4 Recent developments

It is very advantageous to evaluate the welding of aluminum to carbon steel and aluminum to stainless steel together. The similarities and differences between carbon steel and stainless steel enable several different approaches to analyze and understand issues such as weldability, parameter selection and wavy interface formation. That said, these two combinations will be analyzed together.

Carvalho et al. [99–101] undertook a group of analyses regarding the parameters selection, weldability and the pursuit of excellent quality explosive welded joints. From 2017 to 2019, Corigliano et al. [102], Kaya [45], Sherpa et al. [103], Shiran et al. [104,105] and Kaur et al. [106] also studied the welding of aluminum to steel by explosive welding from different approaches.

Regarding the regular achievement of Al-Steel quality welds, using lower collision point velocities was always better in terms of the microstructure and mechanical performance. Carvalho et al. found that collision point velocities above 3000 m/s often result in welding failure for direct welding of Al-SS [99] and Al-CS [100]. Similar results were obtained by Sherpa et al. [103] and Shiran et al. [104] when welding aluminum directly to stainless steel. In both works the results indicated that the best performance is achieved using lower collision point velocity. In addition to collision point velocity, the explosive ratio is also significant when choosing the parameters. Kaya [45] showed that it has a deep influence on the interface, IMCs formation and consequently on the mechanical properties of explosive welds. Regarding the positioning of the materials, the weldability was always improved by using the aluminum alloy as the flyer plate.

According to Carvalho et al. [99], for Al-SS welding, consistent joining could only be produced with the stainless steel positioned as the baseplate. The authors analyzed many welding failures in the welding of Al-SS when the stainless steel was positioned as the flyer plate and reported that the failure in welding stainless steel onto aluminum was related to the time that is needed for the interface to solidify [99]. Shock waves with tensile stresses from the collision and reflected on the surface of the flyer arrive at the interface before the complete solidification of the localized melting and preclude the welding [76,77]. In order to understand the influence of the welding configuration (positioning of the materials in the joint) on the Al-SS weldability, the weldability window was used to evaluate the difference between flyer and baseplate for each property individually [99]. Carvalho et al. performed an analysis of each physical property when the aluminum alloy and stainless steel exchange positions in the joint, indicating the profound influence of the thermal conductivity.

However, since the weldability window has some limitations in evaluating the overall weldability, Carvalho et al. [99] also proposed a new weldability approach based on Efremov and Zakharenko's theory [76,77], using it graphically: the so-called "time-velocity diagrams". The authors show several time-velocity diagrams used for the failure analysis of the welds using stainless steel as the flyer plate. The time-velocity diagrams proved to be a useful and reliable tool to evaluate the weldability in explosive welding, especially when applied together with the weldability window.

Based on the abovementioned theoretical analyses addressed by Carvalho et al. [99], the ideal material to be chosen as the flyer plate in welding of any dissimilar couple should have higher thermal conductivity, specific heat and melting temperature, and lower density when compared to the baseplate. It is evident that it is difficult to find real situations where all the flyer plate's properties mentioned above are favorable to the weldability. Nevertheless, depending on the particular combination, some properties will have a more significant effect on the weldability and should be prioritized. In the case of the Al-SS welding, the property that most affects the weldability is, by far, the thermal conductivity, since there is a ratio of more than 11 times between the conductivity of aluminum and stainless steel. Fig. 6.8 presents the time-velocity diagrams comparing the two different positionings of the materials.

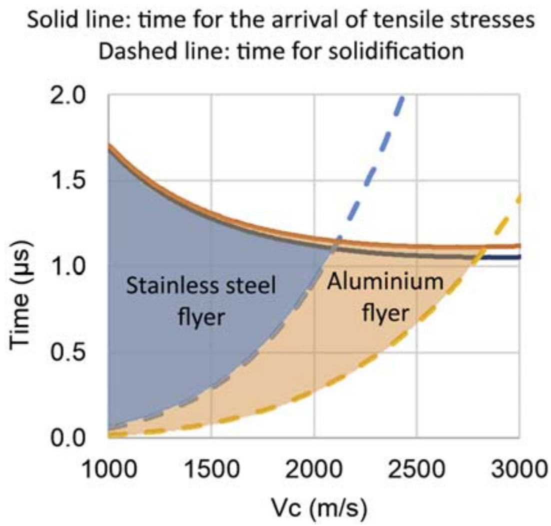

FIG. 6.8 Time-velocity diagrams for the Al-SS weld comparing the stainless steel as the flyer plate (blue) and aluminum as the flyer plate (orange) [99].

With aluminum as the flyer plate, the lines intersect at a higher velocity, indicating a wider range of collision point velocities that can be used to weld this couple, i.e. a better weldability.

Recent literature also provided strong evidence that the welding requirements are not only influenced by the properties of the alloys to be welded but also by the physical properties of the new compounds generated at the weld interface (usually intermetallic phases). Carvalho et al. [100] shows that the appearance of intermetallic compounds at the interface of Al-CS explosive welds increased the solidification time of the interfacial molten material, thereby decreasing its weldability. Therefore, in addition to the usual concerns of the intermetallic compounds related to their harmful effect on the mechanical properties, the IMCs also negatively affect the weldability. The higher the amount of IMCs at the interface, the more significant is their effect on the weldability of the materials, making the weldability window much less effective.

Despite this fact about the intermetallic compounds, there is also compelling evidence that they should not only be seen as harmful. In dissimilar welds that easily nucleate IMCs, when a proper interaction occurs, the nucleation of some intermetallic compounds is inevitable and possibly needed. The occurrence of IMCs is a sign of metallurgical interaction and has been reported by several authors [107−109] as being present in most of the good quality joints. That said, the presence of intermetallic compounds in itself does not indicate a poor-quality explosive weld. Carvalho et al. [101] showed that the most critical knowledge in dissimilar explosive welding is not the discovery of how to produce welds without IMCs, but the discerning of how the IMCs will be distributed within the joint in terms of shape and morphology. That is, knowledge of how to achieve a weld with appropriate metallurgical interaction, an interfacial morphology that can accommodate deformation and that does not have a thick and completely continuous intermetallic layer. Fig. 6.9 shows the wavy morphology that perfectly represents this theory, where the brittle intermetallic region is surrounded (and protected) by deformed ductile material. The above-mentioned results are in agreement with the results obtained by Kaya et al. [45] (welding aluminum to carbon steel) and Shiran et al. [104] (welding aluminum to stainless steel). In both studies the best mechanical results were obtained for joints with considerable

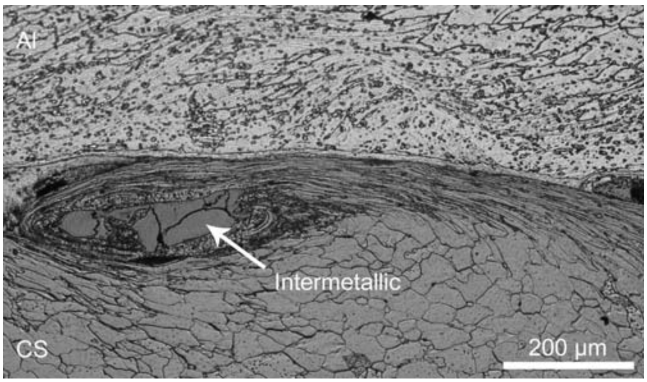

FIG. 6.9 Curled wave with deformed material surrounding completely the intermetallic compound formed at the interface.

intermetallic formation. However, as the results of Shiran et al. [105] show, applications where there will be new thermal cycles (as in some components for transition joints), the presence of intermetallics is critical because the intermetallic layer may significantly increase depending on the thermal cycle.

Explosive welds with characteristics such as in Fig. 6.9 prevent the IMCs from being regions favorable to an uninterrupted propagation of a brittle fracture through the interface and therefore present the best mechanical behavior. Carvalho et al. [101] compared welds with different characteristics. While the Al-SS weld (flat interface, continuous IMCs) presented poor mechanical behavior, the Al-CS weld (wavy interface, IMCs formed in pockets wrapped by deformed material) presented excellent mechanical behavior. The direct comparison between Al-CS and Al-SS welds [101] also helped to understand the effects of the physical properties of the materials. The dissimilarity of the properties between carbon steel and stainless steel notably changed the interface morphology. This proves that the parameter requirements for wave formation on the Al-SS are higher than for the Al-CS. The problem is that in Al-SS, the disproportion in properties between the stainless steel and the aluminum usually makes it very difficult to fulfill these high requirements for a wavy formation because reaching these parameters (high collision point velocity) leads to the failure of the weld [101]. Indeed, in all recent works, such as the studies performed by Kaur et al. [106] Sherpa et al. [103] and Shiran et al. [104,105], the interfacial morphology found for aluminum to stainless steel explosive welding was essentially flat. This is a clear indication that there is a great difficulty to form waves for this metallic combination.

According to Carvalho et al. [101], the Al-CS pair proved to have a much better weldability than the Al-SS. The trials, which were performed with and without an aluminum interlayer, proved that for both pairs, a direct weld between the materials is possible. The use of the interlayer had no beneficial effect on the mechanical properties of the Al-CS welds: an Al-CS steel joint with excellent tensile-shear properties was achieved by direct welding using a low collision point velocity, with the fracture occurring outside the joining region [101]. On the other hand, the Al-SS welding is very difficult to obtain and was considerably improved using an interlayer. The best results in terms of mechanical properties and microstructure were achieved for the direct welding of Al-CS. For Al-SS joining, despite the improvement in mechanical properties and behavior resulting from the use of aluminum as an interlayer, the fracture on the tensile-shear tests occurred inside the interlayer.

5. Conclusions

The current chapter presented an overview of the explosive welding process and the most recent developments of the explosive joining of aluminum to copper, aluminum to carbon steel and aluminum to stainless steel. Based on these studies, aspects related to process development, welding quality and weldability were discussed. The final remarks of this work are outlined below:

- Explosive welding is a joining technology with a very high industrial relevance. However, the industrial application of the process can be strongly expanded by the development of dissimilar joints with optimized mechanical properties. Although many studies

have been published over the years, which strongly increased the knowledge on the process fundaments, intensive research on dissimilar welding is still required;
- The welding between aluminum and copper is possible without the use of unconventional techniques or interlayers for both configurations: aluminum as the flyer or baseplate;
- The welding between aluminum to carbon steel is possible without the use of alternative techniques or interlayers. The available results show that the weldability and properties are better when aluminum is used as the flyer plate;
- The aluminum to stainless steel welding has the worst weldability among the three combinations addressed. The use of an interlayer significantly improves the mechanical properties of the welds.
- For aluminum to copper and aluminum to steel welding, the welds manufactured with lower collision point velocities achieved success more often and presented better quality;
- The wave interface factor (WIF) is a reliable approach to help identify the possibility of a metallic combination forming a wavy interface;
- The weldability is affected by the physical properties of the materials and by the presence of intermetallic compounds. The influence of the physical properties is mainly related to the difference in the values of the properties between the plates being welded;
- The existence of brittle intermetallic compounds at the weld interface does not, in itself, indicate a poor-quality explosive weld joint in terms of mechanical properties;
- The quality of the welded joint comes from the interfacial microstructure and how it can accommodate and distribute the brittle intermetallic compounds.

Acknowledgments

This research is sponsored by FEDER funds through the program COMPETE — *Programa Operational Factores de Competitividade* — and by national funds through FCT — *Fundação para a Ciência e a Tecnologia*, under the project UIDB/EMS/00285/2020.

References

[1] J.E. Gould, Mechanisms of bonding for solid-state welding processes, in: T. Lienert, T. Siewert, S. Babu, V. Acoff (Eds.), ASM Handb. - Vol. 6A Weld. Fundam. Process., ASM International, Materials Park, Ohio, USA, 2011, pp. 171—178, https://doi.org/10.31399/asm.hb.v06a.a0005574.

[2] R.M. Chao, J.M. Yang, S.R. Lay, Interfacial toughness for the shipboard aluminum/steel structural transition joint, Marine Structures 10 (1997) 353—362, https://doi.org/10.1016/S0951-8339(96)00018-4.

[3] L. Tricarico, R. Spina, Mechanical strength of Fe/Al structural transition joints subject to thermal loading, Archives of Materials Science and Engineering 37 (2009) 85—93.

[4] L. Tricarico, R. Spina, D. Sorgente, M. Brandizzi, Effects of heat treatments on mechanical properties of Fe/Al explosion-welded structural transition joints, Materials and Design 30 (2009) 2693—2700, https://doi.org/10.1016/j.matdes.2008.10.010.

[5] S.M. Aceves, F. Espinosa-Loza, J.W. Elmer, R. Huber, Comparison of Cu, Ti and Ta interlayer explosively fabricated aluminum to stainless steel transition joints for cryogenic pressurized hydrogen storage, International Journal of Hydrogen Energy 40 (2015) 1490—1503, https://doi.org/10.1016/j.ijhydene.2014.11.038.

[6] Y. Wei, H. Li, F. Sun, J. Zou, The interfacial characterization and performance of Cu/Al-conductive heads processed by explosion welding, cold pressure welding, and solid-liquid casting, Metals 9 (2019) 237, https://doi.org/10.3390/met9020237.

[7] Y. Kaya, Investigation of copper-aluminium composite materials produced by explosive welding, Metals 8 (2018) 780, https://doi.org/10.3390/met8100780.
[8] S. Liu, J. Banker, C. Prothe, Explosion welding, in: T. Lienert, T. Siewert, S. Babu, V. Acoff (Eds.), ASM Handb. - Vol. 6A Weld. Fundam. Process., ASM International, Materials Park, Ohio, USA, 2011, pp. 690−700, https://doi.org/10.31399/asm.hb.v06a.a0005602.
[9] B. Crossland, Explosive Welding of Metals and its Application, first ed., Oxford University Press, New York, USA, 1982.
[10] V.D. Linse, P.I. Temple, Explosion welding, in: AWS Weld. Handb. − vol. 2 - Weld. Process., eighth ed., American Welding Society, USA, 1991, pp. 765−781.
[11] G.A. Young, J.G. Banker, A. Nobili, B.K. Sareen, W.L. Roth, Explosion welding, in: A. O'Brien, C. Guzman (Eds.), AWS Weld. Handb. Vol. 3 - Weld. Process. Part 2, ninth ed., American Welding Society, Miami, USA, 2007, pp. 303−331.
[12] H. El-Sobky, Mechanics of explosive welding, in: T.Z. Blazynski (Ed.), Explos. Welding, Form. Compact, Springer Netherlands, Dordrecht, 1983, pp. 189−217, https://doi.org/10.1007/978-94-011-9751-9_6.
[13] S.H. Carpenter, R.H. Wittman, Explosion welding, Annual Review of Materials Science 5 (1975) 177−199, https://doi.org/10.1146/annurev.ms.05.080175.001141.
[14] R. Prümmer, The use of lead in explosive cladding, Propellants, Explosives, Pyrotechnics 1 (1976) 103−107, https://doi.org/10.1002/prep.19760010506.
[15] P.O.K. Krehl, Chronology, in: Hist. Shock Waves, Explos. Impact, Springer Berlin Heidelberg, Berlin, Heidelberg, 2009, pp. 169−844, https://doi.org/10.1007/978-3-540-30421-0_3.
[16] G.R. Cowan, O.R. Bergmann, A.H. Holtzman, Mechanism of bond zone wave formation in explosion-clad metals, Metallurgical and Materials Transactions B 2 (1971) 3145−3155, https://doi.org/10.1007/BF02814967.
[17] G.R. Cowan, A.H. Holtzman, Flow configurations in colliding plates: explosive bonding, Journal of Applied Physics 34 (1963) 928−939, https://doi.org/10.1063/1.1729565.
[18] A.S. Bahrani, T.J. Black, B. Crossland, The mechanics of wave formation in explosive welding, Proceedings of the Royal Society A Mathematical Physical and Engineering Sciences 296 (1967) 123−136, https://doi.org/10.1098/rspa.1967.0010.
[19] J.N. Hunt, Wave formation in explosive welding, Philosophical Magazine A 17 (1968) 669−680, https://doi.org/10.1080/14786436808223020.
[20] J.F. Kowalick, D.R. Hay, A mechanism of explosive bonding, Metallurgical Transactions 2 (1971) 1953−1958, https://doi.org/10.1007/BF02913429.
[21] G. Abrahamson, Permanent periodic surface deformations due to a traveling jet, Journal of Applied Mechanics (1961) 519−528, https://doi.org/10.1115/1.3641777.
[22] K.K. Botros, T.K. Groves, Characteristics of the wavy interface and the mechanism of its formation in high-velocity impact welding, Journal of Applied Physics 51 (1980) 3715−3721, https://doi.org/10.1063/1.328157.
[23] S.R. Reid, A discussion of the mechanism of interface wave generation in explosive welding, International Journal of Mechanical Sciences 16 (1974) 399−413, https://doi.org/10.1016/0020-7403(74)90014-9.
[24] R.A. Patterson, Fundamentals of explosion welding, in: ASM Handb. - vol. 6 Welding, Brazing Solder, ASM International, Materials Park, Ohio, USA, 1993, pp. 160−164, https://doi.org/10.31399/asm.hb.v06.a0001351.
[25] X.J. Li, F. Mo, X.H. Wang, B. Wang, K.X. Liu, Numerical study on mechanism of explosive welding, Science and Technology of Welding & Joining 17 (2012) 36−41, https://doi.org/10.1179/1362171811Y.0000000071.
[26] E. Carton, Wave forming mechanisms in explosive welding, Materials Science Forum 465−466 (2004) 219−224, https://doi.org/10.4028/www.scientific.net/MSF.465-466.219.
[27] I.A. Bataev, S. Tanaka, Q. Zhou, D.V. Lazurenko, A.M.J. Junior, A.A. Bataev, K. Hokamoto, A. Mori, P. Chen, Towards better understanding of explosive welding by combination of numerical simulation and experimental study, Materials and Design 169 (2019) 107649, https://doi.org/10.1016/j.matdes.2019.107649.
[28] I. Plaksin, J. Campos, J. Ribeiro, R. Mendes, J. Direito, D. Braga, R. Pruemmer, Novelties in physics of explosive welding and powder compaction, Journal de Physique IV 110 (2003) 797−802, https://doi.org/10.1051/jp4:20020791.
[29] R. Mendes, J.B. Ribeiro, A. Loureiro, Effect of explosive characteristics on the explosive welding of stainless steel to carbon steel in cylindrical configuration, Materials and Design 51 (2013) 182−192, https://doi.org/10.1016/j.matdes.2013.03.069.
[30] J.B. Ribeiro, R. Mendes, A. Loureiro, Review of the weldability window concept and equations for explosive welding, Journal of Physics: Conference Series 500 (2014) 052038, https://doi.org/10.1088/1742-6596/500/5/052038.

[31] A.A. Deribas, I.D. Zakharenko, Surface effects with oblique collisions between metallic plates, Combustion, Explosion and Shock Waves 10 (1974) 358−367, https://doi.org/10.1007/BF01463767.
[32] W.S. Rosset, Analysis of explosive bonding parameters, Materials and Manufacturing Processes 21 (2006) 634−638, https://doi.org/10.1080/10426910600611136.
[33] J.M. Walsh, R.G. Shreffler, F.J. Willig, Limiting conditions for jet formation in high velocity collisions, Journal of Applied Physics 24 (1953) 349−359, https://doi.org/10.1063/1.1721278.
[34] K.K. Botros, T.K. Groves, Fundamental impact-welding parameters-an experimental investigation using a 76-mm powder cannon, Journal of Applied Physics 51 (1980) 3706−3714, https://doi.org/10.1063/1.328156.
[35] V.D. Linse, Procedure development and practice considerations for explosion welding, in: ASM Handb. - vol. 6 Welding, Brazing Solder, ASM International, Materials Park, Ohio, USA, 1993, pp. 896−900, https://doi.org/10.31399/asm.hb.v06.a0001449.
[36] S.P. Marsh, LASL Shock Hugoniot Data, University of California Press, Berkeley, USA, 1980.
[37] J.G. Banker, E.G. Reineke, Explosion welding, in: ASM Handb. - vol. 6 Welding, Brazing Solder, ASM International, Materials Park, Ohio, USA, 1993, pp. 303−305, https://doi.org/10.31399/asm.hb.v06.a0001376.
[38] M.D. Chadwick, P.W. Jackson, Explosive welding in planar geometries, in: T.Z. Blazynski (Ed.), Explos. Welding, Form. Compact, Springer, Netherlands, Dordrecht, 1983, pp. 219−287, https://doi.org/10.1007/978-94-011-9751-9_7.
[39] S. Saravanan, K. Raghukandan, Metallurgical and mechanical properties of wire-mesh reinforced dissimilar explosive cladding, Materials Science Forum 910 (2018) 14−18, https://doi.org/10.4028/www.scientific.net/msf.910.14.
[40] H. Amani, M. Soltanieh, Intermetallic phase formation in explosively welded Al/Cu bimetals, Metallurgical and Materials Transactions B, Process Metallurgy and Materials Processing Science 47 (2016) 2524−2534, https://doi.org/10.1007/s11663-016-0682-1.
[41] Y. Wei, Y. Luo, H. Qu, J. Zou, S. Liang, Microstructure evolution and failure analysis of an aluminum−copper cathode conductive head produced by explosive welding, Journal of Materials Engineering and Performance 26 (2017) 6158−6166, https://doi.org/10.1007/s11665-017-3055-2.
[42] M. Honarpisheh, M. Asemabadi, M. Sedighi, Investigation of annealing treatment on the interfacial properties of explosive-welded Al/Cu/Al multilayer, Materials and Design 37 (2012) 122−127, https://doi.org/10.1016/j.matdes.2011.12.045.
[43] M.M. Hoseini-Athar, B. Tolaminejad, Interface morphology and mechanical properties of Al-Cu-Al laminated composites fabricated by explosive welding and subsequent rolling process, Metals and Materials International 22 (2016) 670−680, https://doi.org/10.1007/s12540-016-5687-4.
[44] K.R. Trethewey, G.T. Little, Explosion-bonded transition joints for structural applications, Construction and Building Materials 3 (1989) 64−72, https://doi.org/10.1016/S0950-0618(89)80002-9.
[45] Y. Kaya, Microstructural, mechanical and corrosion investigations of ship steel-aluminum bimetal composites produced by explosive welding, Metals 8 (2018) 544, https://doi.org/10.3390/met8070544.
[46] A. Gullino, P. Matteis, F. D'Aiuto, Review of aluminum-to-steel welding technologies for car-body applications, Metals 9 (2019) 315, https://doi.org/10.3390/met9030315.
[47] X. Guo, H. Wang, Z. Liu, L. Wang, F. Ma, J. Tao, Interface and performance of CLAM steel/aluminum clad tube prepared by explosive bonding method, International Journal of Advanced Manufacturing Technology 82 (2016) 543−548, https://doi.org/10.1007/s00170-015-7380-z.
[48] S.M. Aceves, G. Petitpas, F. Espinosa-Loza, M.J. Matthews, E. Ledesma-Orozco, Safe, long range, inexpensive and rapidly refuelable hydrogen vehicles with cryogenic pressure vessels, International Journal of Hydrogen Energy 38 (2013) 2480−2489, https://doi.org/10.1016/j.ijhydene.2012.11.123.
[49] P. Corigliano, V. Crupi, E. Guglielmino, Non linear finite element simulation of explosive welded joints of dissimilar metals for shipbuilding applications, Ocean Engineering 160 (2018) 346−353, https://doi.org/10.1016/j.oceaneng.2018.04.070.
[50] B. Predel, Al-Cu (Aluminum-Copper), in: O. Madelung (Ed.), Landolt-Börnstein - Phase Equilibria, Crystallogr. Thermodyn. Data Bin. Alloy, Springer-Verlag, Berlin, Heidelberg, 1991, pp. 1−9, https://doi.org/10.1007/10000866_100.
[51] J. Ouyang, E. Yarrapareddy, R. Kovacevic, Microstructural evolution in the friction stir welded 6061 aluminum alloy (T6-temper condition) to copper, Journal of Materials Processing Technology 172 (2006) 110−122, https://doi.org/10.1016/j.jmatprotec.2005.09.013.

[52] E. Hug, N. Bellido, Brittleness study of intermetallic (Cu, Al) layers in copper-clad aluminium thin wires, Materials Science and Engineering A 528 (2011) 7103–7106, https://doi.org/10.1016/j.msea.2011.05.077.
[53] J.L. Murray, The aluminium-copper system, International Metals Reviews 30 (1985) 211–234, https://doi.org/10.1179/imtr.1985.30.1.211.
[54] L.D. Gulay, B. Harbrecht, The crystal structure of ζ2-Al3Cu4-δ, Zeitschrift für Anorganische und Allgemeine Chemie 629 (2003) 463–466, https://doi.org/10.1002/zaac.200390076.
[55] N. Ponweiser, C.L. Lengauer, K.W. Richter, Re-investigation of phase equilibria in the system Al–Cu and structural analysis of the high-temperature phase η1-Al1−δCu, Intermetallics 19 (2011) 1737–1746, https://doi.org/10.1016/j.intermet.2011.07.007.
[56] T. Izuma, K. Hokamoto, M. Fujita, T. Niwatsukino, Improvement of bond strength of Al/Cu transition joints made by a single-shot explosive welding technique using a Cu intermediate plate, Welding International 8 (1994) 618–622, https://doi.org/10.1080/09507119409548660.
[57] W.E. Veerkamp, Copper-to-aluminum transitions in high direct-current bus systems, in: 42nd Annu. Pet. Chem. Ind. Conf., IEEE, 2002, pp. 187–195, https://doi.org/10.1109/PCICON.1995.523953.
[58] H. Dyja, S. Mróz, Z. Stradomski, Properties of joint in the bimetallic rods Cu-Al and Cu-Steel after explosive cladding and the process of rolling, Metalurgija 42 (2003) 185–191.
[59] S. Berski, Z. Stradomski, H. Dyja, Quality of bimetal Al-Cu joint after explosive cladding, The Journal of Achievements in Materials and Manufacturing Engineering 22 (2007) 73–76.
[60] B. Gülenç, Investigation of interface properties and weldability of aluminum and copper plates by explosive welding method, Materials and Design 29 (2008) 275–278, https://doi.org/10.1016/j.matdes.2006.11.001.
[61] J.Z. Ashani, S.M. Bagheri, Explosive scarf welding of aluminum to copper plates and their interface properties, Materialwissenschaft und Werkstofftechnik 40 (2009) 690–698, https://doi.org/10.1002/mawe.200900415.
[62] M. Asemabadi, M. Sedighi, M. Honarpisheh, Investigation of cold rolling influence on the mechanical properties of explosive-welded Al/Cu bimetal, Materials Science and Engineering A 558 (2012) 144–149, https://doi.org/10.1016/j.msea.2012.07.102.
[63] M. Sedighi, M. Honarpisheh, Experimental study of through-depth residual stress in explosive welded Al–Cu–Al multilayer, Materials and Design 37 (2012) 577–581, https://doi.org/10.1016/j.matdes.2011.10.022.
[64] H. Paul, L. Lityńska-Dobrzyńska, M. Prazmowski, Microstructure and phase constitution near the interface of explosively welded aluminum/copper plates, Metallurgical and Materials Transactions A 44 (2013) 3836–3851, https://doi.org/10.1007/s11661-013-1703-1.
[65] S.Y. Chen, Z.W. Wu, K.X. Liu, X.J. Li, N. Luo, G.X. Lu, Atomic diffusion behavior in Cu-Al explosive welding process, Journal of Applied Physics 113 (2013) 044901, https://doi.org/10.1063/1.4775788.
[66] S. Mróz, P. Szota, A. Stefanik, S. Wasek, G. Stradomski, Analysis of Al-Cu bimetallic bars properties after explosive welding and rolling in modified passes, Archives of Metallurgy and Materials 60 (2015) 427–432, https://doi.org/10.1515/amm-2015-0070.
[67] A. Loureiro, R. Mendes, J.B. Ribeiro, R.M. Leal, I. Galvão, Effect of explosive mixture on quality of explosive welds of copper to aluminium, Materials and Design 95 (2016) 256–267, https://doi.org/10.1016/j.matdes.2016.01.116.
[68] S. Saravanan, K. Raghukandan, K. Hokamoto, Improved microstructure and mechanical properties of dissimilar explosive cladding by means of interlayer technique, Archives of Civil and Mechanical Engineering 16 (2016) 563–568, https://doi.org/10.1016/j.acme.2016.03.009.
[69] M.M. Hoseini Athar, B. Tolaminejad, Weldability window and the effect of interface morphology on the properties of Al/Cu/Al laminated composites fabricated by explosive welding, Materials and Design 86 (2015) 516–525, https://doi.org/10.1016/j.matdes.2015.07.114.
[70] G.H.S.F.L. Carvalho, R. Mendes, R.M. Leal, I. Galvão, A. Loureiro, Effect of the flyer material on the interface phenomena in aluminium and copper explosive welds, Materials and Design 122 (2017) 172–183, https://doi.org/10.1016/j.matdes.2017.02.087.
[71] G.H.S.F.L. Carvalho, I. Galvão, R. Mendes, R.M. Leal, A. Loureiro, Influence of base material properties on copper and aluminium–copper explosive welds, Science and Technology of Welding & Joining 23 (2018) 501–507, https://doi.org/10.1080/13621718.2017.1417783.
[72] G.H.S.F.L. Carvalho, I. Galvão, R. Mendes, R.M. Leal, A. Loureiro, Friction stir welding and explosive welding of aluminum/copper: process analysis, Materials and Manufacturing Processes 34 (2019) 1243–1250, https://doi.org/10.1080/10426914.2019.1644452.

[73] G.H.S.F.L. Carvalho, I. Galvão, R. Mendes, R.M. Leal, A. Loureiro, Weldability of aluminium-copper in explosive welding, International Journal of Advanced Manufacturing Technology 103 (2019) 3211–3221, https://doi.org/10.1007/s00170-019-03841-9.
[74] A. Tajyar, A. Masoumi, Experimental analysis of bonding strength in shape rolling of Al–Cu bimetallic circular pipes into square tubes, Proceedings - Institution of Mechanical Engineers Part C Journal of Mechanical Engineering Science 231 (2017) 4087–4098, https://doi.org/10.1177/0954406216661009.
[75] I.V. Denisov, I.V. Saykov, R.D. Kapustin, Explosion welding of Al + Cu bimetallic joints for electrical contacts, Welding International 31 (2017) 773–776, https://doi.org/10.1080/09507116.2017.1318504.
[76] I.D. Zakharenko, Critical conditions in detonation welding, Combustion, Explosion and Shock Waves 8 (1972) 341–345, https://doi.org/10.1007/BF00742312.
[77] V.V. Efremov, I.D. Zakharenko, Determination of the upper limit to explosive welding, Combustion, Explosion and Shock Waves 12 (1976) 226–230, https://doi.org/10.1007/BF00744893.
[78] S.J. Matthews, D.G. Howden, N.F. Bratkovich, J.F. King, Dissimilar metals, in: AWS Weld. Handb. vol. 4 - Met. Their Weldability, American Welding Society, USA, 1982, pp. 513–547.
[79] B. Predel, Al-Fe (Aluminum-Iron), in: O. Madelung (Ed.), Landolt-Börnstein - Phase Equilibria, Crystallogr. Thermodyn. Data Bin. Alloy, Springer-Verlag, Berlin, Heidelberg, 1991, pp. 1–10, https://doi.org/10.1007/10000866_104.
[80] B. Predel, Al-Cr (aluminum - chromium), in: B. Predel (Ed.), Landolt-Börnstein - Phys. Chem. 12A, Springer-Verlag, Berlin, Heidelberg, 2006, pp. 1–4, https://doi.org/10.1007/10793176_84.
[81] B. Predel, Al-Ni (aluminum - nickel), in: B. Predel (Ed.), Landolt-Börnstein - Phys. Chem. 12A, Springer-Verlag, Berlin, Heidelberg, 2006, pp. 1–5, https://doi.org/10.1007/10793176_104.
[82] ASM Handbook, Volume 3 - Alloy Phase Diagrams, tenth ed., ASM International, Materials Park, Ohio, USA, 1992.
[83] X. Li, A. Scherf, M. Heilmaier, F. Stein, The Al-rich part of the Fe-Al phase diagram, Journal of Phase Equilibria and Diffusion 37 (2016) 162–173, https://doi.org/10.1007/s11669-015-0446-7.
[84] M.I.R. Basariya, N.K. Mukhopadhyay, Structural and mechanical behaviour of Al-Fe intermetallics, in: Intermet. Compd. - Form. Appl., InTech, 2018, https://doi.org/10.5772/intechopen.73944.
[85] A. Szecket, O.T. Inal, D.J. Vigueras, J. Rocco, A wavy versus straight interface in the explosive welding of aluminum to steel, Journal of Vacuum Science and Technology A Vacuum, Surfaces, Film. 3 (1985) 2588–2593, https://doi.org/10.1116/1.572839.
[86] T. Leszczynski, Structure and properties of St41 + A1 aluminium joints produced by explosive welding, Welding International 6 (1992) 347–350, https://doi.org/10.1080/09507119209548200.
[87] Y. Li, H. Hashimoto, E. Sukedai, Y. Zhang, Z. Zhang, Morphology and structure of various phases at the bonding interface of Al/steel formed by explosive welding, Journal of Electron Microscopy 49 (2000) 5–16, https://doi.org/10.1093/oxfordjournals.jmicro.a023791.
[88] J.H. Han, J.P. Ahn, M.C. Shin, Effect of interlayer thickness on shear deformation behavior of AA5083 aluminum alloy/SS41 steel plates manufactured by explosive welding, Journal of Materials Science 38 (2003) 13–18, https://doi.org/10.1023/A:1021197328946.
[89] M. Acarer, B. Demir, An investigation of mechanical and metallurgical properties of explosive welded aluminum-dual phase steel, Materials Letters 62 (2008) 4158–4160, https://doi.org/10.1016/j.matlet.2008.05.060.
[90] L.A. Mal'tseva, D.S. Tyushlyaeva, T.V. Mal'tseva, M.V. Pastukhov, N.N. Lozhkin, D.V. Inyakin, L.A. Marshuk, Metallic layered composite materials produced by explosion welding: structure, properties, and structure of the transition zone, Russian Metallurgy 2014 (2014) 817–825, https://doi.org/10.1134/S0036029514100073.
[91] X. Li, H. Ma, Z. Shen, Research on explosive welding of aluminum alloy to steel with dovetail grooves, Materials and Design 87 (2015) 815–824, https://doi.org/10.1016/j.matdes.2015.08.085.
[92] G. Costanza, V. Crupi, E. Guglielmino, A. Sill, M.E. Tata, Metallurgical characterization of an explosion welded aluminum/steel joint, Metallurgia Italiana 108 (2016) 17–22.
[93] Y. Aizawa, J. Nishiwaki, Y. Harada, S. Muraishi, S. Kumai, Experimental and numerical analysis of the formation behavior of intermediate layers at explosive welded Al/Fe joint interfaces, Journal of Manufacturing Processes 24 (2016) 100–106, https://doi.org/10.1016/j.jmapro.2016.08.002.
[94] T. Izuma, K. Hokamoto, M. Fujita, M. Aoyagi, Single-shot explosive welding of hard-to-weld A5083/SUS304 clad using SUS304 intermediate plate, Welding International 6 (1992) 941–946, https://doi.org/10.1080/09507119209548320.

[95] K. Hokamoto, T. Izuma, M. Fujita, New explosive welding technique to weld aluminum alloy and stainless steel plates using a stainless steel intermediate plate, Metallurgical and Transactions A 24 (1993) 2289–2297, https://doi.org/10.1007/BF02648602.

[96] E. Kakimoto, Joint material of aluminium and stainless steel for welding, Welding International 14 (2000) 614–619, https://doi.org/10.1080/09507110009549238.

[97] X. Guo, J. Tao, W. Wang, H. Li, C. Wang, Effects of the inner mould material on the aluminium-316L stainless steel explosive clad pipe, Materials and Design 49 (2013) 116–122, https://doi.org/10.1016/j.matdes.2013.02.001.

[98] X. Guo, M. Fan, L. Wang, F. Ma, Bonding interface and bending deformation of Al/316LSS clad metal prepared by explosive welding, Journal of Materials Engineering and Performance 25 (2016) 2157–2163, https://doi.org/10.1007/s11665-016-2057-9.

[99] G.H.S.F.L. Carvalho, I. Galvão, R. Mendes, R.M. Leal, A. Loureiro, Explosive welding of aluminium to stainless steel, Journal of Materials Processing Technology 262 (2018) 340–349, https://doi.org/10.1016/j.jmatprotec.2018.06.042.

[100] G.H.S.F.L. Carvalho, I. Galvão, R. Mendes, R.M. Leal, A. Loureiro, Formation of intermetallic structures at the interface of steel-to-aluminium explosive welds, Materials Characterization 142 (2018) 432–442, https://doi.org/10.1016/j.matchar.2018.06.005.

[101] G.H.S.F.L. Carvalho, I. Galvão, R. Mendes, R.M. Leal, A. Loureiro, Microstructure and mechanical behaviour of aluminium-carbon steel and aluminium-stainless steel clads produced with an aluminium interlayer, Materials Characterization 155 (2019) 109819, https://doi.org/10.1016/j.matchar.2019.109819.

[102] P. Corigliano, V. Crupi, E. Guglielmino, A. Mariano Sili, Full-field analysis of AL/FE explosive welded joints for shipbuilding applications, Marine Structures 57 (2018) 207–218, https://doi.org/10.1016/j.marstruc.2017.10.004.

[103] B.B. Sherpa, A. Upadhyay, S. Kumar, V. Mangla, P.D. Kumar, A. Agarwal, Examination of Joint Integrity in parallel plate configuration of explosive welded SS-Al combination, Materials Today: Proceedings 4 (2017) 1260–1267, https://doi.org/10.1016/j.matpr.2017.01.146.

[104] M.R.K.G. Shiran, H. Bakhtiari, S.A.A. Mousavi, G. Khalaj, S.M. Mirhashemi, Effect of stand-off distance on the mechanical and metallurgical properties of explosively bonded 321 austenitic stainless steel - 1230 aluminum alloy tubes, Materials Research 20 (2017) 291–302, https://doi.org/10.1590/1980-5373-mr-2016-0516.

[105] M.K.G. Shiran, G. Khalaj, H. Pouraliakbar, M. Jandaghi, H. Bakhtiari, M. Shirazi, Effects of heat treatment on the intermetallic compounds and mechanical properties of the stainless steel 321–aluminum 1230 explosive-welding interface, International Journal of Minerals, Metallurgy and Materials 24 (2017) 1267–1277, https://doi.org/10.1007/s12613-017-1519-x.

[106] J. Kaur, V. Mangla, J. Singh, S. Kumar, N. Srivastava, Cladding of stainless steel (SS304) on aluminium alloy (AA1100) by explosive welding, Materials Today: Proceedings 5 (2018) 19136–19139, https://doi.org/10.1016/j.matpr.2018.06.267.

[107] D.M. Fronczek, R. Chulist, L. Litynska-Dobrzynska, S. Kac, N. Schell, Z. Kania, Z. Szulc, J. Wojewoda-Budka, Microstructure and kinetics of intermetallic phase growth of three-layered A1050/AZ31/A1050 clads prepared by explosive welding combined with subsequent annealing, Materials and Design 130 (2017) 120–130, https://doi.org/10.1016/j.matdes.2017.05.051.

[108] P. Parchuri, S. Kotegawa, H. Yamamoto, K. Ito, A. Mori, K. Hokamoto, Benefits of intermediate-layer formation at the interface of Nb/Cu and Ta/Cu explosive clads, Materials and Design 166 (2019) 107610, https://doi.org/10.1016/j.matdes.2019.107610.

[109] I.A. Bataev, D.V. Lazurenko, S. Tanaka, K. Hokamoto, A.A. Bataev, Y. Guo, A.M. Jorge, High cooling rates and metastable phases at the interfaces of explosively welded materials, Acta Materialia 135 (2017) 277–289, https://doi.org/10.1016/j.actamat.2017.06.038.

This page intentionally left blank

CHAPTER

7

Ultrasonic welding

Jean Pierre Bergmann, Tobias Köhler, Pascal Pöthig

Technische Universität Ilmenau, Ilmenau, Germany

1. Introduction

Welding processes represent a crucial step in industrial production in order to assembly different parts to each other. On one hand welding should occur in a short time and be as cheap as possible and on the other hand, the joining process should conserve the material properties to allow the integrity of the welded construction. The resulting material properties in the welded area are typically depending on the temperature outline over the time, which defines for example dwelling time at high temperature or the cooling rate.

Welding processes can be carried out at temperatures over melting temperature (liquidus), forming then a common melting pool among the welding partners and a weld after solidification. The welded area has characteristics, which are depending on the mixing of the partners itself. On the contrary, solid-state welding occurs below the melting temperature in the solid-state, whereas not only temperature and time, but also plastic deformation are relevant physical parameters. Basically, the joining occurs over diffusion in the solid state, as diffusion welding, which can be supported from plastic deformation. In this way during the process activation, the energy is reduced. Solid state processes turn to be very interesting in order to weld temperature sensitive metals (or parts) and different metals to each other, which is a recurrent challenging task in research and application [1–5].

Solid-state processes can be grouped depending on the energy source, which can be gases (gas pressure welding), movement (friction welding, ultrasonic welding, explosion welding) or electric current (resistance pressure welding) [1].

Among the solid-state processes for metals, ultrasonic welding gained to a high industrial use especially to join thin sheets (solar heat devices, batteries, busbars, hair pins etc.), cables and wires for supply systems on board or for electrical application. Ultrasonic metal welding allows low welding times and relatively low cost for invest and joint realization in serial production. Parts to be welded can be directly handled and manually placed in the welding device. Due to the low welding time the parts can be almost straight handled after welding.

Some estimation regarding the market development for metal ultrasonic devices confirm that between the years 2020–2024, a growth of approximately 7% (CAGR) will occur.

Advanced Joining Processes
https://doi.org/10.1016/B978-0-12-820787-1.00007-3

According to Technavio [6] the most important driver for the market growth for metal ultrasonic devices are technological advances in the equipment, whereas it has to be added that the raising importance of electromobility is a concurrent advantageous situation. These facts can be pointed out through a parametrization of the welding process, shifting it to a technological mature and digitalization ready process.

Main markets for ultrasonic welding are according to Technovia [6] and Market.us [7]: Electronics, Erospace & Automotive, Life Sciences & Medical and Power.

Metal ultrasonic welding is a method for joining similar or dissimilar metals by applying high frequency vibrations in the welding area. The high frequency ultrasonic energy is usually 20 kHz or above. The ultrasonic vibrations generate a friction-like relative motion between two join partners, which are clamped under a light pressure between the vibrator, also known as a horn, and the anvil. The process occurs in the solid-state within less than 1−3 s − depending on the materials and their thickness − and is characterized by no melting of the base metals [8−11]. Basically, a distinction can be made between two types of ultrasonic welding, depending on how the vibrations are initiated to the part surfaces. In the case of metal welding, the vibrations are parallel to the part surfaces, whereas they are initiated perpendicular in plastic welding. Due to that, the range of weldable materials can approximately be divided in metals and thermoplastics [10,12].

The use of ultrasonic vibrations as a technology to join materials dates indeed back many years. Ultrasonic technology was first used for grain refinement of molten metals in the 1930s. In the 1940s for soldering and with resistance and arc welding as well as for joining plastics in the 1950s. The ultrasonic metal welding process was invented by chance during investigations to improve the grain structure of resistance spot welds. The objective was to decrease the surface resistance without time-consuming preparation of the joining surfaces by adding ultrasonic energy via the spot welding electrodes before the welding current pulse. It was found that the ultrasound alone was sometimes capable to produce a bonding of the metals even if no welding current was flowing. Based on this discovery the introduction of ultrasonic welding in the industrial production between 1954 and 1956 was described as the most important progress in the field of joining technology for metallic materials of these years. Considering the heating of plastics via ultrasound, the first patents for this process were granted in 1951 and 1953. However, not until a decade later ultrasonic welding of plastics was developed to practical maturity and introduced in series production [10,13].

2. Fundamentals of ultrasonic

2.1 Principle of ultrasonics

Sound is generally known as mechanical waves, which requires matter to propagate [13,14]. The matter can be gaseous, liquid or in a solid state. In vacuum, sound propagation is not possible. The sound can be transmitted longitudinally as well as transversely. Whereas in liquids and gases sound is mainly transmitted longitudinally, in solids both forms of transmission can prevail. Furthermore, the propagation medium determines amplitude, wave speed and frequency. Although the ultrasonic range extends to frequencies of a few MHz, most ultrasonic technologies use frequencies from 20 kHz to 100 kHz. Ultrasonic metal welding machines operate usually at a range of 20 kHz [13−16].

Ultrasonic sound can be generated by the excitation of a standing column of air, by a mechanical generator with motor drive as well as by a conversion of electrical energy into mechanical vibration energy of the same frequency. Only the conversion of electrical into mechanical vibration energy is relevant for ultrasonic welding and is based upon the **magnetostrictive** and the **inverse piezoelectric effect** [13].

The **magnetostrictive effect** is based on the fact that a ferromagnetic body experiences an elongation in a magnetic field running parallel to it. If the usually rod-shaped body is then exposed to an alternating magnetic field, it changes the length in rhythm to the field. If the frequency of the alternating field and the natural oscillations of the rod match, resonance phenomena occur. The efficiency achievable with magnetostrictive transducers at 20 kHz is between 50 % and 70 % depending on the used material. With increasing frequency, the efficiency decreases sharply. Therefore, the use of magnetostrictive transducers is limited to frequencies below 50 kHz. Nowadays ultrasonic welding machines are only equipped with magnetostrictive transducers for special applications or if very high power is required [13,17,18].

Today the **inverse piezoelectric effect** is the commonly used principle to generate the ultrasonic sound. In a large number of crystals, electrical charges are generated by deformation due to pressure or elongation (direct piezoelectric effect). A requirement for this effect is the missing of several polar axes respectively the absence of a center of symmetry. Contrary to the direct piezoelectric effect, piezoelectric crystals change their geometry periodically under the application of an alternating electric voltage (**inverse piezoelectric effect)**. During one phase they are pulled, while in the other they are stretched. The inverse piezoelectric effect can be described by the following Eq. (7.1):

$$\varepsilon = d * E_f \tag{7.1}$$

with.

ε is mechanical deformation (compression, elongation)
d is piezoelectric constant
E_f is electric field intensity

While magnetostrictive transducers only achieve an efficiency of 50%–70%, the conversion of electrical energy into mechanical energy realized by piezoceramics in ring form reach an efficiency up to 95% [13,19–21].

2.2 Components of a metal ultrasonic device

A typical ultrasonic welding machine consists of an ultrasonic generator, an ultrasonic oscillator system and the welding device with pneumatic control (suitable bearings for applying the force and an anvil). The ultrasonic oscillator system again comprises of a generator, transducer, booster and horn. Fig. 7.1 shows the schematic assembly of an ultrasonic welding machine as well as the longitudinal induced waves through the horn, which induce the cyclic mechanical deformation and the vibration at the contact site with the parts to be joined.

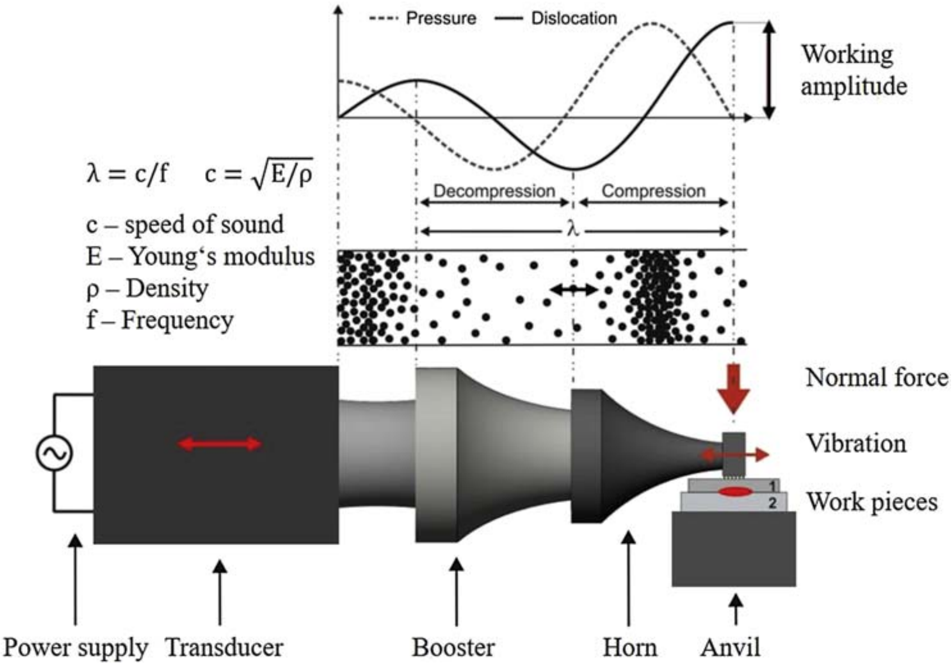

FIG. 7.1 Schematic assembly of an ultrasonic welding machine according to Bergmann [22].

The generator operates with voltages of 220 V or 110 V and transforms the line frequency of 50/60 Hz with great accuracy to the operating frequency, which can vary from 20 kHz to 120 kHz. Depending on the application the power, which these generators convert, is in the range of 10 W for ultrasonic microwelding and over 10,000 W for metal welding. To ensure a constant welding amplitude, a frequency control is integrated in the generators that readjusts the generator frequency according to the resonance frequency of the oscillator system.

The transducer converts the high-frequency current into high-frequency ultrasound waves, which are then amplified in a booster. Here the amplitude of the vibrations is enhanced. At last, a horn delivers the wave to the materials to be welded. Due to the geometry and the dimensions of the horn, the horn acts like the welding tool. Fig. 7.2 shows the measured outline of the horn velocity and displacement.

The layout of a horn takes mainly the determination of relevant parameters, as for example resonance length, nodal points, amplitude and stress distribution over the length in consideration. The maximum amplitude is reached, when the resonance length is achieved. In this case, the horn is working in resonance, with low energy consumption. The nodal points are the points, where the amplitude is zero, while the amplitude represents the displacement of particles in the material from its equilibrium in longitudinal direction [23,24]. Common materials for manufacturing the horn are molybdenum, tool steel, Ferro-Titanit cermets or silver steel [13,25]. The chosen material should present low acoustic losses, which can be described over

$$c = \sqrt{\frac{E}{\rho}} \tag{7.2}$$

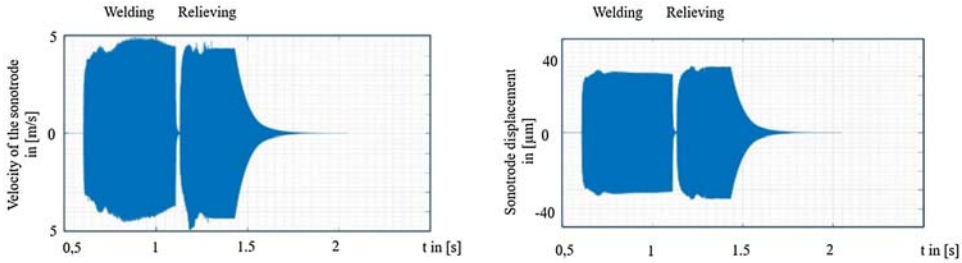

FIG. 7.2 Velocity and displacement of the horn measured with a laser vibrometry on the surface of the horn for the welding time and the relieving impulse.

in order to allow high amplitudes. High amplitudes allows on one hand a higher heat input through frictional heat. Therefore, the design and production of the horn should be very accurate, as deviation from the ideal state leads to a detuning of the oscillator systems, which has influence on the amplitude and on the joint strength [26]. Due the low cycle times and the generated heat during welding an increased temperature at the horn can be detected [27]. On the other hand, high amplitudes also generate a temperature increase at the nodal points indicating a high stress in the horn itself, leading then to failure. The limitations are depending on the horn materials and geometry and can be studied with a harmonic analysis and then a stress analysis [28].

An anvil on the reverse side holds the parts in its position during welding and should have completely other resonance conditions. Horn and anvil have a pattern on the surface in order to deform and hold the material during welding. The anvil is typically of steel or cast iron in order to achieve higher damping properties.

2.3 Ultrasonic metal welding

2.3.1 Welding principles

Conventional ultrasonic devices for metal welding convert the energy into a linear movement in the horizontal plane (Fig. 7.3). New devices allow it, due to another configuration of the horn and the booster, to reach an alternating circumferential rotating vibration in the horizontal plane. This configuration is described as torsional ultrasonic welding and has some advantages regarding the vibration transmission to further parts in the system to be welded Fig. 7.3 [29].

A further configuration of torsional ultrasonic and linear welding is depicted in Fig. 7.4, where even a changing for example in the pressure conditions during welding can be reached.

2.3.2 Joint and material configurations

Ultrasonic metal welding is mainly used in order to weld metal sheets down to 10 µm and up until 1–2 mm, splicing of wires as well as welding of wire to terminal connections. Typical joining configurations are reported in Fig. 7.5.

An overview regarding material combination and thicknesses is presented in a survey for example of the Belgian welding institute (npo) [30], as well as for Aluminum and Copper in

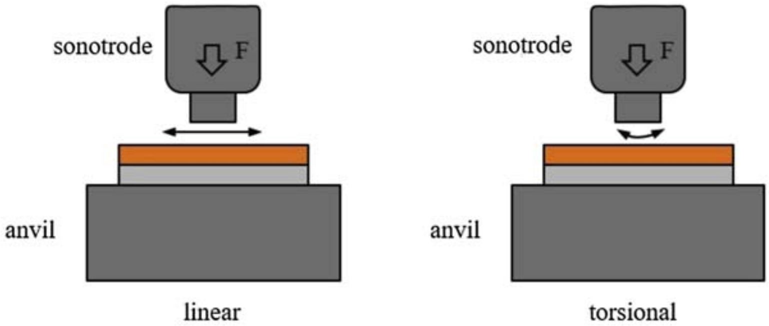

FIG. 7.3 Linear and torsional ultrasonic metal welding.

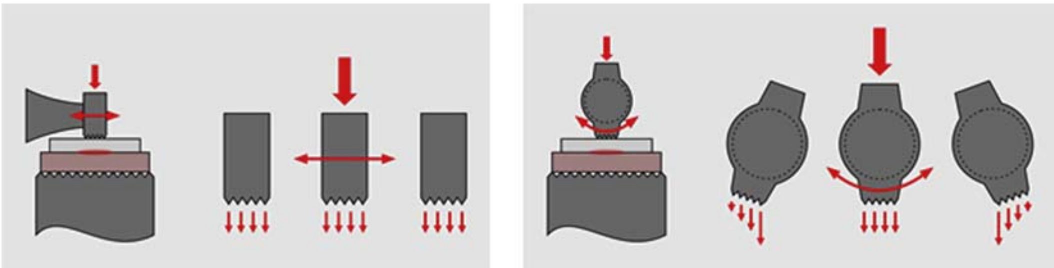

FIG. 7.4 Torsional welding and effect on the loading of the part.

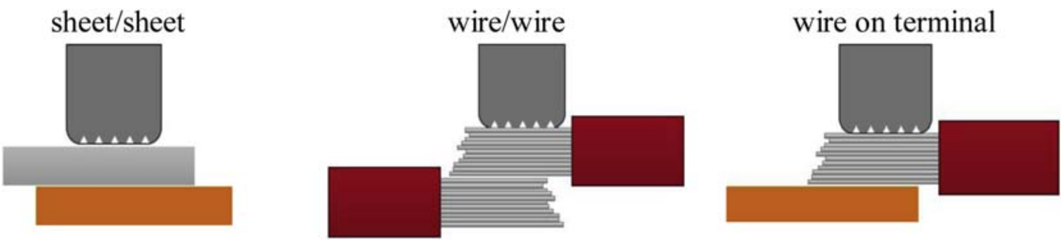

FIG. 7.5 Typical joint configurations in ultrasonic metal welding.

Ni et al. [31] and summarized in Table 7.1. Here an excerpt, merged with further sources from literature is presented and should only give the reader an overview on possibilities and fluctuations. They depend on the size of the horn surface and on the process control method. Depending on the device, the process can be carried out adjusted on an energy to be delivered or on the horn displacement. When achieving the turn-off value the device will shut down.

Ultrasonic metal welding in butt configuration is described for aluminum and copper in Tsujino [40], even though overlap joints are mostly common. To this time, the power of ultrasonic metal devices allows welding of cables and wires until 160 mm^2 (copper) and 240 mm^2 (aluminum).

TABLE 7.1 Overview of material combinations and thicknesses during ultrasonic welding.

Material	Thickness (mm)	Power range of device (kW) or energy (J)	Static pressure/Force	Welding time (s)	Vibration amplitude (μm)	Source
Al/Al	0,01–2,5	2–3 kW	0,14–0,20 MPa	0,005-2	10–100	npo [30]
Al1100/Al1100 with Al-particles	1,2	n.a	0,31 MPa	0,8	42	Ni [31]
Cu–Cu	0,8	4 kW	2250 N	0,9	26	Balz [26]
Cu–Cu	0,2/0,2	2,5 kW	0,2–0,3 MPa	2-2,5	40–50	npo [30]
AA1050/EN CW 004A (torsional)	1/1	n.a.	2000 N/$\phi = 8$ mm	0,75	67,5-90	Köhler [32]
Al–Cu	0,4	n.a	n.a.	n.a.	n.a.	Kreye [33]
Al–Cu	1/1	3 kW	0,5 MPa	0,1-1	12	npo [30]
Al/Cu	0,2/2	2,5 kW	n.a./5 × 5 mm^2	3,5–4,5	28–57	Ganesh [34]
AA5652/Cu	0,8/0,8	30 J	1975 N	0,8	22,5	Ni [31]
AA6111-T4/AA6111-T4	0,93	1,5	1900 N/$\phi = 10$ mm	0,5	5	Jedrasiak [35]
AA6111-T4/DC04	0,93/0,97	1,5 kW	1400 N/$\phi = 10$ mm	0,25-3	5	Jedrasiak [35]
AA6111-T4/AZ31	0,93/1,05	1,5 kW	17,83 MPa	0,3–1,3	5	Jedrasiak [35]
Cu–Cu	0,8	4 kW	2350 N/5 × 7 mm^2	0,2–1,5	n.a.	Yang [36]
AA6061/Ti6Al4V	0,3	3,2 kW	0,3–0,5 MPa	0,09–0,2	n.a.	Zhu [37]
AA6061-T6/Cu	1,0/1,0	1000 J	0,5 MPa		12	Ni [31]
UNS C71500/AA1060	0,3/0,8	3 kW	0,26–0,36 MPa	0,4–0,7	47–68	Das [38]
AA7075-T6/Ti6Al4V (torsional)	1/1	1900 J	2000 N (78,5 mm^2)	n.a.	46	Balle [39]
AA7075-T6/Ti6Al4V	1/1	850 J	1500 N	n.a.	33	Balle [39]
Al-Stainless steel	0,3/0,05	2,4 kW	0,2–0,4 MPa	0,1–0,5	30–60	npo [30]

2.3.3 *Joint formation mechanism*

The joint formation mechanism during ultrasonic welding of metals is content of many studies in literature, whereas different theories were discussed [41]. The process duration is very short and can reach − depending on the parts dimensions − maximum 1 until 2 s.

At the beginning of the process, the horn penetrates the upper sheet with the formation of asperities. At the interface, an initial phase of frictional rubbering can be assumed (Fig. 7.6). Further, the horn settles in the upper sheet and the load leads to a settling of the lower sheet in the anvil as well. Up to this time, the tool displacement is entirely used for plastic deformation concentrated toward the interface, where the material softening is highest [35].

The typical bonding mechanism for bulk material can be summarized as follows Fig. 7.7.

- in a first stage due to the relative movement of the welding parts asperities on the surface are plastic deformed, oxides are for example broken and micro bondings along the weld interface occur,
- in the second stage deformation occurs along the bonding line and in the thermo-mechanically affected zone, a part of the micro bonds are broken but new bonds were formed,
- in the third stage micro bonds grow between the material in order to reach a well-developed bonding zone. At higher energies, the formation of a swirl-like interface can be observed. Work hardening and annealing are occurring nearly contemporarily.

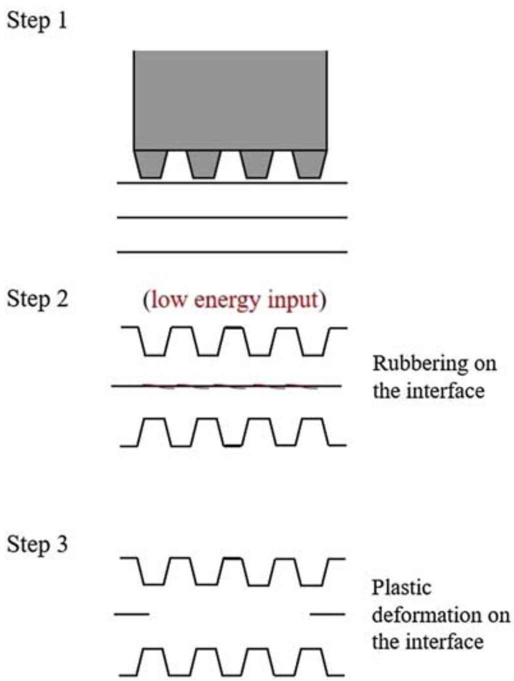

FIG. 7.6 Macroscopic formation of the joint during ultrasonic metal welding.

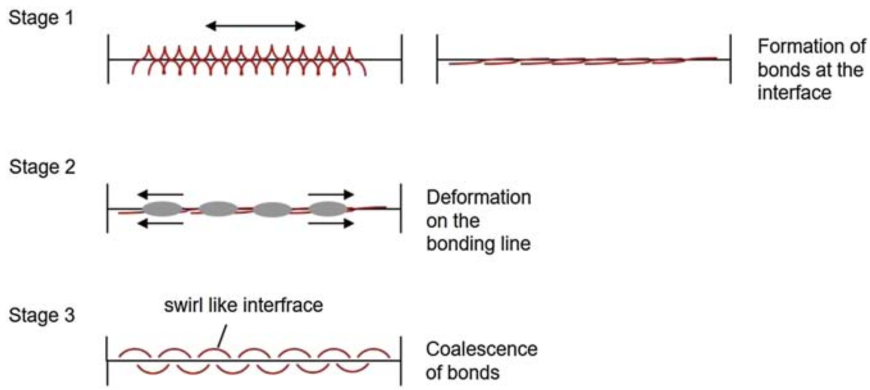

FIG. 7.7 stage-like formation of the joint at the interface.

Relevant process parameters for ultrasonic metal welding are amplitude, time, static loading and energy, as summarized in Table 7.1. Indeed, the process regime defines the effect of the process parameters and the resulting quality of the joint.

Ultrasonic metal welding devices offer the possibility to drive the process in three ways:

- Controlling the energy consumption during welding and shutting down the process, when a defined energy is achieved. The welding time as well as the plunging depth of the horn are resulting variables of the process. The energy ruled process considers the energy in the welding process, so it takes to account the energy necessary to overcome friction at the surface between both plates, the energy in order to achieve sufficient plastic deformation of the plates due to axial force and in the bonding interface. Furthermore, losses in the device are considered as well.
- Controlling time during welding and shutting down the process, when a preset time is achieved. Energy consumption as well as plunging depth are resulting variables.
- Controlling plunging depth and shutting down the process, when a preset plunging depth (or residual thickness of the plate) is achieved. Time and energy consumption are resulting variables.

3. Applications and challenges during ultrasonic metal welding

3.1 Process properties

In the case of sheet/sheet joints it can be assumed, that due to frictional heat the temperature at the interface rises with increasing energy input, resulting in a drop of the flow stress of the material and a higher deformation rate at the interface.

Work hardening, recrystallization and grain growth could be very good described and detected from Yang [36] for welding of copper sheets (see Fig. 7.8). According to the depicted mechanism of joint formation it could be concluded, that with increasing welding energy, the temperature in the interface increased to over 450 °C. At low energy input a reduced grain size in the interface can be recognized, which is connected to dynamic recrystallization. At

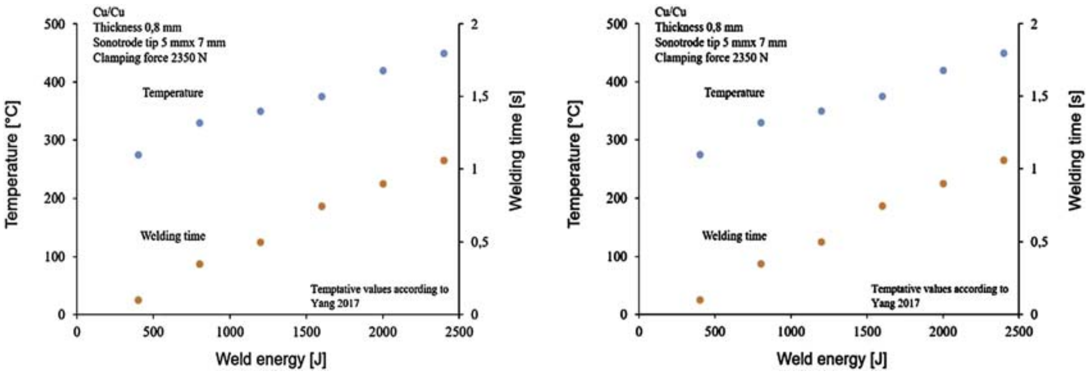

FIG. 7.8 Temperature evolution and weld length depending on weld energy for copper/copper joint according to Refs. [34].

high-energy input, the accumulated heat input at the interface causes a growth of grain size. Nevertheless, the lap shear load rises with higher energy, as the amount of bonded area in the first stage (low energy input) is very low. The failure behavior changes over the weld energy input from an interfacial cleaving to a nugget pullout, when the weld length is over 7 mm (horn tip 7 mm $\times$ 5 mm).

A similar behavior is reported from Jahn [42] for the ultrasonic spot welding of AA6111-T4 in the thickness of 0,9 mm. Jahn [42] describes the process behavior and the resulting properties depending on the geometry of the anvil and the energy input. He asserts that a nugget pullout failure is occurring over energy input of 400 J and is independent on the geometry of the anvil. The difference between these are the dimensions and the patterns. Considering the energy input, the nugget pullout occurs over a weld length of 6–7 mm. Correspondently a swirl like interface is formed at the higher energy input and bifurcation of deformation lines at the interface can be observed. At higher energies (1000 J) the strength reaches a plateau. These findings are confirmed and explained from Bakavos [43] for the same alloy. Bavakos [43] explains furthermore, that an increase of the static load leads to an increase of the tensile shear forces to failure, whereas too high static loading (50 MPa, 1 mm sheet thickness) leads to a thinning of the sheets and a reduction of loadability. Bavakos [43] makes with SEM clear, that swirl like interface occurs due to the sliding and then rotating of the bond interface.

Balz [26] describes the effect of the amplitude on the maximum temperature for a constant weld energy of 1800 J (Cu-Plates with a thickness of 0,8 mm). Balz [26] figures out, that with a higher amplitude from 24 μm to 28 μm the maximum temperature in the welding zone increases over 33%. The evolution of the interface confirms the results in further investigations; particularly a low amplitude leads to a low plastic deformation and only some microbonds. The highest temperature increase is occurring during the first 200 ms. With increasing amplitude, the plastic deformation is enhanced and a change in the heat affected zone occurs. Furthermore, the welding time to achieve the temperature is approximately 20% lower. Nevertheless, the average peel load to failure for the joint reduces with increasing amplitude. A study on the displacement of the horn shows, that with high amplitude the plunging depth increases over 50% and the output power is becoming higher. The relation between time and output power is clear, as:

$$E = P * t \tag{7.3}$$

where.

E is welding energy [J]
P is welding power [W]
t is welding time [s]

At last, a high sensitivity toward the amplitude can be deduced, so that temperature increase in the horn and tolerances in the production and finishing of the horn have to restrict.

As the frictional coefficient between the welding parts changes throughout the welding time and the materials, start bonding after reaching a temperature and plastic deformation level it seems clear, that the power of generator will have an outline as in Fig. 7.9. As reported in Fig. 7.7 at the beginning rubbing at the interface and enhancing the temperature and deformation in order to achieve the nominal amplitude will need a higher welding power. After reaching as the maximum a plateau is formed (Stage 2), where a continuous plastic deformation with work hardening and annealing occurs and a bonding line is formed. In the third stage a stable bonding interface is present, in order to plastic deform further the material at the interface and overcome the flow stress, a higher power is necessary, so that the power increases again. An excessive increase of the power leads then to the formation of voids and cracks as the material will then be overloaded. Lee [44] shows the vibration amplitude at the horn when welding four sheets of copper (3 × 0,2 mm and 1 × 1 mm). Lee [44] depicts the progress of vibration amplitude under processing conditions and confirms, that the vibration amplitude of 60 μm is reached after 0,1 s and remains then constant over the process duration of 0,4 s.

Similar results are reported from Chang [45] for spot welding at AA2xxx alloys. Depending on the normal load (static load) the power consumption and the tip displacement (amplitude) increases, in order to reach an increase of the shear tensile loading of the specimen. Chang [45] could also detect the friction coefficient and the optimal tip displacement at the horn. Furthermore, Chang [45] showed, that over a welding power amount, which means over a defined tip displacement and static loading, the shear tensile load to failure of the

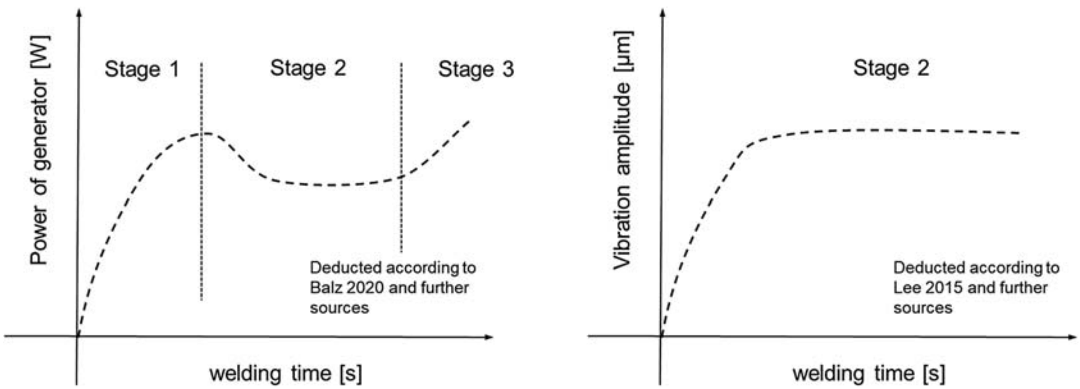

FIG. 7.9 Power of generator and vibration amplitude depending on time.

joints decreases, which is depending on the formation of cracks at the interface (Fig. 7.10). Chang [45] carried out the investigation on a wire on terminal joint, so that sublayer and peripheral cracks could be clearly recognized.

The welding of single wires to each other can be assumed to be comparable to sheet/sheet joints, even if the surface effects are of higher importance. According to Vlad [46], the process of ultrasonic welding for sheets should be quite different from wire-to-wire and wire-to-sheet. Vlad [46] bases her statement on investigation in literature from Pfluger [47] and Hazlett [48]. According to these authors, the interface sliding is less relevant in comparison to external plastic deformation for wire-to-wire joints. Therefore, there should be a lower heat generation at the surface wire-to-sheet and a squeezing of the wire on the surface. According to Joshi [49] there is no sliding and no heating. These theories have been considerably developed and contradicted during the last decades.

Compacting wires via ultrasonic is a very similar process to welding of wire-to-wire. Broda [50] describes the mechanism of bonding in a strand formed by a huge amount of wires. A schematic view is reported in Fig. 7.11. At the beginning, there is a low contact between the wires, while during heat input and plastic deformation there is a coalescence of the wires to each other, which is comparable to the sintering process.

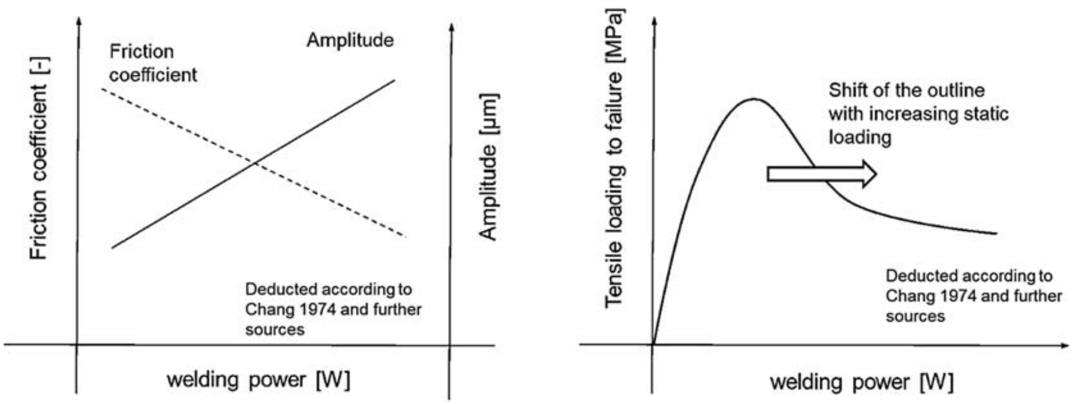

FIG. 7.10 Influence of different process parameters on friction and tensile loading to failure.

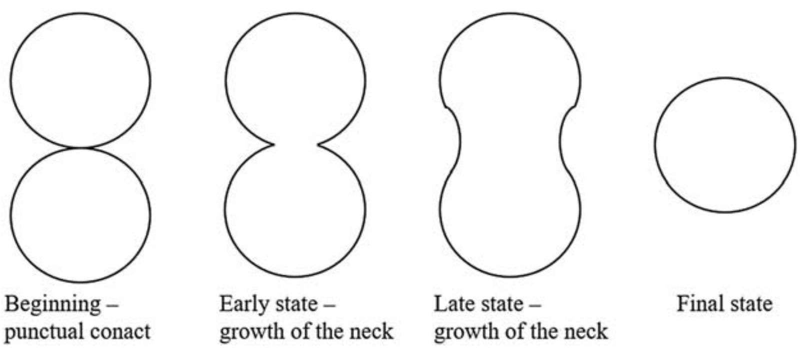

FIG. 7.11 Joint formation during bonding of wires according to Broda [50].

Tsuijno [51] reports for copper wire on plate comparable results to Chang [45], even if in this case the effect of welding time is in the topic. Increasing time leads to a lower tensile strength and compared to welding power to a different formation of the spot.

Splicing of wires is a very large application field for ultrasonic welding. Typically, wires are insulated with different types of insulation. Matos [52] presents results of the splicing of copper to copper wires with insulation of PVC and EFTE. Matos [52] concludes, that the mechanical properties are affected, whereas the reason for it should be dependent on the surface condition of the wires itself. Kuprys [53] investigates the strength of copper wire connections. The authors are able to show, that there is a linear relation between tensile force to failure with the ratio of the perimeter and cross-section of the connections. Furthermore, Kuprys [53] indicates, that the wires should be cleaned by compressed air, in order to reach a higher tensile force. Wagner [39] reports on splicing of aluminum wires with a section of 13 mm^2 and 80 mm^2. He also [39] describes the adherence phenomenon of aluminum to the horn, which is then avoided through standard industrial coating as TiN, TiAlN and a new geometry. The welding zone is in the case of wire-to-wire joint characterized from a high amount of single filaments, which should be connected to each other in order to allow the electric current to pass through. Single filaments of aluminum are still visible after welding. The compaction of aluminum wires is clearly visible in Fig. 7.12 as well. In this case, it can be detected as well, that the compaction is depending on the direction of load and is inhomogeneous in the cable section.

While the region, which is in direct contact to the copper terminal (region 3) is low plastic deformed changing the geometry of the wires, region 2 in the middle has only marginal changes in the geometry, the wires remaining approximately round. In region 1, which is in direct contact with the horn, there is a high compaction, so that the boarder of single filaments cannot be recognized. This behavior allows to assume, that the welding energy is consumed in the upper region, where the relative movement of the wires to each other is enough in order to induce high plastic deformation. The relative movement between the last layer of aluminum wires and the copper substrate is sufficient in order to induce a low deformation of the single wires. Regensburg 2017 showed in this case, that a heating of the copper terminal leads to a fully modified layer in region 3, with a high plastic deformation supporting the energy input over ultrasonic welding. The effect of the different friction condition, as typically cables are stranded and the surface contact between wire and sheet is not homogeneous can be detected and depicted through the outline of amplitude measured at the horn tip.

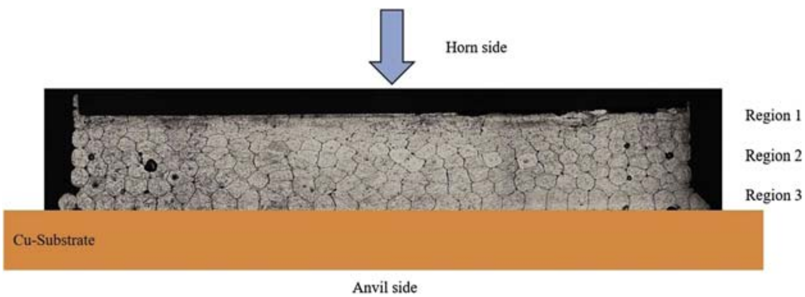

FIG. 7.12 Compaction in aluminum strand according to finding of Regensburg [54].

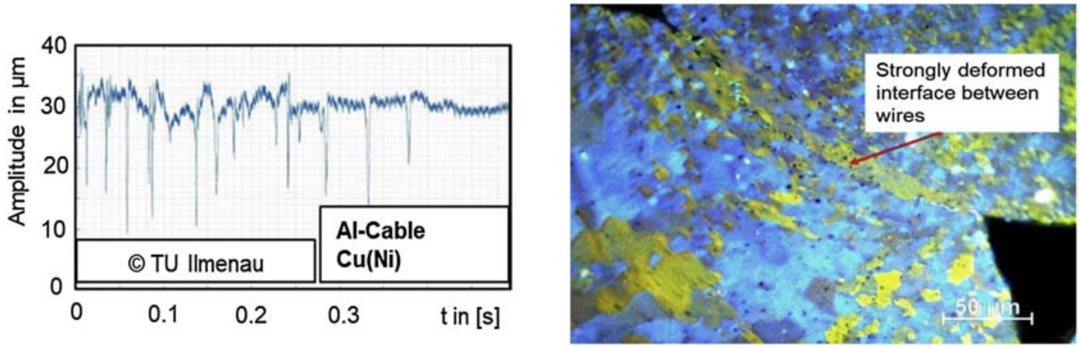

FIG. 7.13 Amplitude of the horn when welding Al-cable to nickel-plated copper sheet and deformation in single wires.

The deformation in the single wires and at the interface between the wires is represented in Fig. 7.13 for aluminum wires according to Regensburg [54].

3.2 An overview over ultrasonic welding of hybrid joints

The high cooling rates and the low temperature during welding makes ultrasonic welding interesting for welding of different metals to each other and avoids formation or growth of intermetallic compounds (IMC).

Intermetallic compounds are formed, based on diffusion processes in combination with certain concentrations in binary or more-elements systems with limited solubility. They are mainly characterized by their inhomogeneity as well as their tendency to generate undesirable joint properties during welding of dissimilar materials, as they are very brittle and form connected during welding. Due to the fact that intermetallic compounds can negatively influence the mechanical joint properties which can lead for example to low ductility of the joint, several work addresses the mechanism of joint formation and characteristics of the interface during ultrasonic welding. Rathod [55] gives an experimental, simple and comprehensive overview on the formation of IMC during solid state welding of aluminum to steel. The formation of IMC occurs, when solid-state solubility is overpassed, while the growth of IMC is then dependent from time and temperature (see Fig. 7.14). The morphology of the IMC in means of its chemical composition and the formation of different Fe_xAl_y had to be considered as well. The effect of alloying elements, as shifting from AA5xxx to AA6xxx is described for diffusion welding in literature (for example Wilden [56]).

A similar summary for the combination of pure aluminum (AA1050) to copper (Cu-ETP) is reported in Bergmann [4].

Ultrasonic welding of SS400 mild steel sheet to AA5052 aluminum alloy sheet was investigated by Watanabe [57]. Watanabe [57] examined the mechanical properties (tensile load) and the interface microstructure by varying the welding conditions i.e. welding time and clamping force. Considering different welding times and a constant clamping force it was found that with 588 N clamping force and 2,5 s welding time the maximum tensile load was reached. With an increase of welding time to 3,0 s the formation of the intermetallic

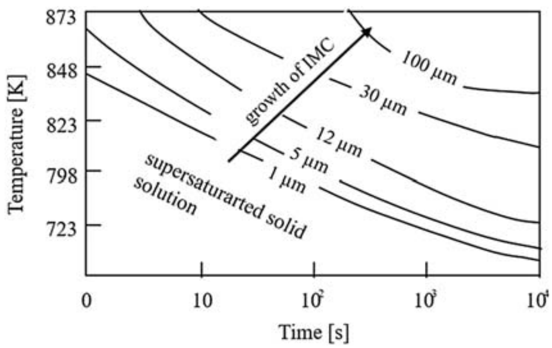

FIG. 7.14 Growth of IMC depending on time and temperature following Rathod [55].

compound Fe_2Al_5 was obtained at the interface, which hence reduced the maximum tensile load achievable.

Panteli [58] reports on high strain rate deformations on intermetallic reactions during ultrasonic welding of AA6111 aluminum and AZ31 magnesium for automotive body applications. According to Panteli [58] the high strain rate deformation was claimed to accelerate diffusion rates in ultrasonic metal welding of different materials. The investigation of the surface between aluminum and magnesium was observed by adjusting different welding energies. At an optimum welding energy of 600 J (welding time 0,4 s) thin reaction layer thickness of 5 μm could be detected. With a welding of 1 s the layer enlarged to 20 μm. It consisted of two intermetallic phases $Al_{12}Mg_{17}$ and Al_3Mg_2, whereas the $Al_{12}Mg_{17}$ phase was first formed early in the process and the Al_3Mg_2 secondly but with a faster expansion. Due to that Al_3Mg_2 was the thickest intermetallic compound at longer welding times. Furthermore, considering the joining of zinc-coated steel and aluminum alloys, Patel [59] and Haddadi [60] analyzed the reaction between aluminum and zinc during ultrasonic spot welding of thin sheets. A thin eutectic Al-Zn film could be found in short period of time, which led to decrease in tensile strength. With longer welding times the formation changed to a dendritic structure due to an increased aluminum concentration.

A detailed overview regarding joint formation and characterization of the joint interface during ultrasonic welding is given by Sanga [41]. Sanga [41] showed that intermetallic compounds were found in many combinations of dissimilar metals for example in AA6111 and Zn coated Steel, AA5754 and $TiAl_6V_4$, AA6061 and pure Cu as well as in AA6061 and SS304. Besides that, it was investigated that intermetallic compounds are contributed to the strength of the joint and joint failures occurred due to the appearance of intermetallic compounds. Actually, heat-affected zone and thermomechanical-affected zone could be found in contrary to the conventional understanding of solid stat welding and the absence of these zones.

Using ultrasonic welding as an intermediate process step in order to weld aluminum with steel is presented in Broda [61]. Broda [61] developed a joining process consisting of two steps. In the first step an additional joining element (DC01) is welded via ultrasonics onto the aluminum material. This additional joining element acts as a buffer layer and forms no intermetallic compounds due to the process of ultrasonic welding. In the second step, the additional joining element is welded via resistance welding onto the steel sheet. Due to this new joining process, a spot weld shear failure and a very ductile joint could be achieved. Further Broda [61] depicted results with good tensile strength properties and replicability.

3.3 Ultrasonic welding of Al/Cu

Further, ultrasonic welding of aluminum to copper is a widely investigated field, especially against the background of the increasing e-mobility market and applications like battery tabs or cable harness production. In these fields, joining of aluminum to copper is a challenging task due to the formation of passivating oxide layers, different melting temperatures, different thermal expansions and different thermal conductivities. Accordingly, pressure-welding processes have been established for the suppression of brittle intermetallic phases as they often occur in fusion welding processes. Nevertheless, the formation of intermetallic compound regions is also possible in pressure welding, such as friction welding, ultrasonic welding and resistance spot welding, with process temperatures below the solidus temperature of the base materials. This leads to reduced mechanical strength properties and increases the specific electrical resistance of the joint. Further challenges arise in particular when joining wire on terminal systems for automotive wiring systems. The use of aluminum conductors and copper arresters can lead to insufficient surface connections, which have a negative effect on the properties of the connection, as they increase the electrical resistance and reduce the mechanical strength. In order to increase process stability, the aim is to increase the contact area of the joint while keeping intermetallic compound formation to a minimum or completely avoid the formation of intermetallic compounds.

The interlayer formation during torsional ultrasonic welding was studied by Regensburg [32]. Regensburg [32] investigated the influence of the amplitude on the bond formation and on the mechanical properties of the overlap joint while the clamping force as well as the process time was kept constant. The investigations were carried out on EN CW 004A and EN AW 1050 1 mm sheets which were joined with amplitudes from 67,5 μm−90 μm. As the temperature is one main driver to build a eutectic or intermetallic phase the temperature profile as a function of time was analyzed (see Fig. 7.15).

At low amplitude, no IMC can be detected by metallographic analysis, as shown in Fig. 7.16.

At an amplitude of 90 μm significant deformation in the outer areas of the joint was detected due to the high peripheral speed and the higher friction-based heat input in this area. Thus, microcracks occurred in the outer areas, which is depicted in Fig. 7.17.

In these areas, the formation of intermetallic phases was also detected by light microscopy. It can be assumed that the crack formation is caused by the immediate proximity of these areas to the maximum sound initiation of the horn and interacts with the simultaneous phase formation. Further, EDX analysis were carried out by Regensburg [32] to specify the intermetallic phases detected by light microscopy (see Fig. 7.18).

In the area of the aluminum interface a composition of 34 wt% copper and 66 wt% aluminum was detected, which indicates the formation of an eutectic like phase region. Furthermore, the analysis showed a comparatively large region with about 53 wt% copper and 47 wt% aluminum. This composition suggests a hypereutectic area. The Al_2Cu phase

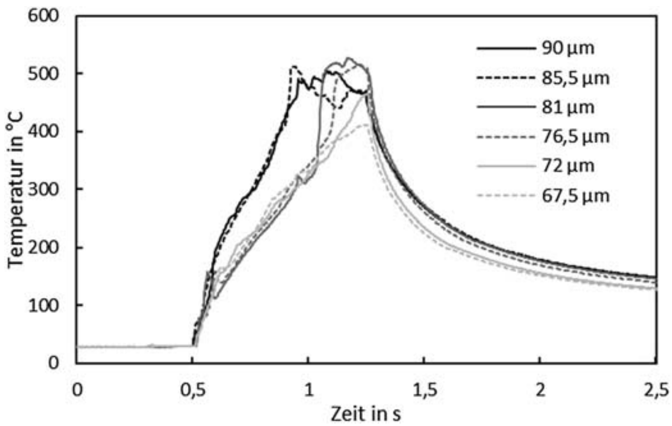

FIG. 7.15 Influence of the amplitude on the temperature profile at the interface.

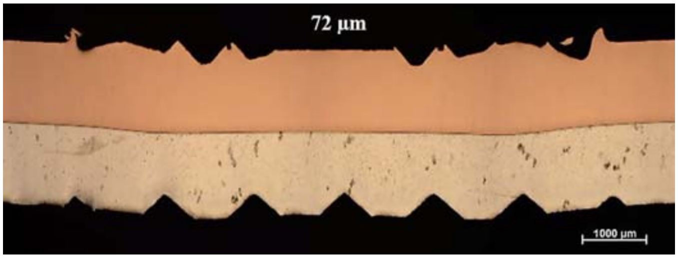

FIG. 7.16 Cross-section at low amplitude (72 µm).

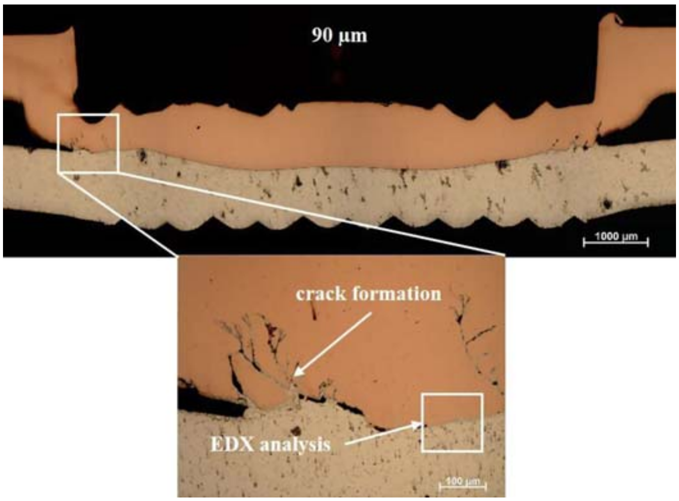

FIG. 7.17 Crack formation at high amplitude (90 µm).

crystallizes at the copper interface. Other copper-rich intermetallic phase regions could not be found due to very short process times and hence greatly reduced diffusion times.

Regarding the failure behavior, differences between low and high amplitude were determined, as it is depicted in Fig. 7.19.

At 72 μm amplitude the aluminum and copper sheets remained mainly undamaged due to the low energy input and plunging depth of horn. For the highest amplitude (90 μm) the failure behavior changes. A high plunging depth of the horn was observed and hence a strong weakening of the upper joining partner (here: copper sheet). Moreover, the crack formation at the outer areas led to further weakening of the copper base material (Fig. 7.17). Therefore, the joint failed in the weakened copper material.

Considering ultrasonic welding of EN AW 1050 to EN CW 004A thin sheets with metallic coatings working as diffusion barrier was investigated within the scope of the IGF Project 19,485 BR/1 at the Technical University Ilmenau.

Nickel is commonly used for enhancing corrosion resistance and diffusion barrier separating aluminum and copper. The nickel coating can have very different chemical compositions, mechanical properties and surface finishing properties depending on the coating process. An overview over the effect of nickel coatings on the mechanical properties of Al-Cu joints welded by US welding in dependence of the welding time is reported in Regensburg [22].

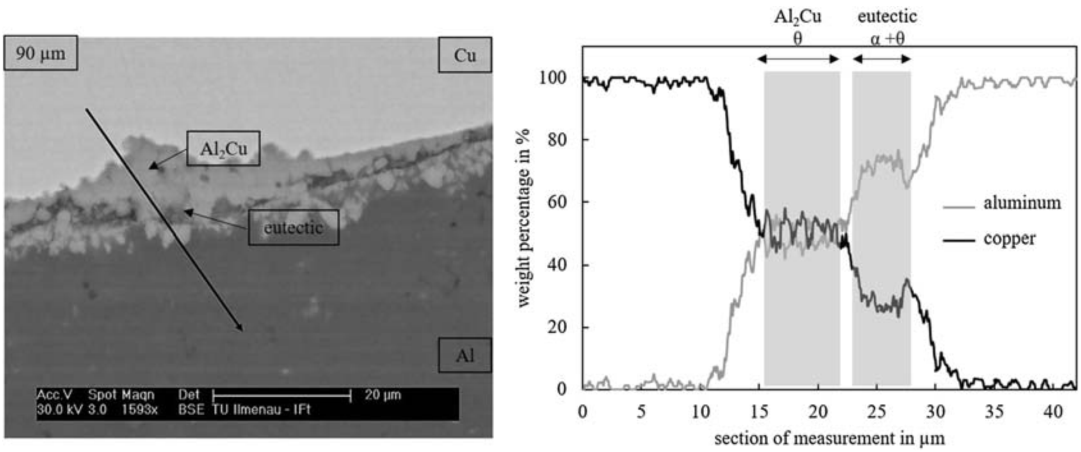

FIG. 7.18 EDX analysis of the phase formation at 90 μm amplitude.

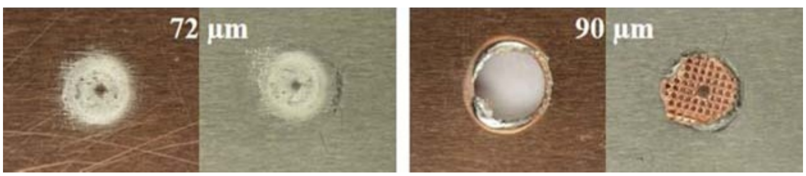

FIG. 7.19 Failure behavior for low (72 μm) and high (90 μm) amplitude.

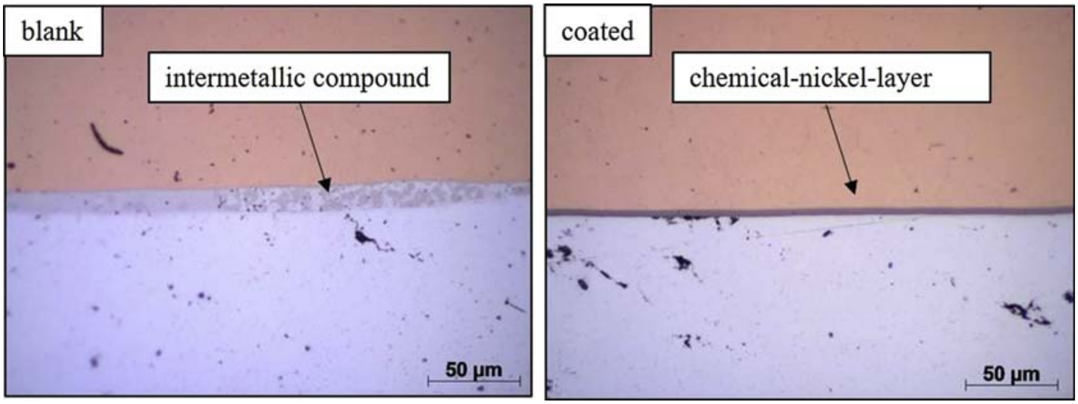

FIG. 7.20 Cross sections of blank sheets and chemical-nickel-coated sheets.

At the coated copper sheets, no interlayer formation could be detected whereas at the blank sheets a small interlayer was found which is depicted in Fig. 7.20.

The interlayer between blank aluminum and copper joints had no significant influence on static strength properties compared to the nickel-coated joints. Respective long-term behavior effects of the coating could be detected. After a thermal treatment for 1000 h at 180 °C the tensile strength decreased for the uncoated sheets compared to the nickel-coated sheets because of the artificially grown intermetallic compound. Subsequent the thermal treated joints were examined via metallographic analysis and scanning electron microscopy (see Fig. 7.21).

Regarding the integrity of the nickel coating a growth of the eutectic phase was detected for the blank sheets due to the thermal treatment (compare Fig. 7.17) whereas in terms of destroyed coatings, due to high plastic deformation in certain areas, the local formation of intermetallic compounds and cracks was observed.

3.4 Ultrasonic welding of aluminum wire to copper sheets

As mentioned above, the welding of aluminum wires to copper sheets can be assumed comparable to sheet-sheet-joints, which has been investigated intensively. Therefore, the bonding mechanism in ultrasonic metal welding has been a central aspect for many researchers, but still no generally admitted consensus has been found yet [41].

Further research addresses monitoring and testing strategies for ultrasonic welded joints. The forming layer of IMC is indeed very thin and the determination of the joining area is very difficult as cables are twisted, stranded etc. IMC and connected area determine the relevant properties like the electrical contact resistance, the temperature increase at operating current or the tensile strength at a given failure load. IMC have very high brittleness as well as high resistivity [62,63]. Especially for lap joints, the evaluation of the bonded area can be challenging and determining it out of the sample failure might not always give the required reproducibility. In the literature, ultrasonic microscopy is one way depicted for determining the area. However, e.g. for electrical applications and lap joints, the resultant contact area between the work pieces can be another important factor, as it determines properties like

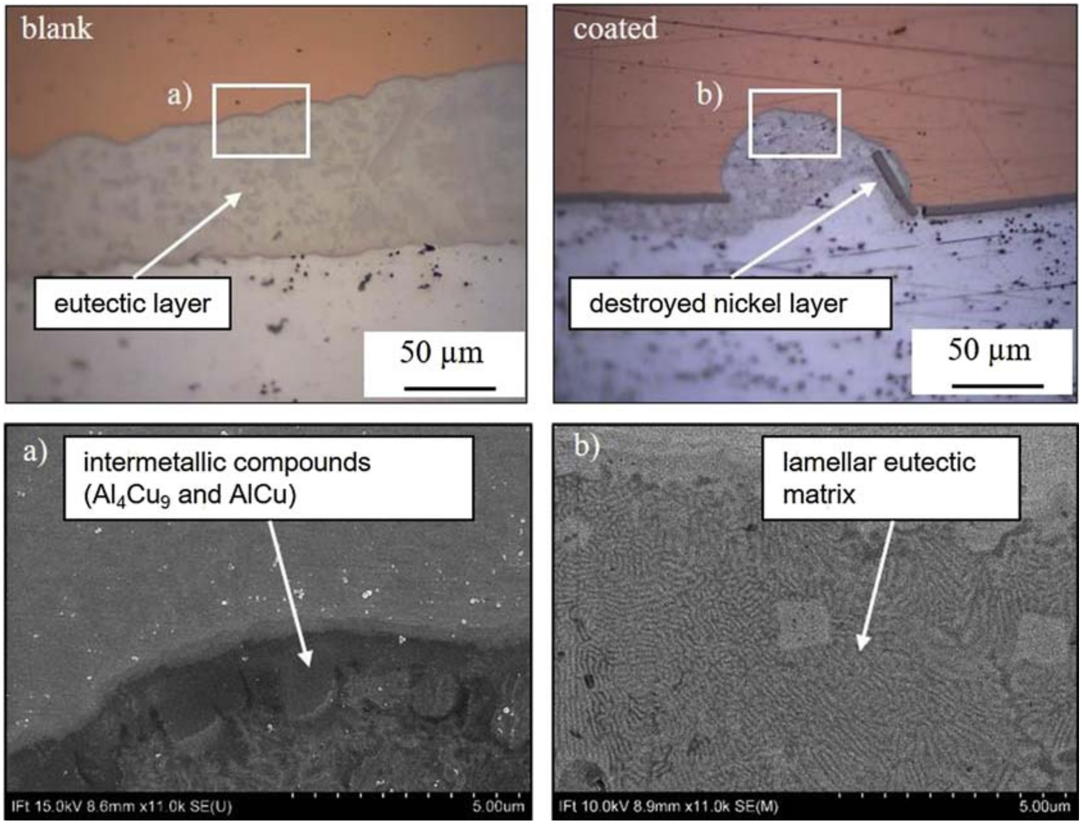

FIG. 7.21 Cross sections and SEM analysis of blank and chemical-nickel-coated sheets.

the electrical contact resistance, the temperature increase at operating current or the tensile strength at a given failure load. Especially for lap joints, the evaluation of the bonded area can be challenging and determining it out of the sample failure might not always give the required reproducibility.

Therefore, a novel approach in order to determine the contact area between solid-state welded dissimilar joining partners was developed and presented in Regensburg [54]. The strategy bases on the assumption, that where a joint was formed during welding, the diffusion layer will grow under heating, so that the formation of brittle intermetallic compounds between ultrasonic welded metals with limited solubility in the solid state will occur. This under the consideration, that diffusion across an interface requires a bond on an atomic scale level. Fig. 7.22 shows a schematical illustration of the developed testing strategy.

Firstly, the joints are subjected to artificial aging at a relatively high temperature in order to propagate significant diffusion mechanisms at the interface. Hence, layers of intermetallic compounds form, which exhibit much higher hardness values than the base materials. In order to demonstrate this strategy, 50 mm^2 EN AW1070 aluminum stranded wire was welded to Ni plated EN CW004A copper contact elements and subjected to 450 °C for 3 h.

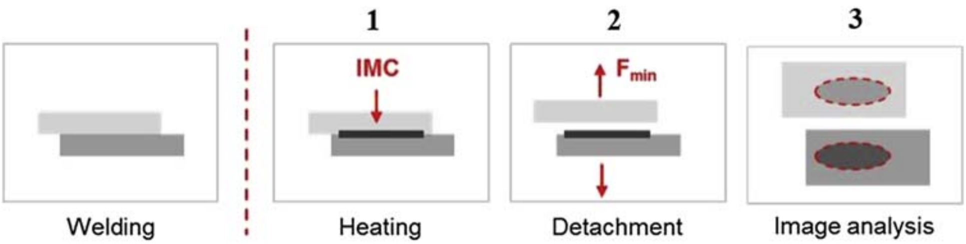

FIG. 7.22 Schematical illustration of the testing strategy.

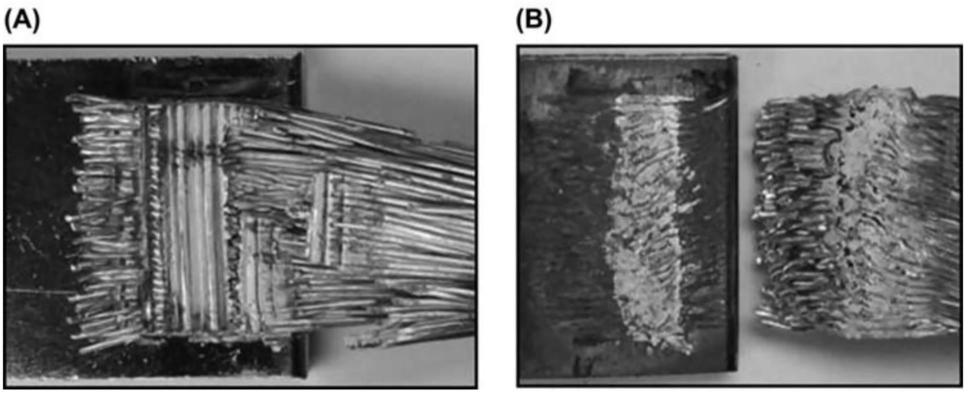

FIG. 7.23 Failure behavior of the joint (A) before and (B) after artificial aging at 450 °C for 3 h.

After the heat treatment, the maximum failure load of the joint is significantly decreased, so that the separation of the joining partners can be performed by applying no or minimal load on the joint. In this way, the interface can be exposed without subjecting the work pieces to plastic deformation, like during tensile testing. Fig. 7.23 illustrates the failure behavior before and after the heat treatment.

Due to the brittle intermetallic compounds, the failure always occurs at the interface and certain layers of the intermetallic compounds stay attached to the Ni plating, leaving an imprint of the actually bonded area (compare Fig. 7.24) as diffusion across the interface requires a microscopic bond as a starting condition.

As those adhesions can be distinguished by a different color, the bonded area can then be evaluated by image analysis. Fig. 7.25 shows the evaluation of the imprint for different welding times and three samples each. With an increasing welding time, the size of the bonded area increases as expected and the values show very low scattering.

The cable is not subjected to macroscopic changes. Subsequently, X-ray analysis of the compaction can be performed after separating the joining partners. Usually, this is inhibited by the shielding effect of the copper contact element and a lateral analysis of the compaction does not provide many insights due to the relatively high weld with compared to the height. For this analysis, a Phoenix Nanomex X-ray inspection system was used and an image analysis was performed on one section in order to compare the void share (share of significantly

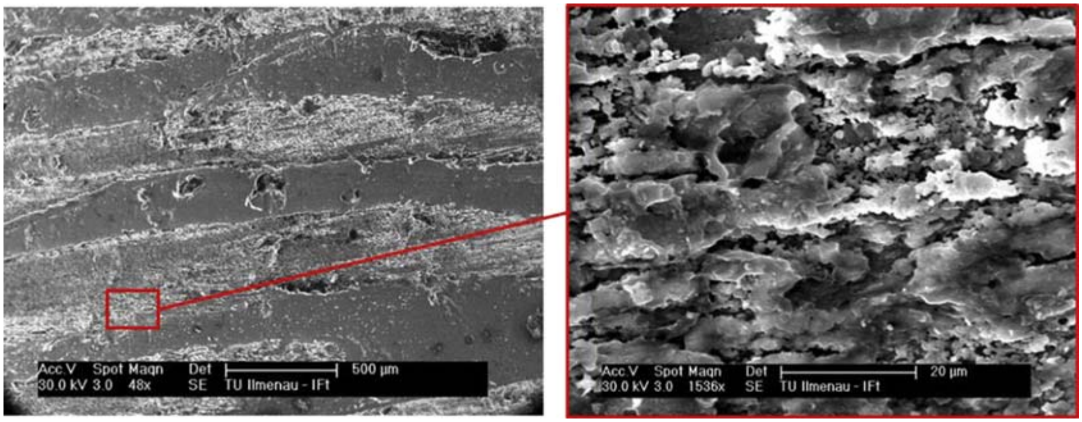

FIG. 7.24 SEM image of the IMC imprint on the Ni surface.

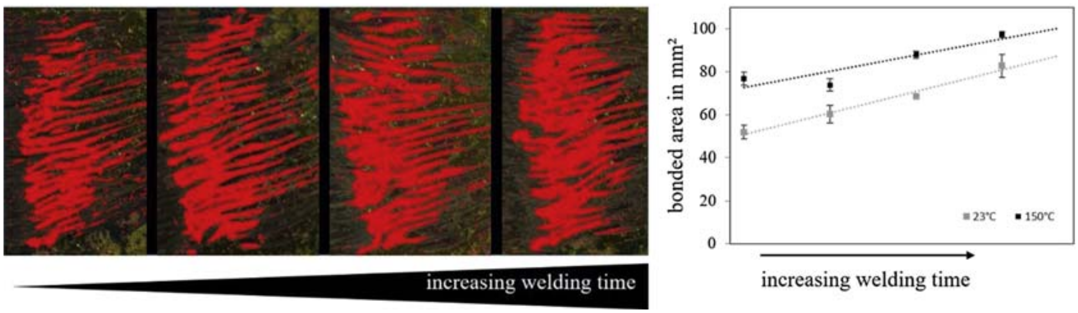

FIG. 7.25 Evaluation of the bonded area for different welding times according to Refs. [48].

less dense areas across a certain area of the strand) between the different parameters. As shown in Fig. 7.26, the compaction significantly increases for higher welding times. The area, which was in contact with the horn, only shows minor irregularities after 1.2s welding time.

This investigation presents a diffusion-based strategy in order to evaluate the bonded area between dissimilar lap joints, which cannot be evaluated otherwise or just according to the failure behavior which may differ depending on the bond quality. The procedure was demonstrated from Regensburg [54]on joints of aluminum stranded wires to nickel plated copper contact elements with pre heating of the terminal up to 150 °C, in order to reduce the energy input when welding and to reach a higher bon quality. It could be demonstrated, that the bonded areas increase as well as the tensile shear load. Over a maximum value of tensile shear load the mechanical properties of the joint decrease again, as the joint between wire and sheet is damaged through the additional energy input after bond formation at the interface. Further investigations show that it also works for plain aluminum-copper joints and that the results of the measured area shows good correlation to the mechanical properties of the joints.

3.4.1 Compaction in ultrasonic welding of wire and sheets

The mechanisms of bonding and joint formation during the ultrasonic welding process have been postulated primarily for sheet-sheet joints. Especially for ultrasonic welding of aluminum stranded wires and copper terminals, an additional process has to be considered: The compaction of the wires. In previous papers, the compaction process has only been described rudimentarily. Systematic investigations regarding the mechanisms during compaction as well as uniform criteria for evaluating the compaction state are missing.

Satpathy [41] investigated ultrasonic welding of thin sheets and categorized the quality of the joint as "under", "good" and "over" based on the density of micro-bonds and the appearance of gaps between the sheets. Similarly, to this categorization ultrasonic welding of 50 mm^2 EN AW1070 aluminum stranded wires to 3 mm EN CW004A copper contact elements were examined. Therefore, the influence of the clamping force on the compaction was investigated via electrical resistance measurements, tensile testing and metallographic analysis. As shown in Fig. 7.27 a certain clamping force and hence compaction is necessary

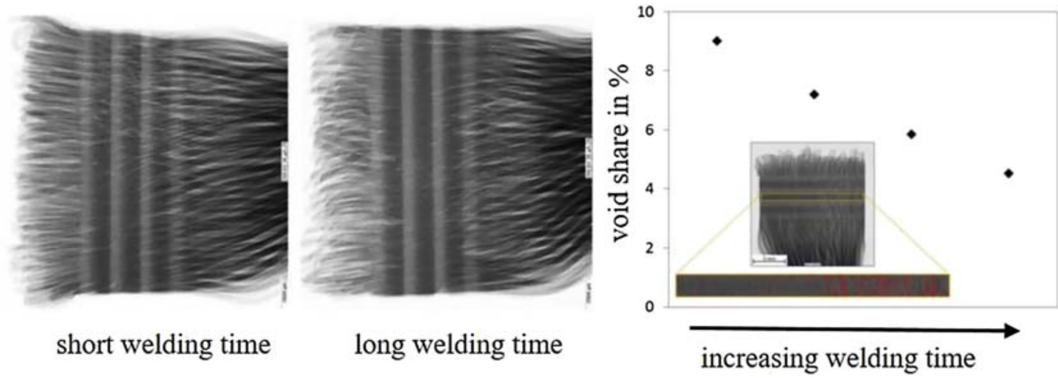

FIG. 7.26 X-Ray analysis of the strand compaction.

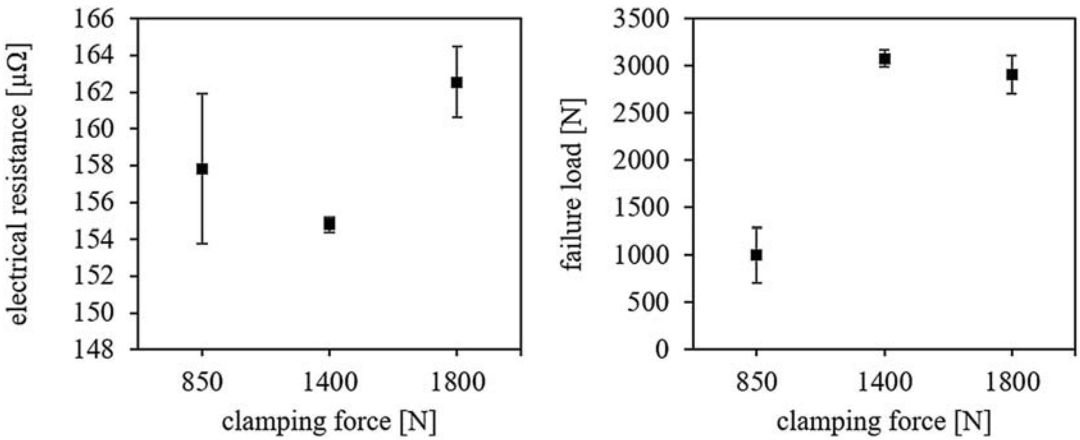

FIG. 7.27 Electrical resistance and failure load of 50 mm^2 wires for different clamping forces.

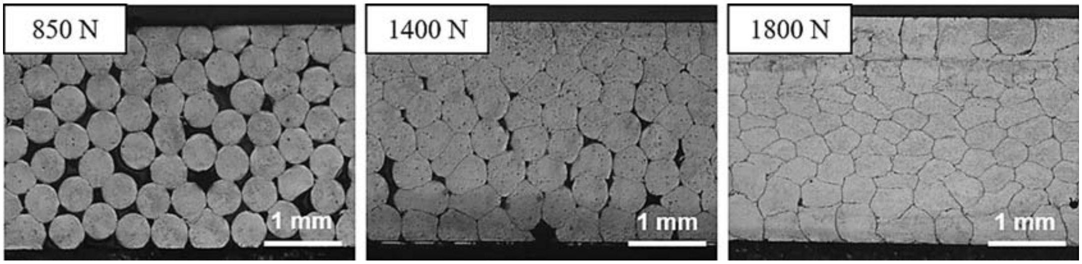

FIG. 7.28 Cross-sections electrolytically ectched for different clamping forces.

to achieve a good electric conductivity and high failure loads. On the contrary high clamping force leads to reduced tensile strength properties and increased electrical resistance.

To specify the compaction of the joints, metallographic analysis of the joints was carried out. Fig. 7.28 shows the cross sections of the joints electrolytic etched using Barker's etchant.

While at 1,25 bar single wires are nearly not deformed and remain approximately round, at 2,5 bar wires are heavily plastic deformed even in the last layer of aluminum wires and the copper sheet. Either for those high clamping forces, the failure behavior occurred due to cracks in the compacted aluminum joint or in the aluminum base material which has been damaged due to high clamping force.

Just as Satpathy [64] classified the joints, a categorization of the wire-sheet joints based on the presented testing methods is possible. Hence, in under weld condition (1,25 bar) wires are nearly round with much gaps in between and less micro-bonds due to low compaction. In good weld condition (2,0 bar) a high bond density could be found with less gaps between the wire and more micro-bonds. However, in over weld condition (2,5 bar) the high compaction of the wires led to cracks or failure in the aluminum base material. Hardly no round wires were visible in cross-sections due to high plastic deformation.

3.5 Simulation and modeling approaches in ultrasonic metal welding

A limited number of studies have been made to simulate and model ultrasonic welding of metals. Elangovan [65] investigated temperature and stress distribution within the scope of an finite element analyze based study. Elangovan [65] developed a model that predicts the temperature in the welding process due to parameters like material thickness, clamping force, welding time and coefficient of friction. The model is also capable to predict the influence of interface temperature and stress distribution on work piece, horn and anvil. The accuracy of this model was limited e.g. on the one hand due to the assumption of constant heat input in the joint area which was calculated from constant friction coefficient and on the other hand by the material thermal properties used that were independent of temperature.

Regarding temperature Kim [66] examined frictional heating in ultrasonic spot welding of aluminum plates and validated the generated data via experimental testing. In the model, it was predicted that frictional heat was generated at three interfaces, which are horn tip and upper specimen, upper and lower specimen and lower specimen and anvil tip. Further Kim [66] used a Johnson-Cook material deformation model which might be debated critically. Concluding Kim found out that frictional heating has an effect on plastic deformation and should be considered while analyzing the welding process and to achieve good correlation with the occurring phenomena in ultrasonic welding.

Jedrasiak [35] modeled the thermal field in dissimilar alloys inferring the power input based on thermocouple. The temperature could be successfully predicted for three material combinations. Jedrasiak [35] also analyzed the growth of intermetallic compound layers at the joint interface for magnesium-aluminum alloy welds as the temperature histories were coupled with a microstructural model.

Similar to Jedrasiak's [35] approach, the modeling of the thermal field was examined for welding of AW1070 aluminum stranded wires to EN CW004A copper sheets. Therefore, the simulation model was calibrated and validated via thermocouple data. Fig. 7.29 depicts the simulated temperature and the experimental measured temperature on the copper sheet. The copper sheet as measuring point was chosen due to the not reliable measurement of the temperature in the joining area.

In contrast, the curves of the joining area temperature, measured with thermocouples, show inconstant deviations between the numerically calculated curves. Therefore, an exact estimation of the joining zone temperature by numerical analysis using temperature measurement by thermocouples is not possible for now [67].

Besides the simulation of temperature during ultrasonic metal welding, other simulation research deals with the vibration behavior of the horn and the ultrasonic assembly before manufacturing. Stănăsel [24] firstly obtained own vibration modes via modal analysis. Based on the modal analysis structural response simulation was carried out to investigate displacement and stress for different modes. Stănăsel [24] showed, that a certain vibration mode corresponds regarding vibration direction at frequency of 19,909 Hz which is very close to the frequency at which the horn was designed.

Further approaches examine the damaging of already welded joints due to a second welding in the immediate vicinity to the first weld. An FEM transient structural approach was used to simulate deformations during the welding process and effects on other parts like joints and machine components (see left-hand side of Fig. 7.30).

The vibration was initiated at the circular section of the horn with an amplitude of 26 μm and a frequency of 20,5 kHz. Right-hand side of Fig. 7.30 shows exemplarily the absolute deformation of anvil, horn aluminum wire, copper sheet and side shifters.

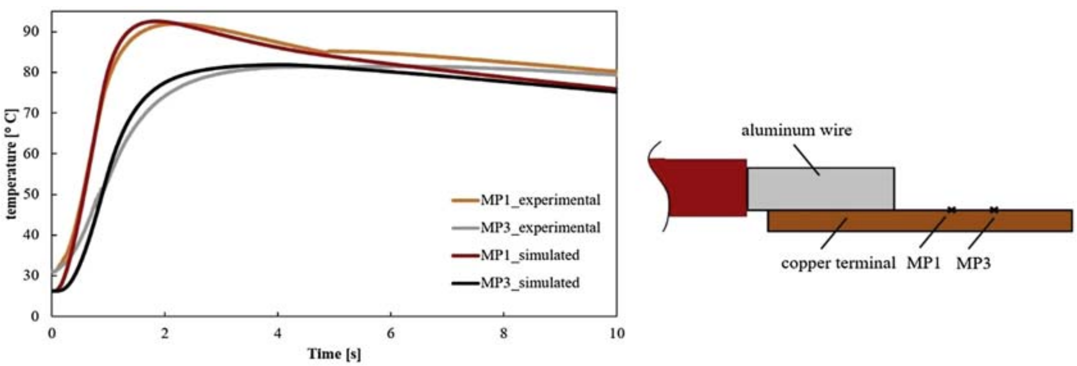

FIG. 7.29 Temperature measurements via simulation and experimental data at copper sheets.

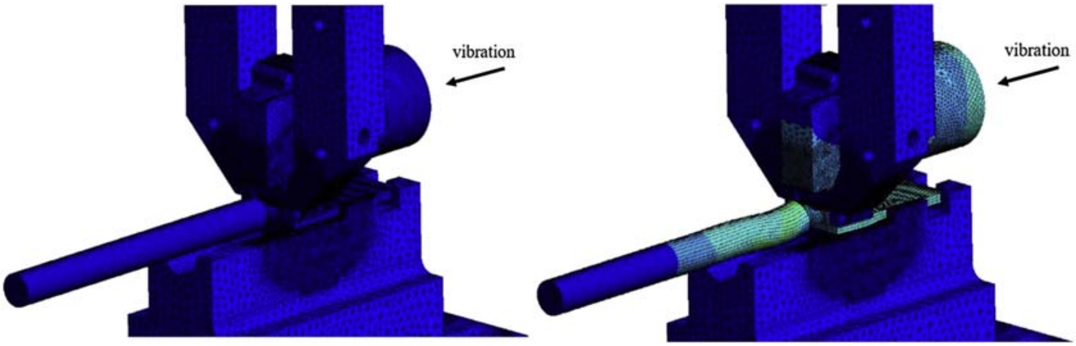

FIG. 7.30 FEM analysis of vibration propagation in wire to sheet ultrasonic welding.

4. Conclusion

In this chapter, current developments in welding principles, joint formation, material specific issues, applications and challenges of ultrasonic welding have been addressed. A short overview about the principles of ultrasonics and components of an ultrasonic metal device was given and linear and torsional welding principle as the most common in ultrasonic metal welding was described.

Despite considerable interest in the joint formation mechanism of ultrasonic metal welding in many studies, the physical understanding of the process is still lacking. In this chapter macroscopic formation of the joint and bonding mechanism at the interface for bulk materials was represented. Further applications and challenges during ultrasonic welding are described. The influence of different process parameters on friction and tensile loading to failure of hybrid joints was shown as well as representative investigation of the joint formation during bonding of wires. Besides, the growth of intermetallic compounds depending on time and temperature for hybrid joints was illustrated.

Special focus was placed on welding of aluminum to copper, in particular on the influence of amplitude and nickel-layer on phase formation. In case of welding aluminum wire to copper sheets, a testing strategy to evaluate the bonded area was described and the effect of compaction on joint properties was analyzed.

Ultrasonic metal welding will continue to gain importance in the future due to the government's efforts to push electromobility and lightweight construction concepts. Accordingly, suitable joining processes as ultrasonic metal welding will also have to develop and remain to be interesting due to the very short process times and process-specific advantages especially in fields of aluminum and copper.

Nevertheless, ultrasonic welding is a quite sensitive welding process toward external influences. Hence a reliable and simple process monitoring is still missing and is surely a worthwhile focus for future research.

References

[1] J.P. Bergmann, Thermische Fügeverfahren: Werkstoff-und Prozesstechnik für das Fügen bei niedrigen Temperaturen, first ed., Mainz, 2008.

[2] E. Schubert, Untersuchungen zum Leichtbau mit Hilfe lasergestützter Mischbauweisen, Strahltechnik 23 (2003).
[3] e.V. Automobiltechnik, Beitrag zum Fortschritt im Automobilleichtbau durch belastungsgerechte Gestaltung und innovative Lösungen für lokale Verstärkungen von Fahrzeugstrukturen in Mischbauweise, FAT-Schriftenreihe 244 (2012).
[4] J.P. Bergmann, F. Petzoldt, R. Schürer, S. Schneider, Solid-state welding of aluminum to copper—case studies, Welding in the World 57 (4) (2013) 541−550.
[5] A. Gullino, P. Matteis, F. D'Aiuto, Review of aluminum-To-steel welding technologies for car-body applications, Metals 9 (3) (2019) 315.
[6] Technavio, Global Ultrasonic Metal Welding Equipment Market 2020−2024, 2019. https://www.businesswire.com/news/home/20191203005425/en/Global-Ultrasonic-Metal-Welding-Equipment-Market-2020-2024. (Accessed 11 March 2020).
[7] J. Pollard, Markt Für Ultraschall-Metallschweißgeräte Massive Entwicklung (2020−2029), 2020. http://strandgazettede.com/2020/03/09/globaler-markt-fur-ultraschall-metallschweissgerate/. (Accessed 11 March 2020).
[8] T.H. Kim, J. Yum, S.J. Hu, J.P. Spicer, J.A. Abell, Process robustness of single lap ultrasonic welding of thin, dissimilar materials, CIRP Annals 60 (1) (2011) 17−20.
[9] S. Kumar, C.S. Wu, G.K. Padhy, W. Ding, Application of ultrasonic vibrations in welding and metal processing: a status review, Journal of Manufacturing Processes 26 (2017) 295−322.
[10] E.A. Neppiras, Ultrasonic welding of metals, Ultrasonics 3 (3) (1965) 128−135.
[11] M.P. Matheny, K.F. Graff, Ultrasonic welding of metals, in: J.A. Gallego-Juárez, K.F. Graff (Eds.), Power Ultrasonics: Applications of High-Intensity Ultrasound, Woodhead Publishing, 2015, pp. 259−293.
[12] E. De Vries, Mechanics and Mechanisms of Ultrasonic Metal Welding, The Ohio State University, 2004.
[13] J. Wodara, Ultraschallfügen Und-Trennen, first ed., DVS Media GmbH, 2004.
[14] Z.S. Al-Sarraf, A Study of Ultrasonic Metal Welding, University of Glasgow, 2013.
[15] H.J. Fahrenwaldt, V. Schuler, Praxiswissen Schweisstechnik: Werkstoffe, Prozesse, Fertigung, fith ed., Springer Vieweg, 2014.
[16] K.-J. Matthes, E. Richter, Schweißtechnik: Schweißen von metallischen Konstruktionswerkstoffen, third ed., Carl Hanser Verlag GmbH & Co. KG, 2016.
[17] E. Hering, G. Schönfelder, Sensoren in Wissenschaft und Technik, Auflage, Viewg+ Teubner Verlag, Wiesbaden, 2012.
[18] L. Kollar, H.-J. Gevatter, Umgebungsbedingungen, in: H.-J. Gevatter (Ed.), Automatisierungstechnik 2: Geräte, Springer, Berlin, Heidelberg, 2000, pp. 19−29.
[19] H.-D. Golde, Ultraschall-Metallschweißen, Verlag Moderne Industrie, 1995.
[20] S. Krüger, Ultraschallschweißen von Glasfasertextilien und Glasfaserverbundwerkstoffen mit Blechen, Technische Universität Kaiserslautern, 2005.
[21] J. Magin, Ultraschalltorsionsschweißen von Aluminium/Titan-Verbunden - Prozessanalyse, mechanische Eigenschaften und Mikrostruktur, Technische Universität Kaiserslautern, 2015.
[22] J.P. Bergmann, A. Regensburg, R. Schürer, F. Petzoldt, A. Herb, Effect of the interface characteristics on the joint properties and diffusion mechanisms during ultrasonic metal welding of Al/Cu, Welding in the World 61 (3) (2017) 499−506.
[23] M. Tadvi, A. Pandey, J. Prajapati, J. Shah, Design and development of sonotrode for ultrasonic drilling, in: ASME 2015 International Mechanical Engineering Congress and Exposition, Houston, Texas, November 13−19, 2015, 2015.
[24] I. Stănăsel, T. Buidos, F. Blaga, Design and fem simulation of ultrasonic welding horn, Nonconventional Technologies Review 18 (1) (2014) 51−55.
[25] Š. Emmer, J. Kováčik, S. Mrkvová, Materials for sonotrode tools, Scientific Proceedings 2013, Faculty of Mechanical Engineering ,STU in Bratislava 21 (1) (2013) 44−50.
[26] I. Balz, E. Abi Raad, E. Rosenthal, R. Lohoff, A. Schiebahn, U. Reisgen, M. Vorländer, Process monitoring of ultrasonic metal welding of battery tabs using external sensor data, Journal of Advanced Joining Processes 1 (2020).
[27] M.F. Zäh, T. Mosandl, K. Schlickenrieder, Ultraschall-Metallschweißen. Steigerung der Prozesssicherheit für das Ultraschall-Metallschweißen, Werkstattechnik 92 (9) (2002) 436−440.
[28] M. Roopa Rani, K. Prakasan, R. Rudramoorthy, Studies on thermo-elastic heating of horns used in ultrasonic plastic welding, Ultrasonics 55 (2015) 123−132.

[29] M. Frost, Ultrasonic TORSIONAL Welding − Understanding the Process Benefits, Expanding Applications and Product Design Possibilities, 2015. https://www.azom.com/article.aspx?ArticleID=12022_11.03.2020.
[30] Belgian Welding Institute npo, Literature Survey: Ultrasonic Welding. https://www.bil-ibs.be/sites/default/files/publicaties/andere/literature_survey_ultrasonic_welding.pdf_11.03.2020.
[31] Z. Ni, J. Yang, S. Li, X. Wang, F. Ye, A review on ultrasonic spot welding of copper alloys, Materials Science and Technology 36 (3) (2020) 264−283.
[32] T. Köhler, M. Raab, A. Regensburg, J.P. Bergmann, Liquid interlayer formation during torsional ultrasonic welding of EN CW004A and EN AW1050, Welding in the World 63 (5) (2019) 1187−1194.
[33] H. Kreye, Melting phenomena in solid state welding processes, Welding Journal 56 (5) (1977) 154−158.
[34] M. Ganesh, R. Praba Rajathi, Experimental study on ultrasonic welding of aluminum sheet to copper sheet, International Journal of Renewable Energy Technology 2 (2013) 161−166.
[35] P. Jedrasiak, H.R. Shercliff, Y.C. Chen, L. Wang, P. Prangnell, J. Robson, Modeling of the thermal field in dissimilar alloy ultrasonic welding, Journal of Materials Engineering and Performance 24 (2) (2015) 799−807.
[36] J. Yang, B. Cao, Q. Lu, The effect of welding energy on the microstructural and mechanical properties of ultrasonic-welded copper joints, Materials 10 (2) (2017) 1−13.
[37] Z. Zhu, K.Y. Lee, X. Wang, Ultrasonic welding of dissimilar metals, AA6061 and Ti6Al4V, International Journal of Advanced Manufacturing Technology 59 (5-8) (2012) 569−574.
[38] S. Das, M.P. Satpathy, B.C. Routara, S.K. Sahoo, S. Gantayat, Mechanical behavior of ultrasonic spot welded aluminum to cupro-nickel sheets for battery tabs, in: IOP Conference Series: Materials Science and Engineering, 2019.
[39] G. Wagner, F. Balle, D. Eifler, Ultrasonic welding of aluminum wires with large cross sections, in: Proceedings of the 12th International Conference on Aluminium Alloys, Yokohama, Japan, 5−9 September, 2010, 2010.
[40] J. Tsujino, T. Ueoka, Y. Fujita, I. Watanabe, Ultrasonic butt welding of aluminum, copper and steel plate specimens, Japanese Journal of Applied Physics 33 (1) (1994) 3058−3064.
[41] B. Sanga, R. Wattal, D. Nagesh, Mechanism of joint formation and characteristics of interface in ultrasonic welding: literature review, Periodicals of Engineering and Natural Sciences 6 (1) (2018) 107−119.
[42] R. Jahn, R. Cooper, D. Wilkosz, The effect of anvil geometry and welding energy on microstructures in ultrasonic spot welds of AA6111-T4, Metallurgical and Materials Transactions A 38 (3) (2007) 570−583.
[43] D. Bakavos, P.B. Prangnell, Mechanisms of joint and microstructure formation in high power ultrasonic spot welding 6111 aluminium automotive sheet, Materials Science and Engineering 527 (23) (2010) 6320−6334.
[44] S. Shawn Lee, T. Hyung Kim, S. Jack Hu, W.W. Cai, J.A. Abell, Analysis of weld formation in multilayer ultrasonic metal welding using high-speed images, Journal of Manufacturing Science and Engineering 137 (3) (2015).
[45] U.I. Chang, J. Frisch, On optimization of some parameters in ultrasonic metal welding, Welding Journal 53 (1) (1974) 24−36.
[46] M. Vlad, Ultrasonic Welding of Aluminum: A Practical Study in Consistency, Part Marking and Control Modes, Iowa State University, 2007.
[47] A. Pfluger, X. Sideris, New developments in ultrasonic welding, SAMPE Quarterly 7 (1) (1975) 9−19.
[48] S.M. Ambekar, T.H. Hazlett, Additional studies on interface temperatures and bonding mechanisms of ultrasonic welds, Welding Journal 49 (5) (1970) 196−200.
[49] K.C. Joshi, The formation of ultrasonic bonds between metals, Welding Journal 50 (12) (1971) 840−848.
[50] T. Broda, Entwicklung von Anwendungsrichtlinien zum Kompaktieren und Schweißen von Kupfer-und Aluminiumlitzen mit konduktiver Widerstandserwärmung, Schlussbericht zum IGF-Vorhaben 17395 BR, Schweißtechnische Lehr- und Versuchsanstalt Halle GmbH (SLV), 2014.
[51] J. Tsujino, Y. Murayama, H. Furuya, Welding characteristics of thin copper wire using complex vibration ultrasonic wire bonding systems, Japanese Journal of Applied Physics 29 (1) (1990) 173−175.
[52] S. Matos, F. Veloso, C. Santos, L. Gonçalves, E. Carvalho, Characterization of ultrasonic metal welding process, Journal of Environmental Science and Engineering (2018) 125−131.
[53] T. Kuprys, J. Janutėnienė, R. Didžiokas, Strength of copper wire connections welded by ultrasonic, Mechanics 65 (3) (2007) 30−33.
[54] A. Regensburg, F. Petzoldt, R. Schürer, P. Hellwig, J.P. Bergmann, Effect of local preheating during ultrasonic welding of Al-Cu joints on strand compaction and bond formation, Welding in the World 61 (3) (2017) 443−451.
[55] M.J. Rathod, M.m. Kutsuna, Joining of aluminum alloy 5052 and low-carbon steel by laser roll welding, Welding Journal 83 (1) (2004) 16−26.

[56] J. Wilden, J.P. Bergmann, Manufacturing of titanium/aluminium and titanium/steel joints by means of diffusion welding, Welding and Cutting 56 (5) (2004) 285−290.

[57] T. Watanabe, H. Sakuyama, A. Yanagisawa, Ultrasonic welding between mild steel sheet and Al−Mg alloy sheet, Journal of Materials Processing Technology 209 (15-16) (2009) 5475−5480.

[58] A. Panteli, J. Robson, I. Brough, P. Prangnell, The effect of high strain rate deformation on intermetallic reaction during ultrasonic welding aluminium to magnesium, Materials Science and Engineering 556 (2012) 31−42.

[59] V. Patel, S. Bhole, D. Chen, Ultrasonic spot welding of aluminum to high-strength low-alloy steel: microstructure, tensile and fatigue properties, Metallurgical and Materials Transactions A 45 (4) (2014) 2055−2066.

[60] F. Haddadi, Microstructure reaction control of dissimilar automotive aluminium to galvanized steel sheets ultrasonic spot welding, Materials Science and Engineering 678 (2016) 72−84.

[61] T. Broda, H. Rudolf, Y. Yang, Kombiniertes ultraschall-widerstandsschweißen an stahl-aluminium-blechverbindungen, in: 14. Kolloquim Widerstandsschweißen und alternative Verfahren, Halle (Saale), Oktober 17, 2012.

[62] W.-B. Lee, K.-S. Bang, S.-B. Jung, Effects of intermetallic compound on the electrical and mechanical properties of friction welded Cu/Al bimetallic joints during annealing, Journal of Alloys and Compounds 390 (1-2) (2005) 212−219.

[63] M. Braunovic, N. Alexandrov, Intermetallic compounds at aluminum-to-copper electrical interfaces: effect of temperature and electric current, IEEE Transactions on Components Packaging & Manufacturing Technology Part A 17 (1) (1994) 78−85.

[64] M.P. Satpathy, B.R. Moharana, S. Dewangan, S.K. Sahoo, Modeling and optimization of ultrasonic metal welding on dissimilar sheets using fuzzy based genetic algorithm approach, Engineering Science and Technology, an International Journal 18 (4) (2015) 634−647.

[65] S. Elangovan, S. Semeer, K. Prakasan, Temperature and stress distribution in ultrasonic metal welding—an FEA-based study, Journal of Materials Processing Technology 209 (3) (2009) 1143−1150.

[66] W. Kim, A. Argento, A. Grima, D. Scholl, S. Ward, Thermo-mechanical analysis of frictional heating in ultrasonic spot welding of aluminium plates, Proceedings of the Institution of Mechanical Engineers - Part B: Journal of Engineering Manufacture 225 (7) (2011) 1093−1103.

[67] T. Köhler, Erarbeiten von Prozessstrategien zum Ultraschallschweißen von Kupfer mit Aluminium unter Berücksichtigung der metallischen Überzüge - IGF-Vorhaben Nr. 19485 BR/1, Schlussbericht, Technische Universität Ilmenau, 2019.

This page intentionally left blank

PART C

Adhesive bonding

This page intentionally left blank

CHAPTER

8

Manufacture and testing

Ricardo J.C. Carbas[a,b], *Catarina Borges*[a], *Eduardo A.S. Marques*[a], *Alireza Akhavan-Safar*[a], *Lucas F.M. da Silva*[b]

[a]**Instituto de Ciência e Inovação em Engenharia Mecânica e Engenharia Industrial (INEGI), Porto, Portugal;** [b]**Departamento de Engenharia Mecânica, Faculdade de Engenharia (FEUP), Universidade do Porto, Porto, Portugal**

1. Introduction

Adhesive bonding has been widely used in several industrial fields, such as the automotive and aerospace industries, driven by its practical advantages over traditional bonding methods. Unlike most conventional joining methods, adhesive bonding does not require the introduction of holes on the structure, which allows for a more uniform stress distribution and avoids stress concentration. Through a continuous bond, it is possible to obtain higher load transmission, stiffness and fatigue resistance. Additionally, adhesives contribute to the weight reduction of the final structure, which is crucial for the transportation sector, where this leads to reductions in energy consumption and emissions. Not only adhesive joints present a lighter alternative to traditional mechanical fasteners, but they also enable the use of composite materials, which are highly sensitive to notches, and the connection of dissimilar materials, further reducing the weight of the designed structure.

Furthermore, adhesives improve the appearance of the designed components, enhance the possibility of joining complex structures, have good corrosion resistance and present vibration damping properties. Moreover, there is an additional stiffening effect due to a wider bonded area used in adhesive joints, which reduces the unsupported and thus unstiffened area when compared with more localized mechanical fastening methods. However, the use of adhesive joints has some inherent disadvantages, such as low peel strength due to the low resistant area, manufacturing constraints associated with the curing of the adhesives and surface preparation of the substrates, high temperature limitations, poor chemical resistance, control of the process and in-service repairs [1].

Adhesive joints must be optimized in order to get the best performance possible for each component, rather than using the design made for mechanical joints and substituting them by

Advanced Joining Processes
https://doi.org/10.1016/B978-0-12-820787-1.00008-5

adhesives. This includes a careful analysis of the methods of application and curing conditions at the design stage, as well as a cautious selection of the type of adhesive to be used.

In adhesive joints design, five key steps must be taken under consideration in order to manufacture an adhesive joint that provides the desired levels of mechanical strength and durability. These main steps are the adhesive selection process, the joint design phase, the selection of the surface treatment, the manufacture process and the control. This chapter comprehends an analysis of how to fully take advantage of adhesive joints and the improvements made in this sector while exploring the innovative processes and techniques developed to minimize its disadvantages.

2. Structural adhesives

2.1 Types of adhesives

Adhesives can be either thermosetting, thermoplastic, elastomeric (rubbers) and hybrid. Thermosetting polymers cure due to chemical reactions at room or high temperature and after this initial cure the adhesive cannot be melted. They can be supplied as one-part or multiple-part systems. One-part systems typically require high temperature to cure and its shelf life is reduced. In multiple-part systems, the adhesive and the hardener are usually supplied separately which translates into higher shelf life, additionally they usually cure at room temperature. Thermoplastic polymers are cured from an initial melted state or by loss of solvent and create a reversible bond since they can be melted again without significant loss of properties. Elastomeric polymers have typically higher elongation, toughness and peel strength and hybrid adhesives consist on a combination of the above. The structural adhesives used in industrial applications are divided into many different chemical families. The most used are epoxies, acrylics, polyurethanes, phenolics and polyaromatics [1–4]. A short summary of the characteristics of each of these chemical families is presented below.

Epoxy-based adhesives can be cured with different hardeners, generating adhesives with different properties, which makes them very versatile. These adhesives can be obtained in one-component or two-components forms. They are commonly used due to their high strength-to-weight ratio, excellent adhesion properties and thermal stability. However, unreinforced epoxies are strong yet very brittle adhesives which makes them too fragile for some structural applications. Therefore, high-performance epoxy adhesives have been created, using different additives, such as nitrile, phenolic, nylon, and polysulfide resins, as well as thermoplastic and elastomeric particles. Toughened epoxies typically contain rubber particles, which increase the ductility and toughness oh the adhesive. Epoxies can be supplied as one-part or two-part systems.

Acrylic polymers usually provide fast cure and high strength but are more expensive than epoxies. They are divided in several families, such as anaerobics, cyanoacrylates and modified acrylic adhesives. Anaerobics are one-part adhesives, which are liquid in presence of air and cure rapidly under the lack of oxygen at room temperature. These materials provide very high bond strength, with the best results being obtained for thin bondlines (less than 0.8 mm). These adhesives can be used with most materials, except polyethylene and fluorocarbons, and are usually used as liquid washers for screws and bolts and sealants to seal porosity in metal castings. Some anaerobics can withstand 230 °C, but they are generally used below 150 °C. Cyanoacrylates are one-part liquid or gel adhesives, with a fast cure at room temperature, which makes them suitable to rapid assemble or repair. They have excellent shear strength but typically have low resistance to severe environments, such as high temperatures and moisture, low toughness, and low peel strength. Modified acrylics have good adhesion to a wide variety of substrates, such as metal, plastic and glass materials, creating strong bonds with high tolerance to somewhat oily and contaminated surfaces. They usually are available in two component packages and their curing time is very short when compared with epoxy or polyurethane-based adhesives which makes them suitable for use in rapid assembly operations. They provide good toughness, peel strength and resistance to moisture.

Polyurethanes adhesives are mostly used for applications that require a flexible joint, such as windshields and panoramic glass roofs in automotive structures, where the adhesive must accommodate the relative movements of the adherends. These adhesives can be supplied as one-part systems, which cure slowly at room temperature when exposed to moisture, and two-part systems, which start to cure upon mixing and the cure can be further accelerated by increasing temperature. Polyurethanes are known for their high ductility and flexibility, also providing high toughness and peel strength. They have good chemical resistance (although inferior to epoxies and acrylics) but are sensitive to moisture and have limited resistance at high temperatures, with their maximum service temperature being around 150 °C.

Phenolic adhesives are commercially available as solutions and films and cure under pressure and high temperature (about 140 °C) for several minutes. These adhesives have a good resistance to severe environments, exhibiting high moisture and temperature resistance. Modifications using synthetic rubbers or thermoplastic can be performed to improve their toughness and peel strength.

Polyaromatic adhesives have excellent thermal resistance and are suitable for high-temperature applications in the eronautical industry. They are usually in films form and can be modified using thermoplastics to improve their toughness. However, they are difficult to process and expensive materials.

Table 8.1 summarizes some generic characteristics for different families of structural adhesives. Characteristics such as typical service temperature that each adhesive can be subjected to, the behavior when subjected to environmental conditions. In addition, some typical applications are shown.

2.2 Adhesive characterization

The experimental tests that are used to mechanically characterize an adhesive can be divided into two main groups: strength tests and fracture tests. Tensile, compressive and shear tests are considered to be strength tests and allow to obtain the adhesive properties in tension, compression, and shear. Fracture tests focus instead on the propagation of cracks through the material and can be performed under tensile, shear or mixed loading conditions [5].

2.2.1 Tensile tests

Bulk tensile tests: The tensile properties of an adhesive, such as the Young's modulus, the tensile strength and strain at failure are typically determined using dog-bone shaped specimens, shown in Fig. 8.1, which are composed solely of bulk adhesive. Bulk tensile specimens are usually manufactured according to the ASTM D412 standard, but some optimization

TABLE 8.1 Characteristics of the main adhesive families.

		Service temperature	Environmental resistance			Applications
			Water	**Solvent**	**Oil**	
Epoxy	One-part	−40 to 180 °C	Excellent	Excellent	Excellent	Aircraft, helicopters, cars, trains, sport equipment, etc.
	Two-parts	−40 to 100 °C	Good	Good	Good	
Acrylic	Anaerobic	−55 to 150 °C	Good	Depends on formulation	Good	Liquid lock washer
	Cyanoacrylate	−30 to 80 °C	Weak	Fair/Good	Good	Optical and electronic industry
	Modified acrylic	−40 to 120 °C	Good	Good	Good	Rapid assemble of structures
Polyurethane		−200 to 120 °C	Fair	Fair/Good	Fair/Good	- Cryogenic applications - Automotive industry
Phenolic		−40 to 180 °C	Excellent	Good	Good	Wood Metal (hybrid phenolics)
Polyaromatic		−40 to 280 °C	Excellent	Excellent	Excellent	- Applications at high temperature - Eronautical and erospace industry

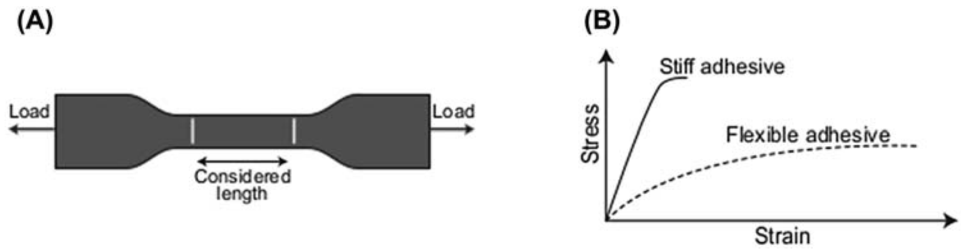

FIG. 8.1 Bulk tensile tests — (A) dog-bone specimen, and (B) typical stress-strain curves of a stiff and flexible adhesive.

studies can also be found in the literature for specific cases, such as Costa et al. [6]. When manufacturing the specimens, it is essential to ensure that air is not trapped in the adhesive, as this would cause voids and, consequently, premature failure of the material.

The specimen is fixed by its wider end sections to a universal testing machine and is uniaxially loaded at a constant crosshead rate until failure occurs. The main objective of this test is to obtain a stress-strain curve. The load is measured by the load cell of the universal testing machine and, consequently, the stress can be determined with the area of the specimen. The strain is determined from the displacement of the considered length and can be obtained using clip gauges or strain gauges. However, whenever possible noncontracting devices should be used, to avoid interference with the material behavior, especially for flexible and ductile adhesives. Therefore, optical methods and digital image correlation have grown in popularity as a suitable alternative although they require more costly equipment.

Butt tensile tests: Tensile strength of adhesives can also be determined using butt tensile tests, schematically shown in Fig. 8.2, which are performed following the ASTM D 2095 standard. The test specimen consists of two cylindrical adherends, bonded with an adhesive layer. The specimen is then loaded perpendicularly to the adhesive layer. To ensure the correct application of the load, the adhesive thickness should be carefully controlled, and this is usually achieved using a specially designed jig equipped with adjustable thickness controlling shims. An inadequate control of the adhesive thickness along the bondline will introduce a cleavage loading component and contribute to wider dispersion of the results.

It is important to note that the stress-strain behavior captured by this test is not representative of the intrinsic behavior of the adhesive, since it can be affected by the constraining effect of the substrates. Therefore, the results obtained by this method cannot be directly correlated with the properties obtained from bulk tensile tests.

2.2.2 Compressive tests

Compressive tests are less common than tensile or shear tests since, generally, it is assumed that the behavior of the adhesive follows the von Mizes model and its tensile and compressive properties are similar. However, adhesives are affected by a hydrostatic stress component, which causes the compressive and tensile strength to be different.

FIG. 8.2 Butt tensile test.

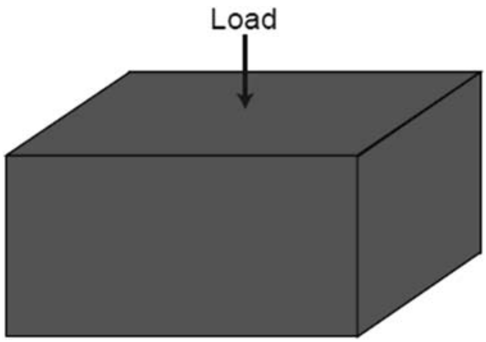

FIG. 8.3 Compressive parallelepipedal specimen following ASTM D 695 standard.

Compressive properties of the adhesive are usually determined using bulk compression tests, following the ASTM D 695. This test suggests a parallelepipedal specimen with a rectangular base, shown in Fig. 8.3.

Alternatively, the ASTM D 695 standard suggests a different specimen, similar to the bulk tensile specimen, which uses less material but is only valid for rigid adhesives, shown in Fig. 8.4. To avoid buckling under compression and guarantee the alignment of this compressive specimen during the test, the specimen is fixed between two blocks. The compression load is then applied to those blocks rather than being directly applied to the specimen.

In both cases the specimen, or the blocks, are compressed between two plates parallel to the surface at a uniform rate until failure occurs. During compressive tests, both the load and displacement are recorded and subsequently, stress-strain curves are determined, similarly to what is done in bulk tensile tests. Load is directly obtained from the universal machine used to perform the test however, displacement should be obtained preferably using non-contact devices to avoid interfering with the test.

2.2.3 Shear tests

Thick adherend shear tests (TAST): The shear properties of an adhesive, such as shear strength, shear modulus and strain to failure can be determined using TAST. While commonly used shear tests, such as the SLJ test, generate higher stress concentrations at the edges of the overlap, and are not capable of accurately measuring the shear properties of the adhesive, the TAST test presents a more uniform shear stress distribution, while remaining easy to manufacture and test. This test can be performed following ASTM D 3983 or ISO 11003-2 standards.

In order to create a more uniform stress distribution and load the adhesive purely in shear, TAST specimens have a small overlap length and the adherends used are very stiff (Fig. 8.5). However, small stress concentrations can still arise at the overlap edges, which can be significant when analyzing brittle adhesives. In those cases, a torsion test should be performed. The

FIG. 8.4 Bulk compression test specimen.

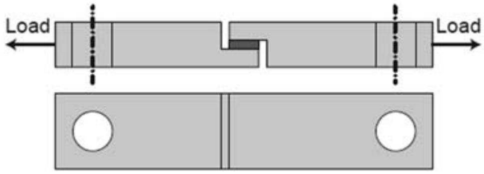

FIG. 8.5 TAST specimen.

stress along the test is determined with the load recorded by the universal testing machine and the area of the overlap. The displacement and, therefore, the strain, can be obtained using an extensometer or digital image correlation. The main difficulty associated with this test is the measurement of the displacement since the adherends are very stiff and the overlap very short, leading to small displacement increments.

Butt torsion tests: Shear properties of an adhesive can also be determined using butt torsion tests, Fig. 8.6. This test induces pure shear loading in the adhesive and, as it is free of stress concentrations, it enables larger strain to failure and, therefore, a higher accuracy for strain than any other test, making it is the preferred method for determining shear properties of the adhesive. Additionally, relatively thick bondlines should be used in order to maximize the adhesive deformation and a precise device to measure rotation should be used.

Butt torsion specimens can be either two solid cylindrical substrates, as shown in Fig. 8.6, or two tubular substrates, Fig. 8.7. The latter have the advantage of having approximately constant shear stress through the whole adhesive layer, since the shear stress is proportional to the radius. However, then are difficult to manufacture because a spew fillet is created inside the tubular adherends, which is difficult to remove and can affect the results. However, if the tubes are thin enough, the influence of this fillet can be neglected.

2.2.4 Fracture tests

Mode I fracture tests: Fracture tests in mode I, which is an opening mode, are performed to determine the energy an adhesive can withstand before crack propagation occurs. Different specimens can be used for the measurement of this energy, such as double cantilever beam (DCB), shown in Fig. 8.8, or tapered double cantilever beam (TDCB), shown in Fig. 8.9. These are standard tests and follow the ASTM D3433 and ISO 25217 standards. In both tests, the

FIG. 8.6 Butt torsion test.

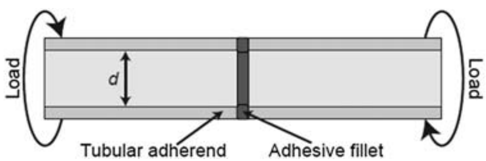

FIG. 8.7 Napkin-ring test specimens.

FIG. 8.8 Double cantilever beam (DCB) test.

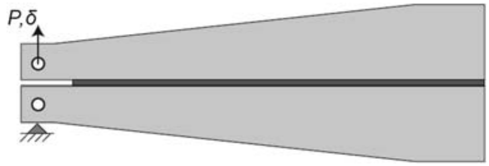

FIG. 8.9 Tapered double cantilever beam (TDCB) test.

adherends are bonded along their length and they are forced to separate with a loading that is perpendicular to the adhesive layer, resulting in an opening effort.

In both the DCB and TDCB tests, it is important that the adherends remain in the elastic domain because, if they deform plastically, the energy being used to deform the substrates will be erroneously added to the fracture energy used by the adhesive layer, leading to wrong results.

To measure the fracture energy, it is required to know the crack length as it propagates, which can be achieved either by direct measurement or by deducing it from the load, P, and displacement, δ, recorded in a testing machine. Adequate data reduction schemes, such as the compliance-based beam method (CBBM) [7], should be used in the latter case. With this method, from the load-displacement curve, the energy release rate in mode I, G_I, as a function of the equivalent crack length, a_{eq}, can be determined. This curve is referred to as R-curve, and it usually presents a *plateau* of stable crack propagation where the energy release rate is constant independently of the a_{eq}, which is the critical energy release rate, G_{Ic}, and represents the adhesive fracture toughness in mode I.

Mode II fracture tests: Fracture tests in mode II, which is a shear mode, are used to determine the fracture toughness in mode II, G_{IIc}. The most common test is the end-notched flexure (ENF) test, as shown in Fig. 8.10, although other tests such as the end-loaded split (ELS), Fig. 8.11, test can also be used for this purpose.

The ENF test consists of two adherends bonded along its length, forming a beam. This beam is simply supported at its edges and loaded at middle length. In one of the edges of the adhesive a pre-crack is introduced, which will propagate as the test progresses. During the crack propagation, and similarly to the DCB test, the crack length should be either directly measured or indirectly deduced from the load, P, and displacement, δ, with an appropriate

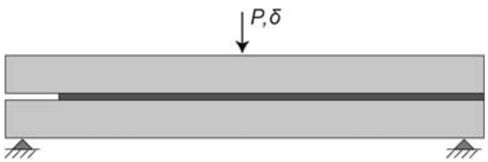

FIG. 8.10 End-notched flexure (ENF) test.

FIG. 8.11 End-loaded split (ELS) test.

data reduction scheme such as the CBBM [7]. In this case, direct measurement of the crack length is particularly challenging because the crack is compressed which makes it very difficult to precisely assess its location.

Mixed-mode fracture tests: In practice, it is uncommon for adhesive joints uncommon to be loaded under pure mode I or pure mode II. In fact, loads are usually composed by a combination of both modes. Mixed-mode fracture tests, which are specifically designed to achieve the desired ratio between mode I and II, are used to experimentally mimic these cases and are crucial to fully understand the adhesive behavior. A wide variety of testes are available to measure the fracture toughness of the adhesive under mixed mode loading, summarized in Table 8.2.

TABLE 8.2 Mixed-mode fracture tests.

Test	Schematic representation
Asymmetric double cantilever beam (ADCB) (Xiao et al. [8])	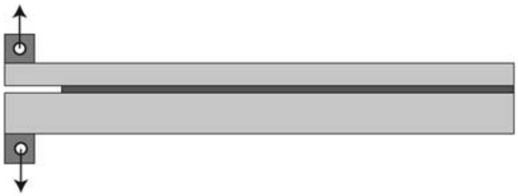
Asymmetric tapered double cantilever beam (ATDCB) (Park and Dillard [9])	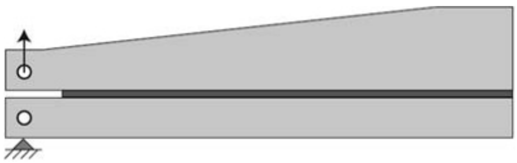
Cracked lap shear (CLS) (Brussat et al.[10])	
Single-Leg bending (SLB) (Yoon and Hong [11])	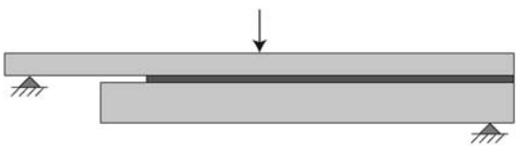

(*Continued*)

TABLE 8.2 Mixed-mode fracture tests.—cont'd

Test	Schematic representation
Arcan (Voloshin and arcan [12]) (left), modified arcan (El-Hajjar and Haj-Ali [13]) (right)	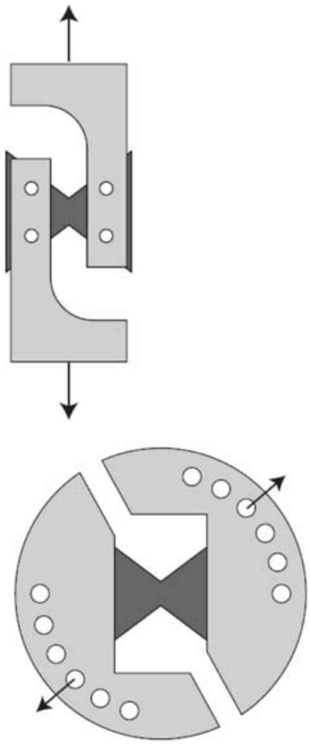
Mixed-mode bending (MMB) (ASTM D6671 [14])	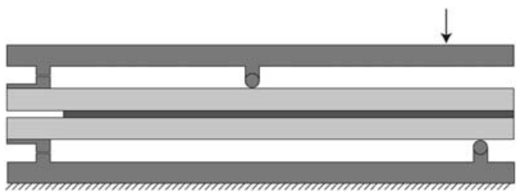
Fernlund and Spelled jig (Fernlund and Spelled [15])	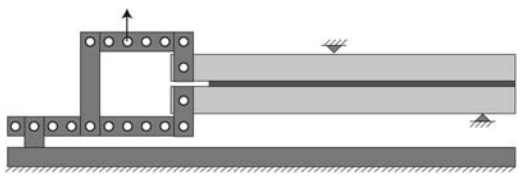

Additionally, an apparatus which is suitable for the study of a wide range of mixed-mode ratios for adhesive joints was recently developed [16,17] and is shown in Fig. 8.12. This apparatus was specifically designed to determine the of the fracture toughness envelope of adhesives. Standard DCB specimens (according ASTM D3433 and ISO 25217 standard) can be

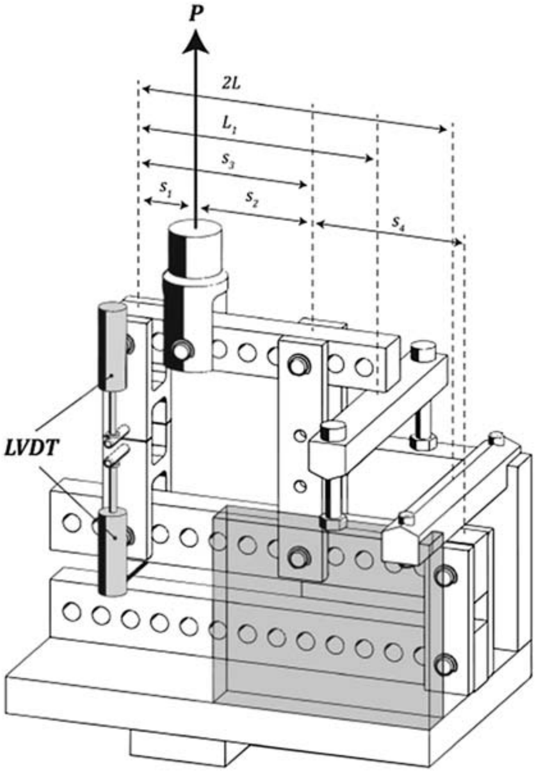

FIG. 8.12 Mixed-mode apparatus device.

used for testing in this apparatus. The apparatus can be configured to apply different modes of loads, including pure mode I (opening), pure mode II (shear) and a variety of mixed modes in-between the pure modes. This wide range of mixed modes is attained by changing the position of the beams that compose the apparatus structure. As the beam position precludes direct measurement of the crack tip location, this measurement is achieved by an indirect method (using the CBBM method), where the crack tip location is estimated using the displacement of each of the specimens' beams, measured using two linear variable differential transformers (LVDT) installed on the apparatus [16,17].

3. Joint design

The design parameters associated with adhesive joints play an important key in achieving the desired the joint strength and durability, enabling the creation of efficient and cost-effective joints. A joint will unavoidably lead to geometrical or/and material discontinuities which can result in high local stress concentrations if a poor design is used. In order to minimize this effect and ensure that a joint will not fail prematurely, an efficient design is required. The adhesive joint design must thus be accomplished by recognizing the limitations of the different joint geometries and by including appropriate restrictions on materials and dimensions, ensuring a durable and strong joint with low manufacturing costs [1,18,19].

3.1 Adhesive joints configurations

In order to ensure that the adhesive joint provides the maximum capacity to resist loading stresses, the loading area should be as large as possible. In addition, the joint should be loaded in shear, taking advantage of the full overlap area instead of concentrating the load in a small area as it typically occurs in a peel loading. However, many other configurations are possible, considering the needs of some specific applications. Generally, adhesive joints configurations can be divided in butt joints, lap joints, cylindrical joints, T joints and corner joints.

3.1.1 Butt joints

Butt joints are among the types of joint simplest to manufacture. However, its resistance to bending loads is low because this type of loading leads to high cleavage stresses in the adhesive. Fig. 8.13 shows some modifications in the geometry of the joint that can be used in order to improve the joint strength, reducing cleavage stresses that act on the adhesive. The tongue and groove butt joint is the most efficient configuration because it is inherently self-aligned and the adhesive works mainly under shear loads [20].

3.1.2 Lap joints

Lap joints are the most used type of joint because due to their simple manufacturing process and the fact that the loading of the adhesive happening mainly in shear. Therefore,

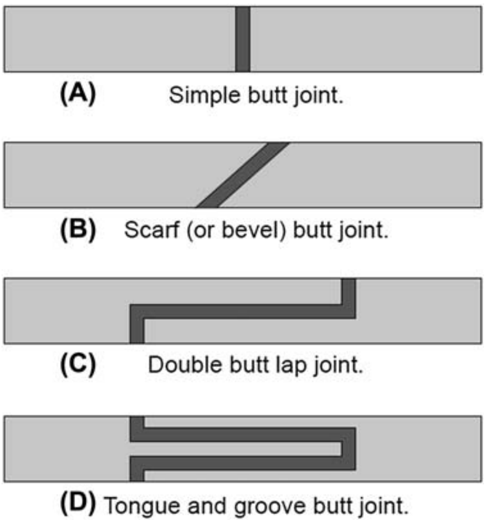

FIG. 8.13 Butt joints. (A) Simple butt joint. (B) Scarf (or bevel) butt joint. (C) Double butt lap Joint. (D).Tongue and groove butt joint.

single-lap joints can be easily found in industrial and academic contexts, providing a quick and practical method for studying a given combination of materials, being very easy to manufacture with simple tooling. The main limitations of these joints are connected to the non-colinear loads applied to the substrates, which will tend to align during load, inducing significant peel stresses, localized at the ends of the overlap. Fig. 8.14 shows some geometrical configurations that can be used to decrease these peel stresses in single-lap joints. The joggle joint is the simplest solution to have load aligned, however, the double lap joint reduces drastically the bending moment, increasing joint strength. Other lap joints configurations such as 'wavy' and 'reverse bent' joints have the minimum peel stresses, leading the highest joint strength [21].

3.1.3 Strap joints

Strap joints can be found in different configurations, as shown in Fig. 8.15. It should be noted that the strap joint with only one strap, similarly to the single lap joint, is subjected to peel stresses due to its non-collinear loading, which induces a bending moment. This bending moment can be reduced by using two straps, leading to a much stronger joint. Of

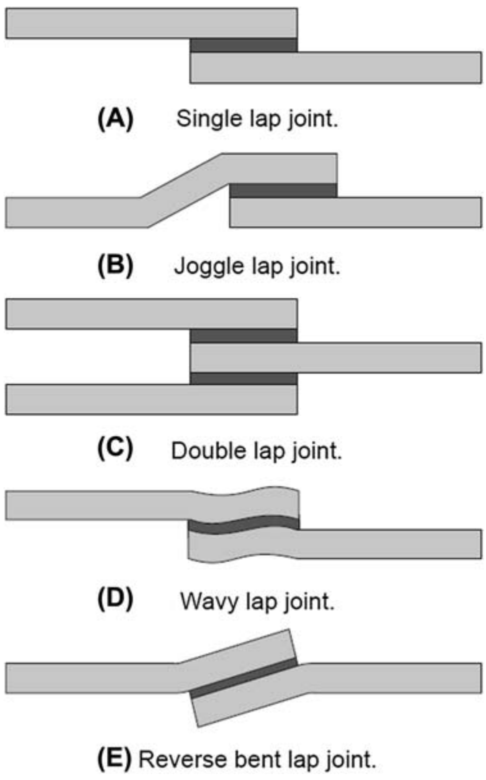

FIG. 8.14 Lap joints. (A) Single lap joint. (B) Joggle lap joint. (C) Double lap joint. (D) Wavy lap joint. (E) Reverse bent lap joint.

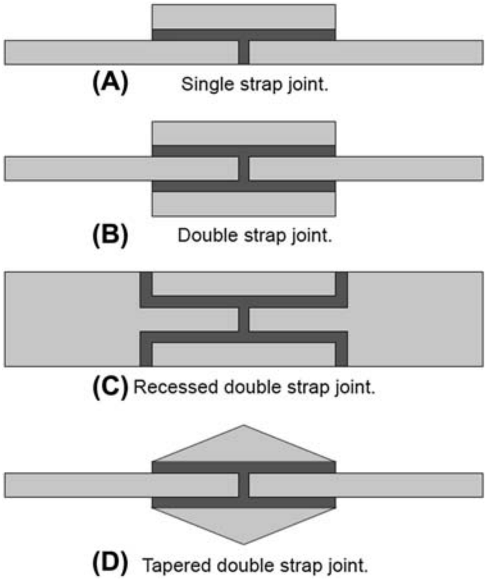

FIG. 8.15 Strap joints. (A) Single strap joint. (B) Double strap joint. (C) Recessed double strap joint. (D) Tapered double strap joint.

the configurations presented, the more efficient types are the strap recessed and tapered joints. However, they require intensive machining, which translates into a much more complex and expensive production process, which might not be economically viable.

3.1.4 Cylindrical joints

Cylindrical joints can be used to sustain axial loads, torsional loads or a combination of the two. For axial loads stress concentrations arise at the ends of the overlap length while for torsion loads there is only the effect of differential straining, as different areas of adhesive along the radius of the substrate are subjected to quite distinct local strains. The manufacture of this type of joints can be achieved using bars and tube adherends, illustrated in Fig. 8.16. Tube shaped adherends provide a larger bonded area however, in some cases, as the tapered adherend tubes, significant machining is required, leading to a much more expensive joint. Is has been shown that the most efficient joint cylindrical joint geometry, considering machining and cost, is the double-lap configuration [22].

3.1.5 T joints

T-joint are joints where two adherends are bonded in perpendicular orientation (90°) although different relative angles (θ) can also be considered, as shown in Fig. 8.17. This type of joint can be support normal (N) or transverse (T) loadings and can be reinforced with additional corner components to minimize the peel loading and increase joint strength, as it can be observed in some configurations presented in Fig. 8.17.

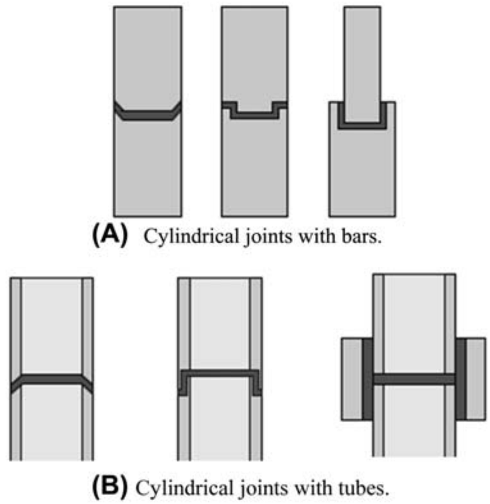

FIG. 8.16 Cylindrical joints. (A) Cylindrical joints with bars. (B) Cylindrical joints with tubes.

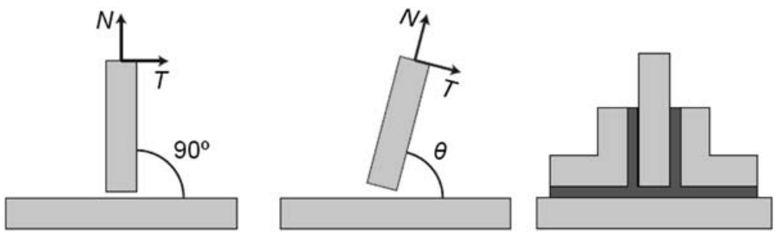

FIG. 8.17 T joints.

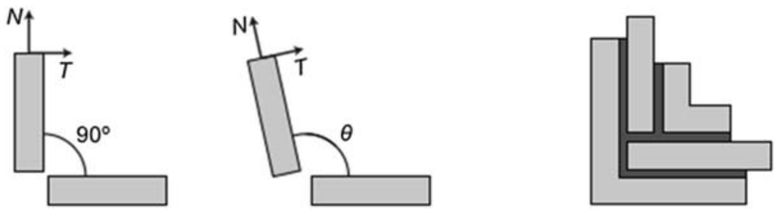

FIG. 8.18 Corner joints.

3.1.6 Corner joints

Fig. 8.18 shows some possible configurations of corner joints, which are similar in concept to the T joints. In these joints, there are also changes that can be made to the base geometry with the aim of reducing peel stresses in the adhesive. Apalak and Davies [23] have found that with regards to stress and stiffness, the transverse loading (T) is the most critical. To reduce the peak stress in the adhesive, one can also increase the thickness and length of the reinforcements.

3.1.7 *Reinforcements*

Industrially, thin plates are used in external parts of some components to increase their rigidity and, it is a common practice to bond those reinforcements. Typically, bonded reinforcements can introduce cleavage stresses in the adhesive layer and, in order to reduce those stresses, a few solutions have been presented, as shown in Fig. 8.19. The solutions presented can follow three different approaches to improve joint strength: increase the bonded area, reduce the stiffness of the edges of the reinforcements or reduce the stiffness of the base.

3.2 Joint strength prediction

There is a wide variety of adhesive joints which can be found in different applications, as explored in the previous section. However, single lap joints are the more common, as the adhesive is loaded in shear and the hole bonded area resists stress. Additionally, the alignment of the loads applied to both adherents induces a flexural moment. Therefore, the analysis of the stress to which the adhesive is subjected has been a critical subject of study, with many

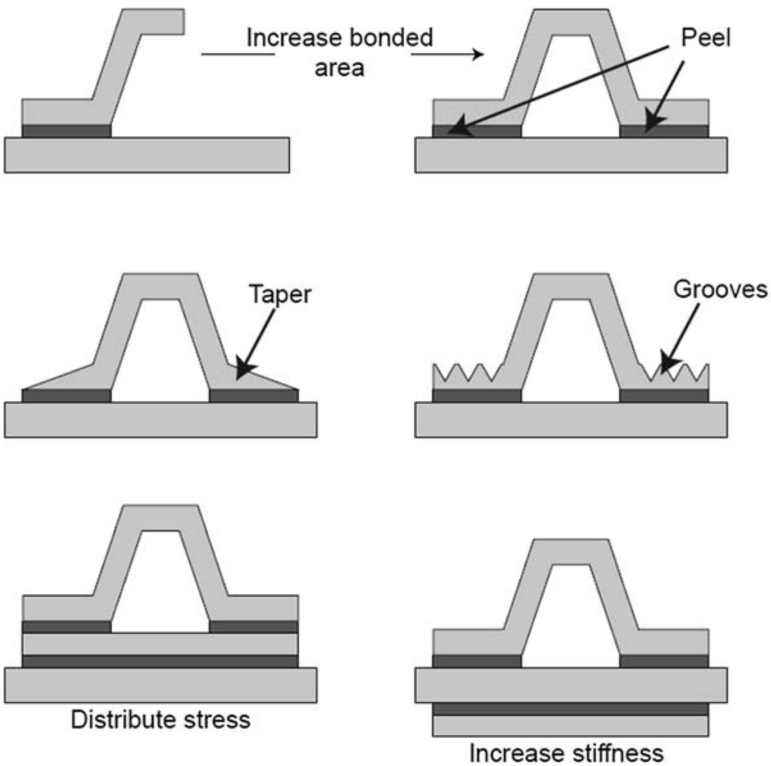

FIG. 8.19 Reinforcements.

different models being proposed to describe the stress levels on the adhesive layer and predict the joint strength.

3.2.1 *Analytical models for stress analysis*

The stresses acting inside the adhesive layer of an adhesively bonded joint can be calculated by analytical methods, as proposed by Volkersen [24], Goland and Reissner [25] and Hart-Smith [26].

The first approach to determine the stress at a SLJ is considering the adherends rigid and that the load is transferred from the adherend to the adhesive through a uniform shear stress distribution, as shown in Fig. 8.20.

In this case, the shear stress is given by:

$$\tau = \frac{P}{bl}$$

where P is the applied load, b is the joint width, and l is the overlap length and t_s is the adherend thickness.

The Volkersen [24] model, shown schematically in Fig. 8.21, improved on this initial analysis by introducing the differential straining or shear lag analysis, i.e., this model considers that the strain of the elements on the edges of the overlap is different from the elements at

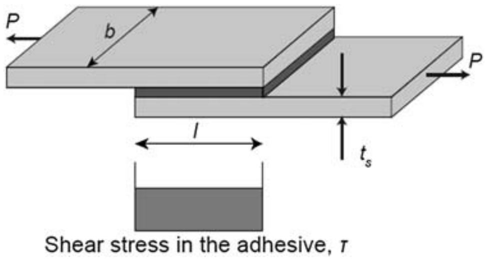

FIG. 8.20 Shear stress in an adhesive in a SLJ, considering a uniform stress distribution.

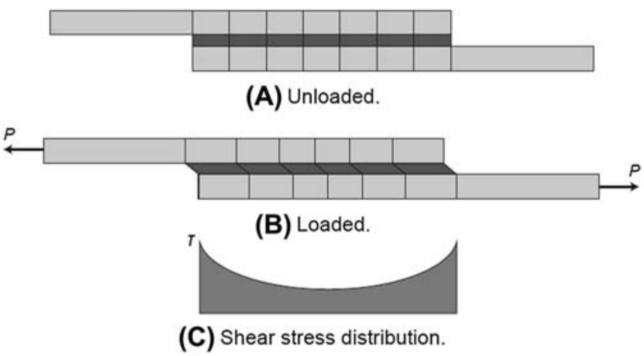

FIG. 8.21 Volkersen analysis. (A) Unloaded. (B) Loaded. (C) Shear stress distribution.

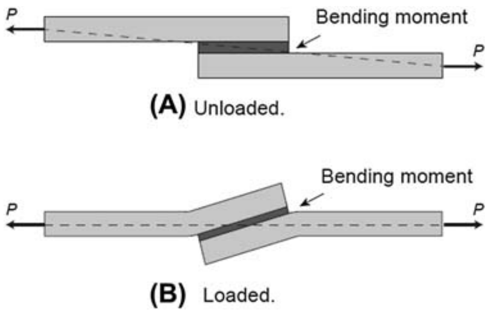

FIG. 8.22 Representation of the Goland and Reissner bending moment factor. (A) Unloaded. (B) Loaded.

the center of the overlap, which creates a non-uniform stress distributions, with higher shear stresses at the ends of the overlap and lower in the middle section.

However, this model does not consider that, as the loads in single lap joints are not collinear, a bending moment is created as the joint rotates due to the alignment of the loads, Fig. 8.22. This rotation induces peel stresses at the ends of the joint additionally to the shear stress already analyzed previously. Moreover, the adherends are no longer simply in tension, but are in fact experiencing a bending moment.

Volkersen [24] and Goland and Reissner [25] only considered the elastic behavior of the adhesive and adherends. However, it is possible for both materials to plasticize, especially at the edges of the overlap which are highly stressed regions. Therefore, Hart-Smith [26] developed a new theory which considers the plastic behavior of the adhesive. Overall, analytical methods such as these, make use of classical linear theories in which some simplifications must be made. As such, these methods are restricted to the analysis of simple structures. These simple approaches find some difficulty in the analysis of composite materials which have anisotropic strength and stiffness properties [18]. Furthermore, when it is necessary to analyze complex structures and other materials with nonlinear properties, which can happen for both the adhesive and the adherend, the use of a numerical tool is highly recommended [1,27]. In response to that problem, for example, finite element method can be used, at it will be explored in the Chapter 10 of this book.

3.2.2 Failure modes

Adhesive joints, with metal substrates, can exhibit three different failure modes: cohesive failure in the adhesive, cohesive failure in the adherend or adhesive (interfacial) failure at the interface between the adherend and the adhesive. These failure modes are shown schematically in Fig. 8.23.

Some acceptable and unacceptable failure modes for all test specimens are illustrated in Fig. 8.24. An example of acceptable failure is cohesive failure of adhesive, which is a rupture of the adhesive joint and normally initiates at a location with the highest stress concentration (at the ends of overlap for single lap joints). An example of unacceptable failure is adhesive failure at the adherend-adhesive interface, which could be an indication of a surface preparation problem and that will result in decreased adhesive joint durability [28,29].

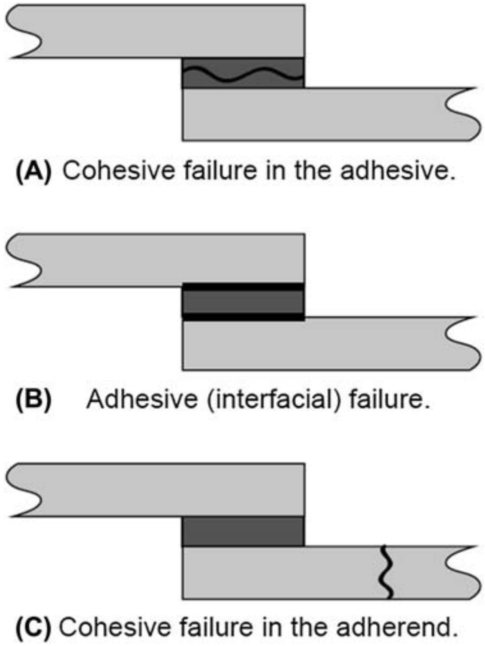

FIG. 8.23 Schematic representation of cohesive and adhesive failure. (A) Cohesive failure in the adhesive. (B) Adhesive (interacial) failure. (C) Cohesive failure in the adherend.

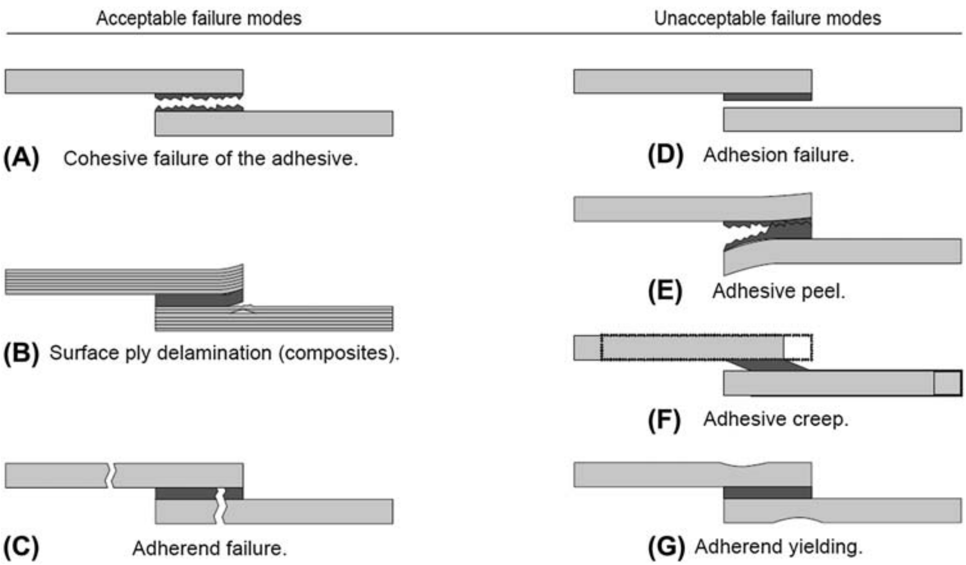

FIG. 8.24 Typical failure modes of adhesively bonded joints. (A) Cohesive failure of the adhesive. (B) Surface ply delamination (composites). (C) Adherend failure. (D) Adhesion failure. (E) Adhesive peel. (F) Adhesive creep. (G) Adherend yielding.

As stated previously, adhesives can be exposed to different mechanical loading conditions. The most common types of stresses are normal, shear, cleavage and peel stresses (Fig. 8.25). The type of stress depends mainly on the way the load is applied, the properties of the adhesive and substrates and on the geometry of the joint.

Adhesives usually behave better when subjected to shear loading because all the area of the adhesive is being used to resist the applied stress. In theory, the same happens when normal stress is applied, but it is almost impossible to create a perfect joint, with the exact same adhesive thickness throughout the overlap, therefore, cleavage stresses will be introduced. In cleavage, the area of the adhesive is not uniformly loaded, which is even worse in peel loadings where the resistant area is reduced to a single line. In practice, a bonded structure must sustain a combination of forces, however the cleavage and peel loads must be reduced much as possible to early failure [30].

3.2.3 Factors that influence joint strength

Mechanical properties of the materials: Both the properties of the adhesive and the adherend will have great influence on the strength of the adhesive joint.

The influence of the **adhesive** can be easily observed when analyzing the stress distribution on a SLJ using a stiff and a flexible adhesive, illustrated in Fig. 8.26.

Joints with more flexible adhesives typically have a more uniform stress distribution and higher elongation, while stiffer adhesives promote higher stress concentration at the ends of the overlap and lower elongation. Flexible adhesives will also have better resistance to peel, fatigue, crack propagation and impact loads. However, these adhesives have lower cohesive strength, lower modulus and reduced heat resistance. Stiff adhesives are typically more cross-linked, are usually employed in structural applications to resist elevated temperatures and aggressive environmental conditioning and provide joints having high stress concentrations [1,31].

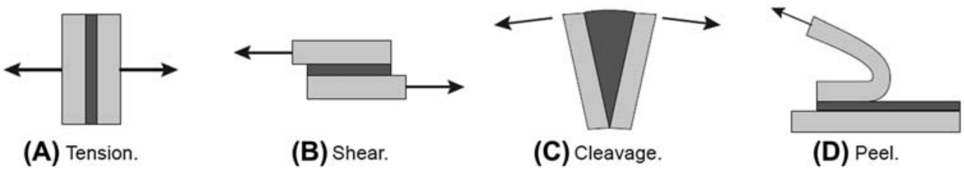

FIG. 8.25 Types of stress on adhesive joints. (A) Tension. (B) Shear. (C) cleavage. (D) Peel.

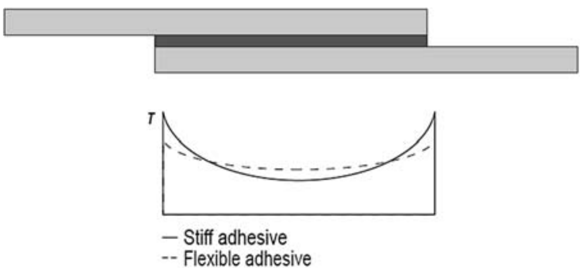

FIG. 8.26 Stress distribution along the overlap for stiff and flexible adhesives.

The properties of the **adherends** can also influence the stress distribution along the adhesive. Non-uniform stress distribution along the adhesive can be caused by the relative displacement of the adherends. The Young's modulus (E) and adherend thickness (ts) of each adherend are important factors in the shear stress distribution. For joints made from thin flexible adherends, there is a tendency for the bonded area to distort, Fig. 8.27. This distortion causes cleavage stress at the ends of the overlap reducing the joint strength. Thicker adherends are more rigid, and the distortion is not as much of a problem as with thin adherends [31].

Adherend yielding can cause a premature failure of the joint, when the stress reaches the yield point of the adherend creating a plastic hinge at the edge of the overlap, as shown in Fig. 8.28. This effect results in a large plastic deformation of the adherend and since the maximum adhesive strain is limited, the joint fails when the maximum adhesive strain is exceeded [1].

When the joints use composite laminate adherends, adherend failure can occur due to the low transverse strength of the composite laminate (thickness direction). Adhesive joints with composites tend to fail in an interlaminar manner due to the high peel stresses at the edge of the overlap (Fig. 8.29).

Overall, adhesive joints with composites have lower interlaminar shear stiffness and shear strength compared to metals. Failure tends to initiate in the composite at the ends of the overlap [29].

Geometrical characteristics: Adhesive thickness and overlap length are two of the geometrical characteristics that affect the strength of a joint loaded in shear.

The adhesive thickness must be kept at an optimum level to maximize the strength of the joint, usually corresponding to a thickness value between 0.1 and 0.2 mm. It has been

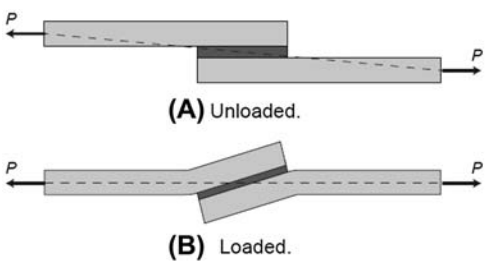

FIG. 8.27 Distortion of adherends in a SLJ. (A) Unloaded. (B) Loaded.

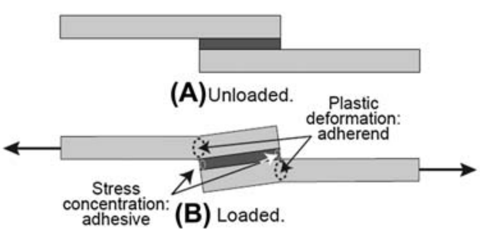

FIG. 8.28 Adherend yielding in a single lap joint. (A) Unloaded. (B) Loaded.

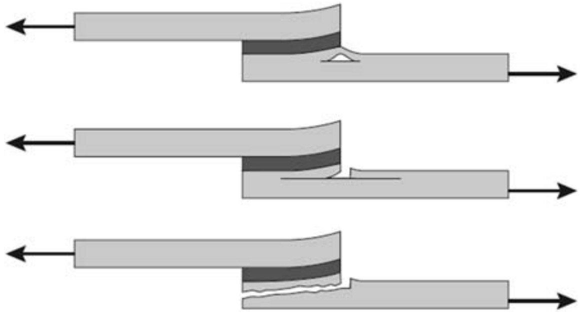

FIG. 8.29 Interlaminar failure of the composite in adhesive joints.

experimentally shown that the strength of the joint decreases with increasing adhesive thickness and, below 0.1 mm, there is also a sudden drop of the joint strength.

Several authors have advanced different explanations to the decrease of joint strength with the increase in adhesive thickness:

- For high adhesive thicknesses, there is the risk of introducing more defects, such as air bubbles and microcracks, as proposed by Adams and Peppiatt [32];
- As the thickness of the adhesive increases, the bending moment increases at the ends of the overlap, resulting in a decrease of joint strength, suggested by Grant et al. [33];
- The interface stresses (peel and shear) increases with increasing bondline thickness and the failure load of a bonded joint decrease, described by Gleich et al. [34] and da Silva et al. [35].

The effect of the **overlap** length is highly dependent on the type of adhesive and on the yielding of the adherend. For ductile adhesives (with more than 20% of strain to failure) and elastic adherends the failure criterion is the global yielding of the adhesive. This joint strength is approximately proportional to the overlap because the adhesive can deform plastically and are the whole overlap. For elastic adherends and brittle adhesives, the joint strength is not proportional to the overlap because the stress is concentrated at the ends of the overlap. For adherends that yield, failure occurs when the yield point of the adherend is exceeded and further increases in the overlap length will not result in additional load being sustained by the joint [1,36,37].

Durability effects: The durability of adhesive joints can be influenced by thermal effects or other environmental effects.

Temperature has been shown to influence the adhesive joint through Dillard and da Silva et al. [1,3,38,39]:

- Shrinkage of the adhesive which is a volume reduction and occurs after the start of gelation in the adhesive;
- Differential thermal expansion. Generally, the thermal expansion coefficients of adhesives are much greater than those of the materials being bonded. These dissimilar expansion coefficients can be reduced by the addition of mineral fillers in adhesives. In addition, if dissimilar substrates are used, they can also have a large difference in thermal expansion between them, which introduces large strains on the adhesive layer;

- Variation of adhesive mechanical properties with temperature. The mechanical properties of adhesives (stress-strain curve and toughness) vary significantly with temperature, through a decrease of strength and stiffness and increase of strain to failure with increasing temperature.

Other environmental effects, such as exposure to radiation, humidity, chemicals, or combinations of all the above, can also influence the durability of the joint. The simultaneous exposure at elevated temperatures, high relative humidity, and mechanical stress can even be highly damaging for certain adhesives, drastically reducing their load carrying capabilities. The combination of oxygen and UV light also causes more extensive damage then both factors separately and causes chemical degradation of adhesives. Water attacks all adhesive joints, reducing significantly the strength of the joint and severely damaging the interface between the adhesive and the adherend, which makes high environmental humidity a possible exclusion factor for the use of adhesive joint, demonstrated by Ref. [40] Costa et al. and Fernandes et al. [41].

As the behavior of the adhesive joint can be affected by this wide variety of factors, usually, it is necessary to test adhesive joints under conditions that are as close to the actual service environment as possible [31,42].

4. Surface treatment

Surface preparation is crucial to ensure good adhesion between the adhesive and the substrate, avoiding premature failure by its interface, which it is ever more important when in presence of severe environmental conditions, such as high moisture levels. In these environments, water may diffuse through the interface, disrupting the adhesion levels and causing a weakening of the joint. While the internal strength of the adhesive and the adherend are easily characterized and controlled, the interface between them is the result of a combination of mechanical, chemical, and physical interactions and its properties can be strongly affected by contaminants.

The main purpose of surface preparation is thus to produce a clean and wettable surface. The effectiveness of different surface treatments can be assessed though the analysis of the contact angle of drop of liquid over the surface of a solid material. Wetting is observed when the surface energy, or surface tension, of the liquid is lower than the surface energy of the solid. Theoretically, the contact angle can range from 0° to 180°, Fig. 8.30, being 0° complete spreading and 180° no wetting (Fig. 8.30).

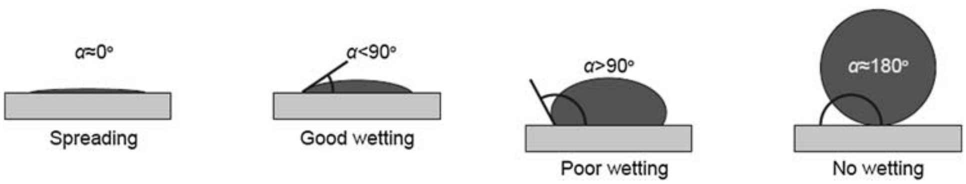

FIG. 8.30 Contact angle measurement.

To increase the surface energy, weak layers must be removed. Some adherends have more tendency to have weak boundary layers attached, such as the oxide layers, corrosion, release agents and contaminants. Therefore, first, the surface must be carefully cleaned with cleaning agents, such as alcohol or organic solvents, to remove any contamination (dust, oil, rust, any mold release agents or other substances from previous manufacturing steps) that may obstruct the wetting procedure and lead to a poor bond quality. Afterward, the pre-treatment of the substrate can range from a simple degreasing to much more complex processes. Surface treatments typically used in adhesive joints can be divided into passive processes and active processes [31]. Passive processes are those where no chemical modification occurs on the adherend surfaces, and include the removal of contaminants or changes to the morphology of the adherend surfaces. This can be achieved by mechanical abrasion, the use of solvents, or other cleaning solutions. Active processes are those that alter the surface chemistry of the adherend through chemical or physical processes. For example, in metallic substrates, the formation of oxide or well-known structure can be promoted, creating stable and strong adherend surfaces. In polymeric materials, this can be achieved by the formation of polar groups that will interact with oxygen and will increase the surface energy and, consequently, the adhesion [4,18].

The surface treatments commonly used to prepare the substrates before bonding can also be further divided into mechanical, chemical, and physical treatments. The most commonly used treatments for each adherend material are summarized in Table 8.3.

4.1 Mechanical treatments

Mechanical treatments consist on the removal of undesirable layers of material and the generation of macro-rough surface textures on metallic surfaces, using abrasive materials. The higher surface roughness will contribute to increase adhesive penetration and improve mechanical interlocking which will facilitate energy dissipation within bondlines. Some examples of these treatments are sanding or grit blasting.

In metallic substrates, with mechanical treatments, good initial levels of adhesion can be observed, however, thin oxides may still be present of the surface of the metal, causing the joint to perform poorly, especially in hot-wet conditions. To suppress that weakness and improve the durability of the joint, primers, coupling agents and chemical treatments can all be used. In polymeric substrates, the use of mechanical treatments is not recommended,

TABLE 8.3 Surface treatments more commonly used as a function on the adherend material.

Material	Mechanical treatments	Chemical treatments	Physical treatments
Aluminum	X	X	
Titanium	X	X	
Steel	X	X	
Polymer		X	X
Composite	X	X	X

since they do not provide improvements to the surface energy, introduce high stresses and damage the substrate.

4.2 Chemical treatments

Adhesive and substrates form chemical bonds, and the strength and durability of the joint is related to the chemical nature of the bond between the adhesive, the substrates and the surface treatment the materials have been subjected to.

To improve adhesion, chemical treatments can also be used for that purpose. In this case, the adherend is immersed in an active solution which can produce chemical conversion coatings. Typical examples of these treatments are FPL, which is a solution of sodium dichromate and sulfuric acid and P2, which is sulfuric acid and ferric sulfate.

Electrochemical treatments are also included in this category. In those treatments the chemical conversion coatings are produced through an electrochemical reaction. Examples of those treatments are phosphoric acid anodizing and chromic acid anodizing. It must be noted that some of these treatments are known to be highly toxic and their use is strictly regulated, which might represent a significant disadvantage associated to the use of these processes.

4.3 Physical treatments

Physical treatments are processes where the chemical structure of the adherend surface is altered by exposure to highly energetic charges or compounds. Examples of these treatments are plasma treatment, laser treatment, flame treatment and corona treatment.

Plasma treatment: Plasma contains charged particles such as positive and negative ions. This treatment promotes the reaction between the surface and the charged particles and allows for gases other than oxygen, for example nitrogen, argon and ammonia, to improve the adhesion and wetting of the surface of adherends. Plasma treatment can be performed at atmospheric pressure, using atmospheric pressure plasma torches, or in a low-pressure chamber.

Laser treatment: Laser treatment can be used to improve corrosion resistance, wear resistance and hardness of metal substrates. In the context of adhesive bonding, laser treatment can be either considered an active or a passive process, depending on the adherend used. When used in metallic adherends, it creates a rough surface on the substrate, promoting mechanical interlocking, and for cleaning the substrate prior to adhesive bonding. When used in polymeric adherends, these treatments also provide chemical modifications to the surface, particularly in treatments performed bellow polymers ablation threshold laser fluency [43,44].

Flame treatment: Flame treatment consists on exposing the adherend to oxygen-containing propane or acetylene gas for a short period of time and promotes the incorporation of functional groups including oxygen at the surface, improving adhesion.

Corona treatment: Corona treatment consists on the application of high voltage between two electrodes, at atmospheric pressure, resulting in various energetic charges that clean and introduce polar groups in the surface of the adherend.

5. Manufacture

Production processes represent a very important step in the industrial usage of adhesive joints. It is at this stage that substrates are brought together, the uncured adhesive becomes solidified, and the initially separated parts form a practical working joint. More generally, the manufacturing process also includes the storage of the materials, the process of metering and mixing the adhesive parts, the adhesive dispensing process, the fixturing of the parts, and the cure process of the adhesive. Proper selection of the production processes can lead to an efficient adhesive joint while an incorrect selection of manufacturing processes can lead to an adhesive joint with an undesired performance and slow and very expensive fabrication [1,5].

5.1 Storage

Correct storage of an adhesive is crucial to ensure its optimal condition at the time of its application on the adherends. The storage factors must be, therefore, analyzed and selected so that the changes in the properties of the adhesive are minimized during this step.

5.1.1 Storage time

The maximum storage time recommended by the manufacturer of the adhesive is known as the shelf life, and it can be found on the adhesive datasheet, which is provided by the supplier. This storage time is typically defined by studying the evolution of the viscosity of the uncured adhesive, which increases over time as shown in Fig. 8.31. Therefore, the shelf life will be considered as the time period in which there are no significant changes to the properties of the adhesive during storage.

During the time an adhesive is stored, several factors will contribute to the variation of properties of the adhesive. These factors can and must be controlled by the adhesive user, such as storage temperature, humidity and the level of exposure to light and other sources of radiation [1].

5.1.2 Storage temperature

Adhesives, as said, are available commercially as one and two-components. Two-component adhesives only start the curing process when the two parts are mixed, which in practice means the cure process is not very sensitive to temperature. Therefore, these adhesives can be stored at room temperature for longer periods. However, in one-component adhesives the curing process is mainly driven by temperature, which means that the higher

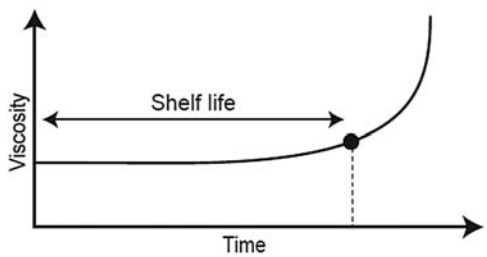

FIG. 8.31 Evolution of the viscosity of the adhesive over time.

the temperature the faster the hardening reaction thus, their shelf life is shorter, and they should be stored at low temperatures in freezers or areas with air conditioners. As an example, considering equivalent adhesives provided by the same manufacturer, one in one-component and the second in two components, the first can require storage temperatures of 2–7 °C for a few months, while the second one might be kept at temperatures from 5 to 25 °C and last up to a year in those conditions.

5.1.3 Humidity

Adhesives are, typically, hygroscopic materials, which means they will absorb water when exposed to it. This water intake is known to contribute to the deterioration of the mechanical properties of the adhesive. Therefore, whenever possible, the adhesive should be stored in low humidity conditions, which can be achieved through dehumidifier equipment or containers filled with hygroscopic salts.

5.1.4 Radiation

Adhesives are polymeric materials which, in its wide majority, are susceptible to degradation by UV radiation. This radiation is a part of the solar spectrum and has enough energy to break the connections between the polymeric chains. To avoid this effect of destruction of the cohesion of the material, adhesives must be stored in low-light or, preferably, dark environments.

5.1.5 Contamination

Contaminants such as dust, sawdust and oils are common in industrial environments and can strongly affect the chemical and mechanical properties of adhesives. Additionally, in adhesive joints, they can act as defects and reduce the strength of the final joint. Adhesive containers must, therefore, be always closed when not in use and the working areas should be as clean as possible. Additionally, filtration systems in storage areas are highly recommended.

5.2 Metering and mixing

When a two-part adhesive is used, the mixing process of the resin and the hardener must be performed correctly, as is the only way to ensure a homogenous mixture of both parts.

Before mixing, the two parts should be carefully weighted following the ratio recommended by the manufacturer, which can be found in the datasheet of the adhesive. Alternatively, the two parts of the adhesive can be drawn from containers with different volumes, with the ratio between the container volumes being the same as the ratio between the two parts of the adhesive. In addition, it is typical for the hardener and the resin to have very different colors, which makes it simpler to visually identify if they are correctly mixed. The mixing process should be carried out until a uniformly colored material is obtained.

During the mixing process, it should also be ensured that no air bubbles are present in the mixture. After curing and under loading, these air bubbles in the adhesive will act as defects and areas of stress concentration. There are different methods to avoid the formation of bubbles such as using a vacuum chamber during the mixture, the use of centrifugal mixing, or ultrasonic mixing. Ultrasonic mixing is particularly important when mixing nanoparticles with the adhesive, such as nano-tubes, cork particles, rubber particles and glass spheres.

FIG. 8.32 Mixing tips.

However, these techniques are very difficult to apply in an industrial environment. Adhesives with low viscosity are simpler to mix, but more viscous adhesives can constitute a challenge in this case, static mixing nozzles are usually used. Static mixing nozzles avoid air entrance to the mixed adhesive, ensure a homogeneous mixture and can easily be used in an automatized system (shown in Fig. 8.32).

5.3 Adhesive dispensing

The manufacturing process of adhesive joints is strongly affected by form of the adhesive chosen, as the application of the adhesive differs greatly between the forms. Adhesives can be supplied in four main forms: paste, liquid, film, and tape, as categorized by Adams [42]. The dispensing methods used for each one of those forms will be discussed below.

5.3.1 Paste

Adhesives available as a paste allow the increase of the precision and repeatability of the manufacturing process. They are formulated to be thixotropic, which means that they remain in the joint and do not flow out during the assembly process. They are also advantageous due to the low waste of adhesive and their ability to create bondlines with a wide range of thicknesses.

Paste adhesives can be supplied in one-part or two-parts and, although in the first case the application is quite straightforward, when a two-part form adhesive is used, extra metering and mixing process are required. Metering can be done either by weight or volume, using scales or measuring cups. As measurement of accurate volumes of adhesives with high viscosity is nearly impossible, they are commonly metered using weight. As stated previously, two-part adhesives are typically supplied in two containers, one with the adhesive and the other with hardener, with the right amount of each component. In this case, the user only needs to combine both, avoiding time consuming and error prone measurements.

Afterward, the application of the adhesive can be done manually using spatulas or hand-operated guns. However, for very viscous adhesives, powered application guns and/or the use of a preheating phase is often necessary to accelerate application rates. Powered applicators are also widely used because they are easily automated. For example, in large scale automotive production, robotic systems are used almost exclusively to apply bondlines, increasing repeatability while reducing application times and waste.

The adhesive should be applied on the bonding surface in such a way as to allow uniform flow over the full bonded area, preferably in a single direction to prevent the appearance of defects. Fig. 8.33 shows the correct procedures to avoid porosities. Applying the adhesive

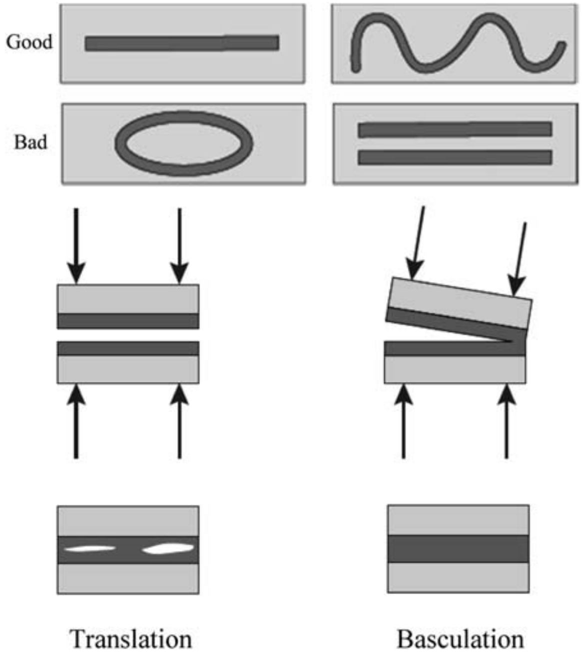

FIG. 8.33 Techniques to apply the adhesive and the adherend to reduce porosity.

following a linear or a zigzagging path, associated at application of the adherend using basculation, provides an escape route and avoids trapping air inside the bondline.

5.3.2 Liquid

Liquid adhesives are particularly easy to apply and to not require specialized equipment. Among the common tools to dispense this form of adhesive are brushes, rollers, syringes, and squeeze bottles. The process can also be automated using robotic glue applicator guns. Liquid adhesives typically have very good wetting capabilities and are especially suited for creating very thin bondlines without the need to apply pressure to the joint. When liquid adhesives are supplied in two-part form, the processes of metering and mixing described for paste adhesives should also be used.

Liquid adhesives are suitable for any geometry however, it must be ensured that they do not flow away from the joint during manufacturing, which may happen due to their low viscosity. It some geometries, this can lead to significant waste of adhesive or even make it impossible to efficiently bond the substrates.

5.3.3 Film

Film adhesives can effectively bond laminate materials and bond components following a highly controlled process and are very common in the erospace industry. Film adhesives consist on a single component adhesive embedded in a carrier, which makes the metering and mixing processes unnecessary.

Joints using film adhesives are highly reproducible, and their application is easily automatable, as the adhesive can be precisely cut and applied to the adherend. These characteristics contribute to minimum waste and bondlines with uniform thickness. However, they are unable to follow curved surfaces, limiting the application of these adhesives to mostly flat or gently curved surfaces. Their production is more complex than paste of liquid adhesive which makes them quite expensive in comparison. Additionally, film adhesives are susceptible to the creation of joints with voids beneath the film and air bubbles, which almost always require the use of autoclaves or vacuum, further increasing the cost associated to the process.

5.3.4 Tape

The use of adhesive tapes is almost limited to non-structural applications, being widespread in industrial applications. This form of adhesive is simple yet highly useful for low strength applications, as it does not require any pre-processing. These adhesives are usually pressure sensitive and do not require any curing procedures to provide adequate shear strengths. Tapes can be applied manually or through automated tape laying machines.

5.4 Fixturing

Fixturing of parts for adhesive bonding is extremely important to ensure that the adherends are correctly aligned, define the thickness of the adhesive layer and the shape of the spew fillet. A variety of devices can be used to fix and apply pressure to the adherends such as springs, binder clips, clamps, weights, presses, vacuum bags, autoclaves and molds.

5.4.1 Pressure application methods

There are some simple methods which can efficiently restrict the adherends such as the use of springs, binder clips and clamps. However, the alignment of those components is not simple and can be time consuming. Additionally, they do not allow the precise control of parameters such as the adhesive thickness, as the localized pressure tends to squeeze the adhesive out of the clamped area. Therefore, when using these simple methods, they should be combined with other method such as microspheres or shims to control adhesive thickness.

Weights and presses allow similar results, as far as adherend restriction is concerned, providing also higher pressure, distributed more evenly along the adhesive joint, which reduces voids and defects in the adhesive. A method to control the adhesive thickness should nevertheless be employed as high pressures can also push the adhesive out of the desired overlap.

Autoclaves and vacuum bags can also be used, these highly specialized equipment uniformly apply load on the materials, by controlling air pressure. They are widely used to manufacture composite structures, as well as bond them. Autoclaves are used to produce large components while vacuum bags are usual employed for smaller parts. The application of compressive loads to the material that is being bonded can be increased by using a combination of the two processes, Fig. 8.34A. Autoclaves can control pressure and temperature, but vacuum bags do not possess that capability, therefore, when vacuum bags are used outside autoclaves and temperature control is needed during the curing stage, they can be used inside a conventional oven, Fig. 8.34B.

5.4.2 *Molds and jigs*

Molds and jigs help the accurate control of all the geometrical parameters of the adhesive joint that is being manufactured such as adhesive thickness and overlap length. Industrial molds are typically manufactured for a specific joint geometry. However, it is possible to design molds that allow some degree of adjustment to its geometry to manufacture different joints.

Molds are usually metallic and should be covered with a release agent so that the adhesive does not bond to the bond. Low surface energy materials, such as Teflon can also be used in the manufacturing of the mold, suppressing the need for a mold release agent. The material of the mold should be the same as the adherends when high temperature is needed for the cure of the adhesive, so that their coefficient of thermal expansion is the same, reducing thermal stresses.

When researching and characterizing adhesive joints, it is very important that the mold used guarantees high quality specimens, with good repeatability. Some techniques used to design these molds are discussed below.

Single lap joints (SLJs) mold: SLJs are the most tested joint geometry, as they represent most real-world applications, therefore, many different molds have been proposed for producing this type of joint, such as the one presented in Fig. 8.35. In this mold, the pins are

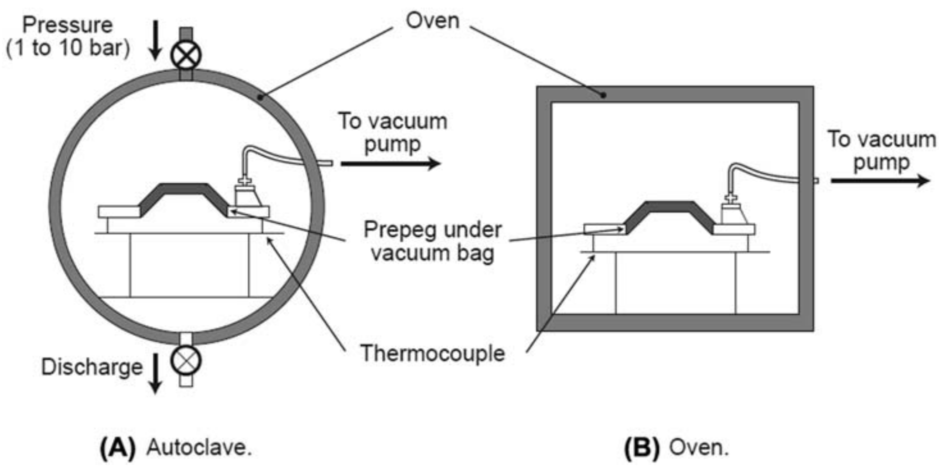

FIG. 8.34 Vacuum bag used in an autoclave (A) and conventional oven (B). (A) Autoclave (B) Oven.

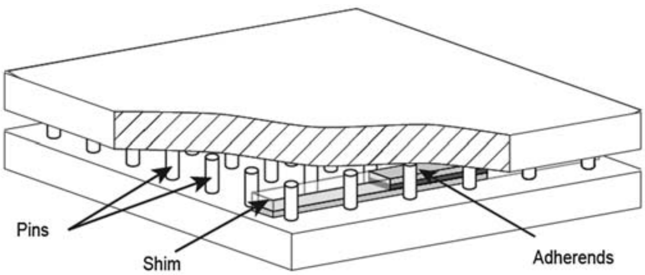

FIG. 8.35 Example of mold to manufacture SLJ.

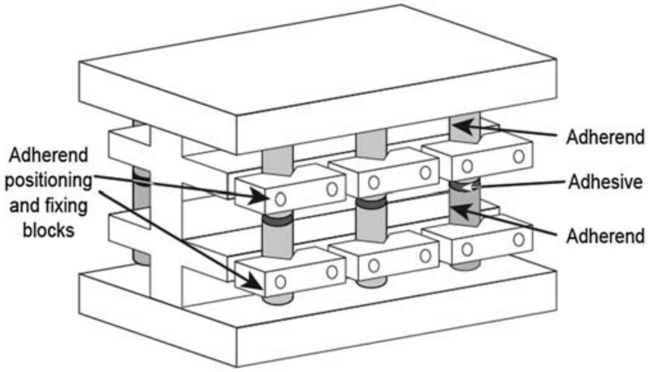

FIG. 8.36 Mold used to manufacture butt joints.

used to align the adherends and the thickness is controlled by specially machined shims [5]. This mold is designed for operating with a hot press, which can provide the necessary temperature and adequate uniformly distributed pressure to cure the adhesive and ensure full contact of the assembly components.

Other important joint used for adhesive characterization is the butt joint, which can be either tested under tensile or torsional loads. The manufacturing process of these joints requires ensuring precise alignment of the adherends and a well-defined adhesive thickness which makes them impossible to fabricate without a specially designed mold, as shown in Fig. 8.36. The alignment of the adherends is guaranteed by machined V-shape grooves, and the adhesive thickness by shims positioned underneath the top screw. Pressure application is not required, and the mold can be placed inside an oven if temperature is necessary for the cure of the adhesive.

T-joints are less common than SLJs for industrial applications, but they are very common in the automotive industry to mimic the geometry of the combination of spot welds and adhesive bonding. The mold for these types of joints places a set of adherends on one side, which are tightened and fully secured. On the other side of the mold a second set of adherends is placed at a predefined distance from the first set, its position is maintained by positioning pins and shims, secured to the top plate by a metal bar with fasteners. Afterward, the top plate is removed from the mold, and adhesive is applied to all the adherends. This is followed by repositioning the top plate that has been removed, fastening it to the mold. The two substrate sets now face each other with adhesive in between, creating the completed joint. To complete cure, the mold can be placed inside an oven.

5.4.3 Techniques for controlling adhesive thickness

A very important parameter for joint strength is the thickness of the adhesive layer, as it is known that failure tends to occur at stress concentration points, which are greater the greater the adhesive layer thickness, as depicted in Fig. 8.37.

Therefore, the control of the adhesive thickness is crucial to ensure that the manufactured bonded structures or components achieve maximum performance. It is known that, for must structural adhesives, the most effective thickness is between 0.1 and 0.2 mm.

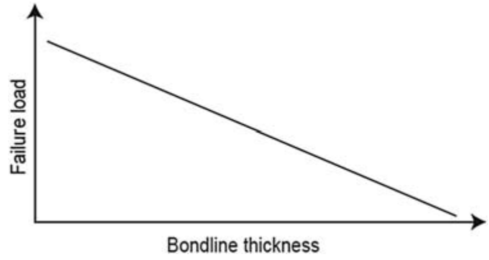

FIG. 8.37 Joint strength as a function of bondline thickness.

There are several practical methods to control the adhesive thickness. These include the use of microspheres, wires and shims. A detailed description of each of these methods is presented in the following paragraphs.

Microspheres: Microspheres can be mixed with the adhesive to control the minimum adhesive layer thickness (see Fig. 8.38). These spheres can be made of different materials such as glass, plastic, and metal. Glass has excellent mechanical and chemical stability at a wide range of temperatures, plastic is used when some deformation is necessary, and metal is used if a thermal or electrically conductive adhesive layer is desired. It is important to keep in mind that the bondline thickness will necessarily correspond to the diameter of the largest spheres and not to their average size.

This method has wide application in the manufacture of precision electronic equipment to ensure accurate component separation. It is used in the manufacture of gas plasma displays, automotive mirrors and other electronic displays. In more structural applications, these spheres are typically uniformly distributed along a high-viscosity epoxy. It is crucial to ensure that the sphere concentration is not excessive, striking a balance between effective control of the adhesive thickness and the excessive introduction of discontinuities or defects. In practice, the use of spheres should have an almost unnoticeable effect on the strength of the adhesive layer.

Wires: Wires are used similarly to microspheres, directly embedded in the adhesive layer (see Fig. 8.39). These wires, which can be o polymeric or metallic nature are available in a wide variety of diameters and allow a precise control of the thickness of the adhesive layer.

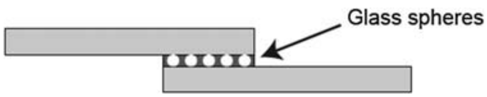

FIG. 8.38 Adhesive thickness controlled by glass spheres.

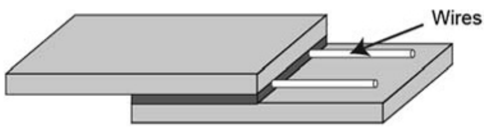

FIG. 8.39 Adhesive thickness controlled by wires.

For example, nylon wire is readily available in many different diameters (for use in fishing wire), which makes it a suitable material for this purpose. However, wires represent a much more substantial defect of the adhesive layer than microspheres and act as a failure locus.

However, wires embedded on the adhesive layer can have other uses beside the control of the adhesive thickness. For example, glass fiber with Bragg grating sensors can be used to monitor the strain of the adhesive layer and act as a means of controlling the adhesive layer thickness during manufacture [45].

Shims: Machined shims can be used to adjust the relative positions of the adherends and create well defined gaps for the adhesive to fill. In some applications, the shims can also be used to ensure the overlap length and the shape of the spew fillet, which are both important for an adequate joint strength (see Fig. 8.40). To ensure that the cured adhesive does not stick to these shims and preclude their removal from adhesive joint, it is necessary to coat the shims with a mold release agent. Calibrated tapes can be used for the same purpose, although they do not allow the control of the shape of the spew fillet. For SLJs, the thickness of the shim should be such to correspond to the thickness of one of the substrates plus the desired thickness of the adhesive.

5.5 Hardening and curing

Adhesives can cure though chemical or physical hardening. Chemical cure of an adhesive consists on the development of strong cross-links between the polymeric chains of the adhesive [46] and can be accelerated by various means, including temperature increase, exposure to UV light and the use of catalyzers such as water vapor or metallic elements. In contrast, physical hardening is a curing process in which the adhesive does not suffer chemical transformations, instead it merely undergoes a physical phenomenon that changes its state from liquid to solid. The most important physical hardening methods are the loss of solvent and hardening from a melted state.

5.5.1 Cure by chemical reaction

Adhesives which cure by chemical reaction are very common, allowing in many cases for strong adhesives with very fast cures, which are attractive for industrial applications. The process can further be accelerated by the increase of temperature, which increases the rate of the cross-linking process of most adhesives. The temperature can be applied using different equipment, which will depend on the geometry of the joint, the mold used and other manufacturing considerations.

Ovens provide uniform temperature distributions, with a rule of thumb stating that only one-third of its free volume should be occupied, to ensure the presence of a large mass of

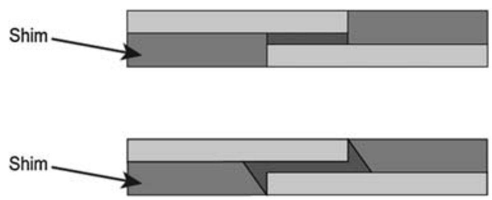

FIG. 8.40 Adhesive thickness controlled by shims.

heated air. Nonetheless, good air circulation should always be guaranteed to avoid the presence of large temperature gradients. Complete bonded structures and smaller molds can be cured inside an oven. If necessary, clamps or weights are placed on the structure or mold to ensure that the components remain aligned and in contact. Hot plates can be used as an alternative to ovens. These are curing devices with resistor-type heating elements embedded in one or two flat surfaces. This equipment can be used for any relatively flat joint or mold geometry and pressure must be applied using clamps or weights. Heater mats, which are small mats with embedded resistors, can also be laid over a portion of the structure to achieve localized heating. These mats are especially well fitted for repairs in the erospace industry reducing the need to disassemble large portions of the airframes.

In ovens, temperature is usually assessed from the air being recirculated inside the oven chamber, which can differ from the temperature of the specimen, especially during the initial heating ramp. The temperature of the specimen can be monitored using a thermocouple placed as close as possible to the adhesive layer. It is also very important to control the humidity level during the curing, since it can strongly affect the properties of the adhesive. Curing time should be considered from the moment the adhesive reaches its curing temperature. After curing is complete, the cooling ramp should be slow and the specimen should reach ambient temperature before being removed, in order to reduce damaging stresses generated by large thermal gradients.

Hot plate presses, as show in Fig. 8.41, are suitable for simultaneously applying temperature and uniformly distributed pressure. This equipment consists of two, pneumatically or hydraulically actuated heated plates. As is the case for hot plates, they are suitable for use with flat specimens or molds but can exert pressure to ensure the absence of voids in the adhesive layer. Molds and jigs designed to use with this equipment should have flat surfaces and be made from a thermally conductive material, such as aluminum, copper or steel. Temperature control should also be performed using thermocouples placed as near as possible to the adhesive.

Induction ovens or coils can also be used for this purpose, where the heat is transferred to the adhesive layer by applying a large electric current to an induction element. By such

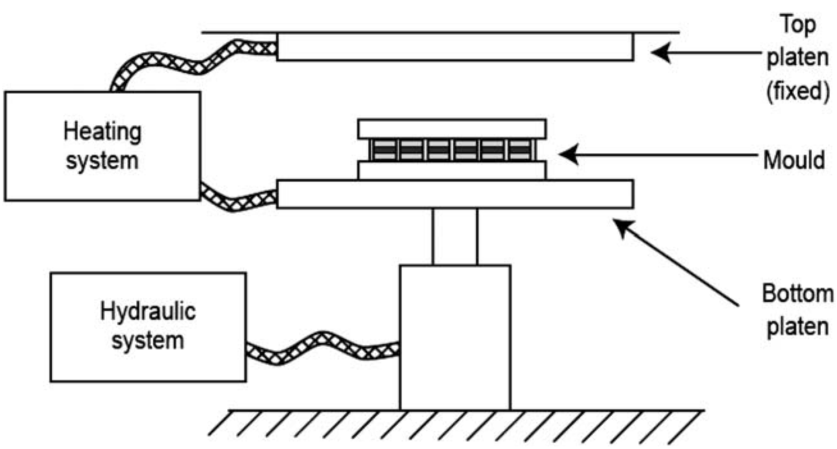

FIG. 8.41 Hot plates press and mold location inside.

method, a powerful magnetic field is generated, and electron eddy currents are thus induced on electrically conducting materials, which will rapidly heat. As this process will only heat conductive materials, it will not directly heat the adhesives. Instead, the temperature of the conducting adherends will increase, consequently heating by thermal conduction adhesive. This process is shown in Fig. 8.42A. Alternative, if non-conductive adherends must be used, conductive particles can be added to the adhesive layer, making it react to the magnetic field. This approach is shown in Fig. 8.42B. This method is particularly interesting for some advanced applications since it allows localized heating to be applied, opening the door for functionally graded curing profiles in the adhesive. This can be achieved focusing the metallic coils in one area or using uneven distributions of conductive particles inside the adhesive.

A particularity of this method is that the control of the temperature inside the adhesive layer cannot be achieved using thermocouples. These sensors rely on metallic wires which interact with the magnetic fields and provide inaccurate results. Therefore, infrared imaging or thermochromic paint must be used as an alternative.

A dielectric cure process, shown in Fig. 8.43, has some similarities to induction heating but heating is achieved via incident microwave irradiation. Under microwave radiations, molecules will vibrate and collide, releasing large amounts of thermal energy. The adhesive can be cured directly in this fashion if it possesses dielectric properties. If not, particles with dielectric properties can be added.

This technique allows for a uniform heating process, where the adhesive reaches the same temperature in all locations at the same time, eliminating the existence of thermal gradients. If a localized heating is required, to achieve some sort of graded curing temperature distribution, dielectric particles can be distributed unevenly throughout the adhesive.

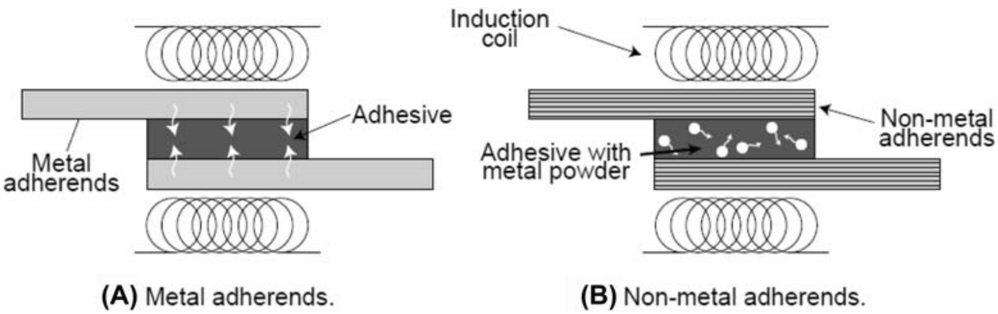

FIG. 8.42 Induction heating on metallic adherends (A) and non-metallic adherends (B). (A) Metal adherends (B) Non-metal adherends

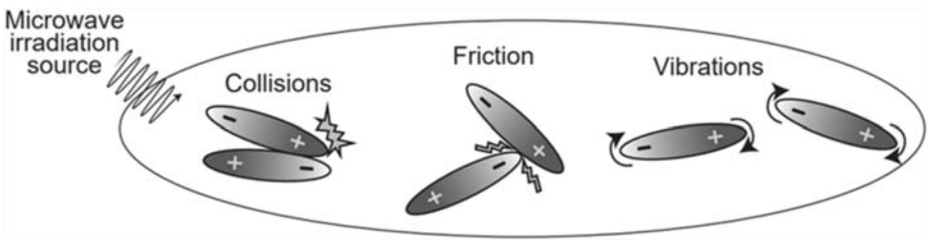

FIG. 8.43 Dielectric heating.

5.5.2 *UV curing*

UV light can be used as a very effective catalyzer for the cure of some specifically formulated one-part adhesives. As the energy is supplied from a radiative source, the cure rate of these adhesives will change drastically with the distance from the UV light source, the intensity of the light source and the thickness of the adhesive.

This method finds very wide application in dental procedures and in the manufacture of electronic and optical components, where a combination of assembly precision and fast curing time is required. Additionally, this technique is quite practical and inexpensive as a simple UV light source suffices.

5.5.3 *Moisture curing*

Moisture acts as a catalyzer to the cure of some adhesives, such as room temperature vulcanizing silicone adhesives and polyurethanes. In this case, the joint must have direct access to the atmosphere to absorb ambient humidity. Curing using this method is usually quite slow, as the water permeates slowly through the adhesive layer. Most importantly, it is fundamental to be aware that for adhesives that cure in this way the outer zones of the adhesive layer appear fully cured, the interior might still be completely uncured.

5.5.4 *Anaerobic curing*

Anaerobic adhesives are adhesives that cure when isolated from oxygen. In this cure mechanism, oxygen inhibits the chemical reaction needed for the cure of the adhesives. When the anaerobic adhesives are placed in some specific joint geometries, the presence of oxygen in the adhesive is very limited, enabling the curing process to initiate. These adhesives are especially well suited as thread locking compounds, as when the adhesive is sealed, for example, between a nut and a bolt, the adhesive is isolated from the atmosphere and the cure is allowed to progress. This process does not require any specific equipment, but it can be accelerated by applying temperature.

5.5.5 *Loss of solvent or water*

The curing process of solvent-based adhesives does not require the development of chemical cross-linking between the polymer chains. In this case, the joints are fully set, and the solvent is evaporated from the adhesive, which occurs quickly after application, increasing the viscosity of the adhesive. Water or organic compounds are both used as solvents. However, water-based adhesives are being increasingly used since they are more environmentally friendly and much safer than organic compounds.

The adherends can be bonded right the adhesive is applied or after some solvent has evaporated, which will increase joint strength, tack and reduce processing time. The time between the adhesive application and the bonding of the adherends is known as set time. If the ideal waiting time is exceeded, most of the solvent will have evaporated and the adhesive will no longer wet the adherends properly, leading to joints with low mechanical strength. This period is known as the open time. An adhesive layer may be reactivated when its open time has been surpassed by spraying, brushing or rolling with a light coat of solvent to return surface tack on the adhesive.

Hot air ovens or infrared heaters can be used to achieve the drying of these adhesives. If organic solvents are used, good ventilation must be ensured, due to their high volatility and fire risk.

5.5.6 Hardening from a melted state

Hot melt adhesives, in contrast with most adhesives, are thermoplastics. These materials cure by simply hardening from a melted state and are applied by projection or extrusion, with the support of a heating systems to melt them prior to its application. The only concern necessary for the curing phase is ensuring that the ambient temperature is low enough for the solidification of the adhesive. Solvent-based adhesives remain soluble in organic compounds after drying, which simplifies cleaning operations and reduces the need for equipment maintenance.

6. Quality control

Quality control of adhesive joints is an essential step to ensure that they perform as designed. This can be carried out by several different testing procedures. Destructive and nondestructive tests are both available to assess the quality of the produced joints [42].

6.1 Destructive tests

Mechanical properties of bulk materials (such as adhesives and adherends) or adhesive joints can be achieved using a wide variety of experimental tests that can be subjected under tensile, compression, shear loads, as discussed in Section 1.2. The most commonly used joint geometry for this purpose is the single lap joint (SLJ), as it balances performance and simplicity of the manufacture process.

Destructive tests are used to determine the strength or fracture properties of bulk materials or joints. Using these types of tests is possible to evaluate the failure mechanism experimentally obtained.

6.1.1 Quasi-static tests

Quasi-static tests are performed to assess the static properties of an adhesive or adhesive joint and can be carried out under different loading conditions. These tests can be performed under load, displacement or strain control; however the tests are normally carried out under displacement control. Quasi-static tests are performed by imposing a constant rate (under displacement, load or strain control) during the testing of the specimen (bulk material or joint). The tests should be performed at slow rates to ensure that the strain rate dependency is not noticeable, allowing for a continuous rearrangement of the stress distribution throughout the test. These tests are carried out to the study structural performance of the bulk material or complete joints. Fig. 8.44 shows a variation of displacement as a function of time, in the first case constant during the test (A) or variable as the rate varies during the test (B).

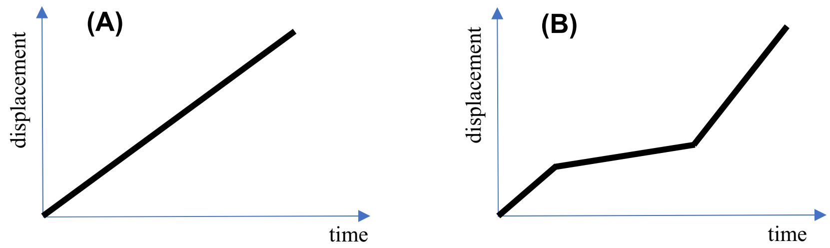

FIG. 8.44 Variation of displacement as a function of time, linear (A) or variable (B).

6.1.2 *High rate and impact tests*

In many adhesive applications, loads can be applied in short time periods as it would happen, for example in the case of vehicle collision. In those situations, two different outcomes can be acceptable: (i) the joint is not damaged; (ii) the joint is plastically deformed and damaged, which might be interesting in the case of a collision because the joint will absorb most of the impact energy and preserve the safety of the occupants of the vehicle.

Adhesives have been also known to exhibit a viscoelastic behavior, which translates into a strain rate dependence of their strength and fracture properties, changing as the loading rates increases. Therefore, it is crucial to accurately characterize the adhesive for the conditions it will be subjected to when in service. Impact conditions can be characterized using different methods, depending on the characteristics and speed wanted for the applied load. For tests up to 5 m/s, which is considered low speed, instrumented pendulum impact tests can be performed. For medium speed, from 5 to 10 m/s, drop weight machines are used. For high-speed, from 10 to 100 m/s, Split-Hopkinson pressure bars are used. Using this machines and setups specially designed for them tensile, shear, fracture and other tests can be performed [47].

6.1.3 *Fatigue tests*

Fatigue tests are performed using the standard test setups used for the characterization of the adhesive or of the adhesive joint. These can be performed under load, displacement or strain control. However, tests are usually carried out under load control. Through load control (the load is applied cyclically) the fatigue behavior of adhesive joints can be characterized using S-N curves, shown in Fig. 8.45, or Paris Law curves, shown in Fig. 8.46.

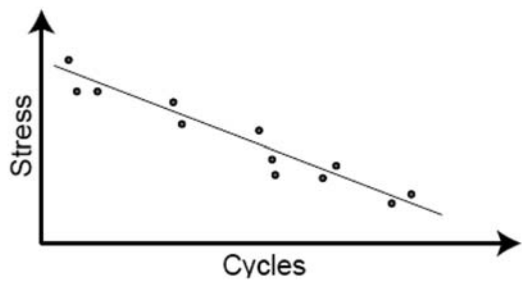

FIG. 8.45 S-N curve.

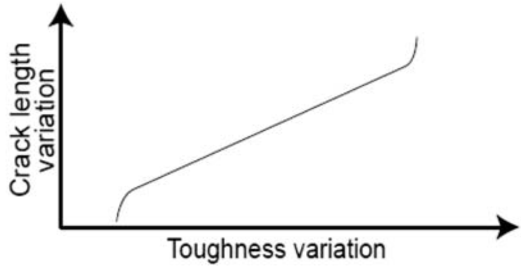

FIG. 8.46 Paris law curve.

S-N curves are related with the crack initiation phase and are used to determine if a joint can perform its duty safely. That is achieved by measuring the number of cycles that joint can withstand when subjected to a given level of stress then, for example if a joint needs to complete 10^4 cycles safely, with the S-N curve, the maximum stress at which those cycles can be performed can be determined. The Paris Law, however, is related with the crack propagation, analyzing parameters such as the crack velocity (variation of the crack length between a specific number of cycles) and fracture toughness threshold (the fracture toughness value immediately before crack propagation occurs). Therefore, while the S-N curves only require the determination of the number of cycles needed for the joint to fail, the Paris Law analysis is much more involved, as it requires periodically measuring the crack length [48].

6.1.4 Creep tests

As stated before, adhesive joints exhibit time dependent behavior, mainly driven by t viscoelastic and viscoelastic nature of the adhesive. These effects can be further exacerbated with increases of the temperature and stress levels applied. Creep tests are thus extremely important to understand the behavior of the adhesive when loaded by different levels of stresses or temperature for long periods of time. It is known that in adhesives creep causes a decrease in stress concentration and an increase of shear strains [49]. The aging affects the relaxation times, but the shape of the creep curve does not change according to Tsou and Dellefave [50].

Several standards exist to normalize the tests used to study the creep behavior of adhesives, such as ISO 889-1, ISO 15109, and ASTM D1780. Those tests typically focus on quantifying the time it takes for the material to fail or deform in a specific manner.

The creep behavior of an adhesive is generally studied through a single lap joint (SLJ) where one of the adherends is fixed and the other is subjected to a load, the former is known as the fixed adherend and the latter as the moving adherend, as shown schematically in Fig. 8.47. The deformation suffered by the adhesive layer over a predefined time period is then recorded as a function of the constant imposed load.

6.2 Non-destructive tests

Destructive tests only allow to confirm the performance of an adhesive joint through the analysis of an equivalent specimen, manufactured using the same procedure. However,

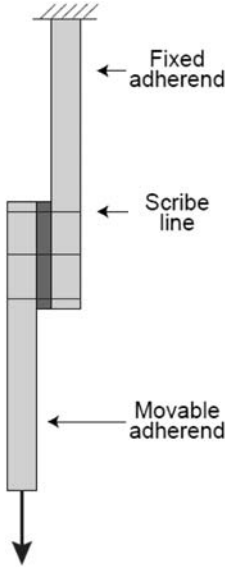

FIG. 8.47 Creep test following the ASTM D1780 standard.

unexpected defects might appear during the manufacture process and the joint may deteriorate significantly during its service life. Therefore, in order to ensure the integrity of practical structures immediately after manufacturing, non-destructive tests must be employed.

The actual strength of the adhesive joint in service is very difficult to determine accurately because every joint has voids and other defects, shown schematically in Fig. 8.48, that can vary from joint to joint.

Poor cure can be caused by several factors. In two component adhesives, it can occur due to an incorrect mixture of the multiple components of the adhesive or if the cure cycle of the adhesive is not respected. In adhesives which cure by catalyzation, it might occur if the catalyst

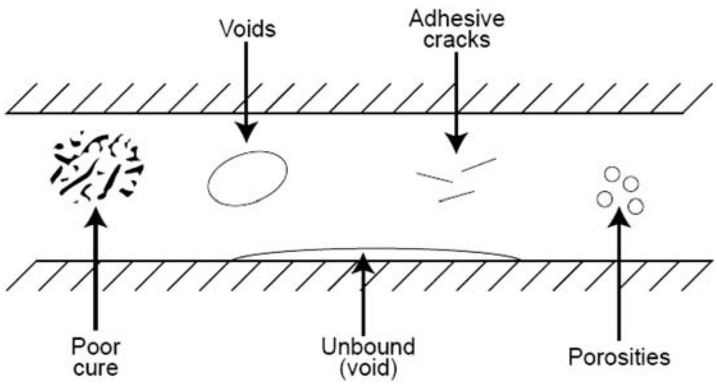

FIG. 8.48 Defects that might be found in adhesive joints.

cannot reach a certain area of the adhesive layer. Voids may occur due to air entrapment inside the bondline, often because of relative movement of the adherends during cure. It is inevitable that some degree of porosity will appear in bondlines due to chemical reaction during cure or by air entrapped in the adhesive. When voids occur near the interface, they are called unbounds. Cracks are a result of thermal stresses, fatigue loads or the application of high stresses. Disbound, or zero volume unbound, occurs when the adhesive does not adhere correctly to the substrate and it is one of the hardest defects to detect using non-destructive tests.

Several methods have been developed to detect defects within the adhesive layer, with different levels of complexity and widely distinct capabilities. As such, the test methodology adopted must be carefully chosen considering the specificities of each adhesive joint and the intended application.

6.2.1 Visual inspection

Visual inspection is the simplest and most inexpensive method of quality control. This method can be quite effective but depends on the skill of the operator. It can be performed mainly be observing the adhesive spew fillet. A good quality fillet indicates good cure, flow of the adhesive and absence of air entrapment. However, a porous adhesive fillet may indicate a high heat up rate or the presence of moisture in the adhesive. Additionally, a quick visual analysis of the contact angle between the adhesive and the adherend, for liquid adhesives, may be a good indicator of its wettability and surface energy and, consequently of the joint strength.

6.2.2 Tap method

The tap method consists on gently impacting the adhesive joint with a light hammer with the intent of analyzing the resultant sound. A clear high-pitched sound means a safe joint where a continuous adhesive layer exists. In contrast, a low deep sound can indicate that the sound is resonating inside a void, a possible indicator of a lack of adhesive in the bond, Fig. 8.49.

The main limitation of this method is that it relies greatly on the experience of the operator and their ability to distinguish a good and a flawed adhesive joint.

6.2.3 Ultrasonic methods

Ultrasonic based methods are among the most used in quality control of adhesive joints, being employed extensively in the eronautical industry. In this method, an ultrasonic pulse is applied to the test area, which will then be reflected and transmitted at each interface of

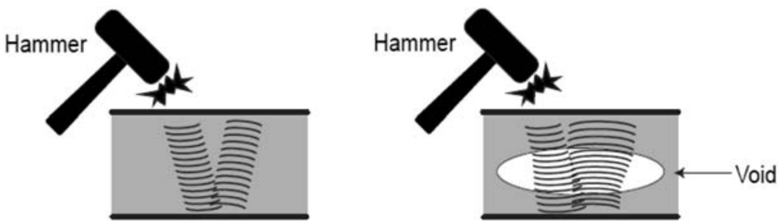

FIG. 8.49 Tap method: adhesive without flaws (left) and adhesive with flaws (right).

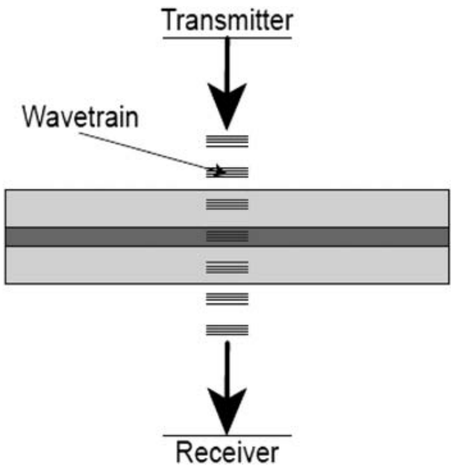

FIG. 8.50 Ultrasonic method.

the joint. When a defect is reached, the pulse will be almost completely reflected due to the high acoustic impedance of air and other gases (Fig. 8.50).

Two alternative test configurations may be used. The first is the "through transmission" technique, where the transmitter and the receiver are located on opposite sides of the adhesive joint, which means the impulse only needs to propagate through the adhesive joint once. The second technique is the "pulse echo", where the transmitter and the receiver are on the same side of the adhesive layer.

6.2.4 Thermal methods

Thermal methods analyze how the heat flows from one side of the overlap to the other, knowing that if the joint is good quality the heat will flow uniformly, which will not happen if voids are present on the adhesive layer. In these methods, a focused heat source is used to heat up the surface of the adhesive bond and the temperature evolution is captured using a thermal imaging camera. Voids will appear as low-temperature spots. The temperature is monitored right after the thermal transient has been applied. The appropriate time depends on the size and depth of the defects, the initial temperature rise, the thermal properties of materials and the thickness of the adherends. The system used to acquire information must be capable of doing so in the appropriate time window, which is typically in the order of 500 ms. When the adherends are metallic, due to their high thermal conductivity, a powerful heat pulse is required. However, for materials with lower thermal conductivity, such as composites, hot air blowers usually provide enough power.

6.2.5 Post fracture analysis

The analysis of the fracture surface of a failed adhesive joint may provide important information about the cause of failure, which may be important for the design and maintenance of similar joints. This analysis may be carried out with a simple visual inspection or using more complex methods such as microscopy and spectroscopy.

Microscopy: Microscopy techniques, such as scanning electron microscopy (SEM) and transmission electron microscopy are commonly used to analyze the fracture surface of adhesive joints. SEM, Fig. 8.51, requires a relatively slow test setup time where the specimen is carefully cleaned and positioned inside a vacuum chamber, which must be free of any contamination.

The surface that will be tested may need to be coated with a thin film of gold (Au) or palladium (Pd), by sputtering, prior to examination. During the test, an electron beam is aimed at the surface and interacts with the atoms of the surface. The resulting signal is used to obtain surface topography data (which is then processed into a 2D image) and the composition of the sample.

Fourier transform spectroscopy: Absorption spectroscopy techniques aim to determine how light is absorbed by a probe at each wavelength, which can be achieved by either projecting several monochromatic light beams at the probe or using a beam containing many different frequencies at a time. This process is repeated using different polychromatic beams and, then, the information is processed by a computer using the Fourier transform algorithm.

The most commonly used technique is the Fourier transform infrared technique (FTIR), Fig. 8.52, which consists on analyzing the infrared spectrum of the sample and comparing it with other samples of which the components are known. Using this technique, it becomes possible to study the formation of new chemical bonds or perform a quantitative analysis for a given component. This technique has a faster preparation time than SEM and does not require the use of a special vacuum chamber.

X-ray photoelectronic spectroscopy (XPS): This process may be used to analyze the influence of surface and interfacial phenomena on the adhesion process. The block of adhesive is

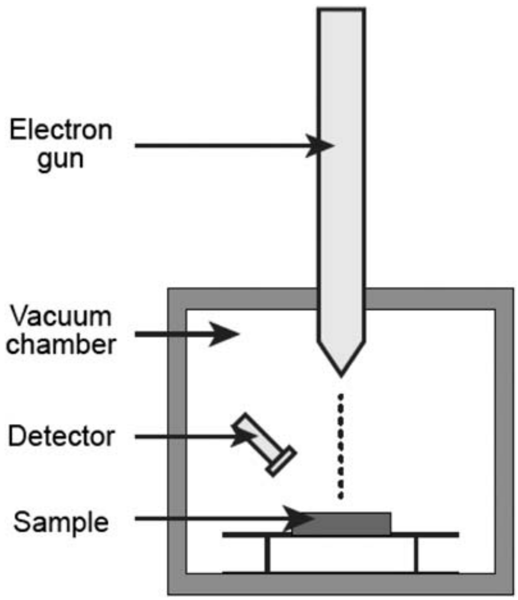

FIG. 8.51 SEM analysis.

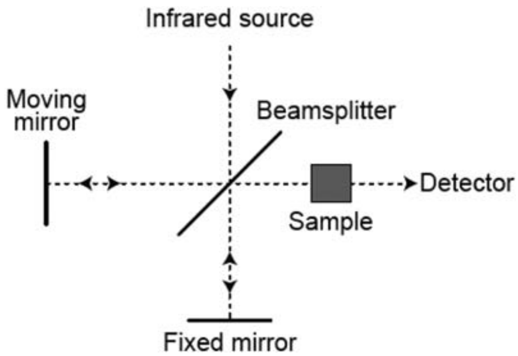

FIG. 8.52 FTIR analysis.

irradiated using x-rays leading to the emission of photoelectrons. These emitted particles are then analyzed by a detector, which will determine the intensity of the photoelectrons as a function of energy and use this data to determine the chemical composition of the sample.

7. Conclusions

The information contained on this chapter is intended to allow a deep understand the major principles and processes related to the manufacture and use of adhesive bonded joints. The major aspects that require judged to be of the most importance in the design of an adhesive joint have been discussed, including the adhesive selection process, joint geometrical design, surface treatments, manufacturing techniques and quality control. Informed design choices regarding these aspects enables the manufacture of structures which can rely on the advantages provided by strong, efficient and durable joints, while being able to be produced in a cost-effective manner.

Acknowledgments

The authors wish to acknowledge the funding provided by Portuguese Foundation for Science and Technology (FCT), under the individual grants SFRH/BPD/96992/2013, as well as the funding provided by Ministério da Ciência, Tecnologia e Ensino Superior — Fundação para a Ciência e a Tecnologia (Portugal), under the projects POCI-01-0145-FEDER-028351, POCI-01-0145-FEDER-028473 and POCI-01-0145-FEDER-029839.

References

[1] L.F. da Silva, A. Öchsner, R.D. Adams, Handbook of Adhesion Technology, second ed., Springer Science & Business Media, Heidelberg, Germany, 2018, ISBN 978-3-319-42087-5.
[2] S.R. Hartshorn, Structural Adhesives: Chemistry and Technology, Plenum Press, New York, USA, 2012, ISBN 9781468477818.
[3] D.A. Dillard, Advances in Structural Adhesive Bonding, CRC Press, Boca Raton, USA, 2010, ISBN 978-1-845-69805-8.
[4] A.V. Pocius, D.A. Dillard, M. Chaudhury, Adhesion Science and Engineering: Surfaces, Chemistry and Applications, Elsevier, Amsterdam, Netherlands, 2002, ISBN 978-0-080-52598-3.

[5] L.F. da Silva, D.A. Dillard, B. Blackman, R.D. Adams, Testing Adhesive Joints: Best Practices, Wiley-VCH, Weinheim, Germany, 2012, ISBN 978-3-527-32904-5.
[6] M. Costa, G. Viana, C. Canto, L. da Silva, M. Banea, F. Chaves, R. Campilho, A. Fernandes, Effect of the size reduction on the bulk tensile and double cantilever beam specimens used in cohesive zone models, Proceedings of the Institution of Mechanical Engineers - Part L: Journal of Materials: Design and Applications 230 (2016) 968–982.
[7] M. de Moura, A. de Morais, Equivalent crack based analyses of ENF and ELS tests, Engineering Fracture Mechanics 75 (2008) 2584–2596.
[8] F. Xiao, C.-Y. Hui, E. Kramer, Analysis of a mixed mode fracture specimen: the asymmetric double cantilever beam, Journal of Materials Science 28 (1993) 5620–5629.
[9] S. Park, D.A. Dillard, Development of a simple mixed-mode fracture test and the resulting fracture energy envelope for an adhesive bond, International Journal of Fracture 148 (2007) 261–271.
[10] T. Brussat, S. Chiu, S. Mostovoy, Fracture mechanics for structural adhesive bonds—final report, in: Tech. Rep., DTIC Document AFML-TR, 1977, pp. 77–163.
[11] S. Yoon, C. Hong, Modified end notched flexure specimen for mixed mode interlaminar fracture in laminated composites, International Journal of Fracture 43 (1990) R3–R9.
[12] A. Voloshin, M. Arcan, Pure shear moduli of unidirectional fibre-reinforced materials (FRM), Fibre Science & Technology 13 (1980) 125–134.
[13] R. El-Hajjar, R. Haj-Ali, In-plane shear testing of thick-section pultruded FRP composites using a modified arcan fixture, Composites Part B: Engineering 35 (2004) 421–428.
[14] ASTM D6671-13e1, Standard Test Method for Mixed Mode I–Mode II Interlaminar Fracture Toughness of Unidirectional Fiber Reinforced Polymer Matrix Composites, ASTM International, West Conshohocken, PA, 2013.
[15] G. Fernlund, J. Spelt, Mixed-mode fracture characterization of adhesive joints, Composites Science and Technology 50 (1994) 441–449.
[16] M. Costa, R. Carbas, M. Benedita, E. Marques, G. Viana, L.F.M. da Silva, E. Yokoi, S. Nakada, T. Furusawa, Static assessment of the mixed-mode behaviour of three epoxy adhesives, Engineering Fracture Mechanics 182 (2017) 552–565.
[17] M. Costa, R. Carbas, E. Marques, G. Viana, L.F.M. da Silva, An apparatus for mixed-mode fracture characterization of adhesive joints, Theoretical and Applied Fracture Mechanics 91 (2017) 94–102.
[18] R.D. Adams, J. Comyn, W.C. Wake, Structural Adhesive Joints in Engineering, second ed., Chapman & Hall, London, UK, 1997, ISBN 978-0-412-70920-3.
[19] M.D. Banea, L.F. da Silva, R.D. Campilho, C. Sato, Smart adhesive joints: an overview of recent developments, The Journal of Adhesion 90 (2014) 16–40.
[20] G.J. Dvorak, J. Zhang, O. Canyurt, Adhesive tongue-and-groove joints for thick composite laminates, Composites Science and Technology 61 (8) (2001) 1123–1142.
[21] G. Fessel, J.G. Broughton, N.A. Fellows, J.F. Durodola, A.R. Hutchinson, Evaluation of different lapshear joint geometries for automotive applications, International Journal of Adhesion and Adhesives 27 (7) (2007) 574–583.
[22] K.S. Kim, W.T. Kim, D.G. Lee, E.J. Jun, Optimal tubular adhesive-bonded lap joint of the carbon fiber epoxy composite shaft, Composite Structures 21 (3) (1992) 163–176.
[23] M.K. Apalak, R. Gunes, Elastic flexural behaviour of an adhesively bonded single lap joint with functionally graded adherends, Materials and Design 28 (5) (2007) 1597–1617.
[24] O. Volkersen, Die nietkraftverteilung in zugbeanspruchten nietverbindungen mit konstanten laschenquerschnitten, Luftfahrtforschung 15 (1938) 41–47.
[25] M. Goland, E. Reissner, The stress in cemented joint, Trans. ASME 66 (1944) A17.
[26] L.J. Hart-Smith, Adhesive-bonded single-lap joints, Douglas Aircraft Co., 1973. NASA Langley report CR 112236.
[27] S. Kumar, K.L. Mittal, Advances in Modeling and Design of Adhesively Bonded Systems, John Wiley & Sons, New Jersey, USA, 2013, ISBN 978-1-118-75407-8.
[28] M.D. Banea, L.F.M. da Silva, Adhesively bonded joints in composite materials: an overview, Proceedings of the Institution of Mechanical Engineers - Part L: Journal of Materials: Design and Applications 223 (2009).
[29] F.C. Campbell, Manufacturing Technology for Aerospace Structural Materials, Elsevier B.V., London, UK, 2006, ISBN 978-0-080-46235-6.
[30] S. Ebnesajjad, Adhesives Technology Handbook, third ed., William Andrew Inc., New York, USA, 2015, ISBN 978-0-323-35595-7.

[31] E.M. Petrie, Handbook of Adhesives and Sealants, vol. 2, McGraw-Hill, New York, USA, 2000, ISBN 978-0-080-46059-8.
[32] R.D. Adams, N.A. Peppiatt, Stress analysis of adhesive-bonded lap joints, The Journal of Strain Analysis for Engineering Design 9 (3) (1974).
[33] L.D.R. Grant, R.D. Adams, L.F.M. da Silva, Experimental and numerical analysis of single-lap joints for the automotive industry, International Journal of Adhesion and Adhesives 29 (4) (2009) 405−413.
[34] D.M. Gleich, M.J.L. Van Tooren, A. Beukers, Analysis and evaluation of bondline thickness effects on failure load in adhesively bonded structures, Journal of Adhesion Science and Technology 15 (9) (2001) 1091−1101.
[35] L.F.M. da Silva, T.N.S.S. Rodrigues, M.A.V. Figueiredo, M.F.S.F. de Moura, J.A.G. Chousal, Effect of adhesive type and thickness on the lap shear strength, The Journal of Adhesion 82 (11) (2006) 1091−1115.
[36] D.F.S. Saldanha, C. Canto, L.F.M. da Silva, R.J.C. Carbas, F.J.P. Chaves, K. Nomura, T. Ueda, Mechanical characterization of a high elongation and high toughness epoxy adhesive, International Journal of Adhesion and Adhesives 47 (2013) 91−98.
[37] L.F.M. da Silva, R.J.C. Carbas, G.W. Critchlow, M.A.V. Figueiredo, K. Brown, Effect of material, geometry, surface treatment and environment on the shear strength of single lap joints, International Journal of Adhesion and Adhesives 29 (2009) 621−632.
[38] L.F. da Silva, R. Adams, Adhesive joints at high and low temperatures using similar and dissimilar adherends and dual adhesives, International Journal of Adhesion and Adhesives 27 (2007) 216−226.
[39] L.F. da Silva, R. Adams, Joint strength predictions for adhesive joints to be used over a wide temperature range, International Journal of Adhesion and Adhesives 27 (2007) 362−379.
[40] M. Costa, G. Viana, L. da Silva, R. Campilho, Environmental effect on the fatigue degradation of adhesive joints: a review, The Journal of Adhesion 93 (2017) 127−146.
[41] P. Fernandes, G. Viana, R.J.C. Carbas, M. Costa, L.F.M. da Silva, M.D. Banea, The influence of water on the fracture envelope of an adhesive joint, Theoretical and Applied Fracture Mechanics 89 (2016) 1−15.
[42] R.D. Adams, Adhesive Bonding: Science, Technology and Applications, CRC Press, Boca Raton, USA, 2005.
[43] G. Crichtlow, C. Cottam, D. Brewis, D. Emmony, Further studies into the effectiveness of CO_2-laser treatment of metals for adhesive bonding, International Journal of Adhesion and Adhesives 17 (2) (1997) 143−150.
[44] P. Laurens, M. Ould Bouali, F. Meducin, B. Sadras, Characterization of modifications of polymer surfaces after excimer laser treatments below the ablation threshold, Applied Surface Science 154−155 (1) (2000) 211−216.
[45] L.F. da Silva, P.M.G.P. Moreira, A.L.D. Loureiro, Determination of the strain distribution in adhesive joints using fiber Bragg grating (FBG), Journal of Adhesion Science and Technology 28 (2014) 1480−1499.
[46] N.P. Cheremisinoff, Handbook of Polymer Science and Technology, vol. 4, Mercel Dekker, New York, USA, 1989, ISBN 978-0-824-78174-3.
[47] J.J.M. Machado, E.A.S. Marques, L.F. da Silva, Adhesives and adhesive joints under impact loadings: an overview, The Journal of Adhesion 94 (6) (2017) 1−32.
[48] A.P. Vassilopoulos (Ed.), Fatigue and Fracture of Adhesively-Bonded Composite Joints, vol. 52, Elsevier, Amsterdam, Netherlands, 2014, ISBN 978-0-857-09812-2.
[49] N. Su, R.I. Mackie, Two dimensional creep analysis of structural adhesive joints, International Journal of Adhesion and Adhesives 13 (1) (1993) 33−40.
[50] A.H. Tsou, D.L. DelleFave, Creep of a glass-flake-reinforced epoxy adhesive for space applications, Polymer 37 (24) (1996) 5381−5386.

This page intentionally left blank

CHAPTER

9

Simulation

Alireza Akhavan-Safar[a], *Eduardo A.S. Marques*[a], *Ricardo J.C. Carbas*[a,b], *Lucas F.M. da Silva*[a,b]

[a]Instituto de Ciência e Inovação em Engenharia Mecânica e Engenharia Industrial (INEGI), Porto, Portugal; [b]Departamento de Engenharia Mecânica, Faculdade de Engenharia (FEUP), Universidade do Porto, Porto, Portugal

1. Introduction

The use of adhesive bonding instead of traditional fastening techniques is increasing in different industries such as the automotive and aerospace industries [1]. Adhesive joints are now widely used for primary structures due to the increased demand for manufacturing light and durable components. In some conditions, such as bonding dissimilar or very thin substrates the use of adhesive bonding is unavoidable.

To reduce the maintenance and inspection costs and also to prevent a catastrophic failure of structures, a precise analysis of the adhesively bonded structures subjected to service loading is necessary. However, the design process of a large scale bonded structure can be extremely complex, requiring detailed knowledge of both the substrate properties and those of the adhesives, which can vary widely from brittle epoxies to highly deformable rubbers [1]. Viscoelastic behavior of the joints combined with complex loading conditions where the stress state is usually multiaxial make the analysis highly complex. The complexity level can further increase if the degradation of the adhesive properties due to environmental and loading conditions are also considered. While some design criteria consider these effects [2], there is still difficulty [3], in creating models that can accurately represent the mechanical behavior of adhesives and adhesive joints under a wide variety of conditions. To analyze the adhesive joints, two different approaches, divided into numerical and analytical methods, can be considered.

Volkersen [4] proposed one of the first analytical models for stress analysis of single lap adhesive joints. His model is the simplest method for stress assessment of adhesive layer in SLJs. However, due to some assumptions, it cannot take into account the effect of edge effects and the moment applied by the eccentricity of the applied load.

Advanced Joining Processes
https://doi.org/10.1016/B978-0-12-820787-1.00009-7

Goland and Reissner [5] in 1944 proposed an Euler based beam model to analyze SLJs. Their model was able to take into account the bending effects. Ojalvo & Eidinof [6] then corrected the Goland and Reissner approach and the model was further developed to take into account the plastic deformation of adhesives [7] and even adherend failure [8]. For ductile adhesives, Crocombe [9] proposed a simple global yielding method for failure assessment of adhesive joints.

Despite the simplicity and low cost of the analytical methods, however, they can be applied on joints with a simple geometry. In terms of material they also have some limitations. Due to their assumptions, the results of analytical methods are not very precise, especially for bonding ends where the stress (strain) is singular. To overcome these shortcomings, the numerical methods considered by researchers are mainly based on finite elements.

Wooley and Carver [10] in 1971 were the first authors who employed finite element method (FEM) for adhesive joint analysis. After few years Adams and Peppiatt [11] considered the FEM technique for failure assessment of adhesively bonded structures. Comparing to the numerical approach, the work of Wooley and Carver [10] was a significant progress in analysis of adhesive joints. However, their model was not able to consider the concepts of fracture mechanics. Based on the principles of fracture mechanics, defects like crack, debonding or delamination exist within the materials. These defects create stress concentration points, which have signification effect on the stress distribution within the joint. By knowing the stress intensity factor at the vicinity of these points, the safe area of working condition of the joints can be obtained as a function of the defect size or the applied load. Different fracture mechanics based criteria including maximum tangential stress (MTS), strain energy density (SED) and maximum tangential strain energy density (MTSED) have been considered by authors [12] to analyze the application of fracture mechanics based methods on failure load prediction of adhesive joints. According to the results, the MTS method can predict the kinking angle of cracks when the adhesive layer experiences mode II dominated stress conditions. When the mode mixity is close to mode I, SED can be a good choice for crack path prediction.

More recently, a combined analytical and fracture mechanics model was proposed to predict the failure of adhesive joints [13]. In this work, using the analytical approach, authors proposed a ratio method to estimate the critical stress intensity factors. Within the framework of fracture mechanics, the effect of substrate stiffness on the stress intensity factor is also studied using analytical and FEM techniques by some authors [13]. However, linear elastic fracture mechanics (LEFM) neglect the damage zone in the vicinity of crack tip. Accordingly, this approach is valid for the case in which the damage ahead of crack tip is small. It also assumes an initial crack like defect within the material. Cohesive zone modeling (CZM) was also developed based on the concepts of fracture mechanics to overcome the mentioned shortcomings [14,15]. CZM is created by defining a damage parameter, considering the damage area around the crack tip. The damage parameter is initially zero where the behavior of the adhesive is linear, that is, in the elastic portion. As damage occurs inside the adhesive layer, the value of damage parameter increases up to a value of one, where failure happens. Although the CZM was initially developed for interfacial damage and was using interfacial element with zero thickness however, it was extended for adhesive joints where the thickness of the cohesive layer is not zero [16]. CZM as a robust technique can be used for failure analysis of adhesive materials subjected to different loading conditions. CZM is able to take into account the effects of degradation due to the cyclic loading [17,18]. It can also take into account the effects of humidity [18] or strain rate [19]. After a conceptual design of the adhesively bonded structures, performing a finite element analysis using a robust tool will provide a designer with an idea about the mechanical behavior of the joints subjected to the service loads. To have accurate results, the problem should be defined precisely. This chapter explains how to simulate the adhesively bonded joints subjected to different loading and environmental conditions. To this effect, the chapter is presented in four sections based on loading and environmental type. The concepts of CZM combined with the extended finite element (XFEM) approach are described first. XFEM, which operates similarly to CZM, is an advanced technique which use the concepts of fracture energy for failure analysis of materials. As most of the joint experiences cyclic loading during their service life, the next section deals with the simulation of fatigue behavior of adhesive joints. Section 4 is focused on modeling of adhesive joints under different loading rate including impact loading. The last portion of the final chapter describes the simulation of moisture uptake in adhesive materials and its effect on joint behavior.

2. Numerical simulation of adhesive joints using CZM and XFEM techniques

Although LEFM based models were successfully considered in various applications, this approach will not work for ductile or toughened adhesives where a large plastic zone or damage area ahead of the crack tip is found. In these conditions, CZM or XFEM can be appropriate approaches for failure analysis of adhesives and adhesively bonded structures. In this section these two methods are discussed in detail.

2.1 CZM

Dugdale [15] and Barenblatt [14] developed CZM in 1950's for use in quasi static loading conditions. It was first developed for brittle materials but then extended for materials with a ductile behavior [20]. CZM is based on the relations between traction acting on the fracture process zone and the corresponding displacement (separation). Considering the fracture process zone ahead of the crack tip is one of the main advantages of the CZM. When the separation reaches a specific value, the damage initiates and increases by increasing the separation. When the separation reaches an ultimate value the crack physically initiates or propagates. Based on the CZM method, for the damaged zone, traction decrease as a function of the separation. The area under the traction separation curve is fracture energy. Different parts of the traction separation laws and a variety of the CZM shapes are discussed in this section. The thickness of the cohesive elements can be zero (Fig. 9.1A) or even it can be set to a finite value (Fig. 9.1B).

Damage can initiate at any cohesive element along the bondline when the criterion of damage initiation is met. However, the cohesive elements should be first defined at the planes of damage. In practice, this means that the damage area should be already known to the designer. However, for adhesive joint in which the failure usually takes place at the bonding areas (within the adhesive layer or the interface of adherend and adhesive), it will be easy to define the damage zones in advance.

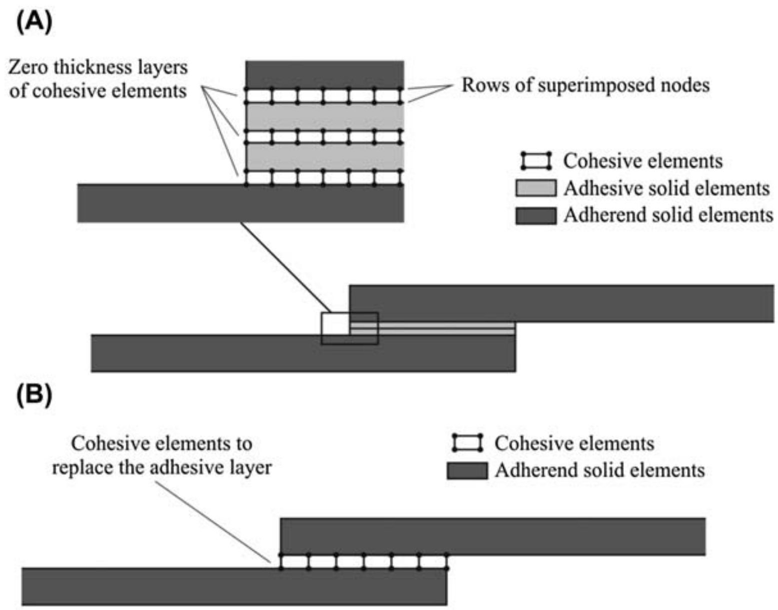

FIG. 9.1 Cohesive elements to simulate zero thickness failure paths – local approach (A) and to model a thin adhesive bond between the adherends – continuum approach (B) in an adhesive joint.

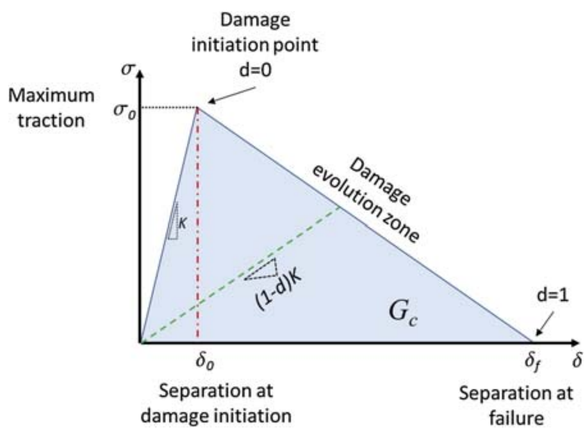

FIG. 9.2 A typical bilinear traction separation law.

As it was mentioned before, there are a variety of CZM shapes available for use. The simplest one is the bilinear shape in which both the initial elastic part and the softening part are linear. A typical bilinear CZM shape is shown in Fig. 9.2.

As it is shown in Fig. 9.2, a damage parameter (d) is defined in this model. The value of d is zero for the initial linear part where the stiffness of the cohesive elements is defined by K. However, as soon as the separation meet the damage initiation criterion, the damage value starts to increase. Loading and unloading during the damage evolution will be performed by a degraded stiffness ((1-d)K) as shown in Fig. 9.2. This CZM shape can be considered for pure loading modes (I, II or III). By knowing the initial stiffness and the maximum traction the values of δ_0 (see Fig. 9.2) can be simply obtained. Then the value of fracture energy will help to define δ_f.

Most of the joints experience mixed mode loading conditions in service. To use the CZM concepts for mixed mode conditions an approach for mixing the pure mode CZM shape should be employed. In this condition first an equivalent displacement should be defined based on the current displacement of elements at each direction. The damage initiation point can be also calculated by damage initiation criteria such as maximum nominal stress or stress, and the quadratic stress or strain criteria. For damage evolution, Power law or the BK (Benzeggagh-Kenane) approach are the two most common methods.

Although bilinear traction separation law is the most considered shape of the CZM, a variety of alternative shapes have been introduced by authors, to better suit different material properties. The first shapes of the CZM were proposed by Barenblatt and Dugdale [21,22]. Barenblatt [21] proposed a nonlinear damage evolution. The Dugdale method [22], for example, was based on a rectangular shape CZM. These shapes were further improved by other researchers such as Needleman, Rice and Wang, Tvergaard and Hutchinson, etc. Triangular [23], linear-parabolic [24], polynomial [25], exponential [26] and trapezoidal [27] CZM shapes have been since considered by other authors. However, the triangular, linear-exponential and the trapezoidal shapes are the most commonly used traction separation laws (Fig. 9.3). Several authors have studied the effect of CZM shape on numerical results. Based on the results of Pinto, Magalhães [28] modeled single lap joints with different substrate configurations and using an accurate CZM shape was found to be significant to predict the load-displacement response of the joint, especially for stiff substrates. Accordingly, it was found that for shear dominated conditions, the CZM shape could be very similar to the load-displacement curve. De Morais [29], Dourado et al. [30], Moroni et al. [31] and Giuliese et al. [32] have all considered triangular shape for their analysis. Based on the results presented by Alfano [33], the shape of CZM has a considerable influence on the numerical results obtained for mode I loading conditions of composite materials. For ductile adhesives the bilinear traction separaton shape underestimates the failure load. For these conditions where the elongation of the adhesive at failure is significant, the trapezoidal shape

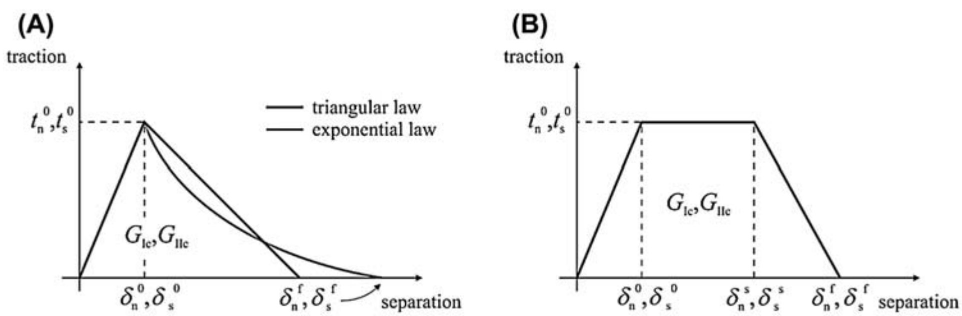

FIG. 9.3 Different shapes of pure mode CZM laws: triangular or linear-exponential (A) and trapezoidal (B).

is recommended by some authors [34,35]. The effect of CZM shape was also studied by Williams and Hadavinia [36] https://www.sciencedirect.com/science/article/pii/S0167844216302671-b0085, Chandra et al. [26] and de Moura and de Morais [37]. According to the presented review, it was found that the shape of the CZM has an important effect on the numerical results but in some studies no significant difference between different CZM shapes have been reported [15,38,39]. However, for brittle materials where the plastic zone size is small, the triangular CZM can be considered as an efficient law for analysis of the joints [40]. This CZM shape has been also considered for intralaminar fracture of composite adherends in bonded structures [41].

The CZM shape affects not only the accuracy of the results, but also the analysis time. For example, the triangular CZM usually face less convergence problem while the trapezoidal CZM sometimes requires more iterations during the solving procedure which is mainly due to the abrupt change of stiffness in the cohesive elements during the damage evolution. As the fracture energies must be kept constant, a larger plateau of constant stress in a trapezoidal law will result in a more abrupt softening slope.

One of the disadvantages of the CZM is its dependency on the joint geometry. From the effective parameters point of view, the fracture energy is the major parameter which govern the damage within the adhesive layer. However, the other parameters (maximum traction and the initial stiffness) should be also set accurately to obtain a precise result. Chen et al. [25] studied the effect of maximum traction in mode I direction in CZM analysis. They tested DCB, ENF and SLJ for pure mode I, pure mode II and mixed mode conditions, respectively. According to their results, when the adhesive layer experiences pure mode II and mixed mode I/II loading conditions, both shear traction and the fracture energies can significantly change the CZM results. However, on the other hand Ji, Ouyang [42], reported a reduction of maximum tensile traction and increase of G_{Ic} for thicker bondlines. It must be noted, however, that some authors [43] believe that the maximum interfacial strength does not change the results significantly.

Several studies deal with the effect of adhesive thickness on mode I and mode II fracture energies. Some authors [44] proposed a new parameter which takes into account the effect of bondline thickness on mode I fracture energy of adhesives with small or intermediate plastic deformations. Based on their results, stress triaxiality ahead of the crack tip and the T stress are two major parameters which change the fracture energy by adhesive thickness in DCB specimens. The effect of adhesive thickness is also considered by other authors [45–47]. Although in some studies, the fracture toughness obtained by fracture tests are considered as a material properties however, Carlberger and Stigh [48] showed that the CZM parameters significantly change with adhesive thickness. Other authors [44,49] also reported the variation of fracture energy as a function of adhesive thickness. Accordingly, the values of CZM parameters is sensitive to the adhesive thickness. Consequently, by changing the bondline thickness the CZM parameters should be set respectively. The effects of substrate thickness on tension and shear fracture energies are also considered by few authors [50,51] for composite materials.

As it was mentioned before, the cohesive layer can be incorporated in finite element software as a zero thickness interface between the substrates. However, for adhesive joints with a finite bondline layer between the substrates, the entire adhesive layer can be replaced by cohesive elements [27,52]. Although the initial stiffness for zero thickness cohesive elements should be set to a high value [53] for finite thickness conditions, the adhesive stiffness can be used for CZM analysis of adhesive materials [54]. The effect of initial stiffness on CZM results have been considered by some authors Daudeville et al. [55] Camanho et al. [56]. In some studies, the initial stiffness of the adhesive is defined by dividing the Young's modulus by the adhesive thickness. Considering the length of the cohesive zone is also important for a precise CZM. Different methods have been proposed by researchers Hillerborg et al. [57], Rice [58], Falk et al. [59], Irwin [60], Dugdale [22], Barenblatt [21] to calculate the cohesive zone ahead of the crack tip. Estimation of the cohesive zone is important as the number of cohesive elements ahead of the crack tip should be enough to cover the process zone. The effect of mesh size is also studied in some works [43]. It should be noted that the size mesh should be sufficiently small to be able to cover the cohesive zone with a sufficient number of elements [61]. To avoid divergence problem during the CZM analysis, sufficient integration points should experience damage evolution ahead of the crack tip [40,62]. To achieve this, some authors [23] have proposed to reduce the initial stiffness by keeping the other parameters constants.

2.2 XFEM

The generalized finite element method (GFEM), commonly referred to as the XFEM is also known as the partition of unity method (PUM). Although mesh refinement may solve some problems in FEM but it increases the time and cost of analysis and also for some problems it will not be the solution. For such cases the XFEM can be applied.

The XFEM is based on enriched nodal shape functions which first proposed by Belytschko and Black [63]. XFEM enrich the degrees of freedom to allow discontinuity of the elements.

XFEM is an energy based approach and, similarly to the CZM, can simulate both crack initiation and crack propagation. Using the XFEM technique, a crack can propagate through the element without the need of remeshing of the area ahead of the crack tip [64]. Also, using the XFEM, the crack path does need to be known in advance. This is the main advantage of the XFEM comparing to the CZM.

During crack propagation, the crack position changes and consequently the position of the discontinuity changes as well. Accordingly, XFEM will update the nodal shape functions of the elements ahead of the updated crack tip. As is the case in CZM, XFEM is also able to use different damage laws to reproduce the failure process of the joints.

XFEM employs the principal or nominal stress or strain criteria to predict the initiation of damage in cohesive elements. The concepts of damage evolution in XFEM are quite similar to those used in CZM, which have been already discussed in detail this section. However, in XFEM, the damage parameter (d) is defined as the average damage values of the edges of the element at crack tip and the crack surfaces.

In XFEM, cracks always propagate orthogonally to the maximum principal stresses/strains, which for example for mixed-mode loading conditions may give inaccurate results. However, in these conditions, the XFEM still predicts the damage initiation points accurately. It predicts the damage initiation by the stress or strain criteria. In terms of the analysis of singular point where the stress can be theoretically infinite, CZM and XFEM behave the same. Based on these approaches the stress level will be never higher than the maximum normal traction stress of the material. Both CZM and XFEM are mesh size independent. However, a mesh size study should always be performed as the number of element along the cohesive zone should not be less than a specific number and also as the stress level at singular point is a function of mesh size and a lower mesh density may change the load level and consequently the corresponding displacement for damage initiation. As is again the case for the CZM method, under compressive stress the enriched elements will not undergo damage.

In some studies, a combination of XFEM-CZM technique is considered [65,66], with good results being reported with the use of a combined XFEM-CZM analysis of single lap joints. Daux, Moës [67] and Sukumar, Moës [68] developed the XFEM for three-dimensional damage and multiple holes and cracks emanating respectively. Elguedj, Gravouil [69] using a new enriched element extended the XFEM for plastic modeling where the new method considers the elastic-plastic fracture mechanics. Contact problems are also considered by some authors [70,71]. Although in some studies [72,73] the XFEM has been applied for specimens where the loading conditions is cyclic but application of this generalized FE model on mixed mode fatigue conditions still requires further work.

3. Fatigue life analysis of adhesives and adhesive joints

Multiaxial stress is a common stress state that the real structures experience during their service load. Simulation of the adhesive joints as a bi-material subjected to quasi static loading conditions was discussed in previous section. However, in practice the loading conditions is mostly cyclic where the adhesive layer experiences multiaxial fatigue degradation. Although most of the joints are shear stress dominated, mode mixity is not constant during the bondline. For example, for single lap joints, the ends of the overlap may be dominated by peel stress and the mode mixity be closer to pure mode I conditions, while the mode ratio is close to pure mode II at the middle of the bondline.

Assessment of such complex adhesively bonded structures is quite challenging as designers must fully understand the real loading conditions that the joints will experience in service. Rocha et al. [73a] and Monteiro et al. [73b] analyzed the mode mixity and load levels on fatigue crack growth in different adhesive systems. They found that despite the significant difference between the mechanical properties, the slope of the Paris law curve is not very different for different adhesives. They used a normalized strain energy release rate in the Paris law relations and considered a compliance approach to obtain the fracture energies. Then they investigated different Paris law relations to find the best relation for adhesive joints in which the curves for different mode mixities and loading conditions are collapsed into a single master curve [73c]. In this section, approaches for the numerical analysis of adhesive joints subjected to cyclic loading are discussed, based on the concepts of the CZM.

According to the CZM, a damage parameter should be defined as a function of the current nodal displacement and the CZM shape of the material. However, to consider the cumulative damage due to the cyclic loading a new damage parameter should be also considered which usually causes a degradation of cohesive properties of the adhesive materials. Several authors have experimentally and numerically studied the fatigue behavior of adhesive joints in terms of the fatigue initiation and fatigue propagation lives. However, in practice as the bondline is very thin it is not easy to experimentally separate the initiation and propagation lives. From the numerical analysis point of view, as soon as the strain energy reaches the fatigue threshold energy the crack initiates. Life after crack initiation up to the final failure of the joint is called fatigue crack propagation life. CZM can estimate both lives. Several efforts have been performed to adapt the CZM and the degradation parameters to estimate the fatigue life of adhesive joints precisely. However, the complexity of the structure and sometimes the lack of a good physical meaning of the methods, makes them limited to very specific applications.

Based on the governing fatigue life, either initiation or propagation, the most appropriate method of analysis of the joints could be greatly different. When most of the life is spent before crack initiation performing a numerical S-N analysis can be a good choice. However, for the joints where the fatigue life is mainly spent in the crack propagation phase, a numerical procedure based on the fracture mechanics approaches is recommended.

For the fatigue life imitation analysis, strain based, stress based or a combination of stress and strain components should be considered as the fatigue parameter. Depending on the material type, in some cases a linear elastic analysis can be sufficient to predict the fatigue initiation life but for more tough or ductile materials, more stress or strain components should be taken into account in the numerical methods. By using a correct fatigue parameter (stress, strain or a combination of them) a precise estimation of the life can be obtained using the S-N approach. Accordingly, two main questions should be answered using this technique. First, which fatigue parameter for the this joint/material should be considered and the second question is that, where exactly this fatigue parameter should be measured within the adhesive layer. Several methods have been developed by answering these two questions. Critical plan and critical distance approaches are the two recent methods which are considered for the total fatigue life estimation of the materials. Kang et al. [74] used maximum structural stress range to predict the total life of the considered adhesive joints. They concluded that by performing a numerical analysis, a stress method can be applied for fatigue life prediction of adhesively bonded structures.

Schneider et al. [75] considered the point method and the line method of the critical distance theory to predict the fatigue life of adhesive joints. They considered scarf and single lap joints bonded with a toughened epoxy adhesive. These authors used a linear elastic analysis to measure the stress level within the adhesive layer. Both uniaxial and multiaxial stress analysis were considered in this work. Some authors considered the maximum tensile stress at overlap ends for fatigue life estimations of lap joints. As it was mentioned before, at the overlap ends of lap joints the stress is mainly tensile and can govern the fatigue response of lap shear bonding. Using a simple FE analysis, combined with the experimentally obtained S-N curve, it was possible to estimate the fatigue life which was in a good agreement with the experimental data.

For the materials with long fatigue crack propagation life and for the structures in which a finite crack propagation is allowed, the fracture mechanics based method instead of the S-N approach is considered. Nowadays, damage tolerance philosophy is used to reduce the weight of the structures, especially in the aerospace sector. Although designing based on the damage tolerance philosophy reduces the complexity and weight of the structures, it needs a precise inspection and maintenance program. Accordingly, an accurate numerical analysis is needed to simulate the fatigue crack propagation of the joint precisely. Stress or strain based method are used in some studies for numerical analysis of fatigue crack propagation in adhesive joints [76–78] however, as it was mentioned before, using the fracture mechanics based methods are recommended for fatigue crack propagation analysis.

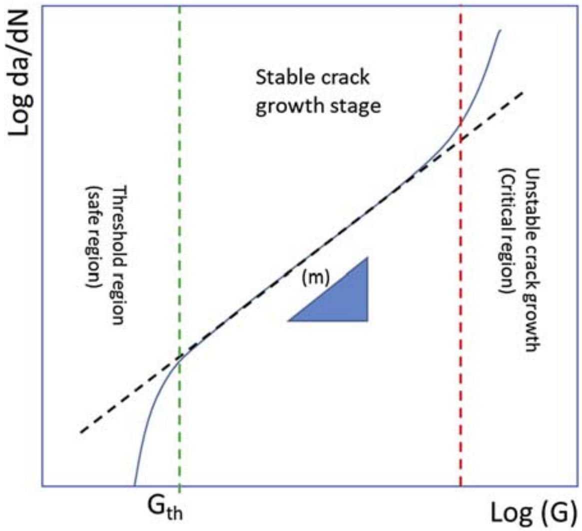

FIG. 9.4 Schematic view of the Paris law curve.

Paris law as a fracture mechanics based method, is the most commonly used approach for assessment of fatigue crack growth in adhesive joints. Different Paris law relations have been considered by authors to simulate the fatigue crack growth in adhesively bonded joints [79–82]. Fig. 9.4 shows a typical Paris law curve where the rate of crack propagation (da/dN) as a function of strain energy (G) is plotted in a log-log diagram.

As it is shown in Fig. 9.4, Paris law curve is divided into three different zones named the initiation part, the stable crack propagation stage and the unstable fatigue crack propagation region. m in Fig. 9.4 shows the slope of the line in stable crack propagation section. m shows the rate of fatigue crack propagation for the considered condition. m not only is a function of the loading condition and material properties but also it depends on the Paris law relation. A lot of effort [81–84] has thus been carried out to introduce a universal Paris law relation that is able to take into account different loading parameters. However, this it is still a challenging and open research topic.

By knowing the Paris law constants, fatigue crack growth can be simulated in bonded substrates. But as the loading conditions may change the Paris law parameters, it is necessary to perform experiments for each loading conditions which is costly and time consuming. To solve this issue, different modifications have been applied on Paris law equations [79,81–84]. The optimum Paris law relation should be able to give similar Paris law constant regardless of the loading condition [73c].

Application of CZM for fatigue analysis of adhesive joints has been considered by some authors [17,18,85,85a]. As it was already mentioned, in addition to the damage parameter (d) used in quasi static analysis, the rate of degradation of the cohesive properties of the adhesive materials should be defined in addition to the damage parameter (d) which is defined for the quasi static conditions. Sometimes the relation to degrade the properties of the adhesive depends on some material constants which should be obtained experimentally. To combine the pure mode I and pure mode II cohesive properties, a mixed mode criterion should be also employed.

Damage mechanics combined with the CZM is also considered in some studies [85] for fatigue analysis of joints. Moroni and Pirondi [86] developed a cohesive zone model for fatigue crack growth analysis of bonded joints. They implemented the model in Abaqus by a user defined subroutine. Katnam et al. [87] studied the effect of load ratio on damage in adhesively bonded joints. They developed a new damage model to be able to take into account the effects of stress ratio. They defined an effective strain for fatigue analysis of a single lap joint. A bi-linear cohesive zone model was used in their analysis.

Strain based fatigue model was also used by Khoramishad et al. [88]. They used CZM concepts to analyze the fatigue behavior of adhesive joints. Some authors proposed a degradation model based on Paris law relation [89]. Costa et al. [18] recently developed a degradation model (Eq. 9.1). According to their model, the maximum traction and the fracture energy will be degraded by the given relation. y in Eq. (9.1) gives the value of the cohesive parameter (e.g. fracture energy) when the element has experienced N number of cycles. The initial value of the corresponded cohesive parameter is y_0 and k as a fitting parameter should obtained using experimental results. N_f is the total fatigue life of the joint which can be estimated using Eq. (9.2).

$$y(N) = y_0\left(1 - \frac{N}{N_f}\right)^k \tag{9.1}$$

$$N_f = \frac{\Delta a}{(da/dN)_a} \tag{9.2}$$

Based on numerical analysis it was shown that by increasing the value of k and threshold energy increases while increasing the value of m leads to a decreases of the threshold energy. Based on this analysis, it was also found that the intercept (C) increases when the value of k decreases [18]. Based on the Costa et al. [18] method the rate of degradation is higher for higher values of k. This model was applied on DCB joints loaded in pure mode I conditions. Based on the obtained results, it was found the total life estimation using Eq. (9.2) gives an accurate estimation for DCB specimens. However, application of this method on joints with different mode mixities and for longer fatigue life needs further investigations. The Costa et al. method was extended to shear loading conditions by some authors. A schematic view of the degradation of the cohesive properties is shown in Fig. 9.5. According to Fig. 9.5 by increasing the fatigue cycles, the maximum traction and the fracture energy of the

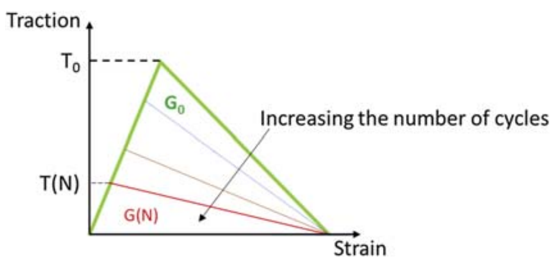

FIG. 9.5 The effect of data degradation on the CZM parameters.

adhesive decrease. Accordingly, the separation corresponding to the damage initiation decrease and damage initiates earlier at higher fatigue cycles.

As described for the quasi static analysis, different CZM shapes can be considered for numerical analysis of the fatigue behavior of adhesive materials, with the triangular law being the simplest and the most commonly used CZM shape. The constitutive equations of the cohesive elements are as follows:

$$\sigma = \begin{bmatrix} \sigma_I \\ \sigma_{II} \\ \sigma_{III} \end{bmatrix} = (1-d)K\begin{bmatrix} \delta_I \\ \delta_{II} \\ \delta_{III} \end{bmatrix} - dK\begin{bmatrix} \langle -\delta_I \rangle \\ 0 \\ 0 \end{bmatrix} \tag{9.3}$$

The Macaulay bracket $\langle -\delta_I \rangle$, defined in Eq. (9.3) is considered as the cohesive elements will not be damaged under compressive stress. The initial stiffness of the cohesive element is defined as K in Eq. (9.3) where d is the damage of the cohesive elements. By knowing the values of the initial stiffness, the amount of damage and the values of the current separation (strain) the traction can be obtained for each integration point and at each time increment.

However, the failure criterion already included in commercial software cannot consider all these aspects of the fatigue analysis. Accordingly, writing a subroutine to define the analysis procedure is necessary. This section deals with the introduction of the most advanced user subroutines which can be used for fatigue analysis of adhesive joints. User element (UEL) in which a customized element is defined and user material (UMAT) where a customized material behavior is defined are the two types of routines that are discussed in this section. UEL uses the concepts of finite element and the constitutive laws of the cohesive elements for numerical simulation of adhesive joints subjected to fatigue. UMAT also calculates the stress at each time increment for each node based on the separation values given by Abaqus.

To employ the UEL, the stiffness matrix of the element should be defined first. Based on the FE concepts the general behavior of the elements can be defined as Eq. (9.4).

$$[K] \times \{d\} = \{f\} \tag{9.4}$$

where $[K]$ is the stiffness matrix, $\{d\}$ is the displacement vector and $\{f\}$ is the vector of the external forces. Eqs. (9.5) and (9.6) show how the stiffness matrix and the vector of the external forces should be calculated.

$$[K] = w[B]^T[T_d][B] \tag{9.5}$$

$$\{f\} = w[B]^T\{T\} \tag{9.6}$$

where w is the element width and $[B]$ is the global displacement-separation relation matrix. $\{T\}$ and $[T_d]$ are also vector and matrix, respectively.

For mode I loadings in the local coordinate system $\{T\}$ and $[T_d]$ should be defined as:

$$\{T\} = \begin{Bmatrix} 0 \\ t(d) \end{Bmatrix} \quad [T_d] = \begin{bmatrix} 0 & 0 \\ 0 & t'(d) \end{bmatrix} \tag{9.7}$$

In Eq. (9.7) $t(d)$ is based on the CZM shape and d0 correspond to the displacement where the damage initiates and $t\prime(d)$is the derivative of $t(d)$. df corresponds to the displacement where d = 1 and element fails.

The UEL was used for fatigue analysis of adhesive joints in pure shear conditions. Comparing to the mode I, the concepts of the UEL can be applied for mode II by applying a minor change as shown in Eq. (9.8).

$$\{T\} = \begin{Bmatrix} t(d) \\ 0 \end{Bmatrix} \quad [T_d] = \begin{bmatrix} t'(d) & 0 \\ 0 & 0 \end{bmatrix} \tag{9.8}$$

To simulate the fatigue behavior of adhesive joints, elements' shape functions and the traction separation law should be defined in UEL. Fig. 9.6 shows a schematic of the mode II loading conditions where (ξ,η) gives the local coordinate and (x,y) corresponds to the global coordinate.

In case of a 4-node element, 4 shape functions should be defined. At a specific ξ coordinate, functions are defined as follows:

$$N_{1.4} = \frac{1}{2}(1-\xi);\ N_{2.3} = \frac{1}{2}(1+\xi); \tag{9.9}$$

where $[N]$ is obtained as follows:

$$[N] = \begin{bmatrix} N_{14} & - & N_{23} & - & N_{23} & - & N_{14} & - \\ - & N_{14} & - & N_{23} & - & N_{23} & - & N_{14} \end{bmatrix} \tag{9.10}$$

$[B]$in Eqs. (9.5) and (9.6) is defined as follows:

$$[B] = [R][N] \tag{9.11}$$

where $[R]$ is the global to local transformations matrix and is calculated as follows:

$$[R] = \begin{bmatrix} \cos\alpha & \sin\alpha \\ -\sin\alpha & \cos\alpha \end{bmatrix} \tag{9.12}$$

Where α is the angle between the coordinate systems (see Fig. 9.6).

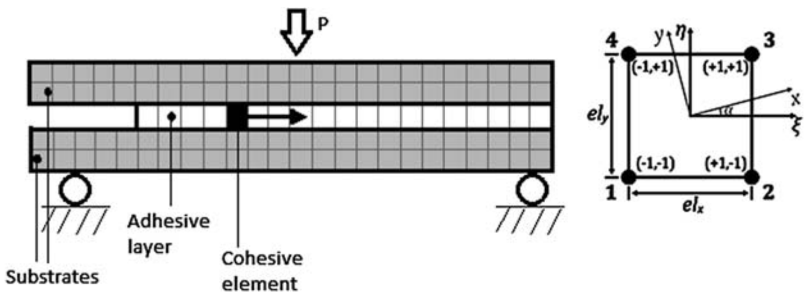

FIG. 9.6 ENF specimen and a cohesive zone element in global (x,y) and local (ξ,η) coordinates.

As it was mentioned before, $t(d)$ and $t\prime(d)$ are defined based on the CZM shape. For a triangular traction separation law two different zones (see Fig. 9.7) can be considered for determining the values of $t_i(d)$, $t_i'(d)$ and G_i. Accordingly, $t_1(d)$, $t_1'(d)$ are defined as follows:

$$t_1(d) = \frac{t_m d}{d_0} \tag{9.13}$$

$$t_1'(d) = \frac{t_m}{d_0}$$

$$t_2(d) = t_m\left(1 - \frac{d - d_0}{d_f - d_0}\right)$$

$$t_2^{'}(d) = \frac{-t_m}{d_f - d_0}$$

where the exponents 1 and 2 denote the zone 1 and zone 2, respectively.

By following the above procedure, the values of fracture energy and separation and subsequently the damage values can be calculated as a function of number of cycles. More details about the procedure can be found in the literature [17,18].

By considering the constitutive equations that govern the mechanical behavior, UMAT can be employed for fatigue life assessment of the adhesive materials, with UMAT being applied at the node level. Based on UMAT, by knowing the displacement of the nodes at each direction, the stress state of the nodes can be calculated and updated considering the mode mixity and the damage value of the nodes. Two commonly used criteria for mixed mode conditions are the power law and the Benzeggagh-Kenane (BK) law. Based on the power law the failure of the joint for mixed mode conditions is governed by Eq. 9.14a.

This relation is for two dimensional conditions however, for a 3D problem an additional term for out of plane fracture energy should be added to Eq. 9.14a.

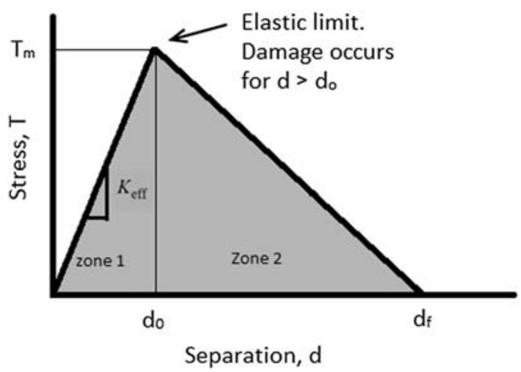

FIG. 9.7 The two defined zones for a bilinear CZM shape.

Eq.9.14b shows the BK relation. If the in-plane shear fracture energy and the out of plane shear fracture energy are the same, then BK can be employed as a mixed mode failure criterion.

$$\left(\frac{G_I}{G_{Ic}}\right)^{\alpha} + \left(\frac{G_{II}}{G_{IIc}}\right)^{\alpha} = 1 \tag{9.14a}$$

$$G_c = G_{Ic} + (G_{shearc} - G_{Ic})\left[\frac{G_{shear}}{G_T}\right]^{\lambda} \tag{9.14b}$$

Where in the BK approach, $G_{shear} = G_{II} + G_{III}$ and $G_T = G_I + G_{shear}$. The energy release rate is calculated at each integration point for a given increment using the reduction factor given in Eq. (9.1). It should be noted that the values of the fracture energy should be degraded based on Eq. (9.1) for cyclic loading conditions. It means that the values of fracture energies in mode I and mode II will decrease by increasing the number of cycles during the fatigue loading. Accordingly, the damage (d) should be updated based on the current state of the nodal stresses/strains and the current values of the fracture energies. Definition of damage depends on the CZM shape. The three most common CZM shapes considered by the authors are the bi-linear, the exponential and the trapezoidal shapes. Accordingly, the damage can be calculated based on Eqs. 9.15a–c, respectively.

$$d = \frac{\delta^f\left(\delta_{eq} - \delta^0\right)}{\delta_{eq}\left(\delta^f - \delta^0\right)} \tag{9.15a}$$

$$d = 1 - \frac{\delta^0}{\delta_{eq}}\left(1 - \frac{1 - e^{\left(-\alpha\left(\frac{\delta_{eq}-\delta^0}{\delta^f-\delta^0}\right)\right)}}{1 - e^{-\alpha}}\right) \tag{9.15b}$$

$$\begin{cases} d = 1 - \dfrac{\delta^0}{\delta_{eq}} & if\ \delta^0 < \delta_{eq} < \delta^s \\ d = 1 - \dfrac{m\delta_{eq} + b}{K\delta_{eq}} & if\ \delta^s < \delta_{eq} < \delta^f \end{cases} \tag{9.15c}$$

where:

$$\delta_{eq} = \sqrt{\delta_I^2 + \delta_{shear}^2}$$

$$\delta_{shear} = \sqrt{\delta_{II}^2 + \delta_{III}^2}$$

$$\delta^{02} = \delta_I^2 + \delta_{II}^2 + \delta_{III}^2 = \delta_I^{02} + \left[\delta_{shear}^{02} - \delta_I^{02}\right]\omega^\lambda \tag{9.16}$$

$$\delta^f = \frac{\delta_I^0\delta_I^f + \left(\delta_{shear}^0\delta_{shear}^f - \delta_I^0\delta_I^f\right)\omega^\lambda}{\delta^0}$$

$$\omega = \frac{G_{shear}}{G_T} = \frac{\beta^2}{1 + 2\beta^2 - 2\beta}$$

$$\beta = \frac{\delta_{shear}}{\delta_{shear} + \delta_I}$$

$$m = \frac{-t^0}{\delta^f - \delta^s}$$

$$b = t^0 - m\delta^s$$

t^0 is the maximum traction, δ_I^0 and δ_{shear}^0 are the damage initiation conditions for normal and shear directions, respectively, and δ_I^f and δ_{shear}^f are displacements at final failure. ω represents the ratio of G_{shear} to G_T which is a function of the mode mixity.

The discussed procedure for UMAT were applied on a single lap joint where the bondline experiences a complex mode mixity during the fatigue loading.

For fatigue analysis of adhesive joints, the current state of strain is considered to calculate the damage and updating the stress state at all integration points based on the degraded values of fracture energy due to the cyclic loads. This process should be repeat for each time increments. As soon as the damage value reaches 1 the node/element will no longer sustain any load.

Using the second approach (UMAT) a DCB joint subjected to a cyclic loading was analyzed. Table 9.1 gives the material properties of the adhesive and the substrates. Initial values of fracture energies for modes I and II was set to 2 N/mm and 10 N/mm respectively. The cycle jump strategy is followed in this analysis where the load is kept constant and equal to the maximum load during the analysis. In this condition the life is controlled by the time increment.

TABLE 9.1 Mechanical properties of the adhesive and substrates [17].

Properties	Substrate	Adhesive
Maximum tensile strength (MPa)	–	31
Maximum tensile strain (%)	–	10.4
Young's modulus (MPa)	210,000	1159
Poisson's ratio (ν)	0.3	

Figs. 9.8 and 9.9 show the joint geometry and the evolution of damage as a function of fatigue cycles, respectively.

It should be noted that change in the loading frequency may change the fatigue life which is due to the changes in strain rate within the adhesive layer. Next section will deal with the effect of strain rate on mechanical behavior of adhesives and adhesive joints.

4. Numerical simulation of adhesive joints at different strain rate and impact conditions

Adhesive properties may significantly change as a function of strain rate [90–92]. Accordingly, considering the strain rate dependent properties of the adhesive materials is essential specially where the impact loading during the service life is expectable. For such applications, the effect of strain rate on mechanical behavior of adhesives and adhesive joints should be assessed to optimize the joints against different loading rates. Performing a numerical analysis instead of doing high strain rate or impact tests will significantly reduce the time and costs. However, to obtain a precise numerical result, not only the properties of the adhesive as a function of the strain rate should be defined correctly, but also an appropriate failure criterion should be employed. Johnson-Cook as a multiplicative model is widely used for strain rate analysis of metals. However, for adhesive materials this approach is also considered to study the effect of strain rate and even the temperature effects on the mechanical response of adhesives and adhesive joints. Cowper-Symonds approach is another strain rate dependent constitutive law. It is an elasto-plastic model which considered for high strain rate analysis of adhesive martials. Using constitutive models is an essential part of the numerical analysis especially for customized materials where writing a subroutine is unavoidable. However, to obtain precise results, an appropriate constitutive model should be defined for the considered material.

Cowper-Symmonds was also considered by Zaera et al. [93] to simulate the impact behavior of a bonded ceramic/metal armour. Using this relatively simple constitutive model, authors were able to reproduce the experimental data sufficiently well for preliminary design calculations. Interfacial stress assessment using the Cowper-Symonds constitutive model was performed by Sawa et al. [94], and Liao et al. [95,96]. They found that the considered constitutive model is able to model the interfacial stress distributions in various types of joint geometries.

The effect of impact loading on behavior of adhesive joints was also numerically investigated by Goda and Sawa [97]. They considered different strain rate from 10^{-4} to 10^{-1} s^{-1} to take into account the effect of strain rate and the plastic flaw. They considered the

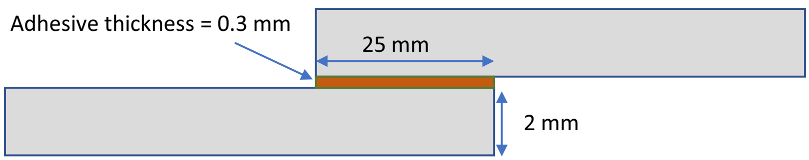

FIG. 9.8 Dimensions of the analyzed SLJ (not scaled), width = 38 mm.

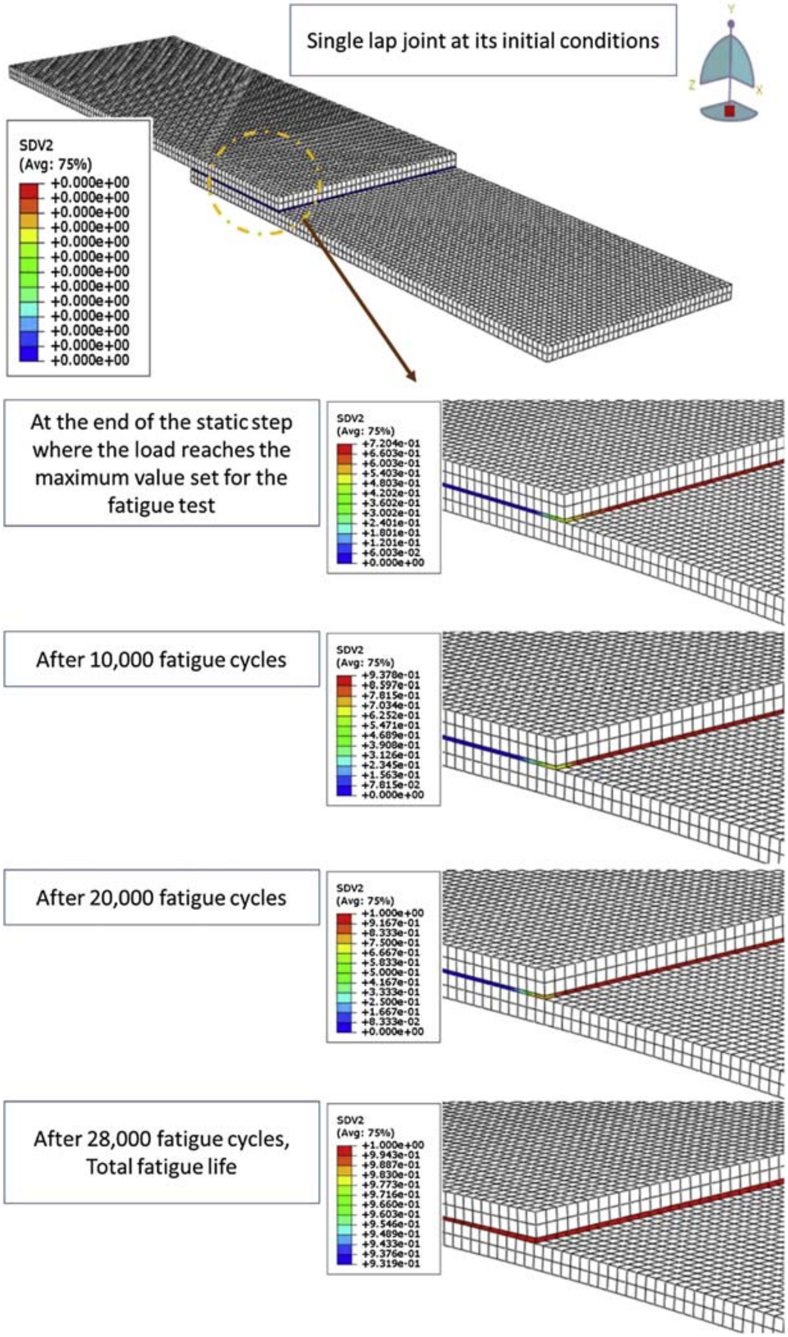

FIG. 9.9 Fatigue life analysis of a DCB joint using UMAT, SDV2 = damage parameter(d).

Cowper-Symonds model. Viana et al. [98], studied experimentally the effect of combined loading rate and temperature on adhesive joints. Goglio et al. [99] studied the effect of strain rate by testing a two-part epoxy adhesive at high strain rates. They considered Cowper-Symonds and Johnson-Cook models to analyze the behavior of the tested adhesive. According to their results, Johnson-Cook model doesn't fit well with the results while the Cowper-Symonds model results for high strain rate was good where a hot curing procedure was employed for preparing the specimens. According to the results reported by Goglio et al. [99] for the intermediate strain rate the Cowper-Symonds gives good results if a cold curing is followed for manufacturing the specimens.

To simulate the high strain rate behavior of adhesive joints, authors have considered different commercial software. DYNA3D was employed by Sawa et al. [100−102] in 2002 to simulate the behavior of adhesively bonded single lap joints subjected to diverse impact loadings. The constitutive dynamic model considered by Sawa et al. [100−102] is as follows:

$$[M][A] + [K][U] = [F] \tag{9.17}$$

where $[M]$, $[A]$, and $[K]$ are the mass matrix, the acceleration vector, and the stiffness matrix, respectively. $[F]$ and $[U]$ are the load and displacement vectors.

A 3D FE analysis using Abaqus® was conducted by Challita and Othman [103]. They performed some high strain rate tests using the split Hopkinson pressure bar (SHPB) on double lap joint (DLJ) specimens with metal substrates. Elastic behavior was assumed for the numerical analysis part for both the substrate and the adhesive. By changing the metal substrates to composite materials Hazimeh et al. [104] studied the effects of material on the high strain rate response of DLJs.

By defining curves of the failure parameters versus the effective strain rate, Yang et al. [105] tried to evaluated the application of a simplified finite element for high strain rate analysis of a toughened adhesive. Dean et al. [106] considered Von Mizes and Drucker-Prager to compare the measured and predicted response of SLJ subjected to impact loading conditions where the strain rates changed from 2.10^{-5} to 115 s^{-1}. They found that although the von Mizes yield criterion is not suitable for toughened adhesives, the linear Drucker-Prager model results were in agreement with the experimental data. According to their results, an elastic-plastic material model with considering the hydrostatic stress is needed. Von Mizes model and a rate dependent Drucker-Prager were also considered by Zgoul and Crocombe [107] to numerically analyze SLJ and thick adherent shear testing (TAST) specimens under high strain rate loading condition. According to their results, none of the von Mizes and the Drucker-Prager models were able to reproduce the experimental data. The von Mizes cannot take into account the effect of hydrostatic stress and in this case the Drucker-Prager model had convergence problems.

Although some constitutive equations have been developed to simulate the behavior of adhesive materials as a function of strain rate, in many cases the strain rate dependency of the material properties is obtained experimentally. This is carried out especially when the CZM approach is considered for analysis of the joint in which the bondline experiences a variety of strain rates and mode mixities during the analysis. CZM was considered by Carlberger et al. [108] in 2007. They found that the CZM approach as a valid method can be used for impact analysis of the joints. CZM method for high strain rate analysis was then considered by several authors [109] where dynamical cohesive models were used for impact analysis of the adhesive joints. However, an average model is used in these conditions where a cohesive law based on the average value of the strain rate is employed during the analysis. Although this simplified approach might be useful to reduce computational cost, this assumption may also introduce a significant error to the obtained numerical results because in practice the adhesive bondline usually experiences different strain rate levels even if the loading rate is kept constant. To overcome this issue, CZM can be developed to reflect the cohesive properties as a function of strain rate in integration point level [109a,109b]. For a customized rate dependent numerical analysis usually a user defined material in framework of a subroutine should be developed based on the obtained experimental data. UMAT or VUMAT are the two most common subroutine which can be considered in Abaqus®. Fig. 9.10 represent a scheme of the integration process of UMAT.

As the stress/strain state at the level of integration points, is usually under mixed mode, it would be more precise if the routine prepared for analysis is constructed to be able to cover

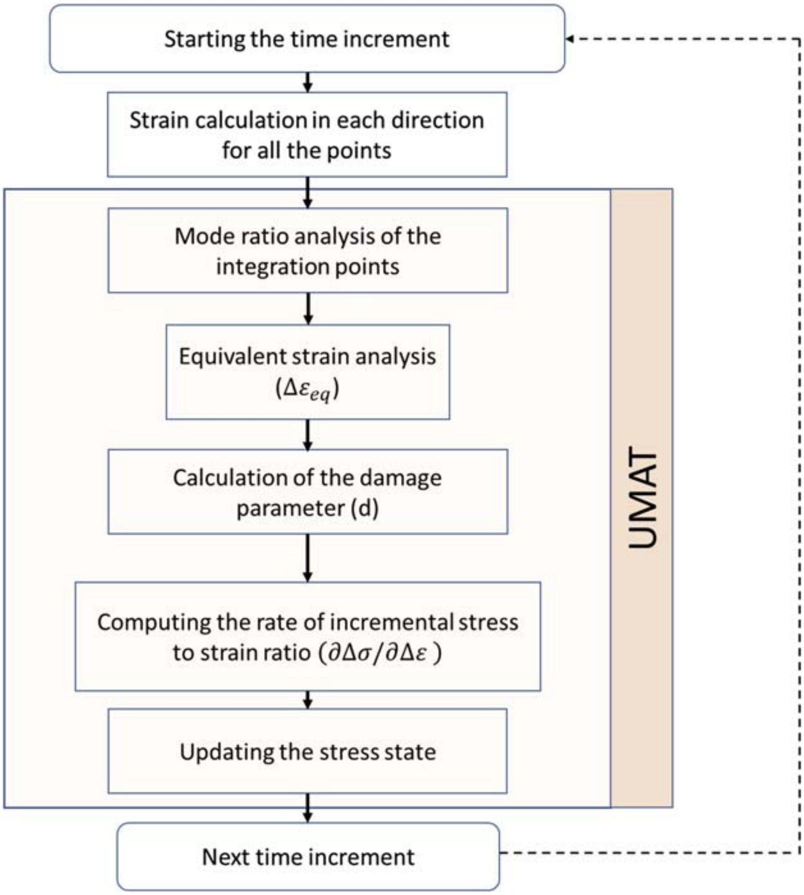

FIG. 9.10 Schematic representation of the UMAT integration process in Abaqus®.

all mode ratios. The concepts of the routine used for strain rate dependency of properties are generally very similar to the cyclic load discussed in previous section. However, the main difference is the variation of fracture energy and maximum traction with increasing the strain rate. Usually the maximum traction increases with the strain rate. However, the effect of strain rate on fracture energy should be also experimentally ascertained. By knowing the maximum traction and the fracture energy as a function of strain rate for different mode mixities and by the use of extrapolation/interpolation techniques, traction and fracture energy for a wide range of strain rates can be calculated. This information is necessary for creating a routine that is able to consider the strain rate in damage analysis of the material. The fracture energy and the maximum traction not only depends on the current strain rate that the integration point experience but also it is a function of mode ratio. The strain rate itself is a function of mode ratio as well. Considering the complex geometry which is usually used in practice and the multiaxial state of loading conditions make the problem more complex. In this case a robust numerical method based on a customized strain rate dependent CZM will be helpful. However, this technique needs sufficient experimental data point to accurately predict the dynamic behavior of the adhesive joints. However, this complete approach is still in its preliminary steps and needs further studies.

5. Numerical analysis of adhesive joints under different environmental conditions

Although they have several important advantages, adhesive joints can suffer degradation induced by environment effects, losing part of their mechanical strength. In many applications such as in automotive and aeronautic industries, joints are sometimes exposed to moist environments during their service life. In such cases, water ingress causes a degradation in mechanical properties of the joints, usually by plasticization phenomenon, as separation of the molecular chains occurs [110]. By absorbing water, adhesives generally become more ductile and weaker and their toughness decreases. To avoid a catastrophic failure, adhesively bonded joints should be designed against these aging conditions.

To analyze the effect of moisture on the mechanical behavior of adhesive joints a complete knowledge about the amount of water at each point should be obtained. This type of analysis has already been carried out extensively by researchers [111−114]. In addition, as the interfacial failure is very common for joints in the aged condition, to simulate the mechanical behavior of these joints, both interfacial [114−117] and adhesive [111,113,114,118,119] properties should be considered as a function of the humidity level. Thus, a numerical analysis can be an useful tool to estimate the mechanical behavior of aged adhesive joints as a function of the water uptake level.

The faces of adhesive layer in adhesive joints exposed to water/moist environment absorb water much faster than the core of the adhesive layer [120]. However, in the case of saturated condition, all points will eventually experience a uniform condition in terms of water uptake and uniform degradation of the mechanical properties. For a numerical simulation at the element level, the amount of water uptake at each element should be precisely calculated and the mechanical properties of each element should be computed accordingly.

Fick's laws are widely used to simulate the water uptake in adhesives [121,122]. Depending on the behavior of the adhesive materials in water uptake, the simple form of the Fick's law or the dual phase Fick's law should be considered. Moisture diffusion can then be analyzed by considering the analogy between heat transfer and the moisture uptake [123]. The equivalent parameters to permeability coefficient, diffusion coefficient and solubility coefficient are thermal conductivity, thermal diffusivity and heat capacity respectively. Accordingly, heat transfer should be used to simulate the water uptake in adhesive materials. DC1D2 and DC2D4 are the two available heat transfer elements in Abaqus for the 1D and 2D heat transfer simulations, respectively.

Several authors have numerically investigated the effect of humidity on the mechanical response of adhesive joints. Roy et al. [124] simulated the moisture diffusion in an adhesive joint using a 2D FE analysis. They considered the interaction of diffusion process and the viscoelastic behavior of the adhesives.

Recently, Israr et al. [125] numerically analyzed the effect of humidity on the crashworthiness behavior of CFRP laminates. They considered the saturated specimens. For numerical simulation, an Abaqus explicit model was considered by these authors. The effect of spew fillet on single lap joints aged by tap water for 30 days was studied by other authors [126]. Similar work was performed by Hua et al. [111] where the von Mizes yielding criterion was considered as the failure criterion. Based on their obtained results, maximum elongation of a bulk specimen is higher than maximum tensile strain of the joint with a similar adhesive. Accordingly, they concluded that the adhesive/adherent interface of an aged adhesive joint is more susceptible to moisture degradation than the adhesive itself. By employing Comsol Multiphysics™, Bordes et al. [127] simulated the aging process of adhesive joints immersed in sea water. They considered double lap and Arcan joints in their studies. To analyze the stress state during aging, they used the experimental data where a relationship between the water content and the loss in adhesive properties was made. Water uptake for a rubber toughened epoxy was simulated by Loh et al. [128]. They numerically analyzed the moisture-dependent swelling coefficient of the adhesive. In their analysis they considered a dual stage uptake model and moisture-dependent mechanical properties of the adhesive.

Residual strength of adhesive joints was investigated by Sugiman et al. [118]. They performed a finite element analysis using CZM technique. Using the numerical method, they measured the residual stresses due to the swelling and thermal strains within the adhesive layer. Based on the experimental results of aged bulk specimens, they developed a bi-linear CZM in which the maximum normal and shear tractions and also fracture energies were defined as a function of the moisture level. In their work, plain strain conditions were considered for the adhesive layer while the substrates were modeled as plain stress. The effect of residual strength of adhesive joints was also studied by other authors using a continuum CZM technique [117]. Liljedahl et al. [129], used CZM where separation in all the loading modes (I, II and III) were accounted for. They considered similar fracture energies regardless of the loading conditions. They determined the cohesive properties of the elements at different aging levels using mixed mode flexure test results. The maximum traction was considered as the onset of non-linear section in load-displacement curve. By fitting the experimental results with the numerical they calculated the fracture energy as a function of the aging level. Accordingly, they found that the fracture energy decreases rapidly initially and then flattens out, where the maximum traction experiences an opposite trend. Based on their work, a 2D analysis of aged joints underestimates the experimental results. They also found that the residual stress due to swelling for a double lap joint may have enhanced the degradation of the properties during the aging process.

3D analysis of aging process was also considered by some other authors [130]. They considered the nonlinear behavior of the bulk adhesives. In their work a CZM was utilized to simulate the interfacial response of the joints. To consider the effect of aging on the CZM properties, they considered a dynamic update of the element materials due to the aging duration. A 3D hex mesh was used for the adhesive, and cohesive elements were considered for the interface. They defined a failure criterion based on the maximum stress/strain for the bulk adhesive where the failure of cohesive layer was defined based on the value of damage parameter.

The effect of the cyclic humidity has also been simulated by some authors [131]. In this work, the moisture history is considered in water diffusing for each cycle. They found a non-Fickian behavior for water absorption while the desorption process was based on Fickian law. They developed a finite element model to take into account the history of water uptake in cyclic aging conditions. They found that the prediction of concentration based on non-history dependent diffusion characteristics over-predicts the moisture concentration in cyclic aging conditioning. A user subroutine, used for defining the materials thermal behavior, was considered by the authors and implemented in Abaqus. They considered the history of the moisture for each point by using the state variables. Their model also considers the dual Fickian law response of the adhesive materials. Based on their results, by neglecting the history dependency of the diffusion rates the results would be over or underestimated. To consider the gradient in the mechanical properties in both dimensions of the adhesive layer, a 3D analysis must be undertaken as the water penetration into the adhesive layer is through two directions [111]. Although both the 2D and 3D analysis are possible, in some cases (listed below) performing a 2D analysis will give very acceptable results:

1. In specimens where the length is considerably smaller than the width. In this case, only the gradient in the length direction is important while the gradient in the width direction is negligible.
2. When the adherents are permeable. In this condition a more uniform water absorption is experienced by the adhesive layer due to the water absorption through the thickness of the substrates.

In more complicated conditions where the diffusion coefficient of the model changes with time (such as in cyclic humidity condition), user filed subroutine or user defined subroutine in Abaqus can be helpful, where the diffusion rate depends on the value of a field variable (which could be the time of the analysis). It should be noted that to compare experimental and numerical results, the average concentration of the water for the model should be compared with the experimental data points.

Most of the studies deal with the diffusion rate of unloaded specimens but in few works [117], authors have considered the water ingress in a specimen while it is loaded. In this condition, the stress state of the adhesive is influenced by the water uptake, which will in turn also be influenced by the stress state of the adhesive [119]. To simulate the degradation of adhesive joints while they are stressed during aging, Han et al. [119] proposed the following analysis steps:

Step 1: Considering a combined thermal-hygro-mechanical condition for a long-term aging procedure where an analogy between the heat conduction and moisture diffusion was made.

To measure the stress dependency of the moisture uptake for an adhesive joint subjected to a constant load, von Mizes stress was considered.

Step 2: Using the amount of moisture uptake and also by considering the value of the strain for each point measured in step 1 to update the properties of the material.

Interfacial moisture diffusion for adhesive joints should be also considered in numerical analysis. Accordingly, the following models are considered:

1. A one dimensional model, where unidimensional beam elements are used to simulate the moisture diffusion along the width of the joint. Considering the experimentally obtained toughness of the joint, by fitting the numerical values, the experimental results will match the calculated moisture uptake. Accordingly, it will be possible to calculate the average diffusion coefficient of the joint through this inverse method.
2. A two-dimensional model, where the interfacial water uptake is simulated separately. In this approach, as it is shown in Fig. 9.11, two layers (one for the bulk adhesive and the other for the adhesive/adherent interface) are simulated to model the water uptake in the adhesive and within the interface separately. Table 9.2 gives example values of the water uptake separately for the two mentioned layers.

Based on the inverse method explained above, it will be possible to measure the coefficient of the moisture diffusion for the interface of adhesive and substrate. Fig. 9.12 shows an example of the computed moisture uptake of XNR 6852-1 adhesive after 24 h of immersion.

Considering Fig. 9.8, across the line segments shown by [AB], [BC] and [CD], no mass transfer occurs. But in line [AD] the equilibrium moisture uptake is attained instantly as it is in contact with the aging environment. Using this methodology, both the average diffusion coefficient and the diffusion coefficient of the interface can be determined. They are shown in Table 9.3. Fig. 9.13 shows a typical numerical result compared with the experimental data. As it is shown in Fig. 9.13, good agreement is observed between the experimental results and the numerical values. The small dispersion observed for the experimental points is expected due to the method used.

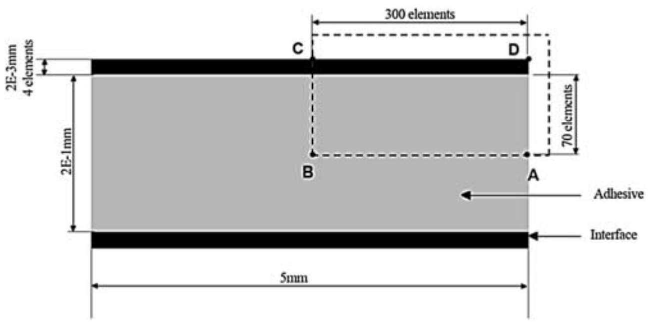

FIG. 9.11 Geometry of the model used to predict interfacial water uptake.

TABLE 9.2 Moisture diffusion parameters of the joints bonded the adhesive studied.

	Aging environment	$D_{average}$ (m^2/s) Obtained with 1D model	$D_{interface}$ (m^2/s) Obtained with the 2D model
XNR 6852-1	Distilled water	6.0E-13	8.0E-14
	Salt water	6.0E-13	8.0E-14

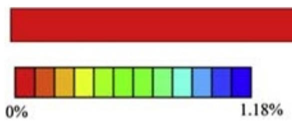

FIG. 9.12 Numerical prediction of the moisture profile of XNR 6852-1 after 24 h of aging. Upper bar represents one-quarter of the adhesive layer while the lower bar represents a color coded scale of the predicted moisture uptake.

TABLE 9.3 Moisture diffusion parameters of an adhesive.

	Aging environment	D_1 (m^2/s)	mwt_1	D_1 (m^2/s)	mwt_2
XNR 6852-1	Distilled water	6.0E-13	0.0095	8.0E-14	0.0023
	Salt water	6.0E-13	0.0080	8.0E-14	0.0006

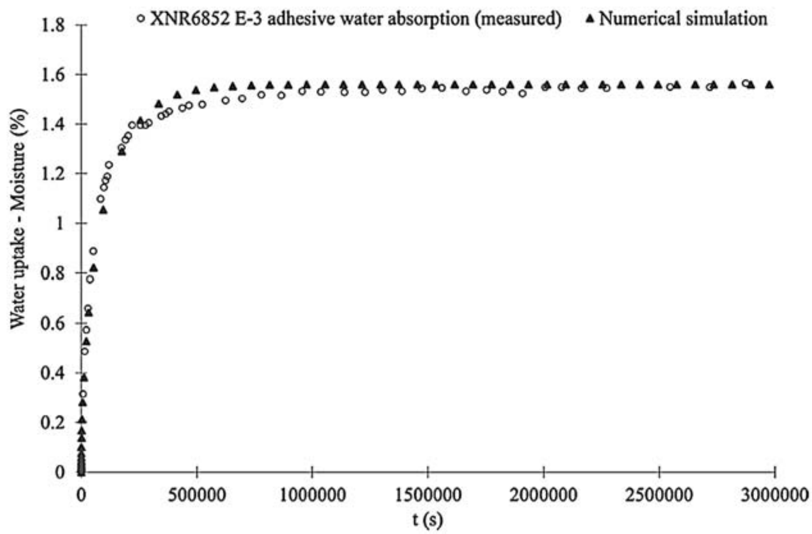

FIG. 9.13 Example of experimental data and numerical prediction for one of the cases under study (XNR 6852 E-3 in deionized water).

As it was explained earlier, to simulate the degradation of adhesive properties as a function of the aging conditions, the cohesive properties should be defined as a function of humidity level. Viana et al. [132,133] studied the effect of moisture and temperature on cohesive properties of adhesive materials. They proposed an empirical relation to update the maximum traction and the fracture toughness as a function of humidity level and temperature. Eqs. (9.18)–(9.20) give an example of these relations where the T_g is the glass transition temperature of the adhesive, σ_y is the maximum traction (yield stress of the adhesive), M is the moisture percentage absorbed by the adhesive and G_c is the fracture energy. The coefficients shown in these equations have been obtained experimentally.

$$T_g = 117.4 - 8.23\,(M)^4 \tag{9.18}$$

$$\sigma_y = -15.4 - 0.75(T - T_g) \tag{9.19}$$

$$G_c = 8.46 - 2.27 \times 10^{-4}(T - T_g)^2 \tag{9.20}$$

Fig. 9.14 shows the comparison of T_g with experimental values. Figs. 9.14 and 9.15 also show the variation of T_g and mechanical properties of the adhesive.

Considering the line fitted with the experimental data, the value of T_g as a function of water uptake can be obtained for any arbitrary humidity level. Accordingly, using Eqs. (9.19) and (9.20), the values of maximum traction and the fracture energy can be calculated as shown in Fig. 9.15.

Based on the results shown in Figs. 9.14 and 9.15, the properties of the adhesive depend on the testing temperature and the T_g of the adhesive. It is important to notice that the values obtained for the fracture toughness correspond only to cohesive fracture of the adhesive and not the interfacial failure.

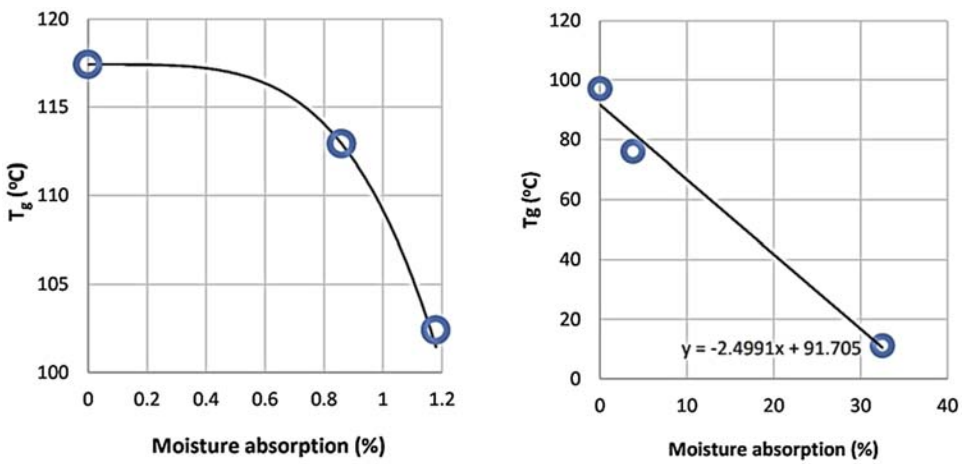

FIG. 9.14 Variation of the T_g with moisture absorbed by the adhesive.

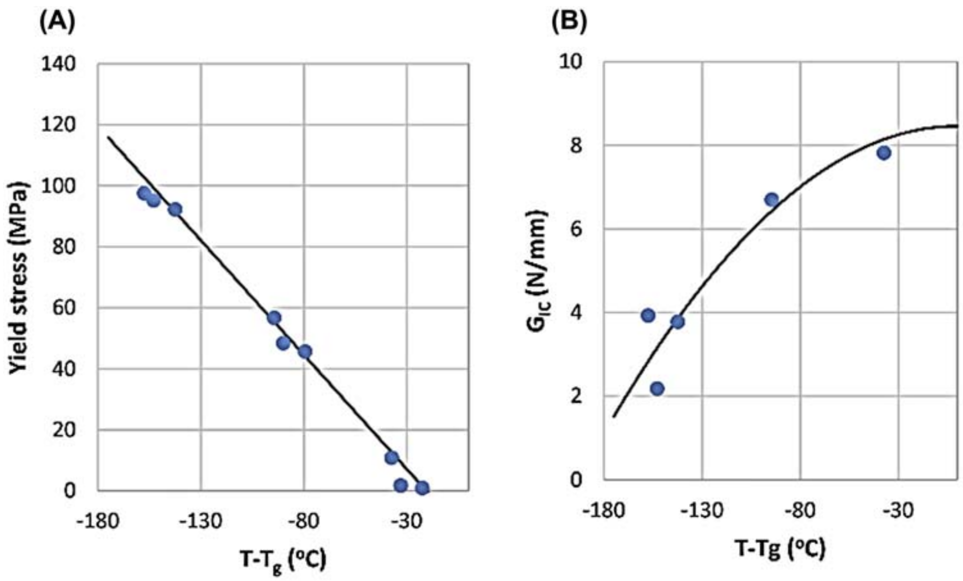

FIG. 9.15 Variation of the yield stress and mode I fracture toughness of the XNR6852 adhesive with $T-T_g$: Column (A) Variation of the strain rate Column (B) Variation of mode I fracture toughness.

Based on the published results it is shown that the simulation of environmental degradation of adhesive materials due to the water absorption is possible even for the more complex conditions where the effect of aging is combined by temperature effect for loaded or unloaded specimens. However, to obtain a precise result out of the numerical simulation, the properties of the adhesive should be defined correctly.

Acknowledgments

The authors wish to acknowledge the funding provided by Portuguese Foundation for Science and Technology (FCT), under the individual grants SFRH/BPD/96992/2013, as well as the funding provided by Ministério da Ciência, Tecnologia e Ensino Superior — Fundação para a Ciência e a Tecnologia (Portugal), under the projects POCI-01-0145-FEDER-028351, POCI-01-0145-FEDER-028473 and POCI-01-0145-FEDER-029839.

References

[1] L.F.M. da Silva, A. Öchsner, R.D. Adams, Handbook of Adhesion Technology, Springer Berlin Heidelberg, 2011.
[2] A.J. Kinloch, Adhesion and Adhesives: Science and Technology, Springer, 1987.
[3] R. Adams, J. Harris, A critical assessment of the block impact test for measuring the impact strength of adhesive bonds, International Journal of Adhesion and Adhesives 16 (2) (1996) 61—71.
[4] O. Volkersen, Die Nietkraftverteilung in zugbeanspruchten Nietverbindungen mit konstanten Laschenquerschnitten, Luftfahrtforschung 15 (1/2) (1938) 41—47.
[5] M. Goland, E. Reissner, The stresses in cemented joints, Journal of Applied Mechanics 11 (1) (1944) A17—A27.
[6] I. Ojalvo, H. Eidinoff, Bond thickness effects upon stresses in single-lap adhesive joints, AIAA Journal 16 (3) (1978) 204—211.

[7] L. Hart-Smith, Adhesive-bonded Double-Lap Joints, National Aeronautics and Space Administration, 1973.
[8] R.D. Adams, J. Comyn, W.C. Wake, Structural Adhesive Joints in Engineering, Springer Science & Business Media, 1997.
[9] A. Crocombe, Global yielding as a failure criterion for bonded joints, International Journal of Adhesion and Adhesives 9 (3) (1989) 145−153.
[10] G.R. Wooley, D.R. Carver, Stress Concentration Factors for Bonded Lap Joints, Louisiana State University and Agricultural and Mechanical College. Division of Engineering Research, 1971.
[11] R. Adams, N. Peppiatt, Stress analysis of adhesive-bonded lap joints, Journal of Strain Analysis 9 (3) (1974) 185−196.
[12] A. Akhavan-Safar, et al., Residual static strength and the fracture initiation path in adhesively bonded joints weakened with interfacial edge pre-crack, Journal of Adhesion Science and Technology 32 (18) (2018) 2019−2040.
[13] S. Rastegar, et al., Prediction of the critical stress intensity factor of single-lap adhesive joints using a coupled ratio method and an analytical model, Proceedings of the Institution of Mechanical Engineers, Part L: Journal of Materials: Design and Applications 233 (7) (2019) 1393−1403.
[14] M.N. Cavalli, M.D. Thouless, The effect of damage nucleation on the toughness of an adhesive joint, The Journal of Adhesion 76 (1) (2001) 75−92.
[15] C. Liljedahl, et al., Damage modelling of adhesively bonded joints, International Journal of Fracture 141 (1−2) (2006) 147−161.
[16] R.D.S.G. Campilho, M.F.S.F. De Moura, J.J.M.S. Domingues, Stress and failure analyses of scarf repaired CFRP laminates using a cohesive damage model, Journal of Adhesion Science and Technology 21 (9) (2007) 855−870.
[17] J. Monteiro, et al., Mode II modeling of adhesive materials degraded by fatigue loading using cohesive zone elements, Theoretical and Applied Fracture Mechanics 103 (2019) 102253.
[18] M. Costa, et al., A cohesive zone element for mode I modelling of adhesives degraded by humidity and fatigue, International Journal of Fatigue 112 (2018) 173−182.
[19] J. Valente, et al., Adhesive joint analysis under tensile impact loads by cohesive zone modelling, Composite Structures 222 (2019) 110894.
[20] M. Heidari-Rarani, A. Ghasemi, Appropriate shape of cohesive zone model for delamination propagation in ENF specimens with R-curve effects, Theoretical and Applied Fracture Mechanics 90 (2017) 174−181.
[21] G.I. Barenblatt, The formation of equilibrium cracks during brittle fracture. General ideas and hypotheses. Axially-symmetric cracks, Journal of Applied Mathematics and Mechanics 23 (3) (1959) 622−636.
[22] D.S. Dugdale, Yielding of steel sheets containing slits, Journal of the Mechanics and Physics of Solids 8 (2) (1960) 100−104.
[23] G. Alfano, M.A. Crisfield, Finite element interface models for the delamination analysis of laminated composites: mechanical and computational issues, International Journal for Numerical Methods in Engineering 50 (7) (2001) 1701−1736.
[24] O. Allix, A. Corigliano, Modeling and simulation of crack propagation in mixed-modes interlaminar fracture specimens, International Journal of Fracture 77 (2) (1996) 111−140.
[25] J. Chen, Predicting progressive delamination of stiffened fibre-composite panel and repaired sandwich panel by decohesion models, Journal of Thermoplastic Composite Materials 15 (5) (2002) 429−442.
[26] N. Chandra, et al., Some issues in the application of cohesive zone models for metal−ceramic interfaces, International Journal of Solids and Structures 39 (10) (2002) 2827−2855.
[27] R.D.S.G. Campilho, M.F.S.F. de Moura, J.J.M.S. Domingues, Using a cohesive damage model to predict the tensile behaviour of CFRP single-strap repairs, International Journal of Solids and Structures 45 (5) (2008) 1497−1512.
[28] A.M.G. Pinto, et al., Single-lap joints of similar and dissimilar adherends bonded with an Acrylic adhesive, The Journal of Adhesion 85 (6) (2009) 351−376.
[29] A. De Morais, Novel cohesive beam model for the End-Notched Flexure (ENF) specimen, Engineering Fracture Mechanics 78 (17) (2011) 3017−3029.
[30] N. Dourado, et al., Bilinear approximations to the mode II delamination cohesive law using an inverse method, Mechanics of Materials 49 (2012) 42−50.
[31] F. Moroni, et al., A numerical investigation on the interlaminar strength of nano modified composite interfaces, Composites Part B: Engineering 55 (2013) 635−641.

[32] G. Giuliese, et al., Cohesive zone modelling of delamination response of a composite laminate with interleaved nylon 6, 6 nanofibres, Composites Part B: Engineering 78 (2015) 384–392.
[33] G. Alfano, On the influence of the shape of the interface law on the application of cohesive-zone models, Composites Science and Technology 66 (6) (2006) 723–730.
[34] P. Feraren, H.M. Jensen, Cohesive zone modelling of interface fracture near flaws in adhesive joints, Engineering Fracture Mechanics 71 (15) (2004) 2125–2142.
[35] R.D.S.G. Campilho, et al., Adhesively bonded repair proposal for wood members damaged by horizontal shear using carbon-epoxy patches, The Journal of Adhesion 86 (5–6) (2010) 649–670.
[36] J. Williams, H. Hadavinia, Analytical solutions for cohesive zone models, Journal of the Mechanics and Physics of Solids 50 (4) (2002) 809–825.
[37] M. De Moura, A. De Morais, Equivalent crack based analyses of ENF and ELS tests, Engineering Fracture Mechanics 75 (9) (2008) 2584–2596.
[38] A. Biel, U. Stigh, Effects of constitutive parameters on the accuracy of measured fracture energy using the DCB-specimen, Engineering Fracture Mechanics 75 (10) (2008) 2968–2983.
[39] P.A. Gustafson, A.M. Waas, The influence of adhesive constitutive parameters in cohesive zone finite element models of adhesively bonded joints, International Journal of Solids and Structures 46 (10) (2009) 2201–2215.
[40] R.D.S.G. Campilho, et al., Strength prediction of single- and double-lap joints by standard and extended finite element modelling, International Journal of Adhesion and Adhesives 31 (5) (2011) 363–372.
[41] D. Xie, et al., Discrete cohesive zone model to simulate static fracture in 2D triaxially braided carbon fiber composites, Journal of Composite Materials 40 (22) (2006) 2025–2046.
[42] G. Ji, et al., Effects of adhesive thickness on global and local mode-I interfacial fracture of bonded joints, International Journal of Solids and Structures 47 (18) (2010) 2445–2458.
[43] A. Turon, et al., An engineering solution for mesh size effects in the simulation of delamination using cohesive zone models, Engineering Fracture Mechanics 74 (10) (2007) 1665–1682.
[44] A. Akhavan-Safar, et al., The role of T-stress and stress triaxiality combined with the geometry on tensile fracture energy of brittle adhesives, International Journal of Adhesion and Adhesives 87 (2018) 12–21.
[45] K. Leffler, K.S. Alfredsson, U. Stigh, Shear behaviour of adhesive layers, International Journal of Solids and Structures 44 (2) (2007) 530–545.
[46] H. Chai, On the correlation between the mode I failure of adhesive joints and laminated composites, Engineering Fracture Mechanics 24 (3) (1986) 413–431.
[47] W.D. Bascom, R.L. Cottington, Effect of temperature on the adhesive fracture behavior of an elastomer-epoxy resin, The Journal of Adhesion 7 (4) (1976) 333–346.
[48] T. Carlberger, U. Stigh, Influence of layer thickness on cohesive properties of an epoxy-based adhesive—an experimental study, The Journal of Adhesion 86 (8) (2010) 816–835.
[49] L.F. da Silva, et al., Mode II fracture toughness of a brittle and a ductile adhesive as a function of the adhesive thickness, The Journal of Adhesion 86 (9) (2010) 891–905.
[50] P. Mangalgiri, W.S. Johnson, R. Everett Jr., Effect of adherend thickness and mixed mode loading on debond growth in adhesively bonded composite joints, The Journal of Adhesion 23 (4) (1987) 263–288.
[51] M.R. Ayatollahi, et al., Effect of notch length and pre-crack size on mode II fracture energy of brittle adhesives, Engineering Fracture Mechanics 212 (2019) 123–135.
[52] M.S. Kafkalidis, M.D. Thouless, The effects of geometry and material properties on the fracture of single lap-shear joints, International Journal of Solids and Structures 39 (17) (2002) 4367–4383.
[53] Z. Zou, et al., Modelling interlaminar and intralaminar damage in filament-wound pipes under quasi-static indentation, Journal of Composite Materials 36 (4) (2002) 477–499.
[54] R.D.S.G. Campilho, et al., Modelling the tensile fracture behaviour of CFRP scarf repairs, Composites Part B: Engineering 40 (2) (2009) 149–157.
[55] L. Daudeville, O. Allix, P. Ladeveze, Delamination analysis by damage mechanics: some applications, Composites Engineering 5 (1) (1995) 17–24.
[56] P.P. Camanho, C.G. Davila, M. De Moura, Numerical simulation of mixed-mode progressive delamination in composite materials, Journal of Composite Materials 37 (16) (2003) 1415–1438.
[57] A. Hillerborg, M. Modéer, P.-E. Petersson, Analysis of crack formation and crack growth in concrete by means of fracture mechanics and finite elements, Cement and Concrete Research 6 (6) (1976) 773–781.
[58] J. Rice, The Mechanics of Earthquake Rupture, Division of Engineering, Brown University Providence, 1979.

[59] M.L. Falk, A. Needleman, J.R. Rice, A Critical Evaluation of Cohesive Zone Models of Dynamic Fracture, 2001.
[60] G. Irwin, Plastic Zone Near a Crack and Fracture Toughness, 1997.
[61] N. Moës, T. Belytschko, Extended finite element method for cohesive crack growth, Engineering Fracture Mechanics 69 (7) (2002) 813–833.
[62] R.D.S.G. Campilho, et al., Tensile behaviour of three-dimensional carbon-epoxy adhesively bonded single- and double-strap repairs, International Journal of Adhesion and Adhesives 29 (6) (2009) 678–686.
[63] T. Belytschko, T. Black, Elastic crack growth in finite elements with minimal remeshing, International Journal for Numerical Methods in Engineering 45 (5) (1999) 601–620.
[64] S. Mohammadi, Extended Finite Element Method for Fracture Analysis of Structures, Blackwell Publishing, New Jersey, USA, 2008.
[65] A. Mubashar, I. Ashcroft, A. Crocombe, Modelling damage and failure in adhesive joints using a combined XFEM-cohesive element methodology, The Journal of Adhesion 90 (8) (2014) 682–697.
[66] F. Stuparu, et al., A combined cohesive elements—XFEM approach for analyzing crack propagation in bonded joints, The Journal of Adhesion 92 (7–9) (2016) 535–552.
[67] C. Daux, et al., Arbitrary branched and intersecting cracks with the extended finite element method, International Journal for Numerical Methods in Engineering 48 (12) (2000) 1741–1760.
[68] N. Sukumar, et al., Extended finite element method for three-dimensional crack modelling, International Journal for Numerical Methods in Engineering 48 (11) (2000) 1549–1570.
[69] T. Elguedj, A. Gravouil, A. Combescure, Appropriate extended functions for X-FEM simulation of plastic fracture mechanics, Computer Methods in Applied Mechanics and Engineering 195 (7–8) (2006) 501–515.
[70] J. Dolbow, N. Moës, T. Belytschko, An extended finite element method for modeling crack growth with frictional contact, Computer Methods in Applied Mechanics and Engineering 190 (51–52) (2001) 6825–6846.
[71] A. Khoei, M. Nikbakht, Contact friction modeling with the extended finite element method (X-FEM), Journal of Materials Processing Technology 177 (1–3) (2006) 58–62.
[72] Y. Xu, H. Yuan, Computational analysis of mixed-mode fatigue crack growth in quasi-brittle materials using extended finite element methods, Engineering Fracture Mechanics 76 (2) (2009) 165–181.
[73] M. Sabsabi, E. Giner, F.J. Fuenmayor, Experimental fatigue testing of a fretting complete contact and numerical life correlation using X-FEM, International Journal of Fatigue 33 (6) (2011) 811–822.
[73a] Ana VM. Rocha, et al., Fatigue crack growth analysis of different adhesive systems: effects of mode mixity and load level, Fatigue & Fracture of Engineering Materials & Structures 43 (2) (2020) 330–341.
[73b] Joao Monteiro, et al., Influence of mode mixity and loading conditions on the fatigue crack growth behaviour of an epoxy adhesive, Fatigue & Fracture of Engineering Materials & Structures 43 (2) (2020) 308–316.
[73c] A.V.M. Rocha, et al., Paris law relations for an epoxy-based adhesive, Proceedings of the Institution of Mechanical Engineers, Part L: Journal of Materials: Design and Applications 234 (2) (2020) 291–299.
[74] H. Kang, et al., Fatigue life predictions of adhesive joint of sheet steels, Procedia Engineering 133 (2015) 518–527.
[75] B. Schneider, V. Beber, M. Brede, Estimation of the lifetime of bonded joints under cyclic loads at different temperatures, The Journal of Adhesion 92 (7–9) (2016) 795–817.
[76] K. Ishii, et al., Evaluation of the fatigue strength of adhesively bonded CFRP/metal single and single-step double-lap joints, Composites Science and Technology 59 (11) (1999) 1675–1683.
[77] M. Imanaka, T. Iwata, Effect of adhesive layer thickness on fatigue strength of adhesively bonded butt, scarf and butterfly type butt joints, International Journal of Fracture 80 (4) (1996) R69–R76.
[78] A. Poursartip, N. Chinatambi, Fatigue damage development in notched (0 2/±45) s laminates, in: Composite Materials: Fatigue and Fracture, Second Volume, ASTM International, 1989.
[79] H. Masaki, et al., Effect of matrix resin on delamination fatigue crack growth in CFRP laminates, Engineering Fracture Mechanics 49 (1) (1994) 35–47.
[80] R. Alderliesten, How proper similitude can improve our understanding of crack closure and plasticity in fatigue, International Journal of Fatigue 82 (2016) 263–273.
[81] G. Allegri, et al., A new semi-empirical model for stress ratio effect on mode II fatigue delamination growth, Composites Part A: Applied Science and Manufacturing 42 (7) (2011) 733–740.
[82] J. Andersons, M. Hojo, S. Ochiai, Empirical model for stress ratio effect on fatigue delamination growth rate in composite laminates, International Journal of Fatigue 26 (6) (2004) 597–604.
[83] D. Atodaria, S. Putatunda, P. Mallick, A fatigue crack growth model for random fiber composites, Journal of Composite Materials 31 (18) (1997) 1838–1855.

[84] R. Ramkumar, J. Whitcomb, Characterization of mode I and mixed-mode delamination growth in T300/5208 graphite/epoxy, in: Delamination and Debonding of Materials, ASTM International, 1985.
[85] J. Munoz, U. Galvanetto, P. Robinson, On the numerical simulation of fatigue driven delamination with interface elements, International Journal of Fatigue 28 (10) (2006) 1136−1146.
[85a] A.V.M. Rocha, et al., Numerical analysis of mixed-mode fatigue crack growth of adhesive joints using CZM, Theoretical and Applied Fracture Mechanics 106 (2020) 102493.
[86] F. Moroni, A. Pirondi, Cohesive zone model simulation of fatigue debonding along interfaces, Procedia Engineering 10 (2011) 1829−1834.
[87] K. Katnam, et al., Load ratio effect on the fatigue behaviour of adhesively bonded joints: an enhanced damage model, The Journal of Adhesion 86 (3) (2010) 257−272.
[88] H. Khoramishad, et al., Predicting fatigue damage in adhesively bonded joints using a cohesive zone model, International Journal of Fatigue 32 (7) (2010) 1146−1158.
[89] F. Moroni, A. Pirondi, A procedure for the simulation of fatigue crack growth in adhesively bonded joints based on the cohesive zone model and different mixed-mode propagation criteria, Engineering Fracture Mechanics 78 (8) (2011) 1808−1816.
[90] R.S. Choudhry, et al., Damage in single lap joints of woven fabric reinforced polymeric composites subjected to transverse impact loading, International Journal of Impact Engineering 80 (2015) 76−93.
[91] L.F. Da Silva, R. Adams, M. Gibbs, Manufacture of adhesive joints and bulk specimens with high-temperature adhesives, International Journal of Adhesion and Adhesives 24 (1) (2004) 69−83.
[92] M.D. Banea, et al., Effect of material on the mechanical behaviour of adhesive joints for the automotive industry, Journal of Adhesion Science and Technology 31 (6) (2017) 663−676.
[93] R. Zaera, et al., Modelling of the adhesive layer in mixed ceramic/metal armours subjected to impact, Composites Part A: Applied Science and Manufacturing 31 (8) (2000) 823−833.
[94] T. Sawa, et al., A study on evaluation of impact strength of adhesive joints subjected to impact shear loadings, in: ASME 2008 International Mechanical Engineering Congress and Exposition, American Society of Mechanical Engineers, 2008.
[95] L. Liao, et al., 3-D FEM stress analysis and strength evaluation of single-lap adhesive joints subjected to impact tensile loads, International Journal of Adhesion and Adhesives 31 (7) (2011) 612−619.
[96] L. Liao, T. Sawa, C. Huang, Experimental and FEM studies on mechanical properties of single-lap adhesive joint with dissimilar adherends subjected to impact tensile loadings, International Journal of Adhesion and Adhesives 44 (2013) 91−98.
[97] Y. Goda, T. Sawa, Study on the effect of strain rate of adhesive material on the stress state in adhesive joints, The Journal of Adhesion 87 (7−8) (2011) 766−779.
[98] G. Viana, et al., Strain rate dependence of adhesive joints for the automotive industry at low and high temperatures, Journal of Adhesion Science and Technology 32 (19) (2018) 2162−2179.
[99] L. Goglio, et al., High strain-rate compression and tension behaviour of an epoxy bi-component adhesive, International Journal of Adhesion and Adhesives 28 (7) (2008) 329−339.
[100] I. Higuchi, T. Sawa, H. Suga, Three-dimensional finite element analysis of single-lap adhesive joints under impact loads, Journal of Adhesion Science and Technology 16 (12) (2002) 1585−1601.
[101] T. Sawa, I. Higuchi, H. Suga, Three-dimensional finite element stress analysis of single-lap adhesive joints of dissimilar adherends subjected to impact tensile loads, Journal of Adhesion Science and Technology 17 (16) (2003) 2157−2174.
[102] I. Higuchi, T. Sawa, H. Suga, Three-dimensional finite element analysis of single-lap adhesive joints subjected to impact bending moments, Journal of Adhesion Science and Technology 16 (10) (2002) 1327−1342.
[103] G. Challita, R. Othman, Finite-element analysis of SHPB tests on double-lap adhesive joints, International Journal of Adhesion and Adhesives 30 (4) (2010) 236−244.
[104] R. Hazimeh, et al., Finite element analysis of adhesively bonded composite joints subjected to impact loadings, International Journal of Adhesion and Adhesives 56 (2015) 24−31.
[105] X. Yang, et al., Modeling of high strength steel joints bonded with toughened adhesive for vehicle crash simulations, International Journal of Adhesion and Adhesives 39 (2012) 21−32.
[106] G. Dean, G. Lord, B. Duncan, Comparison of the Measured and Predicted Performance of Adhesive Joints under Impact − Report (A)206, Centre for Materials Measurement and Technology, Great Britain, 1999. National Physical Laboratory.

[107] M. Zgoul, A.D. Crocombe, Numerical modelling of lap joints bonded with a rate-dependent adhesive, International Journal of Adhesion and Adhesives 24 (4) (2004) 355−366.
[108] T. Carlberger, U. Stigh, An explicit FE-model of impact fracture in an adhesive joint, Engineering Fracture Mechanics 74 (14) (2007) 2247−2262.
[109] A. Haufe, et al., Modelling of weld and adhesive connections in crashworthiness applications with LS-DYNA, in: Proceedings of the NAFEMS Seminar "Simulation of Connections and Joints in Structures". Wiesbaden, Germany, 2010.
[109a] Paulo DP. Nunes, et al., Numerical assessment of strain rate in an adhesive layer throughout double cantilever beam and end notch flexure tests, Proceedings of the Institution of Mechanical Engineers, Part E: Journal of Process Mechanical Engineering (2020), 0954408920916007.
[109b] C.S.P. Borges, et al., A strain rate dependent cohesive zone element for mode I modeling of the fracture behavior of adhesives, Proceedings of the Institution of Mechanical Engineers, Part L: Journal of Materials: Design and Applications 234 (4) (2020) 610−621.
[110] Y.J. Weitsman, Fluid Effects in Polymers and Polymeric Composites, Springer Science & Business Media, 2011.
[111] Y. Hua, et al., Modelling environmental degradation in EA9321-bonded joints using a progressive damage failure model, The Journal of Adhesion 82 (2) (2006) 135−160.
[112] X. Han, et al., The effect of a hot−wet environment on adhesively bonded joints under a sustained load, The Journal of Adhesion 90 (5−6) (2014) 420−436.
[113] Y. Hua, et al., Continuum damage modelling of environmental degradation in joints bonded with EA9321 epoxy adhesive, International Journal of Adhesion and Adhesives 28 (6) (2008) 302−313.
[114] S. Sugiman, A. Crocombe, I. Aschroft, Modelling the static response of unaged adhesively bonded structures, Engineering Fracture Mechanics 98 (2013) 296−314.
[115] C. Liljedahl, et al., Modelling the environmental degradation of the interface in adhesively bonded joints using a cohesive zone approach, The Journal of Adhesion 82 (11) (2006) 1061−1089.
[116] A. Crocombe, et al., Predicting the residual strength for environmentally degraded adhesive lap joints, International Journal of Adhesion and Adhesives 26 (5) (2006) 325−336.
[117] C. Liljedahl, et al., The effect of residual strains on the progressive damage modelling of environmentally degraded adhesive joints, Journal of Adhesion Science and Technology 19 (7) (2005) 525−547.
[118] S. Sugiman, A. Crocombe, I. Aschroft, Experimental and numerical investigation of the static response of environmentally aged adhesively bonded joints, International Journal of Adhesion and Adhesives 40 (2013) 224−237.
[119] X. Han, et al., The strength prediction of adhesive single lap joints exposed to long term loading in a hostile environment, International Journal of Adhesion and Adhesives 55 (2014) 1−11.
[120] A. Ilioni, et al., Prediction of mechanical behaviour of a bulk epoxy adhesive in a marine environment, The Journal of Adhesion 95 (1) (2019) 64−84.
[121] J. Comyn, Kinetics and mechanism of environmental attack, in: Durability of Structural Adhesives, 1983, pp. 85−131.
[122] Y. Lin, X. Chen, Moisture sorption−desorption−resorption characteristics and its effect on the mechanical behavior of the epoxy system, Polymer 46 (25) (2005) 11994−12003.
[123] A. Szekeres, Analogy between heat and moisture: thermo-hygro-mechanical tailoring of composites by taking into account the second sound phenomenon, Computers and Structures 76 (1−3) (2000) 145−152.
[124] S. Roy, et al., A model for the diffusion of moisture in adhesive joints. Part III: numerical simulations, The Journal of Adhesion 27 (1) (1989) 41−62.
[125] H.A. Israr, K.J. Wong, S. Rivallant, Experimental and numerical investigation of humid ageing effects on CFRP laminates crashworthiness behaviours, International Journal of Crashworthiness (2019) 1−12.
[126] A. Crocombe, Durability modelling concepts and tools for the cohesive environmental degradation of bonded structures, International Journal of Adhesion and Adhesives 17 (3) (1997) 229−238.
[127] M. Bordes, et al., Prediction of long term strength of adhesively bonded steel/epoxy joints in sea water, International Journal of Adhesion and Adhesives 29 (6) (2009) 595−608.
[128] W. Loh, et al., Modelling anomalous moisture uptake, swelling and thermal characteristics of a rubber toughened epoxy adhesive, International Journal of Adhesion and Adhesives 25 (1) (2005) 1−12.
[129] C. Liljedahl, et al., Modelling the environmental degradation of adhesively bonded aluminium and composite joints using a CZM approach, International Journal of Adhesion and Adhesives 27 (6) (2007) 505−518.

[130] M. Creyf, et al., A novel finite element model methodology for the generic modelling of adhesive ageing, in: IRF2018: Proceedings of the 6th International Conference on Integrity-Reliability-Failure, 2018. INEGI-INST engenharia mecanica e gestao industrial.
[131] A. Mubashar, et al., Modelling cyclic moisture uptake in an epoxy adhesive, The Journal of Adhesion 85 (10) (2009) 711−735.
[132] G. Viana, et al., Behaviour of environmentally degraded epoxy adhesives as a function of temperature, The Journal of Adhesion 93 (1−2) (2017) 95−112.
[133] G. Viana, et al., Moisture and temperature degradation of double cantilever beam adhesive joints, Journal of Adhesion Science and Technology 31 (16) (2017) 1824−1838.

This page intentionally left blank

CHAPTER

10

Hybrid joining techniques

H. Fricke, T. Vallée

Fraunhofer Institute for Manufacturing Technology and Advanced Materials IFAM, Bremen, Germany

1. Introduction

There are several good reasons why mechanical or thermal connections should be supplemented by adhesive joints [1]: easing stresses, achieving a smoother load transfer [2], raising load capacity, increasing fatigue life [3], reducing vibrations [4], sealing off gases and liquids [5], enhancing corrosion resistance [6] etc. This holds true if looking at hybrid joints from the perspective of bonded joints, where the combination of mechanical/thermal fasteners may greatly simplify manufacturing by fixing adherends while curing, offering additional resistance against peeling stresses, reducing creep deformations, providing load reserves beyond the glass transition temperature of adhesives etc. For the, by far not exhaustive, list of advantages of hybrid joints to be made available to practitioners, it is of paramount importance to understand the fundamental principles that rule the behavior of a hybrid joint, if compared to that of its elementary constituents. The following examples shall illustrate some of the aspects related to the structural behavior of the simplest form of hybrid joints, herein resulting from the combination of mechanical/thermal fastener and adhesive. All examples are taken from practical structural applications.

2. Bolted-bond hybrid joints for structural steel applications

For more than a century now, structural steel construction has relied on two joining techniques: welded and bolted connections. Both welded and bolted connections allow for the transmission of loads in all directions. Bolts, in particular, can act either in traction, in shear, or in a combination of both. For transmitting shear efforts, bolted connections mechanically may act on two different ways. Bolts may just block the relative displacement of the adherends; failure then results of either their capacity to transmit shear (depending upon the material it consist of, and its diameter), or of the load capacity of its adherends (material, thickness, and position of the bolt within the latter). Note that in this configuration

Advanced Joining Processes
https://doi.org/10.1016/B978-0-12-820787-1.00010-3

some relative displacement is always required to activate joint capacity, a feat frequently not wanted. On the other hand, in particular for structural steel applications, bolts may be tightened such to achieve a high level of pre-tensioning, literally pressing the two substrates against each other. In this case, load capacity is almost entirely dependent upon the friction between the adherends, which is expressed by the friction coefficient μ.

Pre-tensioned joints are relatively stiff, as no relative displacement is required to activate loads. The value of the friction coefficient μ is of paramount importance. However, to achieve substantial friction, particularly on the galvanized steel surfaces commonly considered in structural steel, significant surface preparation is required; whatever surface preparation is performed, codes severely limit the design value, typically to values around $\mu = 0.15$. Based upon above-said, it is tempting to consider a hybrid bolted-bonded connection in which bolts would be pre-tensioned, and in which the cured adhesive would conceptually ensure much higher "friction" between the adherends.

To test the concept, a series of experiments was conducted jointly by Fraunhofer IFAM (Bremen, Germany) and Fraunhofer IPG (Rostock, Germany) on large-scale double lap joints (DLJs) composed of two types of substrates: firstly, mirroring a typical situation encountered in civil engineering, galvanized S355 steel plates; secondly, to model a situation encountered in railway, S355 coated steel surfaces. For each type of surface preparation, two different configurations were compared: a purely pre-tensioned bolted connection (subsequently labeled pre-tensioned), and a hybrid connection similar to the first, but in which adhesive was applied at each interface (labeled hybrid). All double-lap joints consisted of inner adherends, 300 mm × 90 mm × 20 mm, and outer adherends 250 mm × 90 mm × 10 mm, overlapping by 120 mm, as shown in Fig. 10.1. All bolts used within this study consisted on M16—10.9, with corresponding sets of washers.

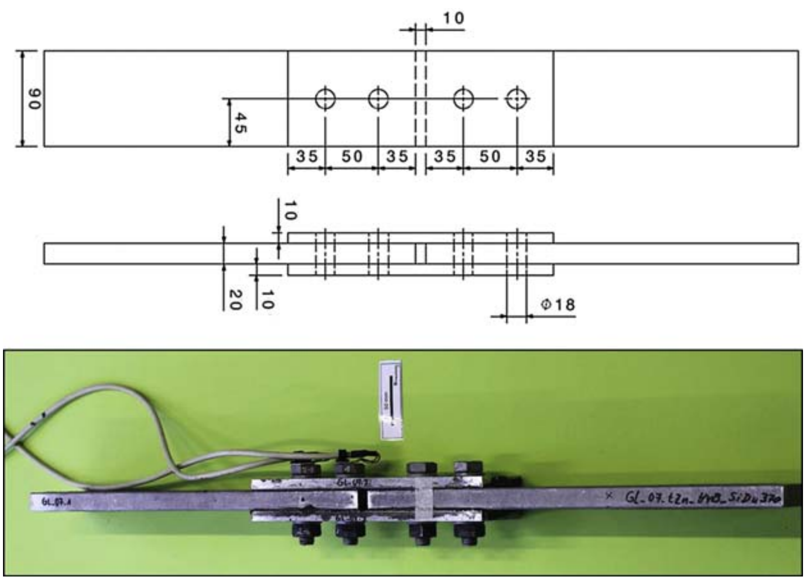

FIG. 10.1 Geometry of the double-lap joints, with the main dimensions in mm. *Credit: Fraunhofer IGP.*

For the hybrid joints, appropriate adhesives have been selected for both surfaces. Without entering in too much detail regarding this selection, it is reminded that adhesive bonding on galvanized surfaces is not trivial, and that is usually requires some form of surface preparation (up to grinding and etching). Through extensive screening, two suitable adhesives for bonding on galvanized steel were selected, which resulted in sufficient strength to rip-off the Zinc-layer, with just minimal surface cleaning by wiping with Isopropanol. Bonding on coated surfaces proved less critical, as the coating is mostly the weakest element that is torn off the steel surface.

Manufacturing of the pre-tensioned specimens, i.e. those without adhesive, consisted in assembling the bolt into the respective holes (with a clearance of 0.1 mm), and tightening. The level of pre-tensioning was measured with instrumented and calibrated bolts, up to a load-level of 100 kN per bolt. The same manufacturing procedure was used to assemble the hybrid joints, safe for the intermediary step of placing the adhesive at each interface. Because of the high pre-load of the bolts, almost all the adhesives was displaced outside the overlaps, safe for some μm. Additionally, all hybrid specimens were left to cure for as long as required by the technical datasheet of the respective adhesive. Joint capacities for the pre-tensioned and hybrid joints were determined in traction tests at a load rate of 1 mm/min, until failure. The load displacement curves, measured at the Fraunhofer IGP (Rostock, Germany) for representative samples are depicted in Fig. 10.1, and joint capacities tabulated in Table 10.1 (Fig. 10.2).

For the galvanized steel, load-displacement of the pre-stressed DLJ-joints exhibit the typical pattern of pre-tensioned bolted connections: loads increase non-linearly up to value of roughly 200 kN, to which corresponds a relative displacement of 0.05 mm, and then remains almost constant, as gliding occurs; the scattering is relatively low, with no obvious outliers. When looking at the hybrid DLJ with galvanized steel, the behavior is significantly stiffer, with almost all load-increase, up to 500 kN, occurring within the first 0.025 mm relative displacement; the scattering, however, is markedly higher, with joint capacities varying between slightly below 350 kN and almost 500 kN. The joint strength data summarized in Table 10.1, shows that, on average, the hybrid joints outperforms the "simple" pre-tensioned joints by +71%, for the adhesive SW7240, and +99%, for the adhesive SikaDur370, respectively. The results also show that, if formulating joint capacities in terms of coefficient of friction, a value of 0.49 would result for the pre-tensioned joint, adhesives achieve values well beyond 0.9, almost the double.

The same analysis performed on the coated steel DLJ allows for the following conclusions. Firstly, load displacement behavior of the pre-tensioned joints increase until a maximum of approx. 75 kN for a displacement roughly equal to 0.018 mm; discarding one outlier, data exhibits very little scattering. The load-displacement curves, shown in Fig. 10.1, of the hybrid joints, on the other hand, increase to much higher values, up to 325 kN at displacements between 0.025 and 0.050 mm. Joint capacities, listed in Table 10.2, show the following: hybrid joints systematically outperform the "simple" pre-tensioned joints fourfold. Expressing these results in terms of coefficient of friction show that the coating does not allow the pre-tensioned bolts to develop more than 0.17, while insertion of the adhesive raises it well beyond 0.75.

Summarizing, the investigations have shown the extremely beneficial effect that hybrid joints exhibit, if compared to "simple" pre-tensioned ones. If a careful adhesive selection is

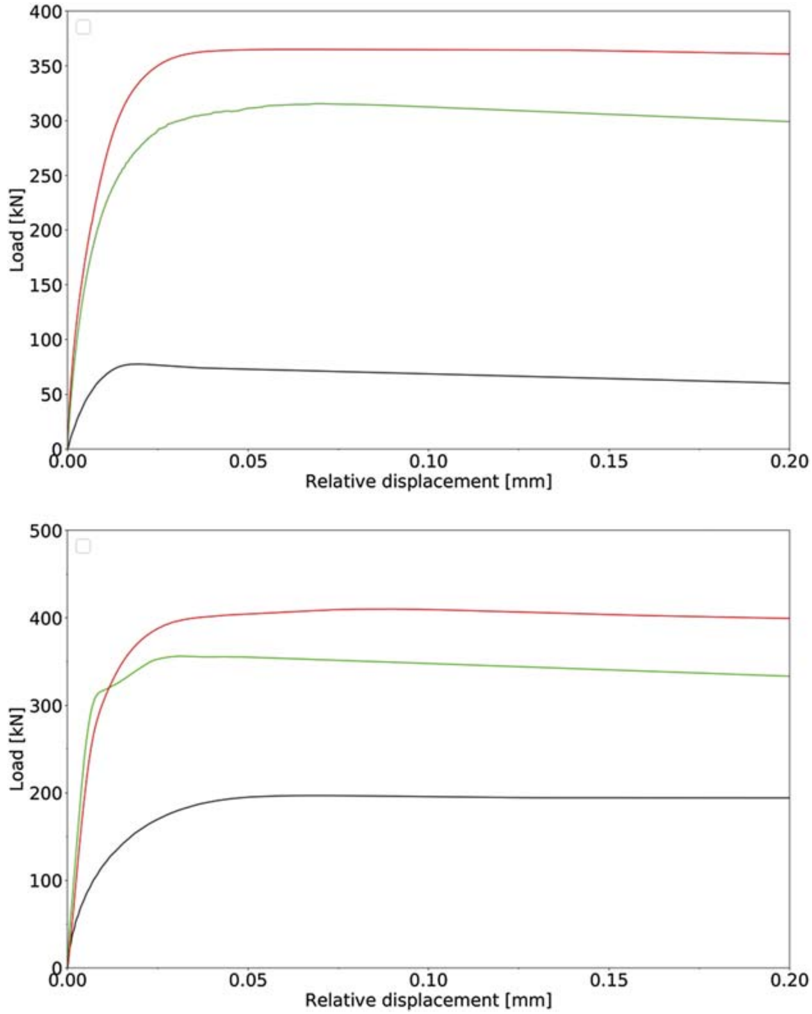

FIG. 10.2 Load displacement curves of typical representatives of the tested DLJ; (top) on galvanized steel surfaces; (bottom) on coated surfaces — black lines denote the pre-tensioned bolted DLJ, the green lines hybrid joints with SW7240, the red lines hybrid joints with SikaDur370.

TABLE 10.1 Experimental results of hybrid joints with galvanized adherends.

Series	Average [kN]	Std.-dev. [kN]	CoV [−]	5%-quantile [kN]
Pre-stressed bolts	214.08	16.17	0.08	185.94
Hybrid, with SW7240	371.53	12.41	0.03	349.19
Hybrid, with SikaDur370	426.03	51.61	0.12	336.23
Pre-stressed bolts	0.49	0.04	0.08	0.42
Hybrid, with SW7240	0.94	0.03	0.03	0.88
Hybrid, with SikaDur370	1.17	0.15	0.13	0.90

TABLE 10.2 Experimental results of hybrid joints with coated adherends.

Series	Average [kN]	Std.-dev. [kN]	CoV [−]	5%-quant. [kN]
Pre-stressed bolts	75.13	9.24	0.12	59.05
Hybrid, with SW7240	316.51	1.42	0.00	313.83
Hybrid, with SikaDur370	356.45	25.39	0.07	308.47
Pre-stressed bolts	0.17	0.02	0.12	0.13
Hybrid, with SW7240	0.78	0.02	0.02	0.76
Hybrid, with SikaDur370	0.91	0.07	0.08	0.78

performed, it is possible to consider the application of adhesives without extensive surface preparation, even on notoriously hard-to-bond surfaces. Joint capacities have shown an increase between 70% and 100% for the galvanized steel surface, depending upon the adhesive, corresponding to a coefficient of friction or roughly 1.0. For the coated surface, hybrid joints lead to increase joint capacities by a factor up to 4.75, with relatively low variation thereof: if expressed in terms of coefficient of friction, values have been increased at least four-fold.

3. Bolted-bond hybrid joints for G-FRP

As for steel, connections involving glass fiber reinforced polymers (G-FRPs) can either be bolted or adhesively bonded, or a combination thereof. While there is a large corpus of literature that deals with bolted [7–9] and bonded [10–12] connections, significantly less has been published for the combination thereof in form of hybrid joints [1,13].

3.1 Illustration on lap shear tests

To illustrate the differences between the different joining techniques, a typical G-FRP double-lap joint consisting of two 5 mm thick outer laminates 500 mm × 100 mm connected to a 10 mm thick inner laminates 500 mm × 100 mm, overlapped by 100 mm. All laminates were structural profiles delivered by Fiberline®. The following means of connection were considered: series (A) adhesively bonded connection, (B) bolted connection using 4M12–8.8, Bt) the same configuration as (B) but with pre-stressed bolts, (C) a combination of (A) and (B), i.e. loose bolts, and Ct) a combination of (A) and Bt), i.e. with pre-stressed bolts. All adhesive layers were 1 mm thick, using SikaDur330®. All joints were subjected to tensile tests, and were performed at the facilities of EPFL (Lausanne, Switzerland). Load-displacement curves are displayed in Fig. 10.3, failure modes in Fig. 10.4, and all ultimate loads reported in Tab. 10.3.

The samples with adhesively bonded joints only, series A, failed in a brittle manner, at an average ultimate load of roughly 145 kN. The joints connected through (loose) bolts, series B, required some initial displacement to develop strength; forces peaked around

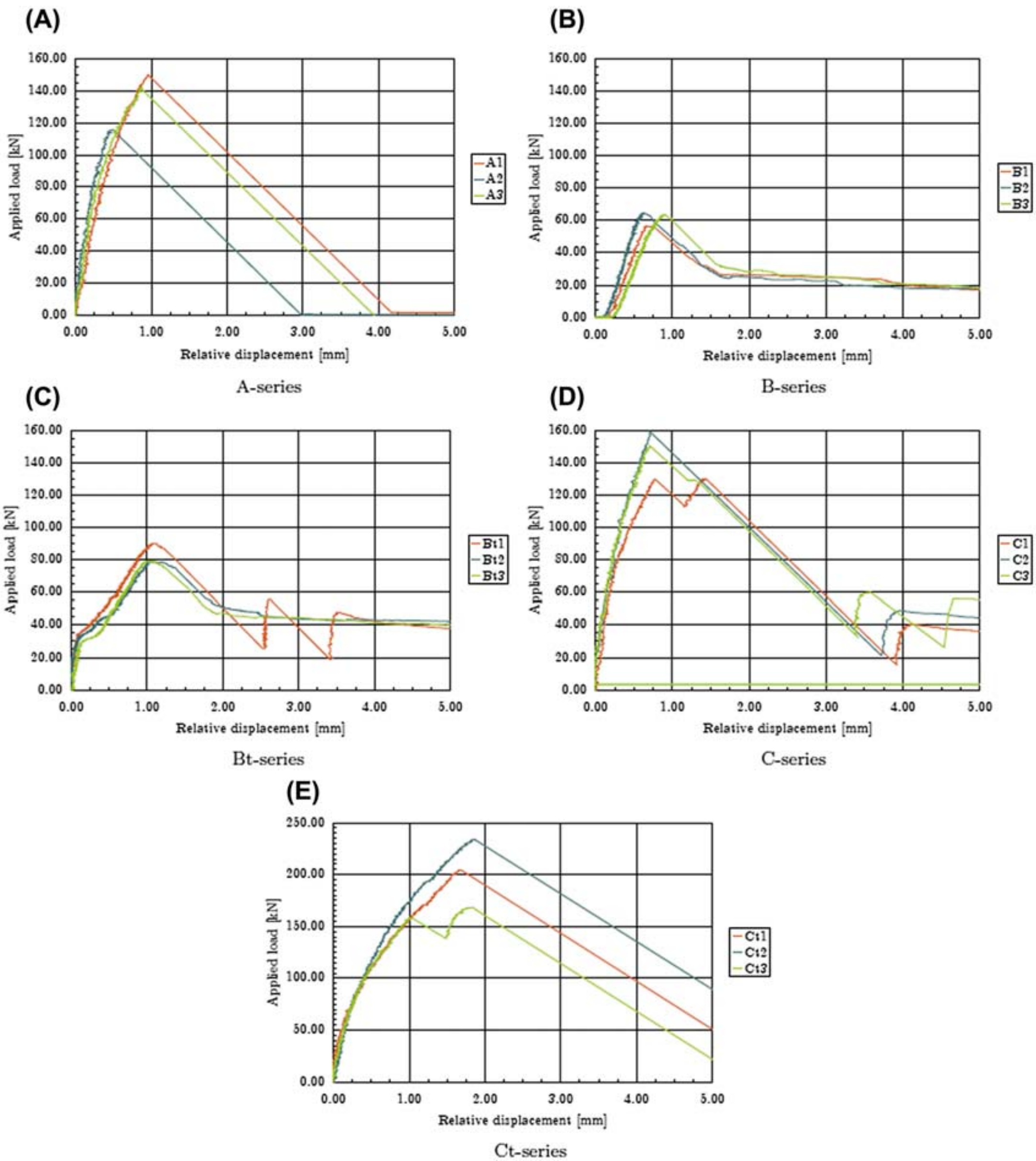

FIG. 10.3 Load-displacement curves of all test series. (A) A-series (B) B-series (C) Bt-series (D) C-series (E) Ct-series.

62 kN (with a small scattering), after which the loads dropped, but were maintained for long relative displacements. By pre-tensioning the bolts, i.e. series Bt, the load-displacement curves first exhibit a (small) stiff part, after which the slope becomes similar to that of series B, ultimate loads peak at values higher by 20 kN than those of the lose bolts, and the scattering

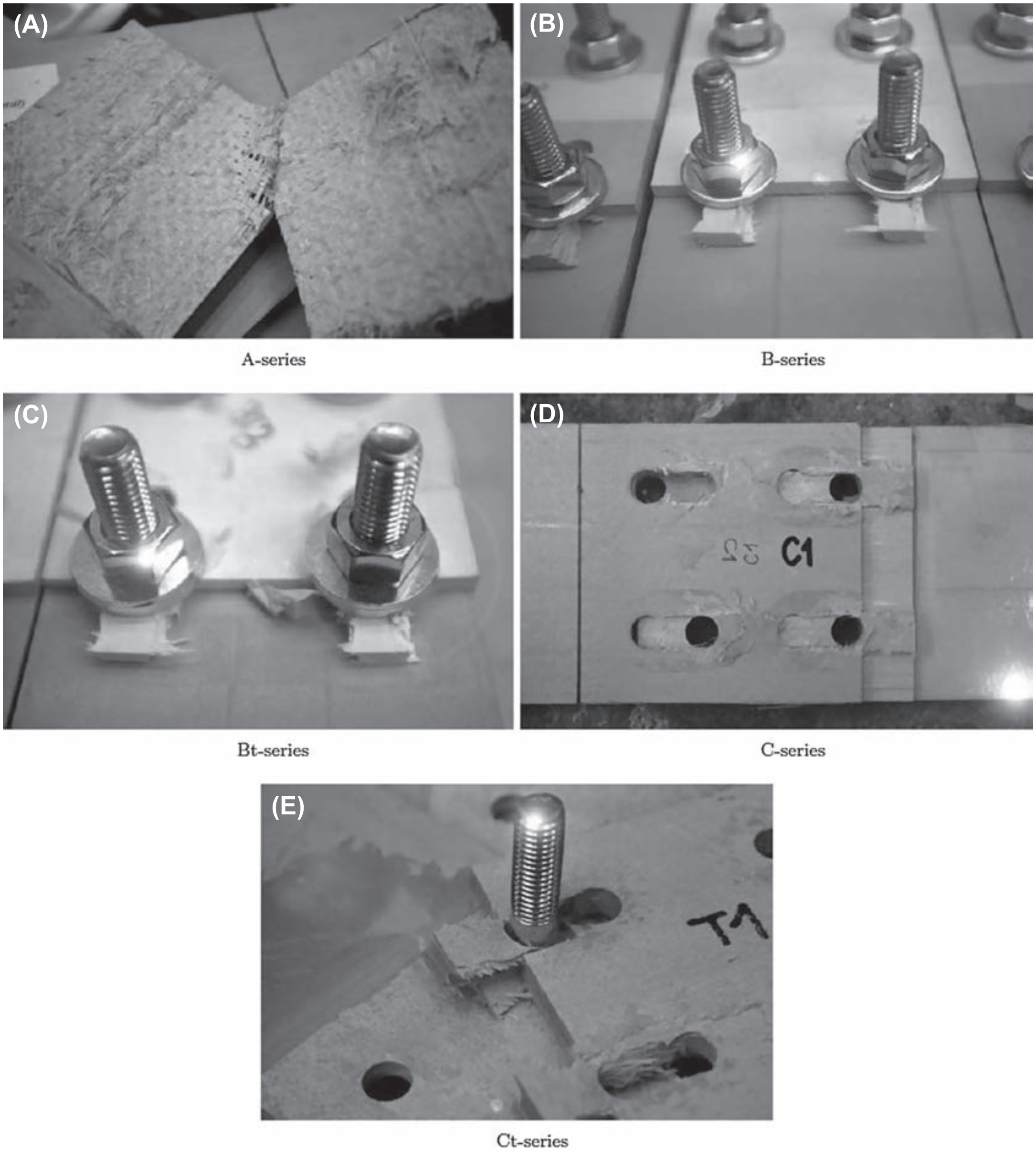

FIG. 10.4 Failure modes of all test series.

remains moderate. Combining the adhesively bonded connection with the lose bolts (series C) results in almost the very same behavior as that of the elementary bonded connection (series A); ultimate loads are almost the same. The mechanical behavior significantly improves if the adhesively bonded connection is combined with the pre-tensioned bolts.

TABLE 10.3 Summary of the experimental results. (A) A-series (B) B-series (C) Bt-series (D) C-series (E) Ct-series.

Series	Ultimate load ? Std.-Dev. [kN]
A, bonded	145.7 ± 3.3
B, bolted	62.3 ± 3.8
Bt, bolts pre-tensioned	82.7 ± 5.2
C, combination of A + B	146.3 ± 12.1
Ct, combination of A + Bt	202.0 ± 27.0

Series Ct features the highest ultimate loads reached throughout all experimental series, which represents an increase of almost 40% of the simple bonded joint); with a quasi linear load-displacement diagram, and a very sudden failure.

Adhesively bonded connections develop the forces in the joints continuously, from the first relative displacements on; and they are usually stiffer, thus little deformation is needed to generate significant forces. In bolted connection, on the other hand, borehole tolerances must first be overcome in order to achieve contact; loads and then generated by locally pressing against the composite substrate, which results in lower stiffness. Accordingly, in a combined bonded and bolted connection, relative displacement in first transformed into force by the adhesive, and the contribution of bolts is minor to inexistent.

To understand why pre-tensioning the bolts significantly enhances the behavior, it is of paramount importance to understand how adhesively bonded joints of G-FRP fail [10,14−16]. As illustrated in Fig. 10.5, failure occurs in the G-FRP by locally exceeding shear stresses and through-thickness tensile stresses. The contribution of these out-of-plane stresses is accounted for in the corresponding failure criteria, e.g. Tsai-Wu [17]. By pre-tensioning the bolts, the out-of-plane stresses at the ends of the overlaps are significantly reduced, ideally annulled, which results in moving away from the failure envelope of the failure criterion ruling the collapse of the joint (Fig. 10.6).

3.2 Illustration on tubular lap shear tests

In another study, tubular G-FRP profiles (Ø40mm, t = 3 mm) were connected to flat G-FRP profiles (100 mm × 3 mm) by means of an aluminum bracket. Three different joining methods were considered: (A) adhesive bonding, using a 1 mm layer of SikaForce7851® applied as illustrated by Fig. 10.7, (B) a series of M8−8.8 bolts, as shown in Fig. 10.7, and (C) a combination of (A) and (B) representing an hybrid joint.

The experimental results are reported in Table 10.4. Ultimate load of the bonded joints, series A, was around 83.3 kN, while the bolted one reached only 44.6 kN, on average. Combining adhesive bonding with bolts did not increase the joint capacity, which in essence achieved the same strength as the bonded one. The difference in capacities between test series A and C was statistically significant; multiple comparison tests showed that there was no significant difference in capacity between the adhesively bonded and the hybrid joints.

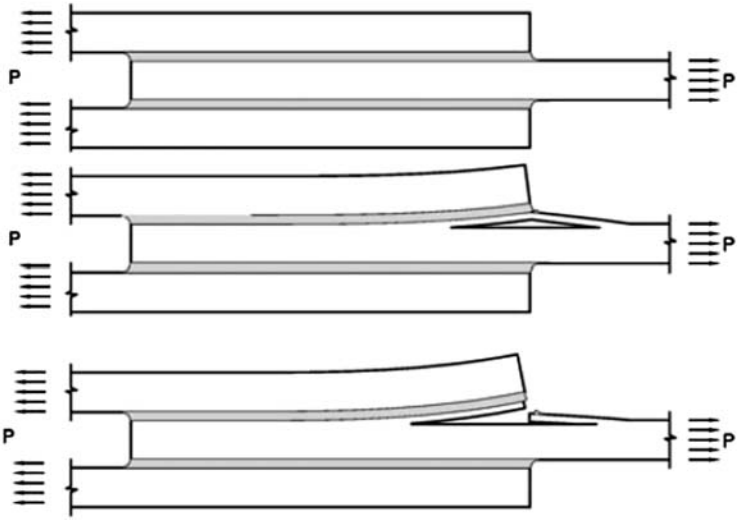

FIG. 10.5 Failure sequence of adhesively bonded joints composed of G-FRP.

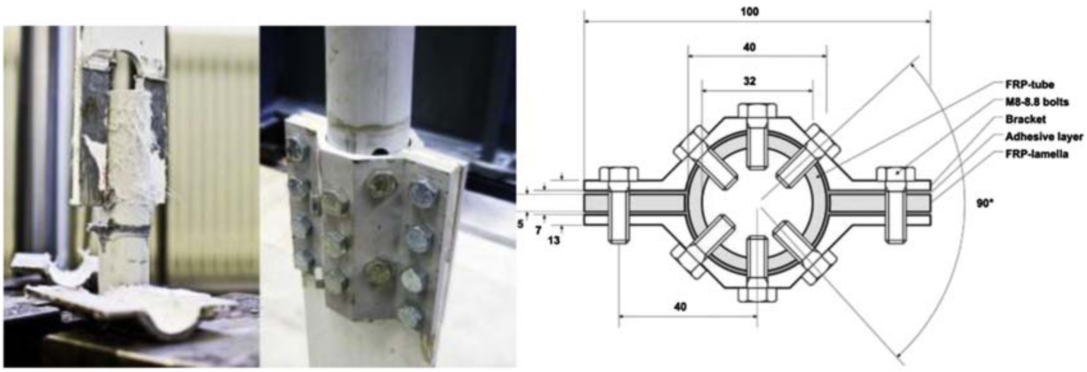

FIG. 10.6 The tubular lap joints (left) general pattern and failure modes, (right) cross-section with dimensions (in mm).

This example clearly shows that for hybrid joints, unless specifically optimized for that purpose, the superposition of means of connections does not necessarily lead to an improvement of the mechanical performance. In particular, that load bearing capacities cannot simply be added up.

4. Hybrid joints in timber engineering

Timber is experiencing a strong comeback as a structural material, a feat due not only to increasing awareness of sustainability and the environment [18], but also to the architectural possibilities [19] offered through modern computer-numerically-controlled machining.

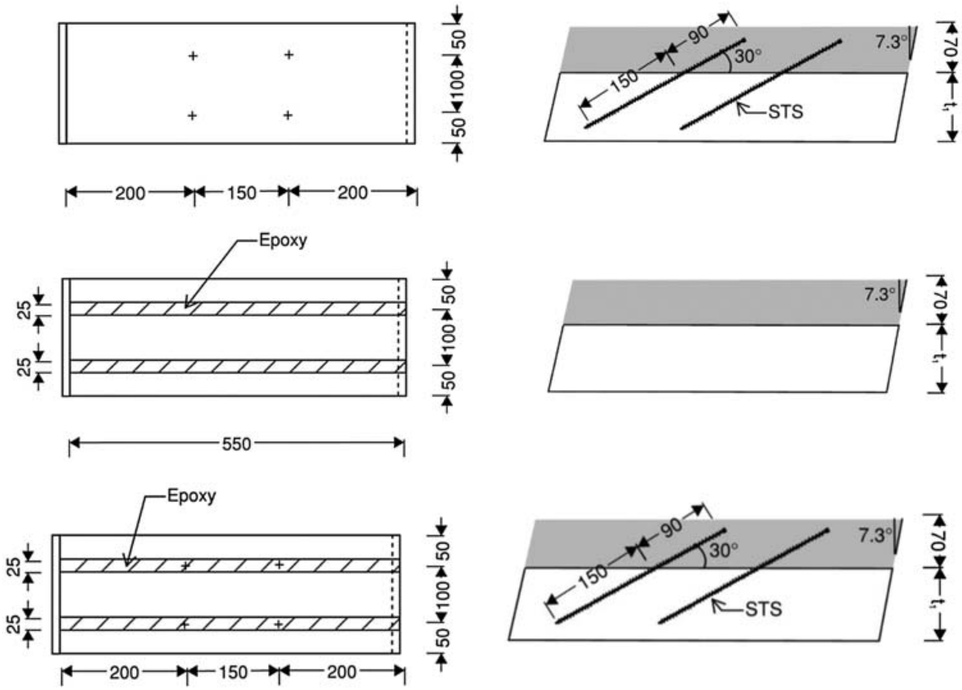

FIG. 10.7 Small-scale specimen layout (dimension in mm): series S (top); series A (middle); and series H (bottom).

TABLE 10.4 Experimental results from the tubular lap shear tests.

Series	Ultimate load ? Std.-Dev. [kN]
A, bonded	83.3 ± 5.9
B, bolted	44.6 ± 3.7
C, combination of A + B	86.4 ± 8.4

Among the novelties related to timber engineering, the use of adhesive bonding as a joining technique is described as one of the most interesting fields of development. The growing interest for adhesive bonding in timber engineering is in great deal due to the fact that traditional mechanical timber joining techniques represent a serious limitation, particularly relevant when timber is used structurally in conjunction with other materials, especially concrete [5,6,20,21], glass [22,23] or steel [24,25].

Timber-concrete-composites (TCC) are structural elements in which a timber component is connected to a concrete layer such to form a composite. The advantageous properties of both materials are exploited and favorable structural and building-physics floor performance is achieved, if compared to timber floors. Usually, the two TCC components are connected with mechanical fasteners where some degree of relative slip cannot be prevented. Alternatively, an almost perfectly rigid connection can be created using adhesives to bond the concrete layer to the timber. The combination of the aforementioned jointing techniques is referred to as hybrid. In this combination, the mechanical fasteners can also be considered as a back-up system for the potentially failing adhesive layer; this fail-safe option provides the incentive designers need to overcome their reluctance toward structural bonding.

In TCC floor design, SLS are often the governing factor. Because of visco-elastic and thermo-hygrometric effects of their constituents, deflections of TCC are dependent upon time (creep), temperature (thermal expansion) and humidity (swelling); which can add up significantly to the elastic ones. The relatively complex behavior of TCC requires special attention from the designer, this is particularly true for adhesively bonded TCC. Tannert et al. [26] investigated the long-term performance of adhesively bonded TCC floor segments (5000 mm long, 490 mm wide and 200 mm deep): after having been loaded for 4.5 years, the segments were tested to failure, resulting in findings that long-term loading caused no significant degradation of the adhesive bond.

4.1 Experimental investigations

As timber products, 89 mm thick LSL and LVL panels were utilized, both readily available flat-plate Engineered Wood Products (EWPs), well suited for one-way span floor applications. The screws used herein were fully threaded Self-tapping screws (STSs) 10 mm × 240 mm ASSY VG provided by MyTiCon Timber Connectors Inc., while Sikadur®32 Hi-Mod was selected as adhesive, a 2K epoxy suitable of bonding wet and cured concrete to timber. All specimens were prefabricated at the Center for Advanced Wood Processing at The University of British Columbia (UBC).

To achieve composite action between timber and concrete, three connector approaches were investigated: (i) mechanical fastening using fully threaded STS, (ii) adhesive bonding; and (iii) hybrid joints combining the adhesive bond with STS. For the third option, the approach taken herein was to provide a bonded connection to meet the SLS stiffness requirements, and to provide a redundant screw connection to meet the ULS strength requirement of the TCC floors.

Six test series were designed: S-1 and S-2 consisting of STS connections tested in LSL and LVL; A-1 and A-2 consisting of adhesive bonds applied in we-wet and we-dry process; H-1 and H-2 consisting of hybrid connections combining STS and adhesive tested in LSL and LVL. Unlike what has been done in previous studies, the adhesive layer was not applied all over the interface, but deliberately limited to relatively narrow strips; more details are provided subsequently. Six replicates per series, thus 36 shear specimens were produced and subsequently tested. The test specimen layouts using the three connector approaches are detailed in Fig. 10.7. All specimens were prefabricated at the Center for Advanced Wood Processing at The University of British Columbia (UBC). The 89 mm thick EWP panels were cut on a Hundegger Robot Drive CNC machine according to the geometry shown in Fig. 10.1.

The shear tests were performed at the UBC Structures Laboratory using a universal testing machine. The geometry according to EN 408 was selected which aligns the loading and reaction surfaces resulting in no rotational moment during loading and eliminates the need for out of plane bracing. The load was applied through a steel bearing plate on the concrete; the specimens were supported by another steel bearing plate beneath the timber as depicted in Fig. 10.8.

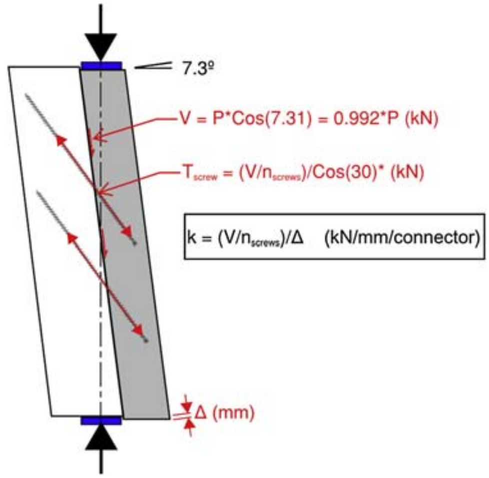

FIG. 10.8 Shear test setup.

4.2 Results

The load-displacement curves in Fig. 10.9 illustrate the individual behavior of all tested shear-test specimens. The relevant strength and stiffness parameters, and their respective variations (CoV), are summarized in Table 10.5. Stiffness was determined at 40 and 100% of the maximum load, corresponding to SLS and ULS load levels, respectively. The two series with STS only (S-1 and S-2) showed very similar behavior, regardless of the EWP considered. The corresponding load-displacement is slightly non-linear from the beginning, and relative displacements of approximately 1 mm are reached when the connection starts to yield. Large displacement capacities are achieved beyond maximum load. All tests with the mechanical fasteners acting alone were stopped after 3 mm relative displacement were reached when the load had dropped to values below 80% of maximum load. The STS connections in LVL (series S-2) reached approximately 10% higher capacity than in series S-1 with LSL (137 kN vs. 123 kN). Variation within each tests series was relatively small, with CoVs of 5% and 6%. All specimens exhibited very similar SLS stiffness with 277 kN/mm, with series S-1 exhibiting larger variability with a CoV of 16% compared to 9% for series S-2. Series S-2 reached their maximum loads at larger deformations, around 1.8 mm compared to the 1.2 mm for series S-1 which resulted in a smaller ultimate stiffness 83 kN/mm versus 113 kN/mm for S-2 with comparable variation (CoVs of 8% and 11%).

In strong contrast, series exhibiting adhesive bonds only (A-1 and A-2) were significantly stiffer with almost no initial slip. They failed at displacements of less than 0.2 mm without any load-carrying capacity after initial failure. The ultimate loads of series A-1 (Wet-Dry) system was significantly higher with 119 kN compared to only 85 kN for series A-2 (Wet-Wet); however, scatter for series A-1 was also higher with 16% versus only 10% for series A-2. Both wet-dry and wet-wet systems, exhibited very high stiffness under service loads, with values of 1340 kN/mm and 1224 kN/mm; variability however was much larger with CoVs of 26% and 33%. Stiffness at failure for both series was still very high with 1009 kN/mm and 867 kN/mm for A-1 and A-2, respectively, but again with large variabilities within the test series with 30% and 24% CoV values.

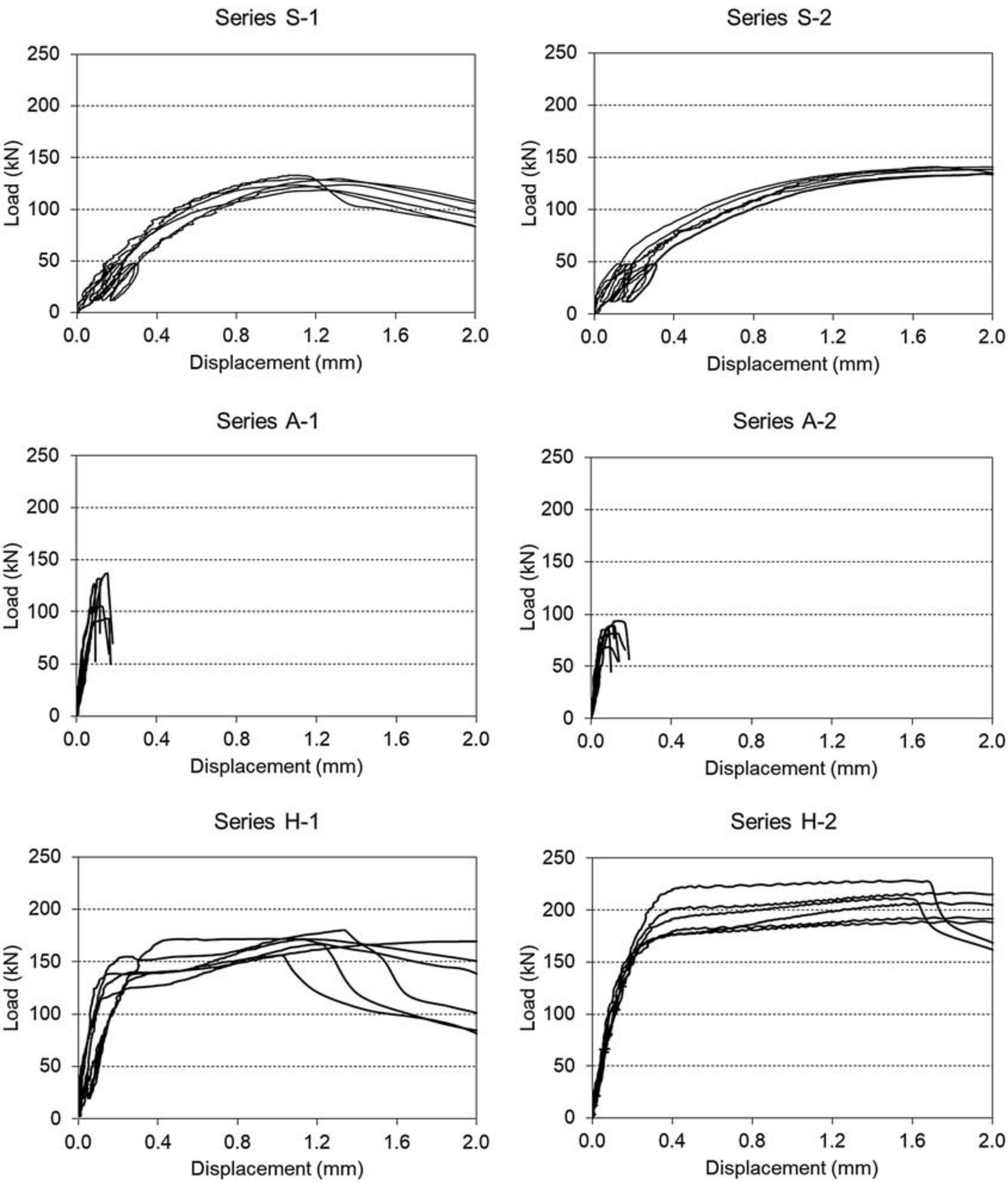

FIG. 10.9 Small-scale shear test load-deformation curves.

TABLE 10.5 Small-scale shear test results (with CoV values in parentheses).

Series	F_{ult} (kN)	k_{SLS} (kN/mm)	k_{ULS} (kN/mm)
S-1	117 (6%)	277 (16%)	113 (8%)
S-2	137 (5%)	275 (9%)	83 (11%)
A-1	119 (16%)	1340 (26%)	1224 (30%)
A-2	85 (10%)	1224 (33%)	867 (24%)
H-1	169 (5%)	1334 (34%)	162 (34%)
H-2	208 (7%)	1159 (27%)	129 (12%)

The hybrid connections combining the screws with the adhesive bond exhibited a truly hybrid load-deformation response. In the first phase, the adhesive bond provided an extremely stiff connection, a phase in which only very small displacement (less than 0.2 mm) were recorded. The stiffness under service loads (SLSs) for both series was as high as those of the adhesively bonded specimens, with 1343 kN/mm and 1159 kN/mm for series H-1 (with LSL) and H-2 (LVL) respectively. Large variability in stiffness within each series was observed with 34% and 27% CoVs. Once the glue line failed, at displacements of approximately 0.2 mm for all hybrid specimens, the screws carried the full shear load, and load capacity was reached at deformation of approximately 1.5 mm relative displacement, similar to what has been observed for series S-1 and S-2. Following the trend observed during the tests with screws alone, hybrid joints with LVL (H-2) reached significantly larger capacities (208 kN) than those in LSL (H-1, 168 kN). Failure loads within each series were associated to low variability with 5% and 7% for series H-1 and H-2, respectively. At failure, (ULS) stiffness was similar to that of the S-series with 162 and 129 kN/mm.

The different failure modes are depicted in the photos of Fig. 10.10. Specimens connected by screws only (series S-1 and S-2) failed in a combination of screw withdrawal and concrete cracking. Adhesively bonded specimens (series A-1 and A-2) failed entirely in the bond line, while the overserved wood fibers on the bond demonstrated proper bond between EWP and concrete. Failures were sudden and brittle. The hybrid specimens (series H-1 and H-2) exhibited mixed failure modes with bond failure, concrete shear failure, and timber shear failure.

4.3 Discussion

The experimental investigations at small-scale level allowed for a direct comparison between the effects of mechanical fastening, adhesively bonding, and the combination thereof, on the mechanical behavior of a complex composite component.

Each of the three considered means of connections exhibited a particular pattern. Load-displacement of the samples with the self-taping screws (S1 and S2) behaved markedly ductile, with large deformations achieved at failure, but also under service loads. Adhesively bonded specimens (A1 and A2) failed, in contrast, in a brittle manner, with deformations

FIG. 10.10 Failed small-scale specimens: screwed (left), adhesive (middle) and hybrid (right).

corresponding to less than 10% of those of the mechanical connected, under service and failure load levels. This situation reflects the dichotomy civil engineers usually encounter: either focusing on ductility at the price of low stiffness, thus penalizing the serviceability of structures; or focusing on strength at the price of brittle failure.

In the hybrid systems (H1 and H2), the screws acted together with the adhesive layer, and failure occurred in distinct phases. Once the glue lines failed, a transition period occurred where the connection slip increased without picking up additional load. This occurred due to the transfer from a very stiff connection (adhesive) to a significantly softer connection (screws). After the screws fully engaged mechanically, they continued to pick up additional load and attained higher ultimate loads than screws on their own. It is posited that some additional load was carried by friction generated between the rough failure surface along the adhesive bond, and the significant clamping component provided by the inclined screws. Accordingly, using the proposed hybrid concept, designers do no longer have to select ductility over stiffness, as both aspects can be covered with one system.

4.4 Conclusions

The work presented the experimental work performed of multi-phase program first with focus on the performance of screwed, adhesively bonded and hybrid TCC configurations. A total of 36 small-scale shear tests were conducted. Based on these tests, the following conclusions were drawn:

- The approach taken in this experimental program was to provide just enough adhesive bond to obtain sufficiently high composite action of the TCC for SLS, and to provide a redundant but less stiff connection of STS, which satisfies the load-resisting requirements at ULS. As a positive side effect, less adhesive is required than if designing for the ULS, and fewer screws are required than if designing for SLS; a higher overall performance is obtained with predictable failure modes.
- Combining mechanical fasteners, herein self-taping screws with adhesive bonding has the potential to combine the requirements for ductile behavior at the level of failure loads (ULS), and stiffness under service loads (SLS). Accordingly, civil engineers are no longer obliged to select ductility against stiffness.
- The hybrid approach provided a fail-safe system for the adhesive bond, as the screws were, at any given moment, able to sustain the design load alone. This feature will ease some of the cones that adhesive bonding is still facing within the community of practitioners.

5. Hybrid mechanical/adhesive joints for the automotive industry

In the automotive industry, mechanical joining is mostly synonymous with clinching, riveting and hamming [28–31]. For clinching and riveting the first step in hybrid joining the two substrates is to apply the liquid adhesive to the joint surface. After the alignment of the metal sheets the mechanical joining process starts. The sheets are fixed in their relative positions from this time and can be further processed. The adhesive is cured during the subsequent oven process.

In hybrid joining [32] processes strong interactions between the two elementary joining steps occur, so that process parameters that have been determined as optimum separately cannot be transferred to the hybrid technology directly. When combining riveting with

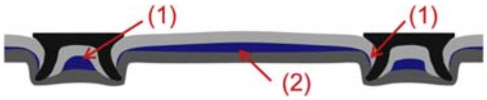

FIG. 10.11 Formation of adhesive pockets (1) in hybrid junctions and (2) between hybrid junctions, see [33].

bonding adhesive pockets may form in the region of the mechanical junctions, and global deformations of the metal blanks between the mechanical joints, cf. Fig. 10.11. Beside experimental studies, numerical descriptions of hybrid joining processes are able to shed additional light on the insights on the influence of several key parameters. Because of the strong interactions between the metals and the adhesives, simulation of hybrid joining processes must integrate liquid adhesives flow and mechanical joining processes in parallel.

The elasto-plastic flow processes of the metal parts and the viscous flow of the adhesive must be calculated simultaneously using a fluid-structure-interaction (FSI) simulation. Specific transfer-procedures couple, for example, a structural domain calculated using structural finite element methods (FEMs) with a fluid domain calculated using computational fluid dynamics (CFDs) by the exchange of boundary conditions at specific corresponding time steps. The reason for coupling of two different software packages in case of FSI is the different nature of solids and fluids. Generally, deformations of solids do not include a change in neighborhood of mass points inside one body; this is effectively solved using the Lagrange approach implemented in most structural FEM codes. The flow of a fluid, in contrast, strongly implies changes of neighborhood inside the material and are better solved using the Eulerian approach. For hybrid bonding, it proved beneficial to use a structural code for the deformation of the solid substrates, and a CFD code for the simulation of the flow of adhesive.

In hybrid bonding processes, hydrostatic pressures [27] inside the adhesive pockets can reach very high values, such to lead to plastic deformations of the metal sheets [34]. The exchange of boundary conditions between the software for the solid metal forming process and the code for simulation of the fluid flow of the liquid adhesive is often limited by questions of numerical stability. Accordingly, very high computational effort, even for a single point hybrid joint, is required [36].

This section focuses on self-pierce-riveting and clinching in combination with adhesive bonding. In the industrial process chain, rivets and clinch-points are set before the adhesive is cured. A FEA reference model is developed for the elementary mechanical joining processes. The model must be expanded with the displacement of the liquid adhesive. Coupled fluid-structure simulations are presented, which include the interaction of the solid matter influenced in the mechanical joining process and the fluid adhesive. In a last step a surrogate model for the multi-point hybrid joint is developed; results of simulations are compared with the results of experiments carried out.

The basis of the simulation of hybrid bonding processes are stand-alone simulations of mechanical joining processes of clinching and self-pierce-riveting [37]. These basic models were extended by the integration of a liquid adhesive layer between the metal sheets. The models must include the measured strength and yield curve of the metals involved on one hand and the rheological flow behavior of adhesive. For the investigations presented herein, three different metals were characterized in Ref. [37]: the two substrates (aluminum AlMg3

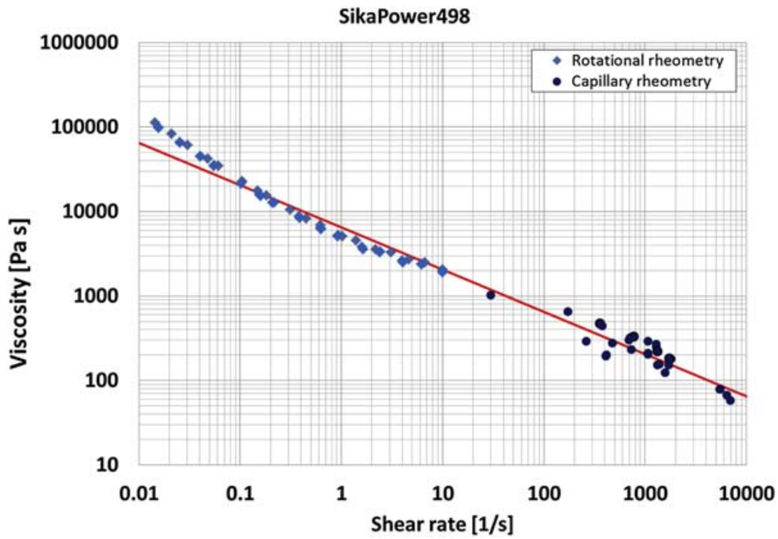

FIG. 10.12 Rheological measurements of a selected adhesive, see [33].

and steel HC340LA). The two substrates exhibited significantly different behavior, and yield strength: $R_{p0.2} = 180$ MPa for the aluminum, resp. $R_{p0.2} = 397$ MPa for the steel. The rivet material exhibited a much higher strength with $R_{p0.2} \approx 1450$ MPa. Rheological measurements performed on the adhesive revealed non-linear visco-elastic flow behavior in general, cf. Fig. 10.12. The adhesive undergoes a strong shear thinning behavior of the adhesive, which was approximated by a straight line, if plotted logarithmically versus viscosity and shear rate.

At first, a reference model for the elementary clinching and the self-pierce-riveting is validated for the simulation. In self-pierce-riveting, the rivet fractures the metal sheet, which has to be taken into account. Concerning the fracture mechanics the processed simulations with the stand-alone reference model for self-pierce-riveting show no strong differences in the final geometry of the mechanical joint and the force-displacement curves using different failure criterions. Computed load-displacement-curves, and the final shape of the hybrid joints, cf. Fig. 10.13, were not very sensitive to the choice of the failure criteria of the metal substrates; thus, the simple ductile model embedded in the standard ABAQUS package.

These simulations greatly help to understand how the adhesive pockets develops in the mechanical joining zone, which forms near the symmetry axis after 0.2 s. For the steel/steel pairing the initial pocket divides into two adhesive pockets with a smaller volume. The aluminum sheet has a lower stiffness, so that it shows higher deformations under the acting forces. As a result, the total amount of the enclosed adhesive at time 0.5 s is higher for the steel/aluminum combination. The punch causes a displacement of the adhesive from the center in radial direction in all material combinations, leading to an accumulation of adhesive in the area of the outer diameter of the punch. At the end of the process, the two distinct pockets of glue in the joint zone are bigger for the pairing aluminum/steel. The riv-bonding process is shown on the right side of Fig. 10.13. After 0.1 s accumulation of adhesive near the axis of symmetry is obvious, while the metal sheets get in contact at position below the rivet shaft. The contact locks the adhesive inside a shrinking center region.

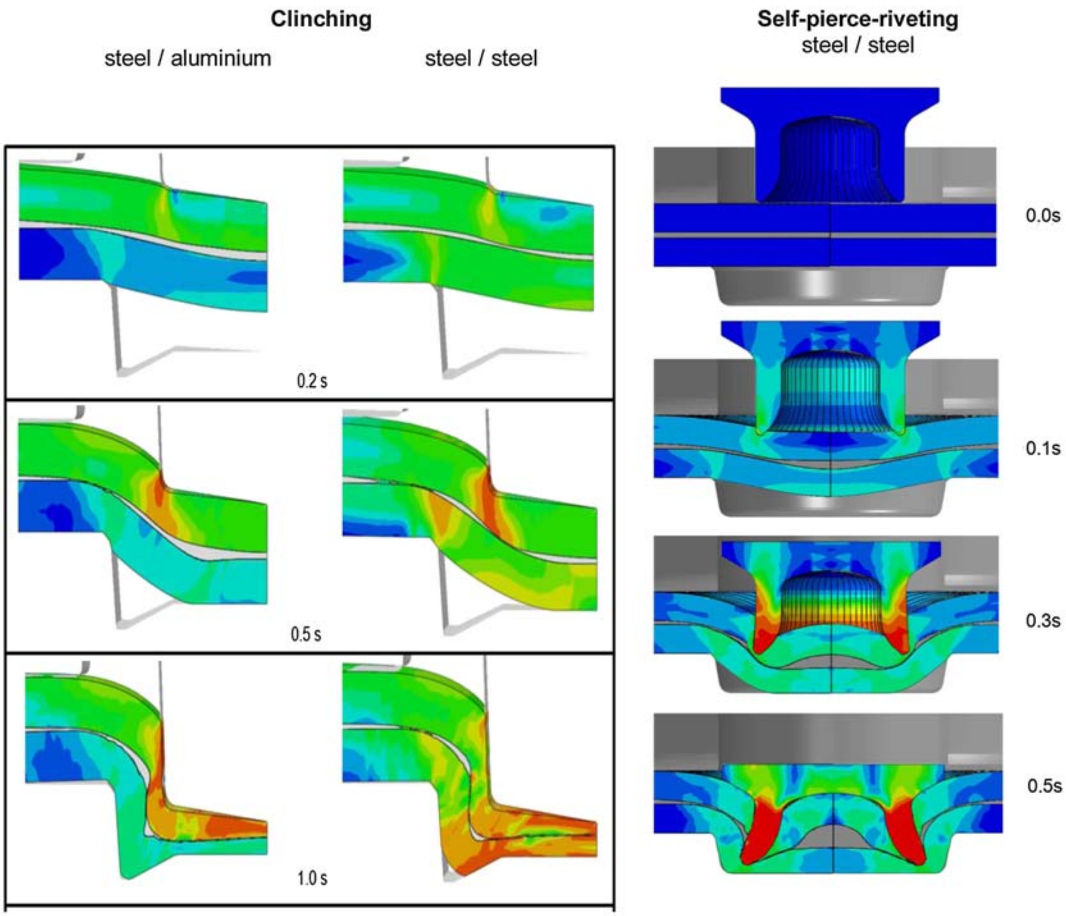

FIG. 10.13 Simulation of the clinch-bonding (left) and the riv-bonding process (right) at different time steps, see [33,37].

The incompressibility of the adhesive and the loss of radial size lead to an increase of the dome height until reaching the final shape of the pockets.

For both simulations, clinch-bonding and riv-bonding, deformation of the metal sheets and the shapes of the adhesive gaps compare well with metallographic sectioning of experimental investigation carried out in parallel. To conclude the simulation method developed here is able to describe the physical processes of single point hybrid bonding correctly, as indicated by Fig. 10.14.

The models described use fully coupled FSI simulation of rotationally symmetric hybrid joining points following correct physics; however, the simulation are computationally very expensive, and therefore limited to $2^1/_2$ D geometries with single point hybrid joints.

Industrial applications usually involve multiple joints embedded in 3D geometries, mostly without symmetries to be exploited. For this purpose, the individual hybrid joining points of a complex part are simplified using simplified surrogate models. The local-to-global

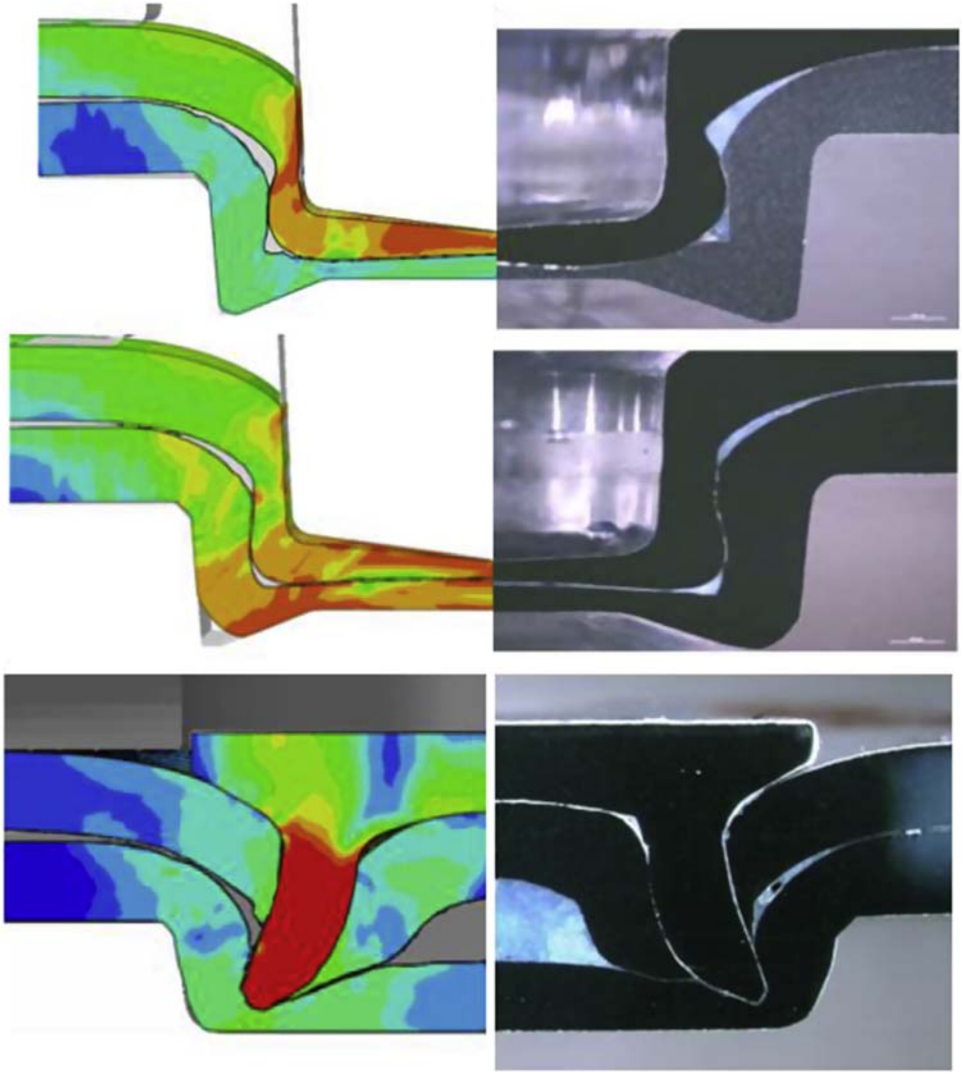

FIG. 10.14 Comparison of the shapes of hybrid bonds; left: numerical simulations, right: metallographic sectioning; top: clinching steel/aluminum; middle: clinching steel/steel; bottom: self-pierce-rivet through steel/steel, see Refs. [33,37].

simulation is divided in a local $2^1/_2$ D model and global 3D model, with a cylindrical connection region located around the jointing point, as illustrated in Fig. 10.15. The local model describes the single hybrid joint using FSI and axial symmetric modeling and the global model describes the flow of adhesive through a 3D structure using imported time dependent boundary conditions derived from the local model [33,35,38].

The simulation connects the local model with the global model using a special type of sub-modeling technique using a python-script, in which the time dependent results of

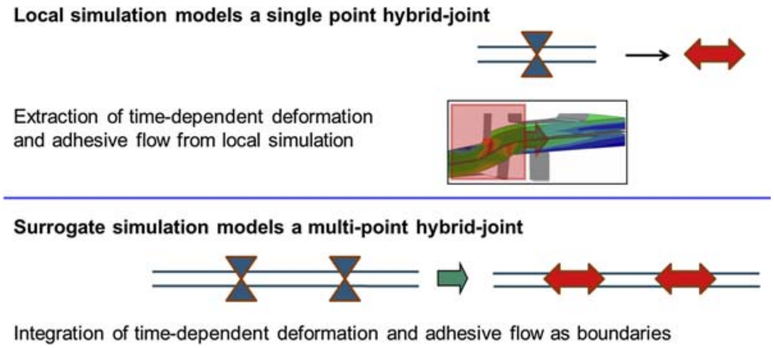

FIG. 10.15 Concept for the simulation of multi-point hybrid joints using a surrogate model for the single point hybrid joint: a $2^1/_2$ D model, situated within a cylindrical boundary just between rivet and blank holder (area marked pink in the figure) generates deflections and flow velocities, a python script extracts this data to be transmitted as boundary conditions to the 3D model (outside the pink area), see Refs. [33,38].

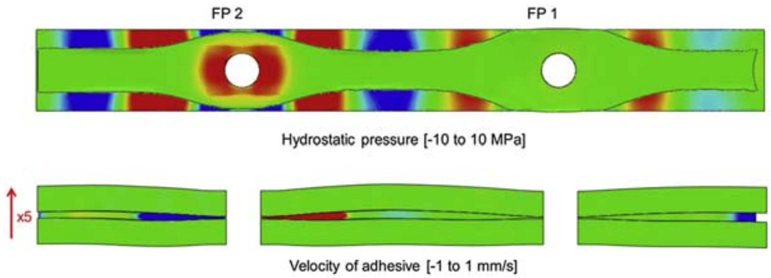

FIG. 10.16 Global 3D model of a two point sample. The first picture shows the distribution of hydrostatic pressure on lower metal sheet and in the adhesive layer viewed from the top. The second picture shows the distribution of the horizontal adhesive velocity in a scaled view from the side (the color scale runs from blue, indicating negative values, to red, indicating positive values; green indicates zero), see Refs. [33,38].

deformation and adhesive flow occurring in the connection region from the local $2^1/_2$ D FSI simulation are extracted and stored in a file. The transformation of data-files to boundaries is automated by a second python-script, which derives the changes in dimension, rotation, translation, time-shift and meshing from the local to the global model. Using the two python-scripts allows to automatically build-up of complex multi-point hybrid joint geometries based upon libraries of materials and adhesive properties, as well as typical hybrid joint elements.

Based on promising validations on small-scale hybrid joints, the method was subsequently used for the simulation of global 3D simulation of samples with two hybrid point joints labeled as JP1 and JP2 illustrated in Fig. 10.16. In a first time step, the rivet at JP1 is set. The second time step corresponds to the setting of the rivet at JP2 resulting in high local hydrostatic pressure gradient in this region; this gradient generates a circular outward wave of adhesive centered on JP2. The merging of the two ebbing waves originating from JP1 and JP2 results in the formation of the central pocket between the two mechanical joints.

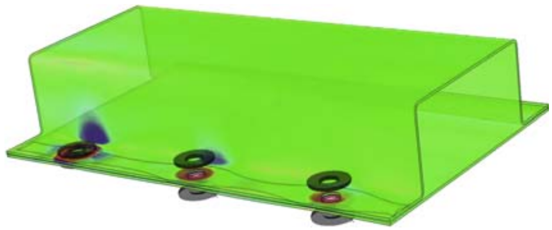

FIG. 10.17 Simulation of a cup profile with three hybrid point joints. The colors show the distribution of hydrostatic stresses [-20 MPa (tension) to +20 MPa (compression)] in the flange. Contour lines show the resulting distribution of adhesive in the flange, see Refs. [33,38].

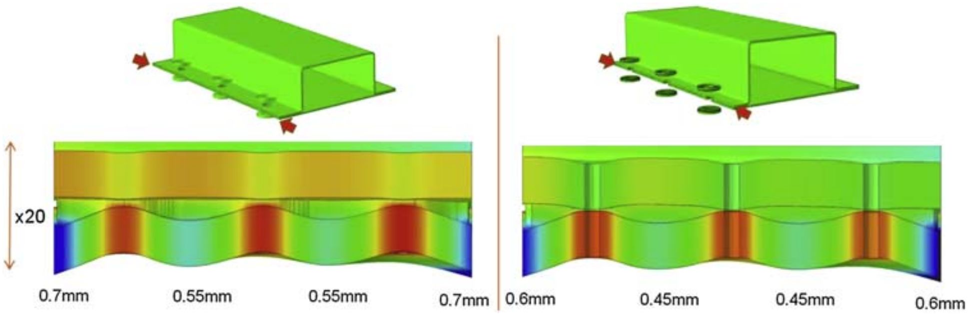

FIG. 10.18 Deformation at the flange of the cup profile at two different cut positions. Colors symbolize the amount of deformation in vertical direction [-0.5 mm–0.05 mm]. The vertical axis is scaled with a factor of 20. Numbers denote the height of the final adhesive gaps, see Refs. [33,38].

Simulations using a surrogate model enable the modeling of much more complex, industry-related, structures without exceeding the capacity of commercially available computer architectures. The validation of the surrogate model at geometrically simple samples sets the basis to describe more complex structures closer to components of automotive body-shells.

A cap profile with three hybrid junction points in the flange is shown in Fig. 10.17 as an example. The adhesive layer in the flange is pressed to its final shape driven by the hydrostatic stresses resulting from the hybrid joining process. The flow of adhesive caused by the mechanical joining process leads to a final deformation of the metal flange of the cup profile. This final deformation is shown for two different positions in Figs. 10.17 and 10.18.

The combined numerical description of the mechanical joining and the adhesive flow helps to understand the hybrid processes and to create solutions for critical joining tasks in industry. Based on the increased process knowledge made possible by the numerical simulations, options for process-optimization of clinch-bonding and riv-bonding processes are derived, leading to a better mechanical performance of the mechanical joint, and reduced pockets of adhesive leading to better surface smoothness. Process can be modified in order to achieve smaller adhesive pockets and bigger undercuts in single point joints. However, the developed simulations for the single point joints are associated with high computational times. Using the developed surrogate model, it is possible dramatically cut CPU time. This allows to study in detail the time-dependent process of much more complex adhesive pocket formation, for example multi-point joining processes. The investigations show that adhesive pockets results as a merging of ebbing waves of adhesive. The worked out techniques can be adapted for industrial use to serve as a tool for further optimization of processes.

6. Welded bond hybrid joints

In industrial applications adhesive bonding is often used in combination with other joining techniques. The reasons for this have already been discussed in the previous chapters:

- There is a need to fix bonded joints in the planned alignment while the adhesive is curing.
- The combination of adhesive bonding and mechanical/thermal joining leads to increased mechanical characteristics of the hybrid joint.
- In addition to improving the mechanical properties, bonding also has a positive effect on the aging properties and media resistance of the hybrid joint.

The elementary resistance spot welding is very often used as a technique for joining metal sheets in the transport sector, in the electrical industry and in electronics production. Different metal combinations can be joined using resistance spot welding. Generally, however, there is the restriction that the joining partner materials must be suitable for welding. Industrial serial processes for the direct resistance spot welding of modern fiber-reinforced plastics with metals are not state-of-the-art. In resistance spot welding [39], energy is supplied to the parts to be welded via electric current. The copper electrodes are positioned above and below the two parts to be joined (see Fig. 10.19). They press the parts to be joined

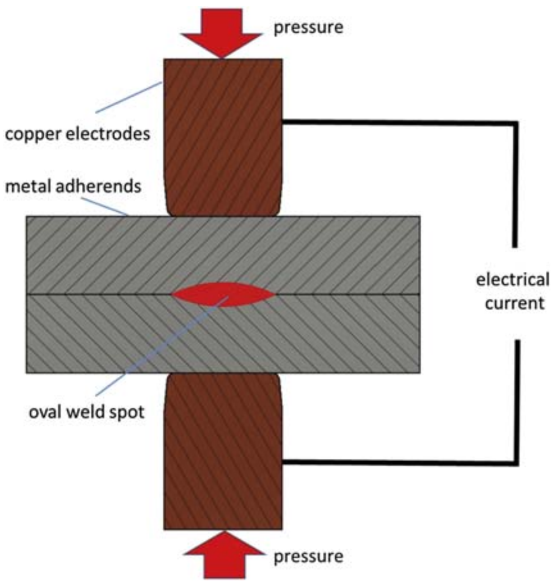

FIG. 10.19 Schematic structure of the resistance spot welding process.

together when the electric current flows. This, however, requires accessibility from both sides of the element. The electric current flowing through the parts to be joined generates locally Joule heat in the joining zone. The joining parts are heated until the required welding temperature is reached. The two adherends are welded at the contact point accompanied by the contact pressure of the electrodes by solidification of the melt, by diffusion or in solid phase. After the material has cooled down, an oval-shaped weld spot is formed between the components [40]. Parameters of the welding process include the welding time, the intensity of the welding current, and the pressing force of the electrodes. The advantages of resistance spot welding are energy efficiency, high potential for automation, and joining without additional aids. The quasi-static tensile and shear strength is often higher than that of mechanical joining connections, although the dynamic strength is often lower.

Spot-weld bonding was already used in aircraft construction in the 50s of the 20th century [42]. In the Soviet Union, the stringers of Antonov and Tupolev airplanes were joined using this technology in various model series. Spot-weld bonding was introduced into automotive engineering later [42]. Test vehicles of the BMW 3 series showed the superiority of the hybrid process over pure welding. An increase in the stiffness of the vehicles of up to 40% could be measured. In addition, acoustic damping properties of the hybrid joining technology in driving operation were observed. In the year 1982 spot-weld bonding was used in series production at BMW for a sunroof frame. A few years later, the process was tested at Volkswagen for use in the Golf 2 cars.

The use of spot-weld bonding in the automotive industry is strongly associated with significant improvements in the formulation of adhesives. The initially selected hard and brittle epoxies, optimized for lap shear strength, could not meet the required properties in crash tests. Under dynamic stress, these adhesives tended to fail unfavorably and abruptly. For this reason, visco-plastic modified adhesives had been developed, and increasingly used for car body construction. With these adhesives, higher energy absorption in crash tests could be achieved. Further developments by adhesive manufacturers focused on improving the adhesion to metals: In the beginning, adhesives in body-in-white were limited to surfaces coated by electrophoretic deposition (EPD). New, often hot-curing adhesives, on the other hand, subsequently enabled bonding on oil contaminated metal sheets. These very high viscosity adhesives are applied in a hot state. They have the ability to absorb small amounts of oil present on the typical automotive metal surfaces. Based on the combination of a simple, inexpensive, fast and mechanically efficient process, spot-weld bonding is now firmly established in automotive industry (Fig. 10.20).

The extension of resistance spot welding to hybrid spot-weld bonding has an extremely positive effect on the mechanical properties of the metal joint. Adhesive bonding supports the quasi-static load capacity of the weld spot [41] and has a positive effect on the dynamic strength of the joint (see Fig. 10.21). The schematic course of a quasi-static force-deformation curve of a spot-welded bonded joint in lap shear test is shown in Fig. 10.20. Here it is assumed that the pure adhesive (blue line) shows almost no ductile behavior. It breaks at high force without plastification. The elementary weld spot (green line) fails at higher strains and lower forces. The spot-weld bond is shown as red line. The breakage of the adhesive of the spot-weld bond occurs at the maximum force at lower strain and the failure of the weld spot at higher strain. The high maximum force and the high maximum deflection of the joint result in a high energy absorption capacity.

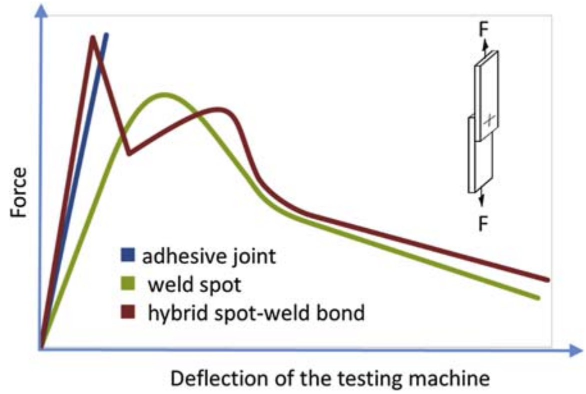

FIG. 10.20 Schematic representation of the force-displacement diagram of the quasi-static test of a resistance spot weld joint.

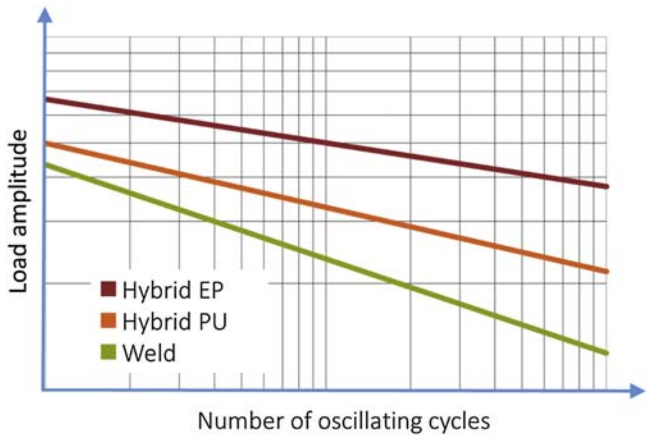

FIG. 10.21 Influence of different classes of adhesives on the fatigue strength of a spot-weld bondings as schematic representation only.

In spot-weld bonding, the adhesive dominates the influence on the dynamic strength of the joint, as shown schematically in Fig. 10.21. A hybrid joint with a high-strength epoxy resin adhesive (Hybrid EP) can carry a higher load amplitude than a joint with a softer polyurethane adhesive (Hybrid PU). The fatigue strength of the elementary welded joint (Weld) reaches significantly lower values compared to the hybrid bonded joints (see Ref. [43]).

For the production of the combined joint, the spot-weldability of the adhesive must be given. The contact pressure of the electrodes partially displaces the fluid adhesive from the joining area before the electric current increases. There is a radial flow of the adhesive from the area of the electrodes, which is dependent on the strength and the time course of the contact pressure. The adhesive is not completely displaced from the joining zone by the contact pressure of the electrodes. When the current is applied, the remaining adhesive is therefore decomposed due to the high temperatures in the area of the welding lens.

A ring of decomposed adhesive also forms around the area of the lens. This area can no longer contribute to the load bearing capacity of the hybrid joint. Occupational health aspects must be taken into account when the adhesive decomposes. But it must be taken into account that gases and vapors also occur during elementary resistance spot welding, especially if the surfaces of the sheets are coated or oiled. The analysis and occupational health assessment of the hazards associated with spot-weld bonding was already discussed in a project carried out in 1995 [44]. When designing the welding parameters for spot-weld bonding, it should be noted that these parameters cannot be adopted from the elementary welding process without further adjustments. The adhesive, which is not displaced by the electrode pressure, forms an additive resistance element in the welding process, which must be taken into account when adjusting the welding current, current time and electrode force.

When comparing the mechanical characteristics of elementary and hybrid processes, the sample shape must always be discussed. In the case of hybrid lap shear test specimens with one weld spot, the adhesive bond can also make a greater contribution to strength than in specimens with the same width and overlap length, but two weld spots, due to the greater proportion of undamaged adhesive bonding area. For the optimization of spot-welded flange connections, the distance between the weld spots must therefore be considered.

A major reason for the frequent use of spot-weld bonding in automotive engineering is the improvement of stiffness compared to elementary welded structures. The fundamental work from Ref. [45] showed that a hat profile joined by hybrid spot-weld bonding with a spot distance of 100 mm is significantly stiffer than a purely spot-welded joint with a spot distance of only 25 mm. On the basis of this finding, it was possible to significantly reduce the number of spot welds of the joined structures by means of further investigations. The source [43] states that the additional bonding of a car body with 4000 weld spots increases the torsional stiffness by about 40%, but halving the number of weld spots of the hybrid joined car body has only a slight effect on the stiffness. The source goes on to explain that hybrid joining increased the stiffness of a new commercial vehicle by about 20% compared to a pure spot-welded structure, and that this advantage of the hybrid process in vehicle life will further increase: the elementary spot-welded structure lost about 20% of its stiffness after one year, compared to only 5% loss with hybrid joining.

7. Concluding remarks

The five examples considered impressively show the advantages in various industries that result from combining mechanical and thermal joining processes with adhesive bonding. However, the examples also show that the joining processes incorporated in the hybrid joint influence each other. The design of the mechanical properties and the planning of the process control of hybrid joining can therefore not be based exclusively on knowledge coming from the elementary joining processes. The special properties of the hybrid joint must be carefully examined. Adhesives play a prominent role in hybrid processes. The selection of the adhesive is not only largely responsible for the maximum forces that can be transmitted, it also has a strong influence on the media resistance, dynamic behavior, stiffness and long-term durability of the structure. From the point of view of adhesive bonding technology, it may be challenging to say, mechanical and thermal processes often have a negative influence on the adhesive layer's ability to transfer loads. Mechanical and thermal joining processes are primarily used for hybrid joints of large series products to fix the components before the adhesive has cured and to reduce the sensitivity to peeling force application. In the future, new approaches will be required to reduce the damaging effects of mechanical and thermal joining processes on the adhesive bond and at the same time to reduce the fixing and resistance to peeling forces.

References

[1] da Silva, F.M. Lucas, A. Pirondi, A. Öchsner (Eds.), Hybrid Adhesive Joints, Springer Berlin Heidelberg, Berlin, Heidelberg, 2011.
[2] B. Bartczak, J. Mucha, T. Trzepieciński, Stress distribution in adhesively-bonded joints and the loading capacity of hybrid joints of car body steels for the automotive industry, International Journal of Adhesion and Adhesives 45 (2013) 42−52, https://doi.org/10.1016/j.ijadhadh.2013.03.012.
[3] N. Chowdhury, W.K. Chiu, J. Wang, et al., Static and fatigue testing thin riveted, bonded and hybrid carbon fiber double lap joints used in aircraft structures, Composite Structures 121 (2015) 315−323, https://doi.org/10.1016/j.compstruct.2014.11.004.
[4] X. He, S. Gao, W. Zhang, Torsional free vibration characteristics of hybrid clinched joints, in: Proceedings 2010 International Conference on Measuring Technology and Mechatronics Automation: Changsha, China, 13-14 March, 2010, IEEE Computer Society Press, Los Alamitos, Calif, 2010, pp. 1027−1030.
[5] A.J. Comer, J.X. Dhôte, W.F. Stanley, et al., Thermo-mechanical fatigue analysis of liquid shim in mechanically fastened hybrid joints for aerospace applications, Composite Structures 94 (7) (2012) 2181−2187, https://doi.org/10.1016/j.compstruct.2012.01.008.
[6] L. Calabrese, G. Galtieri, C. Borsellino, et al., Durability of hybrid clinch-bonded steel/aluminum joints in salt spray environment, International Journal of Advanced Manufacturing Technology 87 (9−12) (2016) 3137−3147, https://doi.org/10.1007/s00170-016-8701-6.
[7] J.T. Mottram, G.J. Turvey, Physical test data for the appraisal of design procedures for bolted joints in pultruded FRP structural shapes and systems, Progress in Structural Engineering and Materials 5 (4) (2003) 195−222, https://doi.org/10.1002/pse.154.
[8] J.T. Mottram, B. Zafari, Pin-bearing strengths for bolted connections in fibre-reinforced polymer structures, Proceedings of the Institution of Civil Engineers - Structures and Buildings 164 (5) (2011) 291−305, https://doi.org/10.1680/stbu.2011.164.5.291.
[9] A.M. Girão Coelho, J.T. Mottram, A review of the behaviour and analysis of bolted connections and joints in pultruded fibre reinforced polymers, Materials & Design 74 (2015) 86−107, https://doi.org/10.1016/j.matdes.2015.02.011.
[10] T. Keller, T. Vallée, Adhesively bonded lap joints from pultruded GFRP profiles. Part I: stress-strain analysis and failure modes, Composites Part B: Engineering 36 (4) (2005) 331−340, https://doi.org/10.1016/j.compositesb.2004.11.001.
[11] T. Keller, T. Vallée, Adhesively bonded lap joints from pultruded GFRP profiles. Part II: joint strength prediction, Composites Part B: Engineering 36 (4) (2005) 341−350, https://doi.org/10.1016/j.compositesb.2004.11.002.
[12] T. Vallée, T. Keller, Adhesively bonded lap joints from pultruded GFRP profiles. Part III: effects of chamfers, Composites Part B: Engineering 37 (4−5) (2006) 328−336, https://doi.org/10.1016/j.compositesb.2005.11.002.
[13] L.J. Hart-Smith, Bonded-bolted composite joints, Journal of Aircraft 22 (11) (1985) 993−1000, https://doi.org/10.2514/3.45237.
[14] T. Vallée, J.R. Correia, T. Keller, Probabilistic strength prediction for double lap joints composed of pultruded GFRP profiles part I: experimental and numerical investigations, Composites Science and Technology 66 (13) (2006) 1903−1914, https://doi.org/10.1016/j.compscitech.2006.04.007.
[15] T. Vallée, J.R. Correia, T. Keller, Probabilistic strength prediction for double lap joints composed of pultruded GFRP profiles − Part II: strength prediction, Composites Science and Technology 66 (13) (2006) 1915−1930, https://doi.org/10.1016/j.compscitech.2006.04.001.

[16] T. Vallée, T. Keller, G. Fourestey, et al., Adhesively bonded joints composed of pultruded adherends: considerations at the upper tail of the material strength statistical distribution, Probabilistic Engineering Mechanics 24 (3) (2009) 358−366, https://doi.org/10.1016/j.probengmech.2008.10.001.
[17] S.W. Tsai, E.M. Wu, A general theory of strength for anisotropic materials, Journal of Composite Materials 5 (1971) 58−80.
[18] M.H. Ramage, H. Burridge, M. Busse-Wicher, et al., The wood from the trees: the use of timber in construction, Renewable and Sustainable Energy Reviews 68 (2017) 333−359, https://doi.org/10.1016/j.rser.2016.09.107.
[19] O. Neumann, J. Hunter, A. Meyboom, et al., Timber shell: wood in building, JEA 3 (2) (2015), https://doi.org/10.15640/jea.v3n2a15.
[20] M. Brunner, M. Romer, M. Schnüriger, Timber-concrete-composite with an adhesive connector (wet on wet process), Materials and Structures 40 (2007) 119−126.
[21] L. Eisenhut, W. Seim, S. Kühlborn, Adhesive-bonded timber-concrete composites − experimental and numerical investigation of hygrothermal effects, Engineering Structures 125 (2016) 167−178, https://doi.org/10.1016/j.engstruct.2016.05.056.
[22] T. Vallée, C. Grunwald, L. Milchert, et al., Design and dimensioning of a complex timber-glass hybrid structure: the IFAM pedestrian bridge, Glass Structure Engineering 1 (1) (2016) 3−18, https://doi.org/10.1007/s40940-016-0007-4.
[23] K. Kreher, J. Natterer, J. Natterer, Timber-glass-composite girders for a hotel in Switzerland, Structural Engineering International 14 (2) (2004) 149−151, https://doi.org/10.2749/101686604777963964.
[24] E. Gonzales, T. Tannert, T. Vallee, The impact of defects on the capacity of timber joints with glued-in rods, International Journal of Adhesion and Adhesives 65 (2016) 33−40, https://doi.org/10.1016/j.ijadhadh.2015.11.002.
[25] T. Vallée, T. Tannert, S. Hehl, Experimental and numerical investigations on full-scale adhesively bonded timber trusses, Materials and Structures/Materiaux et Constructions 44 (10) (2011) 1745−1758, https://doi.org/10.1617/s11527-011-9735-8.
[26] T. Tannert, B. Endacott, M. Brunner, et al., Long-term performance of adhesively bonded timber-concrete composites, International Journal of Adhesion and Adhesives 72 (2017) 51−61, https://doi.org/10.1016/j.ijadhadh.2016.10.005.
[27] P.F. Bariani, S. Bruschi, A. Ghiotti, et al., An approach to modelling the forming process of sheet metal-polymer composites, CIRP Annals 56 (1) (2007) 261−264, https://doi.org/10.1016/j.cirp.2007.05.061.
[28] W. Voelkner, O. Hahn, F. Liebrecht, A. Peetz, Untersuchungen zum Fügen von Feinblechen mittels Durchsetzfügen-Kleben und Stanznieten-Kleben, EFB Forschungsbericht Nr 102 (1997).
[29] M. Peschka, P. Backe, Stanznieten mit Halbhohlniet - Neue Perspektiven beim Fügen hochfester Stahlsorten, Konstruktion 5 (2002).
[30] O. Hahn, T. Draht, V. Thoms, F. Liebrecht, Entwicklung der kombinierten Fügetechnik für Hybridbauweisen am Beispiel Stanznieten-Kleben, Europäische Forschungsgesellschaft für Blechbearbeitung e.V. - Forschungsbericht Nr. 180 (2002).
[31] O. Hahn, T.M. Wibbeke, Optimierung der Fertigungsparameter des Mechanischen Fügens für den Einsatz mit dem Kleben zum Verbinden dünner Bleche, Europäische Forschungsgesellschaft für Blechbearbeitung e.V. - Forschungsbericht Nr. 216 (2004).
[32] L.F.M. da Silva, A. Pirondi, A. Öchsner, Hybrid Adhesive Joints, Springer, Heidelberg, 2011.
[33] H. Fricke, T. Vallée, Numerical modeling of hybrid-bonded joints, The Journal of Adhesion 92 (2016) 652−664.
[34] R. Neugebauer, M. Israel, B. Mayer, H. Fricke, Numerical and experimental studies on the clinch-bonding and riv-bonding process, Key Engineering Materials 504−506 (2012) 771−776.
[35] D. Landgrebe, B. Mayer, S. Niese, H. Fricke, I. Neumann, Adhesive distribution and global deformation between hybrid joints, Key Engineering Materials 651−653 (2015) 1465−1471.
[36] H. Fricke, M. Israel, Unterschiedliche Werkstoffe prozesssicher verbinden-Simulation von Hybridfügeprozessen, Adhäsion Kleben u. Dichten 55 (7/8) (2011) 24−29.
[37] M. Israel, H. Fricke, Qualitätssicherung beim hybridfügen, Europäische Forschungsgesellschaft für Blechbearbeitung e.V. - Forschungsbericht Nr. 330 (2011).
[38] S. Niese, H. Fricke, Taschenbildung und Klebstoffverdrängung zwischen Hybridfügepunkten, Europäische Forschungsgesellschaft für Blechbearbeitung e.V. − Forschungsbericht Nr 424 (2015).
[39] DVS, Widerstandspunktschweißen von Stählen bis 3 mm Einzeldicke - grundlagen, Vorbereitung und Durchführung, DVS-Merkblatt 2902−4 (2001).

[40] G. Habenicht, Widerstandspunktschweißen von hochfesten Stahlblechen im Karosseriebau, TU München, 1987.
[41] F. Eichhorn, O. Hahn, H. Stepanski, Einfluss der Probengeometrie auf die Festigkeit von Widerstandspunktscheiß-Kleb-Verbindungen …, Schweißen und Schneiden 31 (1979).
[42] H. Stepanski, Punktscheißkleben im Automobilbau Teil 1 und Teil 2, Zeitschrift Adhäsion 5/2010, p 30-35 and Zeitschrift Adhäsion 6/2010 p. 35-41.
[43] M. Rasche, Handbuch Klebtechnik, Hanser Verlag, 2012.
[44] W. Hilla, U. Knecht, G. Kötting, G. Lörinci, G. Schmöger, Analyse und arbeitsmedizinische Bewertung der Gefahrstoffe beim Einsatz der Verbindungstechnik Punktschweißen-Kleben, Report BMBF-01 HK 8806 (1995).
[45] O. Gegenbach, Über einige Anwendungen des Metallklebens im Automobilbau, Mitteilungen der Forschungsgesellschaft Blechverarbeitung, 1960.

This page intentionally left blank

Index

'*Note:* Page numbers followed by "f" indicate figures and "t" indicate tables.'

ADVANCED JOINING PROCESSES
Welding, Plastic Deformation, and Adhesion

Edited by Lucas F. M. da Silva, Mohamad S. El-Zein, Paulo Martins

Advanced Joining Processes: Welding, Plastic Deformation, and Adhesion brings together a range of advanced thermal, mechanical, and chemical methods of joining, offering an up-to-date resource for those looking to understand and utilize the very latest techniques.

Efficient joining techniques are critical to a range of innovative applications, with technology in constant development. The first section of the book provides in-depth information on advanced welding techniques, including friction stir, explosive, ultrasonic, laser, electron beam, and computational weld analysis and fatigue of structures. The second section highlights key developments in joining by plastic deformation, adhesive bonding, and hybrid joining. The coverage of each technique is supported by practical guidance, detailed analysis, and finite element simulations.

This is an essential reference for researchers and advanced students in joining, welding, adhesion, materials processing, mechanical engineering, plastics engineering, manufacturing, civil engineering, and automotive/aerospace engineering, as well as engineers, scientists, and R&D professionals, using joining, welding, and adhesion methods, across a range of industries.

Key Features:

- Presents the latest research findings and developments across welding, joining by plastic deformation, and adhesion.
- Includes state-of-the-art methods, such as laser, ultrasonic and electron beam welding, and hybrid joining.
- Offers practical guidance, detailed analysis, and finite element simulations, for all techniques covered.

About the editors:

Lucas F. M. da Silva
Professor of Mechanical Engineering, Faculty of Engineering of the University of Porto

Mohamad S. El-Zein
Manager of Advanced Materials and Mechanics, John Deere

Paulo Martins
Professor of Manufacturing, IDMEC, Instituto Superior Técnico, Universidade de Lisboa, Portugal

ISBN 978-0-12-820787-1

9 780128 207871

ELSEVIER

elsevier.com/books-and-journals